

INFLUENCE OF MACRO-ROUGHNESS OF WALLS ON STEADY AND UNSTEADY FLOW IN A CHANNEL

THÈSE N° 3952 (2007)

PRÉSENTÉE LE 30 NOVEMBRE 2007

À LA FACULTÉ DE L'ENVIRONNEMENT NATUREL, ARCHITECTURAL ET CONSTRUIT

Laboratoire de constructions hydrauliques

SECTION DE GÉNIE CIVIL

ÉCOLE POLYTECHNIQUE FÉDÉRALE DE LAUSANNE

POUR L'OBTENTION DU GRADE DE DOCTEUR ÈS SCIENCES

PAR

Tobias MEILE

Ingénieur civil diplômé EPF
de nationalité suisse et originaire de Fischingen (TG)

acceptée sur proposition du jury:

Prof. L. Laloui, président du jury
Prof. A. Schleiss, directeur de thèse
Prof. W. Hager, rapporteur
Dr M. Jaeggi, rapporteur
Prof. Y. Zech, rapporteur



ÉCOLE POLYTECHNIQUE
FÉDÉRALE DE LAUSANNE

Lausanne, EPFL

2007

*das Wasser rauscht
das Wasser schwoll
ein Fischer sass daran*

...

[Goethe]

Für Erna, Martina und Carole

Abstract

Influence of macro-roughness of walls on steady and unsteady flow in a channel

High-head storage hydropower plants mainly operate their turbines during periods of high energy demand. The sudden starting and stopping of turbines (hydropeaking) lead to highly unsteady flow in channels and rivers. Besides hydropeaking, other anthropogenic actions and natural events such as sluice gate operations, flushing of reservoirs, debris jam and break up, ice jam and break up, sudden stopping and starting of turbines of runoff river hydropower plants, flashfloods or dambreaks can also cause highly unsteady flow.

From an ecological point of view, hydropeaking consists in a non-natural disturbance of the flow regime. Possible mitigation measures aiming to reduce the effect of hydropeaking in a river downstream of the powerhouse can be divided into the installation of detention basins and the improvement of the river morphology. Morphological measures such as macro-roughness at banks might increase the flow resistance as well as the passive retention, which both increase the natural retention capacity of rivers and thus modify the form of the surge wave. In prismatic and nearly prismatic channels, highly unsteady flow conditions can be calculated using the elementary surge wave theory or numerical methods based on the Saint-Venant equations, respectively. For channels with large-scale roughness at the side walls, which may occur by the arrangement of particular morphological measures, no systematic experimental investigations have been done so far on the propagation of surge waves including downstream water-depth and flow velocity.

The aim of this research project was to study how macro-roughness elements at the channel banks influence the unsteady flow conditions due to surge waves. 41 configurations of macro-rough banks and various discharges have been tested in a 40 m long flume with a bed slope of 1.14‰. A special experimental setup has been designed which is able to generate surge waves characterized by different discharge ratios. The first step of the experimental investigations focused on the determination of the flow resistance under steady flow conditions caused by large scale roughness elements at the channel banks, namely rectangular cavities (depressions). In a second step, positive and negative surge waves induced at the channel entrance have been tested in the same geometries. Five different discharge scenarios have been considered for each geometry. For comparison, experiments have also been performed in a prismatic reference channel without macro-roughness elements at the banks.

The analysis of the experiments for steady flow conditions results in the following conclusions:

- The total head-loss is governed by different phenomena such as vertical mixing layers, wake-zones, recirculation gyres, coherent structures and skin friction.

- The flow resistance is significantly increased in the macro-rough configurations due to the disturbance of the bank geometry.
- Three different approaches have been considered in order to relate the additional, macro-rough flow resistance f_{MR} to the forms of the banks by empirical formulas. The first approach is based on a powerlaw optimization, the second one on a model based on form drag and the third one uses the Evolutionary Polynomial Regression method. By separating the observed flow conditions in a square grooved, a reattachment and a normal recirculating flow type, the developed macro-rough flow resistance formulas are in good agreement with the laboratory experiments. Formulas of the second approach are suggested for practical applications in river engineering.
- Water body oscillations in cavities have been observed in axi-symmetric macro-rough configurations. They lead to water-surface oscillations and transverse velocity components. Peaking excitations with heavy oscillations occur for Strouhal numbers values at 0.42 and at 0.84.

The analysis of the experiments with unsteady flow, namely surge waves, shows:

- The elementary surge wave theory for the prismatic reference configuration including secondary waves and wave breaking could be verified in the laboratory flume.
- The absolute surge wave celerity V_w and the celerity c are lower for the macro-rough configurations. The decrease of the absolute surge wave celerity V_w is mainly due to the increased flow resistance and lies between 5% and 25% for both, positive and negative waves coming from upstream.
- Due to the dispersive character, the positive and negative surges from upstream are characterized by a sudden change (front), followed by a progressive change (body) of the water level. The sudden change can be clearly distinguished from the progressive change in the prismatic channel. In the channel with macro rough banks the separation is often hardly visible. The front height decreases between 5% to 25% along the laboratory flume for the prismatic configuration. In the macro-rough channel, the decrease can reach 70%. Behind the wave front of a positive surge, the water level continuously rising to a level which is higher than in the prismatic channel due to the channel bank macro-roughness.
- The decrease of the height of the surge wave front along the channel could be approached fairly good with an empirical relationship applicable for prismatic and macro-rough configurations.

Numerical simulations based on the boundary conditions of the experiments have been done for steady flow tests (2-D simulations). They reveal that the integration of the turbulent stresses is required for the reproduction of the steady flow tests. Test cases with unsteady flow (1-D simulations) show that surge waves in rivers can be computed by integrating the macro-rough flow resistance in the source terms as well as by a modification of the continuity equation taking into account the passive retention.

Keywords: Unsteady flow, steady flow, laboratory tests, macro-roughness, flow resistance, surge wave attenuation and deformation, hydropeaking, river morphology, cavities.

Resumé

Influence de la macro-rugosité des rives sur l'écoulement permanent et fortement non permanent

Les aménagements hydroélectriques à haute chute turbinent les eaux en fonction de la demande en énergie. Le démarrage et l'arrêt rapide des installations provoque des conditions d'écoulement non-permanent et relativement rapidement varié dans les canaux et rivières. D'autres actions anthropogènes et des évènements naturels comme les opérations de vannes, les purges, les ruptures d'embâcles, l'enclenchement et l'arrêt des turbines des aménagements hydroélectriques à basse chute, les crues éclair ou les ruptures de barrage entraînent également des changements rapides de débit sous forme d'intumescences ou ondes de translation.

Du point de vue environnemental, le marnage consiste en une perturbation non naturelle et fréquente du régime d'écoulement. Des interventions pour réduire cet effet en aval des centrales hydroélectriques consistent en l'installation de bassins de rétention et en l'aménagement morphologique du cours d'eau. Certaines mesures morphologiques peuvent augmenter la résistance à l'écoulement et la rétention sur le cours d'eau. Dans des canaux prismatiques et quasi-prismatiques, les écoulements non-permanents et rapidement variés peuvent être calculés par la théorie des intumescences ou à l'aide de méthodes numériques basées sur les équations de Saint-Venant. L'influence des rives contenant des éléments de rugosité de taille importante sur écoulement non-permanent et rapidement varié dans les canaux n'a pas été systématiquement étudiée jusqu'à présent.

Le but du projet de recherche est d'investiguer de quelle manière la macro-rugosité des rives peut influencer les écoulements non permanents. Des essais expérimentaux ont été effectués dans un canal de 40 m de longueur et de 1.14‰ de pente avec 41 configurations géométriques différentes. L'installation expérimentale a été conçue pour générer des intumescences avec des rapports de débit très variables. La première étape, conduite avec différents débits permanents, a permis de caractériser la résistance à l'écoulement de la macro-rugosité des rives, notamment des cavités de forme rectangulaire. Dans la deuxième étape expérimentale, les intumescences positive et négative d'amont ont été étudiées. Au minimum cinq scénarios de débits ont été considérés pour chaque géométrie macro-rugueuse. La configuration à rives rectilignes a servi de référence.

L'analyse des essais en débit permanent avec des rives macro-rugueuses conduit aux conclusions suivantes:

- Les pertes de charge totales le long du canal macro-rugueux sont influencées par des phénomènes divers comme les zones de cisaillement verticales, les zones de sillages, les cellules de recirculation, les structures cohérentes et le frottement de parois.
- La résistance à l'écoulement est significativement augmentée dans les configurations à rives macro-rugueuses. La résistance augmente généralement avec la densité des éléments de rugosité.

- Trois approches ont été considérées pour lier la perte de charge imputable aux macro-rugosité aux caractéristiques des configurations et de l'écoulement. La première approche se base sur l'optimisation d'une loi de puissance, la deuxième sur un modèle considérant les forces hydrodynamiques de traînée et la troisième sur la régression polynomiale évolutive. Les formules empiriques trouvées montrent de bonnes performances dans la reproduction des essais en laboratoire. Une séparation des essais en différents types d'écoulement («square grooved», «reattachment» et «normal circulating») est nécessaire. Des formules de la deuxième approche sont proposées pour des applications liées à la macro-rugosité des rives.
- Des oscillations du plan d'eau dans les cavités ont été observées systématiquement dans les configurations avec des éléments de macro-rugosité axisymétrique. Elles sont combinées avec des vitesses d'écoulement transversales. Des amplitudes maximales sont observées pour des nombres de Strouhal de 0.42 et 0.84.

L'analyse des essais des intumescences positive et négative de l'amont montre que:

- La théorie élémentaire des intumescences s'applique aux essais en canal prismatique en ce qui concerne la vitesse de propagation du front, l'atténuation du front, les ondes secondaires et le déferlement du front.
- Dans les configurations macro-rugueuses, la vitesse de propagation absolue V_w et la célérité c de l'intumescence sont réduites par rapport à la configuration prismatique. Cette réduction est due entre autres à la rugosité additionnelle et se situe entre 5% et 25%, aussi bien pour l'intumescence positive que négative d'amont.
- Les intumescences sont caractérisées par une augmentation rapide du niveau d'eau (front) suivie d'une augmentation progressive du niveau d'eau (corps). Ce comportement est dû au caractère diffusif de l'intumescence. La séparation entre l'augmentation rapide et progressive est bien visible dans le cas prismatique mais peut devenir quasi invisible dans les configurations macro-rugueuses. La réduction de la hauteur du front le long du canal prismatique est de 5% à 25% et peut atteindre 70% dans le cas du canal macro-rugueux. Derrière le front d'une onde positive d'amont, le plan d'eau continue de monter. Due à l'effet de la macro-rugosité le niveau final atteint est plus haut que dans le canal prismatique.
- La réduction de la hauteur du front est exponentielle et elle peut être estimée en utilisant un modèle simple basé sur des coefficients de réduction de la hauteur du front prismatique et macro-rugueux.

La reproduction de certains essais à débit stationnaire par des simulations numériques 2 - D a mis en évidence la nécessité d'inclure un modèle de turbulence qui tient compte des contraintes de cisaillement. Des simulations numériques 1 - D, effectuées pour quelques cas tests ont permis de conclure que les intumescences expérimentales, mêmes celles à fronts raides, peuvent être raisonnablement simulées par la prise en compte d'un frottement macro-rugueux dans les termes source et par la modification de l'équation de continuité afin de tenir compte de la rétention passive supplémentaire.

Mots clés: Ecoulement permanent et non-permanent, essais hydrauliques, macro-rugosité, résistance à l'écoulement, déformation d'intumescences, marnage, morphologie, cavités.

Zusammenfassung

Einfluss von grossmassstäblichen Uferrauheiten auf stationäre und stark instationäre Gerinneabflüsse

Zur Deckung der täglich auftretenden Verbrauchsspitzen an elektrischer Energie turbinieren die Speicherkraftwerke das Wasser der Stauseen gemäss Nachfrage ab. Dies führt in den betroffenen Gewässern zu instationären Abflussbedingungen, auch Schwall und Sunk genannt. Stark instationäre Abflussbedingungen haben nebst dem Betrieb von Speicherkraftwerken vor allem auch andere, natürliche oder anthropogene Ursachen wie den Betrieb von Schleusen und Schiebern, die Spülung von Staubecken, einen Eisstau und -ausbruch, einen Schuttstau und -ausbruch, das rasche Stoppen und Starten von Turbinen von Laufwasserkraftwerken, Sturzfluten oder Damnbrüche.

In alpinen und voralpinen Fliessgewässern stellen tägliche auftretende Abfluss- und Wasserspiegelschwankungen aus gewässerökologischer Sicht insbesondere während der Wintermonate eine Störung des natürlichen Abflussregimes dar. Mögliche Massnahmen zur Verminderung der Auswirkungen von Schwall und Sunk unterhalb der Kraftwerkszentralen umfassen den Bau von Rückhaltebecken oder die Verbesserung der Gewässermorphologie. Flussbauliche Massnahmen wie die untersuchten, grossmassstäbliche Uferrauheiten (GMR) können den Fliesswiderstand und die passive Retention vergrössern. Sie beeinflussen die Rückhaltekapazität des Fliessgewässers und dadurch die Form der sich im Gewässer fortpflanzenden Wellen. In praktisch prismatischen Gerinnen können stark instationäre Abflussvorgänge mit Hilfe der Basistheorie von Schwall- und Sunkwellen berechnet werden oder im numerischen Modell basierend auf den Saint-Venant Gleichungen, falls die Wellen über grössere Strecken ablaufen und die Reibung und Sohlenneigung bedeutend ist. Für Gerinne mit GMR, wie sie möglicherweise durch die Anordnung von bestimmten morphologischen Strukturen entstehen gibt es keine systematischen, experimentellen Untersuchungen.

Ziel des Forschungsprojektes war herauszufinden, wie GMR sich auf Schwall- und Sunkwellen auswirken. Insgesamt 41 Geometrien von GMR wurden für verschiedene Abflussszenarien im Experiment untersucht. Vorgängig wurde eine Versuchseinrichtung entwickelt, welche erlaubt, Schwallwellen unter kontrollierten Bedingungen zu erzeugen. In einem ersten Schritt wurde dann der Fliesswiderstand der GMR in Form von Buchten bestimmt. In einem zweiten Schritt wurden für jeweils fünf verschiedene Abflussszenarien in den selben Geometrien Schwall- und Sunkwellen am Beginn des Gerinnes erzeugt. Versuche in einem prismatischen Kanal ohne GMR dienen als Referenz.

Folgende Punkte gehen aus der Auswertung der Versuche mit stationären Abflüssen hervor:

- Die Gesamtenergiedissipation entlang der Rinne mit GMR ist bestimmt durch verschiedene Phänomene wie vertikale Mischschichten, Wirbelzonen, Rezirkulationszellen und Wandreibung.

- Infolge der Störung der Ufer durch GMR ist der Fliesswiderstand deutlich erhöht.
- Drei verschiedene Ansätze wurden zur Bestimmung von empirischen Formeln für den Reibungsbeiwert verursacht durch GMR verwendet. Der Erste beruht auf der Optimierung eines Potenzgesetzes, der Zweite auf einem Modell welches das Kräftegleichgewicht mittels eines Widerstandsbeiwertes berücksichtigt und der Dritte auf der Methode der Evolutiven Polynomialen Regression. Durch die Unterscheidung in verschiedene Fliesstypen („Wiederanlegende Buchtenströmung“, „Langgezogene Rotationsströmung“, „Kreisförmige Rotationsströmung“) kann der Reibungsbeiwert der GMR berechnet werden. Formeln des zweiten Ansatzes werden zur Berechnung des Fliesswiderstandes durch GMR für Anwendungen im Flussbau vorgeschlagen.
- In gewissen Geometrien und für bestimmte hydraulische Bedingungen sind periodische Schwankungen des Wasserspiegels in den Buchten zu beobachten. Diese sind für Werte der Strouhal Zahl von 0.42 und 0.84 besonders ausgeprägt.

Die Auswertung der Versuche mit instationären Abflüssen zeigte:

- Im prismatischen Laborkanal ist die Basistheorie für Schwallwellen inklusive dem Brechen der Wellenfront und dem Auftreten von Sekundärwellen anwendbar.
- Die absolute (V_w) und relative (c) Fortbreitungsgeschwindigkeit der Front der Schwall- respektive Sunkwelle ist in der Rinne mit Uferformrauheiten reduziert. Die Verminderung beträgt rund 5% bis 25% und ist nebst anderen Ursachen auf die erhöhte Reibung zurückzuführen.
- Aufgrund des dispersiven Charakters sind die im Laborkanal erzeugten Schwall- und Sunkwellen gekennzeichnet durch einen plötzlichen Anstieg des Wasserspiegels (Front) gefolgt von einem allmählichen Anstieg des Wasserspiegels. Im prismatischen Kanal ist der plötzliche vom allmählichen Anstieg deutlich zu unterscheiden während der Unterschied in der Rinne mit Uferformrauheiten zunehmend verschwindet. Die Höhe der Wellenfront vermindert sich um 5% bis 25% entlang dem prismatischen Laborkanal. Mit Uferformrauheiten beträgt die Reduktion der Höhe der Wellenfront bis zu 70%. Der weitere Anstieg des Wasserspiegels hinter der Wellenfront führt jedoch mit GMR zu einem Wasserspiegel der im Vergleich zum prismatischen Kanal erhöht ist.
- Die Abnahme der Höhe der Wellenfront entlang dem prismatischen Kanal und entlang der Rinne mit GMR kann mit einer einfachen empirischen Formel beschrieben werden.

Zwei dimensionale numerische Berechnungen der Versuche mit stationärem Abfluss haben gezeigt, dass zusätzlich zur Wandreibung auch Turbulenzterme eingezogen werden müssen. In eindimensionale Berechnungen konnten mehrere Schwallwellen unter Berücksichtigung des Reibungsbeiwertes der grossmasstäblichen Uferrauheiten im Quellterm der dynamischen Gleichung sowie durch die Anpassung der Kontinuitätsgleichung zum Erfassen der passiven Retention nachgerechnet werden.

Stichworte: Stationärer und instationärer Gerinneabfluss, Experimente, grossmasstäbliche Rauheiten, Fliesswiderstand, Verformung von Wellen, Buchten, negative Rauheit, Schwall/Sunk, Flussmorphologie.

Table of content

<i>Summary</i>	<i>i</i>
<i>Résumé</i>	<i>iii</i>
<i>Zusammenfassung</i>	<i>iv</i>
1 INTRODUCTION	1
2 LITERATURE REVIEW & THEORETICAL BASES	7
2.1 <i>Flow resistance in steady open channel flow</i>	7
2.1.1 Introduction	7
2.1.2 Laminar flow and transition to turbulent flow	8
2.1.3 Turbulent flow	9
2.1.4 Flow in composite and compound channel sections	19
2.1.5 Macro-rough flow	22
2.2 <i>Flow in presence of rectangular cavities - effects of cavities</i>	38
2.2.1 Introduction	38
2.2.2 Cavity flow	39
2.2.3 Groyne fields and embayments	41
2.2.4 Harbours	42
2.3 <i>Unsteady open channel flow</i>	44
2.3.1 Classification of flow types	44
2.3.2 Mathematical formulation and resolution of unsteady non-uniform flow	47
2.3.3 Rapidly varied unsteady and non-uniform flow	50
2.4 <i>Conclusions</i>	76
3 EXPERIMENTAL SETUP & TEST PROGRAM	79
3.1 <i>Test flume</i>	79
3.2 <i>Upstream boundary: Inlet basin</i>	81
3.3 <i>Downstream boundary: Outlet cross section</i>	82
3.4 <i>Macro-roughness configurations</i>	85
3.5 <i>Device for generating positive and negative surge waves</i>	89
3.5.1 Description of the setup for surge wave generation	89
3.5.2 Mathematical model of the surge wave generating setup	90
3.5.3 Model calibration and surge wave discharges	91

3.5.4	Example	94
3.6	<i>Measurement equipment and data acquisition</i>	95
3.6.1	Discharge measurement	95
3.6.2	Water level measurement and recording	96
3.6.3	Velocity measurement	96
3.7	<i>Test procedures</i>	97
3.7.1	Steady flow test procedure	97
3.7.2	Unsteady flow test procedure	98
4	STEADY FLOW EXPERIMENTS	101
4.1	<i>Analysis of leveling and velocity measurements of the steady flow experiments for the macro-rough configurations</i>	101
4.1.1	Classification of the flow based on the geometry and the relative flow depth	101
4.1.2	Characterization of the flow in the widened reach – coherent structures	103
4.1.3	Time-averaged level measurements	105
4.1.4	Time-dependent level measurements	108
4.1.5	Velocity measurements	110
4.1.6	Conclusions of observations in macro-rough configurations	117
4.2	<i>Transverse oscillations of the flow in a macro-rough channel</i>	118
4.2.1	Occurrence of transverse oscillations of the flow	118
4.2.2	Theoretical assessment of transverse oscillations	119
4.2.3	Results of the analysis of the cavity oscillation	124
4.2.4	Conclusions on transverse flow oscillations	131
4.3	<i>Backwater curve computation and resistance quantification</i>	133
4.3.1	Introduction	133
4.3.2	Method applied for the backwater curve computation	134
4.3.3	Equivalent sand roughness of the wall including the macro-roughness $k_{s,w}$	137
4.3.4	Overall and wall friction coefficients f_m and f_w	137
4.3.5	Chezy C and Strickler coefficients K_{st}	141
4.3.6	Discussion of the obtained roughness parameters considering the macro-roughness of the channel banks	145
4.4	<i>Proposition of empirical formulas for the estimation of the flow resistance of the macro-rough banks</i>	148
4.4.1	Empirical flow resistance formulas based on a Powerlaw optimization	148
4.4.2	Semi-empirical flow resistance formulas based on form drag and skin friction	154
4.4.3	Development of empirical formulas with Evolutionary Polynomial Regression	160
4.4.4	Application of the developed empirical and semi-empirical flow resistance formulas for channels with macro-rough banks	166

4.4.5	Backwater curve computation using single head- and skin friction-losses	171
4.5	<i>Summary and conclusions for the steady flow experiments</i>	176
5	UNSTEADY FLOW EXPERIMENTS	179
5.1	<i>Tested scenarios</i>	179
5.2	<i>Classification of the tested waves</i>	180
5.3	<i>Flow conditions for positive and negative surge waves</i>	183
5.3.1	Tests with positive waves in the prismatic configuration	183
5.3.2	Tests with negative waves in the prismatic configuration	185
5.3.3	Tests with positive and negative waves in the macro-rough configurations	187
5.3.4	Dye tests and velocity profiles during the surge waves	189
5.4	<i>Shape of the wave front and secondary waves</i>	193
5.4.1	Detection and measurement methods	193
5.4.2	Observations of the wave front shape and secondary waves in the prismatic configuration	193
5.4.3	Observations of the wave front shape and secondary waves in the macro-rough configurations	195
5.4.4	Comparison of the present with other experiments	196
5.4.5	Conclusions for the shape of the wave front and secondary waves	198
5.5	<i>Unsteady flow data analysis</i>	199
5.6	<i>Characteristic values of positive and negative surge waves from upstream</i>	204
5.6.1	Decrease of the observed absolute wave celerity	204
5.6.2	Attenuation of the wave front height	207
5.6.3	Reasons for the reduction of the absolute wave celerity	209
5.6.4	Distinction of the effects influencing the absolute wave celerity V_w	211
5.6.5	Mathematical description of the attenuation of the wave front height	217
5.6.6	Discharge estimation directly behind the wave front at the end of the macro-rough channel reach	225
5.6.7	Empirical relationships for the surge wave celerity and the attenuation of the surge wave front height obtained by the EPR-method	228
5.7	<i>Conclusions for surge wave experiments in the prismatic and macro-rough configurations</i>	231
6	NUMERICAL SIMULATIONS	235
6.1	<i>2D-simulations of the steady flow experiments</i>	235
6.1.1	Introduction	235
6.1.2	Simulations and results	236
6.1.3	Conclusions for the 2D-steady flow simulations	239

6.2	<i>1D-simulations of the unsteady flow experiments</i>	240
6.2.1	Objectives	240
6.2.2	Theoretical background and model description	240
6.2.3	Simulations and results	241
6.2.4	Conclusions for the 1D-unsteady flow simulations	249
7	SUMMARY, CONCLUSIONS AND OUTLOOK	251
7.1	<i>Summary and conclusions</i>	251
7.2	<i>Outlook</i>	255
7.3	<i>Recommendations for practical engineers</i>	256
	<i>Notations</i>	259
	<i>References</i>	R.1
	<i>Acknowledgement</i>	R.11
	APPENDICES	A.1

1 INTRODUCTION

High-head storage hydropower plants contribute significantly to the electricity production in alpine countries such as Switzerland, where about 60% of the demand is assured by hydropower (Schleiss, 2002, 2007). Reservoirs at high altitudes can store the water of rainfall, snow melt and glacier melt, collecting it in wet and warm periods in summer for its use in winter. The high-head hydropower plants mainly operate their turbines during periods of high energy demand. This kind of operation, called hydropeaking, influences the flow regime of the river downstream of the restitution of the powerhouses. For the problematic of hydropeaking the environmental issues, hydraulic concerns and energetic and economical issues have to be considered.

Environmental effects of hydropeaking

Besides water quality and river morphology, hydropeaking influences on almost all living organisms depending on the river eco-system (Pellaud, 2007). The negative effects have been known for a long time (Vibert, 1939) namely on benthic macro-invertebrates, fishes, periphyton and mosses, aquatic macrophytes and riverbank vegetation. Literature surveys (Baumann and Klaus, 2003; Pellaud, 2007) confirm the stranding of macro-invertebrates due to rapid water level fall or an increase of catastrophic drift during sudden increases in discharge, water levels and flow velocities. Furthermore, the biomass and the richness of species are diminished. Moreover, the composition of the community of macro-invertebrates is altered. A decrease of the biomass and a change of abundance and composition of adult fishes have been reported in different studies (Pellaud, 2007). Juvenile fishes are endangered by drift and stranding and the natural reproduction of fishes is disturbed or even completely hindered (Baumann and Klaus, 2003). Stranding experiments with juvenile brown trout for example (Halleraker et al., 2003) reveal a relationship between habitat quality, fish size, season, ramping rates and habituation to stranding rates. Despite an increasing knowledge of the interactions between hydropeaking and ecology, it is currently still difficult to predict and quantify the biotic responses to hydropeaking. This can be explained by the fact that rivers are often also affected by poor morphology and limited water quality. Furthermore, the impact of hydropeaking strongly depends on the river morphology (Baumann and Meile 2004, Ferrari 2007).

Hydraulic effects of hydropeaking

In a river cross section, hydropeaking is characterized by a frequent change between minimum and maximum flow levels. The amplitude of the variation depends on the maximum and minimum discharge as well as on the river morphology which is including the cross-sectional shape and backwater effects. In a river reach, hydropeaking creates a surge wave propagating downstream. In complex systems

consisting of several storage hydropower plants and tributaries, the unsteady flow conditions resulting from hydropeaking are characterized by the propagation, attenuation and superposition of several positive and negative waves. Propagation and attenuation of the waves are influenced by the channel slope and roughness (Favre 1935) as well as the river morphology (passive retention, Stranner 1996). The duration of the hydropeaking impulse is an additional parameter influencing the flow conditions. It is defined as the duration of the turbine operation. For long duration of impulses and channelized rivers, hydropeaking can be considered as the transition between two steady flow conditions. For shorter impulses and under complex conditions, hydropeaking produces increasingly dynamic effects. Beside the operation of storage hydropower plants, unsteady open channel flow conditions can also result from other anthropogenic activities or natural events (Table 1-1).

Table 1-1: Unsteady flow conditions in open channels caused by anthropogenic activities and natural events.

Occurrence	Anthropogenic	Natural
Often	<ul style="list-style-type: none"> ▪ Hydropeaking due to hydropower storage plants (surge waves) ▪ Surge wave produced by the operation of navigation locks ▪ Flushing of alpine water intakes 	<ul style="list-style-type: none"> ▪ Daily flow cycles in snow and glacier covered river basins ▪ Tidal effects in estuaries ▪ Floods (heavy rainfall, frequency depends on climate)
Rare	<ul style="list-style-type: none"> ▪ Surge waves due to emergency stopping of turbines of run-off-river plants ▪ Flushing of reservoirs and desilting basins ▪ Dambreak waves 	<ul style="list-style-type: none"> ▪ Flood waves (debris jam and break up) ▪ Flood waves (ice jam and break up) ▪ Landslides and glacier breakdowns into reservoirs producing overtopping waves

Energetic and economical issues of hydropeaking

High-head storage hydropower plants have the task to furnish peak energy during high demand periods and to regulate the electricity grid. The economic sustainability of high-head storage power plants and the safety of the electricity supply are therefore closely related to the production of peak energy without constraints. Energetic and economical issues in relation with hydropeaking highly depend on the chosen mitigation measures.

A restricted turbine operation mode may be an efficient measure from an environmental point of view but endangers the energetic and economical sustainability of the electricity production by hydropower plants. The main parameters which allow quantifying the energetic and economical impacts of a restricted turbine operation mode of high head storage hydropower plants are: the installed power and energy production of the power houses as well as the energy prices depending on demand (Wickenhäuser et al. 2005). In most cases hydropeaking mitigation measures at the power house itself by restricting turbine operation are not economical and reasonable from the energy

supply point of view. Therefore, mitigation measures have to focus mainly on reducing the effect of hydropeaking in the river downstream.

Mitigation measures for hydropeaking

Today's river restoration projects intend to give again more space to the rivers in order to improve the flood evacuation capacity and the morphology (Willi, 2005). From an ecological point of view, such restoration projects are most effective if simultaneously water quality and flow regime are satisfactory (Peter et al. 2005). Anthropogenic changes of the natural flow regime are one of the main reasons for the declining health of rivers (Poff et al. 1997).

Mitigation measures to reduce the effect of hydropeaking in a river can be divided in the installation of detention basins and the improvement of the river morphology.

Managed detention basins might be located directly downstream of powerhouses or integrated in the river at strategic locations allowing reducing hydropeaking of several hydropower plants simultaneously (Meile 2006d, Meile et al. submitted). Innovative ideas such as multipurpose schemes (Heller et al. 2007) or the joint operation of high-head storage and run-off-river hydropower plants (Verbund Austrian-Hydropower 2004) can help to minimize economical impacts. Managed detention basins with significant storage volumes can influence on the maximum and minimum daily discharge of the downstream river reach even for long duration impulses (VAW-LCH 2006) and also influence the rate of change of the discharge depending on the management of the basin.

Morphological measures increase the flow resistance and the natural retention capacity of rivers. Thus an attenuation and deformation of the surge wave front is expected. Furthermore, morphological measures allow to increase the flow variability and to create refuges for fishes, macrozoo- and phyto-benthos. The complex interaction of flow and the morphology must be considered in order to reduce the amount of the river portion which is regularly exposed to dry and wet conditions. For long duration hydropeaking impulses, no significant influence on minimum and maximum daily discharge is expected.

Motivation of the research project

The question how morphological measures influence the unsteady flow conditions due to surge waves as a result of hydropeaking was the motivation of the research project.

Unsteady flow in rivers can be assessed either using hydrological methods which applies level pool routing to channels by the calibration of two parameters in the inflow-outflow-storage relationship (Muskingum method). This method is appropriate for streams with small slopes. When the flow becomes increasingly dynamic the complete equations of Saint-Venant (dynamic equations) applies in combination with numerical methods for the resolution.

Stranner (1996) investigated numerically different parameters influencing surge waves from high-head storage hydropower plants. Results show that waves produced by storage plants, can reasonably be calculated with 1D-programs using the Saint-Venant equations. A sensibility study concerning the parameters slope, roughness, type of morphological measures and duration of impulses showed that:

- The unsteady flow is mainly influenced by two processes: the kinematic and the dynamic movement.
- Flow tends asymptotically to normal flow conditions after 1-2 hours in the rivers with small slopes (0.5 ‰) whereas these conditions are reached after only 10-15 minutes in steeper rivers (2 and 3 ‰). Furthermore, the shorter impulses are, the more the surge is diffusive.
- Lateral cavities as morphological measures, increasing the river retention effect, provide the best results when arranged with decreasing density from upstream to downstream for steep slopes. In small sloped rivers, the natural river retention is already relatively important¹ independently of passive retention. The influence of the longitudinal arrangement of passive volumes is negligible, but retention is increased compared to the prismatic case.

For practical applications the influence of parameters such as slope, roughness, morphological measures and duration of impulses can be determined by dimensioning diagrams (Stranner 1996) or using 1D-simulations for specific needs in complex river systems. Special attention should be addressed to the design of morphological measures if the intention is to increase the passive retention. Additional passive retention only occurs when extra volumes are flooded with increasing discharge compared to a prismatic channel. Two-dimensional simulations in three different morphologies (straight channel, alternate bars and braided river) under steady flow conditions show, that additional passive retention hardly occurs in natural river morphologies for a range of discharges typical for hydropeaking (Ferrari 2007). Such volumes probably only arise from man made modified river morphology.

Aim of the study and research objectives

Systematic theoretical and experimental investigations on surge waves in prismatic channels have been conducted by the first time by Favre (1935). No systematic experimental investigations have been done so far on the influence of macro- or large scale roughness elements on the propagation and deformation of positive and negative surge waves. The aim of this study is to investigate experimentally the influence of bank macro-roughness (form roughness) on *steady* and *unsteady flow* conditions, namely surge waves in a channel. For laboratory experiments with a short channel, the tested positive and negative surge waves from upstream are characterized by a steep wave

¹ For durations of impulses of maximum 90 minutes.

front. They differ somehow from most of the unsteady flows caused by hydropeaking in rivers. However, highly unsteady flows in open channel are of relevance for flows influenced by sluice gate operations, flushing of reservoirs, debris jam and break up, ice jam and break up, sudden stopping and start up of turbines of runoff river and storage hydropower plants, dambreaks, flashfloods and so on. Furthermore, findings on the influence of bank macro-roughness on flow resistance and surge wave propagation might be also extended to more gradually varied flows.

The scientific research objectives of the experiments with *steady flow* are defined as:

- Describe how macro-roughness elements at the channel banks physically influence the free surface flow.
- Relate characteristic parameters of macro-roughness elements to the flow resistance.
- Identify simple empirical flow resistance laws which allow to integrate form roughness at the banks into flow resistance computation.

The *unsteady flow* experiments have the following scientific research goals:

- Describe how surge waves propagate, deform and attenuate along a channel with macro-rough banks (complex morphology).
- Highlight the relationship between propagation and deformation of waves and the characteristics of the macro-roughness elements.
- Provide test cases for numerical model calibration.

Regarding practical applications the analysis of the experiments should give inputs to:

- The determination of flow resistance for macro-scale roughness at channel banks.
- The estimation of the influence of macro-scale roughness on the surge wave front height and its propagation speed in a macro-rough channel.

Structure of the report

The work is structured as follows:

- Chapter 2 reviews flow resistance formulas for steady open channel flow, special flow features occurring in flows over cavities as well as the mathematical formulation of unsteady surge wave flow. Moreover, some theoretical developments on the propagation speed of the surge wave front are presented.
- Chapter 3 describes the experimental setup and the test program for the steady and unsteady flow experiments.
- Chapter 4 discusses the results of the steady flow experiments for the channel including macro-roughness at the channel banks. Beside the description of the experiments, different empirical relationships are developed. They are applied to test geometries and more natural like configurations.
- Chapter 5 presents the results of the unsteady flow experiments. The propagation

speed of the surge wave front and the attenuation of the height of the surge wave front are analyzed for both, prismatic and macro rough configurations.

- In Chapter 6 some aspects of the steady and unsteady flow are investigated by numerical simulations.
- Chapter 7 finally gives the conclusions on the result of the experimental work as well as an outlook to further research. It remembers also the practical aspects of this work which are relative to macro-rough flow resistance, groin fields and embayments as well as to surge wave propagation.

2 LITERATURE REVIEW & THEORETICAL BASES

The experimental study of the present research work deals with various subjects of open channel flow. The first subject is the flow resistance in general and particularly the macro-rough open channel flow (§ 2.1). The second subject is the unsteady open channel flow in general, and especially the rapidly varied unsteady flow as well as the effect of roughness and retention on unsteady flow (§ 2.3). Finally the work consists in the analysis of cavity flows in general and deals in particular with special flow features similar as observed in groin fields and embayments (§ 2.2). In the following three chapters the most important aspects summarizing the theoretical considerations of the three mentioned subjects are presented.

At the end of each paragraph, the important points to keep in mind for the further developments and the analysis of the steady and unsteady flow experiments are summarized. They are graphically distinguished as shown in this box.

2.1 Flow resistance in steady open channel flow

2.1.1 Introduction

Flows might be classified regarding the effect of the viscosity relative to the inertia in laminar, turbulent and transitional flows. The turbulent flows can again be divided into three types: smooth turbulent flows, fully rough turbulent flows and transitional turbulent flows. The transition between smooth and fully rough turbulent flows must be clearly distinguished from the transition between laminar and turbulent flow. The transition between laminar and turbulent flow takes place at about $Re = 4R_h U / \nu = 2300$, where R_h is the hydraulic radius, U the mean flow velocity and ν kinematic viscosity of the fluid. The transition between smooth turbulent flow and fully rough turbulent flow depends on both, the Reynolds number and the relative roughness $\varepsilon = k_s / 4R_h$, where k_s is the equivalent sand roughness height. When the relative roughness becomes high, which means that the size of roughness elements approaches the order of magnitude of the flow depth h or the hydraulic radius R_h , the flow is called macro-rough. Open channel flow can be called macro-rough when the water surface is disturbed by the roughness elements. This type of flow has only marginally been studied before 1970 (Dubois 1998). The first systematic investigations on macro-roughness in open channel flow have been done by Bathurst (1978, 1985) and on (macro-) roughness elements in pipe flow by Morris (1955) and Morris and Wiggert (1972). A further separation of the macro-rough flow can be undertaken using the definitions of Lawrence (1997) into well inundated flow regimes, marginally inundated flow regimes and partially inundated flow regimes.

The flow resistance producing the head-loss observed in pipes or open channel flow is governed by different phenomena. For small relative roughness heights viscous friction and turbulent friction in the shear layer dominate. When the size of the roughness elements becomes important compared to the diameter or the flow depth, jet- and wake-dissipation become also important. The main phenomena responsible for the head-losses are linked to the flow types described above as proposed in Table 2-1. Furthermore, different types of flow resistance formulas can be related to the different flow types. In the following chapters (§ 2.1.2 to § 2.1.5) the main formulas and their physical background are briefly presented.

Table 2-1: Flow types, head-loss governing phenomena as well as commonly used types of resistance formulas.

Flow type		Head-loss due to	Resistance equations
Laminar flow ($Re = 4UR_h / \nu < 2300$)		Viscous friction	Hagen-Poiseuille
Transitional flow ($2300 < Re < 4500$)		Viscous and turbulent friction	-
Turbulent flow	Smooth turbulent flow	Turbulent friction in the shear layer; no influence of ε	Prandtl; Von Karman
	Transitional turbulent flow	Turbulent friction in the shear layer (influence of Re and ε)	Colebrook-White
	Fully rough turbulent flow	Turbulent friction in the shear layer; no influence of Re	Nikuradse; various empirical formulas
Macro-rough flow	Well inundated flow	Principally turbulent friction in the shear layer	Nikuradse type formulas with modified constants
	Marginally inundated flow	Turbulent friction in the shear layer & wake dissipation	Constant mixing length model
	Partially inundated flow	Principally jet dissipation and wake dissipation	Drag force based equations

Many studies on friction coefficients based on velocity profile measurements have been performed in pipes for pressurized flow conditions and not particularly for free surface flows. When passing from pressurized pipe to free surface flow, the diameter D is replaced by $4R_h$.

2.1.2 Laminar flow and transition to turbulent flow

Laminar flow is also called streamline flow and occurs when the fluid flows in parallel layers. In open channel hydraulics at prototype scale, laminar flow does not exist practically. In laboratory experiments this kind of flow can occur in low flow velocity and low flow depth areas. In pipe flow, laminar flow occurs when the Reynolds number

$Re = UD / \nu$ is less than 2300. The friction coefficient f for laminar flow is found from the Hagen-Poiseuille formula and is expressed as:

$$f = \frac{64}{Re} \quad (\text{eq. 2.1})$$

The transition from the laminar to the turbulent flow regime ($2300 < Re < 4500$) is characterized by a significant increase of the friction coefficient. No widely used resistance formulas are proposed for this range of Reynolds numbers.

2.1.3 Turbulent flow

The flow resistance equations for turbulent flows have been largely influenced by the approach of Prandtl. They are based on the definition of the boundary layer, the shear stress for uniform flow, the friction velocity and the velocity defect.

2.1.3.1 Smooth turbulent flow

In the smooth turbulent flow, the roughness elements are sufficiently small to be inside the viscous boundary layer. For the smooth turbulent flow regime, Prandtl applied the experimental results of Nikuradse allowing defining the velocity defect in a pipe as:

$$\frac{u_{\max} - u(z)}{u_*} = -5.75 \log \frac{z}{R} \quad (\text{eq. 2.2})$$

where u_{\max} is the maximum velocity at the pipe axis $z=0$, $u(z)$ the velocity at the radial position z , u_* the friction velocity and R the pipe radius. Further developments done by Von Karman based on the definition of the laminar boundary layer, the buffer-layer and the outer layer as well as the introduction of the Reynolds number allowed obtaining the Prandtl-Von Karman resistance formula for turbulent smooth flows in conduits:

$$\sqrt{\frac{1}{f}} = -2 \log \frac{2.51}{Re \sqrt{f}} \quad (\text{eq. 2.3})$$

Since this formula is implicit, Blasius proposed to use the explicit formula $f = 0.3164 / Re$ which gives quasi identical results as the Prandtl-Von Karman formula for $Re < 100'000$. Furthermore, different formulas of the type $f = B + A / Re^n$ are proposed for smooth turbulent flow having the advantage to be explicit and to match well with the Prandtl-Von Karman formula for Reynolds numbers up to $3 \cdot 10^6$. For any smooth turbulent flow resistance formula, the friction coefficient does not depend on the relative roughness but only on the Reynolds number.

2.1.3.2 Fully rough turbulent flow

The second and dominant flow regime in open channel flows is the fully rough turbulent flow. For the fully rough turbulent flow, the roughness elements are sufficiently high to enter into the turbulent boundary layer. Before presenting formulas of fully rough turbulent flows, some considerations about rough surfaces should be mentioned:

- A roughness element is first of all characterized by its geometric height k (Figure 2-1 a). The roughness height is a main characteristic parameter in fully rough turbulent flow, for both pipe and open channel flow and it is related to the skin (surface) of the boundary.
- The relative importance of the roughness must be evaluated regarding the diameter of a pipe or the flow depth, respectively the hydraulic radius of a channel (Figure 2-1 c).
- Roughness elements can have the same height k but do not necessarily have the same form (Figure 2-1 a & b). It is possible to distinguish between undulation roughness for relatively smooth forms and sharp edged roughness, where the viscous sublayer is easily broken.
- Roughness elements can be distributed in different ways over a surface. Either the density of roughness elements of same height and form are varied (Figure 2-1 a & d) or the arrangement of roughness elements are different for a given roughness density and roughness height k (Figure 2-1 d & e). Depressions can be regarded as a roughness too (Figure 2-1 d).

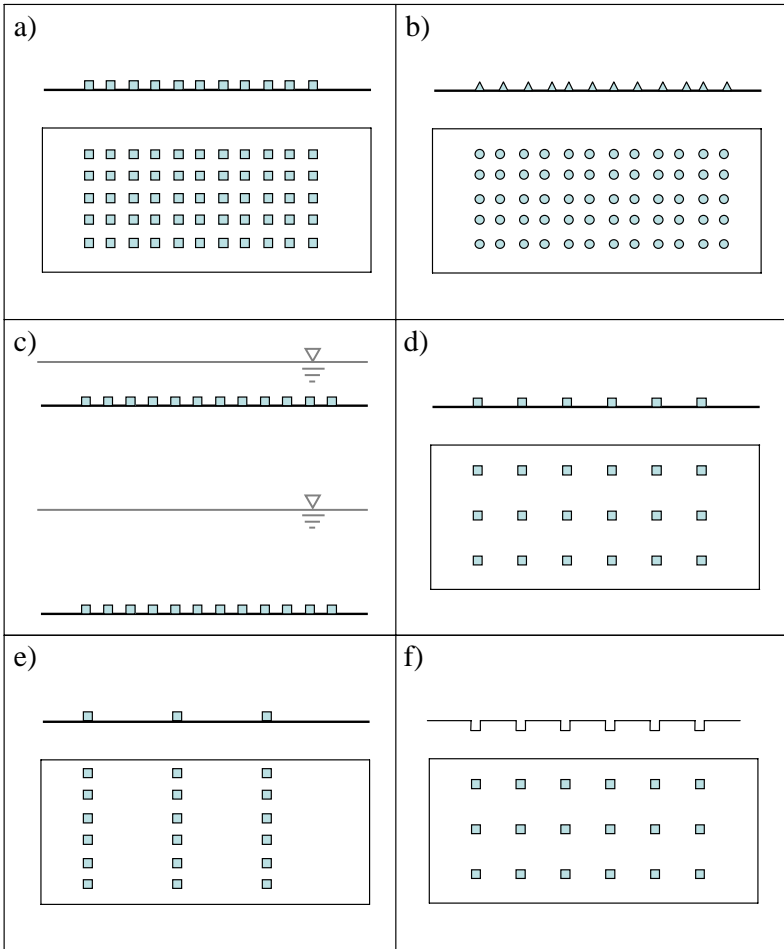


Figure 2-1 : Different roughness types according Carrier (1988): a) & b) same density and height, different forms (cubes versus cones). c) different submergence. d) & e) same density, height and form but different arrangement. f) depression roughness elements.

When using same theoretical considerations as for smooth turbulent flow, the friction coefficient for fully rough turbulent flow is given by:

$$\sqrt{\frac{1}{f}} = -A \log \frac{k}{BD} = -2 \log \frac{k}{3.7D} \quad (\text{eq. 2.4})$$

The values of the constants A and B have been obtained thanks to the exhaustive experiments of Nikuradse. Both formulas are mathematically identical. For sufficiently high Reynolds numbers, Nikuradse found the friction coefficient f to be a function of the relative roughness k/D only. Some points should be clarified when using the Nikuradse formula for fully rough flow:

- The k value of the Nikuradse experiments corresponds to the d_m of the used sand grains. He worked with almost homogeneous grain sizes.
- As the roughness height in the Nikuradse experiments was $d/2$ (the lower part of the grains was immersed in the smoothening concrete and not $k = d$ the k value of formula (eq. 2.4) has only a direct physical meaning for the experiments of Nikuradse.
- The formula can nevertheless be used for many cases by the definition of an equivalent sand roughness value k_s which replaces the k value of formula (eq. 2.4). In general, the hydraulic roughness k_s is not equal to the geometrical roughness height k .
- The experiments of Nikuradse showed a clear dip and rise behavior of the friction coefficient in the transition zone from smooth turbulent to fully rough turbulent flow. No mathematical formulation for this behavior is published by the author of the experiments.

Fully rough flow resistance formulas are widely used. Depending on the specific flow problem, the constants are adapted. The roughness height value is generally related to the bed material and normalized with the flow depth or hydraulic radius.

However, Bezzola (2002) points out an unsolved problem when fitting logarithmic laws on measured velocity profiles. The Von Karman constant can be used in combination with the equivalent sand roughness k_s respectively the constant B since the variation of k_s has the same effect as the variation of $1/B$. Furthermore, the choice of the reference layer ($z = 0$) influences the velocity profile close to the wall.

Finally, when the formula (eq. 2.4) is completed by a wake function allowing to fit the velocity profile better outside of the inner region ($z > 0.2h$), the wake function parameter Π appears as additional calibration parameter.

Important points from the considerations about fully rough turbulent flow are: Friction coefficients may vary for the same channel section, same density and same roughness height when the roughness elements have different forms or skin properties. The friction coefficients can even vary in a given section for identical roughness heights, densities and forms when a specific roughness arrangement is applied. Negative elements (depressions) can be considered as roughness elements too. The theory of fully rough turbulent flow, as proposed by the formula of Nikuradse, theoretically applies only to dense and sharp edged roughness elements with high relative submergence. The use of equivalent sand roughness k_s allows extending the applicability of the fully rough flow resistance formula.

2.1.3.3 Transition from smooth to fully rough turbulent flow

Colebrook followed the theoretical and experimental works of Prandtl-Von Karman and Nikuradse and proposed a mathematical formulation covering all turbulent flow regimes. The proposed formula is the sum of the smooth and fully rough turbulent flow formula, assuming that both exist in the same pipe simultaneously and with the same probability (see Yoo and Singh 2005):

$$\sqrt{\frac{1}{f}} = -2 \log \left(\frac{k_s}{3.7D} + \frac{2.51}{\text{Re} \sqrt{f}} \right) \quad (\text{eq. 2.4})$$

This formula can be graphically represented and the friction coefficient is determined as a function of the Reynolds number and the relative roughness (Figure 2-2). The Poiseuille, Prandtl-Von Karman, Blasius, Moody and Nikuradse curves are also presented in Figure 2-2. When the Colebrook-White formula (eq. 2.4) is used for sections different from circular pipes and open channel flow, the diameter D must be replaced by $4R_h$. Furthermore, if the friction coefficient is determined by this formula in non-circular channel section, a form factor Φ might be applied to the hydraulic radius ($R_{h,eff} = \Phi \cdot R_h$)¹.

Even if the experiments of Colebrook showed that the formula fitted quite well with data from industrial ducts, the Colebrook-White formula does not describe the observed dip and rise of the Nikuradse experiments. The reason for the dip and rise is explained by the quasi homogeneous character of the sand grains of the Nikuradse experiments. The physical explanation is searched in the size of the viscous sub-layer which is decreasing with increasing Reynolds numbers. As long as the roughness elements are inside of the viscous sub-layer, they do not have an effect on the friction coefficient, which obeys to the smooth turbulent laws (Prandl-Von Karman). When the viscous sub-layer becomes sufficiently small for higher Reynolds numbers, the roughness elements point inside the turbulent flow and they takes effect on the turbulent friction. In experi-

¹ This approach can be discussed. The hydraulic radius calculated from the wetted area and perimeter should already take into account the non circular shape. Form factors are nonetheless proposed by different authors (e.g. Schröder 1990).

ments with homogeneous roughness heights, practically all elements begin at the same Reynolds number to act on the turbulent flow. Thus a sudden increase of the friction coefficient corresponding to the fully rough flow is observed. In experiments with heterogeneous roughness heights such as in industrial pipes, the number of roughness elements pointing inside the turbulent flow is gradually increasing and therefore the smooth turbulent friction is progressively replaced by the fully rough turbulent friction (Figure 2-3).

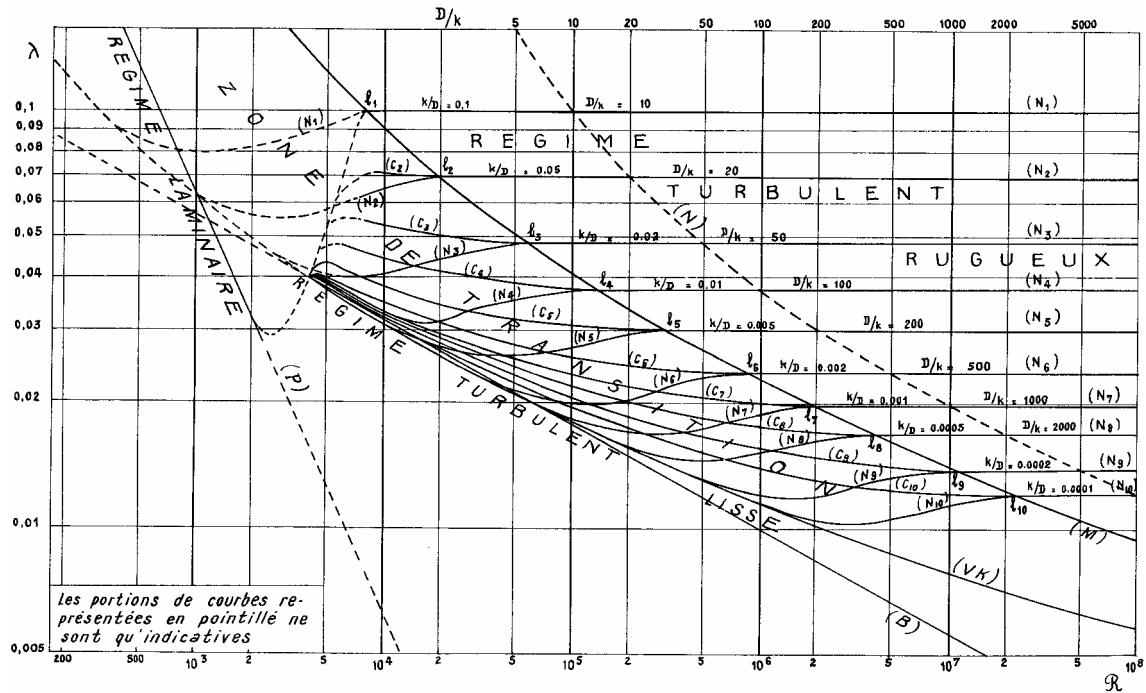


Figure 2-2 : Moody-Stanton diagram as presented in Carlier (1988, original figure). The friction coefficient f is noted here λ . (P) Poiseuille, (VK) Prandtl-Von Karman, (B) Blasius, (M) Moody curves. $(N_1), (N_2), \dots$ Nikuradse-curves. $(C_1), (C_2), \dots$ Colebrook-White-curves. (N) Nikuradse-curve for the fully rough flow with D/k read on the upper x-axis.

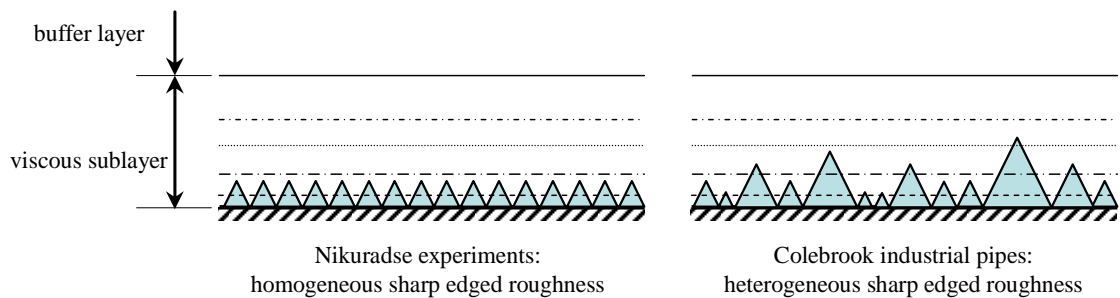


Figure 2-3 : Transition from smooth to fully rough turbulent flow for a uniform size roughness (left) and an industrial pipe (right) with increasing Reynolds numbers. By increasing the Reynolds number, the viscous sublayer decreases in size schematically indicated by the different horizontal lines.

For the transition from smooth to fully rough turbulent flow a significant difference in the behaviour has been noticed between industrial pipes and the artificially roughened pipes. The relationship between the friction coefficients and the Reynolds numbers of artificially roughened pipes of Nikuradse show a dip and rise. The physical explanation is searched in the size of the viscous sublayer depending on the Reynolds number and the roughness heights.

2.1.3.4 Other transitions for turbulent flows and concept of Morris (1955)

Transitions with rising characteristics of the friction coefficient with increasing Reynolds numbers have also been observed by other authors than Nikuradse. Table 2-2 summarizes the Reynolds domain for which increasing friction coefficients have been observed as a function of the relative roughness $\varepsilon = k_s / 4R_h$ (Varwick's data in Kirschmer 1949; Nikuradse 1933) or of the relative roughness spacing $\lambda / 4R_h$ (different sources in Morris 1955).

The ranges and amplitudes corresponding to Table 2-2 are schematically represented in Figure 2-4. The physical explanation for the increase of the friction coefficient with the Reynolds number of the experiments of Nikuradse was given above in § 2.1.3.3.

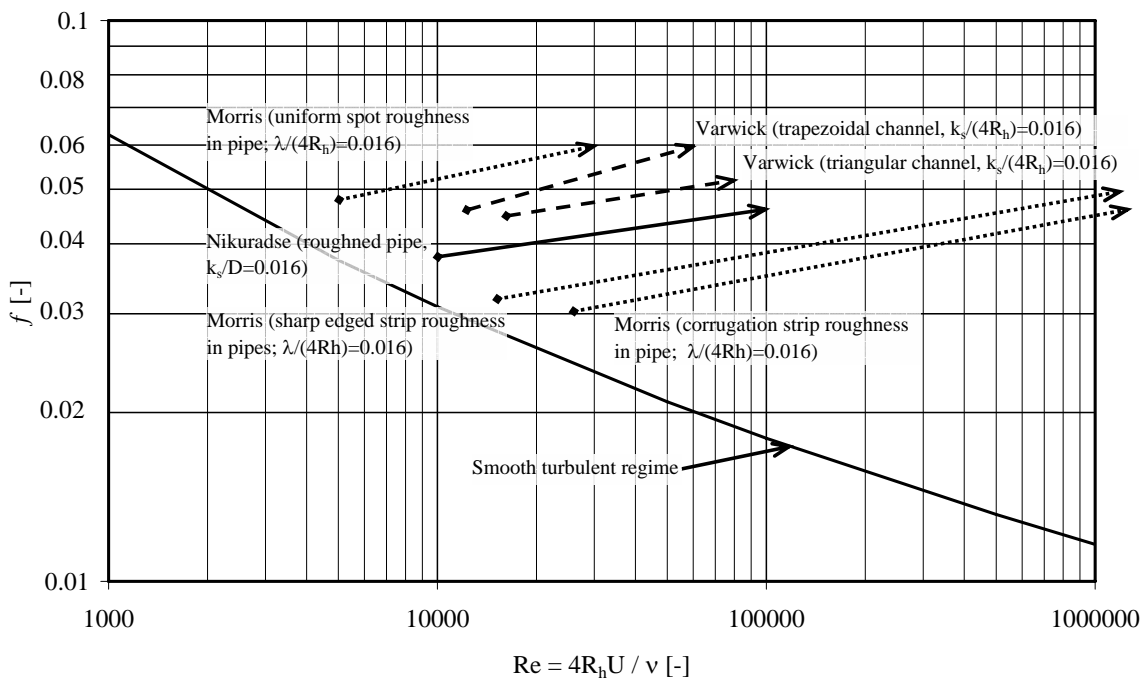


Figure 2-4 : Range of Reynolds numbers with rising characteristics of the friction coefficients for $k_s / 4R_h$ respectively $\lambda / 4R_h$ equal to 0.016. For uniform dense grains, the roughness spacing λ of Morris corresponds to the roughness height k of Nikuradse and Varwick.

Table 2-2: Domain of rising characteristics of friction coefficients Re and f values have been read from the graphics of the corresponding publications. Varwick's data in Kirschmer (1949) and Nikuradse (1933) considers the relative roughness $\varepsilon = k_s/4R_h$ (Varwick's data in Kirschmer 1949; Nikuradse 1933). Different sources in Morris (1955) relates to roughness spacing $\lambda/4R_h$, where λ is the longitudinal spacing of the roughness elements.

Source; application	$k_s/(4R_h)$ [-]; $\lambda/(4R_h)$ [-]	$Re_{\text{start rise}}$ [-]	$Re_{\text{end rise}}$ [-]	$f_{\text{start rise}}$ [-]	$f_{\text{end rise}}$ [-]
Nikuradse (1933); Artificially roughened pipes	0.001	200'000	700'000	0.017	0.019
	0.002	120'000	400'000	0.021	0.023
	0.004	60'000	300'000	0.025	0.028
	0.008	30'000	150'000	0.031	0.036
	0.016	12'100	100'000	0.0388	0.046
	0.032	10'000	100'000	0.055	0.055
Varwick's data ; Arti- ficially roughened trian- gular channel	0.006	80'000	280'000	0.032	0.036
	0.009	60'000	200'000	0.037	0.04
	0.016	16'000	80'000	0.045	0.052
Varwick's data ; Arti- ficially roughened trape- zoidal channel	0.006	80'000	280'000	0.032	0.038
	0.009	40'000	160'000	0.038	0.044
	0.016	12'000	60'000	0.046	0.06
Morris (1955); Corru- gation strip roughness in pipes	0.004	100'000	40'000'000	0.02	0.035
	0.016	25'000	10'000'000	0.03	0.059
	0.050	7'000	200'000	0.043	0.1
Morris (1955); Sharp edged strip roughness in pipes	0.004	50'000	10'000'000	0.021	0.035
	0.016	15'000	5'000'000	0.032	0.058
	0.050	3'500	500'000	0.042	0.1
Morris (1955); Uniform spot rough- ness in pipes	0.004	20'000	100'000	0.03	0.035
	0.016	5'000	30'000	0.048	0.06
	0.050	2'000	8'000	0.08	0.1

The explanation for the data of Morris and Varwick differs from the one of the Nikuradse experiments as points out Chow (1959). He relates the transition of Morris and Varwick's data with another type of flow having higher energy loss (wake-interference flow). This has already been explained reasonably by Morris (1955). With regard to the theoretical developments of § 4.3 (steady flow tests), the main findings and conclusions of Morris' work are presented hereafter (Morris 1955, Morris and Wiggert 1972). He proposed a new concept for the flow resistance in (macro)¹-rough conduits.

¹ The roughness elements in the pipes considered by Morris were not macro-rough regarding their size. Nevertheless, the concept (generation, spreading and dissipation of vortices) applies well to macro-rough flow.

The motivation of the new concept for friction coefficient calculation was essentially based on differences in behaviour between the Colebrook-White formula and the Nikuradse experiments as well as on differences between the Colebrook-White formula and many industrial pipes showing rising or strictly horizontal behaviour of $(f-Re)$ -curves (Harris 1950; Straub and Morris 1950). Additional motivations were the observed dependence of k_s values from the pipe radius and that k_s values have no definite physical meaning except for uniform sand-coated surfaces.

Table 2-3: Flow regimes for turbulent flows for pipes proposed by Morris (1955). f_s : smooth friction factor; f : friction factor; p : total length of perimeter occupied with roughness elements; P : total length of (wetted) perimeter; j : length of the cavity; λ : longitudinal spacing of the roughness elements; C_d : drag force coefficient; V_v : tangential velocity of depression vortex; V_w : velocity near wall; U : average velocity in cross-section; Re_w : wall Reynolds number (Morris 1955).

Regime	Friction factor equation		Variation of f with increase of Re	Variation of f with roughness parameters
Smooth flow	$\frac{1}{\sqrt{f_s}} = -2 \log \left(\frac{2.51}{Re \sqrt{f_s}} \right)$	(eq. 2.3)	Decreases	No effect
Quasi smooth flow	$f = f_s + \frac{p}{P} \frac{j}{\lambda} \left(\frac{V_v V_w^2}{U^3} \right)$	(eq. 2.5)	Decreases	Increases with p/P and j/λ
Semi-smooth (isolated roughness) flow	$f = f_s \left[1 + 67.2 C_d \frac{p}{P} \frac{k}{\lambda} \right]$	(eq. 2.6)	Decreases	Increases with C_d , p/P and k/λ
Hyper-turbulent (wake-interference) flow	$\frac{1}{\sqrt{f}} = -2 \log \left(\frac{\lambda}{3.75 \cdot 4R_h} \right) + \phi(Re_w, shape)$	(eq. 2.7)	Increases	Increases with increasing λ/R_h
Normal (rough) flow	$\frac{1}{\sqrt{f}} = -2 \log \left(\frac{\lambda}{3.75 \cdot 4R_h} \right)$	(eq. 2.8)	Constant	Increases with increasing λ/R_h

As generation, spreading and dissipation of vortices from the wake and separation zones behind the roughness elements is the major source of friction-loss in a fluid flowing over a (macro)-rough surface, the developments of Morris are essentially based on the introduction of the longitudinal spacing of the roughness elements in addition to the geometric roughness height k . Both parameters together replace the equivalent sand roughness height k_s , which has to take into account all physical parameters such as density, height, arrangement and form of the roughness elements. Furthermore, Morris

introduced different drag coefficients C_d for spot (sphere, hemisphere, cube, cone), strip (rectangular, circular, elliptical, semi-circular, triangular) and depression (rectangular slot, hemispherical pit) roughness elements. The developments led to five types of turbulent flows (Table 2-3). The smooth turbulent flow (corresponding to the Prandtl-Von Karman smooth turbulent flow), the quasi-smooth (also called “skimming”) flow, the semismooth (also called “isolated roughness”) flow, the hyper-turbulent (also called “wake-interference”) flow and the normal turbulent flow (corresponding to the fully rough turbulent flow of Nikuradse).

The formulas of Table 2-3 show that in case of isolated roughness flow, the friction coefficient is depending on the density ($p/P\lambda$) and height (k) of roughness elements. According Morris (1955) in the case of wake interference flow, the longitudinal spacing λ becomes more important than the roughness height since the wall Reynolds number Re_w depends on λ too. In case of normal turbulent flow, the friction coefficient is depending on the longitudinal roughness spacing only. Furthermore, the normal turbulent flow corresponds to the fully rough turbulent flow of Nikuradse for which experiments $d = k$ corresponds to λ (Figure 2-3).

Yoo and Singh (2005) proposed the mean friction factor computation method for commercial pipes. Their concept is not based on the separation of the flow into different regimes and the computation of the friction factor using the corresponding formula as proposed by Morris combined with a probabilistic approach. The total friction factor of a pipe is computed by summing the probability weighted contributions of smooth turbulent, rough turbulent or transitional turbulent friction factors. Thus it is possible to compute rising characteristics of friction factors with increasing Reynolds numbers too. Pyle and Novak (1981) working on rough and roughened pipes propose a form drag based computation method taking into account drag coefficients as a function of the form and wall Reynolds numbers, the roughness density and the roughness heights. The geometrical roughness height must be adjusted to an effective roughness height when roughness concentration is higher than 35%. Works on roughened pipes presented by Rouse (1965) show that concentration of roughness elements is as essential as their size. A concentration (also called solidity) of 0.15 to 0.25 yields to a maximum of roughness.

From the findings presented above it is important to remember that friction coefficients do not necessarily show descending or horizontal dependence on Reynolds numbers. Particular arrangement and spacing of roughness elements can lead to rising characteristics in the case of “hyperturbulent flows” due to abnormally intense turbulence and mixing. Parameters as the longitudinal roughness spacing, wall Reynolds numbers, peripheral roughness densities and roughness shapes as well as drag force based approaches might be helpful for the understanding of macro-rough flow types where the size of single roughness elements does not allow anymore considering them as an equivalent roughness.

2.1.3.5 Empirical formulas for fully rough turbulent open channel flow

When fully rough turbulent open channel flow is considered at high Reynolds numbers and with relatively important relative roughness, empirical formulas are widely used due to their simple and explicit character and as they proved sufficient precision for many practical cases. They are called empirical as they are developed in most cases based on experiments. Empirical formulas for rough turbulent open channel flow generally links the mean flow velocity to the hydraulic radius using a power law and the square root of the channel slope:

$$U = \alpha S_0^{\chi_1} R_h^{\chi_2} \tag{eq. 2.9}$$

where α is a dimensional coefficient depending only on the roughness. χ_1 and χ_2 are exponents. The first proposition of such a formula has been made by Chezy in 1775. Most of the empirical formulas have an exponent $\chi_1 = 0.5$. Exceptions are the formulas of Hagen (1854), Flamet (1892), Woltmann (1799). The exponent applied to the hydraulic radius ranges between $0.4 < \chi_2 < 0.714$ (Table 2-4).

Table 2-4: *Some empirical flow resistance formulas for fully rough turbulent open channel flow by diverse authors (summarized from Carlier 1988).*

Authors	Formula	$\chi_1 ; \chi_2$	α
Chezy (1775)	$U = \alpha \cdot S_0^{0.5} \cdot R_h^{0.5}$ (eq. 2.10)	0.5 ; 0.5	$\alpha = C$; Bazin or Kutter formula (Graf et al. 1993)
Gaukler (1868)	$U = \alpha \cdot S_0^{0.5} \cdot R_h^{0.4}$ (eq. 2.11)	0.5 ; 0.4	α : from tables
Forchheimer (-)	$U = \alpha \cdot S_0^{0.5} \cdot R_h^{0.7}$ (eq. 2.12)	0.5 ; 0.7	α : from tables
Christen (-)	$U = \alpha \cdot S_0^{0.5} \cdot R_h^{0.625}$ (eq. 2.13)	0.5 ; 0.625	α : from tables
Hagen (1854)	$U = \alpha \cdot S_0^{0.571} \cdot R_h^{0.714}$ (eq. 2.14)	0.571;0.714	α : from tables
Manning (1891)	$U = \frac{1}{n} \cdot S_0^{0.5} \cdot R_h^{0.667}$ (eq. 2.15)	0.5 ; 0.667	n from tables (Chow, 1959)

Strickler (1923) proposes to use the formula of Manning and to calculate the Strickler coefficient using the characteristics of the alluvial channel as:

$$K_{st} = \frac{1}{n} = \frac{21.1}{d_{average}^{1/6}} \tag{eq. 2.16}$$

where $d_{average}$ is an “average diameter” of the bed material. Strickler (1923) did not precisely define this “average diameter” but he verified that this diameter lies in the middle of the domain between the minimum and maximum diameter of the bed mate-

rial. For typical particle size distributions of rivers, the value of $d_{average}$ rather approaches d_{90} than d_{50} of the bed material (Jaeggi 1984). Furthermore, the mean diameter d_m of the surface layer approximately fits with the d_{90} of the bed material.

Empirical formulas are widely used for the computation of open channel flow problems. The Manning formula (eq. 2.15) in combination with the formula for the resistance coefficient according Strickler (eq. 2.16) is especially employed in Switzerland. Nevertheless, analytical developments comparing the mean flow velocity computed combining of Weisbach-Darcy and Nikuradse formulas with the mean flow velocity found from the Manning-Strickler formula show (Sinniger and Hager 1989, Dubois 1998) that the Manning-Strickler formula gives strictly identical results than the Nikuradse formula only for relative roughness values of $\varepsilon = k_s / 4R_h = 9.17 \cdot 10^{-3}$. Within the limits $9 \cdot 10^{-4} \leq k_s / 4R_h \leq 5 \cdot 10^{-2}$ the computational error on the friction slope S_f remains less than 5%. Already Strickler (1923) found that his coefficient can vary within the same river reach when the relative flow depth changes. In mountain rivers the Strickler coefficient is generally increasing with the discharge whereas in (larger) rivers with smaller channel slopes the Strickler coefficient decreases. These observations could be explained by increasing relative flow depths leading to a smoothening of the roughness elements in mountain rivers respectively the appearance of bed forms (ripples and dunes) in large, small sloped rivers. The variation of Strickler coefficients is at least an indicator for the limited validity of empirical formulas. A field study on 12 river reaches in Switzerland (BWG 2001) shows that the Strickler coefficients found from velocity measurements increases with increasing discharge and flow depth for almost all reaches.

Empirical formulas have limited validity, especially when the size of roughness elements becomes important compared to the flow depth or the hydraulic radius ($h/d < 4 \div 6$). The dimensional coefficient α of formula (eq. 2.9) varies with k_s and also with hydraulic radius R_h .

2.1.4 Flow in composite and compound channel sections

A composite channel is a channel whose wall roughness changes along the wetted perimeter P of the cross section. Thus, the local resistance (wall shear) varies along this perimeter. A compound channel is a channel whose cross section consists of at least two subsections of different geometric shapes. The wall roughness of the different subsections might be identical and the influence of the different subsections is mainly taken into account by the hydraulic radius R_h^1 . Nevertheless, in field applications, compound channels generally are composite channels too. From the physical point of view, composite and compound channel sections influence on the velocity distribution and thus affect the flow resistance.

¹ For cross-sections very different from a circular shape, the hydraulic radius R_h might be replaced by a hydraulically efficient hydraulic radius $R_{h,eff}$.

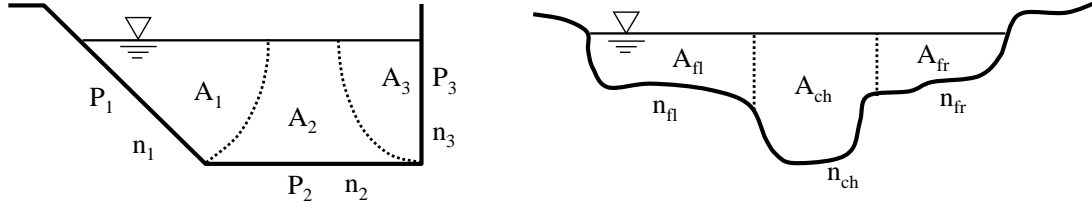


Figure 2-5 : Composite (left) and compound (right) channel section. *A*: area; *n*: Manning coefficient; *P*: wetted perimeter; *ch*: channel; *fl* and *fr*: left and right floodplain.

Yen (2002) reviewed 17 different possibilities to calculate a composite Manning coefficient n_c . Most of them require an assumption on how the composite/compound channel section is divided. Few others are free of this assumption (e.g. Einstein 1934). The concept of the approach of Einstein (1934) is based on the assumption that the total cross sectional mean velocity U is equal to each sub-area mean velocity U_i . The composite Manning coefficient n_c of the section calculates than as:

$$n_c = \left[\frac{1}{P} \sum \left(n_i^{3/2} P_i \right) \right]^{2/3} \quad (\text{eq. 2.17})$$

The composite resistance coefficient of the section can alternatively be calculated also for the composite Weisbach f_c and composite Chezy C_c resistance coefficient using the known relationship between the Mannings n and Weisbach f respectively Chezy C resistance coefficient:

$$\sqrt{\frac{8}{f}} = \frac{R_h^{1/6}}{n\sqrt{g}} = \frac{C}{\sqrt{g}} = C_{adim} \quad (\text{eq. 2.18})$$

where C_{adim} is a dimensionless Chezy coefficient. When combining (eq. 2.17) and (eq. 2.18) the composite friction coefficient f_c is found:

$$f_c = \frac{1}{P} \sum (f_i P_i) \quad (\text{eq. 2.19})$$

The composite Chezy coefficient C_c becomes:

$$\frac{1}{C_c^2} = \frac{1}{P} \sum \left(\frac{1}{C_i^2} P_i \right) \quad (\text{eq. 2.20})$$

The flow resistance computation methods presented up to here (§ 2.1.1 to § 2.1.3) can thus be extended to channel sections of composite roughness and to compound channel sections.

Yen (2002) reveals a lack of available data allowing identifying which of the 17 investigated possibilities gives the most accurate results. For this reason, it has been decided to consider mainly the approach of Einstein (1934) in this work where composite channel section resistance is required.

The presented formulas (eq. 2.17 to eq. 2.21) are based on the uniform cross sectional velocity hypothesis (single channel method SCM). Whereas this assumption is still quite reasonable for a channel section of composite roughness, it becomes more doubtful for a compound channel having a main channel and floodplain(s) where the flow velocities are obviously different from the main channel flow velocity. In this case, the section is divided into subsections and the discharge is computed in each individually (divided channel method DCM). Nevertheless, this method does not take the momentum transfer interaction between main channel and floodplains into account. Bousmar and Zech (1999) therefore present the exchange discharge model EDM for compound channels including the turbulent exchange (momentum flux due to the velocity gradient between main channel and floodplain) and the geometrical transfer (discharge flux due to geometrical changes of the floodplain) between the main channel and the floodplain(s). An additional slope S_a added to the friction slope S_f allows to obtain the head-loss slope for steady flow conditions S_e . Two practical problems are solved by the exchange discharge model: the rating curve computation of a cross-section and the energy slope computation in backwater curve problems.

Recent works including respectively quantifying the momentum exchange between main channel and floodplains has been presented by van Prooijen et al. (2005), McGahey et al. (2006) and Proust et al. (2006). Van Prooijen et al. (2005) concludes that the momentum exchange is dominated by the horizontal coherent structures and the bottom turbulence whereas secondary circulation (geometrical transfer) is of minor importance. McGahey et al. (2006) support these observations by the analysis of the terms of the depth-integrated Reynolds-Averaged Navier-Stokes equations. They show that the hydrostatic pressure term is counteracted principally by the boundary friction but that turbulence due to vertical interfacial shearing and secondary flows contributes to the closure of the equation too. Proust et al. (2006) compared results from different 1D numerical models to compound channel laboratory experiments including an abrupt floodplain contraction. They show that the turbulent exchange becomes small when the mass transfer becomes important. Furthermore, validity of 1D models is shown to be limited when mass transfer becomes severe.

The concept of composite roughness and compound channel flow allows extending the computation of flow resistance to composite channel sections having different roughness on the different walls. Whereas the approach based on the assumption of Einstein (1934) about the uniform flow velocity can be considered as quite correct in composite channel sections, it becomes doubtful in compound channel sections where turbulent exchange and geometrical transfer is significant.

2.1.5 Macro-rough flow

Macro-rough flows can be defined as flows disturbed by elements which size is important compared to the flow depth respectively the hydraulic radius. The roughness elements can cover the entire channel section or only a part of the section as the bottom or the bank. The roughness generating elements may be

- boulders or pebbles,
- artificial elements as cubes, spheres, cones, ...,
- different types of vegetation,
- bed forms in mountain streams and torrents,
- bed forms in mid- and lowland streams or
- abrupt changes of channel sections respectively profile.

In alluvial channels, a characteristic diameter of the particle size curve is used to quantify the importance of the roughness size. Bathurst (1985) classified the roughness into large scale roughness, transitional roughness and small scale roughness. Bray (1987) proposed an extension of this classification including the phenomena responsible for the total head-loss. In addition to the skin friction, jet and the wake dissipation are largely contributing to the total head-loss in macro-rough flows. Furthermore, Herbich und Shulits (1964) relates the main head-loss phenomena in macro-rough flows to the roughness density. For high roughness densities the head-loss is mainly generated the dissipation of jets arriving on the downstream elements whereas in low roughness density arrangements the head-loss is governed by the wake dissipation along shear layers downstream of elements.

Table 2-5: *Classifications of flows according to the size of roughness elements. h : flow depth. d_{84} : characteristic diameter of the particle size curve of the sub-pavement layer (from Bezzola 2002).*

Author	Criteria	Description
Bathurst (1985)	$h / d_{84} < 1$	Large scale roughness
	1 $< h / d_{84} < 4$	Transitional roughness (but still macro-roughness)
	4 $< h / d_{84}$	Small scale roughness
Bray (1987)	$h / d_{84} < 1.6$	Jet- and wake dissipation
	1.6 $< h / d_{84} < 5.3$	Transition to jet and wake dissipation
	5.3 $< h / d_{84} < 10.5$	Transition to turbulent shear layer friction
	10.5 $< h / d_{84}$	Turbulent shear layer friction

Weichert et al. (2006) presents in their work on steep open channels a geomorphic inspired separation into micro-scale (a coarse armour layer), meso-scale (successions of steps and pools), macro-scale (successions of riffles and pools) and reach-scale (a pivot point at the outflow of the flume) features. Roughness or flow resistance parameters are

attributed to the first three geomorphic types whereas the fourth type has to be considered as a geometrical characteristic of the river.

In this study, macro-roughness and macro-rough flow resistance relate to the definition of Bathurst. The roughness is classified macro-rough (large scaled or intermediate scaled) when the flow depth divided by a characteristic size of roughness element remains lower than about 4. Flow resistance formulas and basic concepts of macro-rough flow resistance are presented in the following chapters for different domains: mountain streams and steep open channels (Weichert 2006); boulders and pebbles; bed forms in lowland streams, overland flows; vegetation, artificial roughness and particular developments. Up to here, the friction coefficients have been presented for laminar, smooth turbulent and fully rough as well as transitional flows as $1 / (f)^{0.5}$. In the domain of macro-rough flow, the friction coefficients are generally expressed as:

$$\frac{U}{u^*} = \sqrt{\frac{8}{f}} \quad (\text{eq. 2.21})$$

where U is the mean flow velocity of the section u^* the friction velocity.

2.1.5.1 Mountain streams and steep open channels with large relative roughness

Weichert (2006) reviewed flow resistance formulas in mountain streams and applied them to experimental step-pool data. The following sections of this § 2.1.5.1 are inspired from the above mentioned review. Some points are completed.

Logarithmic laws with modified constants

Various researchers proposed logarithmic formulas for flows with small relative submergence where vortex shedding at the roughness elements causes an important part of the total flow resistance. In comparison to the fully rough flow formula of Nikuradse, only the constants are varied in order to adjust the logarithmic law to the datasets obtained either by laboratory experiments or field measurements. Weichert (2006) gives a selection of equations of the type:

$$\sqrt{\frac{8}{f}} = \frac{1}{\kappa} \ln \left(a \frac{h}{d_c} \right) \quad (\text{eq. 2.22})$$

where d_c is a characteristic diameter, a a constant and κ the Von Karman integration constant.

Some of these formulas using the ratio h / d_{84} for the relative submergence and the Nikuradse formula for fully rough turbulent flow are compared in Figure 2-6. On one hand, the result shows that the formulas of Leopold et al. (1964), Bathurst (1985) and Hager (1992) give friction coefficients quite different from the Nikuradse (1933) formula as they have been developed for large relative roughness and under comparable conditions. For submergence ratios of h / d_{84} significantly less than 1, an important increase of the friction factor f is observed. The difference between the three formulas is

not significant. On the other hand, the formula proposed by Rice et al. (1998) provides friction factors quite similar to the Nikuradse formula which has been developed for fully rough turbulent flows. The difference between the formula of Rice et al (1998) and the other ones explains since the flow regime in natural channels obviously differs from the flow regime in constructed riprap-lined channels which has been investigated by Rice et al. (1998).

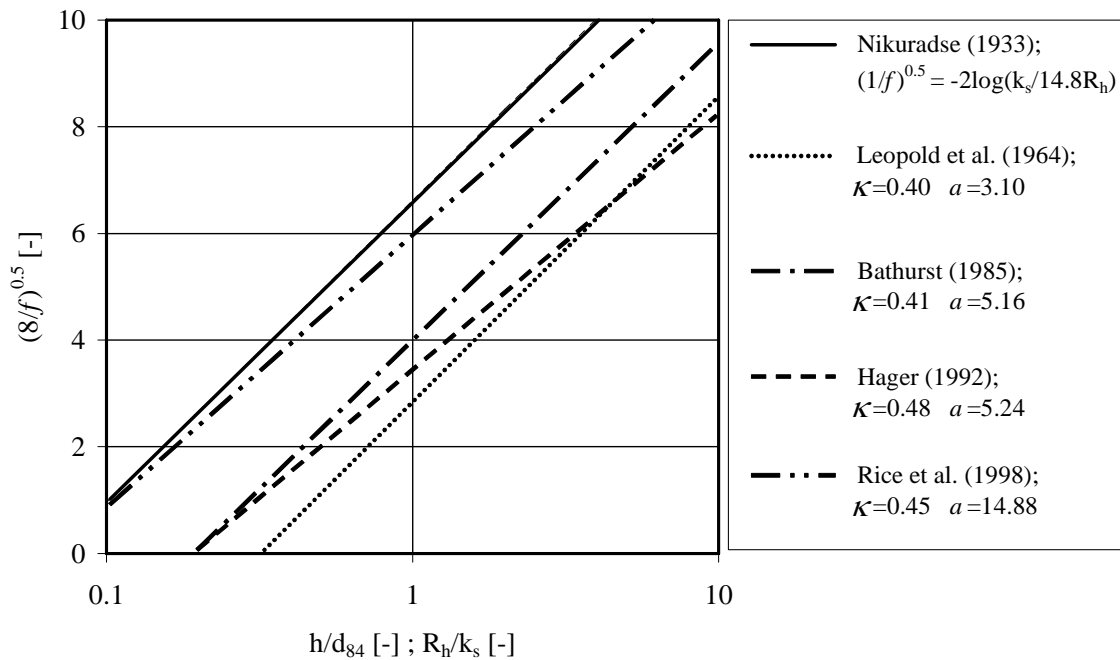


Figure 2-6: Comparison of different logarithmic laws for friction determination in mountain streams and steep open channels.

Modified logarithmic laws

Other logarithmic laws are modified in their form. They are based on correction terms (Table 2-6). Thompson and Campell (1979) as well as Bezzola (2002) apply the correction term to the right side of formula (eq. 2.22) whereas Smart and Jaeggi (1983) suggest considering an effective rather than a geometric slope.

Hybrid approaches consist in an adaptation of the constants of the fully rough flow formula as well as correction terms. As example, Ferro (1999) investigated the flow resistance of a gravel bed channel having bed arrangements characterized by different number of boulders. In a fitting procedure including two stages a first formula is proposed fitting best 464 data points:

$$\sqrt{\frac{8}{f}} = -0.854 + 15.74 \log\left(\frac{h}{d_{84}}\right) \tag{eq. 2.23}$$

where h is the flow depth and d_{84} the characteristic diameter of the particles size curve. In the second stage, this formula has been adapted using an empirical formula to esti-

mate the interception of the flow resistance law based on the characteristics of the bed layer and the boulders. The influence of the proximity to the condition of incipient motion is empirically described too.

$$\sqrt{\frac{8}{f}} = [b_0(\alpha) + 2.2610] + 15.74 \log\left(\frac{h}{d_{84}}\right) - 4.5739 \frac{\tau_*}{\tau_{*cr}} \quad (\text{eq. 2.24})$$

where $b_0(\alpha)$ is an empirical relationship describing the bed layer and the boulders (Ferro 1999), τ_* the Shields parameter and τ_{*cr} the critical Shields parameter. From this formula, it is easily understood that first the constants has been modified and secondly correction terms has been added.

Table 2-6: Modified logarithmic laws. Thompson and Campell (eq. 2.25) Smart and Jaeggi (eq. 2.26): S' : reduced slope; α_s & β_s : J. Bezzola (eq. 2.27): z_{Ro} : thickness of the roughness layer; c_r : correction parameter.

Authors	Formula	Correction term
Thompson and Campell (1979)	$\sqrt{\frac{8}{f}} = \left(1 - 0.1 \frac{k_s}{R_h}\right) \cdot 2.5 \ln\left(12 \frac{R_h}{k_s}\right)$	$\left(1 - 0.1 \frac{k_s}{R_h}\right)$
Smart and Jaeggi (1983)	$\frac{U}{u_*'} = \frac{U}{\sqrt{ghS'}} = 2.5 \ln\left(12.27 \frac{h}{\beta_s}\right)$	$\frac{S'}{S} = 1 - e^{\frac{-\alpha_s h}{d_{90} \sqrt{S}}}$
Bezzola (2002)	$\sqrt{\frac{8}{f}} = c_R \cdot 2.5 \ln\left(10.9 \frac{R_h}{z_{Ro}}\right)$	$c_R^2 = 1 - \frac{z_{Ro}}{h} ; \frac{h}{z_{Ro}} > 2$ $c_R^2 = 0.25 \frac{z_{Ro}}{h} ; 0 \leq \frac{h}{z_{Ro}} \leq 2$

Powerlaws

In addition to the logarithmic laws and modified logarithmic laws, many power laws have been developed for applications in alluvial open channel flows. The power laws relate mean flow velocity to discharge, slope, gravitational constant and characteristic diameter of the channel bed material. Most of them are dimensionally correct whereas others do not respect dimensions (e.g Rickenmann 1996). In general, they have good performance when used for conditions in which they have been developed but show only limited validity and performance when applied to other conditions or datasets.

Laws for macro-and meso-scale features

Finally, for the evaluation of friction of macro- and meso-scale features the concept of composite resistance can be applied. The skin friction is described by the concept of bed shear stress (logarithmic formulas) and the form resistance is expressed by the balance between hydrodynamic and resistance forces. For the practical description of flow

resistance it is often suitable to attribute the spill resistance (wake interference) and free surface distortion also to the form drag. The total friction coefficient becomes:

$$f_{total} = f_{grain} + f_{form} \quad (\text{eq. 2.28a})$$

where f_{total} corresponds to the overall friction coefficient, f_{grain} to the skin friction coefficient of the rough channel bed and f_{form} to the friction due to bed forms. This equation is based on the total shear stress $\tau_0 = \rho g R_h S_0$ and the decomposition of the slope into two components (Meyer-Peter and Müller 1948). It is important to distinguish the composite resistance concept describing the contribution of different phenomenon of a reach (skin friction, form drag) from the composite resistance for a section having different wall characteristics (same phenomenon, different roughness, see § 2.1.4). In the present experimental study, comparing the friction of a prismatic channel to a channel including macro-roughness at the channel side walls (large scale depression roughness leading to form resistance), the concept above will be used as follows:

$$f_m = f_{prism} + f_{MR} \quad (\text{eq. 2.28b})$$

where f_m corresponds to the overall friction. f_{prism} includes all effects contributing to the friction of the prismatic channel but without the macro-roughness elements. f_{MR} accounts for the additional friction due to the macro-rough channel side walls.

Functional relationships with Froude number

Within resistance laws, good correlations are sometimes found for approaches using the Froude number to predict friction coefficients. Nevertheless, as Froude number and friction coefficient are based on the same respectively very similar parameters, good correlation is an evidence and formulas using Froude number in order to explain friction coefficients should be avoided. The functional relationship between Froude number and friction coefficient is shown using the Weisbach-Darcy formula:

$$\frac{8}{f} = \frac{1}{S_f} \frac{U^2}{gR_h} \cong \frac{1}{S_f} Fr^2 \quad (\text{eq. 2.29})$$

Many logarithmic laws, modified logarithmic laws and power laws exist for the computation of the flow resistance in steep open channels. They are able to describe well the flow resistance when the relative flow depth is not too small and when the roughness is produced essentially on the channel bottom as it is the case in mountain rivers. Furthermore, the total resistance may be divided in a part due to skin friction and a part due to form resistance when describing macro-scale features. Functional relationships with Froude numbers should be avoided in resistance laws.

2.1.5.2 Boulders and pebbles

Bezzola (2002) describes in detail the flow around boulders and pebbles and the physi-

cal phenomena leading to the observed flow resistance. Experimental works with the goal to quantify the flow resistance of boulders and pebbles are done by Canovaro et al. (2003; 2004) respectively Canovaro and Solari (2005; 2006). They show results of flows over macro-roughness having different densities and arrangements (random and rows). Pagliara and Chiavaccini (2006a, 2006b) present an experimental study on rock chutes with protruding boulders having different arrangements (random and rows), densities and boulder surfaces (rounded surface and crushed surface). The formulas they developed relate to the meso-scale roughness mentioned in § 2.1.5.1 and are presented below.

The work of Canovaro and Solari (2006) is based on the separation of skin friction and form drag induced flow resistance and points out the following:

- The part of flow resistance due to macro-roughness induced form drag is maximal for pebble densities of 0.1 to 0.2. It reaches 70% to 80% of the total bed shear stress.
- The maximum of total flow resistance is reached within the same range of pebble densities and it is significantly higher than for a channel bed without pebbles or a channel bed completely covered with pebbles.

Using the data of the experimental work a new flow resistance formula taking into account the relative flow depth, the channel slope and the pebble density is proposed by Canovaro and Solari (2006). The outer function (eq. 2.30) includes three inner functions (eq. 2.30a; eq. 2.30b; eq. 2.30c):

$$\sqrt{\frac{8}{f}} = fn\left(\frac{h}{D_s}\right) \cdot [fn(S_0) \cdot fn(\Gamma)]^{D_s/h} \quad (\text{eq. 2.30})$$

$$\text{with: } fn\left(\frac{h}{D_s}\right) = 6.0 \ln\left(\frac{h}{D_s}\right) + 8.5 \quad (\text{eq. 2.30a})$$

$$fn(S_0) = 0.625 S_0^{-0.19} \quad (\text{eq. 2.30b})$$

$$fn(\Gamma) = [\Gamma^{0.75} + \exp(-1.7 \cdot \Gamma^{2.85})]^{-2} \quad (\text{eq. 2.30c})$$

where D_s represent the short diameter of the pebbles, h the flow depth, S_0 the channel slope and Γ the spatial density of pebbles defined as the number of pebbles divided by the maximum number of pebbles necessary to cover totally the channel bottom.

The work of Pagliara and Chiavaccini (2006a, 2006b) on rock chutes includes the analysis of the increase of the flow resistance due to the presence of boulders. The result shows that the presence of macro-roughness (boulders) increases the flow resistance as a function of the ramp slope, the boulder concentration and disposition and the boulders roughness. No significant influence was found for Froude and Reynolds numbers and the relative submergence h/R_b where h is the flow depth and R_b the mean boulder radius. The last finding concerning h/R_b is little surprising but seems valid for the tested range of parameters. Furthermore, this finding is in agreement with the conclu-

sions of Morris showing that the roughness spacing is the main parameter for the flow resistance (wake interference flow) and not the roughness height. Finally, the resistance formula proposed for the total resistance of rock chutes with protruding boulders by Pagliara and Chiavaccini (2006a) is:

$$\sqrt{\frac{8}{f_{total}}} = 3.5(1 - \Gamma)^c S_0^{-0.17} \left(\frac{h}{d_{84}} \right)^{0.1} \quad (\text{eq. 2.31})$$

where Γ presents the boulder concentration, S_0 the ramp slope, h the flow depth, d_{84} the material size of base material for which 84% of material is finer. c is a coefficient varying between -1.6 and -3.0 depending on the disposition (random or rows) and surface (rounded or crushed) of the boulders.

Both formulas (eq. 2.30) and (eq. 2.31) point out the dependence of the flow resistance from the spatial density of pebbles respectively the concentration of boulders. However, both distinguish essentially in the choice of another important parameter which is the relative roughness height. In the case of formula (eq. 2.30) the pebble size is used to determine the relative flow depth whereas the pebble size has no influence in formula (eq. 2.31) where a characteristic diameter of the base material is considered.

Canovaro and Solari (2006b) present the dimensionless Chezy coefficients and the ratio of drag shear stress to the total shear stress $\tau_{drag} / \tau_{total}$ as a function of the ratio strip height (H) to strip wavelength from crest to crest (λ) of regularly arranged strips of pebbles. The maximum values of total resistance as well as the maximum proportion of form drag have been found for values of H / λ ranging around 0.15. The maximum flow resistance and form drag is explained by similar effects than observed by Morris considering wake interference flow causing abnormally intense turbulence and mixing. Furthermore, statistical analysis of the ratio H / λ in natural step-pool beds showed that the highest probability occurs for ratios H / λ between 0.10 and 0.16. This ratio is close to the one maximizing the flow resistance. It can therefore be concluded that natural step-pool sequences tends toward configurations maximizing flow resistance in order to achieve bed stabilization (Abrahams et al., 1995).

From the findings of works with pebbles and boulders it should be remembered that high (macro)-roughness density does not automatically mean high flow resistance. Particular arrangements can lead to maximum flow resistance. The concept of composite flow resistance is applied with success to boulders and pebbles in steep channels. The part of the shear stress attributed to form drag can reach more than 80% of the total shear stress.

2.1.5.3 Bed forms in lowland alluvial streams

Such as for steep open channels, bed forms inducing macro- or form roughness can also occur in lowland alluvial streams. Bed forms and roughness of mountain streams and torrents are mainly related to wide distribution of sediments ranging from sand to large

boulders which leads to a coarse armour layer protecting the underlying material from erosion and to extremely stable channel beds. Bed forms of lowland alluvial streams have been reviewed by Rosier (2007). Bed forms in lowland streams are mainly related to the transport of sediments which are of much smaller size than the ones found in mountain streams. For a first and simple estimation, the Froude number and the sediment transport might serve as a classification parameter (Graf and Altinakar 1995). No sediment transport conditions are associated with plane bed conditions. Sediment transport conditions regarding the Froude number are leading to dune and mini dune ($Fr < 1$), plane bed ($Fr \approx 1$) and antidune ($Fr > 1$) bed form types. Other classifications are not necessarily related to the Froude number but lead to almost the same bed forms. Classification schemes have been proposed by several authors (e.g. Simons and Richardson, 1966).

The shape and dimensions of dunes, the large scale roughness elements considered hereafter, are estimated according van Rijn (1993) or Yalin and de Silva (2001). The proposed relationships are based on flume and field data and points out that typical dune height can reach up to 50% of the flow depth. Such large scale roughness does obviously increasing the flow resistance. Form losses caused by bedforms have to be added to the skin friction.

Assuming that the total or effective dimensionless Chezy resistance factor C_{adim} is due to the sum of friction-losses and energy losses generated by the sudden expansion, C_{adim} is calculated as follows (Yalin and da Silva, 2001):

$$\frac{1}{C_{adim}^2} = \frac{1}{C_{adim,f}^2} + \frac{1}{C_{adim,\Delta}^2} = \frac{1}{C_{adim,f}^2} + \frac{1}{2h} \cdot \underbrace{\left(\underbrace{\delta_r^2 \cdot \Lambda_r}_{\text{ripples}} + \underbrace{\delta_d^2 \cdot \Lambda_d}_{\text{dunes}} \right)}_{\text{form}} \quad (\text{eq. 2.32})$$

where $C_{adim,f}$ is the dimensionless friction factor related to grain roughness and $C_{adim,\Delta}$ the dimensionless bed form resistance factor. h is the flow depth. δ is the steepness and Λ the length of the ripples (r) respectively the dunes (d).

Van Rijn (1984) assumed that the effective roughness height of Nikuradse (k_s) can also be divided into a grain related and a form related part. The total effective roughness (k_s) is proposed to be determined by means of:

$$k_s = \underbrace{3 \cdot d_{90}}_{\text{grain}} + \underbrace{20 \cdot \gamma_r \cdot \Delta_r \cdot \delta_r + 1.1 \cdot \gamma_d \cdot \Delta_d \cdot (1 - \exp(-25 \cdot \delta_d))}_{\text{form}} \quad (\text{eq. 2.33a})$$

where d_{90} corresponds to the material size of the top-layer for which 90% of material is finer. δ_r is the steepness of the ripples, Δ_r is the ripple height and γ_r is a ripple presence factor. δ_d is the steepness of the dunes, Δ_d is the dune height and γ_d is a form factor expressing the influence of dune form on roughness height.

The total dimensionless Chezy resistance coefficient is then calculated as:

$$C_{adim} = 18 \cdot \log\left(\frac{12 \cdot R_b}{k_s}\right) \quad (\text{eq. 2.33b})$$

in which R_b is the hydraulic radius of the bed according to the side wall correction procedure of Vanoni and Brooks (1957).

The main conceptual difference of the approach of van Rijn compared to the approach of Yalin and da Silva is the manner of superposition of skin friction and form drag effects. Whereas Yalin and da Silva only assume that the overall shear stress τ_0 is divided in a skin friction induced shear stress τ_0' and a form drag induced shear stress τ_0'' van Rijn also assumes that the effective roughness heights of Nikuradse are algebraically additive.

Large scale or macro-roughness can also appear in lowland streams as it is revealed in several research works. The concept of composite roughness is considered to be applicable. From the physical point of view, methods separating skin friction and form induced drag are preferable compared to methods based on integral parameters. From the same point of view it may be preferable summing dimensionless friction coefficients rather than equivalent sand roughness values having limited physical meaning.

2.1.5.4 Overland and overbank flow




Overland flow is generally characterized by very low flow depths and velocities and important roughness size (large scale roughness) leading to a disturbed character of the flow. An increase of flow depth and roughness can contribute significantly to more complex flow features, especially when comparing to one dimensional channel or pipe flow conditions for which the widely applied Weisbach-Darcy theory was developed. Lawrence (1997) and Lawrence (2000) points out that for such flow the average degree of inundation consists to the main dimensionless parameter governing overland flow resistance. Three flow regimes are distinguished – the well inundated, marginally inundated and partially inundated flow regime. Table 2-7 presents the flow regimes regarding the average degree of inundation and the proposed flow resistance formula using the inundation ratio Λ as classification parameter.

When regarding formulas (eq. 2.34) to (eq. 2.36) one can show that:

- The architecture of the well inundated flow formula corresponds to the one of fully rough turbulent flow. As this flow regime actually presents flow in presence of micro-scale rather than macro-scale roughness, open channel flow resistance is reasonably applied.
- The second flow regime represents the state in which the flow field is not anymore one dimensional. In this regime, flow separation occurs in the lee of the roughness elements. Jet and wake dissipation are introducing additional flow resistance. The presented formula for this regime was obtained from a similar mixing length model than proposed for turbulent flow in the presence of a boundary.

- When the flow becomes increasingly shallow, the effect of the single roughness elements on the flow resistance becomes important. An approximant relationship between the frictional resistance and the surface roughness is derived using drag force based equilibrium between gravitation and friction force. Formula (eq. 2.36) has been obtained for hemispherical particle of radius $r = k$ as it is assumed that such elements are the most probable in overland flow problems. Nevertheless, analogues formulas could be derived for any other partially inundated roughness elements.

Table 2-7: Well inundated, marginally inundated and partially inundated flow regimes with according flow resistance formulas of Lawrence (1997). k : characteristic roughness height; h : flow depth; Λ : inundation ratio. \underline{P} is the fractional cover or portion of the surface covered by large scale roughness elements and C_D a mean drag coefficient.

Flow regime	Domain of Λ	Flow resistance equation
Well inundated 	$\Lambda = h/k > 10$	$\sqrt{\frac{8}{f}} = \frac{1}{\kappa} \left(\ln \left(\frac{1}{2} \Lambda \right) - 1 \right) + B$ (eq. 2.34)
Marginally inundated 	$10 > h/k > 1$	$\sqrt{\frac{8}{f}} = 1\Lambda \quad \text{or} \quad f \cong 10\Lambda^{-2}$ (eq. 2.35)
Partially inundated 	$1 > h/k$	$f \approx \frac{8}{\pi} \underline{P} \cdot C_D \cdot \min \left[\frac{\pi}{4}; \frac{h}{k} \right]$ (eq. 2.36)

The application of the proposed model of Lawrence (1997) of overland flow frictional resistance to collected data showed quite good agreement (Figure 2-7). Important increase of friction coefficients with the increase of the inundation ratio was found for $0.1 < \Lambda < 1$ and still moderate increase for $1 < \Lambda < 2$. For inundation ratios of $2 < \Lambda < 10$, data are in agreement with the marginally inundated flow resistance and for $\Lambda > 10$ the well inundated resistance formula can be used.

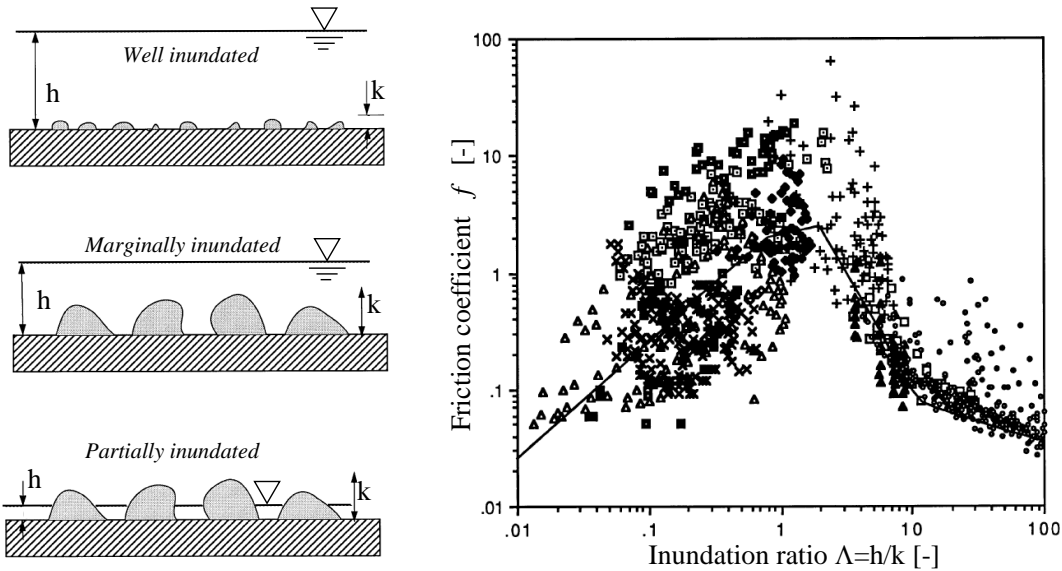


Figure 2-7: Overland flow classification according Lawrence (1997, original figure) and application of formulas to field data from different authors (see Lawrence 1997).

Dubois (1998) investigated partially and marginally inundated flow experimentally using marbles (macro-roughness elements) of same diameter D but different densities p .

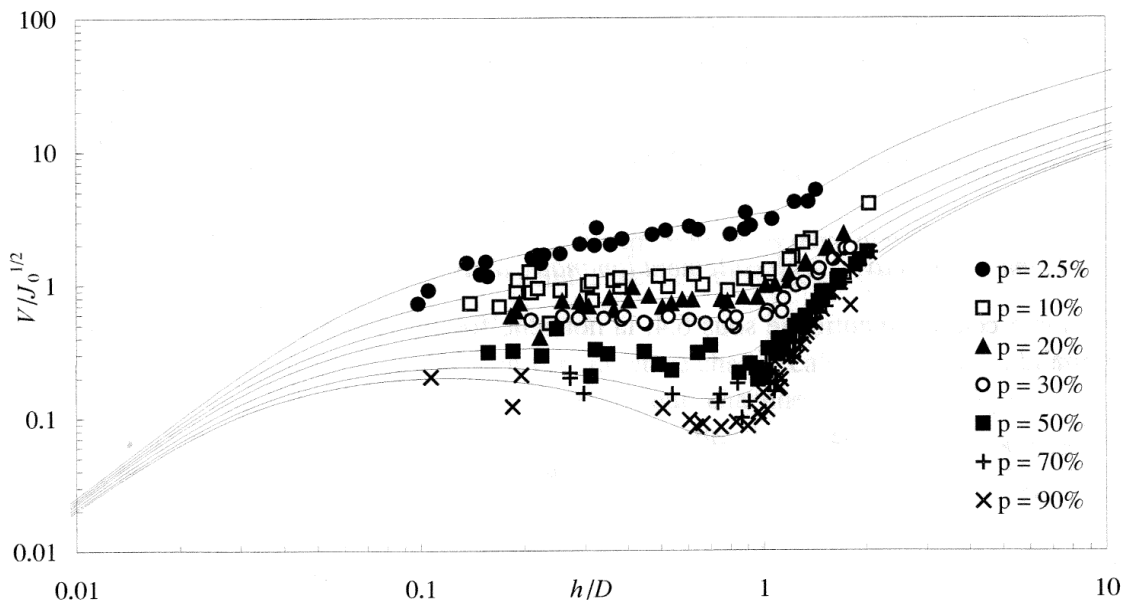


Figure 2-8: Flow resistance over a rough surface according Dubois (1998, original figure) where $V/J_0^{0.5} = (8gR_h/f)^{0.5}$ characterizes the flow resistance.

From the experiments, a new relationship is proposed to compute head loss for partially and marginally inundated flows over rough surfaces (Figure 2-8). For sufficiently dense marbles arrangement, flow resistance is increased for inundations ratios h/D close to the unity.

From the developments of Lawrence (1997, 2000) it is important to note that form drag based resistance laws can be applied with success to flows becoming increasingly shallow. For inundation ratios $h/k < 1$ an important increase of the friction coefficient is confirmed with the increase of the inundation ratio up to $h/k = 1$.

2.1.5.5 Vegetation

Many work has been done on flow resistance of vegetation. The following review is non exhaustive but summarizes some basic concepts. Honsowitz (1988) summarized various aspects influencing the hydraulic capacity of revitalized river reaches. One important aspect is to consider the vegetation. From the different propositions taking into account the rigid vegetation the ones bases on drag coefficients are presented hereafter as they are of relevance for macro-rough flow resistance. In case of flexible vegetation, the flow resistance estimation is usually based on adaptations of logarithmic laws (Kouwen et al. 1969), power laws (Carollo et al. 2005) or form drag based models too (Indlekofer 2003).

When big plants are considered as many rigid single elements, friction coefficients are calculated using following formula (Lindner, 1982):

$$f_{veg} = \frac{4A_{p,i}}{a \cdot b} C_{d,i} \quad (\text{eq. 2.37})$$

where $C_{d,i}$ is the drag coefficient, $A_{p,i}$ the projected area of the element in direction i of the flow, a and b the distance between single (roughness) elements parallel and perpendicular to the flow direction and f_{veg} the friction coefficient due to the vegetation. The difficulty in formula (eq. 2.37) is the estimation of $C_{d,i}$.

An earlier work of Petryk and Basmajian (1975) for application to rigid single elements, proposes to estimate a Manning-Strickler coefficient for vegetation zones $K_{st,B}$. The approach is based on the balance of the forces acting on a control volume and leads to the formula:

$$K_{st,B} = \frac{1}{\sqrt{\frac{C_d R_h^{4/3} \cdot \Sigma A_i}{2gF\Delta} + \frac{1}{K_{st,w}}}} \quad (\text{eq. 2.38})$$

where C_d is the mean drag coefficient for all elements, A_i the projected area of the single element, R_h the hydraulic radius of the vegetated zone; F the flow area of the vegetated zone, Δl the length of the control volume and $K_{st,w}$ the Strickler coefficient of the section

without roughness elements.

Pasche and Rouvé (1985), Mertens (1989), Nuding (1991, 1998) and Schröder (1999) present methods for the estimation of the hydraulic capacity of vegetated channel sections. The common point of their propositions is to consider the boundary between the main channel and the vegetated zone as an imaginary wall. The flow resistance calculation in the vegetated zone is based on the form drag of the vegetation. Mertens (1989) divides the channel which is partially covered by vegetation into 4 areas: 1. in the vegetation next to the channel bank; 2. in the vegetation next to the main stream; 3. in the main stream next to the vegetation; 4. in the main stream far away from the vegetation. Areas 2 and 3 are characterized by macro-turbulence with intense mass- and momentum-exchange. For practical reasons Mertens (1989) proposes to simplify the computation of the hydraulic capacity by considering three different areas only: 1'. the areas inside the vegetation; 2'. the area of the main flow influenced by the roughness of the bed; 3'. the areas of the main flow but influenced by the macro-turbulence induced by the vegetation. Whereas the friction coefficients of areas 2' and 3' are calculated using logarithmic laws with equivalent sand roughness values, the friction coefficient f_B of the area inside the vegetation 1' is calculated using following formula:

$$f_B = f_w + f_{veg} = f_w + 4C_d \frac{h_{veg}}{a} \frac{d}{b} \quad (\text{eq. 2.39})$$

where C_d is the mean drag coefficient for all elements, h_{veg} the mean flow depth in the area with vegetation, d the mean diameter of the roughness elements, a and b the distance between single roughness elements parallel and perpendicular to the flow direction and f_w the friction coefficient due to the skin friction in the zone with vegetation. The vegetation induced part of friction f_{veg} corresponds to the formula (2.24) proposed by Lindner (1982). The basic concepts of the methods of Pasché and Rouvé, Mertens and Nuding are commonly used in practice for the case of unsubmerged rigid vegetation. Many works have been done allowing estimating correctly drag coefficients related to channel vegetation.

Musleh and Cruise (2006) presented experimental results showing increasing drag and friction coefficients with increasing flow depths. The presented drag coefficients range around 15 and are quite high. They probably include effects as interference of the wakes generated at single elements which has been arranged densely for the experiments.

For the estimation of the hydraulic capacity of channels covered with vegetation, the concept of composite roughness can be applied. Rigid vegetation is treated as the sum of obstacles producing form drag. An area influenced by macro-turbulence leading to mass and momentum exchange is located at the interfaces between the main channel and the vegetated parts of the channel section.

2.1.5.6 Particular developments: k - and d -type roughness (Jiménez 2004); drag- and head-loss coefficient model (Smart 2004); artificially roughened bottoms

Some particular developments, difficult to classify in the previous chapters, are shown hereafter. The first one concerns a review of turbulent flows over rough walls by Jiménez (2004) distinguishing into k - and d -type roughness. A second development from Smart et al. (2004) concerns drag coefficient and head-loss coefficient models of gravel bed rivers having relatively large roughness. Finally, two works, one experimental, one numerical with artificially roughened bottoms with transverse bars are shown (Lyapin 1994, Leonardi et al. 2003).

Jiménez (2004) defines the k -roughness as the roughness for which viscosity is irrelevant and the equivalent sand roughness value is proportional to the dimensions of the roughness elements. The ratio of the equivalent sand roughness to the geometric roughness height k_s/k depends on the geometry of the roughness elements and on the solidity (surface covered by roughness elements divided by the total surface). When considering individual drag coefficients C_d for the different forms of individual roughness elements, a relationship between the solidity and the normalized equivalent sand roughness appears. Equivalent sand roughness k_s reaches up to 10 times the geometric roughness height k for solidity close to 0.15 (Figure 2-9).

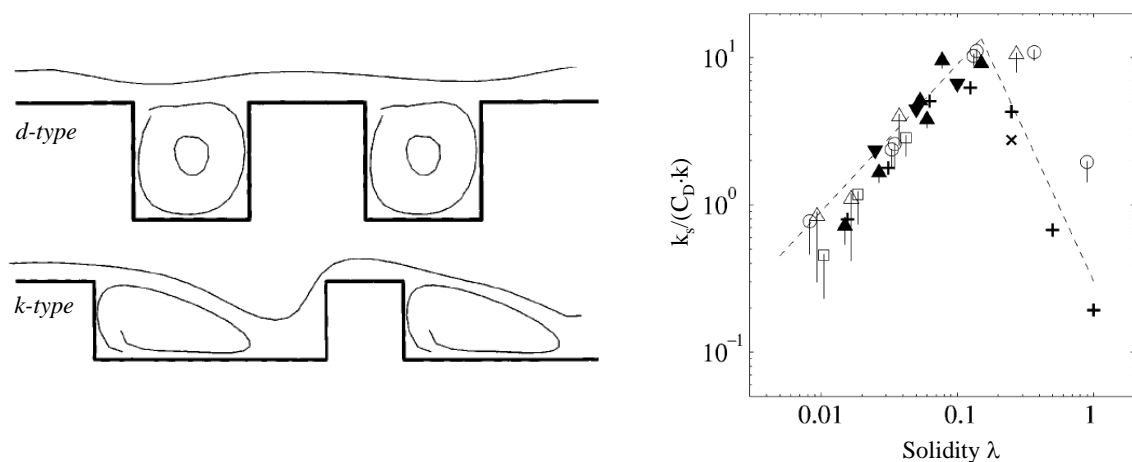


Figure 2-9: Left: d - and k -type slotted walls. Flow is from left to right. Right: Normalized equivalent roughness against solidity. Open symbols, rounded elements (\circ spheres, \triangle cones, $C_D = 0.3$; \square spherical segments, $C_D = 0.13$) from Schlichting (1936). For all others, $C_D = 1.25$. \blacktriangle , spanwise fences (Schlichting 1936); \blacktriangledown spanwise fences (Webb et al. 1971); $+$ spanwise cylinders (Tani 1987); \times spanwise square bars (Bandyopadhyay 1987). The dashed lines have logarithmic slopes 1 and -2. Both figures are taken from Jiménez (2004)

Mainly the data of Schlichting (1936) have been used by Jiménez (2004). d -type roughness elements are defined as grooves which are about square. The equivalent sand roughness values should correlate to the boundary layer thickness (function of the Reynolds number) and are independent on the geometric roughness height. Perry et al. (1969) proposes such relationship for boundary layers over plates roughened by narrow

spanwise square grooves as $k_s = 0.02 \cdot \delta$ where δ is the boundary layer thickness. However, Jiménez (2004) clearly shows that such simplified equation only applies to the experiments of Perry. For other experiments with depressions the equivalent roughness height k_s is not independent on the geometrical roughness height k .

Jiménez (2004) suggests an explanation for the dip and rise of the Nikuradse curves. He expects that roughness elements on a surface have two effects. Principally, they create extra form drag (k -type roughness) but they also influences the viscous generation cycle (d -type roughness) which decreases skin friction. Only when the Reynolds number increases, this viscous cycle is completely destroyed and the form drag takes over.

Smart et al. (2004) propose two models for calculating friction coefficients of relatively rough flow. After the introduction of a volumetric hydraulic radius R_v (volume of water per unit area of bed) a drag coefficient model and a head-loss coefficient model are developed. Such models are accurate for the calculation of friction induced by form drag. The drag coefficient model starts from the drag force equation. Several hypotheses lead to a conceptual formula of the type:

$$\sqrt{\frac{8}{f}} = \frac{U}{U^*} \cong \left(\frac{d_x}{d_z}\right)^{0.5} C \cdot fn\left(\frac{R_v}{d_z}\right) \quad (\text{eq. 2.40})$$

where d_x respectively d_z are the roughness element streamwise respectively vertical size dimension and C the general flow resistance coefficient including the drag coefficient C_d , the sediment shape and the aerial packing density. fn describes a function which is investigated by measuring the parameters U/U^* and d_x/d_z .

The head-loss coefficient model is based on the commonly used loss coefficient in hydraulic situations with complex flow geometry. The head-loss is expressed by $\Delta H = k(U^2/2g)$. Smart applied formula (eq. 2.40) on the flume data and finally obtains two different formulas for use with medium and large scale roughness:

$$\text{medium scale:} \quad \sqrt{\frac{8}{f}} = \frac{U}{U^*} = \left(\frac{d_x}{d_z}\right)^{0.5} C \cdot \left(\frac{R_v}{d_z}\right)^{0.5} \quad \text{for } d_z/R_v < 0.03 \quad (\text{eq. 2.40.a})$$

$$\text{large scale:} \quad \sqrt{\frac{8}{f}} = \frac{U}{U^*} = \left(\frac{d_x}{d_z}\right)^{0.5} C \cdot \left(\frac{R_v}{d_z}\right)^{1.25} \quad \text{for } d_z/R_v \geq 0.03 \quad (\text{eq. 2.40.b})$$

where $C = 3.5$ is a general coefficient. These two formulas were found to perform for flows over rough beds without penetration of roughness elements into the free surface.

Lyapin (1994) investigated experimentally macro-scale ($h/k < 5$) bottom rib roughness in a 5.3 m long channel. Different ratios between the rib height k and the distance between the ribs L have been investigated. The flow either expands ($L/k < 9$) or reattaches ($L/k \geq 9$) to the bottom in the zone between two ribs. Friction coefficients have been estimated based on velocity profiles. Furthermore, computation of the flow resis-

tance is proposed applying an experimental correction factor to a mean volume roughness height in order to find the absolute roughness k_s used in logarithmic laws. Friction coefficients were found higher in the case of reattachment of the flow to the bottom compared to expansion of the flow only.

Leonardi et al. (2003) investigated the same problem, the macro-scale bottom rib roughness, numerically. Thanks to the numerical simulations, they got detailed insight in the pressure distribution around the macro-roughness elements and hence the form drag. The results show that the flow resistance is mainly produced by form drag for ratios of $L/k > 3$ with a maximum of total flow resistance for $L/k = 7$.

The particular developments presented above allow defining k- and d-type roughness elements. In the case of k-type roughness, the equivalent roughness height k_s can reach up to 10 times geometric roughness height corrected by the drag coefficient ($C_d k$) for a solidity of 0.15. The equivalent roughness height of d-type roughness elements is found difficult to relate to the geometric roughness height. The second development points out the need of conceptual models (form drag coefficient respectively head-loss coefficient models) for predicting flow resistance of large scale roughness. In such case, it might be possible to predict accurately friction coefficients without calibration coefficients. Finally, for flow over macro-scale bottom rib roughness, the flow resistance depends on the ratio of the distance between the ribs and the height L/k .

2.2 Flow in presence of rectangular cavities - effects of cavities

2.2.1 Introduction

Since important and quite systematic cavity oscillations have been observed during the experiments with axi-symmetric rectangular widenings, in the following sections a review about cavity flow and cavity oscillations is given.

Many studies exist in hydraulic engineering on groin fields, river embayments (side cavities in open-channel flows), harbours and cavities. Whereas the studies on the first three topics are related to the flow of water, the studies of flow over cavities also deals with other fluids, especially with air in the field of aeronautics.

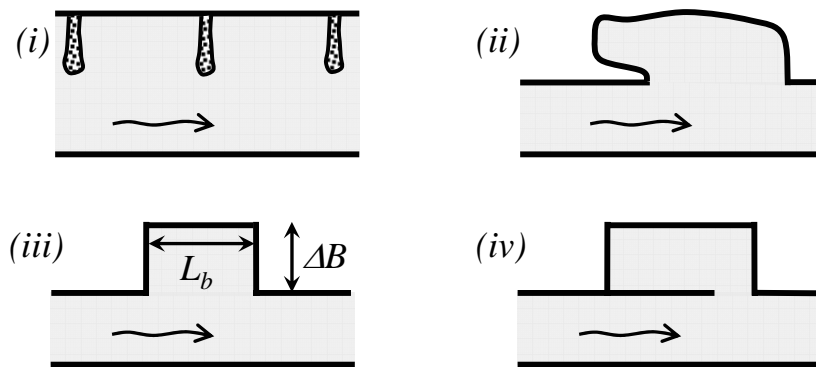


Figure 2-10: Groynes (i), river embayments ("Wando") (ii), cavities (iii) and harbours (iv). ΔB : cavity depth, L_b : cavity length.

In the research field of flow over cavities, the studies generally deal with free shear layer oscillations, feedback mechanisms, resonance phenomenon and passive or active open-loop control schemes (Rowley and Williams 2006, Rockwell and Naudascher 1978). In river embayments (also called "Wando" in Japanese rivers; Nezu and Onitsuka 2002, Muto et al. 2000) coherent horizontal vortices are generated by the shear instability between the main channel and the embayment. By looking at studies on emerged groin fields (McCoy et al. 2006, Weitbrecht 2004, Uijttewaal et al. 2001) the main researches are dealing with the mass-exchange between main channel and groin fields, sedimentation of groin fields, pollutant transport phenomenon and navigation. Finally, studies on harbour hydrodynamics (USACE 2002, Wilson 1972, van Rijn 1994) show the importance of geometry and boundary conditions on the formation of unsuitable seiches in harbours. Even if every of the above mentioned field has its particularities, some similarities can be identified:

- The most important geometrical parameter influencing the flow pattern is the ratio between the cavity depth (ΔB) and the cavity length (L_b).
- The flow in the cavities (or embayments, groin fields) is often influenced by the vortex shedding at the leading edge.

- Recirculation of the flow in the cavity (or embayment, groin field) can induce instabilities leading to an instantaneous flow field which is very different from the mean flow field.
- Surface oscillations can be observed for certain geometrical configurations and hydraulic conditions in case of free surface flow of incompressible fluids (Naudascher 1963, Muto et al. 2000, Nezu and Onitsuka 2002, Wirtz 2004, Ohomoto et al. 2005).

The literature review divided into cavity flow, groin fields and embayments as well as harbours is presented in the following chapters.

2.2.2 Cavity flow

Cavity flow is often unstable and oscillating. Rockwell and Naudascher (1978) grouped unstable flow past cavities into:

- Fluid-dynamic oscillations, where the instability of the shear layer is enhanced through a feedback mechanism.
- Fluid resonant oscillations, where resonance conditions associated either with the compressibility of the fluid or the free surface standing wave phenomena are responsible for the instability.
- Fluid-elastic oscillations, where the interaction with elastic displacement of the boundary leads to the instabilities.

In the case of open channel flow, the wavelength of gravity waves is of the same order of magnitude or smaller than the cavity characteristics L_b or ΔB and fluid resonant cavity oscillations can be present. If $\Delta B / L_b$ is small (shallow cavity), longitudinal standing waves may exist. If $\Delta B / L_b$ is large (deep cavity), transverse waves may be present. Fluid-resonant oscillations of a deep cavity at free surface flow are discussed by Naudascher (1963) for $\Delta B / L_b = 0.5$. Two frequencies of oscillations occurred, one due to the shear-layer instability-feedback mechanism and the other due to a transverse standing wave. Furthermore, resonant oscillations can increase cavity induced drag by 250% if external flow is subsonic¹ (MacGregor and White 1970). Rockwell and Naudascher (1979) mentioned that at high speeds, where the acoustic wavelength is of the same order than the impingement length L_b , consideration of the acoustic speed becomes important. On the other hand, for nearly all oscillations in liquids, the impingement length L_b is much smaller than the acoustic wavelength λ and therefore $L_b / \lambda \ll 1$. In this case, the source and upstream propagation of perturbations may be treated as purely hydrodynamic. Gharib and Roshko (1987) pointed out the difference between the self sustained oscillation mode (low drag regime), where the cavity shear layer stagnates at the downstream corner, and the wake mode (medium drag regime) where large scale motion exist across the line cavity/main flow respectively across the channel centreline in case of two-dimensional flow with axi-symmetric cavities. The

¹ External flow means the main flow along the cavity. When the fluid is water, subsonic conditions are always given in a reasonable field of applications.

wake mode is a purely hydrodynamic case characterized by flow recirculation in the cavity. For the flows studied by Gharib and Roshko (1987) the flow oscillated at the wake mode at ratios $L_b / \Delta B > 1.3$. In addition to the aspect ratio $L_b / \Delta B$, the upstream boundary layer has some importance on the cavity flow conditions. Nevertheless, Rowley et al. (2002), mentioned that as the length or depth of the cavity (relative to the upstream boundary-layer thickness) and/or Mach and Reynolds numbers are increased the flow is characterized by a large-scale vortex shedding from the cavity leading edge. The flow becomes periodic in time, with the fundamental period corresponding to the vortex shedding from the leading edge. The independence of this phenomenon from Mach number indicates that the wake mode is not the result of an acoustic feedback but the feedback is provided by the recirculation of the flow in the cavity, leading to an absolute instability. The main differences between the shear layer and wake mode are

- that the mean streamlines above the cavity are deflected for the wake mode,
- that the flow in the cavity is significantly more recirculating with an impingement point occurring at the cavity downstream wall for the wake mode,
- that the shear layer in case of wake mode is not fixed on the downstream cavity edge.

In addition Rowley et al. (2002) found that growing amplitudes of shear-layer oscillations can initiate wake mode after the oscillations have reached a certain threshold and that the wake mode is characterized by intense oscillations, which are an order of magnitude larger than for the shear layer mode.

Reviews of jet-edge oscillations and cavity oscillations show that prediction of oscillation frequency are achieved with reasonable success for certain geometries (Rockwell and Naudascher 1979). Typically, the frequency of oscillations is expressed in terms of Strouhal number St which is defined as:

$$St = \frac{f \cdot L_b}{U} \quad (\text{eq. 2.41})$$

where L_b is the cavity length (or another characteristic length), U the free stream mean velocity (or another characteristic velocity) and f the frequency of a phenomenon reproducing regularly. Jet-edge, cavity-edge and mixing-layer-edge oscillations show all similar characteristics of frequency jumps with the dimensionless length of impingement (Strouhal number). For shear layer mode oscillations, there is quite a lot of scatter in the measured frequencies at low Mach numbers but in general the data from experiments in water are fairly consistent (Rowley et al. 2002).

The amplitude of oscillations is generally more difficult to predict. Nevertheless, in several studies, peak excitation has been found when oscillations of the shear layer are amplified due to cavity acoustic modes (East 1966, Erickson et al. 1986, Ziada 1994). Typical Strouhal numbers based on the cavity length are $St = 0.3-0.4$ or $St = 0.6-0.9$. Excitation near $St = 0.4$ is characterized by a single vortex in the branch mouth and $St = 0.8$ by two simultaneous vortices (Erickson et al. 1986 ; Ziada 1993). In case of a

free surface deep cavity flow, peak excitations may be observed at the resonant cavity frequency due to a transverse standing wave Naudascher (1963).

2.2.3 Groyne fields and embayments

Flow fields of embayments (also called "Wandoo") and groin fields at emerged situation are quite similar since both are producing shear layer instability at the interface between the main stream and the dead zone which has a circulating flow. Muto et al. (2000) showed that the aspect ratio $\Delta B / L_b$ of the embayment determines the shape and stability of circulating flow. This stability itself has an influence on the mass and momentum exchange coefficients. Therefore, the eddy behaviour is of big importance. Weitbrecht and Jirka (2001) showed that the mass exchange is related to the aspect ratio $\Delta B / L_b$ of a dead zone as well. In general the mean flow in an emerged groin field is dominated by a large single eddy for $0.5 < \Delta B / L_b < 1.5$. For aspect ratios of $\Delta B / L_b < 0.5$ (shallow cavity) a second eddy emerges in the upstream corner of the groin field. For aspect ratios $\Delta B / L_b > 1.5$ the main eddy is splitting into two eddies in the transverse direction (deep cavity). For very long distances between groins, reattachment of the flow is possible which is leading to insufficient bank protection and difficulties for the navigation (Weitbrecht 2004). Even if the mean flow pattern in the groin fields can show a stable two gyre situation, the instantaneous flow field shows a different behaviour. It happens that the gyres are moving in lateral and longitudinal position, which can lead to alternating flow velocities in the main stream. Similar phenomena have been observed as example by Uijttewaal et al. (2001). Large structures are generally generated at the head of a groin or at the leading edge of an embayment. The path of these structures is not always the same. Sometimes they get trapped in the dead zone and sometimes they travel further downstream. This mechanism governs the mass exchange between the main stream and the dead zone and could be compared to the wake mode of cavity flow. For very large aspect ratios $\Delta B / L_b$, Weitbrecht and Jirka (2001) found increased exchange coefficients which are attributed to oscillation effects. The whole water body in a dead zone can start to swing back and forth which leads in this case to additional virtual exchange with the main channel. Nezu and Onitsuka (2002) mentioned the importance of side-cavity open-channel flows which be observed at the riverbank in some Japanese rivers for the fields of river engineering and ecosystem. Such as for the studies mentioned above, coherent horizontal vortices are generated by the shear layer instability between the main channel and the open-channel side-cavity (also called Wandoo).

In several Japanese studies, water surface fluctuations near the spur dikes have been measured or investigated using a water-wave gauge as for example shown in Chen and Ikeda (1996), Ikeda et al. (1999) and Nezu and Onitsuka (2002). Kimura et al. (1997) have found that an amplitude of water surface fluctuations in a Wando increases with an increase in the Froude number. Nezu and Onitsuka (2002) found in her study that the free surface in the Wando is rising when the surface in the main channel is falling, and vice versa. The period of the falling and rising of the water surface was found in good

agreement with the seiche generated in semi-closed open-channel flow.

Studies on groin fields or embayments are generally related to one single cavity or spur dikes on one channel side. Nevertheless, Ohomoto et al. (2005) showed for axi-symmetric spur dikes with an aspect ratio of $\Delta B / L_b = 0.5$ and an expansion ration $ER = 2$ remarkable water surface oscillations in the spanwise direction of the flow (12% of mean flow depth) whereas nearly no oscillations have been observed for the non-symmetric case. The period of water surface oscillation was almost equal to the natural period of sloshing in a rectangular container. The water surface oscillation have been attributed to the interaction of large scale eddies formed in the spur dike zones along both sides of the channel and was probably caused by the separation eddies behind the first spur dike. The same phenomena are investigated and described for prototype scale groin fields at the Elbe-River in Germany (Wirtz 2004).

2.2.4 Harbours

Water surface oscillations can also be observed in harbours where they are attributed to the response of an enclosed or semi-enclosed water body to external forcing. The natural period of these water surface oscillations (also called seiches) is depending on the length and depth of the basin (of the water body) and, as different wavelengths exists for each water body, on the oscillating mode. Seiches with different modes can occur together in a system, however, the uninodal, fundamental oscillation is usually dominant (Wilson 1972).

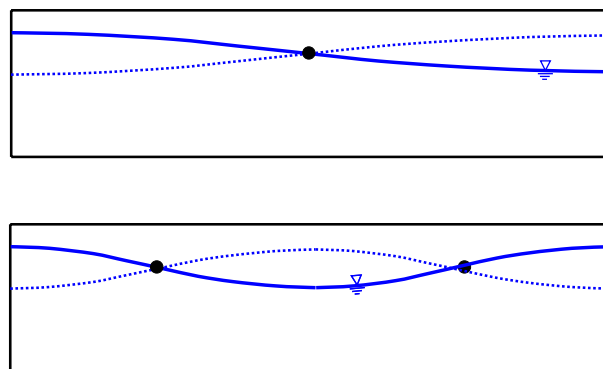


Figure 2-11: First and second mode of seiches of a confined water body.

In general, the causes for seiches are air pressure fluctuations, wind at the surface, heavy rain, snow or hail over a portion of the water body or a flood of a river at one end of the water body. In particular, Sorensen (1978) found that eddies, generated by the currents moving past a harbour opening, may also cause seiches inside the harbour. Seiches can occur in closed and semi-enclosed water bodies. However, some semi-enclosed water bodies may act more like closed systems if the seiches are transverse to the flow (as the case for free surface flow with cavities on both sides of a channel) or if the seiches are longitudinal but the harbour has a narrow entrance (van Rijn 1994). Whereas in regular topography there is almost no damping of the oscillations, rough

topography leads, due to higher bottom friction, to more significant damping (Wilson 1972). A particular point of interest for harbours is the resonant response of the simple rectangular harbour on the amplification factor. The amplification factor for harbour oscillations is defined as the ratio of wave height along the back wall of the harbour to standing wave height along a straight coastline (which is twice the incident wave height). Resonant response of idealized harbours with different geometries is summarized by Zelt (1986).

It may be concluded that cavity oscillations occur under particular geometrical conditions and flow characteristics. An important geometrical parameter is the cavity aspect ratio defined as $\Delta B / L_b$. Periodic behaviour of the oscillations can be related to the Strouhal number. Furthermore, cavity induced flow features influences mass exchange through the line cavity/freestream as well as recirculation of flow inside the cavity.

2.3 Unsteady open channel flow

2.3.1 Classification of flow types

According to Figure 2-12 different type of flows are distinguished in open channel flows. A steady flow is characterized by the independency of the flow velocity and flow area from time¹. Uniform flow is characterized by identical bottom, water surface and energy slope. The **steady uniform** flow consists in the simplest case of open channel hydraulics but do rarely exist since natural channels are usually irregular. Even in artificial channels of uniform section, the occurrence of uniform flow may be relatively infrequent because of control structures (Henderson, 1966). Nevertheless, many engineering problems are calculated following steady uniform flow approach.

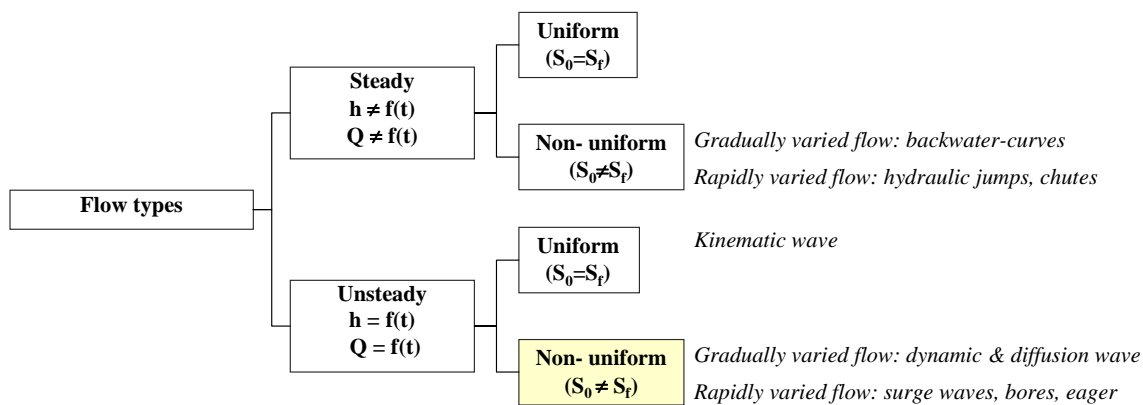


Figure 2-12 : Flow types; h : flow depth, t : time, S_0 : bottom slope, S_f : slope of the energy grade line.

When the flow is **steady but non-uniform**, which is the case in most natural and artificial channels, bottom, water surface and energy slope are not any more identical. Non uniformity in open channel flow is due to a change of geometry (section or/and slope) or a variation of flow resistance (roughness).

If the streamlines of the steady non-uniform flow remain nevertheless relatively parallel, so that the hydrostatic pressure distribution prevails, the flow is called *gradually varied*. Different flow profiles (backwater and drawdown curves) occur in this case of flow which is characterised by not too abrupt changes of the channel sections. They are classified regarding the bottom slope S_0 relative to the critical slope S_{cr} (horizontal $S_0 = 0$; mild $-0 < S_0 < S_{cr}$; critical $-0 < S_0 = S_{cr}$; steep $-S_0 > S_{cr} > 0$; adverse $S_0 < 0$) and the flow depth relative to the normal and critical flow depth (Chow, 1959).

Theory of gradually varied flow is based on several assumptions. In particular, it is assumed that the head-loss at a section is the same as for uniform flow. The inverse of

¹ Steadiness is in this case related to mean flow characteristics and not to variations of the velocity as example due to turbulence or coherent structures. They can occur and are reasonably time dependant.

this assumption is to use the uniform flow formula to evaluate energy slope and thus the corresponding roughness coefficient as it has been done (see § 4.3). Chow (1959) points out that this assumption has never been precisely confirmed but that errors arising from it are small, compared to those incurred from the use of a uniform-flow formula and the roughness selection. The assumption is believed to be more correct in varied flow with increasing than with decreasing velocity.

If streamlines have pronounced curvature, the non-uniform flow is called *rapidly varied*. Rapidly varied flows have some particular features which are mentioned hereafter since they are relevant in the analyses of the steady flow tests: 1) High curvature of flow leads to non hydrostatic pressure distribution. 2) Variation in flow regime takes place on a short distance. Therefore boundary friction is of secondary importance. 3) Rapid changes in water area in rapidly varied flow lead to velocity distribution coefficients much greater than the unity. 4) Separation zones, eddies and rollers may occur in rapidly varied flow. The flow is therefore confined by separation zones rather than by solid boundaries. Examples of rapidly varied steady flows are flows over spillways, hydraulic jumps and flows trough non-prismatic channel sections (see § 4.4.5).

Table 2-8: Wave types of unsteady non-uniform flow in open channels.

Designation (English)	Free surface	Terms considered in (eq. 2.43)	Water surface parallel to bottom	Wave profile change with x	Absolute celerity
Dynamic wave	gradually varied	all terms considered	No	Yes	-
Quasi permanent dynamic wave	gradually varied	$dU/dt = 0$	No	Yes	-
Diffusion wave	gradually varied	$dU/dt = 0$ $dU/dx = 0$	No	Yes	$c_k' = 3/2U$ *
Kinematic wave**	gradually varied	$dU/dt = 0$ $dU/dx = 0$ $dh/dx = 0$	Yes	No	$c_k = 3/2U$ ***
Translation wave (Gravity wave)	rapidly varied	- ****	No	No/Yes	$c_g = U + (gh)^{0.5}$ *****

* The absolute propagation celerity of the diffusion wave is obtained using the Chezy formula and assuming constant bottom slope (Henderson 1966, p. 383).

** The kinematic wave is also called monoclinal rising wave (uniformly progressive flow).

*** The absolute propagation celerity of the kinematic wave is obtained assuming independency of the celerity c_k of the flow depth and using the Chezy formula.

**** Equations of translation waves are obtained directly from the combination of continuity and momentum equations (see § 2.3.3.2).

***** Simplified formulation not taking into account the water level difference before and after the wave front.

As mentioned above, the steady uniform flow is the simplest case in open channel hydraulics. On the opposite scale of complexity is situated the *unsteady non-uniform* flow (Table 2-8). Hydraulic parameters such as discharge, velocity and flow depth are

time and space dependant. Precipitation events of varying intensity and duration, dam breaks, the break up of an ice-jam, the debris jam and break up, the start up and stopping of turbines of runoff or storage hydropower plants and (sluice) gate operations lead to unsteady non-uniform flow. According Graf and Altinakar (1996) unsteady non-uniform flow can again be gradually or rapidly varied. As it is the case for the rapidly varied steady flow, the unsteady, non-uniform and *rapidly varied* flow is characterized by a free surface having sudden change and high curvature. As consequence, assumption of hydrostatic pressure might not be valid on a limited channel reach. A sudden change of the discharge respectively level causes a rapidly varied flow called surge wave (translation wave, gravity wave). Four different types of surge waves (Figure 2-14) are defined (Favre 1935, Chow 1959, Graf and Altinakar 1996): the positive surge wave moving downstream, the positive surge wave moving upstream, the negative surge wave moving downstream and the negative (surge) wave moving upstream.

The celerity of a translation (gravity wave) shows that if Froude number of the (base) flow is equal to $Fr = 1$, the wave front speed corresponds to two times the mean flow velocity of the base flow $c_g = 2U$. A disturbance of the water surface can not move upstream under these conditions. Gravity waves of important height have to be considered as an exception as it will be shown further on. Furthermore it can be shown that a gravity wave is moving faster than a kinematic wave for $Fr < 2$ using the Chezy formula.

The mathematical formulation and the resolution of the equations for the different unsteady non-uniform flow conditions are presented in § 2.3.2. Before, some terms are defined hereafter:

Unsteady flow is a term characterizing conditions in which the discharge changes with time [Source: IATE - Inter-Active Terminology for Europe]. Unsteady flow is equivalent to transient flow but mainly used for free surface flow conditions. Sometimes, flow is also called unsteady if the velocity components change with time. In this work, the flow is called unsteady only when mean flow conditions change.

Transient flow is a flow having hydraulic characteristics varying with time. The term transient is mainly used for pipe flows but also in open channel flow.

A *wave* is called the disturbance in a body of water propagated at a constant or varying speed, often of an oscillatory nature. [Source: UNESCO/WMO; Gloss. Hydrology]

A *flood wave* is the propagation of a flood along the stream channel. The regime during the resulting unsteady flow is determined, in large part, by complex local transfers of energy and of volume. [Source: IATE]

A *positive/negative surge* corresponds to the (rapid) variation in the height of the water level (for example due to a change of discharge) which travels in an open channel with a velocity approximately equal to that of the gravity wave. [Source: IATE]

A *hydraulic bore*/"eagers" expresses either 1) a wave of water having a nearly vertical front, such as a tidal wave, advancing upstream as the result of high tides in certain

estuaries. A similar wave advancing downstream is due to a cloud burst or the sudden release of a large volume of water from a reservoir. Tidal waves are also termed "eagers"; or 2) a standing wave which advances upstream in an open conduit from a point where the flow has suddenly been stopped. The flowing water piles up in the channel against the obstruction that caused the stoppage, and as it reaches a height above the normal water surface, approximately its velocity head, the increased depth of water moves upstream in a wavelike shape. [Source: IATE]

2.3.2 Mathematical formulation and resolution of unsteady non-uniform flow

All motion of fluid substances describes by the Navier-Stokes equations and the continuity equation. These equations applies to laminar flow (Navier-Stokes equations) as well as to turbulent flow (generalized Navier-Stokes equations or Reynolds equations), to free surface flow as well as to pressurized flow, to steady flow as well as to unsteady flow. The Navier-Stokes equations describe the conservation of momentum whereas the continuity equation describes the conservation of mass.

The continuity equation and the momentum equations into the three directions of a coordinate system allow finding the 4 unknowns namely the velocity vector and the pressure (scalar). Nevertheless, the resolution of this simple system of equations – 4 unknowns¹, 4 equations – is not as simple in practice. Resolution of Navier-Stokes equations needs boundary conditions. The exact knowledge of the boundary conditions together with the fact that the equations are non linear of the second order are the main difficulties for their resolution. Some analytical solutions exist nevertheless for particular laminar flow problems with simple boundary conditions (Graf and Altinakar 1995; p. 248ss). For this reason, hydraulic engineers developed simplified formulations especially for free surface or pressurized flow applications. The simplified formulations are based on a number of hypotheses which are considered as reasonable.

In case of gradually varied unsteady and non-uniform flow the hydrostatic pressure distribution assumption is correct and the equation of the one dimensional unsteady, non-uniform flow is developed basically by one of three different possible approaches:

- Chaudhry (1986, p. 386 ss) or Streeter (1967, p. 246 ss) developed the equation from the dynamic equation. To take into account the continuity equation allows simplifying some terms.
- Chow (1959; p. 527) completed the Bernoulli equation by including the loss due to acceleration and (Henderson 1966, p. 90 and p. 286) modified the resistance formula by replacing the total by partial derivatives since the quantities involved may now vary with time as well.
- Finally, the unsteady non-uniform flow equation can be derived from the Navier-

¹ Only correct for laminar flow. In case of turbulent flow, four additional unknowns appear (u' , v' , w' and p').

Stokes equations. First by integration on the vertical assuming hydrostatical pressure distribution ($w \ll u, v$) which leads to the two dimensional Saint-Venant equations and secondly by integration on the horizontal assuming $v \ll u$ which leads to the one dimensional Saint-Venant equations.

The one dimensional equations of Saint-Venant (dynamic equation and continuity equation) are (Graf and Altinakar 1993):

Continuity equation:

$$A \frac{\partial U}{\partial x} + U \frac{\partial A}{\partial x} + \frac{\partial A}{\partial t} = 0 \quad (\text{eq. 2.42})$$

Dynamic equation:

$$\frac{1}{g} \frac{\partial U}{\partial t} + \frac{\alpha U}{g} \frac{\partial U}{\partial x} + \frac{\partial h}{\partial x} = S_o - S_f \quad (\text{eq. 2.43})$$

where Q is the discharge, A the cross sectional surface of the flow, U the mean velocity, h the flow depth, S_o the bottom slope and S_f the friction slope. α is the correction coefficient for the non uniformity the flow velocity and often assumed to be 1. Written in this form, the three terms of the continuity equations are the prism-storage, wedge storage and rate-of-rise terms respectively.

As mentioned above equations (eq. 2.42) and (eq. 2.43) are applicable in case of gradually varied flow. In case of rapidly varied unsteady and non-uniform flow, the resolution of the Navier-Stokes equations is required. The hydraulic engineers however developed analytical solutions for simple problems as for the propagation of surge waves namely by proceeding in a change of reference system. These solutions are presented in § 2.3.3.

If the equations of Saint-Venant (1D or 2D) can not be sufficiently simplified, the analytical resolution becomes impossible. The temporal and spatial variation results in various derivatives even in the 1D case. For the numerical resolution different techniques are available reviewed by Alcrudo (2002):

- Method of characteristics (e.g. Viessman et al. 1972, Giezendanner 1983)
- Method of finite differences (e.g. Graf and Altinakar 1996)
- Method of finite elements
- Method of finite volumes (e.g. Zoppou and Roberts 2000)

The *method of characteristics* is based on the propagation speed of waves in the water. Characteristics are called lines in the x-t space. These lines are straight in the case of the frictionless, horizontal channel and they becomes curved when these parameters are considered. The method has been developed for one dimensional flow problems and the result is section averaged.

The *method of finite differences* is based on the replacement of partial by total derivatives. Explicit and implicit numerical schemes exist. Explicit schemes are easy to calculate but require a particular attention for the computation stability. Furthermore, these schemes

are often found to be non-conservative. Mass or momentum might be created numerically. A second minor disadvantage is that the time step Δt and Δx have to be constant.

The *method of finite elements* is widely used in the continuum mechanics (e.g. structural engineering) but has only limited performance in the domain of hydraulics since discontinuities such as hydraulic jumps or shock waves exist. The principal of the finite element method consists in computing the characteristics of nodes. The continued information is than obtained by interpolation of this information.

The method of *finite volumes* is generally conservative and mathematically “relatively” easy to solve. The fluid is supposed to be a succession of small volumes. The information is attached to the gravity centre of the volumes and the computation deals with the mass and momentum flux across these surfaces (HLL Riemann solver).

The method of characteristics was one of the first used in hydraulics. The method of finite elements is, for the mentioned reasons, rarely used. The application of finite differences is supported by years of experiences and the performances are known as well as the limits. The actual development mainly turns to methods of finite volumes. Finally, the application of the Saint-Venant equations for rapidly unsteady flow is often acceptable, even if pressure distribution is not hydrostatic (Hicks et al. 1991, Mishuev and Komarov 1996, Mingham et al. 1998).

2.3.3 Rapidly varied unsteady and non-uniform flow

2.3.3.1 Types of rapidly varied unsteady and non-uniform flow in channels

Some of the phenomenon causing unsteady non-uniform flow in channels (and shallow reservoirs) can induce rapidly varied flow namely:

- Sluice gate operations (flushing of reservoirs included)
- Debris jam and break up, ice jam and break up (Morse and Hicks 2005)
- Fast opening and shutdown of turbines of run-off-river or storage hydropower plants (Baumer and Beffa 1992)
- Dambreaks (Lauber 1997)
- Tidal effects in river mouth (eagers, mascarets)
- Navigation lock operation (Muser and Meder 1970)
- Transient bore due to landslide in (shallow) reservoir (Zweifel 2004, Zweifel et al. 2006)



Figure 2-13 : Some examples of highly unsteady and non-uniform flow: Top left: Flashflood, <http://www.mckerracher.org> ; Top right: Tidal bore on the Kennetcook River at Scotch Village, Canada. <http://www.glinx.com/~sherm/> Bottom left: Sweetwater dam break on January 30, 1916. <http://www.sandiegohistory.org>. Bottom right: Non breaking surge downstream of Schiffenen on the Sarine River in Switzerland.

A fundamental difference of the various highly unsteady flows is whether downstream base flow exists or not. When considering a channel having an initial flow Q_1 , a sudden

change of the discharge $\pm\Delta Q$ or the flow depth $\pm h'$ causes the formation of a surge wave. The four principally possible surge wave types are presented in Figure 2-14. Surge waves are the topic of the present experimental research.

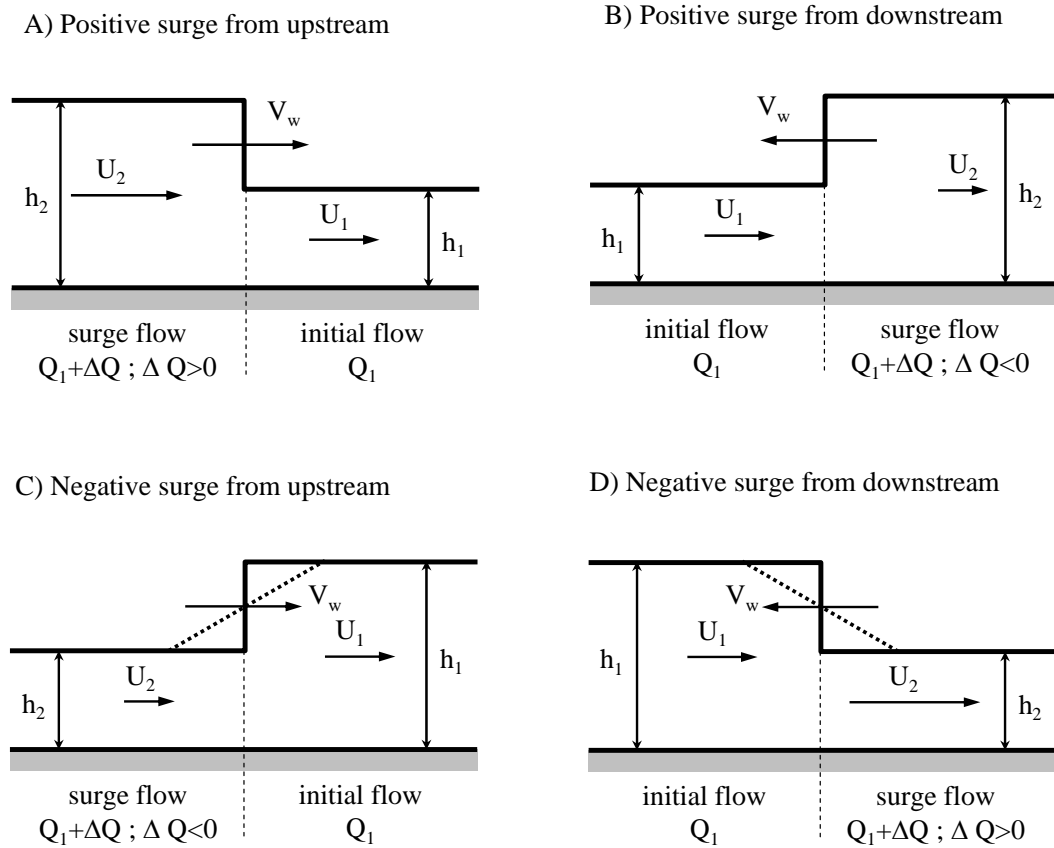


Figure 2-14 : The four different surge wave types. V_w : absolute surge wave celerity observed by a stationary observer. The oblique line of type C) and D) indicate their dispersive character.

2.3.3.2 Mathematical formulation and resolution of rapidly varied unsteady and non-uniform flow

Rectangular prismatic channel sections

Highly unsteady and non-uniform surge wave flows (Figure 2-14) are mathematically solved by using momentum and continuity equation under following assumptions:

- the change of discharge is instantaneous.
- the channel is prismatic and rectangular ($B = \text{cst.}$).
- the channel is frictionless and horizontal.

The development of the surge wave equations is shown for the positive surge moving downstream. When an observer moves along the channel with the absolute wave celerity V_w , the continuity equation writes as:

$$(U_2 - V_w)B \cdot h_2 = (U_1 - V_w)B \cdot h_1 \quad (\text{eq. 2.44a})$$

$$U_2 = \frac{U_1 h_1 + V_w (h_2 - h_1)}{h_2} \quad (\text{eq. 2.44b})$$

The momentum equation becomes:

$$\rho \cdot B \cdot h_2 (U_2 - V_w)(U_2 - V_w) - \rho \cdot B \cdot h_1 (U_1 - V_w)(U_1 - V_w) = \rho \cdot g \cdot B \left(\frac{h_2^2}{2} - \frac{h_1^2}{2} \right) \quad (\text{eq. 2.45})$$

where the term on the left side is the change in momentum of the control volume and the term on the right side represents the hydrostatic pressure forces. When equation (eq. 2.44a) is replaced in (eq. 2.45), the momentum equation simplifies and becomes:

$$(V_w - U_2)B h_2 \rho (U_2 - U_1) = \rho \cdot g \cdot B \left(\frac{h_2^2}{2} - \frac{h_1^2}{2} \right) \quad (\text{eq. 2.46})$$

In the equation above, U_2 is replaced by (eq. 2.44b). When solving for V_w one can find:

$$V_w = U_1 + \sqrt{\frac{g}{2} \frac{h_2}{h_1} (h_1 + h_2)} = U_1 + \underbrace{\sqrt{g h_1}}_A \cdot \underbrace{\sqrt{\frac{h_2}{2 h_1} \left(1 + \frac{h_2}{h_1} \right)}}_B \quad (\text{eq. 2.47})$$

Formula (eq. 2.47) reveals that the absolute wave celerity of a positive surge wave moving downstream is increased comparing to the simplified equation where the term B is considered to be the unity. This assumption is correct in case of a small disturbance of the water level compared to the initial flow depth ($h_2 \cong h_1$).

When the height of the surge wave is known, h_2 is known and the absolute wave celerity V_w (eq. 2.47), the mean flow velocity after the wave front U_2 (eq. 2.44b) and the discharge $Q_2 = B h_2$ are calculated immediately. On the other hand, when h_2 and V_w are unknown but the change in discharge $\Delta Q = Q_2 - Q_1$ is given; h_2 has to be determined iteratively from following equation (Chow 1959):

$$\left(\frac{Q_1}{B h_1} - \frac{Q_1 + \Delta Q}{B h_2} \right) = \frac{(h_1 - h_2) g (h_1 + h_2)}{c \cdot 2 h_1} \quad (\text{eq. 2.48})$$

where c is the celerity:

$$c = \sqrt{\frac{g}{2} \frac{h_2}{h_1} (h_1 + h_2)} \quad (\text{eq. 2.49})$$

The equations and the calculation of the characteristics of a surge wave have been shown here for the positive surge wave moving downstream considering two possible

cases (h_2 known or ΔQ known). The formulas for the other for types of surge waves are developed similarly (Table 2-9). The parameters are defined according to Figure 2-14.

Table 2-9: Absolute wave front celerity of the basic surge wave types including initial flow in a frictionless, horizontal, rectangular channel of constant cross section.

	Positive surge		Negative surge	
From upstream	$V_w = U_1 + \sqrt{gh_1} \cdot \sqrt{\frac{h_2}{2h_1} \left(1 + \frac{h_2}{h_1}\right)}$	(eq. 2.50)	$V_w = U_1 + \sqrt{gh_1} \cdot \sqrt{\frac{h_2}{2h_1} \left(1 + \frac{h_2}{h_1}\right)}$	(eq. 2.51)
From downstream	$V_w = U_1 - \sqrt{gh_1} \cdot \sqrt{\frac{h_2}{2h_1} \left(1 + \frac{h_2}{h_1}\right)}$	(eq. 2.52)	$V_w = U_1 - \sqrt{gh_1} \cdot \sqrt{\frac{h_2}{2h_1} \left(1 + \frac{h_2}{h_1}\right)}$	(eq. 2.53)

Table 2-9 points out that the sign of the different celerity c has to be adapted in order to find correctly the absolute surge wave celerity V_w . The mean flow velocity after the wave front U_2 is calculated in any case from the continuity equation. It is important to conserve the sign of V_w for the computation of U_2 when using (eq. 2.44b). Furthermore, considering the positive and negative surge from downstream it can be confirmed that if surge height is enough important, the wave front can move upstream even for baseflow Froude numbers $Fr_1 > 1$. Following condition on the flow depths is required:

$$\frac{h_2}{h_1} \frac{(h_1 + h_2)}{2h_1} > Fr_1^2 \quad (\text{eq. 2.54})$$

In the case of small amplitude of the disturbance where the second square root becomes equal to one. The equations of Table 2-9 respectively simplifies to:

$$V_w = U_1 \pm \sqrt{gh_1} \quad (\text{eq. 2.55})$$

and the celerity, not anymore able to move upstream, c becomes:

$$c = \pm \sqrt{gh_1} \quad (\text{eq. 2.56})$$

Non-rectangular prismatic channel sections

The equation of the absolute surge wave celerity also for the case of a prismatic channel section which is not rectangular is shown in Favre (1935): The absolute surge wave celerity for the positive surge moving downstream becomes:

$$V_w = U_1 \pm \sqrt{g \left\{ \frac{A_1}{B_1} \left(1 - \tau \frac{h'}{B_1} \right) + \frac{h'}{2} \right\} \left\{ 1 + \frac{h'}{A_1/B_1} \left(1 + \tau \frac{h'}{B_1} \right) \right\}} \quad (\text{eq. 2.57})$$

where A is the area of the section and B and top width of the flow. The subscript 1 is related to the undisturbed flow before the surge wave. h' is the difference of flow depths $h_2 - h_1$. τ is defined here by $2\tau = \cot(\delta) + \cot(\delta')$ where δ and δ' are related to the angle between the water surface and the channel bank (Figure 2-15). The equation above is valuable only if the increase of the flow depth due to the surge wave remain relatively modest such as the area ΔA can be considered having trapezoidal form. The use formula (eq. 2.58) requires positive values of h' for positive surge waves and negative h' for negative surge waves. The sign (+) relates to the surge waves from upstream (positive or negative), the sign (-) to them from downstream.

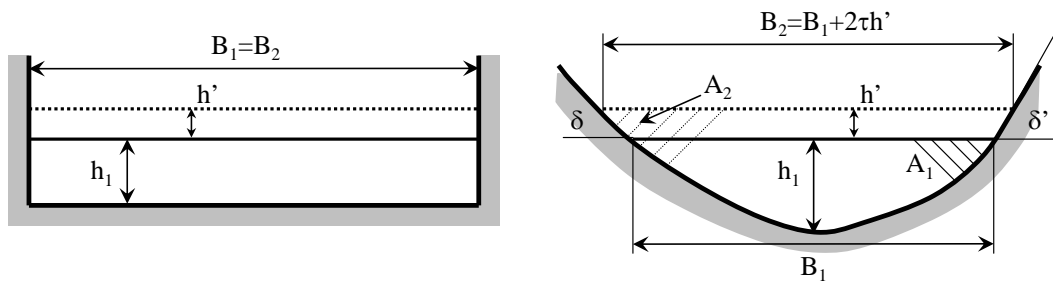


Figure 2-15 : Definition of the parameters of a positive surge wave from upstream in a rectangular (left) and any prismatic (right) channel section.

Furthermore, Favre (1935) simplified formula (eq. 2.58) assuming small increase of the water surface $h' / h_1 \ll 1$:

$$V_w = U_1 \pm \sqrt{g \frac{A_1}{B_1} \left[1 + \left(1 - \frac{2\tau}{3} \frac{A_1}{B_1^2} \right) \frac{3}{4} \frac{h'}{A_1/B_1} \right]} \quad (\text{eq. 2.58})$$

Again, the positive sign (+) relates to the surge waves from upstream (positive or negative), the negative sign (-) to them from downstream. Based on this simplified equation for the absolute surge wave celerity, Favre (1935) proposes an explicit calculation method for surges waves which are superposed to a uniform or gradually varied steady or unsteady baseflow in prismatic configurations including friction and slope.

Secondary waves (Ondes de Favre) and wave front breaking

The surge wave front is known to be followed by secondary waves (Favre 1935, Benet and Cunge 1971, Zairov and Listrovoy 1983, Treske 1994, Chanson 1996, Soares and Zech 2002), commonly called “Ondes de Favre”. The formation of secondary waves is described by Soares and Zech (2002) and is mainly due to non-hydrostatic pressure distributions around the wave front. Whether secondary waves or breaking of the front are observed namely depends on the ratio of the flow depths after (h_2) and before (h_1)

the wave front respectively on the surge Froude number Fr_s defined as:

$$Fr_s = \frac{(V_w - U_1)}{\sqrt{gh_1}} = \sqrt{\frac{h_2}{2h_1^2}(h_2 + h_1)} \quad (\text{eq. 2.59})$$

where V_w is the absolute celerity of the surge wave front and U_1 the mean flow velocity of the baseflow. As secondary waves have crests and troughs, h_2 is representative for the mean flow level after the wave front. Experimental works on secondary waves are summarized in § 2.3.3.3.

Particularity of negative waves from upstream or downstream

The above presented formulas all concern the absolute wave celerity of the surge wave front which is assumed vertical. However, the absolute celerity of a small water volume is a specific and local propriety directly related to the local flow depth and mean velocity of the section as:

$$V_w(h) = U(h) \pm \sqrt{gh} \quad (\text{eq. 2.55})$$

The positive sign corresponds to a disturbance moving downstream and the negative sign to the one moving upstream. From this formula a fundamental difference between positive and negative waves is found as shown at the example of Figure 2-16 for the positive respectively negative wave form upstream.

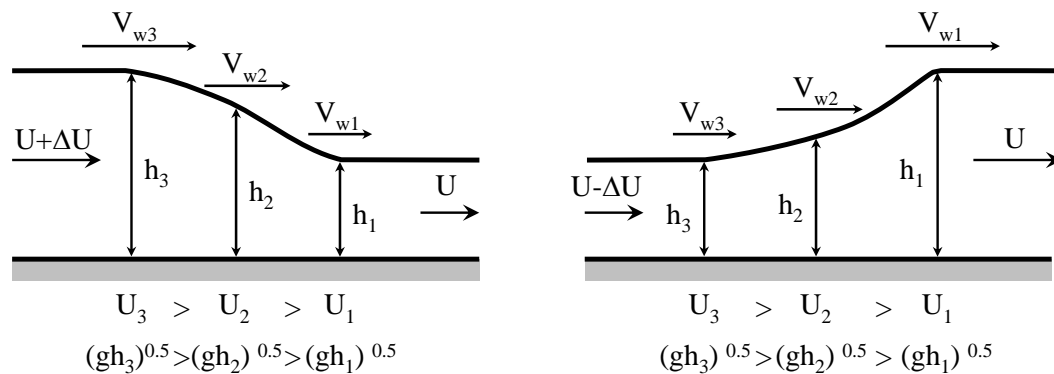


Figure 2-16 : Influence of the local absolute celerity on the profile and formation of a positive (surge) wave (left) and a negative wave (right).

When the increase of discharge is not instantaneously, the initial wave front of a positive wave is not vertical. The absolute wave celerity V_{w3} is higher than V_{w2} which is itself higher than V_{w1} . The wave front is steepening until becoming quasi vertical in the horizontal, frictionless channel. When the wave front is enough steep, breaking conditions might be observed.

When the decrease of discharge happens not immediately, the initial wave front of a negative wave is not vertical. As the absolute wave celerity V_{w1} is higher than V_{w2} itself higher than V_{w3} , the distance between the points at the top and the bottom of the nega-

tive wave (front) is increasing with time. The negative wave is thus flattening in a frictionless and horizontal channel (dispersive character). Even if the change of discharge happens instantaneously and the initial wave front is vertical, the dispersive character is observed.

Negative waves thus do rapidly flatten whether they are from up- or downstream even if it is assumed that they have initially a steep front. In case of a small disturbance, the basic equations of Table 2-9 nevertheless apply. On the other hand, for a height of the surge relatively large, the negative surge wave should be treated as a gradually varied flow. The application of the momentum equation and the continuity equation to a small slice of the negative wave leads to a differential expression relating the velocity U and the flow depth h :

$$\frac{dU}{dh} = \sqrt{\frac{g}{h}} \quad (\text{eq. 2.60})$$

The integration of the equation with the initial conditions $h = h_1$ and $U = U_1$ corresponding to the undisturbed flow conditions leads to following equations for the flow velocity $U(h)$, the absolute wave celerity $V_w(h)$, the wave profile $x(t, h)$ and the discharge $Q(h)$ where t_0 corresponds to the time of the sudden modification of the discharge or water level:

$$U(h) = U_1 - 2\sqrt{gh_1} + 2\sqrt{gh} \quad (\text{eq. 2.61})$$

$$V_w(h) = U_1 - 2\sqrt{gh_1} + 3\sqrt{gh} \quad (\text{eq. 2.62})$$

$$x(t, h) = (U_1 - 2\sqrt{gh_1} + 3\sqrt{gh}) \cdot (t - t_0) \quad (\text{eq. 2.63})$$

$$Q(h) = U(h) \cdot h \cdot B = (U_1 - 2\sqrt{gh_1} + 2\sqrt{gh}) \cdot h \cdot B \quad (\text{eq. 2.64})$$

The four formulas allow calculating the characteristics of a negative wave when the initial undisturbed flow conditions are known as a function of time and space. Furthermore, when eliminating h from (eq. 2.61) and (eq. 2.63) one can express the mean flow velocity as a function of space and time $U(x, t)$:

$$U(x, t) = \frac{U_1}{3} - \frac{2}{3}\sqrt{gh_1} + \frac{2}{3}\frac{x}{t} \quad (\text{eq. 2.65})$$

The gradually varied negative surge wave problem is thus solved analytically assuming initial and boundary conditions known and the frictionless horizontal channel. All main characteristics of the wave such as mean flow velocity in function of space and time are calculated using equations (eq. 2.61) to (eq. 2.65) and the continuity equation for calculating the flow depth and velocity at the location of the discharge change.

Surge wave reflection and superposition

Surge waves are totally or partially reflected at a blind end, at a channel transition leading to a modification of the surge wave discharge (example: surge wave arriving at an abrupt enlargement or contraction of the section), at a lake entrance or at a channel junction. Furthermore, when two surge waves meet, one travelling from downstream, one from upstream, two new surges travelling in the reversed directions get formed. When two surges travelling in the same direction meet, they form one surge of a given height and an absolute front celerity (Favre 1935). Superposition of surge waves can mainly be observed in navigation channels (Muser and Meder 1970) or in tidal river systems but also in rivers influenced by hydropower energy production.

Reflections at dead end, channel transition and entrance to a lake can be treated as proposed in Chow (1959). The following assumptions are considered: the surge heights are small such as $V_w = U + (gh)^{0.5}$; the water is initially at rest ($U = 0$); no energy losses occur at the transitions. Based on the principals of mass and energy conservation as well as on one more hypothesis concerning the celerity of the incoming (c_1) and reflected (c_3) surge, the surge heights h_3' (dead end, lake entrance) respectively h_2' and h_3' (channel transitions) are determined. The reflection coefficient is defined as:

$$C_r = \frac{h_3'}{h_1'} \quad (\text{eq. 2.66})$$

where h_3' is the height of the reflected wave and h_1' the height of the incoming wave. When the incoming surge height and the reflection coefficient C_r , are known, the height of the reflected surge is calculated. The reflection coefficient is a function of the transition geometry. The height of the transmitted wave through a channel transition h_2' is calculated as $h_2' = h_1' + h_3'$. Figure 2-17 summarizes the different cases of total and partial surge wave reflections.

Table 2-10: Summary of the channel conditions, the reflection type and the reflection coefficients (Chow 1959).

Channel condition	Reflection type	Reflection coefficient	Case (Figure 2-17)
Dead end barrier	Positive	$C_r = 1$	A.1 ; A.2
(sudden) contraction	Partially positive	$0 < C_r < 1$	B.1 ; B.2
No transition	None	$C_r = 0$	None; (Figure 2-14)
(Sudden) expansion	Partially negative	$-1 < C_r < 0$	C.1 ; C.2
Lake entrance	Negative	$C_r = -1$	D.1 ; D.2

Table 2-10 summarizes the channel conditions, the kind of reflection and the corresponding reflection coefficients. The entrance of a surge wave into a lake is a particular case of an expansion of the section. The expansion is important and thus the velocity in the lake is assumed zero. The lake water level is not affected by the surge.

When a positive surge arrives in a channel junction, the wave is partially reflected as a negative surge (in fact, a channel junction can be considered as a particular case of an expansion of the section) and two positive surges are transmitted into the two downstream reaches. When considering horizontal and frictionless case, the area included between the three different surge wave fronts is of unique flow depth h in the reflected situation (Figure 2-18).

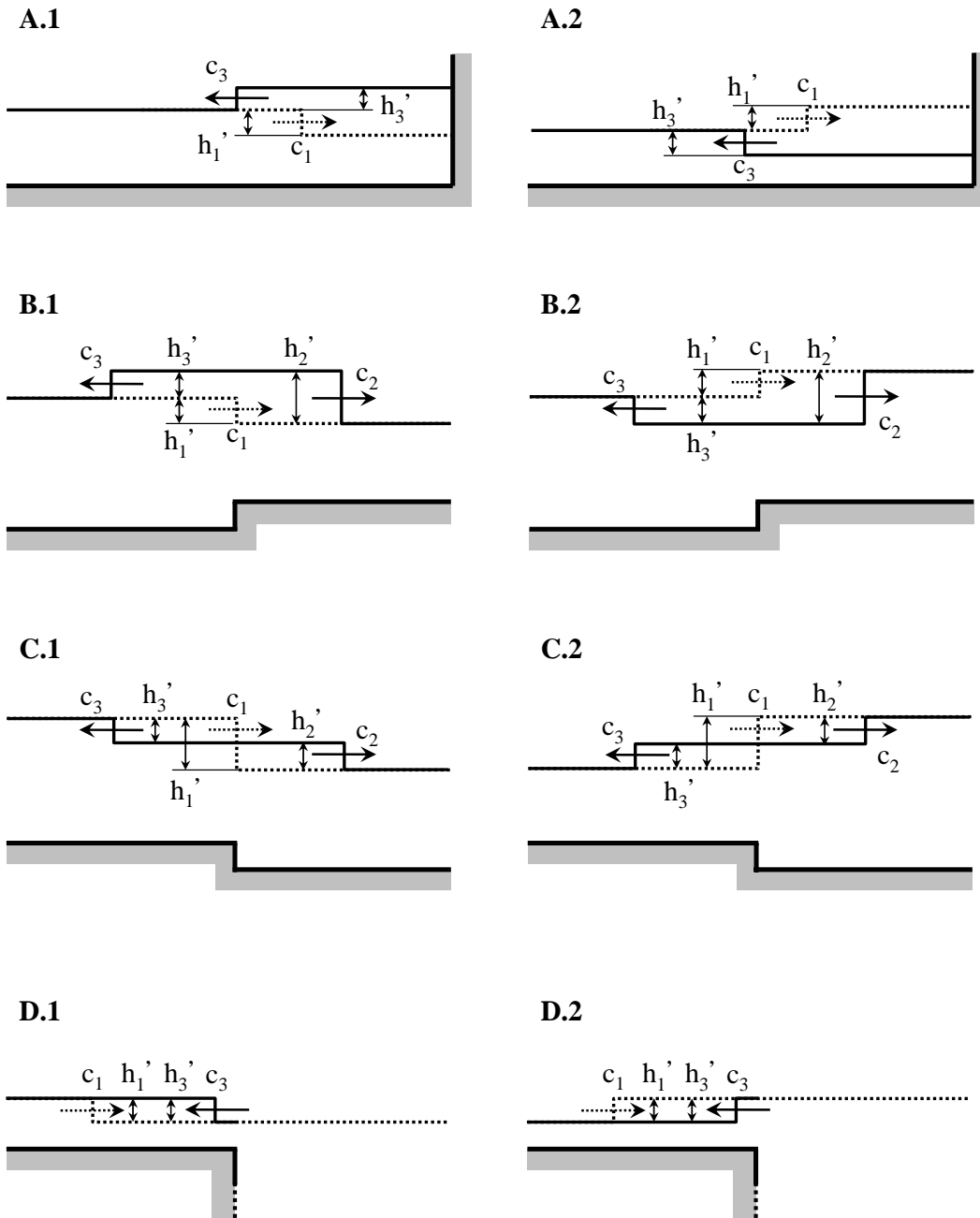


Figure 2-17 : Partial and total reflection of surge waves. A.1 / A.2: Total reflection of a positive / negative surge at a dead end. B.1 / B.2: Partial reflection of a positive / negative surge at a channel contraction. C.1 / C.2: Partial reflection of a positive / negative surge at a channel expansion. D.1 / D.2: Total reflection of a positive / negative surge entering in a lake.

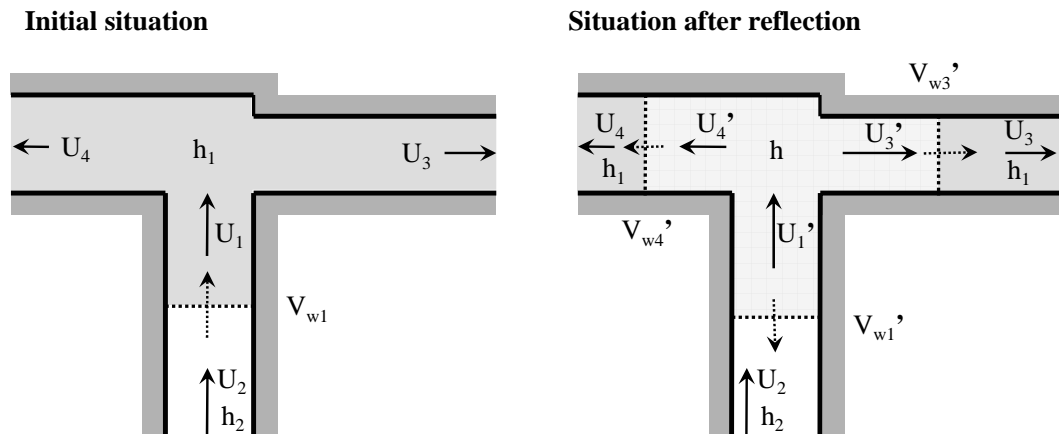


Figure 2-18 : Surge wave through a channel junction.

The 7 unknowns (h , U_2 , U_3 , U_4 , U_1' , U_3' , U_4') are solved when the initial flow conditions (h_1 , U_1) and the flow depth of the incoming surge (h_2) are known considering 7 equations namely:

- the continuity equation through the junction at the initial conditions,
- the continuity equation at the incoming surge,
- the 3 continuity equation at the three surge fronts for the situation after reflection,
- the continuity equation through the junction for the situation after reflection and
- an equation defining the split of the incoming flow into the two following channel branches.

The celerities of the incoming and the three reflected surge wave fronts are calculated using the equations of Table 2-9 respectively the simplified formula $V_w = U + (gh)^{0.5}$. It should be noted that h_1 and h applies to the domain downstream of the surge wave front (initial situation) respectively to the domain contained in between the three surge wave fronts (reflected situation).

Influence of friction and channel slope on the formation of surge wave

Most of the developments and equations presented in this chapter up to here relates to frictionless and horizontal channels respectively to channels where the friction is supposed to be compensated by the bottom slope. The wave profile of an advancing front however changes when friction is considered. This effect might be not important in short artificial channels but it can be significant in long reaches of natural channels (Chow 1959, Jirka 2005). Henderson (1966) qualitatively shows the influence of roughness on the propagation of surge waves. He concludes that for flows having Froude number of the baseflow $Fr_1 < 2$, resistance makes the positive wave more dispersive and delays surge formation (perhaps even indefinitely). When $Fr_1 > 2$, surge formation will always be observed and resistance makes the formation even faster. Independently of Froude number, the resistance makes the negative wave less dispersive. It is however doubtful whether resistance can be so high that negative waves form a steep front.

Favre (1936) showed how to integrate friction and bottom slope in the case of prismatic

channels to surge wave calculations. Nowadays, these two effects are generally accurately integrated into numerical models based on depth averaged 1D or 2D Saint-Venant equations). However according to the best knowledge of the author of this study, no systematic experimental works analysing the effect of macro-roughness on the propagation of surge waves characterized by a steep wave front have been established until these days.

2.3.3.3 Studies/experiments with highly unsteady flow conditions

Experiments with highly unsteady flow conditions in hydraulics mainly cover three domains:

- Dam-break experiments: dam-break waves due to sudden failure of a dam.
- Surge wave experiments: positive and negative surge waves from upstream or downstream due to sluice gate or turbine operation.
- Experiments about secondary waves (Ondes de Favre) following the wave front.

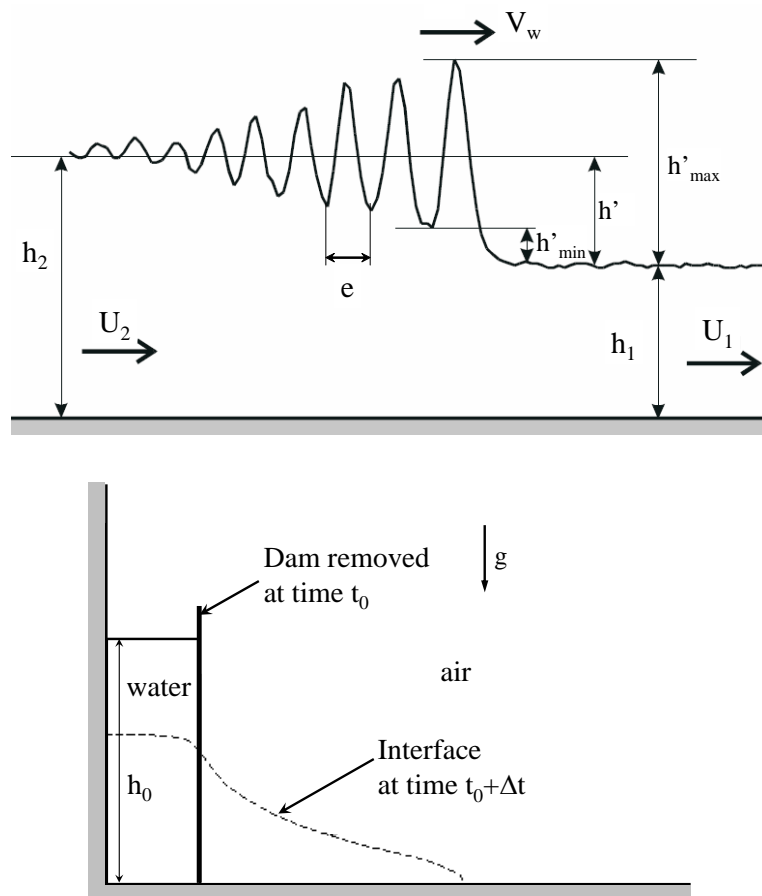


Figure 2-19 : Above: Definition of surge and secondary wave parameters. Below: Definition of dam break flow parameters.

The third category consist in a subgroup of surge wave experiments as secondary waves occur under particular conditions downstream and upstream of surge wave fronts. Table 2-11 summarizes experiments of the three domains. The author of this research reviewed especially published works related to positive and negative surge waves trav-

elling downstream including downstream flow / flow depth since these flows are subject of the study. Table 2-11 contains also the main works on dam-break experiments for which many other experimental studies exist. Detailed review about this particular highly unsteady flow phenomenon was done in Lauber and Hager (1998a, 1998b). The influence of friction on dam-break flow is presented later in this chapter.

Table 2-11: Summary of experiments of highly unsteady flow in channels

Author(s), Year	Title	Main conclusion/finding
Bazin (1865)	Recherches expérimentales relatives aux remous et à la propagation des ondes	Relatively good agreement between observed and calculated absolute wave celerity (see below) of (small) surge waves.
Schoklitsch ; 1917	Über Dambruchwellen (About dam break waves)	Experimental dam break waves do not follow the theory of Ritter at the wave front.
Favre ; 1935	Etude Théorique et Expérimentale des Ondes de Translation dans les Canaux Découverts (Experimental and theoretical developments)	Surge waves due to rapidly varied flow conditions propagate with an absolute wave celerity depending on h_1 and h_2 . The wave front is followed by secondary undulations (wave train; Ondes de Favre).
Faure and Nahas ; 1961	Etude Numérique et Expérimentale d'Intumescences à Forte Courbure du Front.	Good agreement between experiments and numerical model for wave front speed. Slight overestimation of flow depths. Increase of roughness lowers the propagation speed of the wave front.
Benet and Cunge ; 1971	Analysis of Experiments on Secondary Undulations caused by Surge Waves in Trapezoidal Channels	Confirmation of the general behavior of the experiments of Favre (1935) also in trapezoidal channels. Secondary wave amplitude higher at channel banks of compared to rectangular channel.
Ünsal ; 1983	Célérité des ondes de rupture dans un canal a section variable, en régime graduellement varié	Dimensionless celerity depending on the local Froude number of the downstream flow only.
Zairov and Listroy ; 1983	Experimental investigation of the positive travelling surges fore-part observed in canals	Empirical formulas separating into undulating and breaking positive surge waves, Attenuation of secondary waves; waveform and –kinematics formulations.
Treske ; 1994	Undular Bores (Favre-Waves) in Open Channels - Experimental Studies	Confirmation of the general behavior of the experiments of Favre (1935) in trapezoidal channels. Design criteria for the engineers.
Chanson ; 1996	Free surface flows with near critical flow conditions	Comparable near-critical flow conditions for free surface flows (Froude little higher than 1)
Soares and Zech ; 2002	Undular bores and secondary waves – Experiments and hybrid finite-volume modelling	Experimental results in good agreement with earlier studies. Undular bores reproduced by numerical model including extra pressure terms.

Surge wave experiments

The experiments of the “Académie française des science” (Bazin 1865) compared observed absolute surge wave celerities with calculated ones (positive and negative surge from upstream and downstream). The absolute wave celerity was calculated with the formula:

$$V_w = \sqrt{g(h_1 \pm h')} \pm U_1 \quad (\text{eq. 2.67})$$

where h' is the amplitude of the wave. They found good agreement for the absolute wave velocities of the positive and negative surge waves from upstream. For the positive and negative surge wave from downstream they concluded that the formula overestimates the absolute wave velocity for positive surge waves from downstream and underestimates it for negative surge wave from downstream. These results may be explained as the celerity has been calculated by $c = (g \cdot (h \pm h'))^{0.5}$ rather than with $c = (g \cdot h)^{0.5}$ respectively with (eq. 2.50) to (eq. 2.53).

The theoretical and experimental work of Favre (1935) probably consist in the most similar one compared to the present study. The already presented equations (eq. 2.55) and (eq. 2.47) can be obtained from the theoretical work of Favre (1935) when assuming rectangular channel sections. For practical reasons, Favre (1935) proposed to simplify the equations of the absolute wave celerity assuming a water surface variation h' enough small in order to neglect the power of h'/h_1 higher than one. Furthermore, Favre (1935) extended the use of its formulas to situations where the sudden change of discharge is superimposed to a gradually varied steady or unsteady baseflow. The theoretical work has been verified with success by surge wave experiments in a 73.58 m long and 0.42 m wide rectangular and prismatic channel.

Experiments of Ünsal (1983) for the celerity of dambreak waves including a downstream base flow showed that it is possible to calculate a dimensionless celerity when knowing the local Froude number only.

$$A = \frac{c}{\sqrt{gh_0 \left(1 - \frac{h_1}{h_0}\right)}} \frac{h_0}{h_c} \frac{h_0}{(h_0 - h_1)} = 0.85 \cdot Fr^{-0.77} \quad (\text{eq. 2.68})$$

where A is the dimensionless celerity, c the unknown wave front celerity, h_0 the water depth in the reservoir, h_1 the normal depth of the downstream flow, h_{cr} the critical depth of the downstream flow and h_l the effective flow depth. The Froude number is calculated with the effective downstream flow depth and mean flow velocity. As the celerity is dimensionless, all depths included in the formula as reservoir depth, downstream depth, downstream normal and critical depth must be known. It should be pointed out that good results are found with this formula in particular because of the interconnection of the celerity c (left side of the formula) and the Froude number by the physically based term $(g \cdot h)^{0.5}$.

Zairov and Listrovoy (1983) did experiments of positive surge waves from upstream (by a variation of discharge at the channel upstream end) and positive surge from upstream by feeding a constant flow in standing water. Breaking of the positive surge wave front moving downstream is observed when $F_{\Delta} = \Delta Q / (gA / B)^{0.5}$ is greater than 0.75 where $F_{\Delta} [m^2]$ is a dimensional parameter related to the increase of discharge. ΔQ is the absolute change in discharge and A respectively B the flow area respectively the flow width of the undisturbed flow. The mean height of the wave front was found to be decreasing exponentially with the channel distance for the breaking and non breaking conditions. A decrease of 11% occurred under breaking conditions after a channel distance of $600 \cdot h_1$ respectively of 8.5% under non breaking conditions after the same distance. Following empirical relationship was found by the authors for the absolute celerity of a positive surge wave in a rectangular channel ($0.03 < F_{\Delta} < 0.4$):

$$V_w = U_1 + 1.3 \left(\frac{|\Delta Q|}{\sqrt{gh_1}} \right)^{0.095} \quad (\text{eq. 2.69})$$

where U_1 respectively h_1 are the mean flow velocity respectively the flow depth of the undisturbed conditions.

Secondary wave experiments

The first systematic work on secondary waves has been done by Favre (1935). Several other researches allowed completing the knowledge in this domain (Faure and Nahas 1961; Benet and Cunge 1971; Zairov and Listrovoy 1983; Treske 1994; Soares 2002). Experimental works revealed two conditions necessary for the formation of such waves. The first condition is a fast variation of the flow depth in time which is due to a sudden rise of discharge (positive surge from upstream) or the partial or complete closure of a sluice gate (positive surge from downstream). As second condition, the amount of the change has to be within certain limits related to breaking conditions of surge waves.

The importance of secondary waves relative to the initial flow depth increases with the difference of discharge respectively water depth before and after the wave front until breaking conditions of the surge front are reached. After that point, the importance decreases and no secondary waves are observed for highly breaking conditions. At highly breaking conditions the water level is not undulated anymore after the wave front (Favre 1935, Henderson 1966). It is thus possible to have simultaneously breaking conditions at the first undulation of the surge wave front and remaining undulations after it.

The characteristics of published laboratory experiments on secondary waves are summarized in Table 2-12. Table 2-12 shows that breaking conditions are related either to the ratio of flow depths before and after the passage of the wave front (Favre 1935, Benet and Cunge 1971) or to the surge Froude number (Treske 1994). Of particular interest for this study are experiments of positive surge waves in rectangular channels moving from upstream.

Table 2-12: Surge wave experiments in rectangular and trapezoidal flumes/channels leading to secondary waves (Ondes de Favres). Completed from Chanson (1996). L , W_b and S_0 are the length, the width at the free surface and the bottom slope of the channel respectively.

Author (Year)	Direction	Initial flow: $U_1; h_1$	Channel: type ; $L; W_b; S_0$	Breaking condition of first undulation
Favre (1935)	DS ; US	0 ; 0.106÷0.206 > 0 ; 0.109÷0.295	rect. ; 73.6 ; 0.42 ; 0.292‰	$h_2 / h_1 > 1.28$
Benet and Cunge (1971)	DS	0÷0.198 ; 0.057÷0.138	trap. ; 32.5 ; 0.172 ; 0.37‰	$h_2 / h_1 > 1.29 (U_1 = 0)$ $h_2 / h_1 > 1.37 (Fr_1 > 0.1)$
	US	0.59÷1.08 ; 6.61÷9.16	trap. ; * ; 9.0 ; 0.1÷0.15‰	-
	US	1.51÷2.31 ; 5.62÷7.53	trap. ; ** ; 8.6 ; **	-
Zairov and Listrovoy (1983)	DS	> 0 ; -	rect. ; 91 ; 0.7 ; -	$F_A > 0.75^{***}$
Treske (1994)	US	- ; 0.08÷0.16	rect. ; 100 ; 1.0 ; 0.017‰	$Fr_s > 1.38 (h_1 = 0.16 \text{ m})$ $Fr_s > 1.34 (h_1 = 0.08 \text{ m})$
	US / DS	- ; 0.04÷0.16	trap. ; 124 ; 1.24 ; 0‰	$Fr_s > 1.33$
Chanson (1996)	US	0.4÷1.2 ; 0.02÷0.15	rect. ; 20 ; 0.25 ; 3.3÷9.4‰	-
Soares and Zech (2002)	DS	0 ; 0.14÷0.26	rect. ; 26.15 ; 1.0 ; 0‰	

* Oraison power plant intake channel

** Jouques-Saint Estève intake channel

*** $F_A = \Delta Q / (gA/B)^{0.5} [\text{m}^2]$

Favre (1935) found that the secondary waves reach stable conditions after 30 m of the experimental channel for an initial depth of 0.19 m. Systematic tests of positive surge waves from upstream and downstream with and without initial flow velocity U_1 showed a rise of the relative importance of the secondary undulations until a value of $h_2 / h_1 = 1.28$. For higher values, the first undulation is breaking and consequently the secondary undulations diminish. Maximum relative height of secondary waves was $h'_{max} / h' = 2.06$. Furthermore, Favre (1935) reported an exponential decrease of the relative longitudinal distance of secondary wave crests e / h' with the relative wave height h' / h_1 . No equation is proposed for the height of secondary waves or the distance between wave crests but the graphs of Favre allows estimating these parameters easily.

The experiments of Benet and Cunge (1971) include a physical model and two prototype scale channels, all of trapezoidal cross section. Results show on one hand that secondary undulations are increased at the channel banks of trapezoidal sections and on the other hand that initial flow Froude number Fr_1 influences the characteristics of the undulations. Calculation of relative wave length, maximum relative amplitudes at the channel banks and the centre of the channel is proposed by the SOGREAH method for $Fr_1 < 0.1$.

Zairov and Listrovov (1983) provide plots allowing to find h'_{max} , h' and h'_{min} of the first, second and third undulation of a positive surge wave moving downstream. The relative undulation heights are depending on the normalized channel distance x/h_I . Up to a value of $x/h_I = 300$, h'_{max}/h_I are different for the first 3 undulations (formation of the wave train), further downstream of this distance h'_{max}/h_I become identical. Different plots are considered for breaking and non-breaking conditions. The values of h'_{min}/h_I of the first 3 undulations are different up to a distance of about $x/h_I = 600$. Thus, in the present study benefiting of a useful channel length of 38.33 m, stable conditions of the first three undulations may be reached for positive surge waves from upstream having a baseflow depth h_I less than 0.13 m.

Treske (1994) carried out surge experiments in a rectangular and trapezoidal flume. He studied the relationship between surge forms and surge Froude numbers. For $Fr_s < 1.2$, the surge wave was a series of wave train with many secondary waves behind the wave crest. With the increase of Froude number, the undular bore gradually transformed into a usual bore. When the Froude number is $Fr_s > 1.45$, the surge transforms into a completely developed bore (highly breaking).

The experiments of Chanson (1996) dealing with several positive undular surges moving upstream allowed to confirm that the surge wave front was two-dimensional in most cases. In rare cases, the undular surge is stopped and it becomes an undular jump after 5-10 minutes! Contrarily to the undular surge, undular jumps are three-dimensional.

Soares and Zech (2002) present a hybrid finite-volume model able to describe secondary waves. The model is based on Boussinesqu equations which are independent on the hydrostatic pressure assumption. Beside the results of computations of secondary waves which are reproducing well the experiments, the article includes a description of physics of secondary wave initiation. It is summarized as follows (Soares and Zech 2002):

- Starting point is an initially smooth positive wave.
- The wave steepens when travelling downstream as higher local celerity has to be considered for higher depth.
- The wave steepening leads to local extra pressures which are maximised at the points having maximum surface curvature. At the bottom of the wave “front”, the pressure is increased, at the top decreased compared to the hydrostatic pressure.
- These additional pressures lead to pressure gradients along the wave resulting in additional horizontal and vertical velocity components.
- The water surface has to start undulating under such conditions due to the continuity principal.
- Then, either stable undulating conditions or breaking of the undulation is reached.

Dam break experiments

Dam break waves in laboratory experiments are separated into two phases. The movement immediately after the break (lifting of the gate simulating the dam break) is mainly controlled by vertical accelerations. Nevertheless, the vertical acceleration decreases rapidly and the second phase with more gradually varied flow starts. Ritter (1892) developed the analytical solution of this second phase by integrating the Saint-Venant equations for the frictionless and horizontal channel. Experimental works on dam breaks (Schoklitsch 1917, Dressler 1954) pointed out differences between the Ritter solution and the measurements. They are due to the flow resistance especially present for dry downstream river beds. Dressler (1954) and Whitham (1955) proposed analytical solutions for the dam break problem in a channel of infinite width including friction. Finally, Lauber and Hager (1998 a, 1998 b), based on experimental works show that dambreak waves including sloping channels and friction are described well when the initial wave is considered for the first phase and the dynamic wave for the second phase. From the initial wave provides the initial conditions at the upstream boundary of the dynamic wave. Leal et al. (2006) investigated experimentally and numerically the dam-break wave front celerity of fixed and mobile bed with and without water downstream of the dam. Over fixed and mobile bed with dry bottom, the friction coefficient is found the key factor for the reduction of the wave-front celerity. For wet bottom, the wave-front celerity is reduced for increasing values h_3/h_0 (Figure 2-20) which is in agreement with the solution of Stoker (1957). The friction influences the front wave celerity also in the wet bottom case, in particular for low h_3/h_0 .

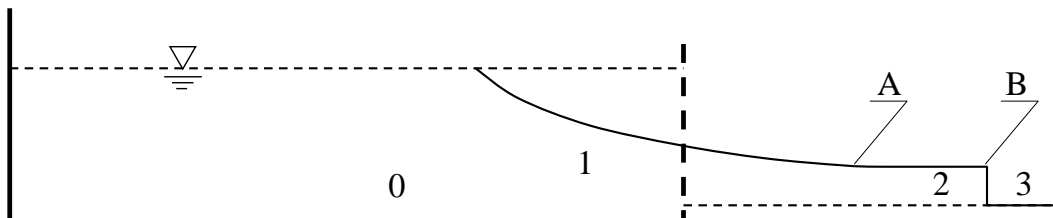


Figure 2-20 : Frictionless horizontal dambreak with downstream water level h_3 (Stansby et al. 1998). Point B describes the positive surge. Point A delimits zone 2 (horizontal water level) from zone 1 (water surface according Ritter).

Formulations including the influence of friction on the wave front propagation speed are summarized in Table 2-13 and shown on Figure 2-21. It can be understood that friction lowers the wave front speed and therefore the volume of water between the wave front of Ritter solution and the friction-influenced surge wave speed has to be stored behind the wave front. Similar effects than for the wave front speed of a dam break wave might be observed for the surge wave front speed when friction is considered.

Dam break waves including downstream water levels resemble somehow to surge wave flows. An analytical solution for the horizontal, frictionless channel is given by Stoker (1957).

$$U_a = U_2 = 2(g \cdot h_0)^{0.5} - 2(g \cdot h_2)^{0.5} \quad (\text{eq. 2.70})$$

$$-V_{wB}h_3 = (U_2 - V_{wB})h_2 \quad (\text{eq. 2.71})$$

$$\frac{h_2}{h_3} = \frac{1}{2} \left[\left(1 + 8 \frac{V_{wB}^2}{(g \cdot h_3)^2} \right)^{0.5} - 1 \right] \quad (\text{eq. 2.72})$$

These equations are solved iteratively by adjusting h_2 until the difference of h_2/h_3 and (eq. 2.72) is less than an accepted error.

Table 2-13: Front propagation velocity of dam break waves. The front propagation speed V_F of the frictionless Ritter solution is compared to formulations including friction.

Author (Year)	Formulas for V_F	Remark(s)
Ritter; 1892	$V_F = 2\sqrt{gh_0}$	Frictionless; horizontal
Dressler; 1954	$V_F = 2\sqrt{gh_0} - 3.59\sqrt{gh_0} \left(\frac{g}{C^2} t \sqrt{\frac{g}{h_0}} \right)^{1/3}$	Approximated solution
Whitham; 1955	$V_F = 2\sqrt{gh_0} - 3.452\sqrt{gh_0} \left(\frac{g}{C^2} t \sqrt{\frac{g}{h_0}} \right)^{1/3}$	Approximated solution
Lauber; 1997	$V_F = 2\sqrt{gh_0} - \left(\frac{g}{C^2} t \frac{1}{0.06h_0} \right)$	Dynamic wave starts at $t = \sqrt{\frac{2h_0}{g}}$

A difference however exists relative to the formation of the wave between the dam break wave (with or without downstream water level) and the positive surge wave from upstream. Whereas the initial phase of a dam break wave consists in a water body having a practically vertical front submitted to gravity, the initial phase of a surge wave might be characterized by a relatively smooth initial wave steepening when travelling up- or downstream. Whereas the hydrostatic pressure distribution hypothesis is particularly incorrect during the initial phase and for increasing time at the dam break wave tip, this assumption becomes invalid at the surge wave front after its development.

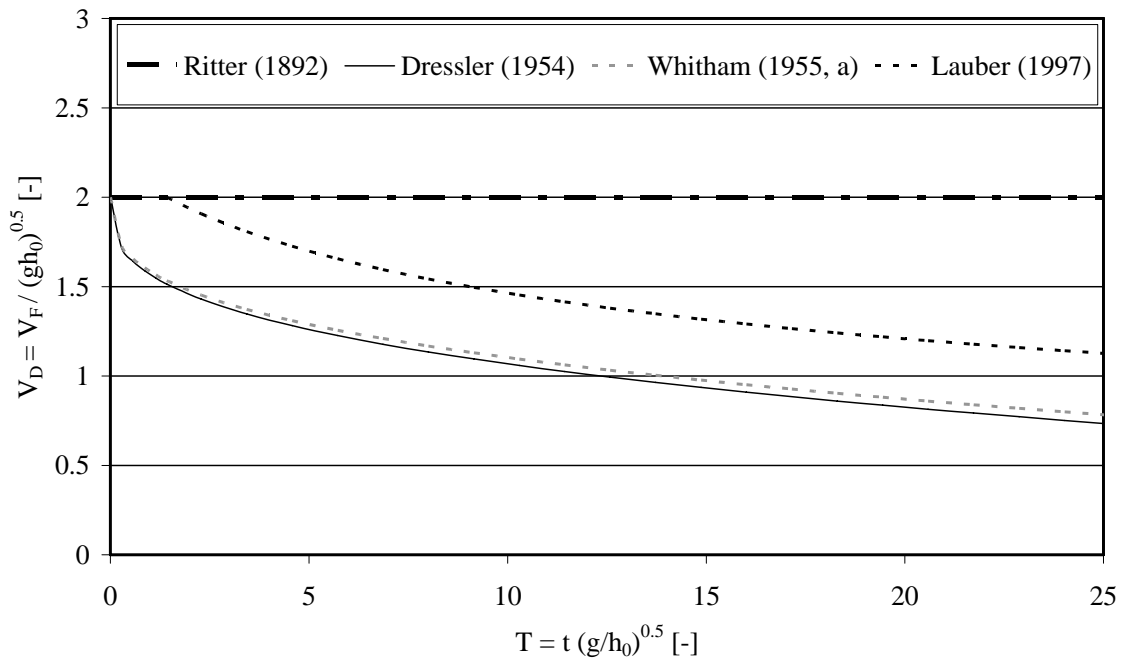


Figure 2-21 : Dimensionless solutions for the front propagation velocity of dam break waves. Following parameters have been chosen for this example: $S_0 = 0$; $f/8 = g/C^2 = 0.00175$; $h_0 = 0.3$ m.

Some common points between dam-break and surge waves exist. However, the formation process of a dam-break wave and a surge wave formed from a sudden change of the upstream discharge differs.

The friction in the dam break problem leads to the reduction of wave-front celerity under both, dry and wet downstream conditions, but especially for low ratios h_3/h_0 . Analytical solution of the surge waves (as tested in the experimental flume of the present research) including friction and bottom slope from the Saint-Venant equations are not possible to find since initial and boundary conditions are significantly more complex than in the frictionless horizontal dambreak problem.

2.3.3.4 Unsteady versus steady friction

Vardy (1992) points out that at high Reynolds numbers the wall shear stress τ_w can usefully be regarded as the sum of a steady component τ_{ws} and an unsteady component τ_{wu} . He found that the method used by Trikha (1975), used to simplify the weighting functions of Zielke (1968) is applicable also at high Reynolds numbers. The calculation procedure however takes into account two empirical constants, which are unfortunately not generally valid.

Eichinger and Lein (1992) mention that the calculation of unsteady flow in pipes is based usually on a steady state friction term although it is known that this term does not describe the real physical phenomena accurately enough. In their work, Eichinger and Lein (1992) propose to compute friction of pipes at steady state either based on the wall

shear stress or the friction power. Friction terms calculated from the wall shear stress (itself computed using the unsteady radial velocity profile) provide good results for laminar and turbulent flow conditions at unsteady state.

Murray (1992) points out several problems in transient analysis of partially full pipe flow which can be considered as an open channel flow. A main problem is that techniques of computation of unsteady free surface flow are generally tested on predominantly steady state flows and depths conditions. More accurate unsteady free surface flow should take into account modified friction term evaluation. Nevertheless, the publication mainly points out the problems and a need of research rather than a precise method for unsteady friction evaluation.

It may be concluded, modified friction term evaluation should theoretically be taken into account when dealing with unsteady flow. However, for most of the applications and numerical models, estimating the unsteady friction with steady state friction formulas is acceptable and widely used, especially in free open channel flow.

2.3.3.5 Some theoretical considerations for positive and negative surges

Frictionless surge wave propagation speed – minimum absolute celerity at $Fr = 0.5$

The first development highlights the effect that the absolute wave celerity which is composed of the mean flow velocity and the wave celerity. The wave celerity is given either by the simplified formula (eq. 2.55) for small water level difference or the complete formula (eq. 2.47) assuming significant difference in water level before and after the wave front. For a given discharge, the mean flow velocity decreases whereas the wave celerity increases. What are the conditions for which one effect becomes more important than the other?

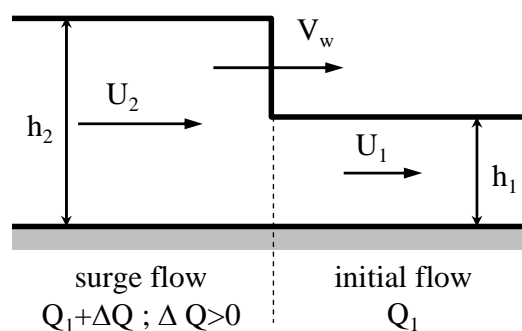


Figure 2-22 : Positive surge from upstream.

When considering a positive surge wave from upstream Figure 2-22 and when choosing a rectangular channel of width B , a regular bottom slope S_0 , a discharge Q , and a flow resistance given by $f/8$ the absolute wave celerity is calculated according to Table 2-14 (simplified or “exact” formula). The Weisbach-Darcy formula is used to compute a realistic normal flow depth h_1 even if the channel is assumed frictionless. The use of the

complete formula for the celerity requires the choice of a ΔQ and the computation of the flow depth h_2 by the formulas developed in Chow (1959). The calculation of h_2 is implicit and has to be done separately for sub- and supercritical flow due to computational reasons.

Table 2-14: Computation of the wave celerity of a positive surge from upstream.

Use of simplified formula for celerity	Use of complete formula for celerity
Step 1: Calculation of h_1 with Weisbach-Darcy:	
$S_0 = f \frac{U_1^2}{8g} \frac{1}{R_h} = \frac{f}{8g} \left(\frac{Q}{Bh_1} \right)^2 \frac{B+2h_1}{Bh_1} \quad \text{or} \quad h_1 = \left(\frac{Q}{B} \right) \left[S_0 \frac{8g}{f} \frac{Bh_1}{B+2h_1} \right]^{-0.5}$	
Step 2: Calculation of h_2 not required!	Step 2: Calculation of h_2 : subcritical flow (Chow 1959; 19-16): $h_2 = h_1 - \frac{\left(\frac{Q}{Bh_1} \right) - \left(\frac{Q + \Delta Q}{Bh_2} \right)}{\sqrt{\frac{g}{2} \frac{h_2}{h_1} (h_1 + h_2)}}$ supercritical flow (Chow 1959; 19-18) $h_2 = \left[\frac{B}{Q + \Delta Q} \left(\frac{Q}{Bh_1} + \frac{h_2 - h_1}{c} \left(\frac{h_1 + h_2}{2h_1} \right) g \right) \right]^{-1}$
Step 3: Calculation of V_w :	Step 4: Calculation of V_w :
$V_w = \frac{Q}{Bh_1} + \sqrt{gh_1} \quad (\text{eq. 2.55})$	$V_w = \frac{Q}{Bh_1} + \sqrt{\frac{g}{2} \frac{h_2}{h_1} (h_1 + h_2)} \quad (\text{eq. 2.47})$

Figure 2-23 shows the results of the computations for the chosen parameters $Q = 50$ l/s; $\Delta Q = 25$ l/s, $B = 1$ m and $f/8 = 0.01$ for various channel slopes S_0 . Analysis of similar graphs but having different numerical values of the parameters reveals the following:

- When considering the simplified formula for the celerity $c = (g \cdot h)^{0.5}$, the absolute surge wave celerity V_w is increasing for Froude numbers $Fr_1 < 0.5$. The decrease of the mean flow velocity U_1 is less important than the increase of the celerity c . For channel slopes leading to Froude numbers $Fr_1 > 0.5$, V_w is increasing too. The increase of the mean flow velocity is more important than the decrease of the celerity. A minimum absolute surge wave celerity is always observed for a Froude number $Fr_1 = 0.5$. In this case, the mean flow velocity of the baseflow U_1 is half of the celerity $c = (g \cdot h)^{0.5}$.
- The absolute surge wave celerity corresponds to $V_w = 2U_1$ for Froude numbers $Fr_1 = 1$ since the mean flow velocity U_1 is equal to the celerity $c = (g \cdot h)^{0.5}$.

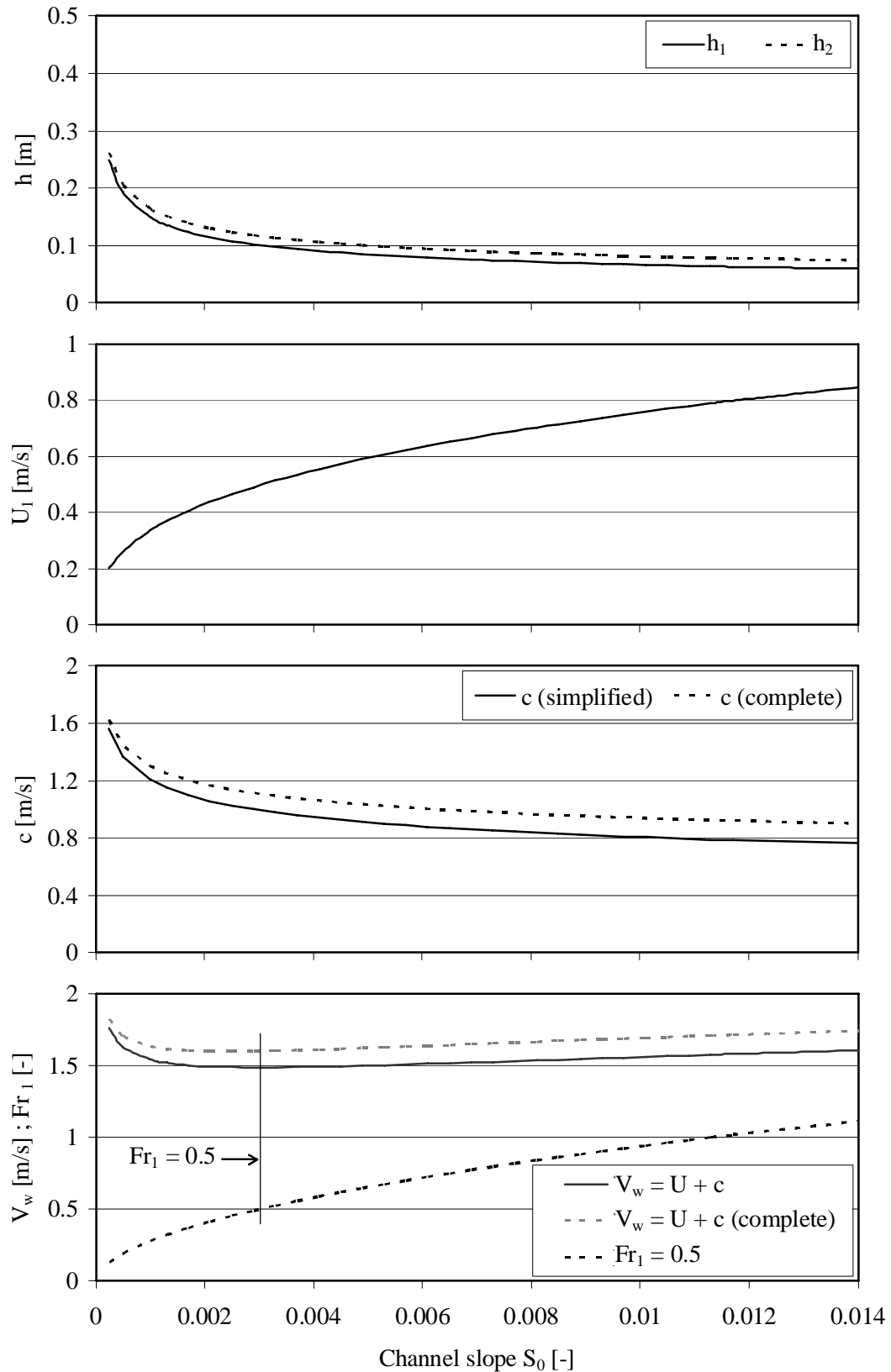


Figure 2-23 : Calculated flow depths h_1 (before) and h_2 (after) the surge; mean flow velocity U_1 ; celerity c ; absolute surge wave celerity $V_w = U_1 + c$ and Froude number of the base flow Fr_1 for a surge wave having a base flow $Q_b = 50$ l/s, an additional flow $\Delta Q = 25$ l/s, $B = 1$ m and $f/8 = 0.01$ as a function of the channel slope.

- When the complete formula is considered for the calculation of the celerity c , the Froude number leading to minimum absolute surge wave celerity is shifted to values slightly lower than 0.5 since U_1 is identical but the celerity of the complete formula is higher than the celerity of the simplified formula for a positive surge from upstream.

Minimum absolute celerity for Froude numbers $Fr_1 = 0.5$ is mathematically show by differentiation of (eq. 2.55) where h_1 is expressed with Fr_1 :

$$\frac{dV_w}{dh_1} = -\frac{Q}{B}h_1^{-2} + 0.5\sqrt{g}h_1^{-0.5} = -\frac{Q}{\underbrace{Bh_1}_{U_1}}\frac{Fr_1^2}{U_1^2}g + 0.5g\frac{Fr_1}{U_1} = -\frac{Fr_1^2}{U_1}g + 0.5g\frac{Fr_1}{U_1} \quad (\text{eq. 2.7})$$

Minima respectively maxima of V_w depending on Fr_1 correspond to $dV_w/dh_1 = 0$ leading to:

$$\frac{dV_w}{dh_1} = 0 = -\frac{Fr_1^2}{U_1}g + 0.5g\frac{Fr_1}{U_1} = -Fr_1 + 0.5 = 0 \quad (\text{eq. 2.74})$$

The Froude number leading to minimum value of V_w becomes thus $Fr_1 = 0.5$. The identical development can be done for a negative surge wave from upstream. Minimum absolute surge wave celerity in this case is found for $Fr_1 = 0.5$ too where Fr_1 is related to the situation of the flow before the passing of the wave front.

The absolute wave celerity is depending on both, the mean flow velocity and the flow depth. If the simplified formula is considered (eq. 2.55), the absolute surge wave celerity becomes minimal for $Fr_1 = 0.5$. As the Froude number is affected by the slope and the flow resistance, the absolute wave celerity is indirectly influenced by the flow resistance too. At least theoretically, it is possible to find a channel roughness leading to Froude equal to 0.5 for a given slope and discharge. Furthermore, the absolute surge wave celerity is quite constant for flow conditions leading to Fr_1 close to 0.5. In back-water-curves having local Froude numbers close to 0.5, the absolute surge wave celerity is expected to be more or less constant since a reduction of the celerity c is compensated by an increase of the mean flow velocity U_1 for $Fr_1 < 0.5$ and vice versa if $Fr_1 > 0.5$.

Wave celerity for a positive surge wave including friction and bottom slope

The second development reveals the effect of friction and bottom slope on the positive surge wave celerity. The mathematical approach starts from the continuity and momentum equation which are then developed in the same way than for the frictionless horizontal channel.

Considering the positive surge wave moving from upstream to downstream in a rectangular channel having a constant bottom slope S_0 and a steady flow resistance given by $f/8$. The channel width is B . The flow conditions downstream of the surge wave front are given by the initial flow depth h_1 and the mean flow velocity U_1 whereas the conditions upstream are given by $h_2 > h_1$ and U_2 . The absolute surge wave celerity is V_w . The length of the control volume L is such that hydrostatic pressure distributions exist at its downstream and upstream end. From the momentum principal one can find (e.g. Chow 1959):

$$\frac{1}{g}(V_w - U_2)Bh_2\rho(U_2 - U_1) = F \quad (\text{eq. 2.75})$$

where F is the unbalanced force and ρ the density of the fluid. In the case of the frictionless horizontal channel, F is equal to the difference between the hydrostatic pressures on the areas Bh_2 and Bh_1 . When the bottom slope and channel friction are considered, F is expanded with bottom and friction related components leading to:

$$F = \rho B \left(\frac{h_2^2}{2} - \frac{h_1^2}{2} \right) + \rho BL \left(\frac{h_1}{2} + \frac{h_2}{2} \right) S_0 - F_f \quad (\text{eq. 2.76})$$

where F_f is the friction component of the unbalanced force. This term can be expressed using the definition of the bottom shear stress τ_0 :

$$F_f = \frac{1}{g}\tau_0 PL = \frac{1}{g}\gamma R_h S_f PL = \frac{1}{g}\gamma \frac{B\bar{h}}{B+2\bar{h}} S_f (B+2\bar{h})L = \rho BL \left(\frac{h_1}{2} + \frac{h_2}{2} \right) S_f \quad (\text{eq. 2.77})$$

where P is the wetted perimeter, R_h the hydraulic radius, γ the specific weight and \bar{h} the averaged height of the flow upstream and downstream of the wavefront. Alternatively the control volume can also be divided into a part downstream and a part upstream of the wave front and the friction component of the unbalanced force becomes thus:

$$F_f = \frac{\rho BL}{2} (h_1 S_{f1} + h_2 S_{f2}) \quad (\text{eq. 2.78})$$

When introducing (eq. 2.78) or (eq. 2.78) in (eq. 2.76) and (eq. 2.76) in (eq. 2.75) the momentum equation for a prismatic rectangular channel writes:

$$\frac{1}{g}(V_w - U_2)h_2(U_2 - U_1) = \underbrace{\frac{1}{2}(h_2^2 - h_1^2)}_{\text{pressure term}} + \underbrace{\frac{1}{2}L(h_1 + h_2)(S_0 - S_f)}_{\text{channel slope \& friction terms}} \quad (\text{eq. 2.79a})$$

or alternatively (eq. 2.79b):

$$\frac{1}{g}(V_w - U_2)h_2(U_2 - U_1) = \underbrace{\frac{1}{2}(h_2^2 - h_1^2)}_{\text{pressure term}} + \underbrace{\frac{1}{2}L(h_1 + h_2)S_0}_{\text{channel slope term}} - \underbrace{\frac{1}{2}L(h_1S_{f1} + h_2S_{f2})}_{\text{friction slope term}}$$

The continuity equation is written as:

$$U_2 = \frac{U_1 h_1 + V_w (h_2 - h_1)}{h_2} \quad (\text{eq. 2.44b})$$

Such as for the horizontal frictionless channel, (eq. 2.44b) can be replaced in (eq. 2.79a or b). After simplifications the absolute surge wave celerity for the sloping channel including friction writes as:

$$c^2 = (V_w - U_1)^2 = \underbrace{\frac{g}{2} \frac{h_2}{h_1} (h_1 + h_2)}_{\text{"A"}} + \underbrace{\frac{g}{2} \frac{h_2}{h_1} \frac{(h_1 + h_2)}{(h_2 - h_1)} L(S_0 - S_f)}_{\text{"B"}} \quad (\text{eq. 2.80a})$$

or alternatively (eq. 2.80b):

$$c^2 = (V_w - U_1)^2 = \underbrace{\frac{g}{2} \frac{h_2}{h_1} (h_1 + h_2)}_{\text{"A"}} + \frac{g}{2} \frac{h_2}{h_1} \frac{(h_1 + h_2)}{(h_2 - h_1)} L S_0 - \frac{g}{2} \frac{h_2}{h_1} \frac{(h_1 S_{f1} + h_2 S_{f2})}{(h_2 - h_1)} L$$

From (eq. 2.80a) the following can be derived:

- The classical form (eq. 2.47) of the celerity of a positive surge wave from upstream is obtained when the channel is frictionless and horizontal ($S_0 = S_f = 0$). Term "B" is equal to zero in this case.
- The classical form of the celerity of a positive surge wave from upstream can also be found if the friction is assumed to be compensated by the bottom slope ($S_0 = S_f$) at the control volume.
- According to the continuity equation (eq. 2.44b) the difference in discharge ΔQ is reduced and/or the depth h_2 when the absolute wave celerity is below that in a frictionless horizontal channel
- When the friction slope is less than the bottom slope the term "B" becomes positive and thus the celerity is higher than in the case of the frictionless horizontal channel.
- The length of the control volume is a priori an unknown but an important parameter for the modification of the celerity by friction and bottom slope of a steep front positive surge wave.

The friction slope S_f might be calculated with the Weisbach-Darcy formula leading to:

$$S_f = \frac{1}{2} \frac{f}{8g} \frac{U_1^2}{R_{h1}} + \frac{1}{2} \frac{f}{8g} \frac{U_2^2}{R_{h2}} \quad (\text{eq. 2.81})$$

where U_2 is the mean flow velocity upstream of the surge wave front. U_2 can be again replaced by (eq. 2.44b) issued from the continuity principal.

The influence of friction and bottom slope on the equation (eq. 2.80a and b) is illustrated with an example. Following parameters are chosen: different channel slopes S_0 ; the channel width B ; a baseflow Q , a length of the control volume and various channel flow resistance given by $f/8$. The flow depth downstream of the positive surge wave h_1 is calculated from these parameters using the Weisbach-Darcy formula. It is then assumed that a sluice gate operation upstream produces an increase of the flow depth of h' leading to $h_2 = h_1 + h'$.¹ Figure 2-24 shows the influence of friction and bottom slope on the surge wave celerity. The absolute surge wave celerity V_w calculated from the equation including friction and bottom slope (terms “A” & “B”) is compared to the equation developed for horizontal and frictionless conditions (term “A” only).

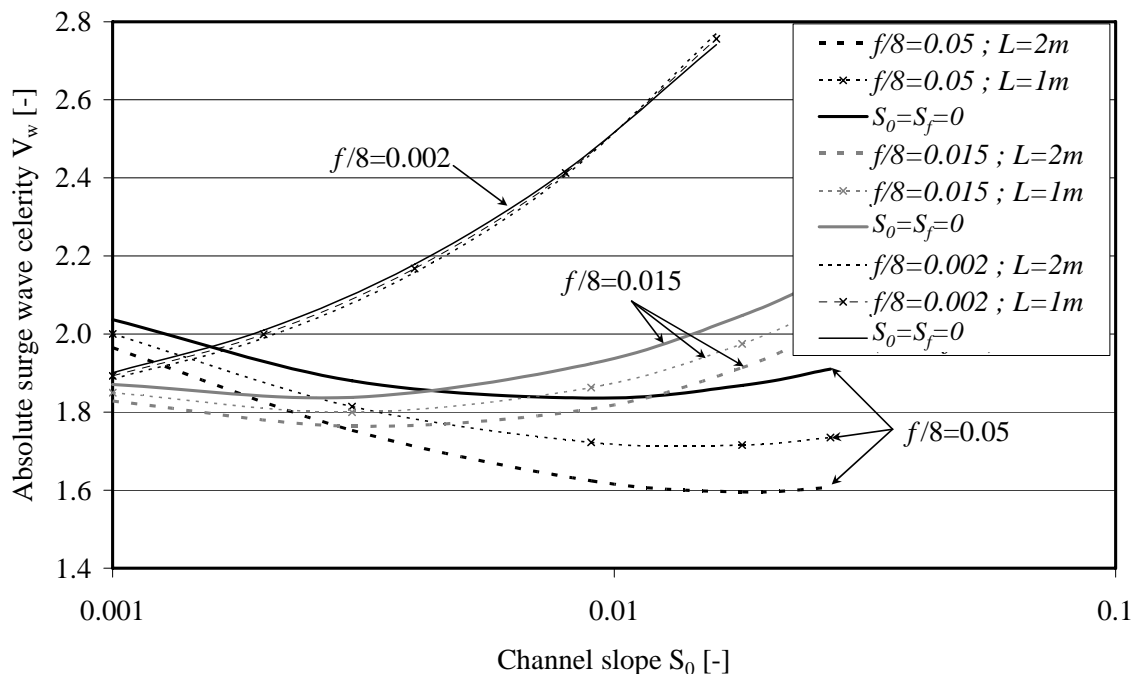


Figure 2-24 : Absolute wave celerities V_w : base flow $Q = 50$ l/s, $B = 1$ m, $h' = 0.05$ m as a function of the bottom slope for three different friction coefficients and two different lengths of control volume.

The figure includes two effects and points out the characteristics of (eq. 2.80a). The first effect has already been described above and is related to the minimum of the absolute celerity for Froude number of the base flow $Fr_1 = 0.5$. For a channel resistance of $f/8 = 0.002$, Froude numbers are higher than 0.5 for all slopes and the absolute surge wave celerity increases with the slope. For the other two friction coefficients

¹ Theoretically it would be more rigorous to choose a difference in discharge ΔQ and calculating the flow depth h_2 as $h_2 = h_1 + \Delta Q/V_w$ and introduce this term in formula (eq. 2.51). The three unknowns of the problem (V_w , h_2 , U_2) can be solved by three equations namely: the momentum equation, the continuity equation of the control volume and the equation $Q_2 = U_2 h_2$. Nevertheless, it is much more efficient for this example to chose h_2 directly.

($f/8 = 0.015$ and $f/8 = 0.050$) the drop and rise of V_w is observed. The second effect relates to the influence of the friction related term of the modified momentum equation. It appears that friction obviously has an influence on the wave celerity but it becomes visible only when relatively high friction coefficients and/or important length of the control volume are considered. The effect of the length is shown by the comparison of 2 m and 1 m length of the considered control volume.

When considering the case of $f/8 = 0.002$, the effect of a bottom slope higher than the computed friction slope becomes visible. For a channel slope higher than 0.01 the calculated friction slope is lower than the bottom slope and the absolute celerity including the friction becomes more important than the frictionless one. When the hypothesis of a large channel is assumed, the normal depth h_1 and the friction slope S_f can be computed with h instead of R_h . For this case it is possible to show that the change to absolute surge wave celerity higher than for the horizontal frictionless channel takes place at $Fr = 2$ respectively for bottom slopes corresponding to 4 times to $f/8$ (Darcy-Weisbach).

From the second development presented above it is concluded that friction has an influence on the absolute surge wave celerity but only when the friction coefficients are relatively high and when the length of control volume of the modified momentum equation is not too small. Effect of bottom slope and friction influences the wave celerity controversially and both effects might compensate each other (e.g. horizontal frictionless channel). In the particular case of a bottom slope higher than the friction slope, the absolute celerity is higher than the horizontal frictionless one for identical flow depths h_1 and h_2 . An important but a priori unknown parameter in equation (eq. 2.80a and b) is the length L of the control volume.

2.4 Conclusions

The literature review revealed a need of further research on macro-rough flow resistance and its influence on surge wave flow as well as highly unsteady flow. The originality of the experimental investigations of the present study is:

- To describe qualitatively and quantitatively the effect of macro-scale roughness on the flow resistance in channels with macro-roughness at banks for subcritical flow conditions.
- To conduct systematic surge wave experiments of positive and negative surges in complex geometries under controlled laboratory conditions. The experiments include flow depth and flow velocity downstream of the surge wave front.
- To investigate the influence of the macro-scale roughness on surge wave propagation and deformation.

To the author's best knowledge, these three points have not been investigated system-

atically until now. The research follows earlier works conducted at the Laboratory of Hydraulic Constructions (LCH-EPFL) on the influence of macro-roughness on surface flows (Dubois 1998), of vertical ribs placed at outer bank in armoured channels (Hersberger 2003) and the effect of macro-roughness elements on the energy dissipation in stepped chutes (André 2004).

3 EXPERIMENTAL SETUP & TEST PROGRAM

Experiments under steady and unsteady flow conditions have been performed in the test flume at the Laboratory of Hydraulic Constructions LCH at EPFL. The main goal of the **steady flow** tests was to highlight and to understand for a large number of geometrical configurations the influence of macro-roughness elements on the flow conditions. The **unsteady flow** tests (positive and negative surge waves traveling downstream) had the purpose to reveal how the surge wave propagation and deformation are influenced by the macro-roughness elements. This chapter contains all relevant information about the experimental setup and the steady and unsteady experiments.

3.1 *Test flume*

The channel has a useful length of $L_{tot} = 38.33$ m and a mean slope of $S_0 = 1.14\%$ (Figure 3-1, Figure 3-2 and Figure 3-3). The channel base width is $B = 0.485 \pm 0.002$ m and remained constant during all the tests.

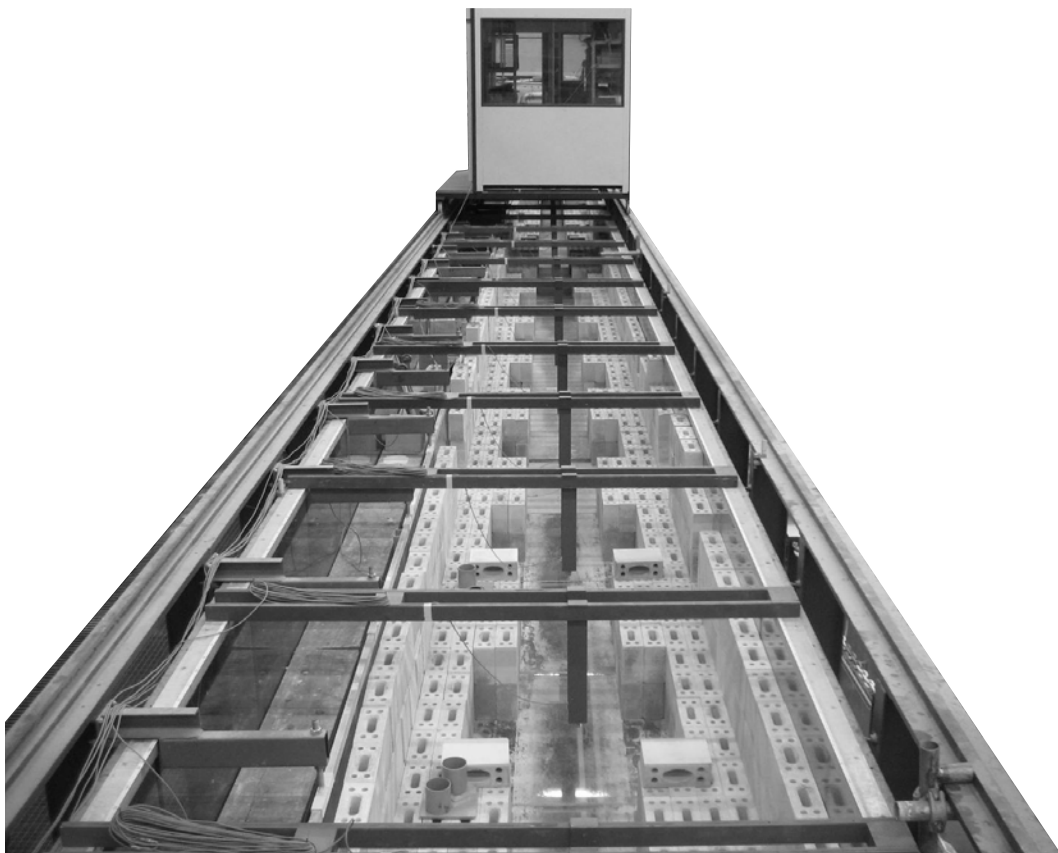


Figure 3-1: *Laboratory flume of the Laboratory of Hydraulic Constructions (LCH) at EPFL viewed from downstream.*

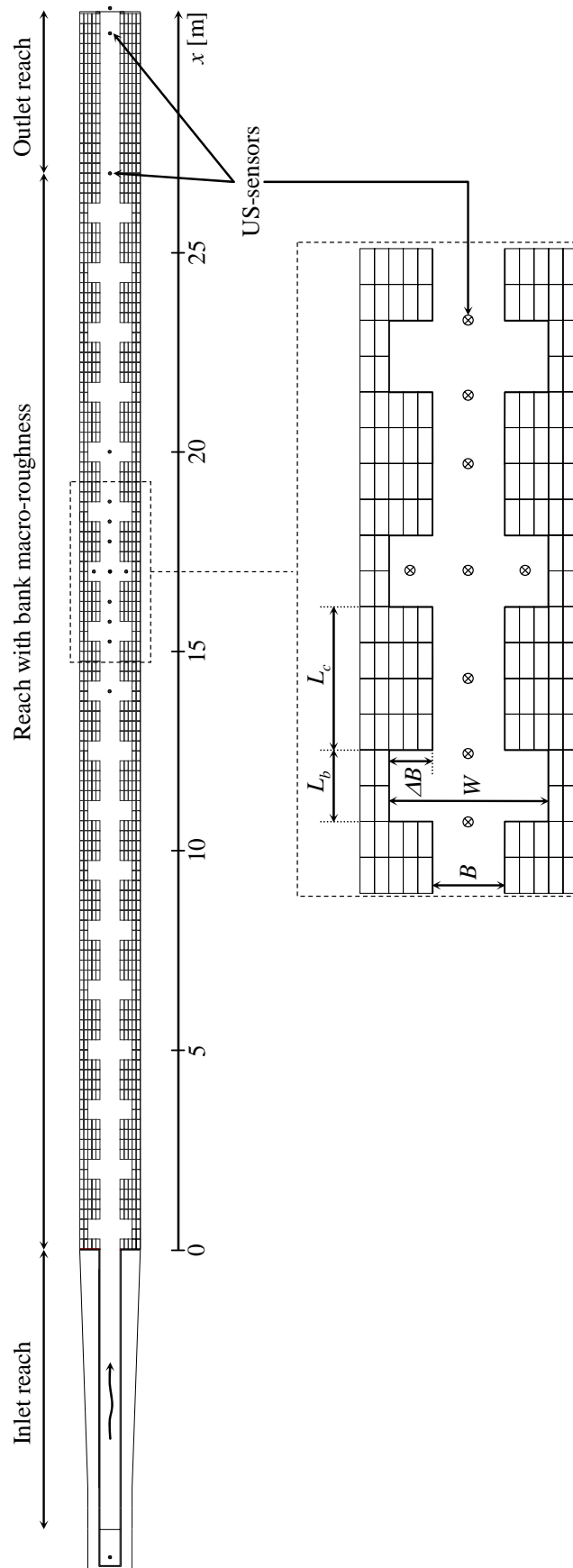


Figure 3-2: Plan view of the test flume divided into an inlet reach, a reach with bank macro-roughness elements (rectangular cavities) and an outlet reach.

The channel is divided from upstream to downstream into an inlet reach with a length $L_{in} = 7.40$ m, a reach with rectangular cavities at the side walls (bank macro-roughness elements) with $L_{MR} \cong 26.85$ m and an outlet reach with $L_{out} \cong 4.0$ m (Figure 3-2). The exact lengths of L_{MR} and L_{out} depend on the arrangement of the macro-roughness elements. The sidewalls of the reach with rectangular cavities and the outlet reach are formed by limestone bricks which allow changing easily the geometrical configurations. The equivalent sand roughness of this limestone bricks has been determined by means of backwater curve computations in a rectangular prismatic configuration ($k_{sw} = 0.021$ mm) without macro-roughness elements. In the same way the equivalent sand roughness of the bottom was determined ($k_{s0} = 0.001$ mm). The channel bed is fixed and no sediment transport is considered. The flow is controlled from downstream due to a particularly shaped cross section.

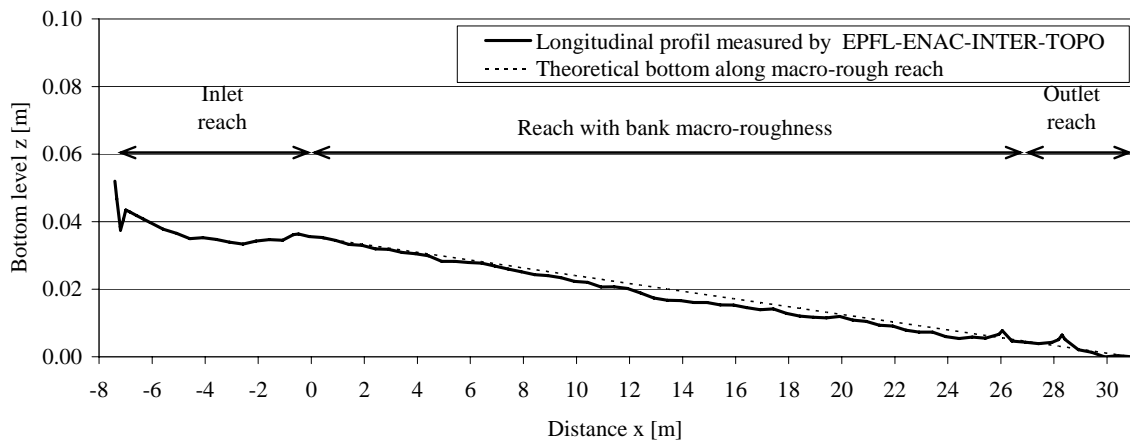


Figure 3-3: High precision longitudinal profile of the test flume measured by the geodetic engineering laboratory TOPO at EPFL.

The imprecision compared to a theoretical bottom of constant slope between the end of the inlet reach and the end of the channel is of ± 0.003 m. Even if Figure 3-3 reveals some geometrical imprecision's, with regard to the vertical distortion, the slope can be considered about constant along the macro-rough reach. However, for the computation of the backwater-curves (see § 4.3), the exact geometry has been taken into account in order to exclude errors related to the channel slope.

3.2 Upstream boundary: Inlet basin

The fully automatic water supply system of the laboratory delivers the water into the inlet basin located upstream of the inlet reach. This basin forms the upstream boundary condition of the inlet reach. The inlet basin has a length of 2.0 m, a width of 1.6 m and a depth of about 1.5 m measured from the channel bottom. The free surface of this basin is covered by a reinforced PVC plate having an opening of 0.9 m length and 0.5 m width corresponding to the one of the inlet reach. The inlet basin is shown in Figure 3-4.

The longitudinal profile of the alimentation basin and the first 2 m of the inlet reach are presented in Figure 3-5.

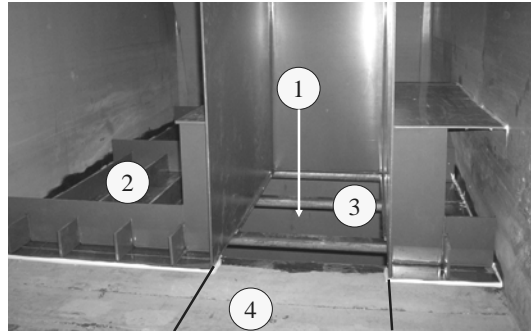


Figure 3-4: Inlet basin (1) covered by a reinforced PVC plate (2) with an opening (3) conducting to the upstream part of the inlet reach (4). The inlet reach is shown without lateral side walls (picture taken during the construction).

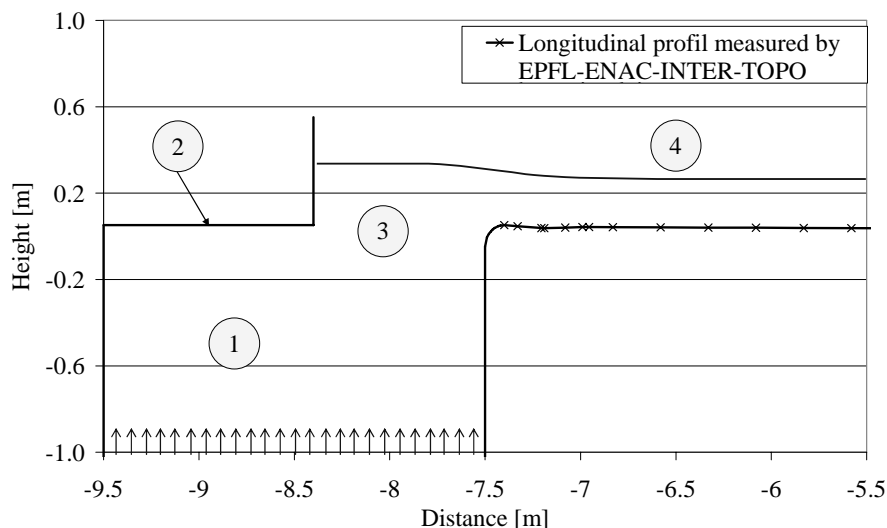


Figure 3-5: Section through the inlet basin and the first two meters of the inlet reach. $x = 0$ m is located at the end of the inlet reach.

3.3 Downstream boundary: Outlet cross section

Without particularly shaped cross section, a backwater curve (type M_2 , e.g. Henderson 1966) would be observed in the channel. Therefore, a particularly shaped cross section was placed at the downstream end of the outlet reach. Its geometry was optimized in order to simulate a long channel at uniform flow depth. Flow conditions were subcritical during the tests due to the small slope and the section at the outlet for the range of desired discharges¹. The geometry of the section has been optimized using an approach proposed by Carlier (1988).

¹ For some channel sections corresponding to the irregularities of the longitudinal profile, near critical flow conditions were observed for the discharges $Q < 0.007 \div 0.008$ m³/s.

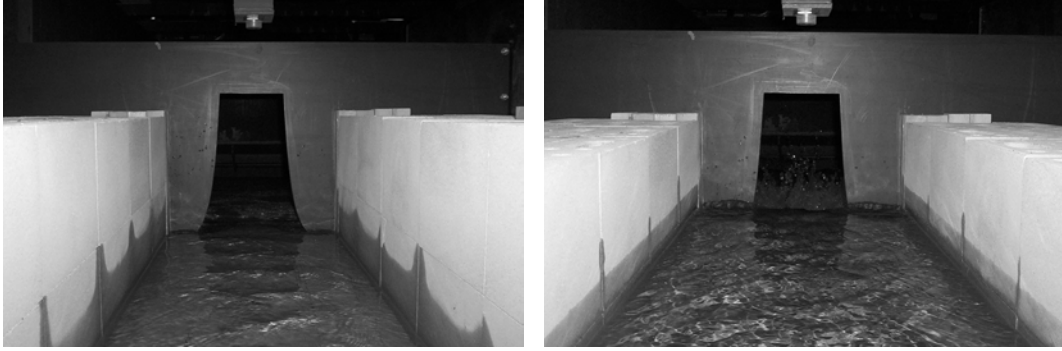


Figure 3-6: Outlet section for different discharges.

According to Figure 3-7 the discharge dQ of a small horizontal slice dz can be written as:

$$dQ = \mu B(z) \sqrt{2g(h-z)} dz \quad (\text{eq. 3.1})$$

where μ is the contraction coefficient and $B(z)$ the flow width at the vertical position z .

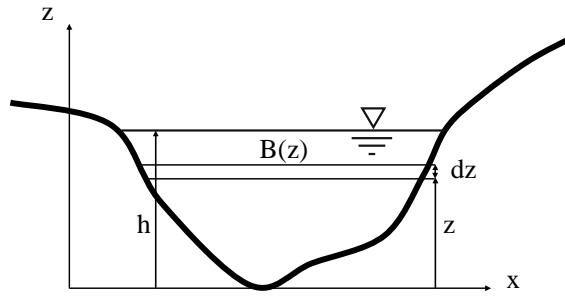


Figure 3-7: Definition of the parameters for the computation of the outlet section geometry.

The integration of equation 3-1 over the flow depth h allows finding the discharge Q of the cross section as:

$$Q(h) = \mu \sqrt{2g} \int_0^h B(z) \sqrt{(h-z)} dz \quad (\text{eq. 3.2})$$

$B(z)$ can be used to adjust the behavior of the $Q(h)$ function. For example if a behavior according to the Strickler law is wished, $Q(h)$ can be expressed as:

$$Q(h) = K_{st} A(h) R_h(h)^{2/3} S_f^{1/2} \quad (\text{eq. 3.3})$$

where K_{st} is the Strickler coefficient, $A(h)$ the flow area, $R_h(h)$ the hydraulic radius and S_f the friction slope. The friction slope S_f is the same as the bottom slope S_0 for uniform flow. The function $B(z)$ describing the form of the cross-section can now be found by minimizing the difference of the equations (eq. 3.2) and (eq. 3.3) for a range of desired discharges:

$$\text{Min}(\Delta Q) = \text{Min} \left[\mu \sqrt{2g} \int_0^h B(z) \sqrt{(h-z)} dz - K_{st} A(h) R_h(h)^{2/3} S_f^{1/2} \right] \quad (\text{eq. 3.4})$$

The proposed particularly shaped cross section has a major advantage over the classical and widely employed movable flap gate. For a quite important range of discharges no manipulations are needed between steady flow tests having different discharges. The method described above has been used to find an adequate geometry of the downstream section for the test flume. The minimization of equation (eq. 3.4) for a range of discharges from 0 to 0.25 m³/s applying the Strickler law ($K_{st} \cong 92 \text{ m}^{1/3} \text{ s}^{-1}$, $S_0 = 0.00114$, $B = 0.485 \text{ m}$, $\mu = 0.9$) permitted to find the function $B(z)$ as:

$$B(z) = 0.1462 z^{0.25} \quad (\text{eq. 3.5})$$

Figure 3-8 shows the comparison between the wished behavior of the channel outlet section and the one obtained with the particularly shaped cross section (eq. 3.2). The choice of K_{st} is related to an a priori estimation of the channel roughness.

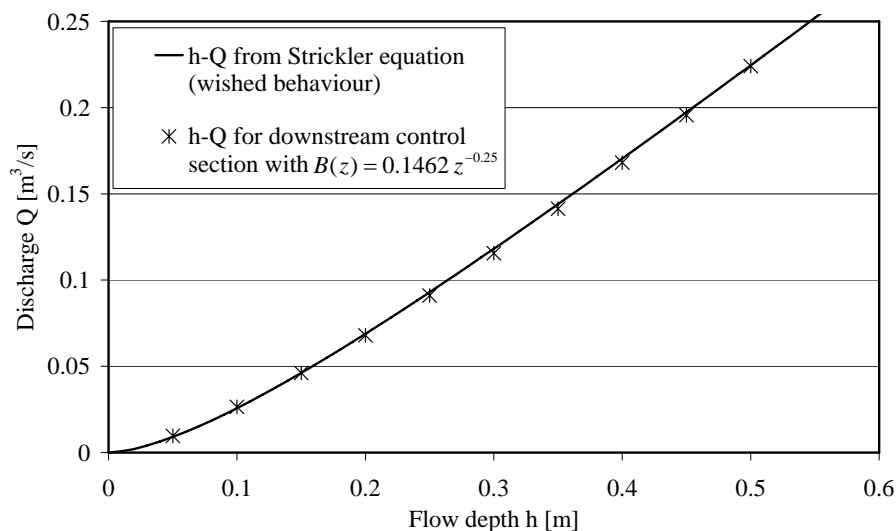


Figure 3-8: Comparison between the wished relationship Q - h and the behavior obtained with the selected outlet section.

Finally, the effective behavior of the channel outlet section has been verified by water level measurements along the channel for different discharges. A water surface parallel to the channel bottom indicates uniform flow conditions. Figure 3-9 shows the water level measurements for different discharges¹. The measured water surface is mostly parallel to the bottom. Some remaining minor deviations from the uniform flow depth must be explained by the irregularities of the channel longitudinal profile.

¹ This result has been obtained after minor modifications of the geometry of the outlet section. The theoretical geometry based on the estimated K_{st} value led to a backwater curve of the type M_1 since the effective Strickler coefficient of the channel is higher than 92.

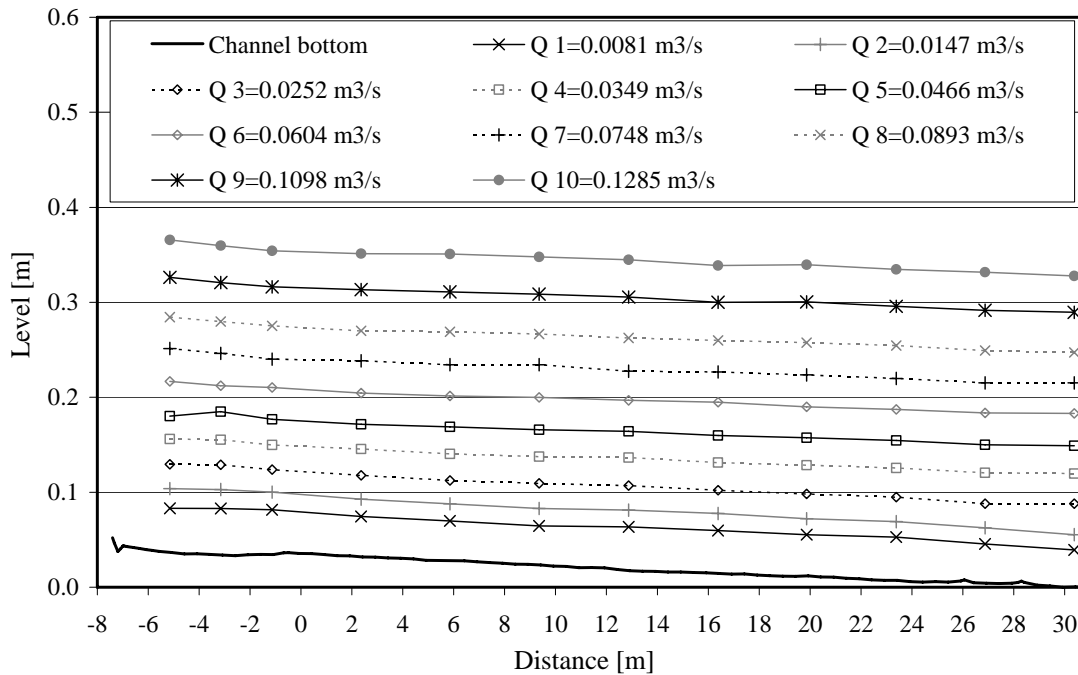


Figure 3-9: Water level measurements for different discharges with the selected downstream particularly shaped cross section.

3.4 Macro-roughness configurations

(Macro)-roughness elements can be classified into spot roughness, strip roughness and depression roughness elements (Morris and Wiggert 1972). They can be located either on the bottom (André 2004) and/or at the banks of a channel (Hersberger 2003) as well as on the whole perimeter in case of pipeflow (Morris 1954). The arrangement of the macro-roughness elements can be either regular or random (Canovaro 2005).

The macro-roughness elements considered in this research are large scale depression roughness elements at both channel banks (also called cavities or widenings in the text). As mentioned above, the sidewalls of the reach with macro-roughness elements and the outlet reach are formed with limestone bricks (Figure 3-11). The limestone bricks are 0.25 m long, 0.10 m wide and 0.19 m high. Two superimposed horizontal layers of bricks have been placed in the channel allowing thus a maximum flow depth of 0.38 m. The chosen modular system allowed to change efficiently the geometrical arrangement of the macro-roughness elements.

Three geometrical parameters – the length of the cavity L_b , the distance between two cavities L_c and the depth (or lateral extent) of the cavity ΔB – have been systematically varied during the tests (Figure 3-2). The base width $B = 0.485$ m remained constant during all the tests. The aspect ratio of the cavity is defined as $\Delta B / L_b$. The aspect ratio of the cavities including the river width is defined as $(B + 2\Delta B) / L_b$. The expansion ratio is defined as $(B + 2\Delta B) / B$. The geometrical proprieties of the 36 different tested configurations are summarized in Table 3-1. A prismatic channel with constant width

$B = 0.485 \text{ m}$ has been used as reference for the 36 macro-rough configurations. The bottom level is the same in the main channel and in the cavities.

Table 3-1: Geometrical properties of the tested axi-symmetric configurations.

Configuration	L_b [m]	L_c [m]	ΔB [m]	$\Delta B / L_b$ [-]	$(B + 2\Delta B) / L_b$ [-]	$(B + 2\Delta B) / B$ [-]
111	0.5	0.5	0.1	0.2	1.37	1.41
112	0.5	0.5	0.2	0.4	1.77	1.82
113	0.5	0.5	0.3	0.6	2.17	2.24
114	0.5	0.5	0.4	0.8	2.57	2.65
121	0.5	1.0	0.1	0.2	1.37	1.41
122	0.5	1.0	0.2	0.4	1.77	1.82
123	0.5	1.0	0.3	0.6	2.17	2.24
124	0.5	1.0	0.4	0.8	2.57	2.65
141	0.5	2.0	0.1	0.2	1.37	1.41
142	0.5	2.0	0.2	0.4	1.77	1.82
143	0.5	2.0	0.3	0.6	2.17	2.24
144	0.5	2.0	0.4	0.8	2.57	2.65
211	1.0	0.5	0.1	0.1	0.685	1.41
212	1.0	0.5	0.2	0.2	0.885	1.82
213	1.0	0.5	0.3	0.3	1.085	2.24
214	1.0	0.5	0.4	0.4	1.285	2.65
221	1.0	1.0	0.1	0.1	0.685	1.41
222	1.0	1.0	0.2	0.2	0.885	1.82
223	1.0	1.0	0.3	0.3	1.085	2.24
224	1.0	1.0	0.4	0.4	1.285	2.65
241	1.0	2.0	0.1	0.1	0.685	1.41
242	1.0	2.0	0.2	0.2	0.885	1.82
243	1.0	2.0	0.3	0.3	1.085	2.24
244	1.0	2.0	0.4	0.4	1.285	2.65
411	2.0	0.5	0.1	0.05	0.3425	1.41
412	2.0	0.5	0.2	0.10	0.4425	1.82
413	2.0	0.5	0.3	0.15	0.5425	2.24
414	2.0	0.5	0.4	0.20	0.6425	2.65
421	2.0	1.0	0.1	0.05	0.3425	1.41
422	2.0	1.0	0.2	0.10	0.4425	1.82
423	2.0	1.0	0.3	0.15	0.5425	2.24
424	2.0	1.0	0.4	0.20	0.6425	2.65
441	2.0	2.0	0.1	0.05	0.3425	1.41
442	2.0	2.0	0.2	0.10	0.4425	1.82
443	2.0	2.0	0.3	0.15	0.5425	2.24
444	2.0	2.0	0.4	0.20	0.6425	2.65

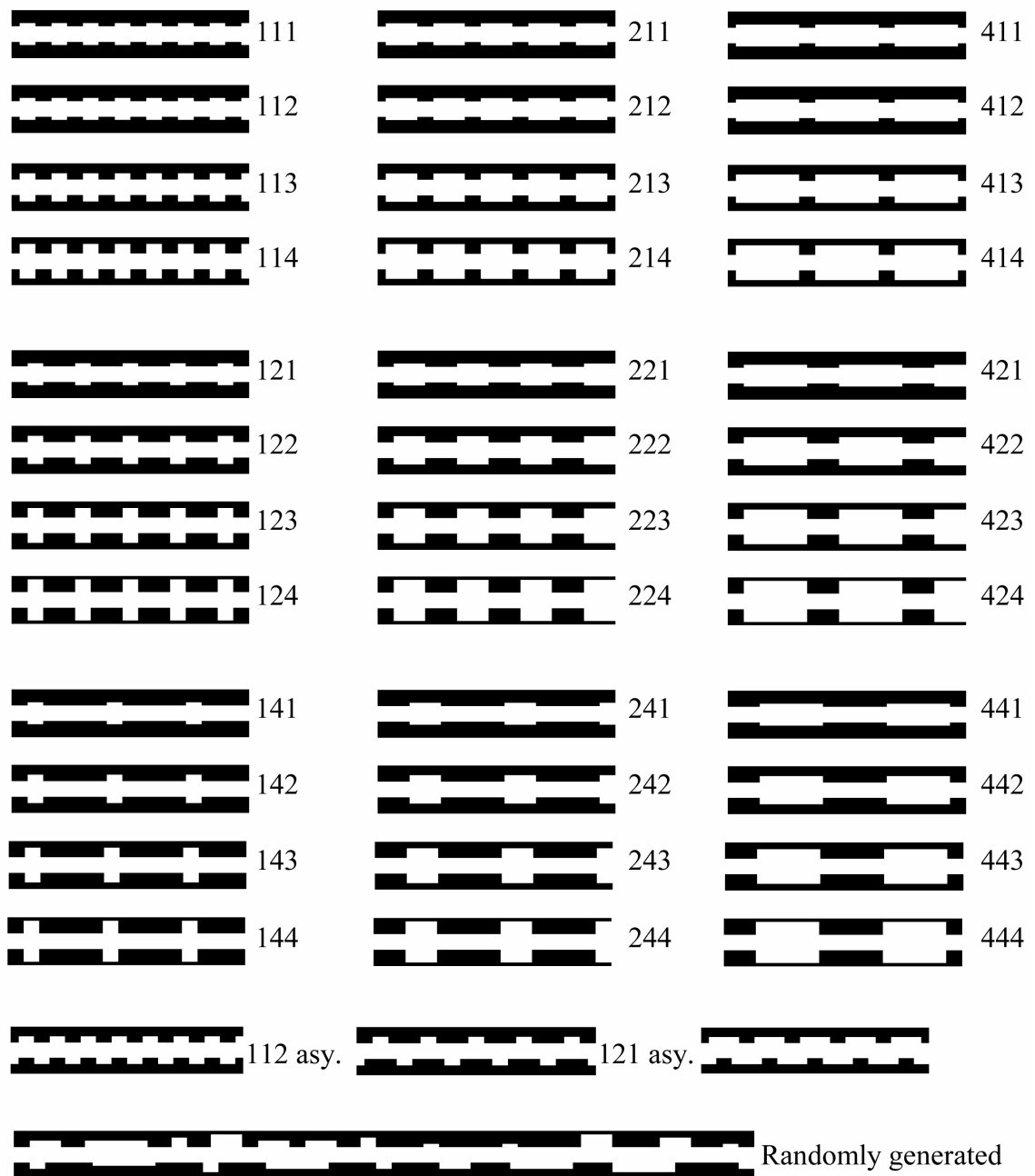


Figure 3-10: The 36 investigated axi-symmetric macro-rough configurations.

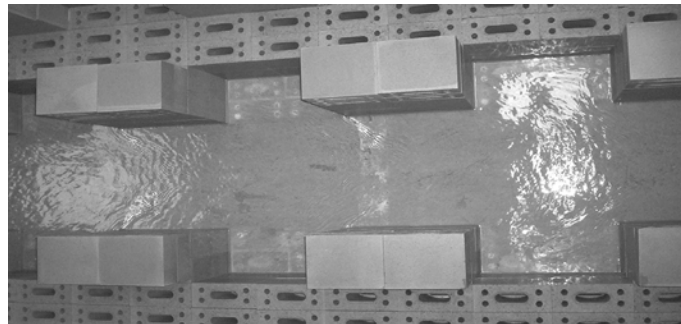


Figure 3-11: Example of the cavities (macro-roughness at banks) built using the modular system of limestone bricks. Example of configuration 111.

The denomination of the different test geometries is explained in Figure 3-12. The geometrical proprieties can be obtained directly from the configuration name. The first number indicates the cavity length L_b as a multiple of B , the second number is related to the distance between two cavities L_c as a multiple of B and the third number defines the cavity depth ΔB as a multiple of $B/5$.

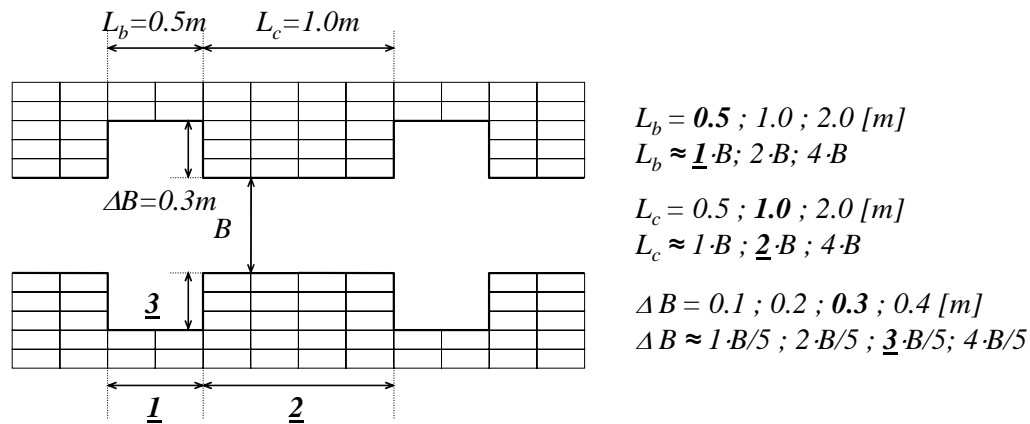


Figure 3-12: Denomination of the different test configurations. Example: configuration 123.

Three of the 36 axi-symmetric configurations have been tested in an asymmetric arrangement by applying a longitudinal displacement $(L_b + L_c) / 2$ to one channel bank (configurations 112a, 122a and 212a). In addition to the 36 axi-symmetric and the 3 asymmetric configurations, a randomly generated configuration has been analyzed (Figure 3-10).

In order to obtain the random arrangement of the bank macro-roughness, both bank geometries have been constructed going from upstream to downstream choosing the succession of the cavities randomly from the 36 different geometrical configurations.

All tested configurations (1 prismatic, 36 axi-symmetric, 3 with a longitudinal displaced channel bank and 1 with randomly generated cavities) are shown in Appendix 4-1.

3.5 Device for generating positive and negative surge waves

3.5.1 Description of the setup for surge wave generation

The main challenge during the adaptation of the existing test channel for the experiments of this study was the realization of a setup generating positive and negative surge waves with well defined characteristics. The setup (Figure 3-13) described hereafter has been designed and built based on following elements:

- An upper basin (1) placed on the flume over the inlet basin with a separate water supply system (2) and a crest spillway (3).
- Six different pipes (4) connecting the upper basin (1) with the inlet basin (5).
- A flap gate (7) at the end of every pipe.
- An opening/closure device (6) for the fast opening of one or several flap gates (7)

The connection between the flap gates and the opening/closure device is ensured by a rope. The opening of the flap gates is initiated by the release of the rope and driven by the difference of the water head between the upper basin and the inlet basin. The closure of the flap gates is realized by a fast pulling on the rope(s) which is (are) immediately fixed in the opening/closure device. Due to the sudden release or hold back of water, positive or negative surge waves are generated in the channel. Four of the six pipes connecting the upper and inlet basin have been used for the present research (Table 3-2). Two of the four pipes are equipped with a diaphragm between the upper basin and the pipe inlet.

Table 3-2: Characteristics of the pipes connecting the upper basin to the inlet basin for the generation of surge waves.

Denomination	Inner diameter [mm]	Surface [mm ²]	Particularity
82.1	82	5281	Diaphragm of diameter 42 mm
82.2	82	5281	Diaphragm of diameter 53 mm
82	82	5281	-
100	100	7854	-

The upper basin has an effective length of 2.97 m, a width of 2.13 m and a depth of 1.11 m. The spillway crest is placed at 2.21 m above the bottom level of the channel inlet section which is located at $x = -7.40$ m. The function of the spillway is to discharge the difference between the inflow into the upper basin from the supply system and the flow passing through the pipe(s).

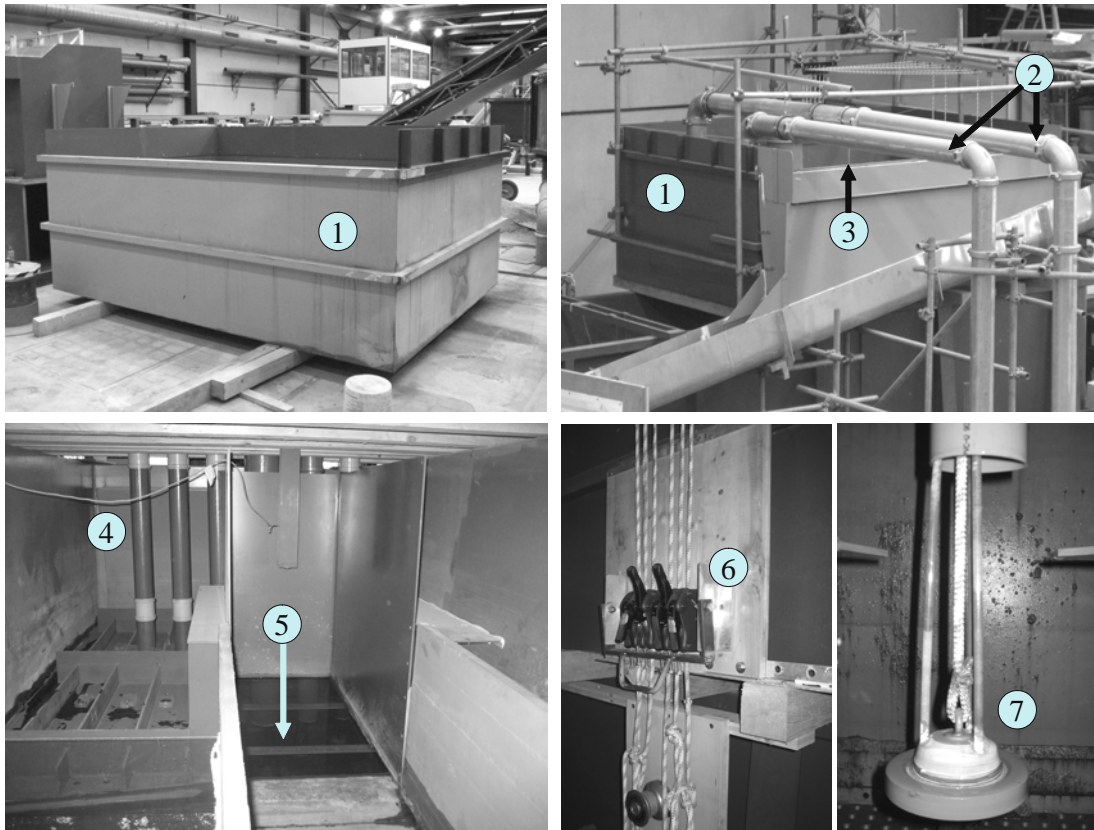


Figure 3-13: Setup generating positive and negative surge waves. Top left: Upper basin (1) under construction. Top right: Overview of the upper basin (1), with water supply pipes (2) and the crest spillway (3) placed on experimental flume. Bottom left: Pipes (4) connecting the upper basin with the inlet basin (5). Bottom right: Opening/closure device (6) and flap gates (7) at the pipe ends.

3.5.2 Mathematical model of the surge wave generating setup

The discharge passing from the upper basin into the channel is calculated with a mathematical model of the setup generating the positive surge waves. It is based on the subdivision of the setup into four elements (Figure 3-14):

- The upper basin with the crest spillway
- The pipes connecting the upper basin and the inlet basin
- The inlet basin with the rectangular opening
- The outflow into the inlet reach

The formulation of the model takes into account following equations:

- In the upper basin: continuity equation and overfall formulas.
- For the pipes: momentum equation and head-loss formulas for single and linear head-loss
- In the inlet basin with the rectangular opening: continuity equation.
- For the outflow into the inlet reach: continuity equation and the formula for the wave celerity.

Following hypotheses are assumed:

- Vertical velocity of the water surface in the upper basin is zero
- The water is non compressible
- The pipes are non extensible
- The wave height is considered to be small compared to the flow depth at the channel inlet section $x = -7.4$ m. This is correct for small time steps.

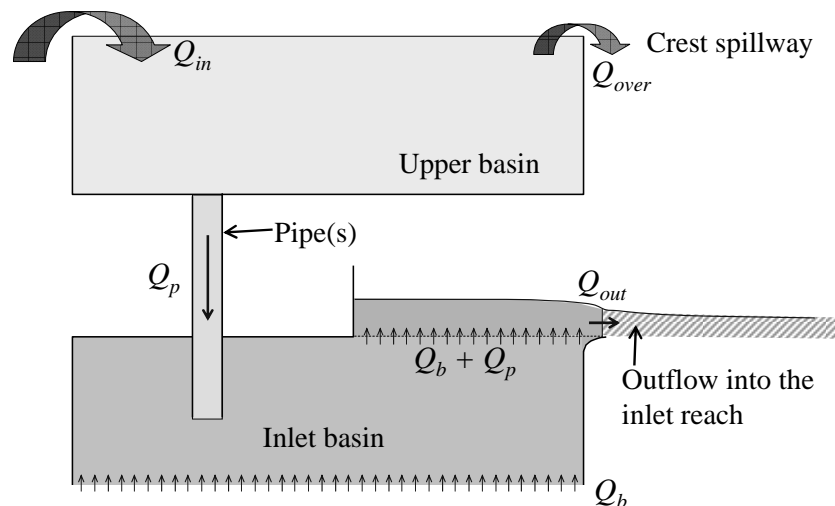


Figure 3-14: Elements of the mathematical model of the surge wave generating setup.

The mathematical model of the surge wave generating setup has been integrated into an Excel Worksheet. The detailed mathematical formulation of the model is shown in Appendix 3-1.

3.5.3 Model calibration and surge wave discharges

The mathematical model of the setup generating surge waves has been calibrated in a first step operating every pipe individually by the adjustment of the pipe diameter for pipe “100” and pipe “82” respectively by the adjustment of the diameter of the diaphragm of pipe “82.1” and “82.2”. In order to find these adjustments, the test procedure has been as follows:

- Complete filling of the upper basin and the inlet basin using the water supply system.
- Stop of the pumps of the water supply system.
- Verification of the leak tightness (stable water surface in the upper basin)
- Start of the data acquisition of the level measurement in the upper basin.
- Opening of one single flap gate (pipe “100” or pipe “82” or “82.1” or pipe “82.2”).
- Measurement of the water level in the upper basin during its emptying.

The emptying velocity $dH(t)/dt$ of the upper basin predicted by the non-calibrated mathematical model can be compared to the measured emptying velocity during the calibration test. Figure 3-15 shows the emptying during the calibration test and the emptying of the non-calibrated mathematical model. By the calibration of the mentioned parameters, it was possible to adjust perfectly the two emptying velocities.

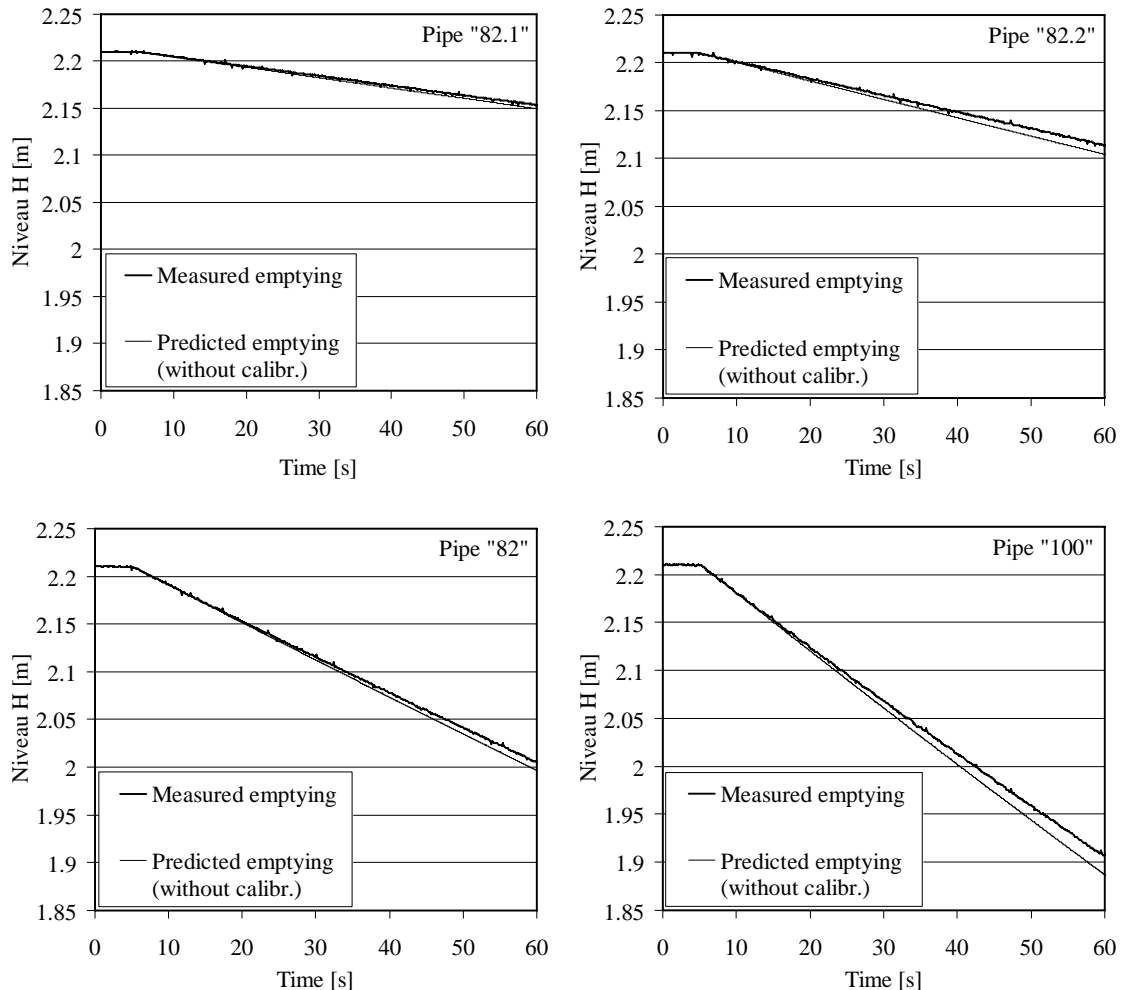


Figure 3-15: Measured and predicted water levels in the upper basin during its emptying for the single pipe cases (pipe "82.1", pipe "82.2", pipe "82" and pipe "100")

In order to validate this calibration, the different combinations of the four pipes have been tested using the same procedure described above. Figure 3-16 shows the measured and predicted emptying of 4 of totally 15 possible combinations. All graphs of the predicted and observed emptying are shown in Appendix 3-2. The validation of the calibrated mathematical model shows its accuracy for the prediction of the outflow into the inlet reach.

Figure 3-17 shows the values of the discharges which can be generated by using the 16 combinations issued of the four pipes. As the discharge is not only depending on the combination of the pipes, but also on the baseflow Q_b and the inflow into the upper

basin Q_{in} , these values are indicative. Table 3-3 indicates for each wave discharge whether the corresponding pipes are open or closed.

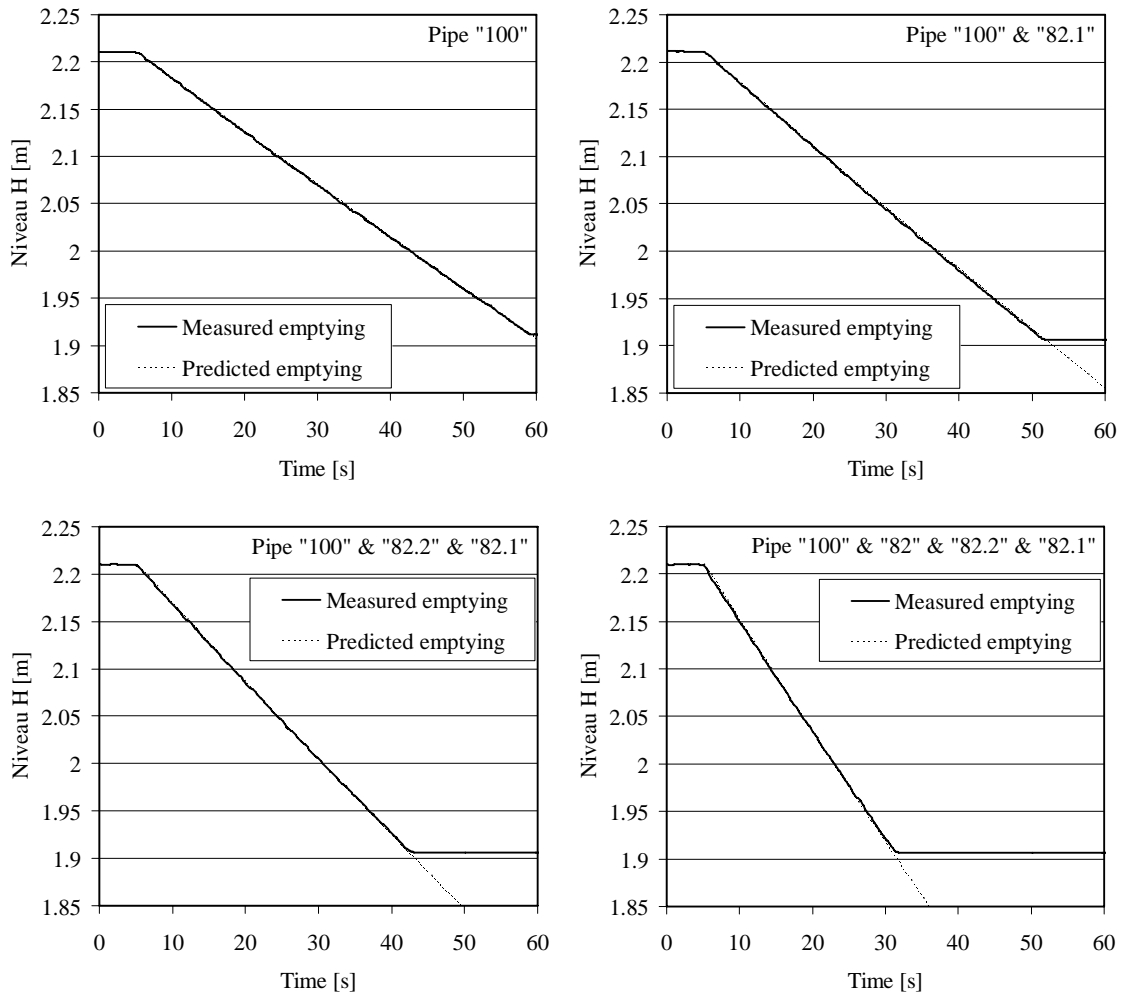


Figure 3-16: Measured and predicted water levels in the upper basin during its emptying for different cases with the calibrated mathematical model.

Table 3-3: Different wave discharges in $[m^3/s]$ for the opening of one or several flap gates (1: flap gate open; 0: closed). Inflow to the upper basin $Q_{in} = 0.090 m^3/s$; the baseflow is $Q_b=0 m^3/s$.

	1	2	3	4	5	6	7	8	9	10	11	12	13	14	15
"100"	0	0	0	0	0	0	1	0	1	1	1	1	1	1	1
"82"	0	0	0	1	1	1	0	1	0	0	0	1	1	1	1
"82.2"	0	1	1	0	0	1	0	1	0	1	1	0	0	1	1
"82.1"	1	0	1	0	1	0	0	1	1	0	1	0	1	0	1
Q_p [m^3/s]	0.007	0.011	0.018	0.024	0.031	0.036	0.037	0.042	0.043	0.048	0.054	0.061	0.067	0.072	0.078

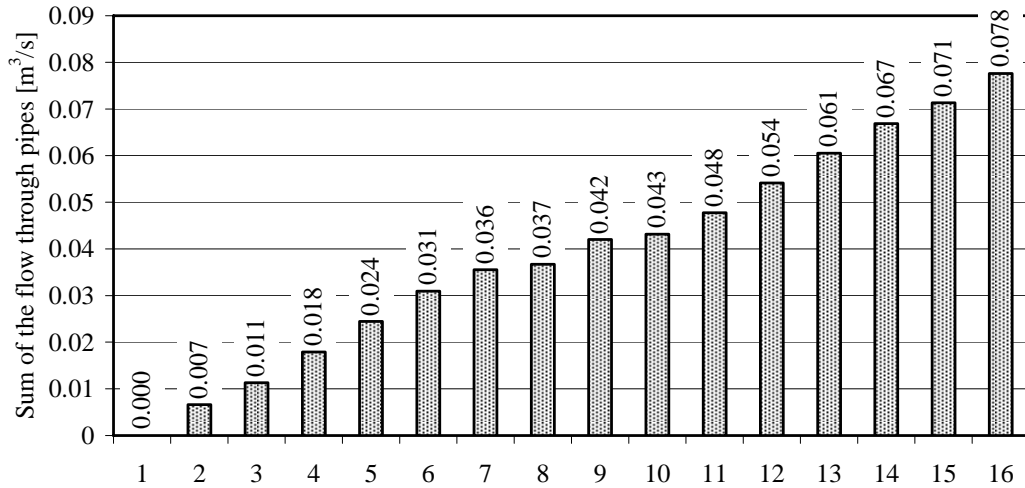


Figure 3-17: Computed values of the wave discharge with the mathematical model of the surge wave generating setup. Inflow to the upper basin is $Q_{in} = 0.090 \text{ m}^3/\text{s}$; the baseflow is $Q_b = 0 \text{ m}^3/\text{s}$.

3.5.4 Example

One example of the results obtained with the calibrated mathematical model of the surge wave generating setup is presented hereafter (Figure 3-18). The baseflow into the inlet basin is $Q_b = 0.010 \text{ m}^3/\text{s}$, the inflow into the upper basin $Q_{in} = 0.020 \text{ m}^3/\text{s}$. All pipes are closed at the beginning. The overflow of the upper basin is therefore $Q_{over} = Q_{in} = 0.020 \text{ m}^3/\text{s}$. At time $t = 0 \text{ s}$, pipe “82” and pipe “82.2” are opened. After a short time, the outflow into the inlet reach Q_{out} passes from Q_b to $Q_b + Q_{p,82} + Q_{p,82.1}$.

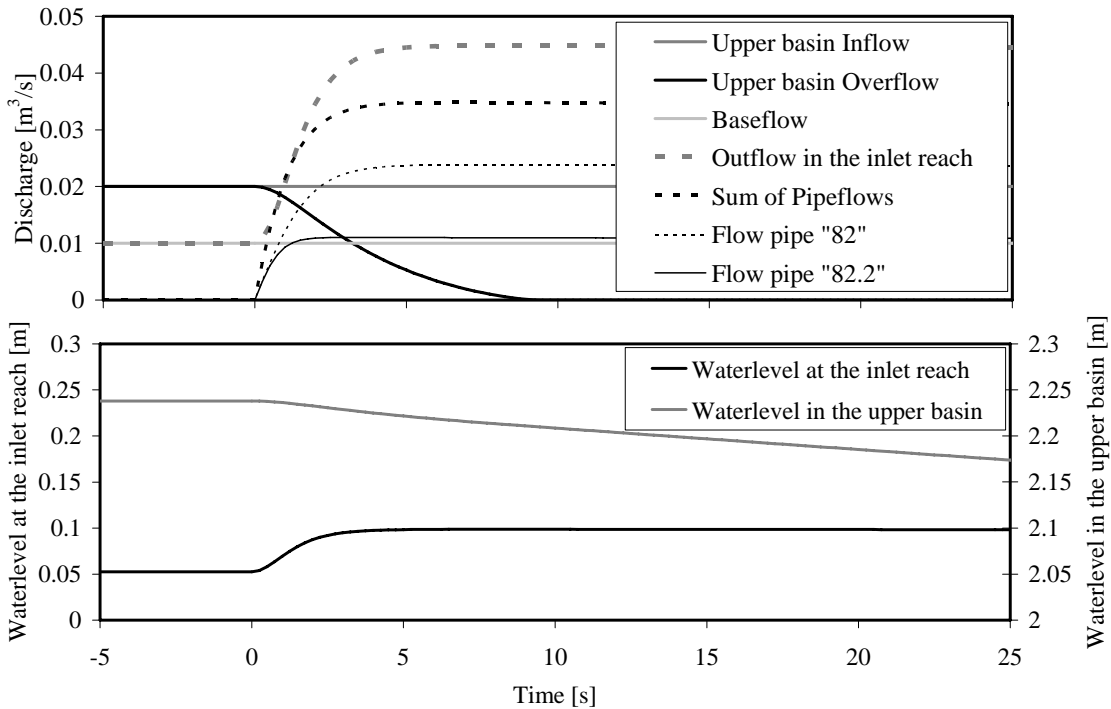


Figure 3-18: Above: Evolution of the different discharges calculated with the calibrated mathematic model. Below: Evolution of the computed water levels.

Since the sum of the pipeflow is higher than the inflow into the upper basin, the upper basin is slowly emptied¹. After 9.5 seconds the upper basin overflow thus becomes zero as the upper basin water level reaches the overflow crest at 2.11 m. Figure 3-18 indicates that the time needed to pass from the baseflow to the final outflow into the inlet reach is about 4 seconds. In order to obtain good agreement between the observed and calculated value of this time, it has been necessary to introduce an additional calibration parameter to the model which allows taking into account the inertia of the water body contained in the upper basin and in the inlet basin. These terms have been neglected in the mathematical model but can be easily reintegrated by the inertia calibration factor.

3.6 Measurement equipment and data acquisition

Discharges, water levels, velocity profiles and pressure measurements have been recorded during the tests. The main unit (desktop computer) regulated the discharge and acquired the water level measurements. The velocity unit (notebook) acquired independently of the main unit a 1D-velocity profile at the channel axis (Figure 3-19).

3.6.1 Discharge measurement

The discharge during the tests was controlled by an electromagnetic flow meter, which is part of the laboratory equipment and it was regulated from the data acquisition computer. The guaranteed precision of the pumps is $0.0025 \text{ m}^3/\text{s}$ (1% of the maximum flow scale). Automatic recordings of the discharge showed that the precision is even considerably higher ($\pm 0.0005 \text{ m}^3/\text{s}$). During all tests, the inflow into the inlet basin and the inflow into the upper basin have been recorded.

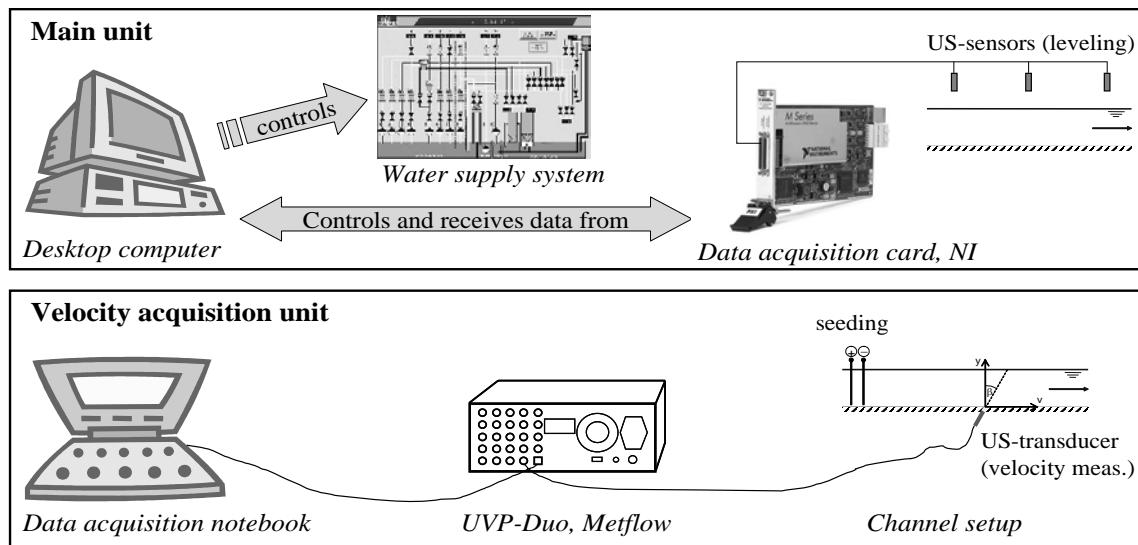


Figure 3-19: Data acquisition units.

¹ For the systematic tests, the inflow into the upper basin is always sufficiently high to avoid this emptying.

3.6.2 Water level measurement and recording

The water level raw data (voltage between 0 and 10 V) have been recorded with ultrasonic (US) sensors. For the steady flow tests a sampling rate of 16 Hz was used and for the unsteady flow tests a sampling rate of 32 Hz. The voltage was transformed into a distance to a reference level by calibration of every ultrasonic sensor. Thus it was possible to determine the water level under each ultrasonic sensor and consequently the flow depth. For the steady flow tests, the data have first been filtered by replacing erroneous measurements with the average of their neighbors and then averaged over 60 s. For the unsteady flow tests the data have also been filtered but only averaged over 0.15625 s (moving average over 5 values). The moving average over 5 values was identified to be the best compromise between a necessary smoothing of the measurements and the ability to measure water levels during rapidly varied unsteady flow.

For the steady flow tests the ultrasonic sensors have been located as indicated on Appendix 4-1. One sensor was placed over the inlet basin, four sensors upstream of section $x = 16.92$ m, three sensors at section $x = 16.92$ m (right side widening, channel axis and left side widening), four sensors downstream of section $x = 16.92$ m, one sensor in the outlet reach and finally one sensor at the outlet section. This relatively dense arrangement of sensors has been chosen in order to follow the evolution of the water surface in different sections along the macro-roughness elements.

To measure the propagation and deformation of positive and negative surge waves along the channel, a large number of ultrasonic sensors have been distributed homogeneously along the channel. The locations of the ultrasonic sensors for the unsteady flow tests are summarized in Appendix 3-3.

3.6.3 Velocity measurement

A 1D-velocity profile using the Ultrasonic Doppler Shift effect (Takeda 2002) has been recorded for the steady and some unsteady flow tests in the channel axis at location $x = 16.92$ m. Data acquisition has been performed by means of the Ultrasonic Velocity Profiler (UVP-DUO) instrument from Met-Flow SA (2002). This instrument allows obtaining quasi instantaneous 1D-velocity profile over the channel depth. For some additional tests, the same instrument has been used with modified firmware allowing access the demodulated echo amplitude (Birkhofer et al. 2006). The ultrasonic transducer with an emitting frequency of 2 MHz and an active diameter of 0.01 m was provided from Imasonic SA (Besançon, France). It has been installed inside the channel bottom and pointed downstream with an angle of $\beta = 30^\circ$ from the vertical. The flow was not disturbed by the transducer which was installed 0.01 m under the bottom-level of the channel. The free space between the transducer and the bottom level was filled with a contact ultrasound gel (P.J. Dahlhausen & Co. GmbH, Germany) covered with a self-adhesive tape (Figure 3-20).

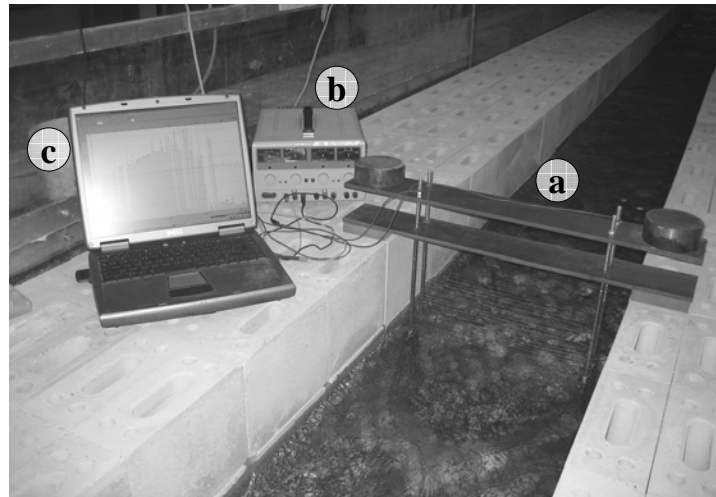
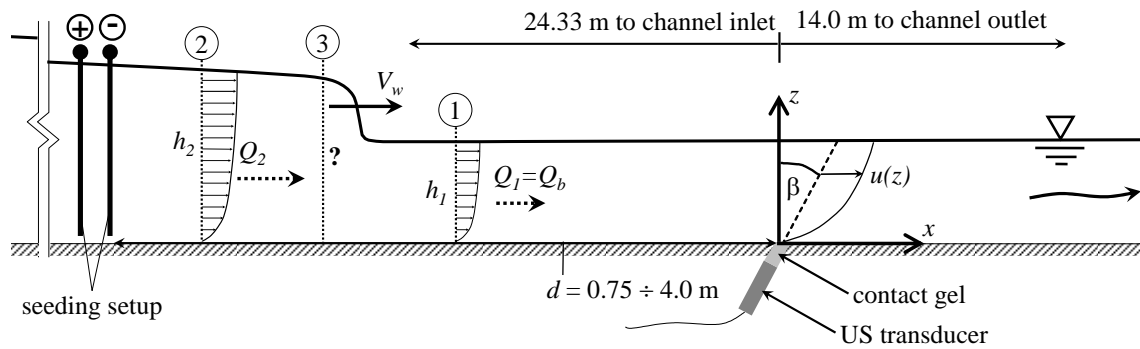


Figure 3-20: Above: Schematic view of the installation of the US-transducer in the channel axis at $x = 16.92$ m. Below: The setup used for the data acquisition (below): a) setup generating hydrogen bubbles b) power supply c) data acquisition notebook.

Preliminary tests showed very low acoustic scattering level. It was necessary to produce artificial seeding of the flow. By seeding of hydrogen bubbles it was possible to get good velocity measurements under steady and even rapidly varied unsteady flow conditions. The setup used for the production of hydrogen bubbles and the data-acquisition are shown in Figure 3-20. Details about the manufacturing of the setup, its power supply and operation as well as details about data acquisition are presented in Meile et al. (2006, 2007 accepted for publication).

3.7 Test procedures

3.7.1 Steady flow test procedure

For the tests with steady flow conditions, 12 different discharges for every geometrical configuration have been analyzed. The range of discharges varied from about $0.005 \text{ m}^3/\text{s}$ up to $0.120 \text{ m}^3/\text{s}$. The test procedure for the tests with steady flow conditions can be summarized as follows:

1. Regulation of the discharge.

2. Observation of the flow until steady flow conditions appear.
3. Documentation of special phenomena and observations (including photos, video and dye-tests).
4. Determination of the discharge by reporting instantaneous values measured by the electromagnetic flow meter.
5. Recording of the water levels by measurement of 960 values (one minute recording with 16 Hz).
6. Verification of stable water levels from the recordings.
7. Recording of the velocity profile.
8. Regulation of the discharge to the next higher one.

During the tests, it was important first, to verify stable discharge conditions and secondly, to be sure about stable water levels. Especially at low discharges in macro-rough configurations, few minutes are required before obtaining stable water levels after the modification of the upstream discharge (due to the filling/emptying of the cavities).

3.7.2 Unsteady flow test procedure

Every geometrical configuration has been tested under 5 to 30 rapidly varied unsteady flow conditions, called scenarios. A scenario is defined by its baseflow and the additional flow due to the opening of one or several flap gate(s). Six different base flows have been combined with five different surge waves (Table 3-4). The values of the total discharge after opening of the flap gates are approximate. Exact values have to be determined depending on the baseflow and the inflow into the upper basin during the experiments using the mathematical model (§ 3.5.2).

Table 3-4: Scenarios (**bold**) for the tests with unsteady flow. The total discharge Q_{total} after the complete opening of flap gates and stabilization of the flow is indicated in the brackets in [l/s].

Opened pipe(s)	baseflow [l/s]					
	≈6	≈11	≈19	≈35	≈49	≈63
“82.1”	1 (12.5)	6 (17.3)	11 (25.9)	16 (41.4)	21 (55.4)	26 (69.3)
“82.2”	2 (17.2)	7 (21.9)	12 (30.5)	17 (46.0)	22 (59.9)	27 (73.8)
“82.1”& “82.2”	3 (23.6)	8 (28.4)	13 (36.9)	18 (52.3)	23 (66.2)	28 (80.1)
“82”&“82.1”	4 (36.5)	9 (41.1)	14 (49.7)	19 (65.0)	24 (78.8)	29 (92.6)
“100”&”82.1”&”82.2”	5 (59.6)	10 (64.2)	15 (72.5)	20 (87.7)	25 (101.3)	30 (115.0)

Figure 3-21 indicates the ratio of the flow into the inlet reach after the complete opening of the corresponding flap gates (Q_{total}) and the baseflow (Q_b). For a small baseflow the ratio varies between about 2 and 10, for the highest baseflow between about 1 and 2.

Thus, the tests with unsteady flow conditions cover a large range of surge waves going from very important additional flows ($\approx 900\%$) to only small variations of the flow ($\approx 9\%$).

Scenarios 3, 8, 13, 18, and 23 have been tested for every configuration. The other scenarios have generally been tested only for the geometrical configurations with $\Delta B = 0.2$ m and $\Delta B = 0.4$ m. Detailed information about the tested scenarios for every configuration is given in Appendix 3-4.

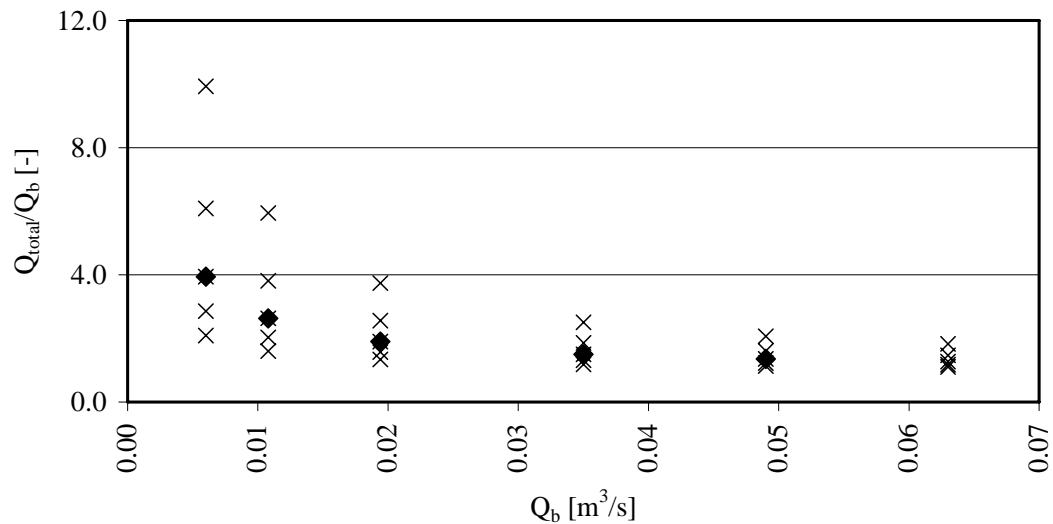


Figure 3-21: Combination of baseflow discharge Q_b and total discharge Q_{total} for the different unsteady flow tests (scenarios). ◆: Scenarios tested for all geometries. ×: Additional scenarios tested for geometries with $\Delta B = 0.2$ and $\Delta B = 0.4$.

The test procedure for the tests with unsteady flow conditions can be summarized as follows:

1. Regulation of the baseflow and the inflow to the upper basin.
2. Observation of the baseflow until steady flow conditions appear.
3. Determination of the discharge (baseflow and inflow to the upper basin) by reporting instantaneous values measured by the electromagnetic flow meter.
4. Start of the recording of the waterlevels by measurement of 11520 (9600) values corresponding to 6 (5) minutes at 32 Hz.
5. Start recording with the video camera situated laterally at the outlet reach.
6. Opening of the flap gates corresponding to a certain scenario after about 0.5 minutes of recording.
7. Observation and documentation of the positive surge wave.
8. Stop of the video camera.
9. Closure of the flap gates corresponding to a certain scenario after about 30 s of recording.
10. Observation and documentation of the negative surge wave.

For geometrical configurations with large cavities as well as for important surge waves completely steady flow conditions could not be reached between the opening and closure of the flap gate(s). Nevertheless, the flow conditions at the beginning of the negative surge flow (wave) can be considered as quasi steady.

4 STEADY FLOW EXPERIMENTS

This chapter includes all results from the experiments with steady discharge. § 4.1 gives a description of the flow in the macro-rough channel issued from observations and measurements. In § 4.2 one phenomenon, which was observed during the experiments, is developed in detail: the transverse oscillations of the flow. The flow resistance parameters as Strickler-coefficients K_{st} , Chezy-coefficients C and equivalent sand roughness values k_s are shown and discussed in § 4.3. § 4.4 contains three macro-rough resistance laws: one issued from a Powerlaw optimization, one obtained from an extension and adaptation of the Morris' approach (1955, 1972) for flow in rough conduits and one found by Evolutionary Polynomial Regression EPR. Finally, § 4.5 concludes on the steady flow tests.

4.1 Analysis of leveling and velocity measurements of the steady flow experiments for the macro-rough configurations

4.1.1 Classification of the flow based on the geometry and the relative flow depth

Various geometrical configurations having different aspect and expansion ratios (Table 3-1) and hydraulic conditions have been analyzed during the steady flow tests. The bottom slope remained constant during the tests. Nevertheless, as the head-loss of the macro-roughness elements produces backwater curves in the experimental channel, the friction slope changes with the discharge. This led to very different flow characteristics (Figure 4-1).

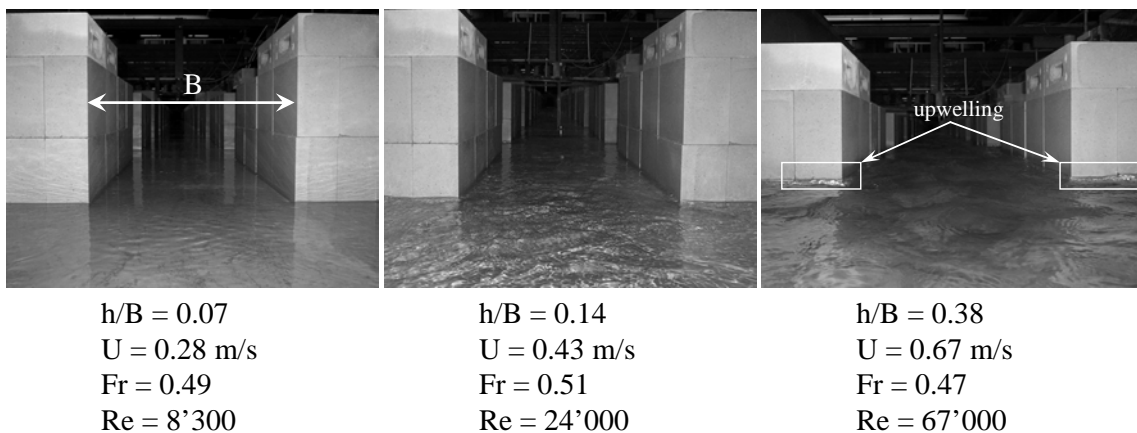


Figure 4-1: Types of flow for a low (left), medium (middle) and high (right) discharge in configuration 223 ($L_b = 1$ m, $L_c = 1$ m, $\Delta B = 0.3$ m). U , Fr and Re are relative to the small section at base width B .

Approximately, the different behaviors of the flow can be divided into three different regimes: a low discharge flow ($h/B < 0.12$), a medium discharge flow ($0.12 < h/B < 0.30$) and a high discharge flow ($h/B > 0.30$). The more the discharge and therefore the relative flow depth increases, the more the flow behavior becomes three dimensional. For the low discharge flow, the water surface is generally flat (smooth) and develops small ripples at the surface. For the medium discharge flow, the water surface becomes more "wavy" but the aspect remains still relatively homogeneous over the entire surface. Finally, when the relative flow depth h/B exceeds the value of 0.3, the water surface gets wavy and heterogeneous. A zone of upwelling flow appears at the downstream end of the widening, indicating that the flow hits the sudden contraction. This zone occupies either a part of the width ΔB or the whole width ΔB of the widening. A succession of photos illustrating the flow at different discharges and relative flow depths is given in Appendix 4-2. It includes two different geometrical configurations (222 and 142).

Besides the relative flow depth, the aspect ratio of the cavity $\Delta B/L_b$ is an important parameter allowing to classify of the steady flow into different categories. The more this parameter is small, the more easily the flow reattaches to the side walls of the cavity. The more $\Delta B/L_b$ approaches the value one ($\Delta B/L_b \rightarrow 1$), the more a single, circular gyre appears inside the cavity. A simple classification into reattachment and recirculation flow, based on the discharge and the cavity aspect ratio $\Delta B/L_b$, is presented in Figure 4-2.

	Low discharge flow $h/B < 0.12$	Medium discharge flow $0.12 < h/B < 0.3$	High discharge flow $h/B > 0.3$
$\Delta B/L_b = 0.8$			
$0.1 < \Delta B/L_b \leq 0.6$			
$\Delta B/L_b \leq 0.1$			

Figure 4-2 : Schematic classification of the flow as a function of the relative flow depth and the aspect ratio of the cavity. PIV flow patterns according Weitbrecht (2004).

The smallest value of $\Delta B/L_b$ that has been tested is 0.05. In this case, the flow clearly reattaches to the cavity side wall for all investigated discharges. If $\Delta B/L_b$ is 0.1, the low discharge flow does not reattach, but an elongated primary gyre and a very small secondary gyre can be observed. When the discharge increases, the flow reattaches to the cavity side wall and a recirculation gyre develops next to the leading edge. The increase of the discharge leads to a slight displacement of the reattachment point upstream.

The highest value of $\Delta B / L_b$ that has been tested is 0.8. In this case, a single and almost circular gyre is located in the cavity. The increase of the discharge leads to an increase of the rotating velocity of the gyre and of the mass exchange.

For cavity aspect ratios $\Delta B / L_b$ between 0.1 and 0.6, the observations indicate a recirculation of the flow with a primary and secondary gyre. For relatively high discharges, the exact size and arrangement of the gyres are difficult to detect and depend on the value of $\Delta B / L_b$. For relatively small discharges, dye tests and flow patterns from velocity measurements correspond qualitatively well to the ones observed in studies on flow recirculation and mass exchange in groyne fields (Uijttewaal 2001, Uijttewaal 2005, Weitbrecht 2004).

In all cases, the secondary gyre is rotating with a much smaller velocity than the primary gyre. When dye is introduced into this secondary gyre, it remains longer than in the primary eddy before being successively removed by interaction with a dynamic gyre. This gyre is not shown in Figure 4-2 since it presents time-averaged flow fields. The proposed schematic classification could be confirmed with dye visualizations (Appendix 4-3).

4.1.2 Characterization of the flow in the widened reach – coherent structures

Coherent structures are generated at the leading edge of the cavity due to the velocity gradient between the main stream and the cavity. The coherent structures are travelling downstream in the mixing layer and their size increases from upstream to downstream. They are travelling either into the cavity or remain next to the main stream. The coherent structures have been identified by turbulence intensities of the transverse velocity components, obtained from UVP measurements. The measurements of Figure 4-3 indicate that in configuration 224 ($L_b = 1.0$ m, $L_c = 1.0$ m, $\Delta B = 0.4$ m) for a discharge of 36 l/s ($h / B = 0.28$), the mixing layer increases in size and is deviated into the cavity.

The coherent structures that frequently shed at the leading edge of the cavity are well visible in some geometrical configurations, especially for low and medium discharges. The vortices, which alternately shed from the cavity leading edge at the right and left side of the channel axis, are the most significant in configurations with high expansion ratios. Furthermore, the alternate vortices are better visible for relatively long cavities ($L_b = 1.0$ m or $L_b = 2.0$ m), where they have time to develop, but they are also present for in shorter cavities $L_b = 0.5$ m. In combination with the alternate vortex shedding, the water body, contained in the main channel and the right and left side widening, oscillates transverse to the main flow direction. The water body oscillations are leading to periodic water surface oscillations which, at certain Strouhal numbers, have peaking values related to standing waves in the spanwise direction to the flow. The frequency of the oscillations is increasing with the flow depth and the relative wave-heights are depending on both, geometric and hydraulic conditions. In § 4.2 the results concerning the transverse oscillations of the flow are discussed in detail.

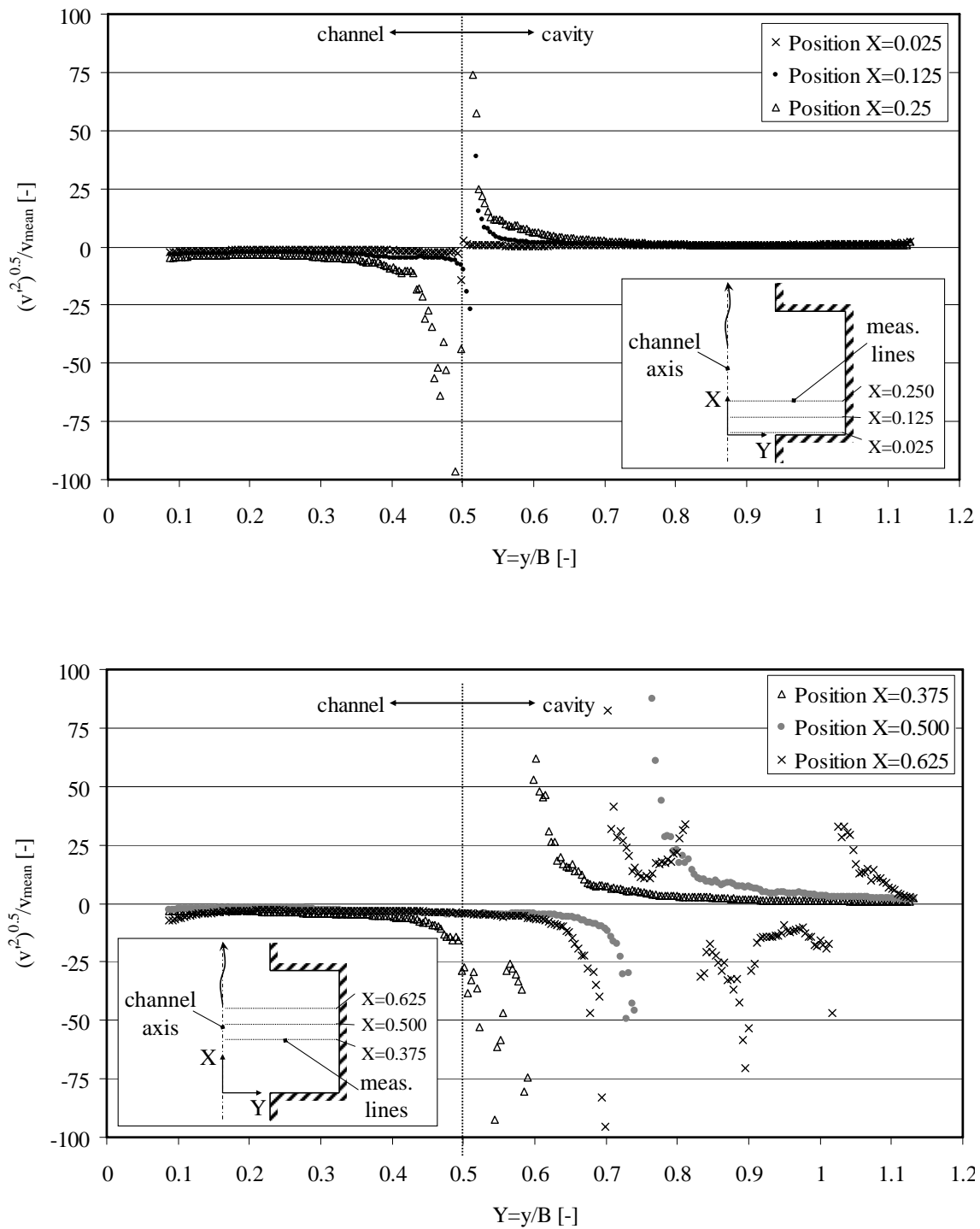


Figure 4-3 : Turbulence intensity of the transverse velocities v . $X = x / L_b$ with $x =$ streamwise distance from the cavity leading edge. $Y = y / B$ with $y =$ spanwise distance from the channel axis. The first three positions (above) indicate the increase of the vertical mixing layer in the first part of the cavity. The second three positions (below) indicate the further increase and the deviation into the cavity.

4.1.3 Time-averaged level measurements

Level measurements have been done during the experiments with a steady discharge using ultrasonic sensors. They have been placed at characteristic locations of a macro-rough channel reach (along the channel axis and in the cavities) upstream and downstream of position $x = 16.92$ m (Table 4-1). The exact locations for the ultrasonic sensors are indicated in Appendix 4-1.

Table 4-1: Arrangement of the US-sensors in the macro-rough reach (steady flow tests).

y-positions	x-positions			
	beginning of the widened reach	middle of the widened reach	end of the widened reach	middle of the contracted reach
along the channel axis				
in the cavities		left side cavity ($y = +(B / 2 + \Delta B / 2)$)		
		right side cavity ($y = -(B / 2 + \Delta B / 2)$)		

In the following, examples of the time-averaged water level measurements are shown in order to highlight the influence of the different geometrical parameters (L_b , L_c and ΔB). In Figure 4-4 the flow depths of configuration 222 are compared with the prismatic configuration for different discharges. The following observations can be made:

- Uniform flow conditions occur in the prismatic configuration for all discharges.
- The large scale macro-roughness elements increase significantly the flow depths for flows with high discharge.
- The large scale macro-roughness elements have only a limited influence on the flow depths for low discharge flows. This is due to the reduced influence of the side walls for low h / B -ratios.
- The water surface is still sloping, especially for higher discharges. This indicates that the uniform depth is not reached for the configurations with macro-roughness elements at the position $x = 16.92$ m of the channel (backwater curve of type M2).

Furthermore, the water levels are influenced by the local position along the macro-rough channel reach. As expected, flow depths under subcritical flow conditions ($Fr < 1$) are increased in the widened channel sections.

Figure 4-5 shows the influence of the cavity depth at the example of configurations 221, 222, 223 and 224 (3 different discharges):

- No significant influence of the parameter ΔB is observed on the time-averaged flow depths. It is important to reveal that this observation is not generally valid. In other geometrical configurations, the parameter ΔB might influence the backwater curves.

- Again, an increase of the water level in the widened part of the channel is observed corresponding to the theory of subcritical flow through widenings.

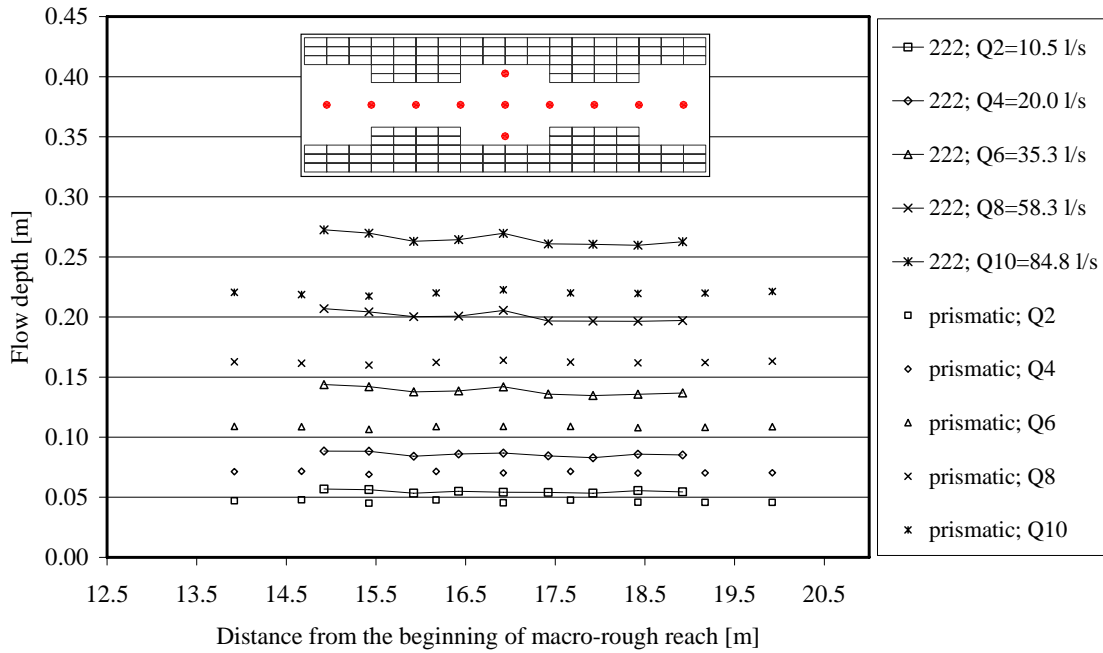


Figure 4-4: Time-averaged flow depths for different discharges of the configuration 222 ($L_b = 1\text{ m}$, $L_c = 1\text{ m}$, $\Delta B = 0.3\text{ m}$) and the prismatic channel.

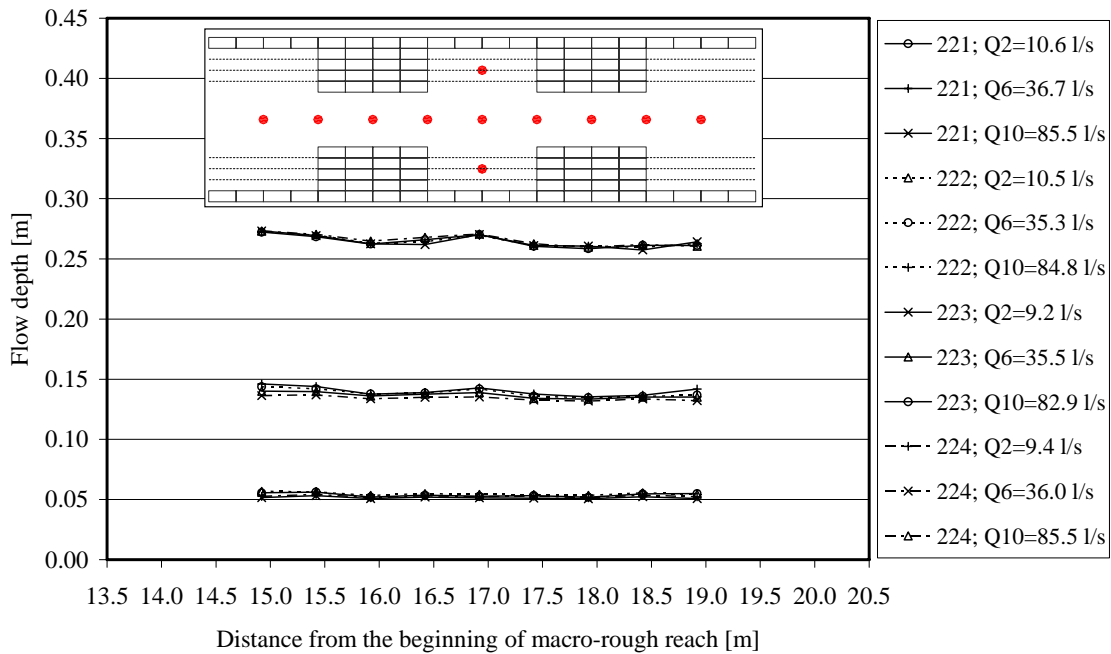


Figure 4-5: Time-averaged flow depths for 3 different discharges of configuration 221 ($L_b = 1\text{ m}$, $L_c = 1\text{ m}$, $\Delta B = 0.1\text{ m}$), 222 ($\Delta B = 0.2\text{ m}$), 223 ($\Delta B = 0.3\text{ m}$) and 224 ($\Delta B = 0.4\text{ m}$). No influence of the parameter ΔB can be observed (superimposed curves).

The time-averaged flow depths of three configurations having different cavity densities but identical cavity geometries are shown in Figure 4-6. It appears that the distance between two cavities L_c influences somehow the flow depths and that the difference increases with increasing discharge.

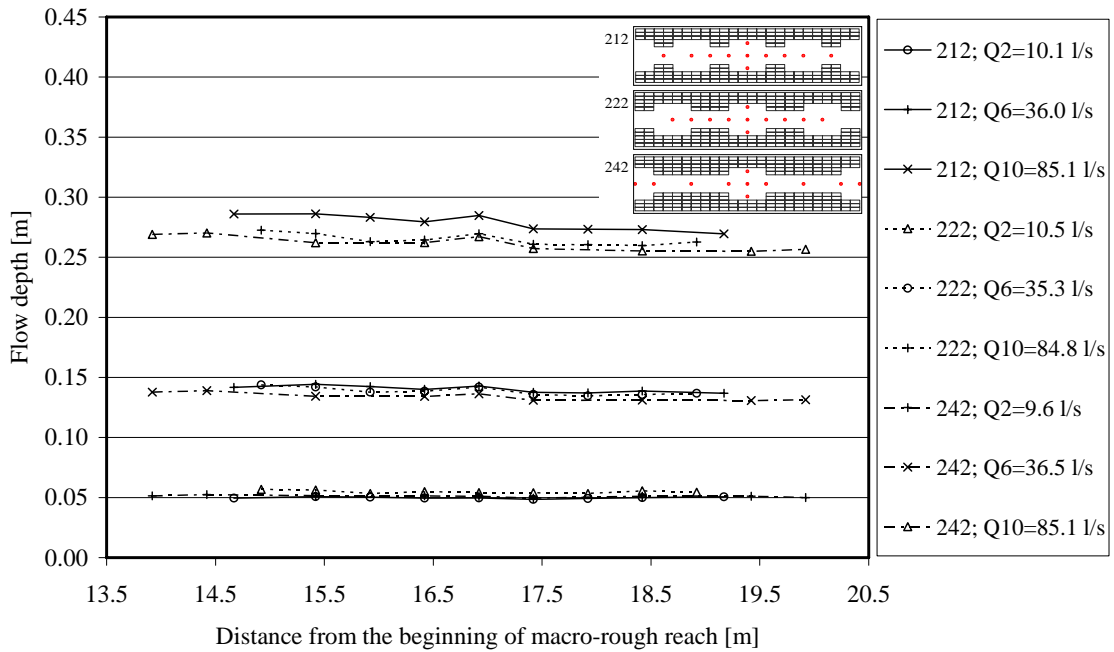


Figure 4-6: Time-averaged flow depths for 3 different discharges of configuration 212 ($L_b = 1.0$ m, $L_c = 0.5$ m, $\Delta B = 0.2$ m), 222 ($L_b = 1.0$ m, $L_c = 1.0$ m, $\Delta B = 0.2$ m), 242 ($L_b = 1.0$ m, $L_c = 2.0$ m, $\Delta B = 0.2$ m).

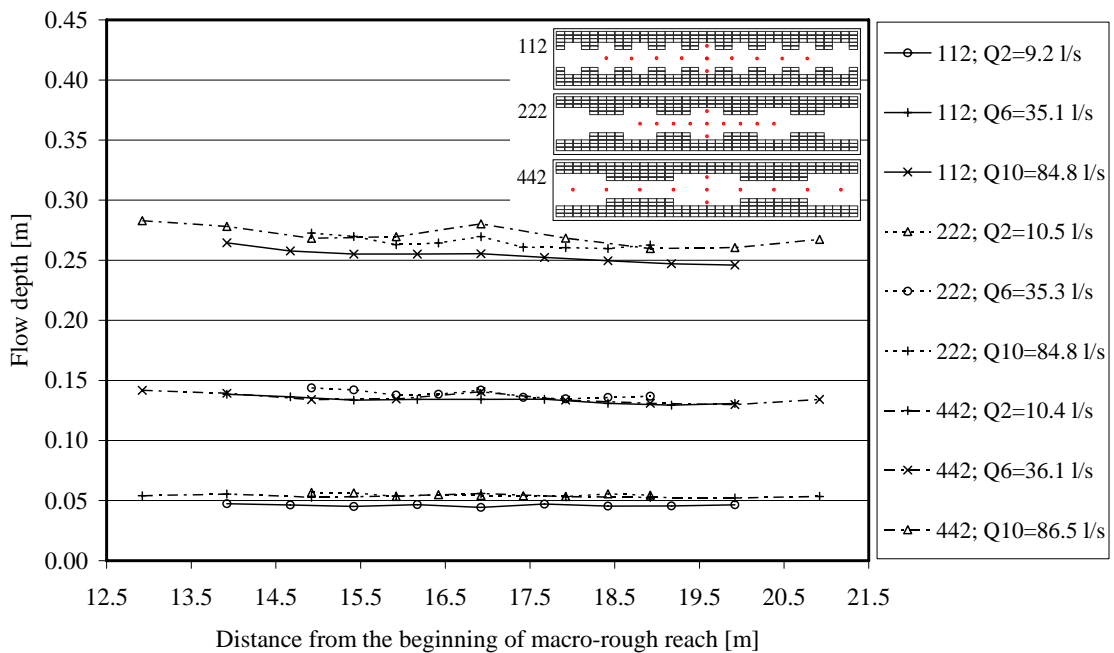


Figure 4-7: Time-averaged flow depths for 3 different discharges of configuration 112 ($L_b = 0.5$ m, $L_c = 0.5$ m, $\Delta B = 0.2$ m), 222 ($L_b = 1.0$ m, $L_c = 1.0$ m, $\Delta B = 0.2$ m), 442 ($L_b = 2.0$ m, $L_c = 2.0$ m, $\Delta B = 0.2$ m).

Finally, in Figure 4-7 the influence of the cavity length L_b on the flow depths is compared. All configurations 112, 222 and 442 have the same proportion of the widened parts of the channel (50%). As the cavity width is the same for all configurations, they automatically have the same additional surface compared to the prismatic reference configuration. However, longer cavities are leading to higher flow depths and the difference increases with the discharge.

The comparison of flow depths helps to identify first trends between the geometry and the flow resistance of a configuration. Generally, the flow-depth is increasing with the cavity length L_b , with the density of cavities and the width of the cavities ΔB . Nevertheless, the levelling data reveal many exceptions of these general trends. Only the determination of roughness related parameters based on backwater curve computations, such as presented in § 4.3, allows the adequate comparison of the 36 geometrical configurations.

4.1.4 Time-dependent level measurements

The analysis of the level measurements as a function of time allowed to confirm stable mean water levels. Furthermore, the variations of the water levels around their time-averaged position at different locations of the macro-rough reach could be quantified. Periodic water surface oscillations have been detected by the two US sensors located in the left respectively right side cavity of the widened reach.

Figure 4-8 shows the time-dependent water depths of configuration 124 ($L_b = 0.5$ m, $L_c = 1.0$ m, $\Delta B = 0.4$ m) for a discharge of $Q_5 = 28.1$ l/s. Periodic water surface variations are significant at the sensors located above the cavities, whereas a more random behaviour is found for all sensors along the channel axis ($y = 0.0$ m). Such periodic water surface oscillations have however only been detected in certain geometries and for a specific range of discharge. In Figure 4-9 the time-dependent flow depths for two different geometrical configurations are compared – one with periodic water surface oscillations and the other without. The periodic water surface oscillations, visible in the cavities of configuration 124, have also a minor influence on the water surface at the channel axis which can be explained by the periodic displacement of a surface wave. Details about occurrence, frequency and amplitude of the periodic water surface oscillations are given in § 4.2.

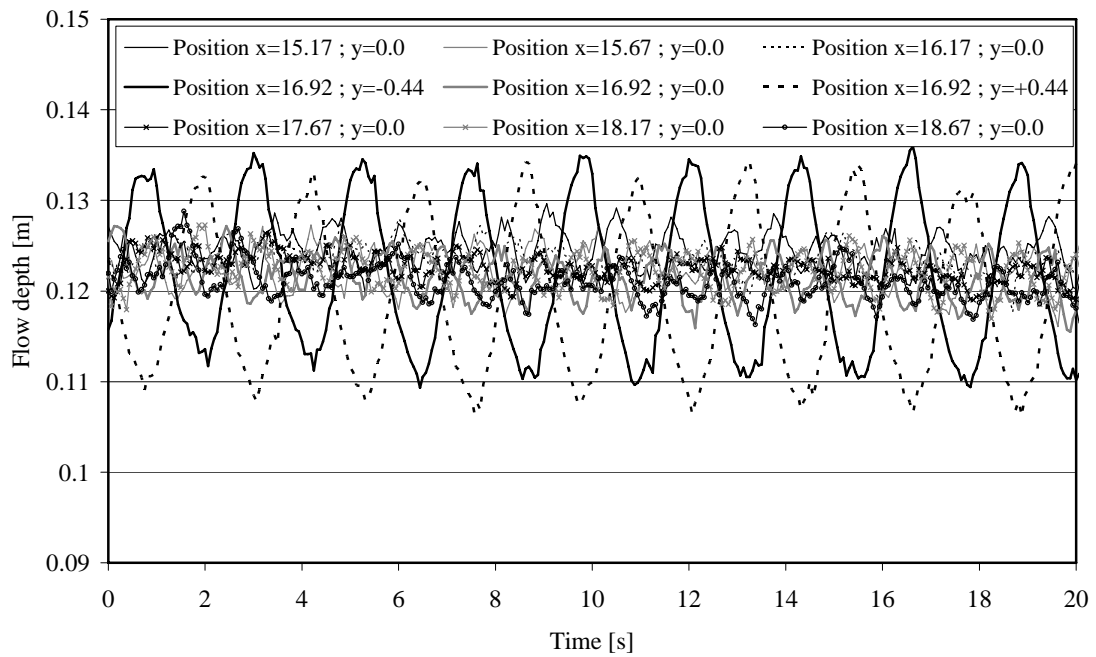


Figure 4-8: Time-dependent flow depths for 9 US sensors of configurations 124 ($L_b = 0.5$ m, $L_c = 1.0$ m, $\Delta B = 0.4$ m) and discharge $Q_5 = 28.1$ l/s. x and y positions in [m].

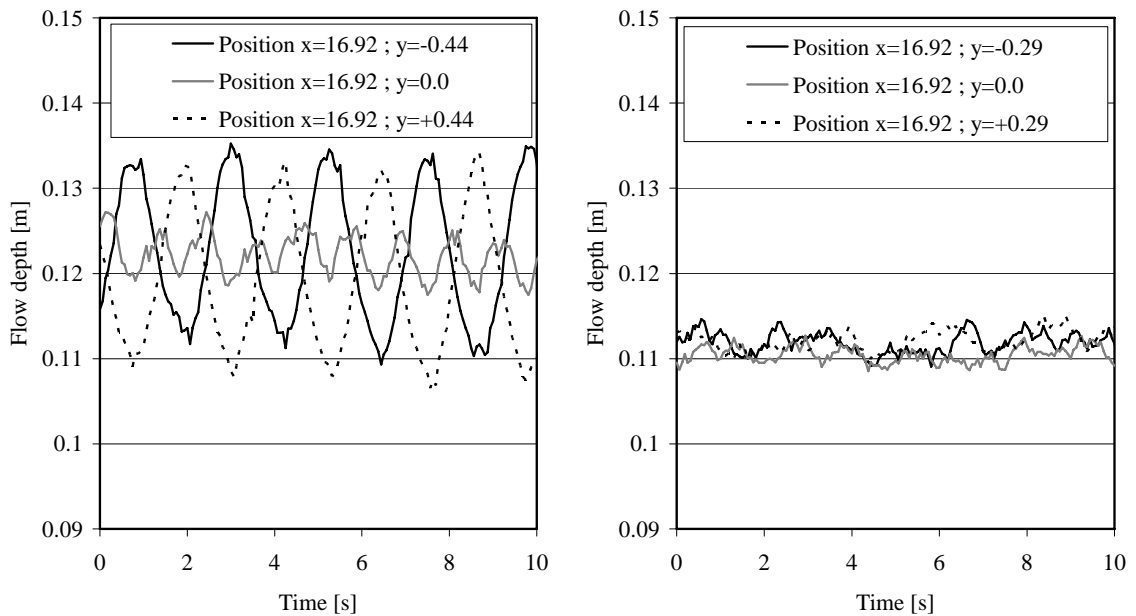


Figure 4-9: Time-dependent flow depths for the US sensors at position $x = 16.92$ m for configurations 124 ($L_b = 0.5$ m, $L_c = 1.0$ m, $\Delta B = 0.4$ m) (left) and 221 ($L_b = 1.0$ m, $L_c = 1.0$ m, $\Delta B = 0.1$ m) (right). In both cases the discharge is of 28 l/s. x and y positions in [m].

4.1.5 Velocity measurements

Velocity measurements by UVP technique were helpful for the detection and description of several phenomena existing in the channel with large scale macro-roughness elements at the channel banks namely:

- the reattachment and recirculation of the flow
- the quantification of the backflow in the cavity
- the expansion of the flow arriving into the widened channel reach
- the contraction of the flow at the end of the widened reach
- the detection of the stagnation point at the downstream end of the cavity
- the detection of coherent structures
- the detection of transverse velocity components (two dimensional flow)

The accomplished velocity measurements, their purpose, the configurations and the discharge are listed in Table 4-2.

Table 4-2: *Performed velocity measurements.*

Test geometry	Discharge	Type of measurement	Purpose
All	$Q1$ to $Q8$ ($Q12$)	Vertical velocity profile (u-component) at channel axis	Influence of the widening on the vertical profile
221	$Q1 \cong 6$ l/s	1D velocity (streamwise) in the sections $x=15.92; 16.17; 16.42; 16.67; 16.92;$ $17.17; 17.42; 17.67; 17.92$	Reattachment and recirculation of the flow, effect of the expansion and contraction
222	$Q3 \cong 19$ l/s		
223	$Q4 \cong 48$ l/s		
224			
224	$Q \cong 36$ l/s	1D velocity (spanwise = transverse to the main flow) at different cavity locations	Transverse velocity components, Stagnation point

4.1.5.1 Vertical velocity profiles

Figure 4-10 (top) shows the time-averaged u -components of the velocity measurements in the channel axis at position $x = 16.92$ m. The results for configuration 144 ($L_b = 0.5$ m, $L_c = 2.0$ m, $\Delta B = 0.4$ m) are presented on the left and for configuration 221 ($L_b = 1.0$ m, $L_c = 1.0$ m, $\Delta B = 0.4$ m) on the right side. For configuration 144, the cavity aspect ratio of 0.8 results in a single recirculation gyre whereas in configuration 221, complete reattachment of the flow at the side walls is observed for higher discharges. These two different flow behaviour explain the differences in the velocity profiles.

For configuration 144, the single recirculation gyre avoids the lateral expansion of the flow and the mean flow velocities regularly increase with the discharge. For configuration 221, it can be supposed that the flow recirculates in the cavity for a low discharge

($U_{UVP} \cong U_{mean}^+$) but reattaches for higher ones ($U_{UVP} \cong U_{mean}^-$): the increase of the discharge is thus partially compensated by the increase of the effective flow area. Therefore, the mean flow velocity does not increase in the same regular way than for configuration 144.

Figure 4-10 (bottom) semi-quantitatively confirms this behaviour. In configuration 144, the mean flow velocity from UVP measurements is close or even slightly higher than the theoretical velocity $U_{mean}^+ = Q / (Bh)$, since the effective flow area does not increase in the widened channel reaches. In configuration 221 the mean flow velocity from UVP measurements is approaching to the theoretical mean velocity $U_{mean}^- = Q / [(B + 2\Delta B)h]$ because the flow reattaches to the cavity side wall. The transition from recirculating (low discharge) to reattachment (high discharge) flow is confirmed by the velocity measurements.

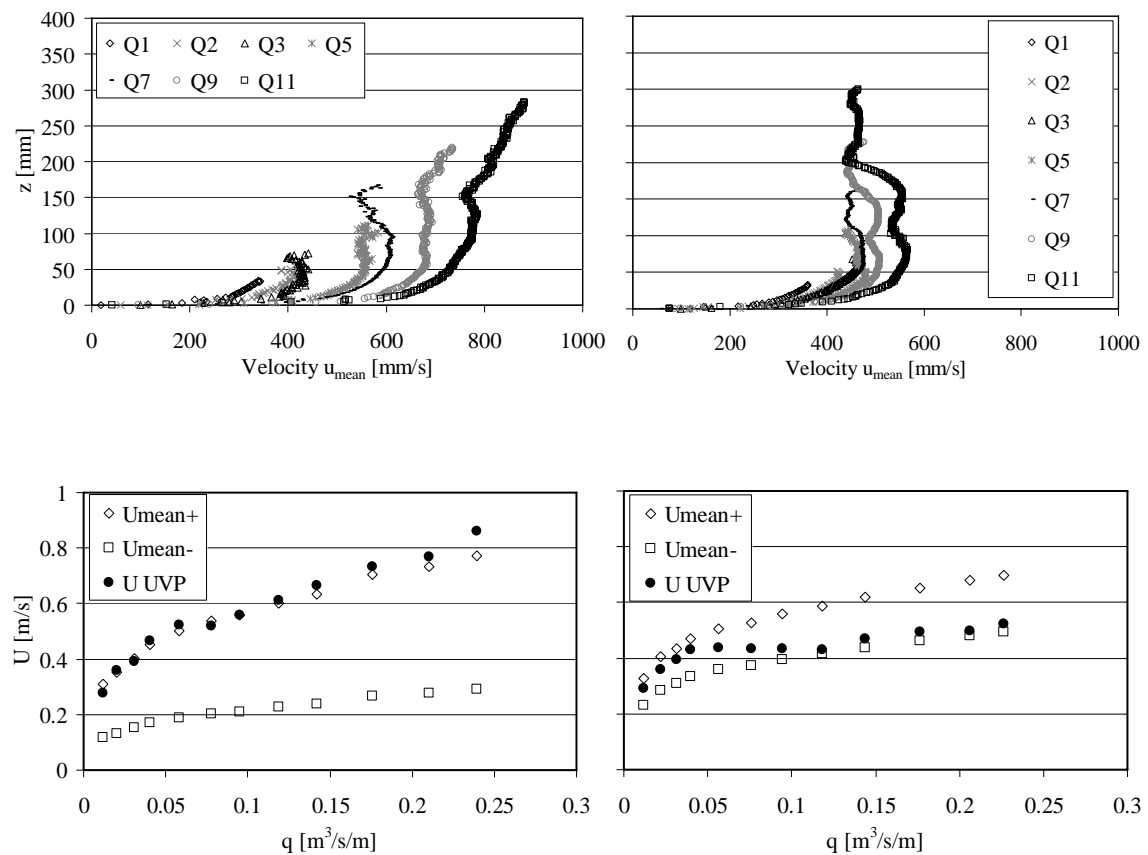


Figure 4-10: Above: Vertical velocity profiles for seven different discharges. The geometrical configurations are 144 (left) and 221 (right). Below: Comparison of the mean flow velocity of the vertical profile obtained from UVP measurements with the theoretical mean flow velocities $U_{mean}^+ = Q / (B \cdot h)$ and $U_{mean}^- = Q / [(B + 2\Delta B) \cdot h]$. Position of the measurement according Figure 4-11 at $x = 16.92$ m.

The somehow unusual upper part of the vertical velocity profiles of configuration 221 can be explained as follows. In general, in cases where complete reattachment or at least expansion of the flow is expected inside the widened part of the cavities, the highest

velocities are not measured next to the water surface (see also Appendix 4-1). Two reasons are responsible for the modification of the profile. They are both related to the orientation of the ultrasonic transducer pointing downstream with an angle $\beta = 30^\circ$ from the vertical (Figure 4-11). The inclination of the ultrasonic transducer is necessary for identifying the u -velocity components assuming 1D flow.

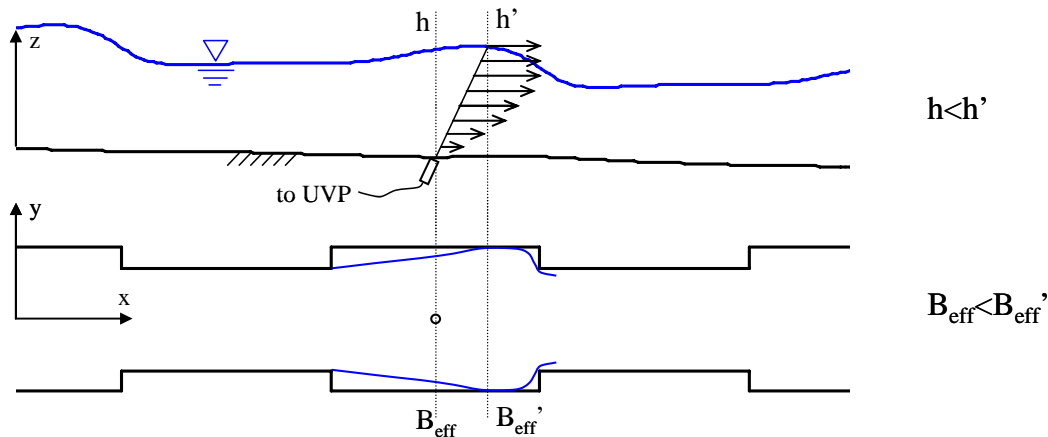


Figure 4-11: Schematic representation of the flow through an enlarged channel part. Above: Longitudinal profile with increased z -components. Below: Plan view.

The first reason is that the horizontal velocity components of the flow are detected along the measurement line inclined of 30° and not exactly on the vertical line above the measurement location. As the flow spreads more and more from upstream to downstream in the widened channel part, the velocities measured at higher z -levels correspond to x -locations with higher effective flow areas. The second reason relates to the theory of the water levels in sudden transitions for subcritical flow conditions (Formica 1955, Chow 1959 p.464) and has been confirmed by numerical 2D simulations. The flow depth increases progressively from upstream to downstream in the widened channel part before decreasing suddenly through the contraction. Again, as the measurement line is not vertical above the measurement location, but inclined with 30° downstream, the velocities measured at higher z -levels correspond to x -locations with higher mean flow depths and therefore lower mean velocities. The sum of these two effects is leading to the observed decrease of the upper part of the measured velocity profile for configurations with an expansion of the flow in the widening.

4.1.5.2 Velocity measurements at different cross sections (u -components)

The difference between recirculation and reattachment of the flow found from § 4.1.5.1 is qualitatively confirmed by the measurements of cross sections u -components (done for configurations 221 to 224). In Figure 4-12 the horizontal velocity profiles taken at $z = 0.5 \div 0.6 h_{max}$ are shown. For a discharge of about 49 l/s the measurements confirm the reattachment of the flow in configuration 221, whereas the flow circulates in the cavities of configuration 224. Observations of dye tests (Appendix 4-3) correspond qualitatively well to the measurements of horizontal velocity profiles (Appendix 4-4).

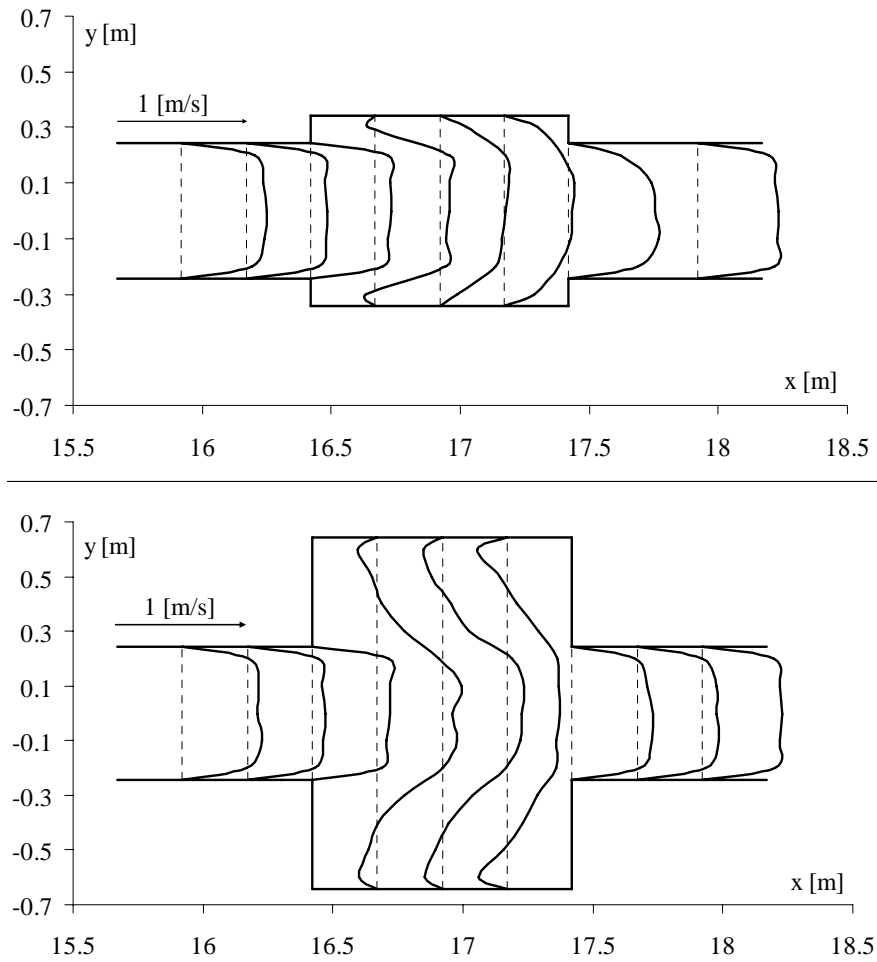


Figure 4-12: Horizontal velocity profiles at the level $z = 0.5 \div 0.6 h_{max}$ for configuration 221 (above) and 224 (below). The dashed line indicates a velocity of $u = 0$ [m/s] for a given section. Discharge $Q \cong 49$ l/s.

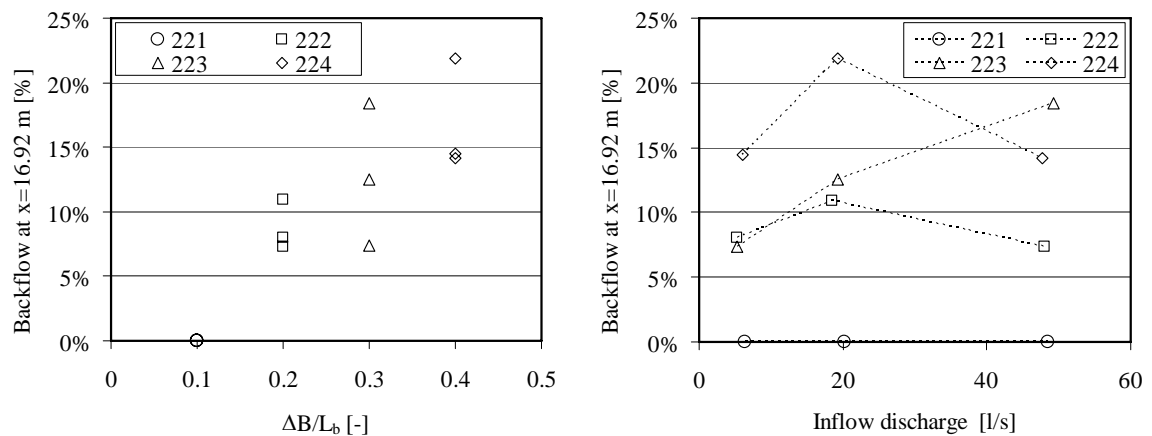


Figure 4-13: Estimated backflow in the cavity at the distance $x = 16.92$ m (cross-section in the middle) relative to the inflow into the cavity as a function of the aspect ratio $\Delta B / L_b$ (left) and the inflow discharge (right).

The backflow can be estimated from the horizontal profile of the velocity measurements (Figure 4-13). The backflow is 0% in configuration 221 where reattachment was found and reaches maximum values of 25% in case of a medium discharge in configuration 224. It can be noted that the backflow is increasing with the aspect ratio $\Delta B / L_b$. Due to the measurement uncertainty and due to the fact that only the z -level ($z = 0.5 \div 0.6 h_{max}$) was considered, the obtained values fix the order of magnitude but not absolute values.

The measurements of the u -components of the velocity in different sections allow to get an idea of the alpha respectively beta coefficients related to the non-uniformity of the velocity profile, i.e. the energy (Coriolis) coefficient respectively the momentum (Boussinesq) coefficient. Due to the strong deformation of the velocity profile, these two coefficients hardly increase in the widened channel reach when calculated over the whole width. (Figure 4-14).

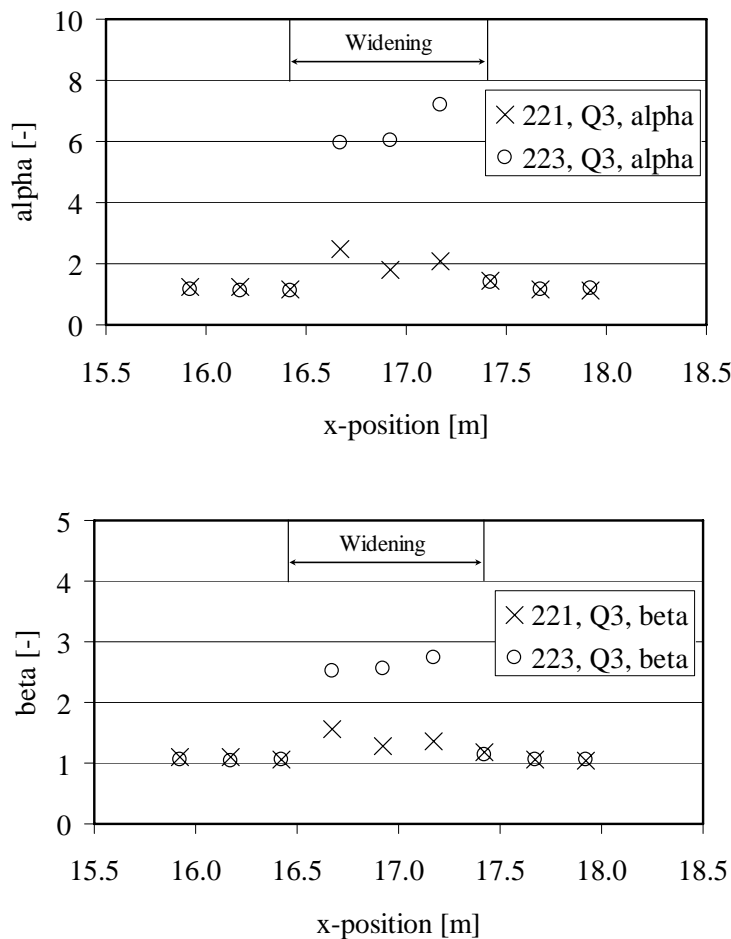


Figure 4-14: Alpha (energy) and beta (momentum) coefficients resulting from the non-uniformity of the velocity profile. Configuration 221, $Q = 20.1$ l/s and configuration 223, $Q = 19.3$ l/s.

In the case of reattachment of the flow respectively by considering an active flow area for the other cases, it would theoretically be possible to determine the single head-loss using the alpha and beta coefficients by combining the energy and momentum equation

(Appendix 4-5). The resolution and measurement precision of the available data as well as the difficulty in the definition of an active flow area and the interpolation of the velocities to the controlling cross sections did not allow to compute the energy slope precisely considering one contraction and expansion of the flow only. The head-losses will be quantified by the analysis of the backwater curve over a long distance (§ 4.3).

4.1.5.3 Lateral velocity measurements at different locations along the widened reach (v-components)

Finally, velocity components transverse to the main flow direction have been measured. They allow to highlight the relation between the water surface oscillations and the movement transverse to the main flow direction of the water body contained in the widened reach. The configuration 224 ($L_b = 1.0$ m, $L_c = 1.0$ m, $\Delta B = 0.4$ m; $Q = 36$ l/s) with significant and periodic water surface oscillations was used for this verification. The measurements have been done at a z-level $z = 0.5h_{max}$ (ca. 0.07 m). The main frequencies of the time-dependent water levels and the transverse velocity components (v-components) are identical ($f = 0.467$ Hz; Figure 4-15). Furthermore the observed maximum velocity value ($v = \pm 55 \div 60$ mm/s) corresponds to the theoretical one found by the formula of sloshing in a container ($v = \pm 60$ mm/s).

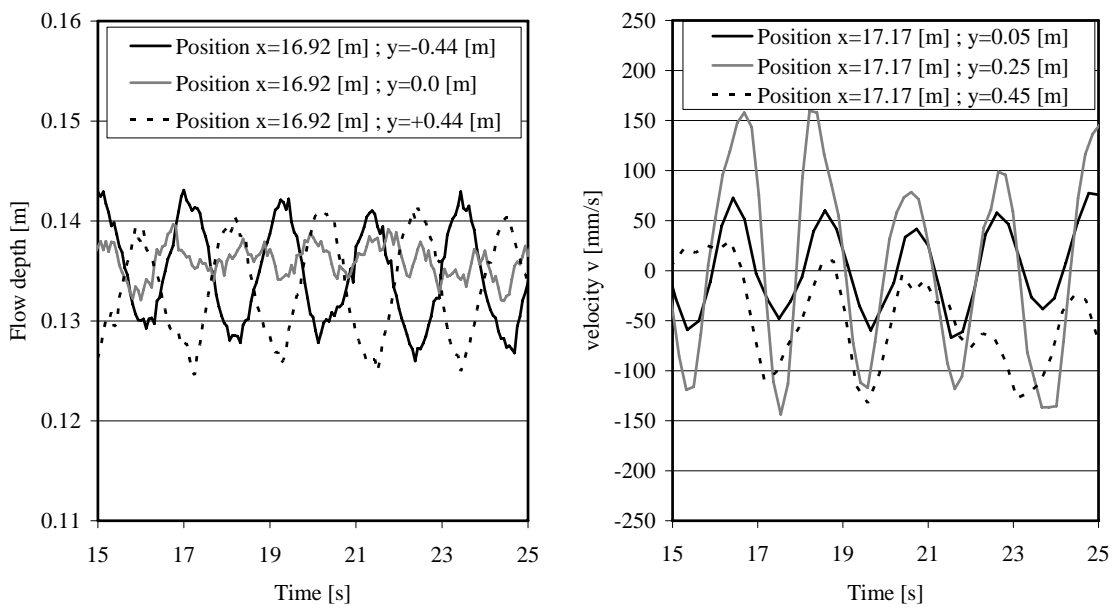


Figure 4-15: Water surface oscillations in the cavities (left) and time-dependent transverse velocity components at the channel axis (right) for configuration 224, $Q = 36$ l/s.

The time averaged components of the transverse flow also allow identifying the regions where the mean flow is directed inside the cavity due to the diffusion of the flow respectively where it recirculates back to the main stream (Figure 4-16, above). It can be confirmed that the mass exchange is from inside to outside of the cavity at its upstream part (negative v-components) whereas the water enters the cavity at its

downstream part (positive v -components). The highest mean transverse velocities from the main channel to the cavity are observed next to the downstream cavity wall.

Finally it was possible to determine the time-averaged position of the stagnation point at the downstream wall of the cavity (Figure 4-16, below) which is located 0.03 m from the cavity downstream edge respectively 0.273 m from the channel axis.

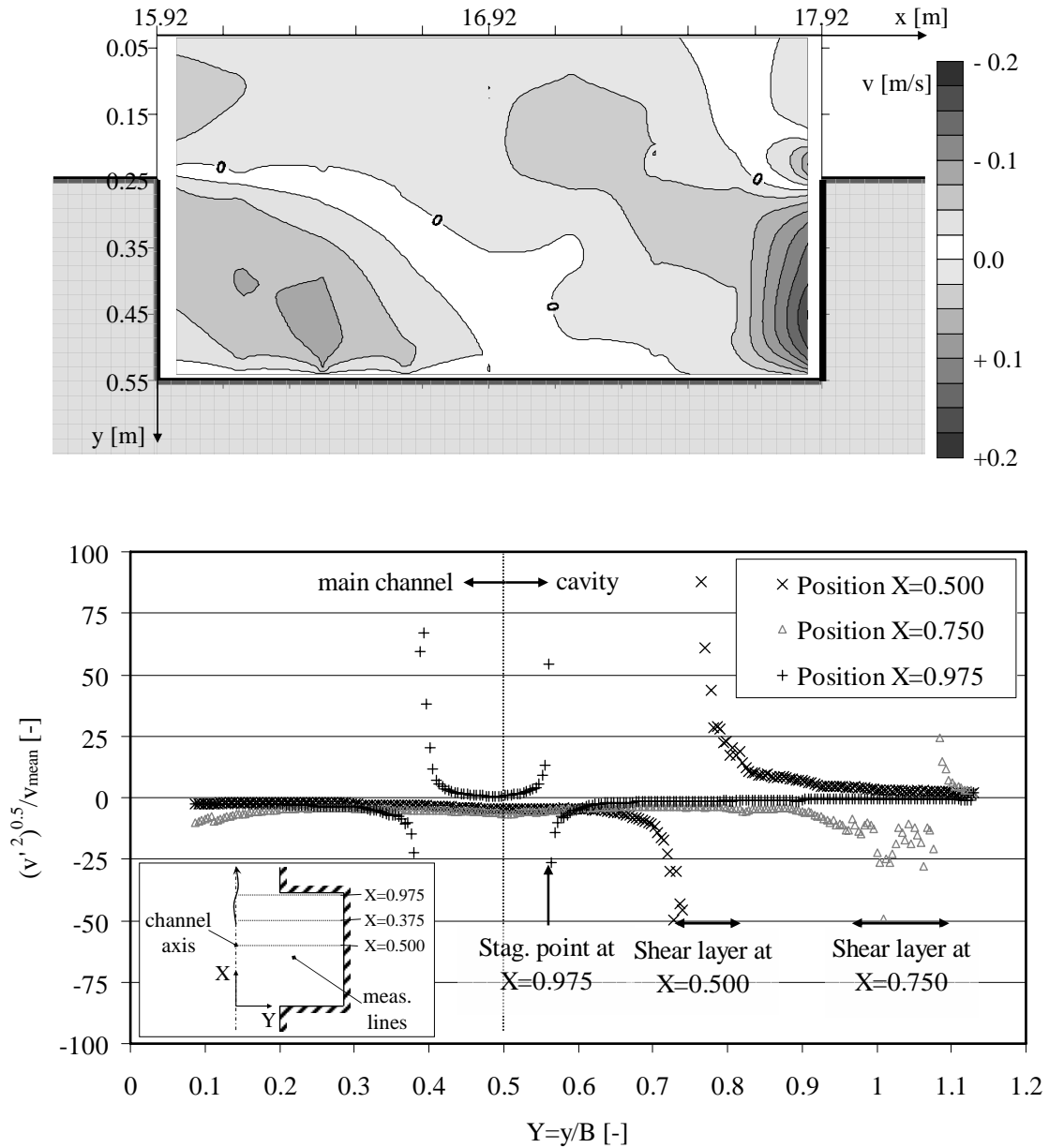


Figure 4-16: Inflow and outflow regions (above) and position of the stagnation point at the downstream cavity wall (below) for configuration 224; $Q = 36$ l/s; $X = x / L_b$ with $x =$ streamwise distance from the cavity leading edge; $Y = y / B$ with $y =$ spanwise distance from the channel axis.

4.1.6 Conclusions of observations in macro-rough configurations

The observations of the flow pattern as well as the water level and the velocity measurements in a channel with macro-roughness elements at the banks confirm that the flow has steady characteristics from a time-averaged point of view. Nevertheless, the flow characteristics are highly unsteady if instantaneous patterns are considered. They result from the superposition of several complex phenomena such as recirculation gyres, coherent structures, vertical mixing layers, wake-zones and transverse oscillations of the flow schematically illustrated in Figure 4-17.

Not all of the mentioned phenomena exist with the same relative importance in all geometrical configurations. However, all active phenomena contribute to the head-loss along the macro-rough channel. In this chapter, the increased head-losses have been shown by comparing water levels of prismatic and macro-rough configurations. In the chapters (§ 4.3 and § 4.4), the roughness of the investigated configurations, including all effects of the above mentioned phenomena, will be identified with the help of some hydraulic concepts based on different assumptions.

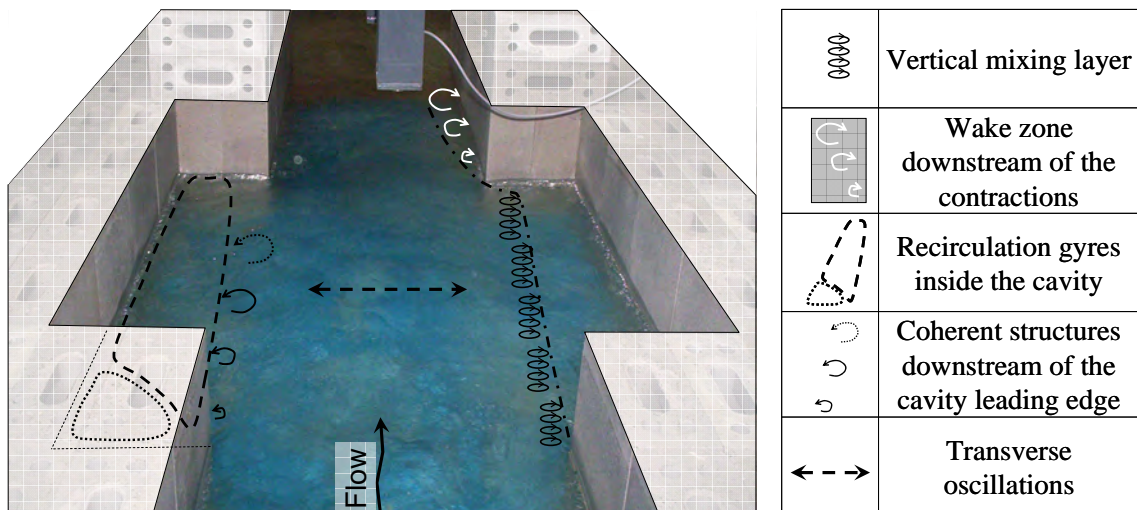


Figure 4-17: Schematic representation of the different phenomena observed in the channel with macro-rough banks (large scale depression roughness).

4.2 Transverse oscillations of the flow in a macro-rough channel

The work shown in this chapter has been published in a summarized version in the proceedings of the 32. IAHR conference (Meile et al. 2007).

4.2.1 Occurrence of transverse oscillations of the flow

Oscillations of a waterbody can occur in groyne fields, river embayments (side cavities in open-channel flows), harbours and cavities (Figure 4-18).

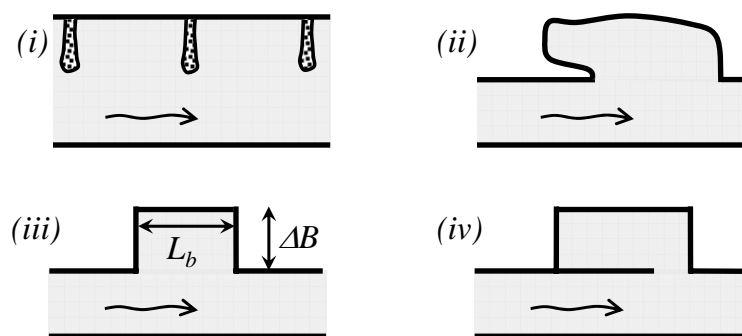


Figure 4-18: (i) Groyne fields, (ii) river embayments "Wando", (iii) cavities and (iv) harbours.

Regarding research on flow over cavities, the studies generally deal with free shear layer oscillations, feedback mechanisms, resonance phenomenon and passive or active open-loop control schemes (Rowely and Williams 2006; Rockwell and Naudascher 1978). In river embayments (also called "Wando" in Japanese rivers; Nezu and Onitsuka 2002; Muto et al. 2000) horizontal coherent structures (vortices) are generated by the shear instability between the main channel and the embayment. The main studies on emerged groyne fields (McCoy et al. 2006; Weitbrecht 2004; Uijttewaal et al. 2001) address the mass-exchange between main channel and groyne fields, sedimentation of groyne fields, pollutant transport phenomenon and navigation. Finally, studies on harbour hydrodynamics (USACE 2002; Wilson 1972; van Rijn 1994) highlight the importance of geometry and boundary conditions on the formation of unsuitable seiches in harbours. Between the above mentioned studies, the following similarities can be identified:

- The most important geometrical parameter influencing the flow pattern is the ratio between the cavity depth and the cavity length (aspect ratio $\Delta B/L_b$).
- The flow in the cavities (or embayments, groyne fields) is often influenced by the vortex shedding at the leading edge.
- Recirculation of the flow in the cavity (or embayment, groyne field) can induce instabilities leading to an instantaneous flow field which is very different from the mean flow field.

- Surface oscillations can be observed for certain geometrical configurations and hydraulic conditions in the case of free surface flows of incompressible fluids (Naudascher 1963; Muto et al. 2000; Nezu and Onitsuka 2002; Wirtz 2004; Ohomoto et al. 2005).

Most of the existing studies treat a single cavity (embayment) or spur dikes at only one channel side. In the present research, a large range of widening geometries with different aspect and expansion ratios has been investigated in a 40 m long channel with cavities at both sides of the main channel (Figure 4-19). Different subcritical free surface flow conditions have been investigated. In some experiments, significant transverse oscillations of the water bodies, formed by the water contained in the widened reaches, have been observed. The resulting, periodic water surface oscillations are initiated and maintained by hydrodynamic oscillations, called the wake mode type (Gharib and Roshko 1987). At certain Strouhal numbers, resonance related to free surface standing waves leads to peak values of the water surface oscillations.

4.2.2 Theoretical assessment of transverse oscillations

The definition of the geometrical parameters used in the present study is summarized in Figure 4-19 where B is the channel base width, ΔB the widening depth, L_b the widening length and L_c the longitudinal distance between the widenings. $W = B + 2\Delta B$ is the channel width including the widenings. The aspect ratio of the rectangular widening is defined as $\Delta B / L_b$. The aspect ratio of the widenings including the river width is defined as $(B + 2\Delta B) / L_b$ and the expansion ratio is defined as $(B + 2\Delta B) / B$.

The mean water level h is the time-averaged response from the m water level measurements h_i at the locations of the ultrasonic sensors (L), (M) and (R) (Figure 4-19). The mean wave-height a quantifies the water surface oscillations around the mean water level h and is calculated taking into account the standard deviation.

$$h = \frac{1}{m} \sum_{i=1}^m h_i \quad (\text{eq. 4.1})$$

$$a = 2\pi \left(\frac{1}{m} \sum_{i=1}^m (h_i - h)^2 \right)^{1/2} \quad (\text{eq. 4.2})$$

As the ultrasonic sensors, measuring the oscillating movement of the water surface, are located at y -positions $y = \pm(B/2 + \Delta B/2)$, the mean wave-height a is not directly representative for the maximum water surface oscillations at the extremity of the widenings, where $y = \pm(B/2 + \Delta B)$. Assuming a sinusoidal water surface (Figure 4-19, below) the mean wave-height a_+ can be calculated at locations $y = \pm(B/2 + \Delta B)$ with (eq. 4.3). Furthermore, as the channel width including the widenings $W = B + 2\Delta B$ varies for the different geometrical configurations, the mean wave-heights a or a_+ are not directly comparable for the different geometries. Assuming again a sinusoidal water surface, a representative mean wave-height can be calculated at locations $y = \pm B/2$ using (eq. 4.4).

$$a_+ = a \left[\sin \left(\frac{B/2 + \Delta B/2}{B/2 + \Delta B} \frac{\pi}{2} \right) \right]^{-1} \quad (\text{eq. 4.3}) \quad a_{B/2} = a_+ \sin \left(\frac{B/2}{B/2 + \Delta B} \frac{\pi}{2} \right) \quad (\text{eq. 4.4})$$

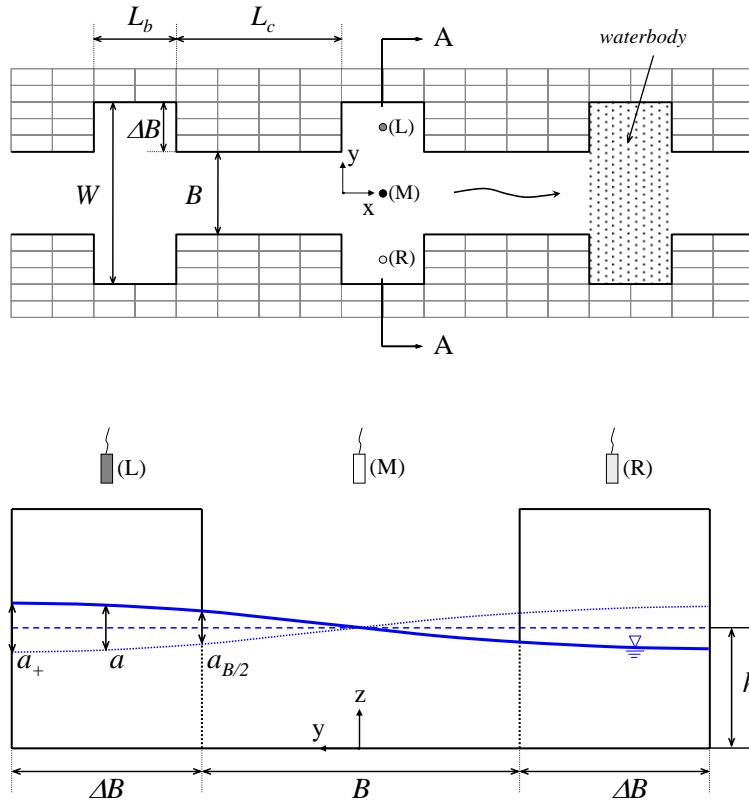


Figure 4-19: Below: Definition of the geometrical parameters of the tested configurations. Situation (above) and cross-section A-A (below). (L), (M) and (R) US-sensors.

The different mean wave-heights a , a_+ or $a_{B/2}$ can be normalized with the mean water level h which allows getting relative wave-heights using (eq. 4.5a), (eq. 4.5b), (eq. 4.5c).

$$a_r = \left(\frac{a}{h} \right) \quad (\text{eq. 4.5a}) \quad a_{r+} = \left(\frac{a_+}{h} \right) \quad (\text{eq. 4.5b}) \quad a_{r_{B/2}} = \left(\frac{a_{B/2}}{h} \right) \quad (\text{eq. 4.5c})$$

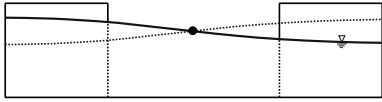
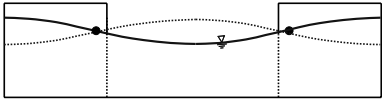
The following (eq. 4.6) can be applied for the calculation of the natural frequency f^n of the water body in a rectangular basin assuming the n order mode sloshing perpendicular to the mainstream. In case of low water levels compared to the width of the waterbody $h/W \ll 1$, this equation can be simplified. The term $\tanh(n\pi h/W)$ becomes $n\pi h/W$ and equation (eq. 4.6) becomes the formula for the frequency of seiches (eq. 4.7).

$$f^n = \frac{1}{2\pi} \sqrt{\frac{n\pi g}{W} \tanh \left(\frac{n\pi h}{W} \right)} \quad (\text{eq. 4.6}) \quad f^n = \frac{n\sqrt{gh}}{2W} \quad (\text{eq. 4.7})$$

A fast Fourier transformation (FFT) has been done in order to identify the power-spectrum of the free surface oscillations where the frequency of the observed transverse oscillations f_{FFT} corresponds to the frequency of the most powerful surface oscillations. In addition, the FFT analysis allowed identifying the phase P of the water surface oscillations. A phase difference ΔP_{L-R} close to 180° indicates that the water surface oscillations in the left and right side widenings are alternating (mode $n = 1$). A phase difference ΔP_{L-R} close to 0° or 360° indicates that the water surface oscillations in the left and right side widenings are produced simultaneously (mode $n = 2$).

Different criteria have been chosen in order to decide if water surface oscillations are present or not during the experiments (Table 4-3). They are based on the water level measurements h_i of the three ultrasonic sensors located in the left side widening, in the channel axis and in the right side widening (Figure 4-19, below). The criteria can be summarized as presented in Table 4-3 for the first two modes $n = 1$ and $n = 2$.

Table 4-3: Criteria allowing to identify water surface oscillations of mode $n = 1$ or $n = 2$. (L) concerns the left widening, (R) the right widening and (M) the channel axis.

		
	$n = 1$ (first mode)	$n = 2$ (second mode)
Criterion 1: based on phase difference ΔP_{L-R}	if $170^\circ < \Delta P_{L-R} < 190^\circ$, criterion 1 is satisfied	if $abs(\Delta P_{L-R}) < 20^\circ$, criterion 1 is satisfied
Criterion 2: based on the relative wave-heights at (L), (M) and (R).	if $0.5 \cdot (a_{rL} + a_{rR}) / a_{rM} > 1.05$, criterion 2 is satisfied	if $0.5 \cdot (a_{rL} + a_{rR}) / a_{rM} < 0.95$, criterion 2 is satisfied
Criterion 3: based on the calculated (eq. 4.6) and observed main frequencies (FFT).	if $f_{FFT L} - f_{cal}$ or $f_{FFT R} - f_{cal} < 0.05$; criterion 3 is satisfied	if $f_{FFT L} - f_{cal}$ or $f_{FFT R} - f_{cal} < 0.1$; criterion 3 is satisfied

Based on the observations, the level measurements and the FFT analysis, it can be assumed that if all three criteria of the first ($n = 1$) or second ($n = 2$) mode are satisfied, periodic water surface oscillations of the corresponding mode are fairly sure. If two of the three criteria are satisfied, periodic water surface oscillations are still possible. Finally, if only one or no criterion is satisfied, there are no periodic water surface oscillations of this mode. In the first mode, the water body is oscillating between the widening on the right and left side which is leading to significant transverse flow velocities in the main channel. In the second mode, transverse flow velocities are also present, but their importance is less than for mode $n = 1$.

The Reynolds number is defined by (eq. 4.8) using the hydraulic radius R_h of the section

at base width B and the mean flow velocity U . The Strouhal number St is a dimensionless number describing oscillating flow mechanisms taking into account a frequency, a characteristic length and a characteristic velocity. Different definitions, depending on the choice of the characteristic length and velocity, exist for the Strouhal number. In the present study, the Strouhal number is calculated with the length of the widening L_b according to (eq. 4.9).

$$Re_m = \frac{U R_h}{\nu} \quad (\text{eq. 4.8})$$

$$St = \frac{f^n L_b}{U} \quad (\text{eq. 4.9})$$

Maintaining water surface oscillations needs some energy. This energy can be compared to the total observed head-loss along the channel (§ 4.3). Based on the following reflections it is possible to estimate the importance of the energy “loss” induced by periodic oscillations of the water body for the dominating mode $n = 1$ (Table 4-3):

- The potential energy E_{pot1} in the situation 1 (corresponding to the inclined/curved water surface) is higher than the potential energy E_{pot2} in the situation 2 (corresponding to a horizontal water surface).
- The difference between the potential energy ΔE_{pot1-2} must be provided at least one time to the system (if assumption is made that there is no friction-loss in transverse direction).
- A part of $x\%$ of this energy difference has to be provided to the system at every oscillation (if assumption is made that $x\%$ of the energy difference is lost at every oscillation due to damping).
- The comparison of the potential energy difference ΔE_{pot1-2} with the total observed energy dissipation due to friction and form drag along the channel (§ 4.3) allows to quantify the importance of the transverse oscillations on the total head-loss along the channel.

The potential energy in situation 1 can be calculated as:

$$E_{pot,1} = \rho g L_b \int_{-o}^o (h + a') \left(\frac{h + a'}{2} \right) dy \quad \text{with} \quad a' = 0.5 a_+ \sin \left(\frac{y \pi}{o} \right) \quad \text{and} \quad o = \frac{B}{2} + \Delta B$$

After solving, the equation becomes:

$$E_{pot,1} = \rho g L_b \frac{1}{2} \int_{-o}^o (h^2 + 2ha' + a'^2) dy$$

The integration can be done separately for the three terms in the brackets. The result for the second term is zero. The results for the first and third term are:

$$E_{pot,a} = \frac{1}{2} \rho g L_b h^2 (B + 2\Delta B) \quad E_{pot,c} = \frac{1}{16} \rho g L_b a_+^2 (B + 2\Delta B)$$

Finally, as the cinematic energy of situation 1 is zero, the total (potential) energy in

situation 1 is:

$$E_{S,1} = E_{pot,1} = \rho g L_b (B + 2\Delta B) \left(\frac{1}{2} h^2 + \frac{1}{16} a_+^2 \right) \quad (\text{eq. 4.10})$$

The potential energy in situation 2 (horizontal water surface) is calculated immediately as:

$$E_{pot,2} = \frac{1}{2} \rho g L_b h^2 (B + 2\Delta B) \quad (\text{eq. 4.11})$$

The cinematic energy in situation 2 can be calculated using $\bar{V}_{t \max}$ being the transverse velocity averaged in space:

$$E_{cin,1} = \frac{1}{2} \rho L_b h (B + 2\Delta B) (\bar{V}_{t \max}^2) \quad (\text{eq. 4.12})$$

Finally the total energy (potential and cinematic) in situation 2 is:

$$E_{S,2} = \rho L_b h (B + 2\Delta B) \left(\frac{gh}{2} + \frac{\bar{V}_{t \max}^2}{2} \right) \quad (\text{eq. 4.13})$$

An upper limit for the additional head-loss due to the transverse oscillations can thus be estimated using the difference between the potential energy $\Delta E_{pot,1-2}$ which is:

$$\Delta E_{pot,1-2} = \rho g L_b (B + 2\Delta B) \left(\frac{1}{16} a_+^2 \right) \quad (\text{eq. 4.14})$$

Therefore the difference of potential energy of situations 1 and 2 can be calculated directly from the mean wave-heights a_+ . This $\Delta E_{pot,1-2}$ can be compared to the energy dissipation per distance ($L_b + L_c$) due to friction and form drag (§ 4.3). It is calculated as:

$$\Delta E_{f,L_b+L_c} = \rho g \nabla h_f = \rho g B h (L_b + L_c) S_f (L_b + L_c) \quad (\text{eq. 4.15})$$

where ∇ is the volume of water contained in one sequence ($L_b + L_c$) at base width and S_f the friction slope.

Finally, the ratio $\Delta E_{pot,1-2} / \Delta E_{f,L_b+L_c}$ allows estimating an upper limit of the part of energy dissipation due to the transverse oscillations relative to the totally observed energy dissipation.

Furthermore, the transverse velocity averaged in space \bar{V}_{\max} can be calculated by comparison of the total energy of situation 1 and 2:

$$\rho g L_b (B + 2\Delta B) \left(\frac{1}{2} h^2 + \frac{1}{16} a_+^2 \right) = \rho L_b h (B + 2\Delta B) \left(\frac{gh}{2} + \frac{\bar{V}_{t \max}^2}{2} \right)$$

which leads after simplification to:

$$\bar{V}_{\max} = \frac{a_+}{8} \sqrt{\frac{g}{h}} \quad (\text{eq. 4.16})$$

\bar{V}_{\max} is the transverse velocity averaged in space at the time corresponding to situation 2,. This velocity is lower than the maximum horizontal velocity in a standing wave at the node, calculated as Sorensen (1986):

$$V_{\max} = \frac{a_+}{2} \sqrt{\frac{g}{h}} \quad (\text{eq. 4.17})$$

4.2.3 Results of the analysis of the cavity oscillation

4.2.3.1 Flow reattachment and water surface oscillations

Observations during the tests showed that reattachment of the flow to the side walls of the widened channel reach avoids respectively reduces transverse movements of the flow and therefore water surface oscillations. A simplified approach based on numerical simulations is proposed to separate the large number of experiments into those with reattachment of the flow and those with a recirculation of the flow in the widenings. The main parameters responsible for the reattachment of the flow are the aspect ratio $\Delta B / L_b$ and the Reynolds number Re_m of the incoming flow. Numerical simulations have been done using *FLOW-3D* for the test configurations 221, 222, 223 and 224 for 6 different discharges ($11'000 < Re < 84'000$). Reattachment of the flow was found for the two highest discharges of configuration 221. For all other discharges, recirculation of the flow occurred (Figure 4-20, above). Considering a linear separation of the domain between reattachment and recirculation of the flow, reattachment can be assumed if the following two criteria are fulfilled.

- $\Delta B / L_b < 0.2$
- $Re_m \geq 520'000 \cdot (\Delta B / L_b)$

The separation is considered to be valid for Reynolds numbers of the incoming flow less than 90'000 and for $0.1 < \Delta B / L_b < 0.2$. For the present study it might be possible to extend the validity of the lower limit to $\Delta B / L_b = 0$ (since there is reattachment by definition for $\Delta B / L_b = 0$).

Within the simulated configurations and discharges it was found that the larger a widening is, compared to its length, the higher is the recirculation flow (backflow). According Rowley et al. (2002) such kind of backflow in cavities might produce an absolute instability, which provides the feedback mechanism, leading to hydrodynamic cavity oscillations of the type “wake mode”.

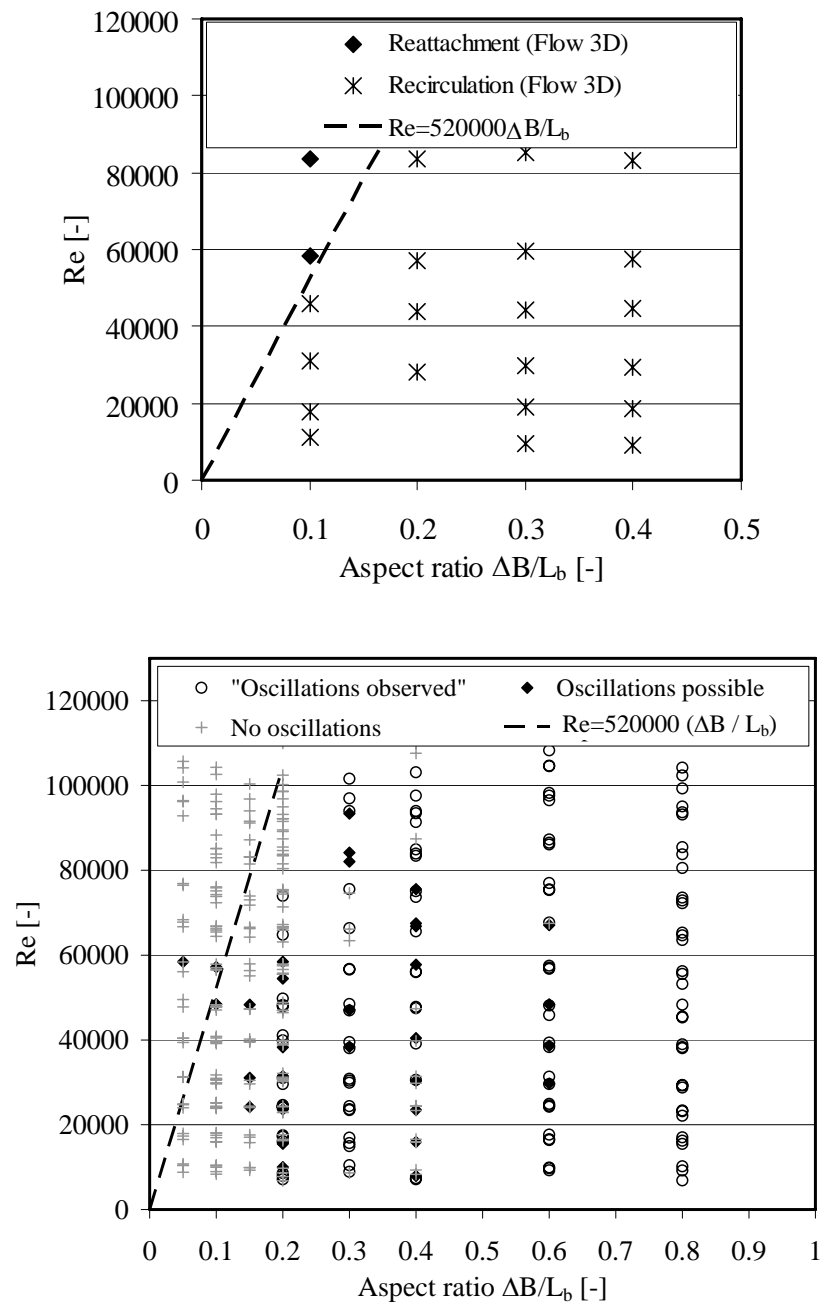


Figure 4-20: Above: Recirculation or reattachment of the flow for the simulated cases using FLOW-3D. Below: Experiments with observed, possible and without transverse oscillations (mode $n = 1$), represented in the recirculation-reattachment domain.

The separation between reattachment and recirculating flow is qualitatively validated by the observations on the physical model using the criteria defined for the identification of transverse oscillations of the water body (Table 4-3). As transverse oscillations are avoided by the reattachment of the flow, experiments with periodic water surface oscillations (all criteria fulfilled) respectively possible periodic water surface oscillations (2 of 3 criteria fulfilled) should be located in the recirculation domain. Figure 4-20 (below) effectively shows that:

- there is no experiment with observed water surface oscillations (3 criteria fulfilled) located in the reattachment domain and only 2 of the 31 experiments with possible water surface oscillations (2 criteria fulfilled).
- most experiments with observed water surface oscillations (3 criteria fulfilled) are located clearly in the recirculation domain, distant from the separation line between the two domains.
- experiments without transverse oscillations are either in the reattachment domain or located close to the limit which is indicating a reduced backflow.

Water surface oscillations of the second mode ($n = 2$) have only been observed (3 criteria fulfilled) for few discharges of configuration 122 and 142.

4.2.3.2 Frequency of the periodic water surface oscillations and vortex shedding

Figure 4-21 shows the comparison between the observed and calculated frequencies with the exact (eq. 4.6) and simplified (eq. 4.7) formula for all experiments including observed transverse oscillations of the first mode (3 criteria fulfilled). As higher frequencies correspond to higher flow levels for a given geometry and mode, it can easily be understood that the simplified equation deviates from the exact equation for higher frequencies, where the assumption of relative flow depth $h/W \ll 1$ is not valid anymore.

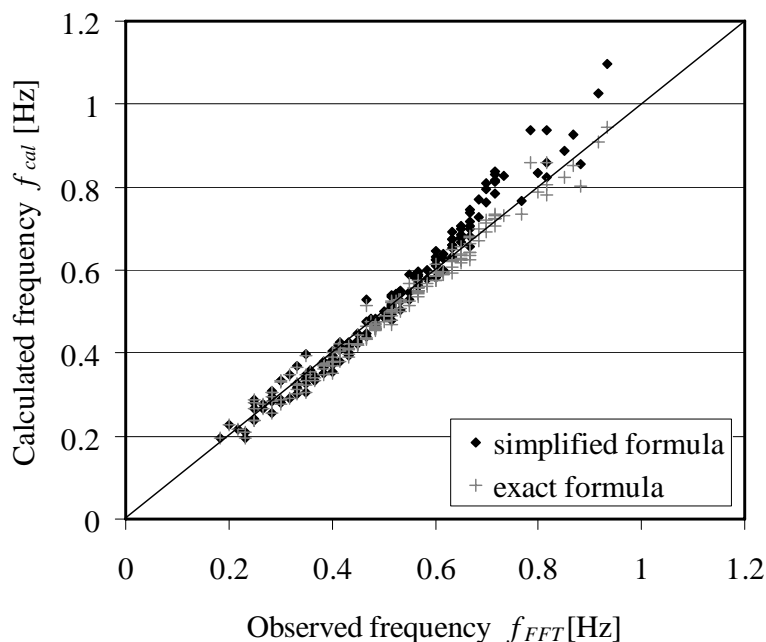


Figure 4-21: Comparison between the calculated and the observed frequencies for the exact (eq. 4.6, sloshing in a rectangular basin,) and approximate (eq. 4.7, seiches) equation for all experiments with transverse oscillations of mode $n = 1$.

Table 4-4: Comparison between the vortex shedding frequency (f_{shed}), the frequency of water surface oscillation (f_{FFT}) and the calculated frequency (f_{cal}) with (eq. 4.7).

Conf.	214	214	223	223	223	224	224	224	224	224	414	414
Q ; [m ³ /s]	0.036	0.046	0.009	0.015	0.020	0.009	0.049	0.059	0.071	0.085	0.015	0.021
h ; [m]	0.132	0.164	0.051	0.068	0.086	0.052	0.173	0.196	0.226	0.262	0.074	0.091
f_{shed} ; [Hz]	0.500	0.500	0.333	0.383	0.433	0.300	0.516	0.567	0.600	0.667	0.350	0.367
f_{FFT} ; [Hz]	0.467	0.517	0.333	0.383	0.417	0.300	0.500	0.533	0.567	0.600	0.300	0.200
f_{cal} ; [Hz]	0.435	0.479	0.326	0.374	0.422	0.279	0.493	0.524	0.557	0.591	0.334	0.370

For some configurations and discharges, the vortices shed at the leading edge of the widening have been clearly detected during the experiments. For example, for the configuration 224 with a discharge of $Q = 49$ l/s ($h = 0.173$ m, $Re = 58'950$) 31 vortices per minute are shed at the leading edge. The frequency of vortex shedding is therefore $f_{shed} = 0.516$ Hz. This value is close to the calculated frequency ($f_{cal}^{n=1} = 0.493$ Hz, (eq. 4.7) and observed frequency ($f_{FFT} = 0.500$ Hz; Figure 4-21) of the water surface oscillations. A comparison of the frequency of vortex shedding with the calculated and observed frequencies of the water surface oscillations is presented in Table 4-4. It can thus be concluded, that vortex shedding and water surface oscillations are coupled phenomena.

4.2.3.3 Transverse velocities components in the widening

The assumption that the periodic oscillations at the water surface are due to the periodic, transverse oscillations of the water body contained in the widened channel reach has been verified for configuration 224 ($\Delta B / L_b = 0.4$; $ER = 2.64$; $Q = 36$ l/s) by the measurement of the transverse velocity components at different locations of the widening. The main frequency of the water surface oscillations ($f_{FFT} = 0.467$ Hz), which is close to the Eigenfrequency of the water body ($f_{cal} = 0.438$ Hz), corresponds to the frequency of the cycle observed in the transverse velocity components ($f_v = 0.467$ Hz). Figure 4-22 shows the cyclic behaviour of the transverse velocities near the channel axis ($y = -0.05$ m). For the v -velocities at the cavity-freestream separation line ($y = -0.243$ m) Figure 4-23 shows a similar result. The measured transverse velocities of Figure 4-22 are higher at positions 1 to 7 than for Figure 4-23 which is explained by the continuity equation in the transverse direction relative to the main flow¹.

Furthermore, the maximum measured transverse velocities are of the same order of magnitude than the maximum horizontal velocity $V_{max} = 0.06$ m/s, calculated by means of (eq. 4.16) (see also Appendix 4-6).

¹ Please note that the y-axis of Figure 4-22 and Figure 4-23 have not the same scale.

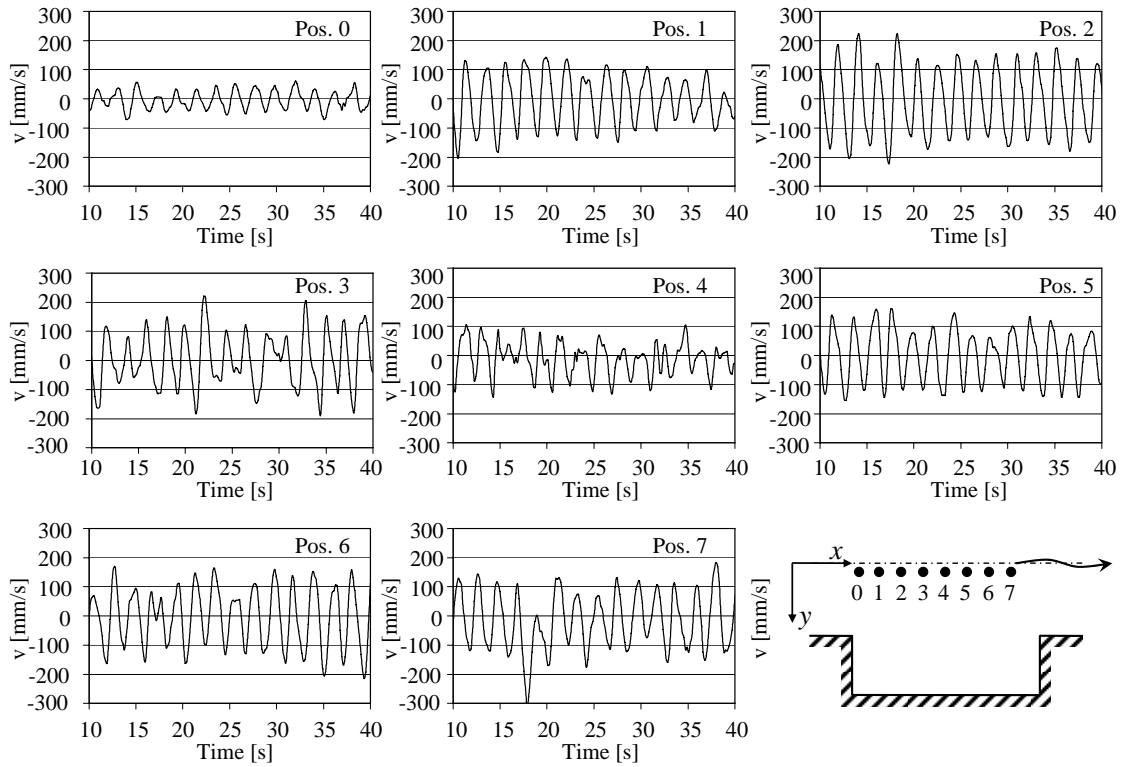


Figure 4-22: Transverse velocity components near the channel axis ($y = 0.05$ m) measured by the ultrasonic velocity profiler for different positions (see bottom right of the figure). The z -level is at the mean flow depth ($z = 0.066$ m).

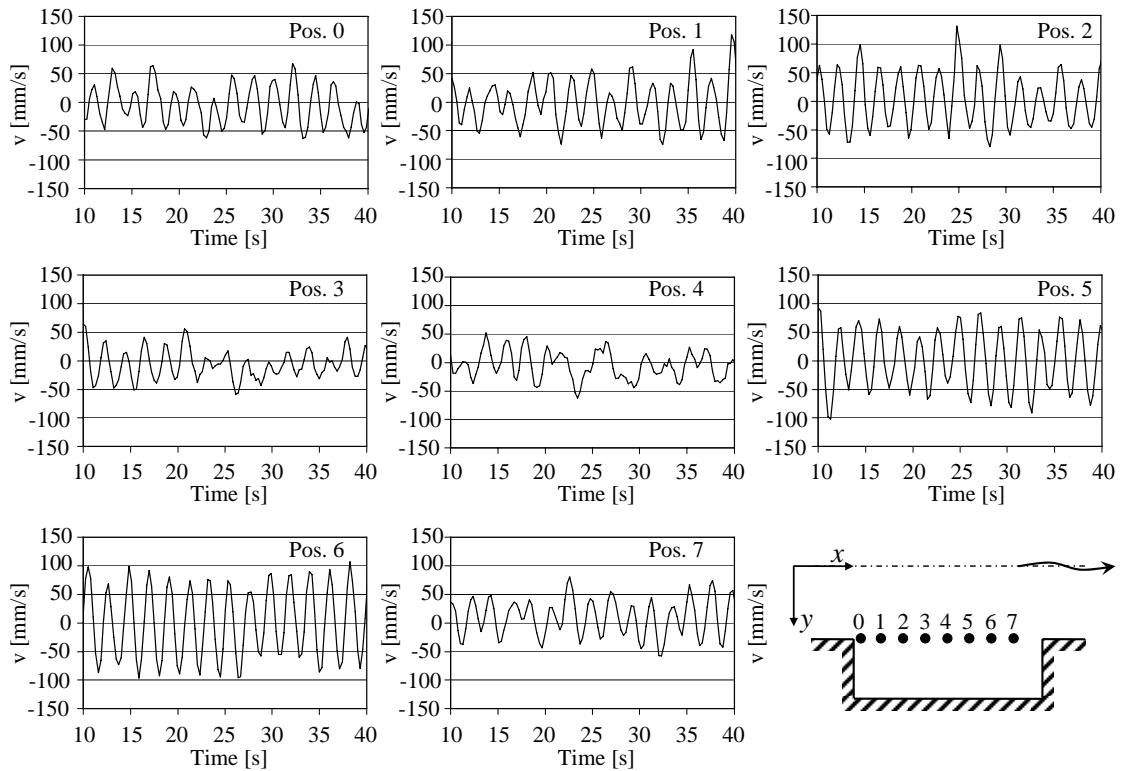


Figure 4-23: Transverse velocity components near the separation line cavity – main flow measured by the ultrasonic velocity profiler for different positions (see bottom right of the figure). The z -level corresponds to the mean flow depth ($z = 0.066$ m).

4.2.3.4 Amplitude of water surface oscillations

The amplitude of water surface oscillations in the widenings, depending on the geometrical characteristics of the cavities and the flow characteristics, would be useful to know for practical applications. A clear correlation has been found between the Strouhal number and the relative height of water surface oscillations. The Strouhal number is obtained from the calculated frequency (eq. 4.7) depending on the flow depth h and the width W of the waterbody, the widening length L_b as well as the mean flow velocity in the main channel U . Figure 4-24 and Figure 4-25 reveal peaking values of the relative mean wave-heights for Strouhal numbers near $St = 0.42$ and $St = 0.84$. The relative mean wave-heights can – but do not necessarily – reach values of about 30% ($St = 0.42$) respectively 22% ($St = 0.84$) at the side walls (Figure 4-25).

The figures also reveal that experiments producing transverse oscillations (all criteria fulfilled) are leading (logically) to the most important water surface oscillations. The experiments finally show that the relative mean wave-heights are below 3% if the flow reattaches to the side walls of the widening.

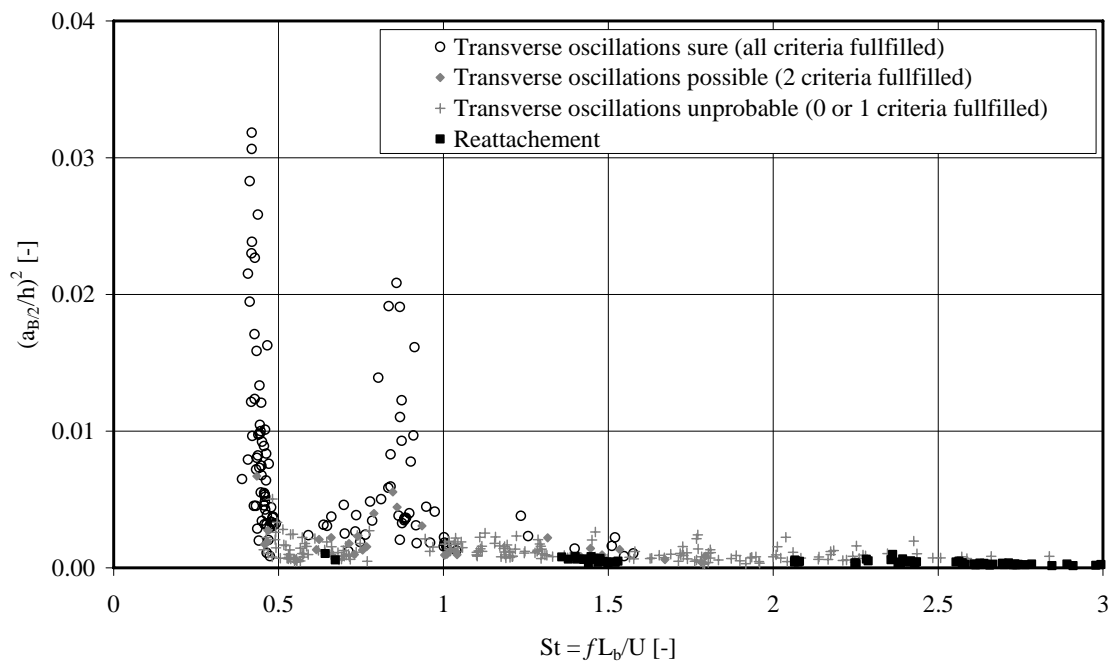


Figure 4-24: Square value of the relative wave-height at $y = \pm(B/2)$ as a function of the Strouhal number based on the calculated frequency (eq. 4.7), the mean freestream velocity U and the widening length L_b . A value of $(a_{B/2}/h)^2 = 0.04$ corresponds to a relative mean wave-height of 20% at $y = \pm B/2$.

In order to prevent significant water surface oscillations, which are the result of transverse water body movements between the left and right side widenings, Strouhal numbers near 0.42, 0.84 or 1.26 should be avoided by an adequate choice of the cavity dimensions. Axi-symmetric configurations as tested in the experiments clearly promote water surface oscillations. Water surface oscillations of 12% of the mean flow depth

have also been detected by Ohomoto et al. (2005) for axi-symmetric spur dikes with an aspect ratio of $\Delta B / L_b = 0.5$ and an expansion ratio of $(B + 2\Delta B) / B = 2$. For a comparable geometry and flow depth, the water surface oscillations found at the present study are in the same order of magnitude with about 14% to 17% of the mean flow depth.

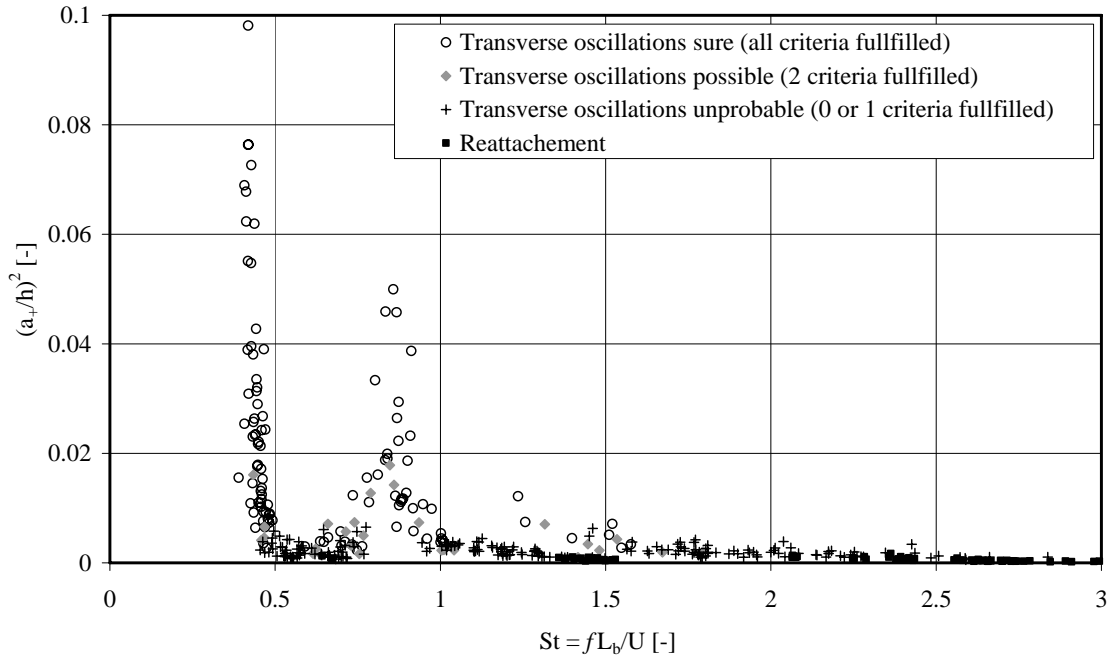


Figure 4-25: Square value of the relative wave-height at $y = \pm(B/2 + \Delta B)$ as a function of the Strouhal number based on the calculated frequency (eq. 4.7), the mean freestream velocity U and the widening length L_b . A value of $(a_+/h)^2 = 0.1$ corresponds to a relative mean wave-height of 31.6% at the side wall of the widening.

4.2.3.5 Influence of the longitudinal distance between widenings

In addition to the aspect ratio $\Delta B / L_b$ and the expansion ratio ER , the distance between widenings L_c has been varied during the experimental study. Intensification of the water surface oscillations is observed with increasing distance L_c (Appendix 4-6). Nevertheless, there is no influence on the general behaviour with peaking values of the amplitudes at Strouhal numbers of 0.42 and 0.84. It can therefore be concluded that the interaction between two opposite widenings is favouring important water surface oscillations, whereas the interaction between widenings along the channel (for example due to vortex structures travelling downstream) reduces water surface oscillations due to a disturbed incoming flow.

4.2.3.6 Energy dissipation due to transverse oscillations

An upper limit of the energy dissipation due to the transverse oscillations can be calculated using (eq. 4.14). This upper limit for the energy dissipation due to the transverse oscillations is related to the observed energy dissipation in the channel for the different configurations (eq. 4.15) using the ratio $\Delta E_{pot,1-2} / \Delta E_{f,L_b+L_c}$. Detailed results are

presented in Appendix 4-6. The maximum value of the ratio between the energy dissipation due to the transverse oscillations and the total observed energy dissipation reaches 13.6% for configuration 114 at the highest discharge. For cavities with an aspect ratio $\Delta B / L_b < 0.3$, transverse oscillations are exceptional. The upper limit of the energy dissipation due to the transverse oscillations is significantly less than 1% in this case. For aspect ratios $\Delta B / L_b \geq 0.3$, transverse oscillations are often observed. The upper limit of the energy dissipation due to the transverse oscillations can reach 5% to 10% of the observed total dissipation in the channel. However, as the calculated energy dissipation due to the transverse oscillations represents an upper limit (complete damping is assumed at every oscillation) and since in a regular topography there is almost no damping of the oscillations (Wilson 1972), the energy dissipation resulting from the transverse oscillations can be completely neglected comparing to skin friction and form drag. On the other hand, transverse oscillations may influence the drag coefficients of the cavities. Gharib and Roshko (1954) showed an increase of 250% of the cavity drag coefficient in case of cavity oscillations of the wake mode type.

4.2.4 Conclusions on transverse flow oscillations

Experiments with series of rectangular widenings (cavities) at both side walls of the main channel have been performed in a 40 m long laboratory flume. The tested arrangements of the widenings are symmetric to the channel axis. Various widening lengths L_b , widening depths ΔB and distances between the widenings L_c have been analyzed in 36 different configurations covering aspect ratios $\Delta B / L_b$ from 0.05 to 0.80 and expansion ratios $(B + 2\Delta B) / B$ from 1.41 to 2.65. Furthermore, 12 different discharges have been investigated for each geometry. For particular geometrical configurations and hydraulic conditions, periodic water surface oscillations have been observed in the widenings. Table 4-5 summarizes the factors related to the geometry and the flow which either favor or prevent water surface oscillations.

Table 4-5: *Factors favouring and preventing important and periodic water surface oscillations in a channel with cavities (large scale macro-roughness on banks).*

Factors favouring periodic oscillations	Factors preventing periodic oscillations
Axi-symmetric and regular arrangement of the cavities	Randomly arranged cavities (varying ΔB , L_b , L_c)
Strouhal numbers close to 0.42 and 0.84	Reattachment of the flow to the side walls
High expansion ratios $(B + 2\Delta B) / B$	Strouhal numbers different from 0.42 and 0.84
Relatively high aspect ratios $\Delta B / L_b$	Cavities only at one channel side
Undisturbed flow conditions at the cavity leading edge	Uneven bed topography (leads to damping)

If no periodic oscillations are observed, the relative mean wave-heights are in general significantly less than 5% at the lateral side walls of the widened channel sections. On

the other hand, the mean wave-height can reach up to 30% of the mean flow depth in case of strong water surface oscillations. Since the transverse velocity components, measured near the channel axis show the same periodic behaviour, it must be concluded that the phenomenon corresponds to seiching of a confined water body (free surface standing wave in the transverse direction to the main flow) even if the water body is only semi-confined.

The observed frequencies of the oscillations, identified by an FFT-analysis of the water level measurements, corresponds to the Eigenfrequencies calculated for the water body formed by the water contained in the widened reach. This frequency can be predicted with (eq. 4.6) for small relative flow depths or (eq. 4.7) for higher relative flow depths. The first mode of the free surface standing wave with a single node at the channel axis is largely dominating. The vortex shedding frequency at the leading edge of the widening was the same as the observed frequency of the water surface oscillations. These two phenomena are consequently coupled.

The amplitude of water surface oscillations is more difficult to predict than the frequency. Nevertheless, if the flow reattaches to the side walls of the widened channel reaches, no periodic water surface oscillations are observed and the relative mean wave-heights remain small. The reattachment of the flow avoids the formation of large scale (unstable) recirculation eddies in the rectangular widening and the hydrodynamic feedback mechanism leading to the wake mode misses.

Furthermore, the experiments allowed to identify critical Strouhal numbers around $St = 0.42$ and $St = 0.84$ at which peak excitations of the water surface oscillations occur. These Strouhal numbers should be avoided if practical applications require a reduction of water surface oscillations and transverse movements of the flow. Finally, the determination of an upper limit of the energy required for maintaining the transverse oscillations shows that this effect can be neglected completely in most of the configurations.

4.3 Backwater curve computation and resistance quantification

4.3.1 Introduction

The preceded chapters have shown the diversity of phenomena governing the total head-losses along the macro-rough channel. Some water level measurements have also been shown. Systematic comparison of the different macro-rough configuration requires the identification of roughness parameters. They have been derived from a backwater curve computation starting from downstream.

Channel slope and the particularly shaped cross section at the outlet have initially been chosen in order to obtain almost uniform flow depth along the prismatic channel without macro-roughness elements. The design of the outlet section placed at the end of the outlet reach allowed to achieve these conditions for more or less the whole range of tested discharge. Only for very small discharges supercritical flow conditions occurred in the outlet reach ($Q \leq 7 \div 8$ l/s). This is not due to the overall channel slope or the outlet section but due to the small geometrical irregularities of the channel bottom. However, there is no effect of this supercritical flow on the roughness parameters as the backwater curve computation started upstream of the critical section.

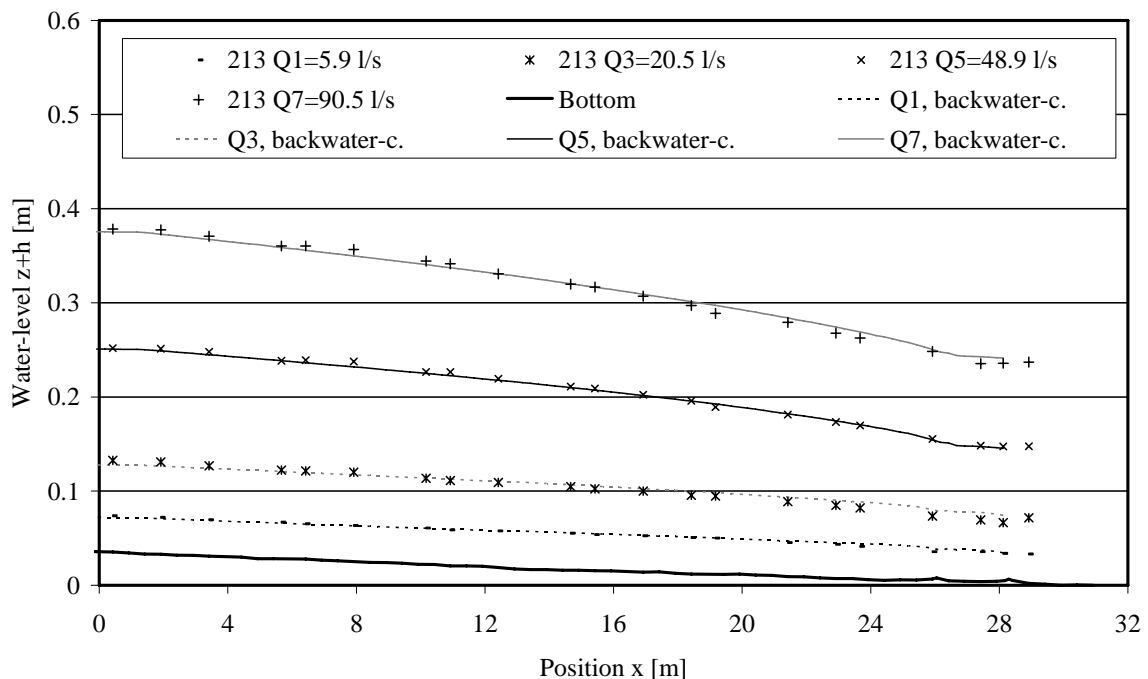


Figure 4-26: Backwater curve calculated along the channel for the example of configuration 213 ($L_b = 1.0$ m, $L_c = 0.5$ m, $\Delta B = 0.3$ m).

When macro-roughness elements are considered, the flow is still at uniform depth in the outlet reach of the channel but a backwater curve starts at the downstream end of the macro-rough channel reach (Figure 4-26).

Starting point of the backwater curve computations was the position $x = 28.12$ m. This position is located upstream of the main irregularity of the longitudinal profile of the channel. It is obvious that some measured points do not exactly fit the calculated backwater curve since they are not located in the sections having the base width B but at the beginning, in the middle or at the end of widened the channel part.

The backwater curve computation from downstream to upstream allowed identifying the roughness parameters as the equivalent sand roughness k_s , the Strickler coefficients K_{st} or the Chezy coefficients C of the 36 different geometrical configurations. The utilized technique is also called “inverse roughness modelling” (Sieben 2003, Ramesh et al. 2000).

4.3.2 Method applied for the backwater curve computation

The backwater curve computation is based on a one dimensional prismatic approach for a highly non prismatic channel. The following assumptions have been made:

- The channel is divided into a prismatic inlet reach, a reach with macro-roughness elements (axi-symmetric rectangular cavities) leading to a higher roughness of the channel banks and a prismatic outlet reach in which the backwater curve computations starts.
- The head-losses due to the macro-roughness elements (form drag) are considered as an additional linear head-loss like the skin friction of the prismatic channel.
- The channel is considered as prismatic but with composite roughness (side wall roughness is different from the bottom roughness).
- A logarithmic law is used for the friction computation.
- The friction of the composite channel section is calculated following the method of Einstein (1934) for the conceptual¹ subdivision of the section. Eq. 2.19 is used for the weighting of the friction coefficients.
- The backwater curve is computed using the standard step method.
- The calibration of the parameter related to the roughness is done by minimization of the sum of squares of differences between the calculated and measured values of flow depth (objective function). Only US-sensors located in a section at base width B are considered for the calibration.

The formulas employed for the inverse roughness modeling are given hereafter. The energy equation is used for the backwater curve computation and the standard step method leads to:

$$\left(h_{i+1} + z_{i+1} + \frac{U_{i+1}^2}{2g} \right) - \left(h_i + z_i + \frac{U_i^2}{2g} \right) = \overline{S}_{fm} (x_{i+1} - x_i) \quad (\text{eq. 4.18})$$

¹ The subdivision of the section is conceptual, not physical (Yen 2002).

where S_f = friction slope; h = flow depth; x = channel section; z = bottom level; U = mean velocity related to the base width B . The subscript m indicates that the friction slope is composed of a wall friction (subscript w) including effect of the macro-roughness and a bottom friction (subscript 0). The subscript i refers to the position along the channel.

The friction slope is calculated by the Darcy-Weisbach formula:

$$\overline{S_{f_m}} = \overline{f_m} \frac{\overline{U}^2}{8g\overline{R_h}} \quad (\text{eq. 4.19})$$

where R_h = hydraulic radius; f = friction coefficient. The horizontal bar indicates that averaged values of sections i and $i + 1$ are taken into account (iterative computation).

The channel has been considered as a section of composite roughness. If the assumption of the approach of Einstein (1934) for a section of composite roughness applies, it can be written:

$$\frac{R_{h0}}{f_0} = \frac{R_{hw}}{f_w} = \frac{R_{hm}}{f_m} = \frac{U^2}{8g\overline{S_{f_m}}} \quad (\text{eq. 4.20})$$

where R_{h0} = hydraulic radius referred to the bottom; R_{hw} = hydraulic radius referred to the wall; R_{hm} = hydraulic radius referred to the section at base width B .

The friction coefficient of the section f_m is calculated according to (eq. 2.19). This formula is obtained from the Darcy-Weisbach formula using Einstein's approach for composite channel sections.

$$f_m = \frac{Bf_0 + 2hf_w}{B + 2h} \quad (\text{eq. 4.21})$$

where f_0 = bottom friction coefficient; f_w = wall friction coefficient including the effect of macro-roughness of the widenings.

The bottom and wall friction coefficients can be determined iteratively with the following logarithmic laws:

$$\frac{1}{\sqrt{f_0}} = -K_1 \log \left(\frac{k_{s0}}{K_2 R_{h0}} + \frac{K_3}{4Re_0 \sqrt{f_0}} \right) \quad (\text{eq. 4.22a})$$

$$\frac{1}{\sqrt{f_w}} = -K_1 \log \left(\frac{k_{sw}}{K_2 R_{hw}} + \frac{K_3}{4Re_w \sqrt{f_w}} \right) \quad (\text{eq. 4.22b})$$

where Re_0 = Reynolds number related to the bottom; Re_w = Reynolds number related to the wall; $k_{s,0}$ = equivalent bottom sand roughness; $k_{s,w}$ = equivalent wall sand roughness including the effect of macro-roughness of widenings. $K_1 = 2.03$, $K_2 = 10.95$ and

$K_3 = 1.70$ are the constants utilized by Rouse (1946). Backwater curve computations for the prismatic channel showed good agreement of the hydraulic behaviour of the laboratory flume with these constants.

The hydraulic radius R_{h0} , R_{hw} , and the Reynolds numbers Re_0 and Re_w are calculated as:

$$R_{h0} = \frac{R_{hm}}{f_m} f_0 \quad (\text{eq. 4.23a}) \qquad Re_0 = \frac{U R_{h0}}{\nu} \quad (\text{eq. 4.24a})$$

$$R_{hw} = \frac{R_{hm}}{f_m} f_w \quad (\text{eq. 4.23b}) \qquad Re_w = \frac{U R_{hw}}{\nu} \quad (\text{eq. 4.24b})$$

The equivalent sand roughness of the wall $k_{s,w}$, which includes the effect of macro-roughness of the widenings, has been used to fit the calculated water levels with the observed ones. A dataset of $k_{s,w}$ -values is obtained by this way. The $k_{s,w}$ -values can either be determined globally for all discharges of one geometrical configuration (global values; Table 4-6) or individually for every discharge of the geometrical configuration (single values).

Table 4-6: Definition and advantages / disadvantages of global, final and single values of wall roughness and overall roughness / flow resistance parameters.

Denomination :	Description	Advantages / Disadvantages
Global roughness parameter :	Values which provide the best results between the observed and calculated water surface for all discharges leading to $Re_m > 60'000$.	Errors minimized for several backwater curves. Values are thus stable towards levelling errors. / Do not always well reproduce low discharges experiments.
Final roughness parameter :	Values which are asymptotically reached for the highest tested discharges. Normally very close to global values.	Idem global roughness parameters.
Single roughness parameter :	Values which are issued from the calibration of the water surface separately for every discharge.	Fits well the water surface of the calculations and the observations. / Do not respect the inherent character of a roughness parameter (a priori constant).
Wall roughness parameter :	Values only related to the roughness of the wall (including the effects of the macro-roughness, index w)	Independent on the channel width, applicable to various base widths B . / Dependent on the hypotheses for separating bottom and wall roughness.
Overall roughness parameter :	Values related to the section of composite roughness (index m)	Reflect the general behaviour in the test flume and for flumes with comparable geometries. / Merge wall and bottom roughness effects.

The wall friction coefficients f_w including the effect of macro-roughness can be extracted from (eq. 4.22b). The friction coefficients of the section f_m can be extracted from (eq. 4.21). The f_m -values correspond to a more general information than the f_w or

$k_{s,w}$ -values. Moreover, f_m -values are practically independent on the hypothesis made by the introduction of (eq. 4.20) to (eq. 4.24) and nearly constant along the channel for a given discharge and a given macro-rough configuration.

The equivalent sand roughness of the wall $k_{s,w}$, the wall friction coefficients f_w and the friction coefficients f_m represent three different data sets related to the macro-rough configurations. The quantitative results of these parameters are presented in the following § 4.3.3 as well as several derived quantities.

4.3.3 Equivalent sand roughness of the wall including the macro-roughness $k_{s,w}$

The equivalent sand roughness of the wall $k_{s,w}$ was the calibration parameter in the backwater curve computation method. The results of two test series are shown in Appendix 4-1. Generally good agreement is found between the values issued from the first test series (ES) and the second test series (EnS). For the following analysis, only the values and measurements of the second test series (EnS) are considered as the adjustment of computed and measured backwater curves has been done over a longer channel distance than for the first test series (ES).

For most cases the equivalent sand roughness of the wall is increasing with the unit discharge before attending asymptotically final values (Appendix 4-1). The increase could be shown in the same way as a function of the measured flow depth, the mean flow velocity or the Reynolds numbers since all these parameters increase similar to the unit discharge. The reason for the increase of the equivalent sand roughness of the wall is that for low relative flow depths h/B , the wall roughness cannot be fully mobilized. The final value of the equivalent sand roughness is always significantly lower than the geometrical parameter ΔB despite for configurations 111 ($L_b = 0.5$ m, $L_c = 0.5$ m, $\Delta B = 0.1$ m), 211 ($L_b = 1.0$ m, $L_c = 0.5$ m, $\Delta B = 0.1$ m) and 212 ($L_b = 1.0$ m, $L_c = 0.5$ m, $\Delta B = 0.2$ m).

For a given cavity length L_b , the equivalent sand roughness generally increases with a decrease of the distance between the cavities L_c as well as with an increase of the cavity depth ΔB . However, the equivalent sand roughness values of the wall do not follow these general trends for all configurations and the relation is almost not linear. As examples are mentioned configurations 141 to 144 ($L_b = 0.5$ m, $L_c = 2.0$ m) for which a sudden increase of $k_{s,w}$ is noticed for $\Delta B = 0.4$ m. For configurations 411 to 414 ($L_b = 2.0$ m, $L_c = 0.5$ m) no more increase of $k_{s,w}$ can be observed for $\Delta B = 0.2$ to 0.4 m.

4.3.4 Overall and wall friction coefficients f_m and f_w

Two further parameters have been found directly from the backwater curve computation method: the wall friction coefficients f_w and the friction coefficients of the composite channel section f_m . They are presented for all configurations in Figure 4-27 as a function of the Reynolds number Re_m of the section at the base width B respectively in Figure 4-28 as a function of the wall Reynolds number Re_w (eq. 4.24b). The observed range of

friction coefficients of the prismatic reference configuration is given on the same plots.

With regard to the friction coefficients of the section (f_m -values) of Figure 4-27 the following observations can be highlighted:

- The macro-roughness elements lead to significantly increased f_m -values compared to the prismatic reference channel.
- The macro-roughness leads to rising characteristics of the f_m-Re_m curves, especially for Reynolds numbers $Re_m > 25'000 \div 30'000$.
- For short widenings ($L_b = B$), no further increase of f_m -values seems to be produced for Reynolds numbers $Re_m > \sim 60'000$. For long widenings ($L_b = 2B$ or $4B$), the increase of f_m -values is still present but reduced for Reynolds numbers $Re_m > \sim 70'000$.
- According Morris (1972), the global behaviour of the composite channel section follows a kind of wake interference (also called hyperturbulent) flow for Reynolds numbers $Re_m > 25'000 \div 30'000$. Quasi-smooth flow is remarked for geometries with short widenings ($L_b = B$) and Reynolds numbers $Re_m > 60'000 \div 70'000$.
- Differences in f_m -values between the 36 different geometrical configurations exist, although they are not as important as the difference between the prismatic reference and the configurations with macro-roughness.

Regarding the wall friction coefficients (f_w -values) of Figure 4-28 the following can be observed:

- The wall friction coefficients f_w are higher than the friction coefficients of the section of composite roughness f_m due to the low bottom friction coefficients f_0 .
- Quasi constant f_w -values can be observed for short and deep cavities with an aspect ratio $\Delta B / L_b = 0.8$ (conf. 114, 124, 144) for wall Reynolds numbers up to $100'000$ before they decrease for higher wall Reynolds numbers. This is also visible but less evident for cavities with an aspect ratio of $\Delta B / L_b = 0.6$ (configurations 113, 123, 143).
- The rising characteristics found from the f_m-Re_m curves still exist after the separation of the wall and bottom friction. This indicates a kind of wake interference flow also when regarding the wall friction coefficients only.
- Kind of stabilization of the wall friction coefficients f_w -values is observed for most geometrical configurations for wall Reynolds number higher than about $100'000$.

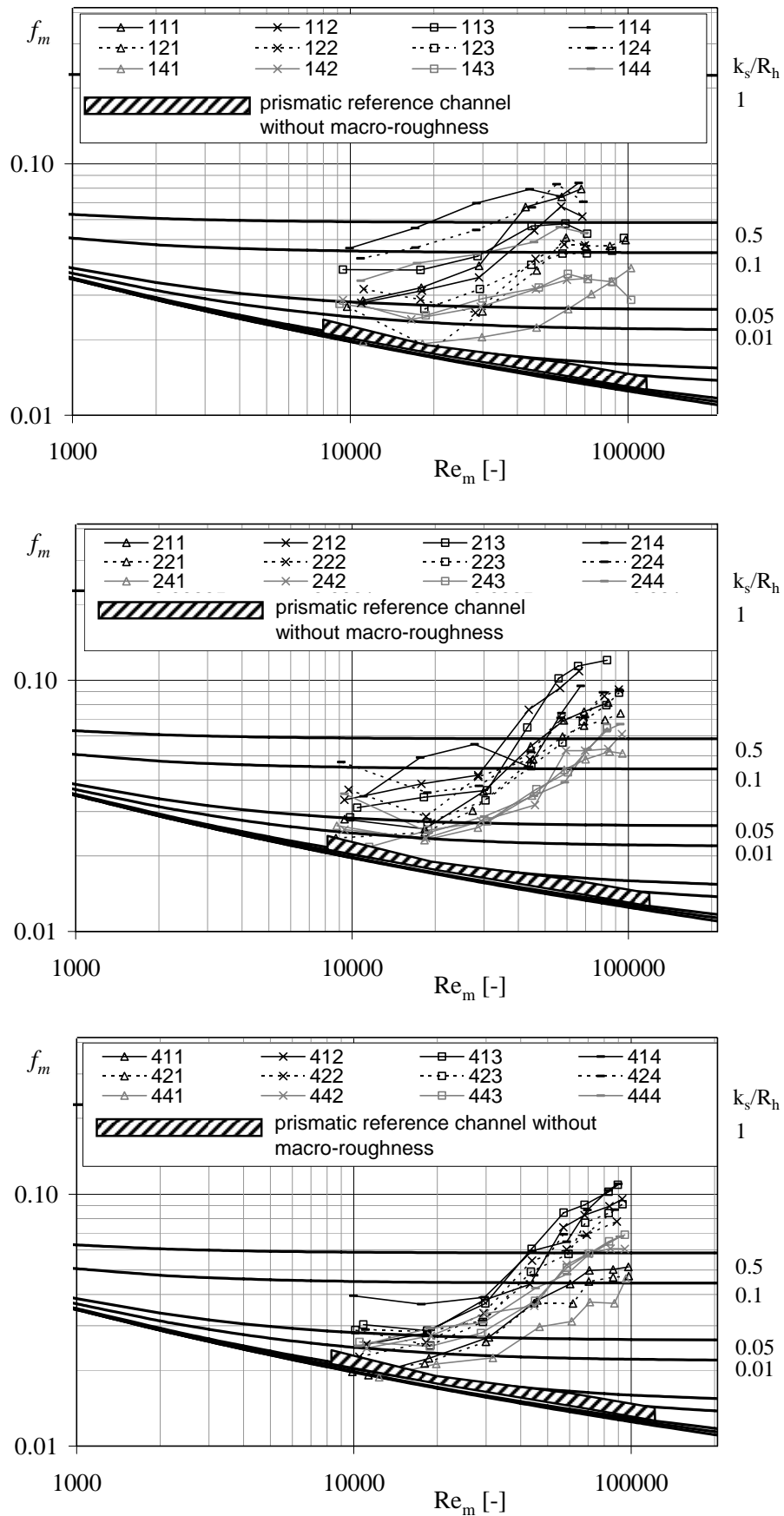


Figure 4-27: Friction coefficient of the composite channel section f_m (including MR) as a function of the Reynolds number Re_m of the composite channel section (relative to B).

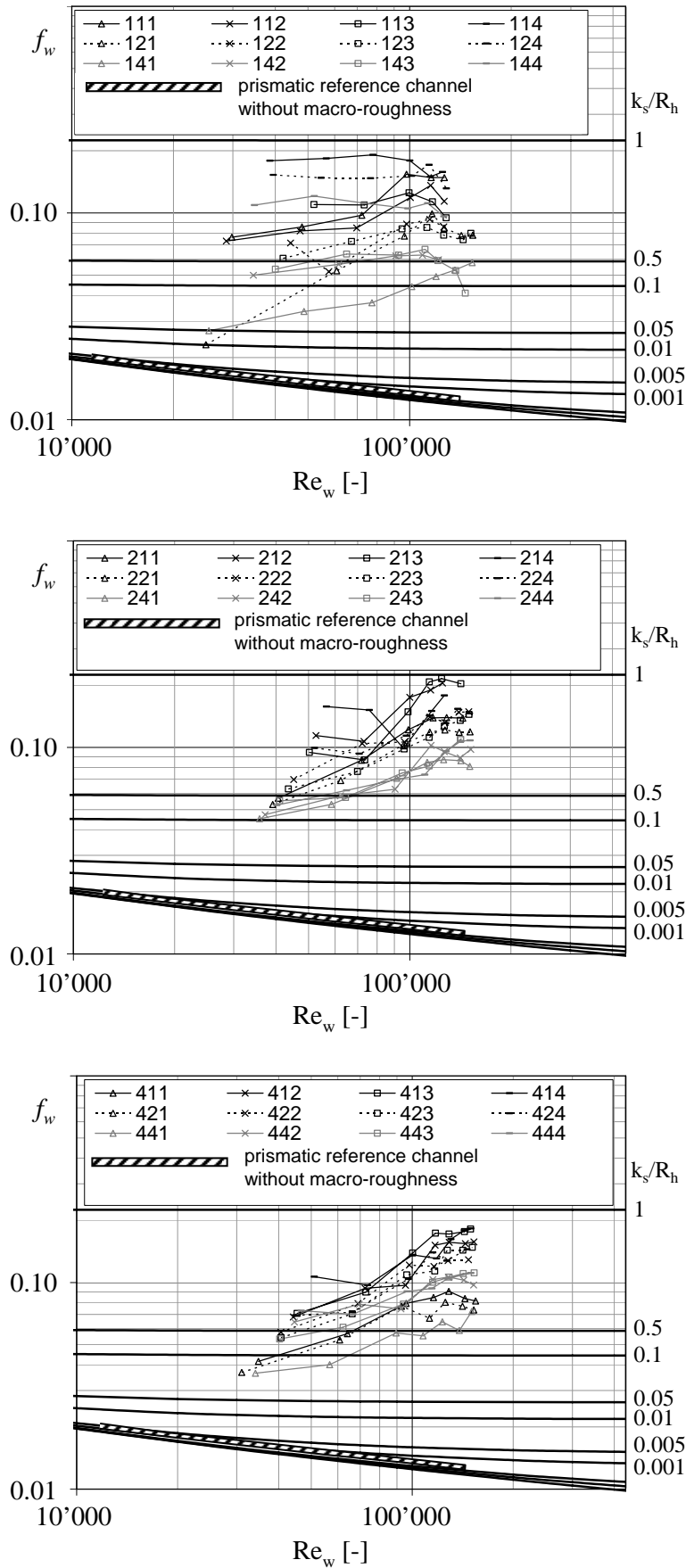


Figure 4-28: Wall friction coefficient f_w (including MR) as a function of the wall Reynolds number Re_w (eq. 4.24b).

Figure 4-27 and Figure 4-28 show qualitatively and quantitatively the influence of macro-roughness elements (rectangular widenings) at the side walls on friction coefficients. The curves differ from any logarithmic or power law presented in § 2.1.5 since with increasing flow depth (or Reynolds numbers) the friction coefficients increases for most of the configurations. However, the form drag based friction law of Lawrence (1997) correlates somehow with the experimental data when it is conceptually translated into the situation of channel bank macro-roughness. In Figure 4-29, the partially inundated friction factor (Lawence 1997) is calculated as the sum of the prismatic friction coefficient and a contribution due to the channel bank macro-roughness. This second contribution has been interpreted as:

$$f_m = f_{m,prism} + \xi \frac{L_b}{L_b + L_c} C_d \Delta B R_{hm} \quad (\text{eq. 4.25})$$

where ξ [m^{-2}] is a constant C_d is the drag coefficient, $L_b / (L_b + L_c)$ the linear widening density, ΔB the cavity depth and R_{hm} the hydraulic radius of the section.

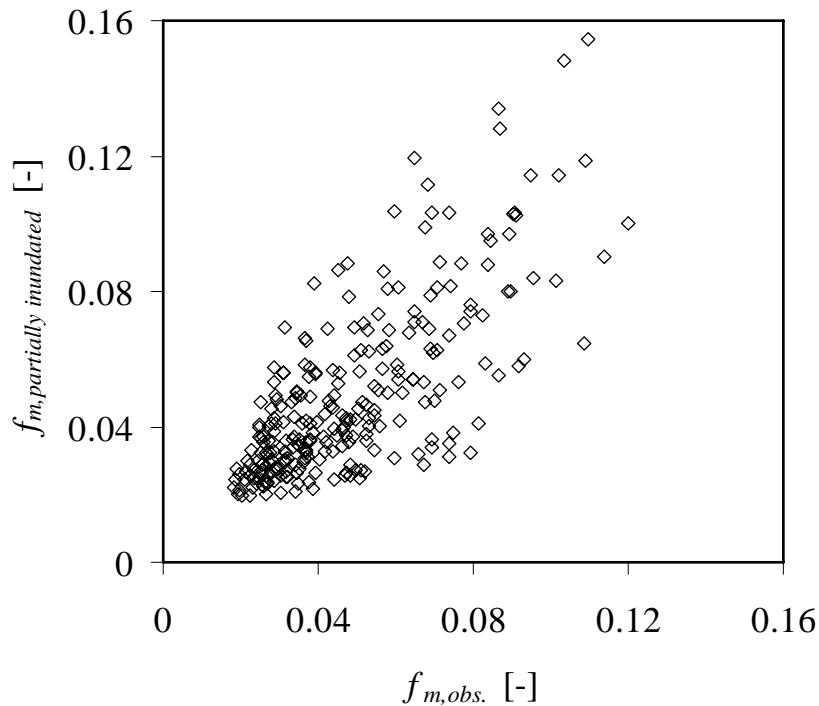


Figure 4-29: Formula of Lawrence (1997) for partially inundated flow interpreted for and compared to the steady flow test with channel bank macro-roughness.

4.3.5 Chezy C and Strickler coefficients K_{st}

Using the relation between the most frequently used resistance formulas in open channel flow, Manning-Strickler, Darcy-Weisbach and Chezy (Yen 2002), other resistance parameters can be derived from the friction coefficients presented above.

$$\sqrt{\frac{8}{f}} = \frac{K_{st} R_h^{1/6}}{\sqrt{g}} = \frac{C}{\sqrt{g}} = \frac{U}{\sqrt{g R_h S_f}} \quad (\text{eq. 4.26})$$

where f , K_{st} , C and R_h are related to the section of composite roughness (index m) respectively to the wall (index w). The calculated coefficients $K_{st,m}$, $K_{st,w}$, C_m and C_w do not provide real additional information or knowledge about the flow in the macro-rough channel section. They are however illustrative and the values of $K_{st,m}$, $K_{st,w}$, C_m and C_w are given for all tests in Appendix 4-1.

The following observations and reflections are made with regard to the roughness related parameters of Figure 4-30 and Appendix 4-1:

- All Chezy coefficients of the wall (C_w -values, final values) are situated between $39.0 \text{ m}^{0.5}/\text{s}$ and $19.5 \text{ m}^{0.5}/\text{s}$. The C_w -value determined for the wall without macro-roughness elements is $78.0 \text{ m}^{0.5}/\text{s}$. The Chezy coefficients related to the wall are thus reduced 2 to 4 times.
- The C_w -values are generally decreasing with the unit discharge before attending asymptotically a stable (final) value. This indicates that for high discharge flows, where the wall-roughness strongly influences the flow resistance, constant Chezy coefficients can be considered for a given geometrical configuration.
- The Strickler coefficients related to the wall $K_{st,w}$ have practically the same behaviour as the Chezy coefficients C_w . This is explained by the relation between the two parameters ($C_w = R_{hw}^{1/6} \cdot K_{st,w}$) and by relative constant values of $R_{hw}^{1/6} = 0.725 \div 0.825 \text{ m}^{1/6}$.
- The Strickler or Chezy coefficients of the section of composite roughness $K_{st,m}$ and C_m are logically higher than the ones related to the wall (due to the low bottom friction) and tend asymptotically to a final value. For the range of tested discharges it seems that the final values are not always reached. There is still an influence of the bottom on the overall friction¹.

If the unit discharge values $q < 0.05 \text{ m}^3/\text{s}/\text{m}$ are not considered (low h/B and less influence of the wall roughness) most of the $K_{st,m}$ -values range between $70 \text{ m}^{1/3}/\text{s}$ and $35 \text{ m}^{1/3}/\text{s}$ (prismatic reference: $113 \text{ m}^{1/3}/\text{s}$). The C_m -values are between $50 \text{ m}^{0.5}/\text{s}$ and $25 \text{ m}^{0.5}/\text{s}$ (prismatic reference = $71 \div 79 \text{ m}^{0.5}/\text{s}$).

The final values of the wall Chezy-coefficients C_w (Figure 4-30) can be considered as an accurate roughness characteristics of the macro-rough configurations for two reasons. First, the final values correspond to the highest discharge and therefore to the highest flow depth. The influence of the wall is governing and the result is independent of a possible error of the bottom roughness estimation. Secondly, a possible error of the

¹ Such as for large rivers, where the bank roughness has no more influence on the overall roughness, it can be considered that for sufficiently high relative flow depths h/B the bottom roughness has no more influence on the overall roughness.

discharge (or level) measurement has the less influence for the highest flow depth.

It appears that even the “smoothest” macro-rough configuration is two times rougher than the configuration without macro-roughness elements (prismatic channel). Within all macro-rough geometries, the C_w -value passes from $39 \text{ m}^{0.5}/\text{s}$ for configuration 143 ($L_b = 0.5 \text{ m}$; $L_c = 2.0 \text{ m}$, $\Delta B = 0.3 \text{ m}$) to $19.5 \text{ m}^{0.5}/\text{s}$ for configuration 212 ($L_b = 1.0 \text{ m}$; $L_c = 0.5 \text{ m}$, $\Delta B = 0.2 \text{ m}$). Furthermore, the ranking of Figure 4-30 indicates the difficulty to relate roughness parameters to a certain geometrical configuration for different reasons:

First, only small differences of C_w -values can be observed for geometries having however very different geometrical proprieties. 60% of the tested geometries are situated between $C_w = 27 \text{ m}^{0.5}/\text{s}$ (conf. 244) and $C_w = 19.5 \text{ m}^{0.5}/\text{s}$ (conf. 212). Secondly, the ranking does not always follow the intuition. Who would have thought a priori that configuration 123 with deeper cavities is smoother than configuration 121? Who would have thought a priori that 123 is smoother than 243? Why is the C_w -value of 411 so different from 412, 413 and 414? Why 113 and 112 are smoother than 111?

For the better understanding of the influence of the different geometrical proprieties on the roughness, the test configurations are divided (Figure 4-30) into widening types ($L_c > L_b$), intermediate types ($L_c = L_b$) and groyne types ($L_c < L_b$). The subdivision allows making the following observations:

- The roughness is generally higher for groyne types than for widening types. According to the developments of Morris (1972) about macro-roughness elements, the relative roughness spacing seems to be the important parameter for the quantification of the roughness.
- Within the groyne types, the roughness generally increases with ΔB whereas the roughness decreases with increasing L_c and/or L_b .
- For the intermediate types, which all have the same proportion of widened channel length compared to the total channel length (50%), the roughness increases also with increasing ΔB .
- For the widening types it is remarked that the higher ΔB respectively L_b , the higher becomes the roughness. Furthermore, the higher L_c , the smaller becomes the roughness.

The above mentioned observations are valid for a lot of cases. Nevertheless, due to particular flow behaviours such as recirculation or reattachment of the flow, some exceptions are observed. These exceptions indicate that additional parameters as the cavity aspect ratio or the expansion ratio have to be taken into account.

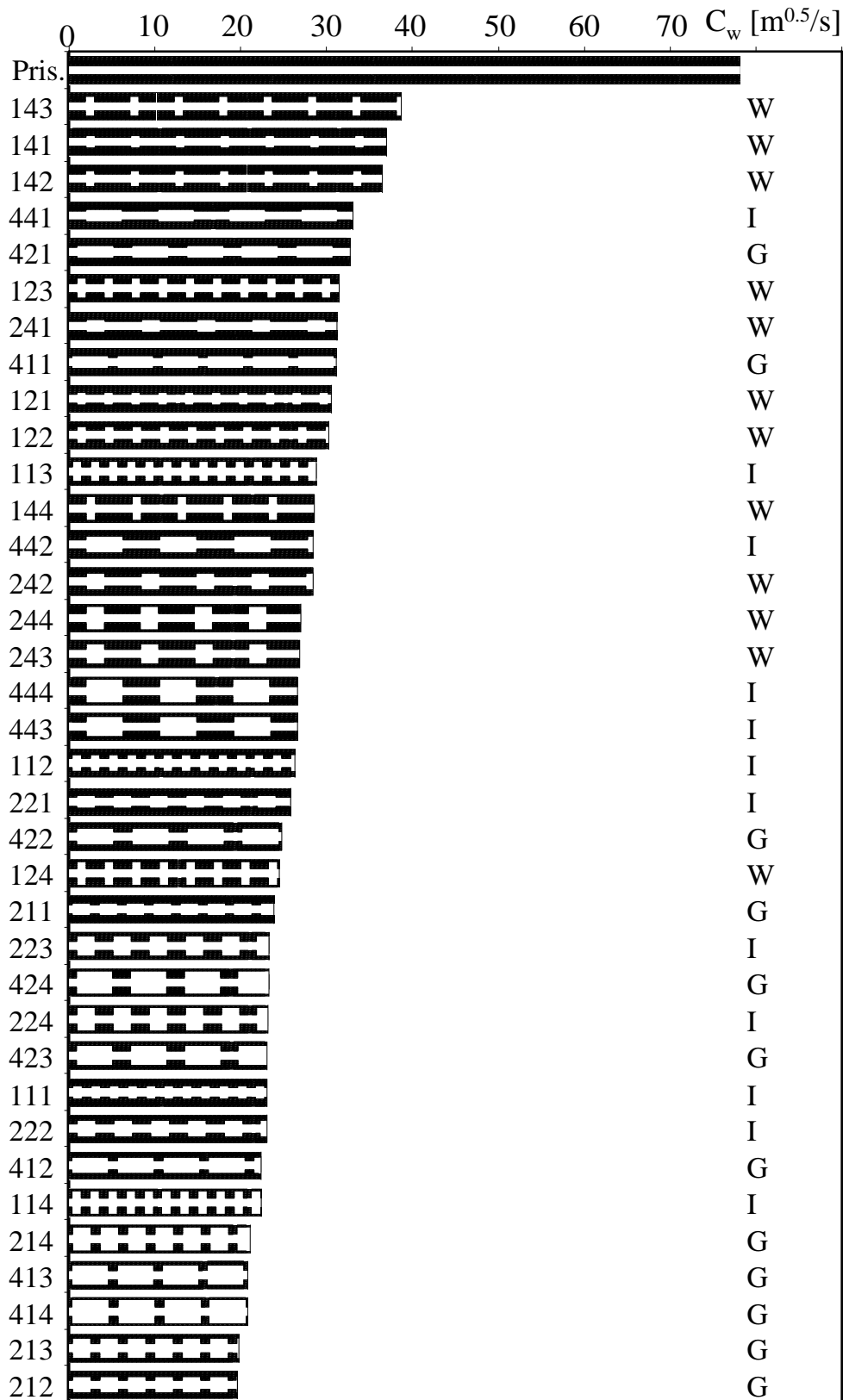


Figure 4-30: Values of the final Chezy coefficients related to the wall C_w for all geometrical configurations. The length of the bars illustrates the C_w values found by back-water curve computation. W: widening type geometries, I: Intermediate type geometries, G: Groyne type geometries. At the top: smoothest configurations. At the bottom: the roughest configurations.

4.3.6 Discussion of the obtained roughness parameters considering the macro-roughness of the channel banks

From a **qualitative point of view**, in open channel flow, it is the behaviour of the flow in and over a specific roughness geometry rather than the roughness itself which has to be classified “macro-rough”. When flow depth and velocity are sufficiently high, the effect of the macro-roughness elements disappears and flow tends towards the normal rough flow conditions (Bathurst 1985). Macro-rough flow behaviour can be observed in natural geometries when the flow depth is very low compared to the roughness elements (mountain stream) as well as in man made geometries with artificial, often regularly disposed roughness elements such as investigated here. Especially in the latter case, the friction coefficient might increase with increasing Reynolds number. In natural overland and overbank flows, the friction factor increases with rising relative flow depths, observed for partially inundated flow regimes (Lawrence 1997). Macro-roughness on channel banks favours flow resistance behaviour such as observed for partially inundated flows (Figure 4-29).

The laboratory experiments showed that part of the flow resistance is only mobilized for increasing Reynolds number. This behaviour of friction coefficients is comparable with other studies. The macro-rough geometrical parameters of this study varied from 0.5 m to 2.0 m for L_c and L_b and from 0.1 m to 0.4 m for ΔB and the hydraulic radius related to the wall (eq. 4.23b) varied from 0.05 m to 0.25 m. Thus, the increase of the friction coefficients in the present study takes place at another geometric scale of roughness elements. For comparison, the dimensions of roughness elements of other experimental investigations (Table 2-2), showing comparable behaviour, can be summarized as follows:

- Nikuradse, artificially roughened pipes (grain diameters = 0.0001 m to 0.0016 m; diameters of pipes = 0.025 m to 0.100 m)
- Warwick, artificially roughened channels (roughness heights 0.0004 m, 0.002 m and 0.004 m; hydraulic radius 0.01 m to 0.072 m)
- Morris (including roughness heights and spacing of very different size but in general with a roughness spacing smaller than 0.07 m and a roughness height smaller than 0.05 m; including data from Schlichting, Powell, Streeter and Bazin).

The analysis of the parameters related to the roughness allowed:

- a better understanding of the different phenomena of the macro-rough flow (increasing and then stabilization of the roughness-related parameters).
- to distinguish fully rough turbulent flow from macro-rough turbulent flow in a channel reach (decreasing respectively increasing characteristics on the friction coefficient – Reynolds number plots).
- to identify parameters of the flow resistance for steady flow conditions, which are the basis for the analysis of the experiments with unsteady flow.

From the **quantitative point of view**, the obtained equivalent roughness parameters are summarized in Table 4-7. The mean, minimum and maximum values are given for groyne, intermediate and widening type geometries. They are compared to the prismatic reference. A distinction is made between the roughness parameters of the wall (index w) and the composite channel section (index m).

Table 4-7: *Final* equivalent roughness parameters related to the wall (w) and to the composite channel section (m). Average (A), maximum (+) and minimum (-) values for groyne, intermediate and widening type geometries.*

Roughness parameter		Prismatic reference	Groyne type			Intermediate type			Widening type		
			A	-	+	A	-	+	A	-	+
Equivalent sand roughness	$k_{s,w}$ [mm]	~0.02-0.03	132	35	199	93	33	135	49	15	101
Wall Chezy coefficient	C_w [$m^{0.5}/s$]	78	23.6	19.6	32.7	25.8	22.3	32.9	31.0	24.4	38.6
Wall Strickler coefficient	$K_{st,w}$ [$m^{1/3}/s$]	110	31.0	24.9	42.7	34.0	29.3	47.0	40.7	29.7	52.4
Wall friction coefficient	f_w [-]	0.0129	0.152	0.074	0.205	0.122	0.072	0.158	0.088	0.058	0.132
Section Chezy coefficient	C_m [$m^{0.5}/s$]	79	30.5	25.6	40.7	33.5	29.3	41.2	39.7	33.3	48.1
Section Strickler coefficient	$K_{st,m}$ [$m^{1/3}/s$]	113	42.8	35.8	57.0	47.3	40.7	57.9	56.3	47.9	68.6
Section friction coefficient	f_m [-]	0.0123	0.089	0.047	0.120	0.072	0.046	0.092	0.052	0.035	0.071

* Final values correspond to the highest investigated discharge.

The experiments showed that the equivalent sand roughness height is generally significantly smaller than the geometric depth of the widenings AB . The average equivalent sand roughness is smaller for “widening type” geometries than for “intermediate type” geometries, whereas the latter is smaller than the one of “groyne type” geometries. The increase of the roughness parameters between the different types is mainly explained by the dimensionless parameter $L_b / (L_b + L_c)$. This parameter characterizes the cavity density and is higher for widening- than groyne type geometries.

Since the differences between the macro-rough configurations are small, it is important to consider the sensitivity in view of **measurement errors**. The measurement precision of calibrated US-sensors is ± 1 mm for time-averaged measurements. As the water surface of the flow in the macro-rough channel is not smooth, the precision might decrease to ± 2 mm. The sensitivity analysis on the backwater curve computation reveals that assuming a systematic measurement error of 2 mm to 3 mm, configuration 243 could pass between configuration 242 and 244 (Figure 4-30). With a systematic

error of 1 mm, configuration 213 would be rougher than configuration 212. However, a systematic measurement error of more than 50 mm would be required that configuration 143 would become the most rough. It can therefore be concluded that a minor rearrangement of the geometrical configurations could occur when repeating the tests several times but that no major change of the ranking has to be expected.

4.4 *Proposition of empirical formulas for the estimation of the flow resistance of the macro-rough banks*

In this chapter three different approaches are used in order to propose macro-rough flow resistance formulas. The first approach is based on the dimensionless analysis (§ 4.4.1). The second approach gives a semi-empirical formula which is physically based on a drag coefficient model (§ 4.4.2). The third approach uses Evolutionary Polynomial Regression EPR (§ 4.4.3). Alternatively to these three approaches, it is possible to recalculate backwater curves along the macro-rough channel by a modified Borda-Carnot approach (§ 4.4.5).

The observed friction coefficient of the section f_m is the sum of the friction coefficient of the prismatic reference f_{prism} and a macro-rough friction coefficient f_{MR} due to the channel bank macro-roughness. The prediction of f_{MR} by resistance laws makes possible the calculation of the friction coefficient of the section as $f_m = f_{prism} + f_{MR}$.

4.4.1 Empirical flow resistance formulas based on a Powerlaw optimization

The dimensional analysis is a common tool in hydraulic engineering which allows identifying the dominant parameters involved in a physical phenomenon. The use of the Π -Theorem of Buckingham (1914) allows to reduce a general problem with N variables and M basic dimensions to a problem having N minus M dimensionless parameters.

In general flow problems, the pressure coefficient depends on the Reynolds, Froude, Mach and Weber numbers. Mach numbers can be neglected in incompressible flows. The Weber number relates the surface tension forces to the fluid's inertia. This number is generally considered for vortex initiation.

Mach, Weber, Froude and Reynolds numbers – Similitude of the laboratory flume

In the present study the Mach number is neglected as the fluid is assumed incompressible. The Weber number ranges between 40 (for low discharges) and 2200 (for high discharges). As vortices have been detected also for low discharges, it is admitted that Weber numbers were sufficiently high to permit vortex formation under all test conditions. Nevertheless, as values of $We > 120$ are required to avoid scale effects (Jain et al. 1978), tests at low discharges ($Q < 20$ l/s) will not be considered for the development of macro-rough flow resistance formulas.

Froude number lies in the range $0.37 < Fr < 0.62$ when considering the cross section of the main channel (base width $B = 0.485$ m). Subcritical conditions are thus relevant. Reynolds numbers at the same section, calculated as $Re_m = U \cdot R_{hm} / \nu$, vary between 8'000 and 105'000. According to the Colebrook-White formula, this range is typically associated to fully turbulent flow conditions. The experiments showed that part of the

flow resistance is mobilized only with increasing Reynolds numbers § 4.3.4.

It might not possible to consider the Froude similitude only when upscaling the results to prototype scale. If the configurations tested in the laboratory flume should be compared to a prototype configuration, Froude and Reynolds similitude's have theoretically to be considered simultaneously. Empirical relationships obtained from the experimental data may have limited validity when applied to other scales, since the respective Reynolds numbers change significantly.

For the experiments in the macro-rough channel, the dimensional analysis was performed with the method of Rayleigh by relating the pressure drop Δp per length Δl to the variables of the problem. Analogous to the pipe flow problem (Graf and Altinakar 1993) it can be written:

$$\frac{\Delta p}{\Delta l} = \xi R_h^a B^b \Delta B^c L_b^d L_c^e U^f \rho^g \mu^h k_s^i \quad (\text{eq. 4.27})$$

The variables R_h , U , ρ , μ , k_s are well known from dimensional analysis of the pipe flow whereas the variables B , ΔB , L_b , L_c are specific to the macro-rough configurations. ξ is a constant. Thus, the dimensional relationship becomes:

$$M^1 L^{-2} T^{-2} = L^a L^b L^c L^d L^e (L T^{-1})^f (M L^{-3})^g (M L^{-1} T^{-1})^h L^i \quad (\text{eq. 4.28})$$

From the exponents it is possible to write:

$$L \quad : \quad -2 = a + b + c + d + e + f - 3g - h + i \quad (\text{eq. 4.29})$$

$$M \quad : \quad 1 = g + h \quad \text{or} \quad g = 1 - h \quad (\text{eq. 4.30})$$

$$T \quad : \quad -2 = -f - h \quad \text{or} \quad f = 2 - h \quad (\text{eq. 4.31})$$

When replacing (eq. 4.30) and (eq. 4.31) in (eq. 4.29) it can be found:

$$-2 = a + b + c + d + e + 2 - h - 3 + 3h - h + i \quad \text{resp.} \quad a = -1 - b - c - d - e + 2 - h - i$$

Equation (eq. 4.27) than becomes:

$$\frac{\Delta p}{\Delta l} = \frac{h_r \rho g}{\Delta l} = \xi \left(\frac{U^2 \rho}{R_h} \right) \left(\frac{B}{R_h} \right)^b \left(\frac{\Delta B}{R_h} \right)^c \left(\frac{L_b}{R_h} \right)^d \left(\frac{L_c}{R_h} \right)^e \left(\frac{\mu}{\rho U R_h} \right)^h \left(\frac{k_s}{R_h} \right)^i \quad (\text{eq. 4.32})$$

The final result of the dimensional analysis is similar to a friction coefficient when dividing formula (eq. 4.32) by $\xi (U^2 \rho / R_h)$ and choosing $\xi = 1/8$.

$$f_m = \frac{h_r}{\Delta l} \frac{2g}{U^2} 4R_h = f\left(\frac{B}{R_h}; \frac{\Delta B}{R_h}; \frac{L_b}{R_h}; \frac{L_c}{R_h}; \text{Re}_m; \frac{k_s}{R_h}\right) \quad (\text{eq. 4.33})$$

Thus, the total friction-loss depends on the Reynolds number and the relative roughness (skin friction) and the dimensionless characteristics of the macro-rough configurations. Since friction coefficients can be summed up, it is possible to split the coefficient f_m into a friction coefficient due to the macro-roughness elements and a friction coefficient due to the skin friction. Parameters related to the macro-rough configurations appear only in the f_{MR} -coefficient. The relative roughness k_s/R_h of the prismatic channel without macro-roughness appears in the f_{prism} -coefficient which corresponds to the friction coefficient observed in the prismatic channel. It accounts for the bottom and wall roughness but not for the macro-roughness. The Reynolds number is present in both formulas.

$$f_{MR} = f\left(\frac{B}{R_h}; \frac{\Delta B}{R_h}; \frac{L_b}{R_h}; \frac{L_c}{R_h}; \text{Re}_m\right) \quad (\text{eq. 4.34})$$

$$f_{prism.} = f\left(\text{Re}_m; \frac{k_s}{R_h}\right) \quad (\text{eq. 4.35})$$

A formula between the dimensionless parameters and the macro-rough friction coefficients was established by two additional steps:

- Calculation of the macro-rough friction coefficient f_{MR} of the experiments as:

$$f_{MR} = f_m - f_{prism} \quad (\text{eq. 2.28b})$$

- Separation of the experiments according to the concepts of Morris (1955) and Jiménez (2004). For practical reasons, the following purely geometrical criteria are proposed. This separation is in agreement with most of the steady flow tests even if it differs little from (eq. 4.18).

⇒ Reattachment flow (isolated roughness flow): $\Delta B / L_b < 0.1$

⇒ Square grooved flow (quasi smooth flow): $\Delta B / L_b = 0.8$

⇒ Normal recirculation flow: all other cases

The correlations between the parameters found from the dimensional analysis and the experimental macro-rough friction coefficients are graphically represented in Figure 4-31. In addition to the dimensionless parameters found by means of formula (eq. 4.34), some parameters issued from Morris' approach have been added.

The Pearson product-moment correlation coefficient R^2 can be used to estimate the correlation of X and Y . It quantifies the extent of a linear relation between two data sets and its square value ranges between 0 and 1. The Pearson coefficient is defined as:

$$R^2 = \frac{(n \cdot \Sigma XY - \Sigma X \cdot \Sigma Y)^2}{(n \cdot \Sigma X^2 - (\Sigma X)^2) \cdot (n \cdot \Sigma Y^2 - (\Sigma Y)^2)} \quad (\text{eq. 4.36})$$

where n is the number of samples, X is the dependent variable and Y is the dimensionless parameter. The result is summarized in Table 4-8.

Table 4-8: Square values R^2 of the Pearson product-moment correlation coefficient quantifying the extent of linear relationship between the macro-rough friction coefficients f_{MR} and different parameters.

flow type	B / R_{hm}	L_b / R_{hm}	L_c / R_{hm}	$\Delta B / R_{hm}$	Re_m	$(L_b+L_c)/R_{hm}$	$(L_b+L_c)/\Delta B$
Normal recirculating	0.482	0.003	0.469	0.069	0.309	0.257	0.122
Reattachment	0.537	0.344	0.376	0.043	0.400	0.552	0.352
Square grooved	0.298	0.314	0.827	0.314	0.172	0.853	0.665

From Table 4-8 the following can be observed:

- The Pearson product momentum correlation is high if linear relation between two variables exists. Some relationships between f_{MR} -values and the dimensionless parameter (L_c / R_{hm} ; $(L_b+L_c) / R_{hm}$; $(L_b+L_c) / \Delta B$) are obviously not linear (Figure 4-31).
- The relative flow width B / R_{hm} and the Reynolds number Re_m apparently have an influence on the friction coefficient for normal circulating and reattachment flow types. Square grooved flow types are less or not influenced by this dimensionless parameter.
- The relative roughness spacing $(L_b + L_c) / R_{hm}$ is an important parameter for reattachment and square grooved flow types, which corresponds to the results of Morris (1955).
- Looking to the low values of the Pearson coefficients (Table 4-8), the normal recirculating flow which includes the largest numbers of data, will be the most difficult to predict.
- The square grooved flow type is highly dependant on $(L_b + L_c) / \Delta B$. This dimensionless parameter is comparable to the one of Morris defined for skimming flow.

For the square grooved, reattachment and normal recirculating flow types it was possible to find a macro-rough flow resistance formula of the type:

$$C_{adim,MR} = \sqrt{\frac{8}{f_{MR}}} = \xi \cdot A^\alpha \cdot B^\beta \cdot C^\gamma \dots \quad (\text{eq. 4.37})$$

where A , B , C ... are dimensionless parameters (Table 4-8) and α , β , γ , ... the exponents of the power law. ξ is a constant.

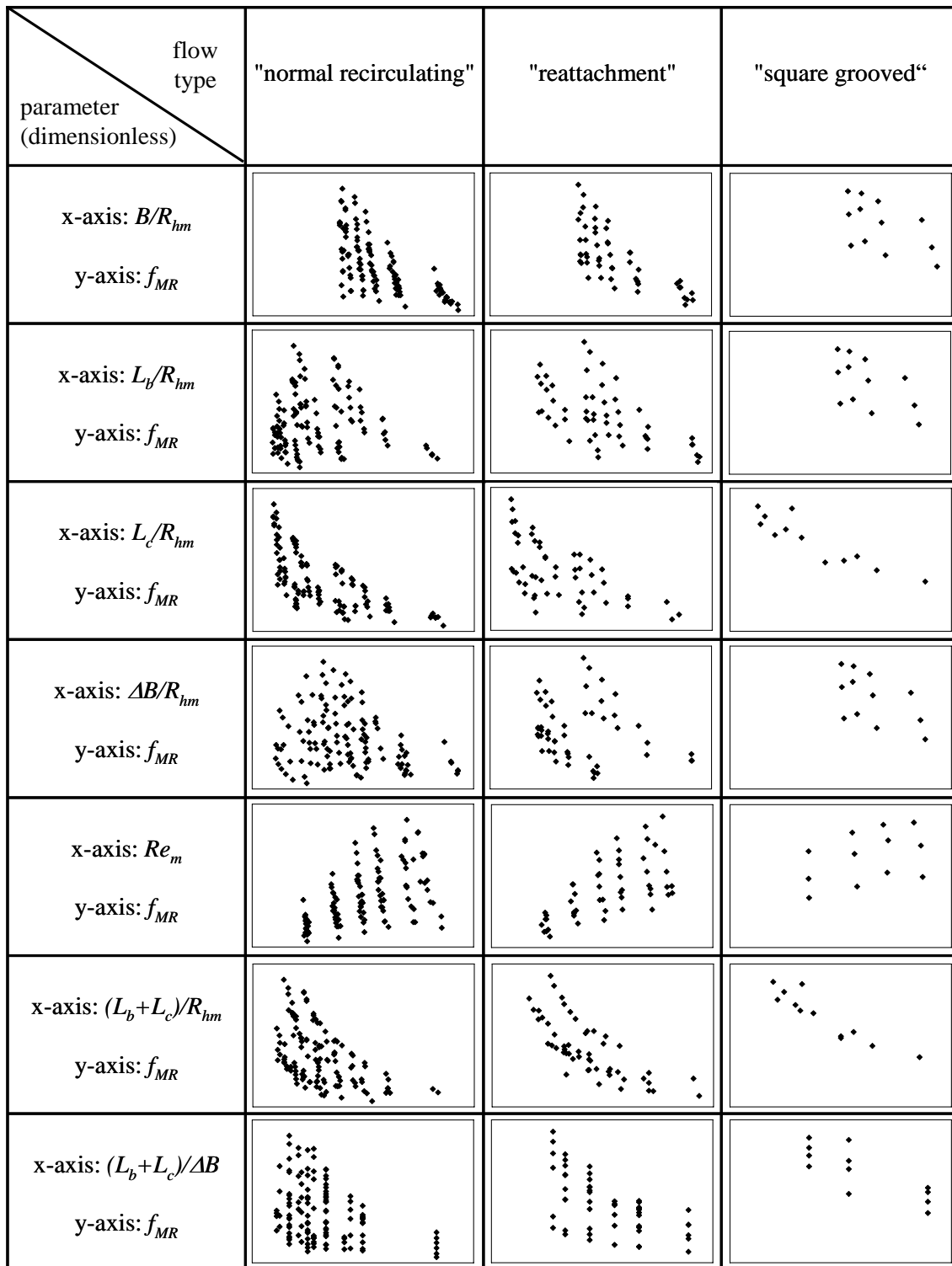
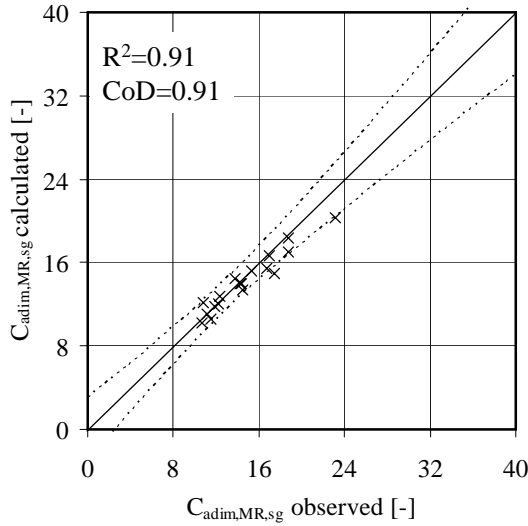


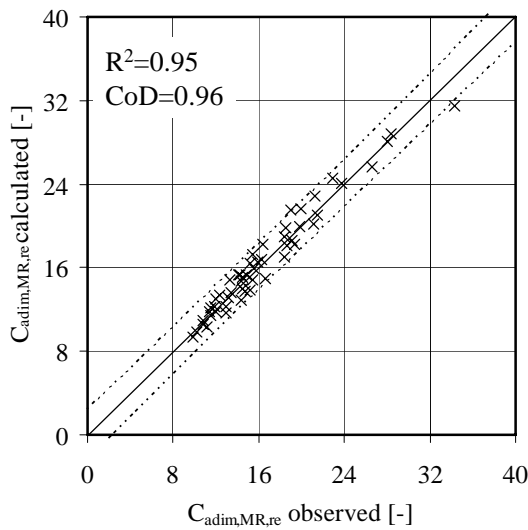
Figure 4-31: Graphical analysis of the relation between the macro-rough friction coefficients f_{MR} (x-axis) and different dimensionless parameters (y-axis).



Square grooved flow type:

$$C_{adim MR,sg} = \sqrt{\frac{8}{f_{MR,sg}}} = 5 \cdot \left(\frac{L_b + L_c}{R_{hm}} \right)^{1/3}$$

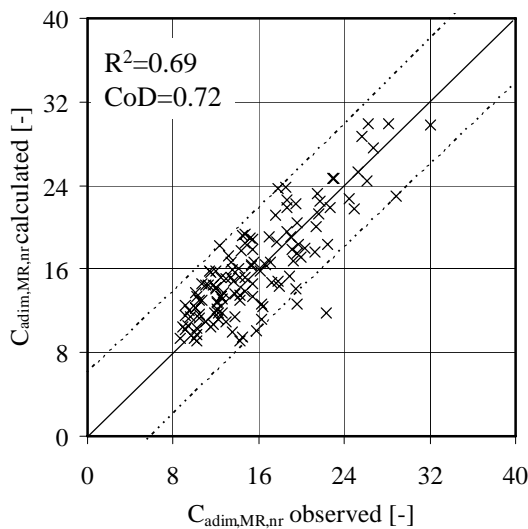
(eq. 4.38)



Reattachment flow type:

$$C_{adim MR,re} = \sqrt{\frac{8}{f_{MR,re}}} = \left(\frac{L_b + L_c}{\Delta B} \right)^{0.43} \left(\frac{B}{R_{hm}} \right)^{0.5}$$

(eq. 4.39)



Normal recirculating flow type:

$$C_{adim MR,nc} = \sqrt{\frac{8}{f_{MR,nc}}} = \left(\frac{L_b + L_c}{\Delta B} \right)^{0.43} \cdot [\log(\text{Re}_m)]^{0.24} \cdot \left(\frac{B}{R_{hm}} \right)^{0.9}$$

(eq. 4.40)

Figure 4-32: Friction coefficients from empirical formulas based on the Powerlaw optimization. Comparison between calculated and observed dimensionless Chezy coefficients $C_{adim MR} = (8/f_{MR})^{0.5}$. R^2 : correlation coefficient. CoD: coefficient of determination (also Nash coefficient). The dashed lines (- - -) represents the 95% confidence bound.

The calculated and observed dimensionless Chezy coefficients are compared in Figure 4-32. For the square grooved and reattachment flow types, the observed dimensionless Chezy coefficients are in relatively good agreement with the calculated ones. As expected, the prediction of the dimensionless Chezy coefficients for the normal recirculation flow type, corresponding to the largest number of data shows the highest scatter.

The resistance formula for the “square grooved” flow type (eq. 4.47) depends only on the constant $\zeta = 5$ and the dimensionless roughness spacing $(L_b + L_c) / R_{hm}$. This dimensionless parameter has already been identified as the main parameter influencing the flow resistance by Morris (1972) for the skimming flow case.

For the “reattachment” flow type (eq. 4.48), the constant becomes $\zeta = 1$. The first dimensionless term describes the cavity characteristics and has an exponent of 0.43. The second term takes the cross section geometry into account with an exponent of 0.9.

The empirical resistance formula for the “normal recirculating” flow type (eq. 4.49), is similar to the reattachment flow type. Nevertheless, the turbulence characteristics $\log(\text{Re}_m)$ of the flow are taken into account with an exponent of 0.24. However, due to the high scattering, this formula has limited applicability.

4.4.2 Semi-empirical flow resistance formulas based on form drag and skin friction

4.4.2.1 Definitions

The following approach is based again on the separation of skin friction in a prismatic channel and the form drag due to the macro-roughness elements at the banks ($f_m = f_{prism} + f_{MR}$). A mathematical formulation according Morris (1955) is used. The separation into “square grooved”, “reattachment” and “normal circulating” flow types is considered again. Furthermore, the “square grooved” flow types are separated into cases of low discharge (low Re_m , heavy oscillating) and the high discharge (higher Re_m , less oscillating). With this separation, which is confirmed by the observations of the experiments, quite good agreements are found between the predicted and the observed dimensionless Chezy-coefficients.

The separation criteria are summarized as follows:

- *Normal recirculating flow type* with one main and two secondary recirculation cells: $0.15 \leq \Delta B / L_b \leq 0.6$
- *Reattachment flow type* without main recirculation cell: $\Delta B / L_b \leq 0.1$
- *High discharge square grooved flow type* with one recirculation cell: $\Delta B / L_b \geq 0.8$ and $\text{Re}_m \geq 60'000$
- *Low discharge square grooved flow type* with heavy transverse oscillations of the flow: $\Delta B / L_b \geq 0.8$ and $\text{Re}_m \leq 60'000$

4.4.2.2 Mathematical model

The definitions used for the mathematical model based on the drag force are shown in Figure 4-33.

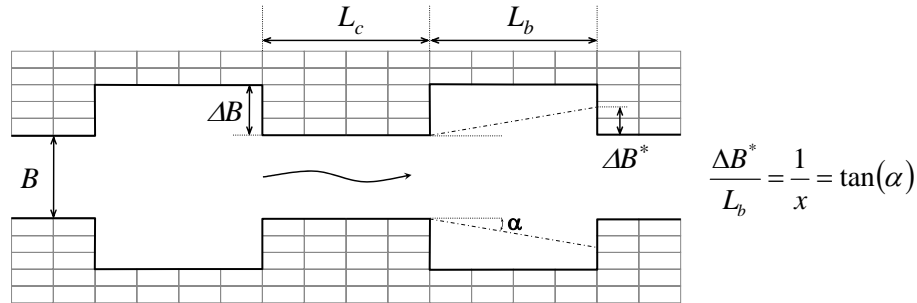


Figure 4-33: Definition of the parameters of the drag force based head-loss model.

The drag force formula can be written as:

$$F_r = C_d A_r \rho \frac{U^2}{2} = \Delta p A \quad (\text{eq. 4.41})$$

where F_r is the drag force, C_d the drag coefficient, A_r the area on which the drag acts, U the mean velocity¹ in the main channel at base width B , Δp the pressure drop and A the flow surface in the main channel. When replacing the pressure drop $\Delta p = \gamma \cdot h_r$ and $h_r = S_{f,MR} \Delta x = S_{f,MR} (L_b + L_c)$ one obtains:

$$C_d A_r \frac{U^2}{2g} = S_{f,MR} (L_b + L_c) A$$

In this formula, the macro-rough friction slope is replaced by:

$$S_{f-MR} = f_{MR} \frac{U^2}{8gR_{hm}} \quad \text{where : } f_{MR} = f_m - f_{prism}$$

and (eq. 4.41) becomes:

$$C_d A_r = f_{MR} \frac{1}{4R_{hm}} (L_b + L_c) A \quad \text{with}$$

$$A = B \cdot h \quad \text{and}$$

$$A_r = 2\Delta B^* \cdot h \quad \text{where : } \Delta B^* = \min(\Delta B ; L_b / x)$$

ΔB^* is the minimum value of the geometric cavity depth and an effective cavity depth considering a certain expansion of the flow ($1/x$) inside of the cavity (Figure 4-33).

¹ This assumption is quite rough since the flow velocity close to the roughness elements is lower than the mean flow velocity (see Appendix 4-7) but it allows to simplify the formula.

When all these terms are introduced in formula (eq. 4.41), the macro-rough friction coefficient f_{MR} respectively the total friction coefficient of the channel section f_m becomes:

$$f_{MR} = C_d \frac{8R_{hm} \Delta B^*}{B(L_b + L_c)} \quad (\text{eq. 4.42})$$

$$\Delta B^* = \min(\Delta B; L_b / x) \quad (\text{eq. 4.43})$$

$$f_m = f_{prism} + C_d \frac{8R_{hm} \Delta B^*}{B(L_b + L_c)} \quad (\text{eq. 4.44})$$

Moreover the drag coefficient C_d can be found from the experimental results by choosing $\tan(\alpha)$ or the expansion of the flow $\tan(\alpha) = l/x$ by choosing C_d . When the expansion of the flow is assumed to be $\tan(\alpha) = 1/6$ for example, the experimental C_d -values tend to a value of 0.55 for the reattachment flow type at Reynolds numbers higher 55'000 whereas in the recirculation case they are lower (Appendix 4-7).

The above presented mathematical approach has been applied to reattachment and normal recirculating flow types. For the square grooved flow type at relatively high Reynolds numbers the macro-rough friction coefficients are calculated according to the skimming flow approach from Morris (1972). The formula is based on the energy required to maintain the rotation of the gyre in the groove of a pipe. It has been modified for the present experimental study dealing with macro-roughness elements at the side walls as:

$$f_{MR} = \left(\frac{2h}{B + 2h} \right)^\alpha \cdot \left(\frac{L_b; \Delta B}{L_b + L_c} \right)^\beta \cdot \left(\frac{c_w \cdot V_w}{U} \right)^3 \quad (\text{eq. 4.45})$$

where α and β are calibration parameters. V_w / U is the wall velocity ratio and fixed at 2/3 (Appendix 4-7, Morris 1955). c_w is the ratio between tangential velocity of the gyre and the near wall velocity V_w . For skimming flow geometries according Morris (1972) “;” signifies that either L_b or ΔB could be used.

As the cavity in the Morris approach is square grooved, either the cavity length L_b or the cavity depth ΔB can be used. In the present study, the length L_b is 25% higher than ΔB . The first term $[2h / (B + 2h)]^\alpha$ represents the part of the total perimeter covered by the cavities corrected by an exponent α (open channel instead of pipe flow).

4.4.2.3 Application of the form drag based approach to the experimental data

The macro-rough friction coefficient for the *reattachment flow type* $f_{MR, re}$ is given by:

$$f_{MR, re} = C_d \frac{8R_{hm} \Delta B}{B(L_b + L_c)} \quad (\text{eq. 4.46})$$

This equation corresponds to (eq. 4.42) but since the flow reattaches to the side wall, $\Delta B^* = \Delta B$ and (eq. 4.43) is not required. The calibrated C_d coefficient found from the experimental data is $C_d = 0.475$. The comparison of observed and calculated macro-rough friction coefficients $f_{MR,re}$ respectively dimensionless Chezy coefficients $C_{adim,MR,re}$ is given at Figure 4-34 (middle).

Quite good agreement is found between measured and calculated values despite for the experiments indicated with (o). They correspond to the low discharge experiments with an aspect ratio of $\Delta B / L_b = 0.1$. As mentioned in § 4.1.1, the flow may not completely reattach to the side wall but recirculates respectively the roughness is not fully mobilized. Most of these cases are better solved by the normal recirculating flow type formula (Figure 4-35, on the left).

The macro-rough friction coefficient of the *normal recirculating flow type* $f_{MR,nc}$ can be calculated as:

$$f_{MR,nc} = C_d \frac{8R_{hm} \Delta B^*}{B(L_b + L_c)} \quad (\text{eq. 4.42}) \quad \text{with} \quad \Delta B^* = \min(\Delta B; L_b / x) \quad (\text{eq. 4.43})$$

The same C_d coefficient of 0.475 can be used. Nevertheless, the value of x was not found constant but depends on the Reynolds number and the aspect ratio of the cavity. x can be expressed by the following, fully empirical formula:

$$x = \left(\frac{Re_{lim}}{Re_m} + x_0 \right) \left(\frac{L_b}{\Delta B} \right)^{0.18} \quad (\text{eq. 4.47})$$

where $Re_{lim} = 150'000$ and $x_0 = 4.5$.

This empirical formula gives a better fit to the friction coefficients for the lower Reynolds number flows. Physically, this can be explained either by a less expansive flow for low discharge or by lower drag coefficients at lower Reynolds numbers (which would be quite unexpected). Therefore, the correction has been applied to the expansion of the flow $\tan(\alpha) = 1/x$ and not to C_d . The comparison of observed and calculated macro-rough friction coefficients $f_{MR,nc}$ respectively dimensionless Chezy coefficients $C_{adim,MR,nc}$ in Figure 4-34 shows acceptable agreement:

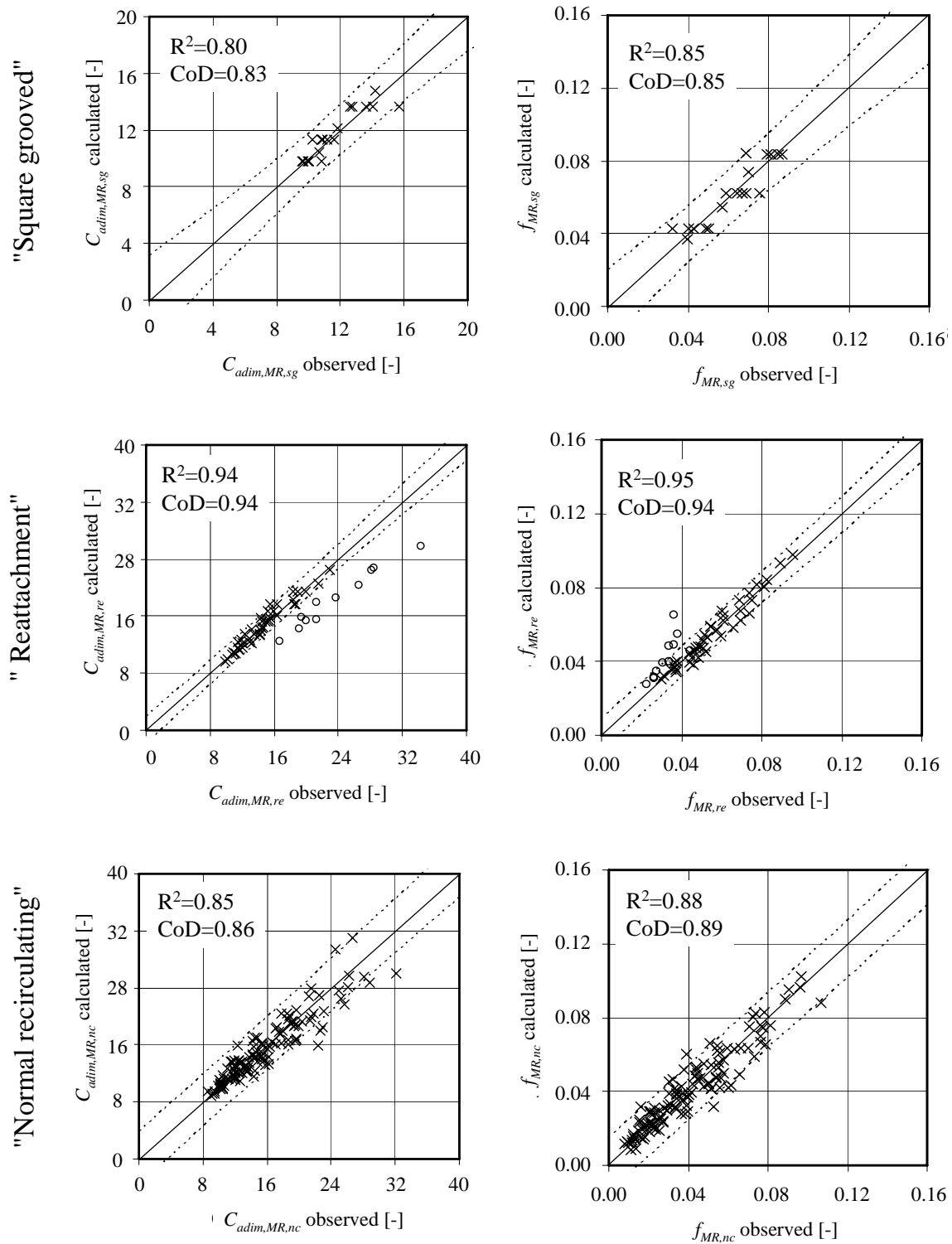


Figure 4-34: Friction coefficients obtained from the semi-empirical model for square grooved (eq. 4.48) reattachment (eq. 4.46) and normal recirculating (eq. 4.42), (eq. 4.43), (eq. 4.47) flow types. Comparison between calculated and observed macro-rough dimensionless Chezy coefficients $C_{adim,MR}$ and macro-rough friction coefficients f_{MR} . R^2 : correlation coefficient. CoD: coefficient of determination (Nash coefficient). The square grooved types correspond to high discharge ones having values of $Re_m > 60'000$. The dashed lines (- - -) represents the 95% confidence bound.

The macro-rough friction coefficient for *square grooved flow type* $f_{MR,sg}$ for Reynolds numbers higher than 60'000 is given by:

$$f_{MR,sg} = \left(\frac{2h}{B+2h} \right)^\alpha \cdot \left(\frac{L_b}{L_b + L_c} \right)^\beta \cdot \left(\frac{c_w \cdot V_w}{U} \right)^3 \quad (\text{eq. 4.48})$$

where $\alpha = 0.525$, $\beta = 0.75$, $V_w / U = 2/3$ and $c_w = 0.85$.

Formula (eq. 4.48) is issued from formula (eq. 4.45) which is inspired from the skimming flow type formula (Morris 1972). The cavity length L_b is the better parameter for describing the cavity than the cavity depth ΔB . The value of $c_w = 0.85$ seems quite high compared to the estimation ($c_w = 0.5 \div 0.75$) of Morris and Wiggert (1972). The comparison of observed and calculated macro-rough friction coefficients $f_{MR,sg}$ respectively dimensionless Chezy coefficients $C_{adim,MR,sg}$ in Figure 4-34 shows also good agreement. Since only few values are available for this flow type, the experimental data of the steady flow tests (first series ES) and the second series (EnS) have been assembled.

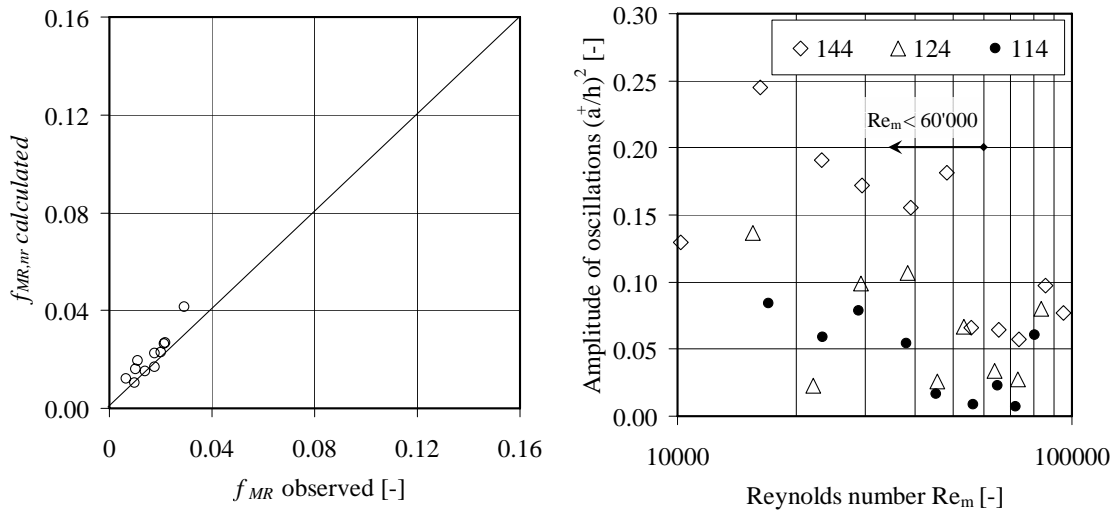


Figure 4-35: Left: Friction coefficient comparison of the low discharge flows of the “reattachment” configurations. Friction coefficient calculated with the normal recirculating formula. Right: Square values of the amplitudes of the cavity oscillations as a function of the Re_m .

The applicability of the physically based formula (eq. 4.48) to the square grooved flow type at lower Reynolds numbers than 60'000 has been checked. Unfortunately, the formula clearly overestimates the friction coefficients for low Reynolds numbers. The first term of (eq. 4.48) does not reduce the friction coefficient sufficiently in order to compensate the decreasing influence of the wall.

It was thus verified whether the friction coefficients of the square grooved flow type at lower Reynolds numbers can be reasonably calculated with the normal recirculating flow type. When applying (eq. 4.42), (eq. 4.43) and (eq. 4.44) to this flow type, the fric-

tion coefficients are however clearly underestimated. From the physical point of view, the underestimation might be explained by the important cavity oscillations which are especially significant for the square grooved flow types at Reynolds numbers less than 55'000 (Figure 4-35, on the right). According Naudascher (1963) resonant oscillations can increase cavity induced drag by 250%. It may be concluded that further experimental investigations would be required for a correct description of the square grooved flow type at low Reynolds numbers.

4.4.2.4 Conclusions on the semi-empirical form drag and skin friction based formulas

The formulas for the reattachment and normal recirculating flow type developed in this section are based on the isolated roughness flow type according Morris (1955, 1972). The wall velocity ratio has been chosen $V_w/U = 1$ in order to simplify the formulas and due to a lack of detailed information about this parameter. This choice has an influence on the drag coefficient of the sharp edged cavity C_d which would be 2.25 or 4 times higher when assuming a ratio of $V_w/U = 2/3$ respectively $V_w/U = 1/2$ ($C_d' = 1.07 \div 1.90$). These C_d' values correspond well to the drag coefficients proposed by Morris (1972) for the rectangular depression roughness.

From a physical point of view, the reattachment flow type is similar to the isolated roughness flow type according Morris. Therefore, the best agreement between calculated and observed friction coefficients is found for this flow type. For the normal recirculating flow type the agreement is still quite good. The expansion of the flow inside the cavity has to be taken into account by an empirical formula based on the Reynolds number of the flow and the cavity geometry. Additional investigations in a short flume including only a few widenings would be necessary to justify or reject this proposition.

The adapted, physically based mathematical model can predict the observed friction coefficients of the square grooved flow with good agreement for $Re_m > 60'000$. For lower Reynolds numbers, no satisfying mathematical description could be found since only limited data is available. The difficulty to quantify correctly d-type roughness has already been mentioned by Jiménez (2004).

From the author's point of view, the description of the macro-roughness flow resistance by a form drag based model seems to be the best approach. The necessary subdivision in square grooved, reattachment and normal recirculating flow types is physically based and further investigations on a smaller model would make possible the determination of the drag coefficients of macro-roughness elements other than rectangular cavities.

4.4.3 Development of empirical formulas with Evolutionary Polynomial Regression

4.4.3.1 Introduction

With the evolution of informatics, new techniques for data treatment were developed as the Evolutionary Polynomial Regression EPR. It combines the genetic programming

symbolic regression (genetic algorithms to find the structure of the expression) with conventional numerical regression (least squares optimization). The EPR technique can be classified as a grey box approach (Giustolisi and Savic 2003), requiring less physical knowledge about the phenomenon than a white box model (mathematical relation between parameters based on first principals; physical laws) but more than black box models (Artificial Neural Networks ANN, Genetic programming GP). White box models can be easily understood since they are physically based. On the other hand black box models can deal with a large number of input variables and find functional relationship of complex phenomena. Overfitting is a known phenomenon for grey as well as for black box models. The term overfitting describes the ability of finding such a flexible mathematical model that can even correctly predict target values for input data including measurement errors. When such model is applied to input data which have not been used for the construction of the model, the prediction becomes significantly less accurate compared to the data used for the model construction. A well known technique to avoid overfitting is to divide the dataset into a training and validation set.

In order to find the functional relation between flow resistance coefficients and the input variables, the evolutionary polynomial regression toolbox EPR, developed by Giustolisi and Savic (2003), has been used for following reasons:

- The EPR technique has provided good performance on similar problems namely the interpolation of Colebrook-White formula for friction factor prediction of corrugated pipes (Giustolisi 2004).
- The EPR technique is considered as a grey and not a black box model which gives probably physically more concluding results than a black box model.
- Some tests with the software on simple cases revealed user-friendly and fast computations.
- The software allows to build and to evaluate the mathematical model separately by dividing the available data into a training and a test set.

The main characteristics of the software are (Giustolisi and Savic 2003):

- Two stage technique: The structure of the model is identified first (genetic algorithms). Then, the parameters are optimized (estimation of constants by solving a Least Squares linear problem)
- Some techniques help to avoid overfitting such as: 1) complex model with many terms are penalized 2) controlling the constant values which probably describe noise (constants close to zero).

Details of the EPR technique and a comparison between monomial and genetic programming, respectively genetic programming and evolutionary polynomial regression are given in Laucelli et al. (2005), Giustolisi (2004) and Giustolisi and Savic (2006).

4.4.3.2 Application and results of the EPR-approach to the experimental data

At the first stage, basically dimensional parameters (B , L_b , L_c , ΔB , R_h , h) and the dimensionless parameter Re_m have been provided as input variables to the EPR software for the prediction the macro-rough dimensionless Chezy coefficient $C_{adim,MR}$. The goal of this first stage was to identify how parameters act together. Then, only dimensionless parameters have been used to develop macro-rough flow resistance formulas based on the findings of the first stage. The separation into square grooved, reattachment and normal recirculating flow types has been considered with the purpose to compare EPR with the previous approaches (§ 4.4.1 and § 4.4.2).

The first stage revealed that the dimensionless parameters identified by the Pearson product-moment correlation method (see Table 4-8) mainly correspond to the parameters found by EPR. On the other hand, by using dimensional geometrical parameters such as B , L_b , ΔB , R_h , etc. the EPR software was not able to reasonably predict the roughness-related parameters. Some numerical instabilities in the optimization procedure occurred for the reattachment and normal recirculating flow types.

Table 4-9: *Dimensionless parameters provided to the EPR toolbox parameters retained by the EPR toolbox in the proposed formulas.*

Flow type	Introduced dimensionless parameters into EPR	Retained parameters by EPR
Normal recirculating	$\frac{L_b + L_c}{L_b}$; $\frac{B}{R_{hm}}$; $\frac{\Delta B}{L_b}$; $\frac{L_b + L_c}{\Delta B}$; $\log(Re_m)$	$\frac{L_b + L_c}{L_b}$; $\frac{B}{R_{hm}}$; $\frac{L_b + L_c}{\Delta B}$
Reattachment	$\frac{L_b + L_c}{R_{hm}}$; $\frac{B}{R_{hm}}$; $\log(Re_m)$; $\frac{L_b + L_c}{\Delta B}$	$\frac{B}{R_{hm}}$; $\frac{L_b + L_c}{\Delta B}$
Square grooved	$\frac{L_b + L_c}{R_{hm}}$; $\frac{B}{R_{hm}}$	$\frac{L_b + L_c}{R_{hm}}$

At the second stage, the macro-rough dimensionless Chezy coefficient $C_{adim,MR}$ have been predicted for the three different flow types (square grooved, reattachment, normal recirculating) using the dimensionless parameters already presented in § 4.4.1. Low discharge flow data ($Re_m < 25'000$) have not been considered for the macro-rough flow resistance formulas. Finally, in order to avoid overfitting, the available data have been randomly divided into a training set (2/3 of the data) and a validation set (1/3). The separation was not applied to the data providing from the square grooved flow type, since very few data are available for this case. The formulas shown hereafter result from a systematic procedure including the variation of the predefined structures and options of the EPR-toolbox (Appendix 4-8). Not all provided dimensionless parameters have been utilized by the toolbox for the model construction (Table 4-9), namely the cavity

aspect ratio $\Delta B / L_b$ for the normal recirculating flow type, the Reynolds number and the dimensionless roughness spacing $(L_b + L_c) / R_{hm}$ for the reattachment flow type and the dimensionless width B / R_{hm} for the square grooved flow type.

The best formulas found by the EPR technique in view of the correlation coefficients and the simplicity of the model structure are summarized hereafter:

Square grooved flow type :

$$\sqrt{\frac{8}{f_{MR,sg}}} = 0.215 \cdot \left(\frac{L_b + L_c}{R_{hm}} \right) + 8.88 \quad (\text{eq. 4.49})$$

Reattachment flow type:

$$\sqrt{\frac{8}{f_{MR,re}}} = 1.79 \cdot \ln \left[\left(\frac{B}{R_{hm}} \right)^2 \cdot \frac{L_b + L_c}{\Delta B} \right] + 0.008 \cdot \left(\frac{B}{R_{hm}} \right)^2 \left(\frac{L_b + L_c}{\Delta B} \right) \quad (\text{eq. 4.50})$$

Normal recirculating flow type:

$$\sqrt{\frac{8}{f_{MR,nc}}} = 5.40 \cdot \ln \left[\left(\frac{B}{R_{hm}} \right) \cdot \frac{L_b + L_c}{L_b} \right] + 0.006 \cdot \left(\frac{B}{R_{hm}} \right)^2 \left(\frac{L_b + L_c}{\Delta B} \right) \cdot \ln \left(\frac{B}{R_{hm}} \right) \quad (\text{eq. 4.51})$$

The second term of the formula for reattachment and normal recirculating flow type can also be written as:

$$\left(\frac{B}{R_{hm}} \right)^2 \cdot \left(\frac{L_b + L_c}{\Delta B} \right) = \underbrace{\left(\frac{B}{R_{hm}} \right)}_A \cdot \underbrace{\left(\frac{B}{\Delta B} \right)}_B \cdot \underbrace{\left(\frac{L_b + L_c}{R_{hm}} \right)}_C \quad (\text{eq. 4.52})$$

Formulas (eq. 4.49) to (eq. 4.51) can be discussed as follows:

- The square grooved flow resistance formula (eq. 4.49) mainly depends on a constant. With the first term of the formula the macro-rough dimensionless Chezy coefficient is adjusted in order to consider the relative roughness spacing. Furthermore, the flow resistance is independent from B / R_{hm} . Since only one base width $B = 0.485$ m has been investigated an extrapolation of the formula for the square grooved flow type to cavities having a length L_b very different from B has to be avoided.
- The reattachment flow type formula (eq. 4.50) depends on two terms. The main contribution comes from the first term including the relative flow width $(B / R_{hm})^2$. It quantifies the importance of the influence of the banks and the dimensionless parameter $(L_b + L_c) / \Delta B$, which corresponds exactly to the parameter k / λ proposed by Morris for the isolated roughness flow. A minor contribution comes

from the second term depending again on the relative flow width B/R_{hm} , on the ratio $B/\Delta B$ and on the dimensionless cavity wavelength $(L_b + L_c)/R_{hm}$. From the physical point of view an increase respectively decrease of one of the geometrical parameters influences the $C_{adim,MR}$ coefficient in a logical way. Since B/R_{hm} and $(L_b + L_c)/R_{hm}$ are important for low flow depths, the small constant of 0.008 can be explained. Neglecting this second term leads to a significant decrease of Nash and correlation coefficients.

- The normal recirculating flow type formula (eq. 4.51) depends also on two terms. The main contribution comes from the first term including the relative flow width B/R_{hm} quantifying the influence of the banks and the dimensionless parameter $(L_b + L_c)/L_b$. The second term is similar to the reattachment flow type with an additional term taking into account the relative flow width B/R_{hm} . From a physical point of view, the change of the different geometric parameters affects the flow resistance in a logical way.

Figure 4-35 summarizes observed and calculated dimensionless Chezy coefficients for the training and validation data set. Quite good agreement can be found for all flow types. Nevertheless, limited data were available for the square grooved flow type. The normal circulating flow type is the most difficult to correctly predict. The proposed formulas apply to macro-roughness elements on channel banks having comparable geometrical characteristics as in the present study. Furthermore, the skin frictional flow resistance of the bottom and walls has to be added to the macro-rough flow resistance. In wide channels, the influence of macro-roughness elements on channel banks almost completely disappears since B/R_{hm} becomes high.

During the optimization process, the following alternative formulas have been found for the normal circulating and the reattachment flow type.

Reattachment:

$$\sqrt{\frac{8}{f_{MR,re}}} = 0.06 \cdot \left(\frac{B}{R_{hm}}\right) \cdot \left(\frac{L_b + L_c}{\Delta B}\right) + 0.12 \cdot \left(\frac{B}{R_{hm}}\right)^2 + 5.77 \quad (\text{eq. 4.53})$$

Normal recirculating:

$$\sqrt{\frac{8}{f_{MR,nc}}} = 0.66 \cdot \frac{B}{R_{hm}} \cdot \ln \left[\frac{B}{R_{hm}} \left(\frac{L_b + L_c}{L_b} \right)^2 \right] + 4.62 \quad (\text{eq. 4.54})$$

They have a comparable performance on the training and validation data sets than formulas (eq. 4.50) and (eq. 4.51). The structure resemble to the formula of Nikuradse for the fully rough turbulent flow. However, the application of (eq. 4.50) and (eq. 4.51) is preferred to formulas (eq. 4.53) and (eq. 4.54) since in the latter ones, a macro-rough friction term remains even if the macro-roughness elements disappear completely.

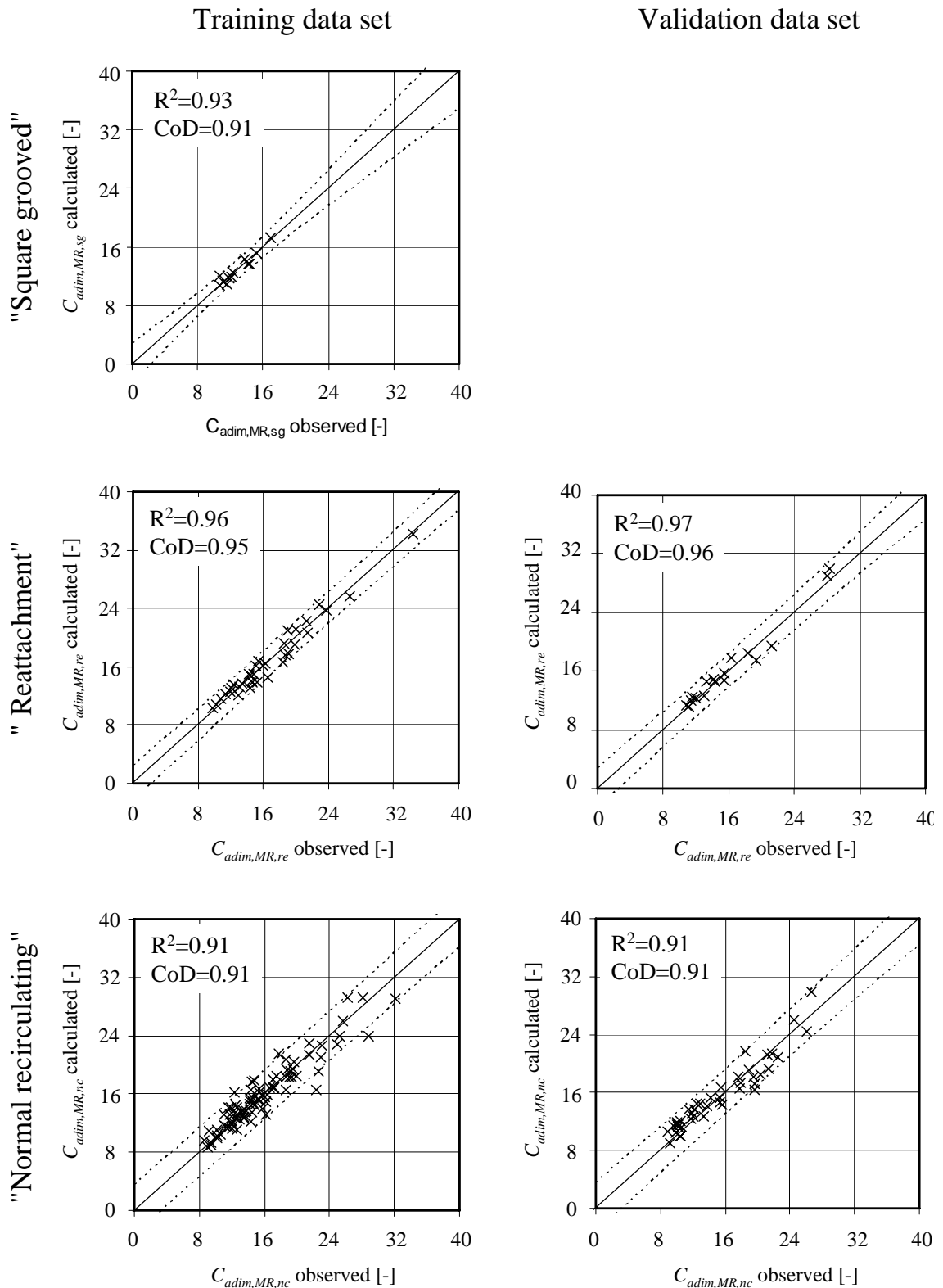


Figure 4-36: Comparison between observed and calculated macro-rough dimensionless Chezy coefficients for the formulas from EPR. On the left are presented the correlations for the training data set. On the right are presented the correlations for the validation data set. The dashed lines (---) represents the 95% confidence bound.

4.4.3.3 Conclusions on the empirical formulas obtained from EPR

Evolutionary polynomial regression (EPR) is an efficient tool to identify relationships between the geometrical parameters of the tested macro-rough configurations and the flow resistance. By the division of the flow into square grooved, reattachment and normal recirculating flow types, quite good correlations have been found between observed and predicted macro-rough friction coefficients. The preliminary selection of adequate dimensionless parameters was necessary in order to obtain good results. It can therefore be concluded that the use of EPR in combination with dimensionless analysis is better than the dimensionally aware use of EPR. All developed formulas highlight the importance of the roughness spacing ($L_b + L_c$) either normalized with the hydraulic radius R_{hm} (square grooved flow type), the cavity depth ΔB (reattachment and normal recirculating flow type) or the cavity length L_b (normal recirculating flow type). The normalized channel width (B / R_{hm}) is also an important parameter since it describes the relative importance of the channel banks. All formulas have a general structure which can be physically explained. The available data have been divided into 2/3 for the model construction and 1/3 for the validation. Validation is important when proceeding with Evolutionary Polynomial Regression or Genetic Programming tools in order to avoid overfitting.

4.4.4 Application of the developed empirical and semi-empirical flow resistance formulas for channels with macro-rough banks

The formulas found by the three different approaches (empirical formula by Powerlaw optimization; Evolutionary Polynomial Regression EPR; semi-empirical form drag based model) have been applied to nine different examples.

4.4.4.1 Geometry and flow depths of the test examples

As a first example three geometries from the investigated macro-rough geometries are tested (Figure 4-37). The prismatic friction coefficient is assumed to be $f_{prism} = 0.0123$ corresponding to the test flume roughness. The second three geometries have dimensions which could occur in a natural channel (Figure 4-38). The prismatic friction is taken into account with a Strickler coefficient of $K_{st,prism} = 30 \text{ m}^{1/3} \text{ s}^{-1}$. For the third three examples the size of macro-roughness elements is decreased compared to the channel base width (Figure 4-39). The friction coefficient for the prismatic contribution is again calculated from a Strickler coefficient $K_{st,prism} = 30 \text{ m}^{1/3} \text{ s}^{-1}$.

The mean flow velocity is calculated at the channel base width B . Since friction coefficients can be summed up, the macro-rough friction coefficient is added to the prismatic (skin) friction.

When choosing a macro-rough geometry and a flow depth, the flow resistance f_m and friction slope S_f can be calculated explicitly for a given discharge. This friction slope can either be used for the computation of the normal flow depth or for the computation of backwater curves (gradually varied flow).

The flow depth is assumed 3 m for the prototype scale applications and 0.2 m for the macro-rough configurations tested in the model. The result of the application of the three different approaches for these test examples is summarized in Table 4-10.

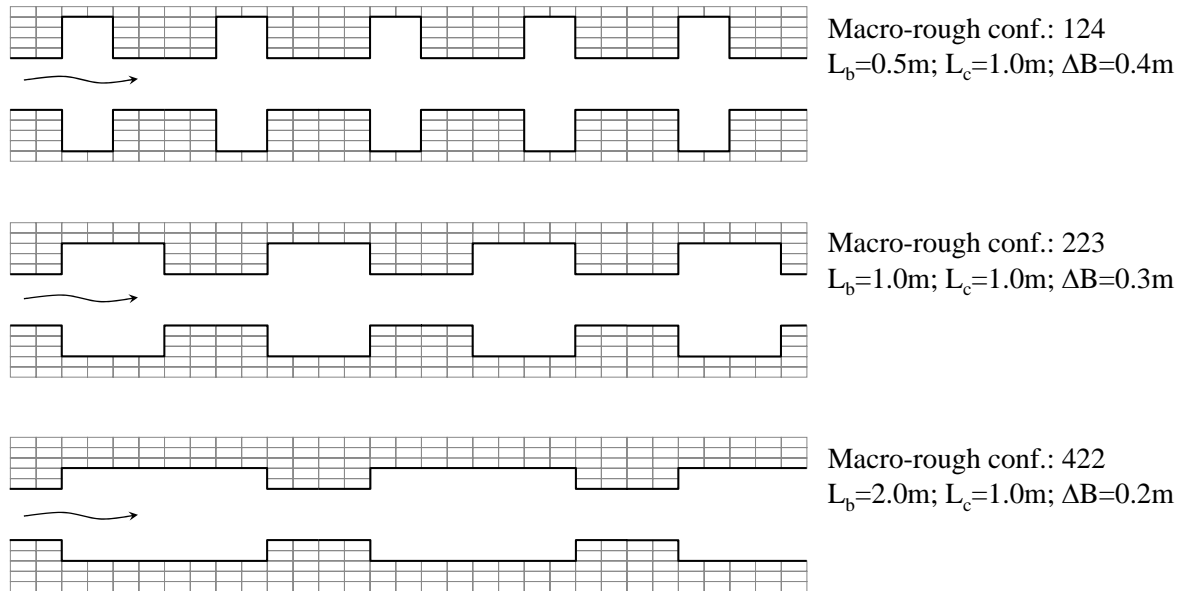


Figure 4-37: Test configurations with square grooved (124), normal recirculating (223) and reattachment (422) flow type.

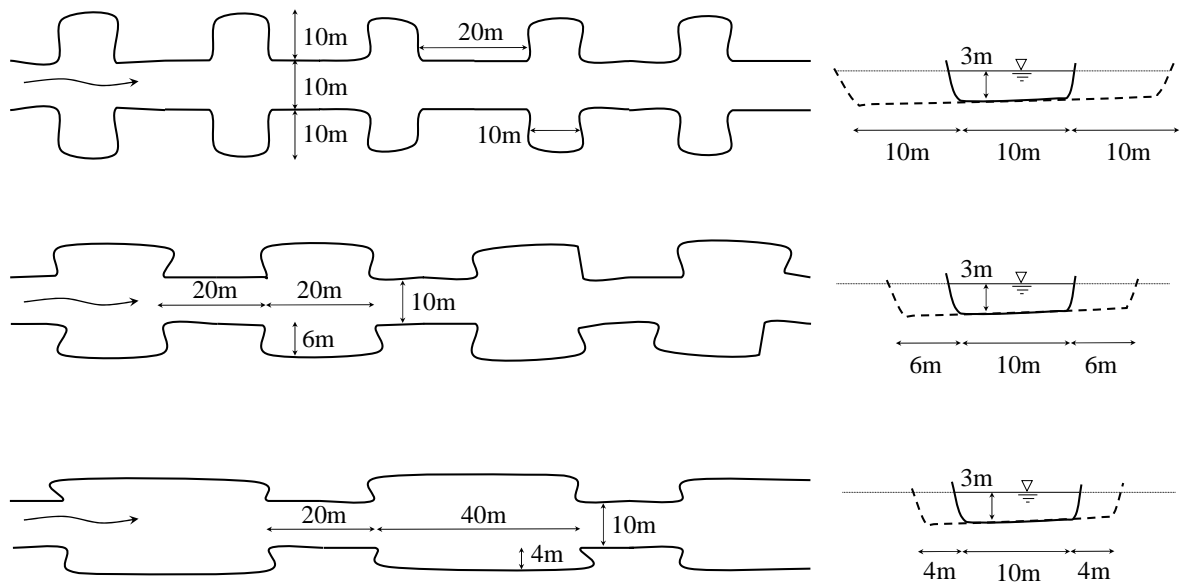


Figure 4-38: Natural like geometrical configurations at prototype scales for square grooved, normal recirculating and reattachment flow types.

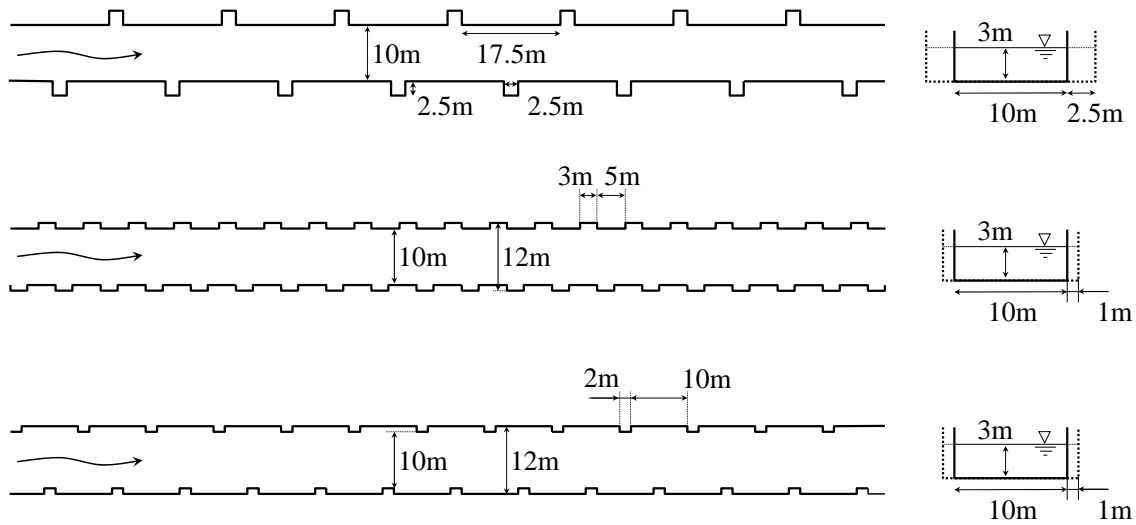


Figure 4-39: Asymmetrical configurations at prototype scale with small cavity dimensions compared to the width B for square grooved, normal recirculating and reattachment flow types.

Table 4-10: Dimensionless macro-rough Chezy coefficients $C_{adim,MR}$, macro-rough friction coefficients f_{MR} and friction coefficient of the section $f_m = f_{prism} + f_{MR}$ obtained from the developed empirical formulas. First value of a column = empirical formula based on the Powerlaw optimization / second value = semi empirical formula based on form drag / third value = formula based on EPR.

Test cases	Param.	Square grooved	Reattachment	Normal recirculating
Formula		eq.4.38 / eq.4.48 / eq.4.49	eq.4.39 / eq.4.46 / eq.4.50	eq.4.40 / eq.4.42 / eq.4.51
Macro-rough test conf. (Figure 4-37)	$C_{adim,MR}$	11.2 / 11.7 / 11.3	10.2 / 10.7 / 11.0	11.4 / 10.9 / 10.5
	f_{MR}	0.064 / 0.058 / 0.063	0.077 / 0.070 / 0.066	0.062 / 0.067 / 0.072
	f_m	0.076 / 0.071 / 0.075	0.089 / 0.082 / 0.078	0.074 / 0.079 / 0.084
Natural like conf. at prototype scale (Figure 4-38)	$C_{adim,MR}$	12.6 / 13.0 / 12.3	14.5 / 13.0 / 14.3	14.7 / 11.4 / 15.7
	f_{MR}	0.050 / 0.048 / 0.053	0.038 / 0.048 / 0.039	0.037 / 0.062 / 0.052
	f_m	0.121 / 0.118 / 0.123	0.110 / 0.118 / 0.109	0.108 / 0.133 / 0.103
Asymmetrical conf. at prototype scale (Figure 4-39)	$C_{adim,MR}$	11.0 / 18.7 / 11.2	13.1 / 11.6 / 13.2	16.6 / 13.0 / 17.0
	f_{MR}	0.066 / 0.023 / 0.064	0.046 / 0.059 / 0.046	0.029 / 0.047 / 0.028
	f_m	0.137 / 0.094 / 0.135	0.117 / 0.130 / 0.117	0.100 / 0.118 / 0.098

4.4.4.2 Discussion of the results of the application of the three different approaches

The results can be discussed as follows:

- For the macro-rough test configurations (Figure 4-37), the formulas of all approaches lead to dimensionless Chezy coefficients, macro-rough friction coefficients and friction coefficients of the section which are very close for a certain test case.
- This is also valid for the natural like configurations at prototype scale (Figure 4-38) despite for the application of the form drag based formula to the normal recirculating flow. In this case, the obtained friction coefficient is higher than that obtained with the EPR formula or the formula based on the Powerlaw optimization. The difference is mainly due to the estimation of the expansion of the flow as a function of the Reynolds number. At prototype scales, Reynolds numbers are high and therefore the flow expansion increases (eq. 4.47).
- For the asymmetrical configurations with small cavity dimensions compared to the flow width B (Figure 4-39), the friction coefficients for the square grooved flow type given by the EPR technique and the empirical formula based on the Powerlaw optimization are significantly higher than the one given by the physically based formula (eq. 4.48). This result can be explained since only one base width has been investigated. Consequently, the flow resistance formulas found by the EPR technique and the Powerlaw optimization do not depend on B / R_{hm} .
- Since the macro-rough friction coefficient f_{MR} is added to the friction coefficient of the prismatic configuration f_{prism} (skin friction of the laboratory flume), the relative difference of f_m between the three formulas (EPR, empirical, form drag based) is less than for f_{MR} .

4.4.4.3 Application range of the empirical formulas

From the presented examples and the test conditions in the laboratory flume, the application range of the formulas considering channel bank macro-roughness can be given as follows:

- The ratio of the flow depth to the channel width h / B must be contained between 0.1 and 0.75: Ratios higher than 0.75 are anyhow rare in open channel flow. Furthermore, the lower limit might be extend to zero since the macro-rough friction coefficients of the channel bank macro-roughness f_{MR} becomes very small and even an error of 100% has neglecting effect on the total flow resistance f_m .
- The resistance formula based on the Powerlaw optimization and the one obtained from EPR for the square grooved flow type should be used only for cavity geometries having L_b and ΔB approximately equal to B since the ratio B / R_{hm} respectively $2h / (B + 2h)$ are not explicative variables.
- The resistance formula based on the Powerlaw optimization and the one obtained from EPR for the reattachment and normal recirculating flow types should be used

only for roughness spacing in the range of the experiments, since they are not physically based. The limits of the dimensionless parameters are summarized in Table 4-11.

- The Froude numbers during the tests ranged between ~ 0.3 and ~ 0.7 .
- The friction slopes during the experiments ranged between $0.001 < S_f < 0.005$.

Table 4-11: Range of the dimensionless geometrical parameters of the normal recirculating (first value) / reattachment (second value) flow type for the application of the flow resistance formulas based on ERP and the Powerlaw optimization.

Parameter	R_{hm} / B	$(L_b + L_c) / R_{hm}$	$(L_b + L_c) / L_b$	$(L_b + L_c) / \Delta B$
Minimum value	ca. 0.0	ca. 9 / ca. 12	ca. 2 / ca. 1.5	ca. 3.3 / ca. 12
Maximum value	ca. 0.3	ca. 67 / ca. 65	ca. 5 / ca. 3	ca. 25 / ca. 40

4.4.4.4 Conclusions of the application of empirical formulas to examples

At model scale as expected, all types of formulas (based on EPR, on the Powerlaw optimization and the form drag model) can be applied alternatively for the corresponding flow type (square grooved, reattachment, normal recirculating). According to the rather bad correlation coefficients, the formula based on the Powerlaw optimization (eq. 4.50) for the normal recirculating flow type ($0.1 < \Delta B / L_b < 0.8$) is not recommended for use.

The EPR formula (eq. 4.49) and the one based on the Powerlaw optimization (eq. 4.48) for square grooved flow types should not be applied when the dimensions of the cavities (depression macro-roughness elements) are very different from the flow width B . For reattachment (eq. 4.46) and normal recirculating (eq. 4.42, eq. 4.43 and eq. 4.47) flows at prototype scale, the application of the form drag based approach generally leads to the highest macro-rough friction coefficients due to the higher expansion of the flow at prototype scale. However, this approach is recommended since it is physically based and since higher friction coefficients include some safety for practical applications.

All formulas are based on a one-dimensional approach for non-prismatic channels. The extra elevations of water levels in the widened reach under subcritical flow conditions have to be considered as follows: For the square grooved flow type, no extra surface elevation is observed. For the reattachment and the normal circulating flow type, the elevation can be calculated based on the specific head $H_s = h + U^2/2g$ including the sudden expansion assuming the effective flow width $B + 2\Delta B^*$ neglecting the bottom slope and skin friction over a short distance.

In any case, at prototype scale for rivers with low ratios h / B ($\cong R_{hm} / B$), the influence of the channel bank macro-roughness decreases and the friction estimation of the section becomes less dependent on the choice of the formula. At high ratios R_{hm} / B , the consideration of the channel bank macro-roughness becomes substantial.

4.4.5 Backwater curve computation using single head- and skin friction-losses

As an alternative to the developed empirical formulas which include all effects of the macro-roughness in the friction coefficient f_{MR} , the backwater curves can be computed considering the single head-losses produced by sudden expansions and contractions of the flow and the distributed skin friction-loss due to the channel roughness.

The computation of the backwater curve is based on the total energy $H = z + h + U^2/2g$ between two channel sections at base width including one sudden contraction and one sudden expansion of the flow (Figure 4-40). The alpha coefficient is assumed to be 1.

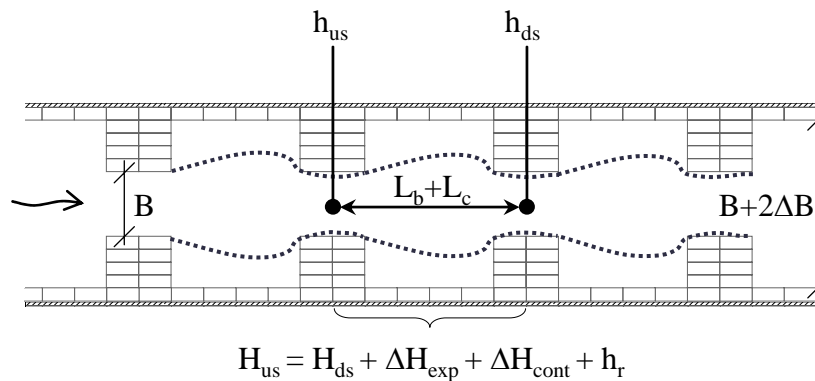


Figure 4-40: Backwater curve computation through a sequence of one sudden contraction and expansion.

The geometric width at the enlarged section $B + 2\Delta B$ is considered for the calculation of the single head-losses. Since the active flow area is, in most cases less than the geometric width, a correction term $G = f(B; L_b; L_c; \Delta B) \leq 1$ is applied to the single head-losses and the distributed skin friction-losses. The correction term depends on the geometrical macro-rough configuration.

The equation of the total energy between two sections becomes (Figure 4-40):

$$z_{us} + h_{us} + \frac{\left(\frac{Q}{B h_{us}}\right)^2}{2g} - G[\Delta H_{exp} + \Delta H_{cont} + h_r] = z_{ds} + h_{ds} + \frac{\left(\frac{Q}{B h_{ds}}\right)^2}{2g} \quad (\text{eq. 4.55})$$

where z = bottom level; h = flow depth; Q = discharge; B = base width. ΔH_{exp} = single head-loss for the expansion; ΔH_{cont} = single head-loss for the contraction; h_r = the linear head-loss. The index us refers to the upstream section, ds to the downstream section.

The single head-losses for the sudden expansions are calculated as (Henderson 1966):

$$\Delta H_{exp} = \frac{\left(\frac{Q}{B h_{us}}\right)^2}{2g} \left[\left(1 - \frac{B}{B + 2\Delta B}\right)^2 + \frac{2 Fr_{us}^2 B^3 (2\Delta B)}{(B + 2\Delta B)^4} \right] \quad (\text{eq. 4.56})$$

where $B + 2\Delta B$ = geometric width flow width at the enlarged section; Fr_{us} = Froude number at the upstream section.

The single head-loss for the sudden contraction ΔH_{cont} is calculated following Sinniger and Hager (1989):

$$\Delta H_{cont} = \xi \frac{\left(\frac{Q}{B h_{ds}}\right)^2}{2g} \quad (\text{eq. 4.57})$$

with ξ given by Matthew (1975):

$$\xi = \left(1 - \frac{B}{B + 2\Delta B}\right)^{2 - (\alpha/\pi)} \sin^2(\alpha/2) \quad (\text{eq. 4.58})$$

where α = contraction angle (in the present case 90°).

As further simplification, the flow depth of the downstream section (at width B) is used for the velocity head $U^2 / 2g$ and the Froude number. Thus, the head-loss for the sudden expansion and contraction becomes:

$$\Delta H_{exp} + \Delta H_{cont} = \left[\left(1 - \frac{B}{B + 2\Delta B}\right)^2 + \frac{2 Fr_{ds}^2 B^3 (2\Delta B)}{(B + 2\Delta B)^4} + \left(1 - \frac{B}{B + 2\Delta B}\right)^{2 - (\alpha/\pi)} \sin^2(\alpha/2) \right] \frac{\left(\frac{Q}{B h_{ds}}\right)^2}{2g} \quad (\text{eq. 4.59})$$

Finally, the linear head-loss between two sections is calculated using Strickler formula. For a value of $K_{st} = 113 \text{ m}^{1/3} \text{ s}^{-1}$ according the prismatic configuration, the linear head-loss becomes:

$$h_r = (L_b + L_c) \cdot \left(\frac{\frac{Q}{B h_{ds}}}{K_{st} R_h^{2/3}} \right)^2 \quad (\text{eq. 4.60})$$

The results from this approach show:

- Good agreement between calculated and observed water levels (Figure 4-41 ; Appendix 4-9) are obtained when the flow reattaches to the cavity side walls (root means square error RMS = 0.0054 m). The formulas for a sudden expansion (Henderson 1966) and the empirical formula for a sudden contraction (Matthew 1975) give good results in the case of flow reattachment as they have been devel-

oped for such conditions. All the geometrical configurations with flow reattaching to the side walls have cavity aspect ratios $\Delta B / L_b \leq 0.1$.

- An overestimation of the head-loss is observed for all configurations without reattachment of the flow when no correction term G is applied.
- It is difficult to define a generally applicable correction term G as a function of the macro-rough geometry. Nevertheless, following trends have been observed:
 - 1) The expansion ratio $(B + 2\Delta B) / B$ has the biggest influence.
 - 2) Considering the aspect ratio $\Delta B / L_b$ slightly increases the quality of the fitting of the backwater curve.
 - 3) Also the parameter $(L_b + L_c) / L_b$ has an influence, even if this parameter should be already included in formula (eq. 4.53).

For these reasons, the correction term has been defined as:

$$G = \left(\frac{B + 2\Delta B}{B} \right)^\alpha \left(\frac{\Delta B}{L_b} \right)^\beta \left(\frac{L_b + L_c}{L_b} \right)^\gamma \tag{eq. 4.61}$$

The first term takes into consideration the expansion ratio $(B + 2\Delta B) / B$, the second one the cavity aspect ratio $\Delta B / L_b$ and the third term $(L_c + L_b) / L_b$ represents the cavity density. High values of $(L_c + L_b) / L_b$ indicate that the distance L_c between the widenings is increasing and interaction of flow features between successive cavities is unlikely.

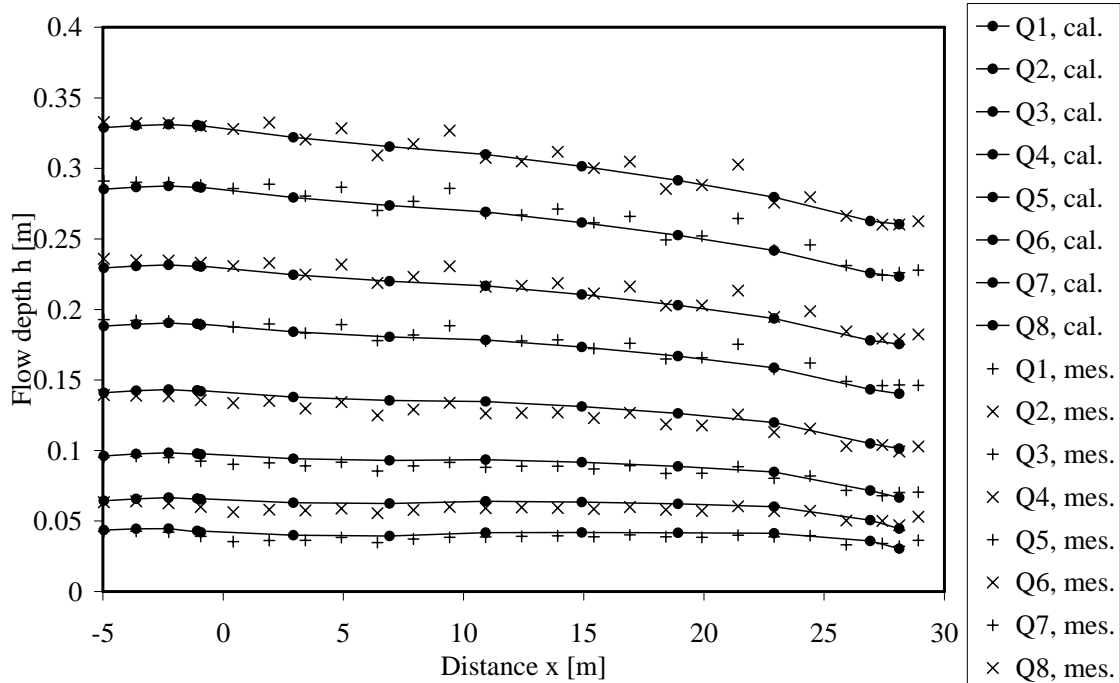


Figure 4-41: Example of the backwater curve computation with “Borda-Carnot” approach considering sudden contractions and expansions for configuration 442 with $L_b / \Delta B = 10$ (reattachment of the flow).

Two possibilities have been studied for finding the α , β and γ exponents. First, it was tried to find a good overall fitting for all configurations and discharges. Then, the usual separation into “square grooved”, “reattachment” and “normal circulating” flow was considered.

The results of the optimization for discharges Q_3 ($\cong 19$ l/s) and higher are summarized in Table 4-12. The root mean square errors of the computed water levels are compared to the root mean square errors of the backwater curves calculated without geometrical correction (RMS_0 : $\alpha, \beta, \gamma = 0$; $G = 1$). The number # indicates the number of backwater curves used for the optimization of the exponents.

Table 4-12: α , β and γ exponents applied to the correction term for single and linear head-losses (eq. 4.55). The value of the root mean square error RMS_0 corresponds to coefficients $\alpha = \beta = \gamma = 0$ ($G = 1$). # of backwater-curves used for the calibration of the exponents.

	α [-]	β [-]	γ [-]	RMS [m]	RMS_0 [m]	# Q [-]
All cases (1)	-0.79	-	-	0.0151	0.0316	189
All cases (2)	-1.09	-0.20	-	0.0123	0.0316	189
All cases (3)	-0.86	-0.20	-0.26	0.0106	0.0316	189
Reattachement	-	-	-	0.0054	0.0054	52
Reattachement (3)	-0.18	0.00	0.10	0.0049	0.0054	52
Square grooved (1)	-1.13	-	-	0.0100	0.0569	12
Square grooved (3)	-1.65	0.00	0.50	0.0065	0.0569	12
Normal recirculating (1)	-0.80	-	-	0.0156	0.0345	125
Normal recirculating (2)	-1.22	-0.28	-	0.0137	0.0345	125
Normal recirculating (3)	-0.93	-0.35	-0.44	0.0102	0.0345	125

The approach presented above (eq. 4.56) can be slightly improved by keeping the linear head-loss fully active ($G = 1$). In this case, the energy equation for the backwater curve computation becomes:

$$z_{us} + h_{us} + \frac{\left(\frac{Q}{Bh_{us}}\right)^2}{2g} - h_r - G(\Delta H_{exp} + \Delta H_{cont}) = z_{ds} + h_{ds} + \frac{\left(\frac{Q}{Bh_{ds}}\right)^2}{2g} \quad (\text{eq. 4.62})$$

In Table 4-13 the new exponents α , β and γ of the correction term (eq. 4.61) and the root mean square errors are summarized. The RMS-errors are reduced by a factor $\cong 3.5$ (normal recirculating) to $\cong 10$ (square grooved) compared to a computation of the backwater curves without application of the correction term (RMS_0).

Table 4-13: α , β and γ exponents applied to the correction term for single head-losses only (eq. 4.62). The value of RMS_0 corresponds to coefficients $\alpha = \beta = \gamma = 0$ ($G = 1$). # of backwater-curves used for the calibration of the exponents.

	α [-]	β [-]	γ [-]	RMS [m]	RMS_0 [m]	# [-]
All cases (1)	-0.95	-	-	0.0143	0.0316	189
All cases (2)	-1.30	-0.23	-	0.0119	0.0316	189
All cases (3)	-0.90	-0.26	-0.49	0.0097	0.0316	189
Reattachment	-	-	-	0.0054	0.0054	52
Reattachment (3)	-0.22	0.00	0.14	0.0051	0.0054	52
Square grooved (1)	-1.32	-	-	0.0077	0.0569	12
Square grooved (3)	-1.74	-0.12	0.45	0.0057	0.0569	12
Normal recirculating (1)	-0.97	-	-	0.0151	0.0345	125
Normal recirculating (2)	-1.43	-0.32	-	0.0135	0.0345	125
Normal recirculating (3)	-1.03	-0.64	-0.64	0.0095	0.0345	125

4.4.5.1 Conclusions regarding the Borda-Carnot approach for backwater curve computation

The approach based on the energy equation through channel transitions is an alternative backwater curve computation method, which gives very good results when the flow reattaches to the cavity side wall. For this reattachment flow type, no correction of the effective flow width respectively the head-loss terms is required. For low discharge flows, the head-loss is slightly underestimated and for high discharge, the flow depths are underestimated in some cases (Appendix 4-9).

For the square grooved and normal recirculating flow types, the single head-losses and the skin friction-losses have been corrected by a term taking into consideration the dimensionless parameters expansion ratio, cavity aspect ratio and cavity density.

The correction term can be applied to the single head-losses and the skin friction-losses respectively to the single head-losses only. The application of the experimental data reveals slightly higher performance in the later case.

Applying a correction term to formula (eq. 4.61) allows to reduce the root mean square errors by a factor of 3.5 (normal recirculating flow type) to 10 (square grooved flow type).

4.5 Summary and conclusions for the steady flow experiments

Flow conditions in the channel with macro-rough banks

The cavity geometry and also the flow conditions in the main channel have mainly an influence on the flow pattern inside the cavity. For cavity aspect ratios $\Delta B / L_b \leq 0.1$, the flow reattaches to the sidewalls except for very low discharge conditions with $h / B < 0.12$. Important oscillations transverse to the main flow direction occur at Strouhal numbers close to 0.42 and 0.84. This flow feature creates water surface oscillations inside the cavity. It is produced by a hydrodynamic feedback effect provided from the backflow. Since the main frequency of the observed water surface oscillations and the main frequency of the measured transverse velocity component are identical with the one of vortices shedding periodically at the cavity leading edge, the phenomena are assumed to be coupled. For practical applications, it is possible to avoid such oscillations by considering the criteria found with the help of the steady flow tests (Table 4-14).

Table 4-14: Factors favouring and preventing important and periodic water surface oscillations in a channel with cavities (large scale macro-roughness on banks).

Factors favouring periodic oscillations	Factors preventing periodic oscillations
Axi-symmetric and regular arrangement of the cavities	Randomly arranged cavities (varying $\Delta B, L_b, L_c$)
Strouhal number close to 0.42 and 0.84	Reattachment of the flow to the side walls
High expansion ratios $(B + 2\Delta B) / B$	Strouhal numbers different from 0.42 and 0.84
Relatively high aspect ratios $\Delta B / L_b$	Cavities only at one channel side
Undisturbed flow conditions at the cavity leading edge	Uneven bed topography (leads to damping)

Roughness parameters of the channel bank macro-roughness

The experimentally investigated cavities can be considered as macro-roughness elements (depression roughness) since their size is important compared to the hydraulic radius. Different phenomena are responsible for the total head-loss along the macro-rough channel such as vertical mixing layers, wake-zones, recirculation gyres, coherent structures and transverse oscillations of the flow. The backwater curve computation allowed identifying the overall flow resistance in terms of friction coefficients f , Chezy coefficient C and Strickler coefficient K_{st} . It could be shown that disturbing the flow by macro-roughness elements leads to a significant increase of the flow resistance compared to the prismatic reference configuration. The increased flow resistance has to be considered in practical applications including flood protection. However, this increase becomes significant only with increasing relative flow depths h / B . The differ-

ence between the prismatic reference configuration and the 36 macro-rough configurations is important whereas the differences between the 36 macro-rough configurations itself are more difficult to identify. The relative roughness spacing was found to be the most important parameter for the determination of the friction coefficients.

Empirical formulas for channel bank macro-roughness

From the three investigated possibilities which allow all to calculate friction coefficients for the channel bank macro-roughness, the formulas summarized in Table 4-15 are recommended for use. The application range is defined in § 4.4.4.3.

Table 4-15: Recommended formulas issued from the empirical and semi-empirical approaches for the calculation of the macro-rough friction coefficient of the channel bank macro-roughness f_{MR} . $C_d = 0.475$ is the drag coefficient of a rectangular cavity and $Re_{lim} = 150'000$ respectively $x_0 = 4.5$ are empirical parameters describing the flow expansion in (eq. 4.47).

Flow type	Geometrical criteria	Formula
		issued from the Powerlaw optimization:
Square grooved flow type	$L_b \cong \Delta B \cong B$	$C_{adim\ MR,sg} = \sqrt{\frac{8}{f_{MR,sg}}} = 5 \cdot \left(\frac{L_b + L_c}{R_{hm}} \right)^{1/3} \quad (\text{eq. 4.38})$
		issued from the form drag based approach:
Reattachment flow type	$\Delta B / L_b \leq 0.1$	$f_{MR,re} = C_d \frac{8R_{hm} \Delta B}{B(L_b + L_c)} \quad (\text{eq. 4.46})$
		issued from the form drag based approach:
Normal recirculating flow type	$0.1 \leq \Delta B / L_b \leq 0.75$	$f_{MR,nc} = C_d \frac{8R_{hm} \Delta B^*}{B(L_b + L_c)} \quad (\text{eq. 4.42})$
		$\Delta B^* = \min(\Delta B ; (L_b / x)) \quad (\text{eq. 4.43})$
		$x = \left(\frac{Re_{lim}}{Re_m} + x_0 \right) \left(\frac{L_b}{\Delta B} \right)^{0.18} \quad (\text{eq. 4.47})$

In order to obtain the total friction of the channel section f_m , the friction coefficient of the channel without macro-roughness f_{prism} is summed up with the friction coefficient f_{MR} issued from Table 4-15. The friction coefficient of the prismatic channel (natural or artificial) can be determined by commonly used formulas presented in § 2.1.

Further experimental works can be concentrated on short models including only few macro-roughness elements. Provided that the head-loss can be precisely described, they would allow extending the form drag based model to macro-roughness elements other than rectangular slots. Furthermore, it might be possible to describe more precisely the

expansion of the flow $\tan(\alpha) = I/x$ influencing ΔB^* and the wall velocity ratio V_w/U . Thus, the fully empirical calculation of ΔB^* with (eq. 4.43) and (eq. 4.47) could be confirmed or eventually replaced by a more physically based and prototype oriented approach.

5 UNSTEADY FLOW EXPERIMENTS

5.1 Tested scenarios

Positive and negative waves from upstream have been examined in the prismatic reference configuration as well as in 36 axi-symmetric, in 4 asymmetric and in a randomly generated macro-rough configuration. Table 5-1 summarizes the test discharges as well as two characteristic dimensionless wave parameters HP_1 and HP_2 defined as:

$$HP_1 = \frac{Q_{total}}{Q_b} \quad (\text{eq. 5.1})$$

$$HP_2 = \frac{Q_{total} - Q_b}{0.5 \cdot (Q_b + Q_{total})} = \frac{Q_w}{Q_{mean}} \quad (\text{eq. 5.2})$$

The ratio of the total discharge Q_{total} to the baseflow discharge Q_b ranges between $1.10 < HP_1 < 10.02$ indicating that the total discharge including the unsteady discharge is up to 10 times higher than the baseflow. The ratio of the difference Q_w to the average discharge Q_{mean} ranges between $0.10 < HP_2 < 1.64$.

Table 5-1: Summary of the baseflow discharge (Q_b) and the total discharge (Q_{total}) including the discharge of the surge wave Q_w introduced at the upstream end of the channel for the prismatic configuration.

Scenario	1	2	3	4	5	6	7	8	9	10	11	12	13	14	15
Q_b [l/s]	6.0	5.9	6.0	6.2	5.9	10.7	10.7	10.7	10.7	10.7	19.2	19.1	19.0	18.9	18.7
Q_{total} [l/s]	12.5	17.0	23.6	36.7	59.4	17.2	21.8	28.3	41.1	64.1	25.7	30.2	36.5	49.2	71.8
Q_{total} / Q_b	2.09	2.90	3.96	5.94	10.02	1.61	2.04	2.64	3.83	5.98	1.34	1.58	1.92	2.60	3.84
Q_w / Q_{mean}	0.71	0.98	1.19	1.42	1.64	0.47	0.68	0.90	1.17	1.43	0.29	0.45	0.63	0.89	1.17
Scenario	16	17	18	19	20	21	22	23	24	25	26	27	28	29	30
Q_b [l/s]	34.7	34.8	34.4	34.9	35.0	49.1	48.7	48.8	48.7	48.6	62.3	61.0	60.8	61.0	60.9
Q_{total} [l/s]	41.1	45.7	51.8	64.9	87.7	55.5	59.6	66.0	78.5	100.8	68.6	71.8	77.9	90.6	112.9
Q_{total} / Q_b	1.18	1.32	1.50	1.86	2.50	1.13	1.22	1.35	1.61	2.08	1.10	1.18	1.28	1.49	1.85
Q_w / Q_{mean}	0.17	0.27	0.40	0.60	0.86	0.12	0.20	0.30	0.47	0.70	0.10	0.16	0.25	0.39	0.60

The values of Table 5-1 correspond to the tests of the prismatic reference configuration. They are approximately the same for the channel configurations with macro-rough banks (Appendix 5-1). The baseflow discharge has been measured with the electromag-

netic flowmeter. The wave discharge is calculated from the calibrated surge wave model for every configuration and scenario (§ 3.5).

5.2 *Classification of the tested waves*

First, a detailed classification of the tested waves is done for the positive waves from upstream in the prismatic configuration. Then, the classification is extended to the non-prismatic configurations and to the negative waves.

The wave classification criteria for shallow water waves of Ponce et al. (1978) and those proposed in a recently published work of Chung and Kang (2006) are employed. Three preliminary steps are necessary in order to classify the waves:

- 1) Verification of the shallow water wave hypothesis (Henderson 1966) $\lambda/h > 50$ where λ is the wavelength and h the flow depth.
- 2) Identification of the evolution of the wave front along the channel regarding its formation and stabilization of the shape.
- 3) Estimation of the time to peak value t_p which is a characteristic unsteady flow parameter.

Shallow water hypothesis: The channel has a length of 38.33 m and a maximum available flow depth of 0.38 m. The positive wave is generated by opening the flap gates of the surge wave setup. The negative wave is generated by the closure of the gates and has never been produced before the arrival of the positive wave at the channel end. The relative wave length is therefore at least $\lambda/h > 101$ and the shallow water wave hypothesis is verified.

The **evolution of the wave front** and the determination of the time to peak value are done simultaneously by analyzing the steepness of the wave front at different locations along the channel. Three different ultrasonic sensors are considered. Sensor 0 ($x = -7.71$ m) is located above the inlet basin, sensors 5 and 13 are situated at a distance of $x = 0.42$ m and $x = 12.42$ m from the end of the inlet reach. The time to peak values t_p determined from the level recordings are presented as a function of HP_2 in Figure 5-1 for the three different sensors.

The **time to peak value** is a function of HP_2 at ultrasonic sensor 0 ($x = -7.71$ m). Further downstream this time has been found almost independent from the discharge characteristics of the wave ($x = 0.42$ m and $x = 12.42$ m). When regarding the values of t_p at $x = 0.42$ m and $x = 12.42$ m, it can be concluded that the wave becomes in general slightly steeper along the channel but that already after the inlet reach, a quite stable wave form is achieved. At the upstream end of the channel ($x = -7.71$ m) the time to peak values are about 1 to 10 times higher. At the sensor 0 ($x = -7.71$ m), they are consequently influenced by the inertia of the wave generating setup, whereas the time to peak values at locations $x = 0.42$ m and $x = 12.42$ m are smaller due to the overrun phenomenon. The opening time and the inertia of the surge wave generation setup

(§ 3.5) is however small enough in order to get a positive wave with a steep front. After a short channel distance the wave characteristics are independent of the flap gate opening time. This observation is in good agreement with Favre (1935) indicating that operation times up to values of 6 seconds do not influence the shape of the formed surge.

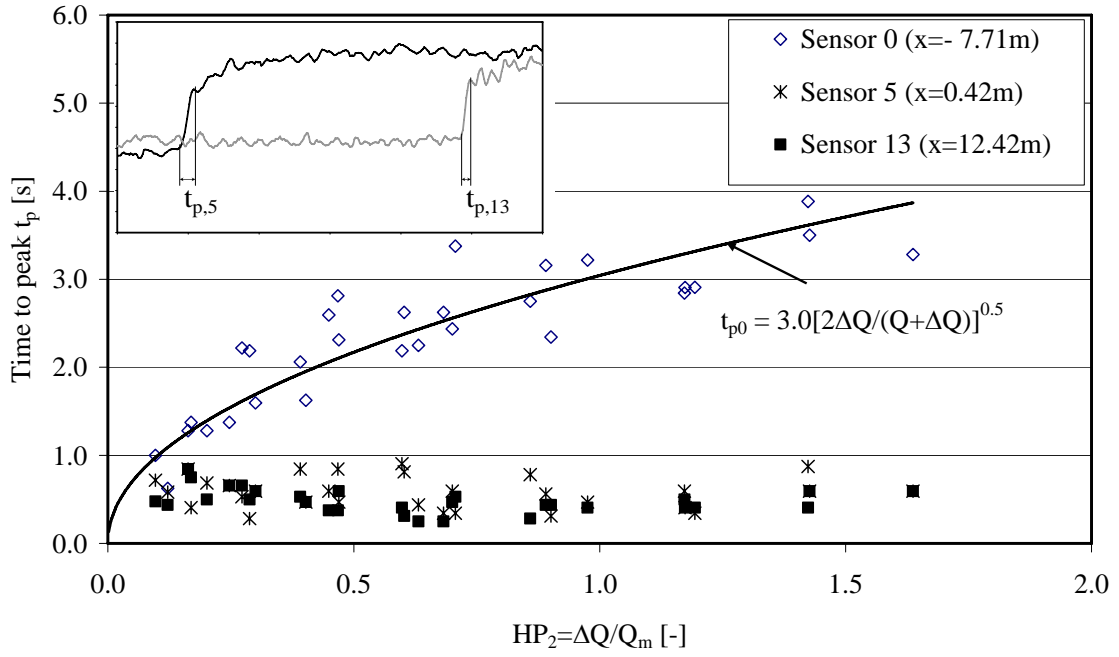


Figure 5-1: Time to peak values t_p at the ultrasonic sensors 0 ($x = -7.71$ m), 5 ($x = 0.42$ m) and 13 ($x = 12.42$ m) for all 30 scenarios of the prismatic reference configuration.

From the time to peak values both required wave classification parameters, namely the Froude number of the baseflow Fr_1 and the modified friction number G_{1m} , can be calculated as (Chung and Kang 2006):

$$Fr_1 = \frac{U_1}{\sqrt{gh_1}} \quad (\text{eq. 5.3})$$

$$G_{1m} = \frac{2gS_0t_p}{U_1} \quad (\text{eq. 5.4})$$

where U_1 and h_1 are the mean flow velocity and flow depth related to the baseflow, S_0 is the bottom slope and t_p the estimated time to peak.

To classify the waves the criteria of Ponce et al. (1978) and the classification diagram of Chung and Kang (2006) are applied (Figure 5-2). Both approaches confirm that the investigated scenarios produce gravity waves at locations $x = 0.42$ m and $x = 12.42$ m. As soon as the waves travelled along the inlet reach, they are transformed into gravity waves even if some of them have to be considered as dynamic waves at $x = -7.71$ m.

The time to peak values of the negative waves have been determined for sensor 0 ($x = -7.71$ m). For the sensors further downstream, this parameter becomes difficult to identify since negative waves have a dispersive character. The time to (negative) peak ranges between 0.8 and 3.5 seconds for most of the scenarios at sensor 0 ($x = -7.71$ m). The determination of the Froude number Fr_1 and the modified friction number G_{1m} reveal that most of the negative waves in the prismatic configuration can be considered as gravity waves at the upstream end of the test flume. Due to the dispersive character, the negative waves become dynamic waves when travelling downstream.

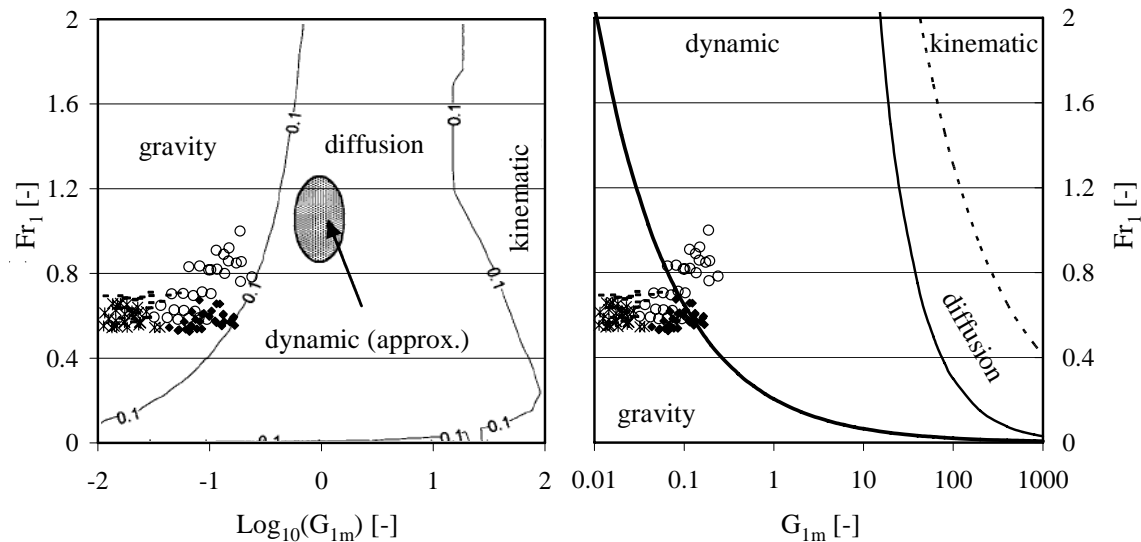


Figure 5-2: Experimental waves from upstream on the wave classification diagram. Left: criteria according Chung and Kang (2006). Right: criteria of Ponce et al. (1978). Positive wave: (○) at $x = -7.71$ m, (◻) at $x = 0.42$ m, (*) at $x = 12.42$ m. Negative wave: (◆) at $x = -7.71$ m.

No further investigations are needed for the classification of the positive and negative waves from upstream in the different macro-rough configurations for following reasons:

- The flow depths in the inlet reach are increased under the influence of macro-roughness elements due to backwater effects.
- For a given discharge and channel width, the increase of the mean flow depth affects the Froude number with a power $Fr_1 = f(h_1^{-1.5})$ whereas the G_{1m} number is affected by $G_{1m} = f(h_1^1)$. The decrease of Fr_1 is consequently more important than the increase of G_{1m} .
- The relationship separating gravity from dynamic waves according to the criteria of Ponce is $Fr_1 = (0.042 / G_{1m})^{0.5}$. Thus, the increase of the flow depth for a given discharge makes the waves more gravity-like (Figure 5-2, right side). If the wave classification diagram from Chang and Kung (2006) is used, the interpretation differs, since the line separating the gravity wave and the dynamic wave domain takes another form. However, the change in flow depth due to macro-roughness elements is not significant enough to leave significantly the gravity domain.

It may be concluded that the tested positive waves are all gravity waves at the end of the inlet reach for both, prismatic and macro-rough configurations. The investigated negative waves are mainly gravity waves at origin but they transform into dynamic waves along the channel due to their dispersive character.

5.3 *Flow conditions for positive and negative surge waves*

5.3.1 Tests with positive waves in the prismatic configuration

After the opening of the flap gates of the setup generating the waves, the positive surges are rapidly formed and they reach stable conditions at the front for most scenarios already at the end of the inlet reach. Under non-breaking conditions the wave train formed by secondary waves continues to increase in length and number of undulations along the channel (§ 5.4). Under highly breaking conditions, the wave front is characterized by air entrainment and a non-undulating water surface behind the wave front. When breaking of the wave front has been observed after the inlet reach, it remained until the channel end. The positive surge waves travel along the whole channel until reaching the particularly shaped cross section at the outlet. At the downstream end of the channel, basically four different behaviours of the positive waves have been observed and confirmed by the level measurements (Table 5-2):

- Partial reflection of the surge wave under supercritical flow in the outlet reach. Froude number is temporarily higher than $Fr = 1$. The partial reflection is high enough and a positive surge moves upstream.
- Very small reflection unable to move upstream under the temporarily supercritical flow conditions in the outlet reach after the passage of the positive surge wave from upstream.
- Partial reflection of the surge wave under subcritical flow conditions in the outlet reach. The reflection is sufficiently high and a positive surge moves upstream.
- Very small reflection which is unable to move upstream under subcritical flow conditions in the outlet reach.

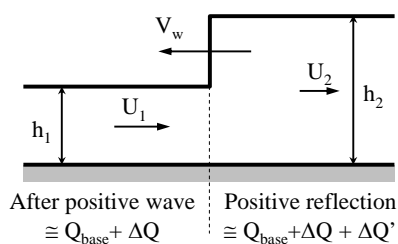
Supercritical flow conditions after the wave front are observed for scenarios 1 to 15 having a baseflow Q_b less than 20 l/s. Positive surge waves moving upstream due to partial reflection at the particularly shaped cross section at the outlet are observed for scenarios having an additional discharge of at least 17 l/s. According § 2.3.3.2 the reflection is combined with a change in discharge $\Delta Q'$. This change has been roughly estimated at $x = 24.42$ m with equations (eq. 2.48) and (eq. 2.49) using the level measurements before (h_1) and after (h_2) the positive surge wave from downstream (Table 5-3).

Table 5-2: Classification of the scenarios of the positive surge waves from upstream in the prismatic configuration relative to the flow conditions in the outlet reach.

	Scenarios with temporarily supercritical flow at $x = 28.12$ m and 28.92 m	Scenarios with subcritical flow conditions all the time at $x = 28.12$ m and 28.92 m
Positive surge moving upstream (reflection verified at $x = 24.42$ m)	5 9, 10 14, 15	18, 19, 20 23, 24, 25 28, 29, 30
No surge wave moving upstream (no reflection or too small to be detected at $x = 24.42$ m)	1, 2, 3, 4 6, 7, 8 11, 12, 13	16, 17 21, 22 26, 27

Table 5-3: Estimation of the reduction of the discharge due to the partial reflection of the positive surge wave from upstream at the particularly shaped cross section at the outlet. Level and discharge data from tests.

Scen.	Q_b	ΔQ^*	h_1	h_2	U_2	V_w	$\Delta Q'$	$\Delta Q'^{**}$
[-]	[l/s]	[l/s]	[m]	[m]	[m/s]	[m/s]	[l/s]	[%]
5	5.9	53.5	0.127	0.134	0.90	-0.20	-0.7	-1.1%
9	10.7	30.4	0.103	0.107	0.78	-0.21	-0.4	-1.0%
10	10.7	53.4	0.135	0.143	0.91	-0.22	-0.9	-1.4%
14	18.9	30.3	0.118	0.122	0.82	-0.24	-0.5	-1.0%
15	18.7	53.1	0.147	0.159	0.91	-0.27	-1.6	-2.2%
18	34.4	17.3	0.133	0.139	0.75	-0.38	-1.1	-2.1%
19	34.9	30.1	0.147	0.158	0.82	-0.36	-1.9	-2.9%
20	35.0	52.7	0.167	0.193	0.89	-0.35	-4.4	-5.0%
23	48.8	17.2	0.165	0.170	0.79	-0.48	-1.2	-1.8%
24	48.7	29.9	0.178	0.190	0.82	-0.48	-2.8	-3.5%
25	48.6	52.3	0.197	0.223	0.88	-0.47	-5.9	-5.9%
28	60.8	17.1	0.193	0.199	0.79	-0.58	-1.7	-2.2%
29	61.0	29.7	0.203	0.215	0.84	-0.55	-3.2	-3.6%
30	60.9	52.0	0.221	0.244	0.90	-0.53	-5.9	-5.3%



* The additional discharge ΔQ after the wave front would be equal to Q_w only in the frictionless and horizontal channel or at the upstream end of the channel. For the estimation of the partial positive reflection, this assumption is accepted.

** Reduction relative to $Q_b + \Delta Q$.

The reflection of the surge wave is reduced when the flow conditions in the outlet reach are supercritical (Table 5-3). The reflected positive wave from upstream is nevertheless

able to move upstream for some scenarios and leads to a relative reduction of the initial discharge $\Delta Q' / (Q_b + \Delta Q)$ of maximal 2.2%. Under subcritical flow conditions the reflection leads to a reduction of the initial discharge between 1.8% and 5.9%.

It may be concluded that the reflection at the particularly shaped cross section at the outlet is negligible for an additional discharge $\Delta Q < 18$ l/s (maximum reflection 1.7 %). After a while, stable discharge conditions are achieved at the outlet section and quasi steady flow conditions occurs along the experimental channel. The discharge corresponds to about $Q_b + \Delta Q \cong Q_b + \Delta Q - \Delta Q'$.

5.3.2 Tests with negative waves in the prismatic configuration

When the flow reaches quasi steady conditions, the negative surge wave from upstream is initiated by the closure of the upstream discharge control device. The front of the negative surge reduces its steepness when moving downstream due to its maximum local wave celerity $V_w(h)$ at the wave tip. When arriving at the particularly shaped cross section at the outlet, the negative wave is also partially reflected. For a few scenarios, summarized in Table 5-4, a reflection of the negative (surge) wave from upstream could be observed with the level measurements at $x = 24.42$ m.

Table 5-4: Estimation of the increase of the discharge due to the partial reflection of the negative (surge) wave from upstream at the particularly shaped cross section at the outlet. Level and discharge data from tests.

	Scen.	h_1' [m]	U_1' [m/s]	Q_1' [l/s]	h_2 [m]	U_2 [m/s]	V_w [m/s]	$\Delta Q''$ [l/s]	$\Delta Q''^{**}$ [%]
	10	0.137	0.576	38.3	0.131	0.628	-0.545	1.6	2.5%
	15	0.154	0.513	38.3	0.148	0.561	-0.680	2.0	2.8%
	25	0.199	0.512	49.4	0.187	0.597	-0.822	4.8	5.0%
	28	0.189	0.664	60.9	0.185	0.693	-0.676	1.3	1.7%
	29	0.207	0.660	66.2	0.196	0.736	-0.709	3.8	4.3%
	30	0.222	0.559	60.2	0.21	0.640	-0.857	5.0	4.7%

** Reduction relative to $Q_b + \Delta Q$ (= discharge before the passing of the negative surge).

The partial negative reflection is estimated by calculating the flow parameters after the negative wave Q_1' and U_1' first (eq. 2.61 to eq. 2.64). Then, the reflected flow $Q_2 = Q_1' + \Delta Q''$ and U_2 can be calculated. The partial reflection of the negative surge wave from upstream leads to an increase of the discharge in the flow influenced by the negative reflection (Table 5-4). The amount of the increase ranges between 2.5% and 5% of the discharge before the passing of the negative (surge) wave from upstream.

After the arrival of the negative (surge) wave at the outlet section, the downstream boundary condition is permanently adjusted as a function of the discharge. Directly after

the arrival of the negative (surge) wave, the flow depth and discharge are first decreasing rapidly and then exponentially with a lower gradient until reaching the final conditions corresponding to the initial discharge Q_b (Figure 5-3). The initial flow depth and discharge are first reached at channel sections upstream and than at channel sections downstream, similar to a flood wave.

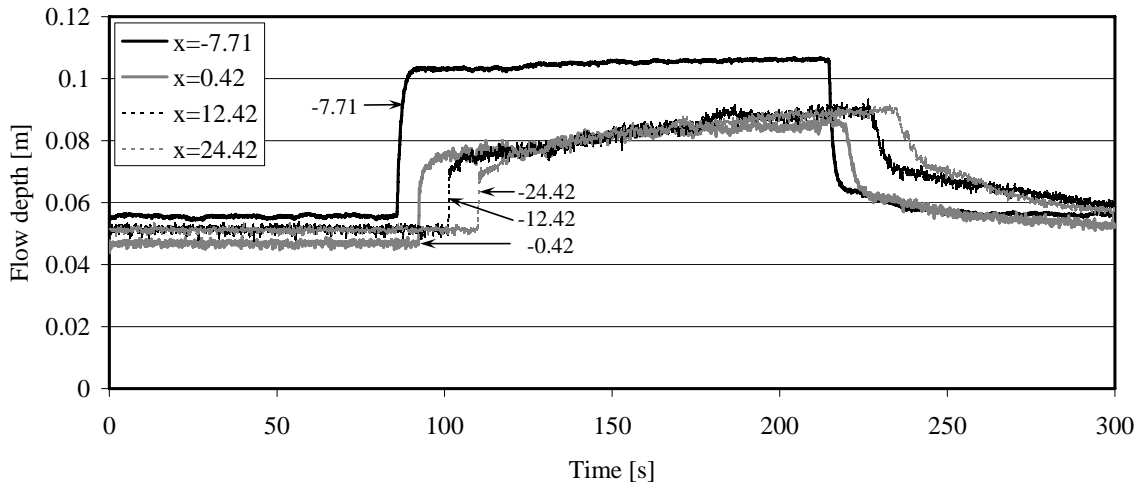


Figure 5-3: Example of a positive surge followed by a negative surge wave measured with ultrasonic sensors at different locations along the channel for the prismatic configuration; test scenario 8: $Q_b = 10.70$ l/s, $Q_{total} = 28.30$ l/s. The opening time of the flap gates for scenario 8 corresponds to approximately 3 seconds.

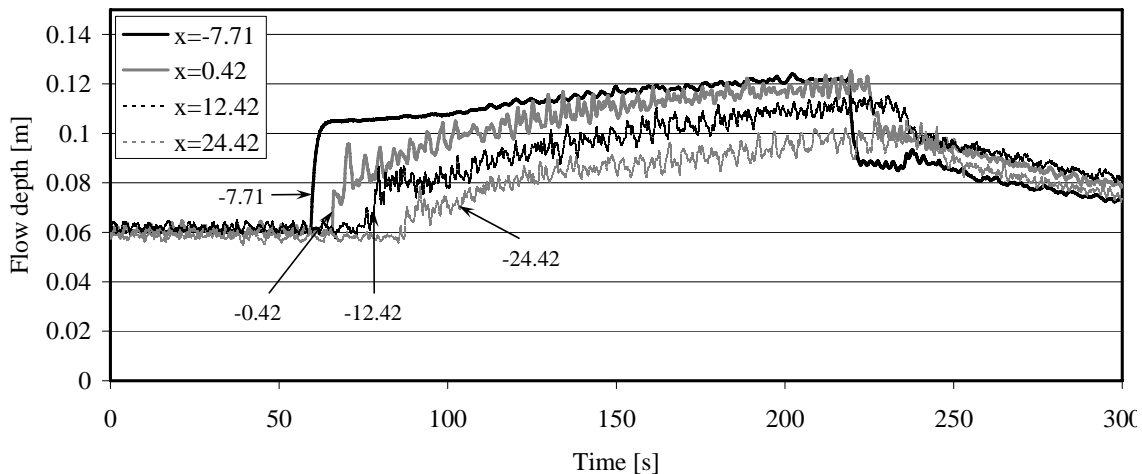


Figure 5-4: Example of a positive surge followed by a negative surge wave measured with ultrasonic sensors at different locations along the channel for the macro-rough configuration 222: $L_b = 1$ m, $L_c = 1$ m, $\Delta B = 0.2$ m; test scenario 8: $Q_b = 10.95$ l/s, $Q_{total} = 28.47$ l/s). The opening time of the flap gates for scenario 8 corresponds to approximately 3 seconds.

5.3.3 Tests with positive and negative waves in the macro-rough configurations

At least five of the 30 scenarios tested in the prismatic reference configuration have also been investigated in the 36 axi-symmetric, the 4 asymmetric and the randomly generated configuration with macro-roughness at the channel banks.

In general, the observations made in § 5.3.1 are also valid for moderate macro-rough configurations characterized by relatively small additional surfaces (high L_c , small L_b and ΔB). Nevertheless, for increasing additional flow areas due to the depression macro-roughness elements, some significant differences are observed (Figure 5-4):

- The positive wave is characterized by a first and **sudden increase** of the flow depth due to the wave front and a second **progressive increase** of the flow depth after the wave front. The more a configuration is macro-rough (many and important rectangular widenings), the more the proportion of progressive increase compensates the sudden increase.
- An **attenuation** of the height of the positive surge moving downstream can be observed visually along the macro-rough reach especially for scenarios leading to a steep breaking front in the inlet reach. The attenuation is due to the filling of the depression macro-roughness element and is also favoured by the partial reflections of the surge at each downstream border of the rectangular widenings (see Figure 5-9).
- **Breaking** conditions of the front observed after the formation of the surge in the inlet reach can disappear along the macro-rough reach and transform into a non-breaking wave front followed by secondary waves. This observation is contrary to the prismatic case where the breaking wave front travelled along the whole channel. Furthermore, **secondary waves** which are formed in the inlet reach can disappear completely. This point is detailed in § 5.4.
- The **aspect of the water surface** in the macro-rough configurations is more heterogeneous compared to the prismatic configuration already before the passage of the positive wave. This difference is pronounced after the passage of the wave where the water surface of the macro-rough configurations is characterized by intense superposition and reflection of surface waves. These surface waves should not be mixed up with the periodic oscillations described in § 4.2.
On the other hand, the aspect of the water surface becomes quite homogeneous after the passage of the negative wave mainly due to the sudden decrease of the flow velocity (Froude number).
- When **transverse oscillations** occur at baseflow conditions, they are generally amplified after the passage of the positive and reduced again after the negative wave.
- A special behaviour is observed for the US-levelling at position $x = -7.71$ m in the macro-rough configurations after the closure of the flap gates as well as for all sensors in the inlet reach. After a sudden decrease, the water level progressively

decreases during approximately 14 seconds. Then, the water level suddenly increases before decreasing again progressively (Figure 5-5, above). This behaviour is due to a partial negative reflection of the negative surge when it arrives in the first expansions of the macro-rough reach. A small positive surge moving upstream in the inlet reach is resulting. This phenomenon is visible especially for configurations with big cavities ($L_b = 4 \cdot B$ and $\Delta B \geq 0.2$).

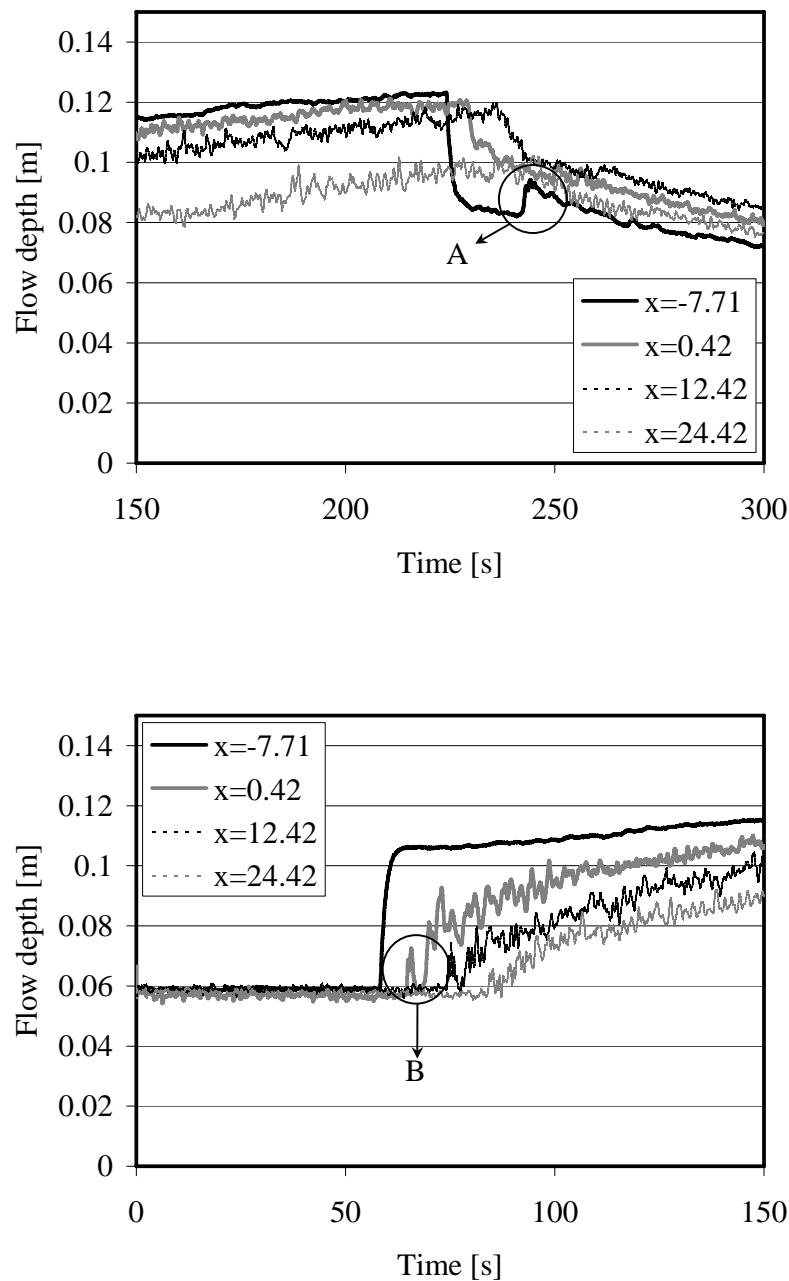


Figure 5-5: Above: Negative reflection of a negative wave leading to a positive surge moving upstream (A) for configuration 412, scenario 8. Below: Moving hydraulic jump inside of the widened channel reach for the positive surge from upstream (B) for configuration 442, scenario 8.

- A second special behaviour is observed when the additional discharges of the positive surge from upstream and the cavity length are high ($L_b = 2$ m and $L_b = 1$ m). When the positive surge arrives at the enlarged channel reach, the central part of the wave front continues in the main channel practically at the same velocity. On the other hand, the lateral parts of the wave front are deformed (Figure 5-9) and reflected at the downstream border of the widened reach. This reflection can be so important that a positive surge moving upstream (moving hydraulic jump) forms inside of the widened channel reach (Figure 5-5, below). This behaviour is mainly observed in the upper part of the macro-rough channel reach.

It may be concluded that the surge wave flow in the configurations with macro-roughness at the channel banks differs from the surge flow in prismatic configurations as follows:

- Partial positive and negative reflections of the surge waves occur in the depression macro-roughness elements.
- The wave front attenuates and deforms. Whereas it is two dimensional in the prismatic configuration, it becomes 3 dimensional in the configurations with macro-roughness at the channel banks.
- Surface waves are pronounced after the passage of the positive wave from upstream and again reduced after the negative wave from upstream.

5.3.4 Dye tests and velocity profiles during the surge waves

Dye was introduced in the flow for some test with low discharge at baseflow conditions. The surge wave front first catches up the cloud and after a short moment its location is more downstream of the cloud. For high baseflow discharge conditions, the same behaviour exists but it is difficult to observe since the dye is rapidly dissolved. When dye is introduced into the flow before the passage of the negative wave, the velocity of the dye cloud drops significantly after the passage of the wave and it disperses rapidly due to the dispersive character of negative waves. In the central part of the channel, the path of the dye is straight for the axi-symmetric macro-rough configurations as well as for the 4 asymmetric macro-rough configurations. As long as the main channel is not penetrated by obstacles, the straight path seems not to be significantly disturbed.

Two possible explanations for the catching up and passage of the dye cloud by the positive surge wave front can be given. Both are related to the vertical velocity profile of the flow:

- The first explanation is that the flow of a positive surge has two layers, namely a slower layer corresponding to the baseflow in the lower part and a faster layer corresponding to the additional flow in the upper part.
- The second explanation is that in a logarithmic velocity profile the local flow velocities close to the surface are higher than close to the bottom. Thus, dye introduced close to the bottom moves slower than dye introduced close to the free surface, even under completely steady flow conditions.

In order to verify whether the first or second explanation is governing, some unsteady velocity profiles have been measured (Figure 5-6). Detailed results of these measurements and the effect of seeding with hydrogen bubbles are presented in Meile et al. (2007, accepted for publication). The characteristics of the tested surge waves, the main results and conclusions are summarized hereafter.

Table 5-5 shows the test conditions where Q_b is the steady baseflow and Q_w the additional discharge introduced at the upstream end of the channel (24.33 m upstream of the measurement location). h_1 , Re_1 , Fr_1 and U_1 are related to the steady discharge. U_2 and h_2 are related to the flow immediately after the surge front. Q_2 is the estimated discharge directly behind the wave front and is not equal to $Q_b + Q_w$ since the channel is not frictionless and horizontal.

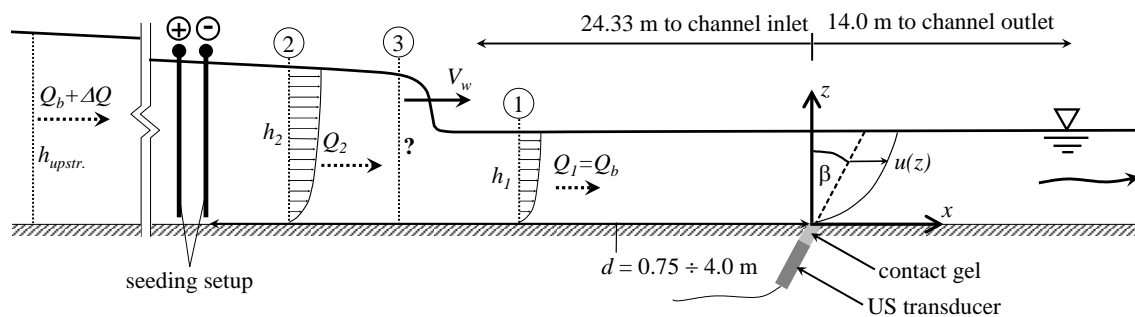


Figure 5-6: Experimental set-up and schematic definition of the surge wave characteristics before (index 1) and after (index 2) the surge wave front moving with an absolute celerity V_w . Q is the discharge and h the flow depth. Velocity profiles are investigated before (1), after (2) and during (3) the surge wave front. The total flume length is 38.33 m.

Table 5-5: Hydraulic test conditions of the three investigated surge waves: Q_b (steady baseflow discharge), h_1 (flow depth of baseflow), $U_{1,cal}$ (mean velocity of baseflow), Re_1 (Reynolds number of baseflow), Fr_1 (Froude number of baseflow), Q_w (additional discharge introduced at flume entrance 24.33 m upstream of the measurement location), h_2 (flow depth directly after front), $U_{2,UVP}$ (mean velocity from UVP), Q_2 (discharge directly after front), V_w (absolute surge wave celerity) experimentally and theoretically.

Q_b [m ³ s ⁻¹]	h_1 [m]	$U_{1,cal}$ [ms ⁻¹]	Re_1 [-]	Fr_1 [-]	Q_w [m ³ s ⁻¹]	h_2 [m]	$U_{2,UVP}$ [ms ⁻¹]	Q_2 [m ³ s ⁻¹]	$V_{w,exp}$ [ms ⁻¹]	$V_{w,th}$ [ms ⁻¹]
0.0056	0.035	0.33	9500	0.56	0.0175	0.057	0.62	0.0170	(?)	1.07
0.0057	0.035	0.34	9600	0.57	0.0306	0.065	0.79	0.0249	≈ 1.10	1.32
0.0056	0.035	0.33	9500	0.56	0.0535	0.088	0.96	0.0410	≈ 1.30	1.38

For the smallest surge wave of $Q_w = 0.0175 \text{ m}^3/\text{s}$, the sampling frequency of a single velocity profile $1 / \Delta T = 5.32 \text{ Hz}$ is too low for measuring a profile exactly during the

passage of the wave front¹. For the second and third surge wave of $Q_w = 0.0306 \text{ m}^3/\text{s}$ and $0.0535 \text{ m}^3/\text{s}$ respectively, a "two-layer type" velocity profile has been detected during a short period corresponding to the passage of the positive surge. In the lower part of the velocity profiles, the velocities during the passage of the positive surge waves are situated always between the velocities before and after the passage of the wave. In the upper part of the velocity profiles, downstream velocity components are increased during the passage of the wave. This indicates a separation of the flow into an upper, faster part moving on a lower, slower part. This behaviour is however observed only during a very short period respectively within a short distance of the surge wave body. An approximately "uniform flow type" velocity profile is re-established over the entire flow depth within less than 0.2 s. For a baseflow depth h_1 of 0.035 m and a surge wave height h' of 0.024 m, the distance is less than 0.25 m. For the same baseflow depth and a surge wave height h' of 0.053 m, the distance is less than 0.55 m.

It can thus be concluded that the catching up and passing of the dye cloud by the positive surge wave front is mainly due to the logarithmic velocity profile and only little due to the "two layer type" velocity profile existing during a very limited laps of time only. The measured velocity of the upper layer is in acceptable agreement with the theoretical absolute celerity $V_{w,th}$ calculated from the flow depths. No significant mass exchange exists between the baseflow layer and the upper layer since the fast moving upper part remains free of dye. Finally, the discharge immediately behind the surge front can be estimated ($Q_2 = B \cdot h_2 \cdot U_{2,UVP}$) and compared to the initial surge wave discharge at the upstream end of the channel. For the three analyzed positive surge waves from upstream the ratio of $Q_2 / (Q_b + Q_w)$ lies between 69% and 74%.

The seeding of hydrogen bubbles 2 m upstream of the measurement location was found to be an efficient technique to get qualitatively and quantitatively accurate velocity measurements at high temporal resolution. They allow gaining insight in the physics of the highly unsteady surge waves. For the investigated, breaking conditions of the wave front, non hydrostatic pressure distributions (accelerated velocity profile) are limited to a very small part of the wave. This explains physically the disappearance of the secondary waves (Soares and Zech 2002) in case of breaking conditions (see § 5.4).

¹ A single velocity profile is obtained by averaging 256 profiles recorded at the maximum sampling frequency of the UVP-Duo instrument. This is necessary in order to obtain reasonable profiles.

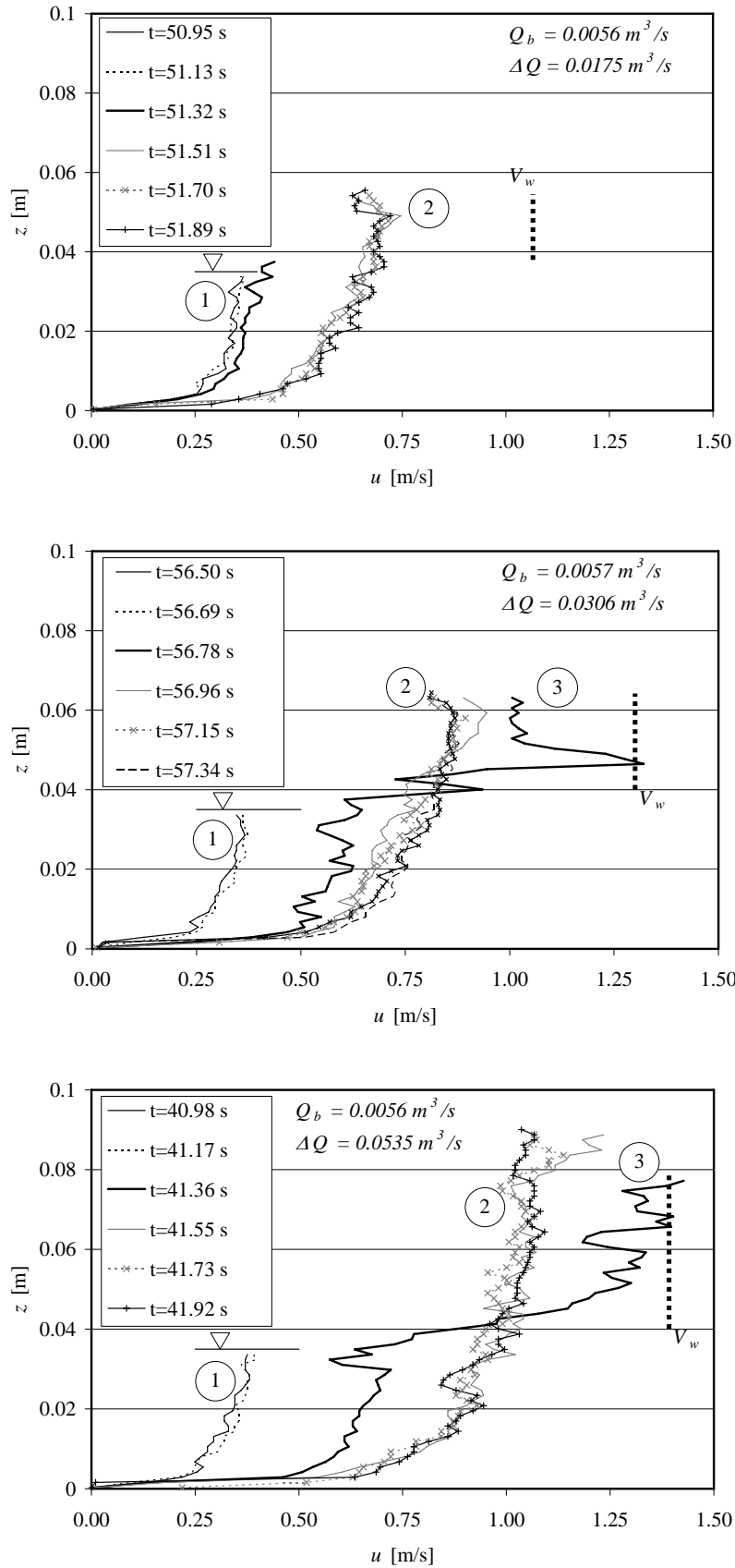


Figure 5-7: Velocity profiles during the passage of the wave front for different scenarios in the prismatic reference configuration. (1), (2) and (3) according Figure 5-6.

5.4 *Shape of the wave front and secondary waves*

5.4.1 Detection and measurement methods

The shape at the wave front and secondary waves (Ondes de Favre) have been observed and reported for all tests by filming¹ laterally in the outlet reach the flow through a transparent channel window of 0.75 m length. The centre of the observation window was located at the channel distance $x = 29.3$ m. Illumination of the flow allowed to get shadow effects for detecting well the flow depths before, during and after the wave front. Thanks to a regular grid on the transparent wall, the flow depths could be determined with a precision of ± 0.0025 m.

5.4.2 Observations of the wave front shape and secondary waves in the prismatic configuration

From the 30 different positive surge waves in the prismatic configuration, secondary waves have been observed in 15 cases (Table 5-6) at the observation window. In 2 other cases, breaking of the first undulation has been observed. This first, breaking undulation was however followed by a wave train. In 6 cases, the wave front showed highly breaking flow conditions and was not followed by any undulation. In the last 7 cases, neither secondary waves nor breaking flow conditions have been observed (Table 5-6). These last 7 cases were characterized by a small and sudden increase of the water level at the wave passage.

Highly breaking conditions were observed in the prismatic configuration for depth ratios higher than $h_2/h_1 \cong 1.6$ respectively for surge Froude numbers higher than $Fr_s \cong 1.5$. Breaking of the first undulation was observed at $h_2/h_1 \cong 1.42$ respectively $Fr_s \cong 1.32$. For ratios $h_2/h_1 < 1.1$ respectively $Fr_s < 1.06$, no secondary waves have been detected. These values are in the range reported in Table 2-12. The value of $h_2/h_1 \cong 1.42$ describing the limit of the breaking of the first undulation is nevertheless slightly higher compared to the values of Favre (1935; $h_2/h_1 \cong 1.28$) or Benet and Cunge (1971; $h_2/h_1 \cong 1.29$). This is probably due to the initial velocity of the baseflow. For a baseflow having Froude number of 0.1, Benet and Cunge (1971) observed also a higher value of $h_2/h_1 \cong 1.37$.

¹ Sony Digital Handycam Carl Zeiss Vario-Sonnar DCR-TRV15E (24pictures/second) with wide angle.

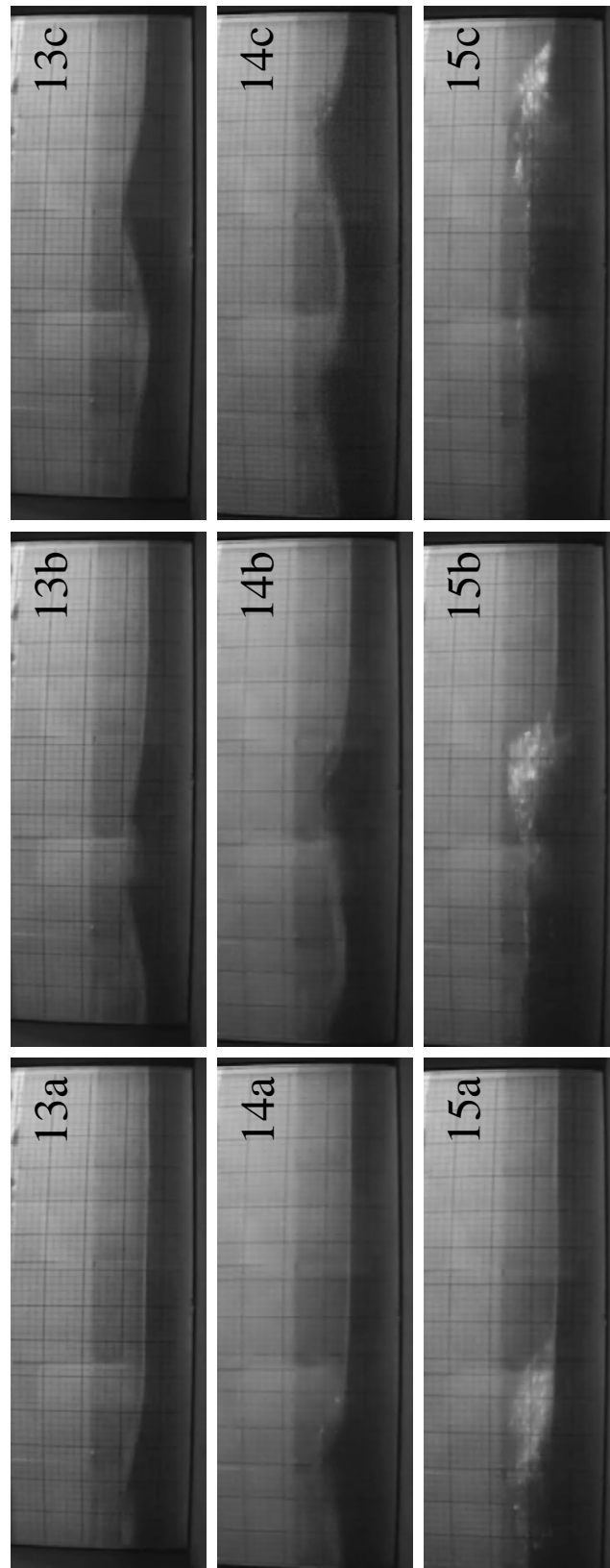


Figure 5-8: Surge waves with secondary waves (13a to 13c; 14a to 14c) and without secondary waves (15a to 15c) for scenarios 13, 14 and 15 (see Table 5-6). a, b and c correspond to the times $t_a = 0.0$ s, $t_b = 0.125$ s and $t_c = 0.250$ s.

Table 5-6: Summary of flow conditions at the front observed in the prismatic configuration. Cases **s**: secondary waves; Cases **s_b**: secondary waves with breaking of first undulation; Cases **b**: highly breaking conditions. h_1 (just before) and h_2 (just after the wave front) are representative water levels measured in the downstream half of the experimental channel close to the location of the video camera.

Scenario	1	2	3	4	5	6	7	8	9	10	11	12	13	14	15
Q_b [l/s]	6.0	5.9	6.0	6.2	5.9	10.7	10.7	10.7	10.7	10.7	19.2	19.1	19.0	18.9	18.7
Q_{total} [l/s]	12.5	17.0	23.6	36.7	59.4	17.2	21.8	28.3	41.1	64.1	25.7	30.2	36.5	49.2	71.8
Fr_s [-]	1.19	1.32	1.48	1.73	2.13	1.12	1.20	1.32	1.50	1.78	1.08	1.13	1.20	1.33	1.53
h_2/h_1 [-]	1.26	1.43	1.65	2.00	2.55	1.16	1.27	1.43	1.67	2.07	1.10	1.17	1.27	1.44	1.72
Observ.	s	(s)_b	b	b	b	s	s	s	b	b	-	s	s	s_b	b
Scenario	16	17	18	19	20	21	22	23	24	25	26	27	28	29	30
Q_b [l/s]	34.7	34.8	34.4	34.9	35.0	49.1	48.7	48.8	48.7	48.6	62.3	61.0	60.8	61.0	60.9
Q_{total} [l/s]	41.1	45.7	51.8	64.9	87.7	55.5	59.6	66.0	78.5	100.8	68.6	71.8	77.9	90.6	112.9
Fr_s [-]	1.05	1.07	1.12	1.19	1.31	1.03	1.05	1.08	1.13	1.22	1.01	1.04	1.06	1.10	1.18
h_2/h_1 [-]	1.06	1.10	1.15	1.25	1.42	1.04	1.07	1.11	1.18	1.29	1.02	1.05	1.08	1.14	1.24
Observ.	-	s	s	s	s_b	-	-	s	s	s	-	-	-	s	s

5.4.3 Observations of the wave front shape and secondary waves in the macro-rough configurations

In configurations including macro-roughness elements, the surge wave propagation is affected by the storage of water in the cavities and the partial reflection of the surge wave front in the widened channel sections (Figure 5-9). The surge wave front and secondary waves are two-dimensional in the straight channel and become three-dimensional in the widenings since the streamwise velocities are higher in the extension of the main channel than in the cavities. The combination of all these effects results in an attenuation of the surge wave speed and front height as well as in the reduction respectively disappearance of the secondary waves along the macro-rough channel.

Roughness elements along the macro-rough reach modify the wave front shape and the secondary waves. Compared to the corresponding scenarios of the prismatic channel, following changes can be observed in the outlet reach (observation window):

- 1) Either, the highly breaking surge wave front observed in the prismatic configuration changed into a wave front followed by secondary waves for the configuration including macro-roughness elements.
- 2) Or the highly breaking surge wave front (prismatic configuration) changed into a (sudden) rise of the water surface. No secondary waves are observed anymore.

- 3) Or the non breaking wave front followed by secondary waves (prismatic configuration) changed into a (sudden) rise of the water surface at the observation window. No secondary waves are observed anymore.

Appendix 5-2 summarizes the observations about the breaking of the wave front and the secondary waves in the macro-rough configurations in comparison to the prismatic reference for all tested scenarios.

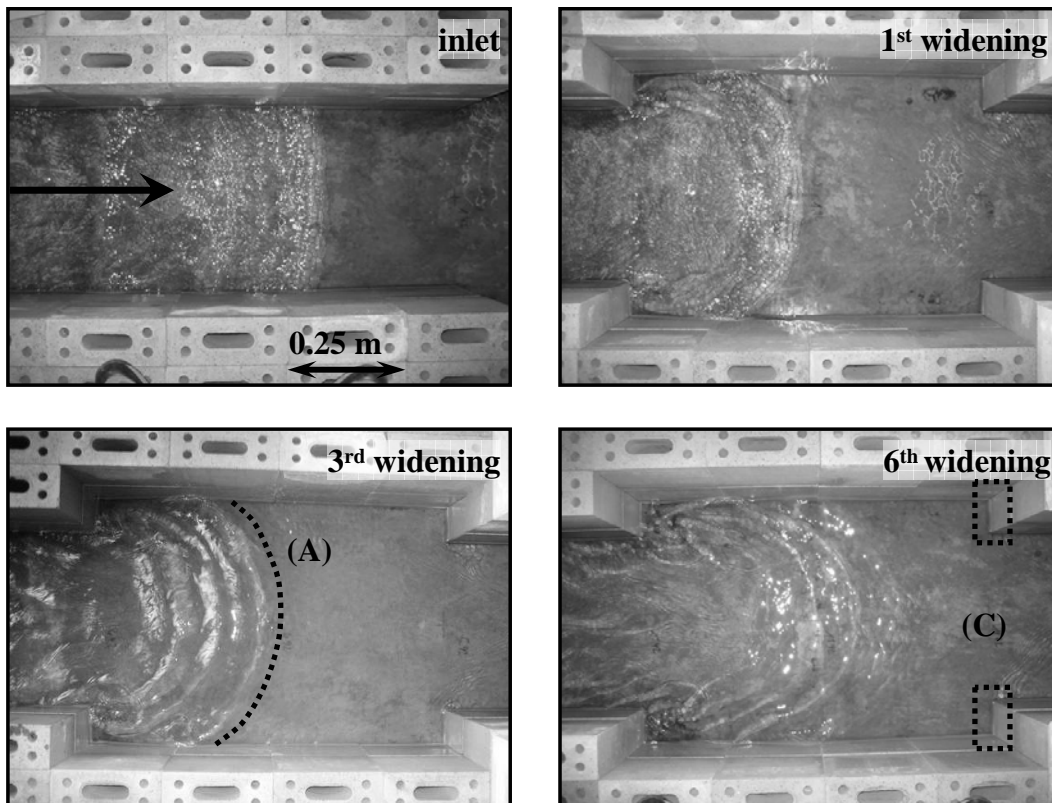


Figure 5-9: Positive surge wave from upstream for scenario 3 in configuration 211 ($L_b = 1.0$ m; $L_c = 0.5$ m, $\Delta B = 0.1$ m. $Q_b = 6.38$ l/s; $Q_{total} = 24.93$ l/s. (A) Deformation and (C) reflection of surge wave.

5.4.4 Comparison of the present with other experiments

The amplitude of the secondary waves h'_{max}/h_1 has been compared with the experiments of Favre (1935), Treske (1994) and Soares and Zech (2002) (Figure 5-10; see also Figure 2-19). Only channels with rectangular channel sections of constant width and experiments of positive surge waves from upstream have been considered. In the present experiments, the level of the trough of the secondary wave was not obvious to detect on films and the value of the difference ($h'_{min}-h_1$) is often very low. Figure 5-10 shows in general good agreement with other experiments, nevertheless with relatively high scattering due to the precision of detection of the characteristic values h_1 , $h_{2,max}$, $h_{2,min}$ and h_2 on the films. The values h'/h_1 are aligned as the surge Froude number Fr_s is calculated from the flow depths h_1 and h_2 before and after the surge wave front (eq. 2.59).

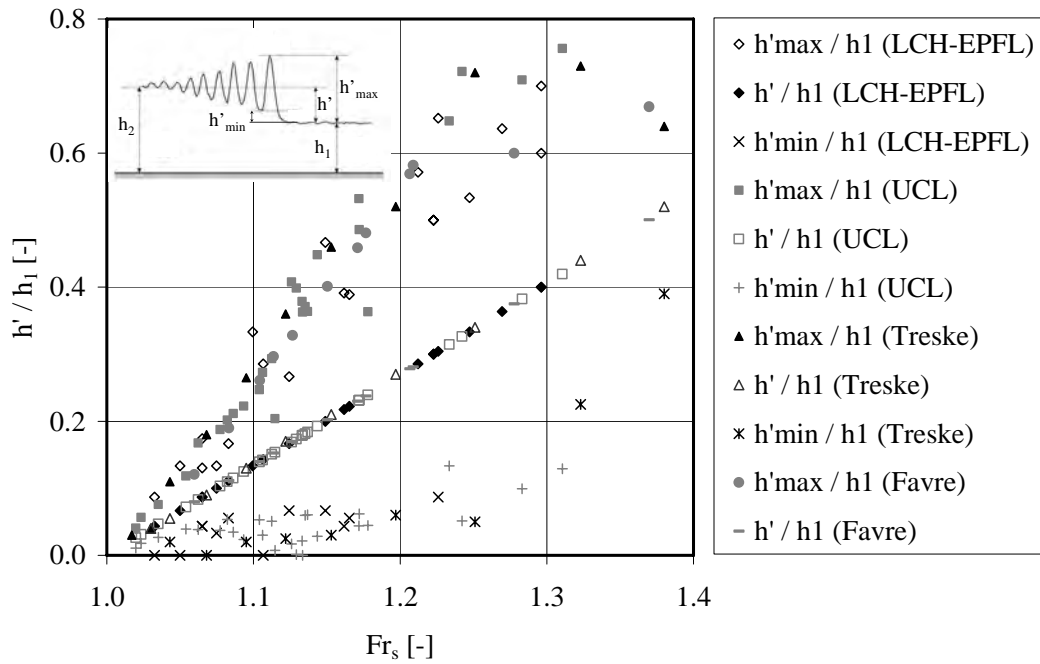


Figure 5-10: Secondary wave characteristics h'/h_1 ; h'_{max}/h_1 and h'_{min}/h_1 of several experimental investigations as a function of the surge Froude number Fr_s .

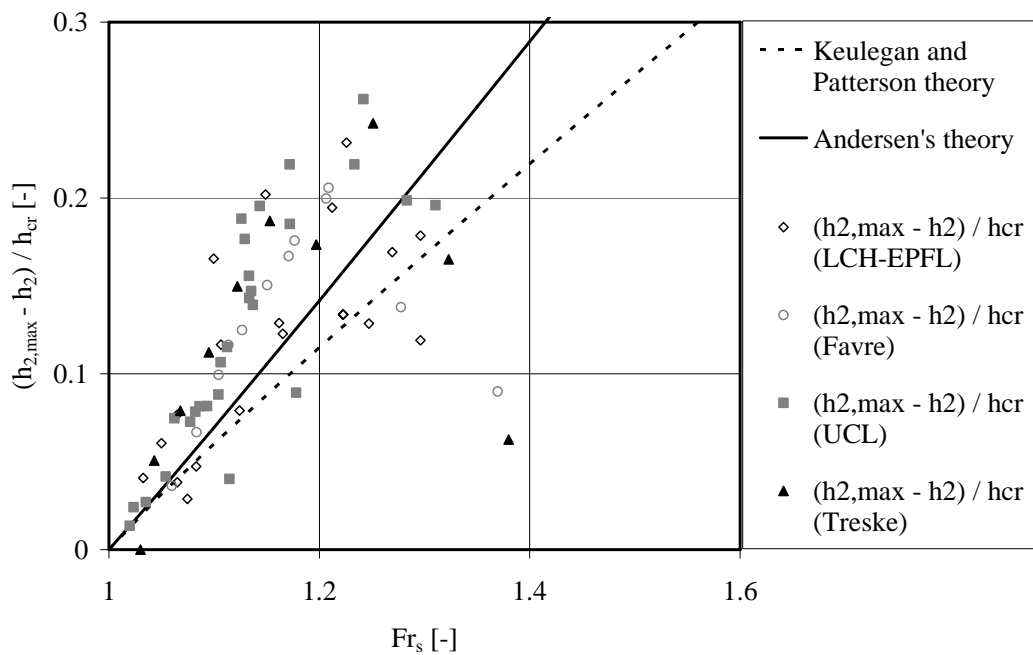


Figure 5-11: Amplitude of the first undulation $(h_{2,max} - h_2)/h_{cr}$ of several experimental investigations as a function of the surge Froude number Fr_s .

Figure 5-11 compares the wave amplitude of the first undulation defined as $(h_{2,max} - h_2)$ of the different experimental works to the correlation of Keulegan/Patterson's respectively Andersen's theory. As shown by Chanson (1996), both theories slightly underestimate the wave amplitude of the first undulation. The critical depth value h_{cr} in Figure 5-11 is obtained by combining the equations for Fr_s (eq. 2.59) and V_w (eq. 2.49) and by setting $Fr_s = 1$. The critical depth value becomes:

$$h_{cr} = \frac{1}{2} \frac{h_2}{h_1} (h_1 + h_2) \quad (\text{eq. 5.5})$$

Water level measurements with ultrasonic sensors did not give precise values of $h_{2,max}$ and $h_{2,min}$ due to the high water surface curvature. The position of the wave crests as a function of time was however detected without difficulty and the spacing of the wave crests is calculated by multiplying the time between to wave crests with the observed absolute celerity of the surge wave front as:

$$e = (t_{II} - t_I) \cdot V_w \quad (\text{eq. 5.6})$$

where t_{II} respectively t_I are the times of the first and second wave crest of the wave train and V_w the absolute observed front wave speed.

The relative spacing e/h' of the wave crests decreases as a function of the relative surge wave height. For the prismatic reference configuration, the observed spacing between the first and second crest is stabilized at ultrasonic sensor 13 since no major difference can be observed compared to ultrasonic sensor 21. At ultrasonic sensor 5, the distance between the first two wave crests is not established yet especially for relative surge wave heights $h'/h_1 < 0.25$. The relative spacing of well established secondary waves observed in the laboratory flume of the present study is given by:

$$\frac{e}{h'} = 4.5 \left(\frac{h'}{h_1} \right)^{-5/4} \quad (R^2 = 0.96) \quad (\text{eq. 5.7a})$$

Considering also the data of Favre (1935) the formula becomes:

$$\frac{e}{h'} = 4.5 \left(\frac{h'}{h_1} \right)^{-7/5} \quad (R^2 = 0.98) \quad (\text{eq. 5.7b})$$

5.4.5 Conclusions for the shape of the wave front and secondary waves

Secondary waves are accompanying the positive surge waves from upstream when the ratio of the flow depth after and before the surge is higher than 1.1. Their height increases until the value h_2/h_1 reaches 1.42 for which the first undulation is breaking. For higher values, the relative height of secondary waves decreases rapidly until they disappear completely for highly breaking flow conditions which are reached for a value of $h_2/h_1 \cong 1.6$.

The characteristics of the secondary waves observed in the prismatic channel are qualitatively and quantitatively in agreement with other experimental investigations and field studies of the same phenomenon. The empirical formula (eq. 5.7a) describes the relative spacing of succeeding crests of the wave train. The height of secondary waves in prismatic channels (rectangular section) is determined graphically from Figure 5-10.

For the macro-rough configurations, the shape of the surge wave front is modified from breaking into a smooth front followed by secondary waves or from a smooth front followed by secondary waves into a sudden increase of the water level only.

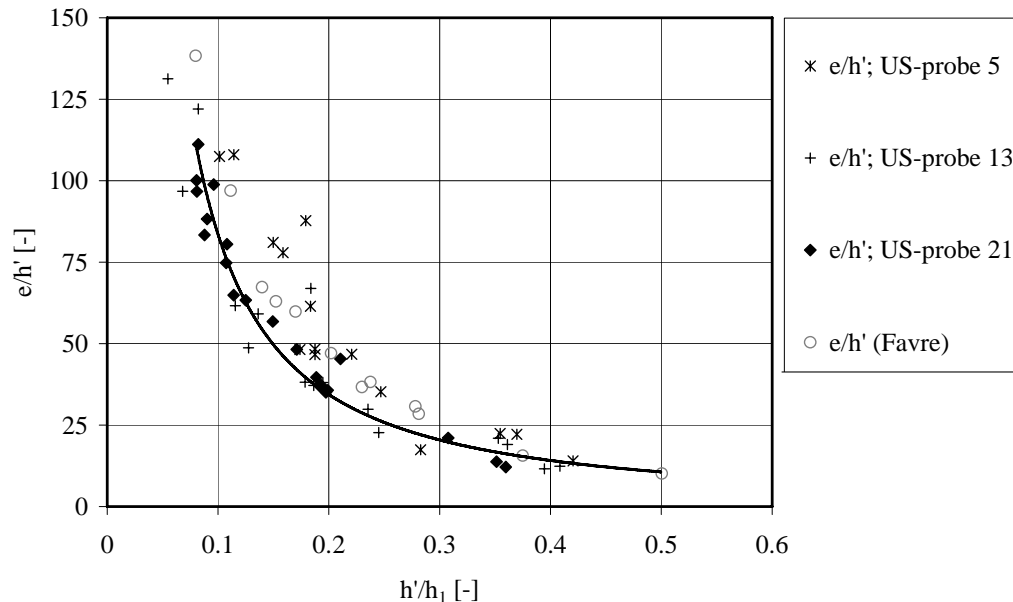


Figure 5-12: Relative spacing of the crests of secondary waves as a function of the relative surge wave height. Ultrasonic sensor 5, 13 and 21 are located at the channel sections $x_5 = 0.42$ m, $x_{13} = 12.42$ m and $x_{21} = 24.42$ m. Position $x = 0$ m corresponds to the end of the inlet reach.

5.5 Unsteady flow data analysis

For the analysis of special aspects such as the partial reflection of positive and negative surge waves at the outlet section (§ 5.3) or the flow conditions at the wave front (§ 5.4), the level measurement data have been extracted manually. Automatic identification of characteristic values of the surge wave was hoped by an adequate data treatment. The best solution found after trials on test data sets includes following steps:

- 1) Initial smoothing of the level measurements by a moving average over 5 values (=0.15625 seconds)
- 2) Elimination of superposed surface variations by the use of a moving maximum (321 values = 10 seconds, Figure 5-13).
- 3) Second derivation (maximum curvature) of the curve obtained under 2)
- 4) Summing up of the positive values of the curve obtained under 3)
- 5) Derivation of the curve obtained under 5).

The two maximum values identified by step 5), corrected by +6 s respectively -6 s, correspond to the arrival of the positive respectively the end of the negative surge wave front at a given location. The correction is necessary due to a shift caused by moving

maximum and the mathematical operations. The same steps apply also to the determination of the end of the positive respectively the arrival of the negative surge wave front. The only difference consists in summing up the negative values of the curve obtained under 3) instead of the positive ones. All couples $h-t$ of the curve presented in Figure 5-14 are identified from this procedure.

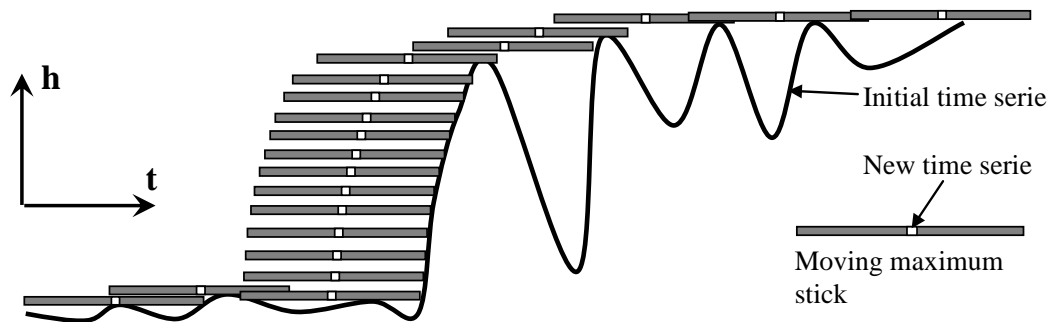


Figure 5-13: Principle of the moving maximum for elimination of secondary surface variations. The moving maximum is calculated such as a moving average by assigning to a time t_i always the maximum value contained in the interval $[t_i - 5s ; t_i + 5s]$.

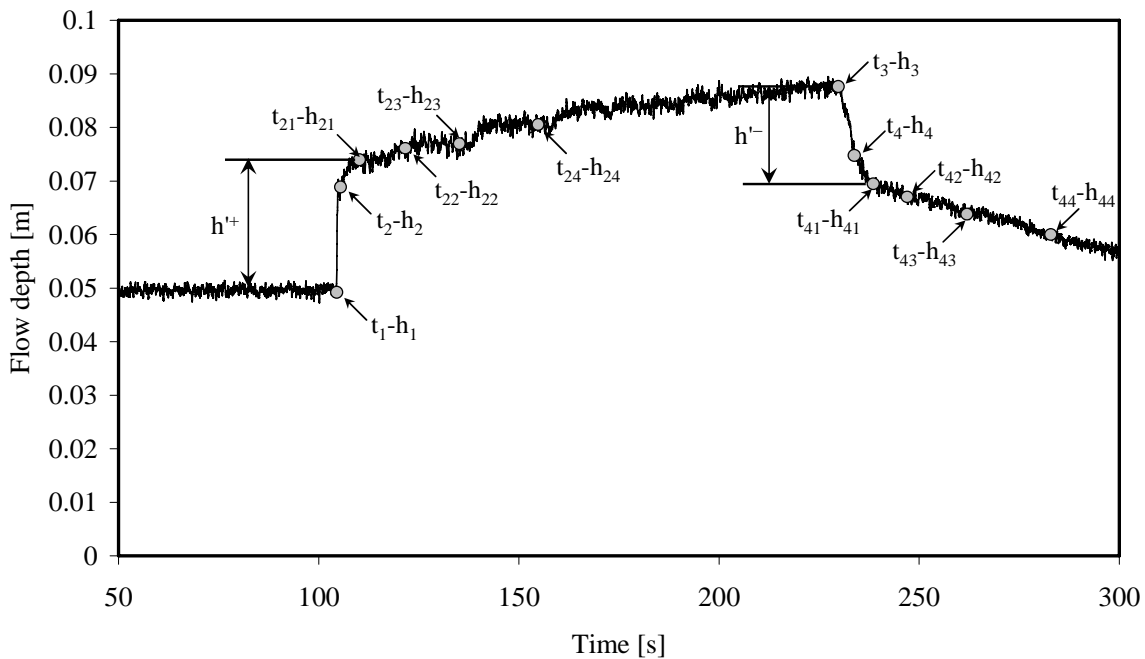


Figure 5-14: Couples $h-t$ of a scenario in the prismatic configuration. t_1, t_2, t_3 and t_4 identified by the fully automatic procedure, t_{31}, t_{32}, t_{33} and t_{34} respectively 5, 10, 15 and 20 seconds after t_2 and t_{41}, t_{42}, t_{43} and t_{44} respectively 5, 10, 15 and 20 seconds after t_4 .

Despite this sophisticated data treatment, the unsteady flow tests were difficult to analyse, especially in the macro-rough configurations characterized by very weak levelling signals (Figure 5-15).

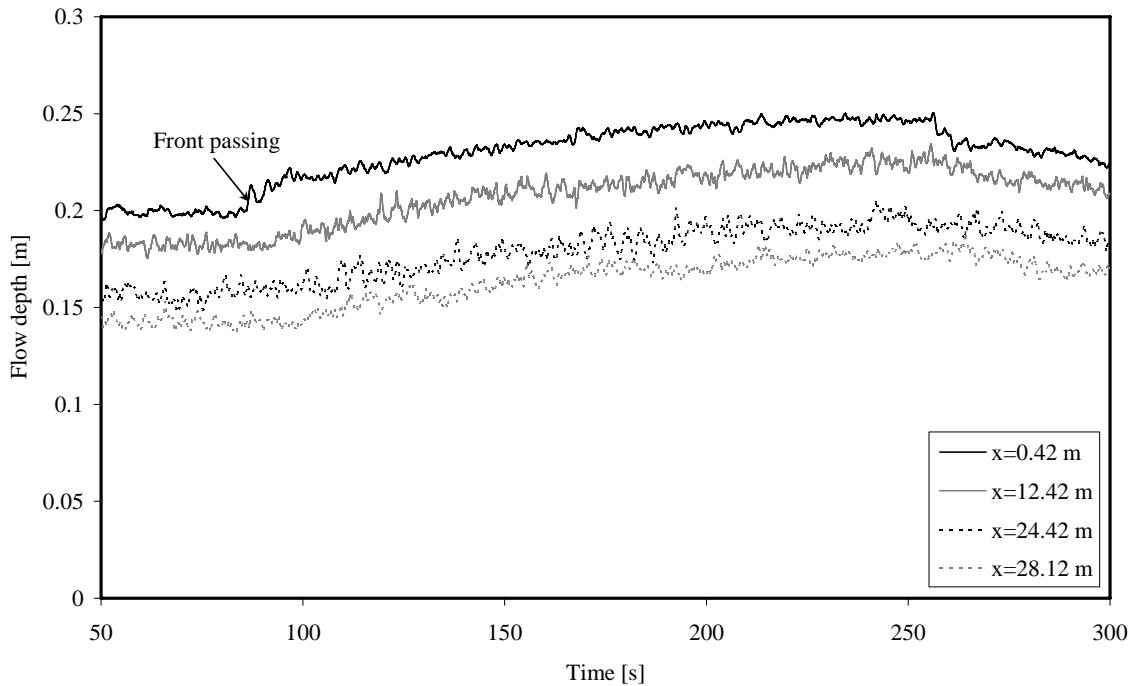


Figure 5-15: Example of a time series with weak leveling signals. Configuration 423, scenario 23. The passage of the wave front is well detectable only at the beginning of the macro-rough channel ($x = 0.42$ m).

Averaging is not an adequate solution neither since important information on the wave front is lost. Therefore it was necessary to pass from a fully automatic to a semi-automatic procedure including the following steps:

- 1) Initial smoothing of the level measurements by a moving average over 5 values ($=0.15625$ seconds)
- 2) Determination of the begin of the wave front t_l for a sensor at the end of the inlet reach and for a sensor in the outlet reach or close to the outlet reach (manually). Calculation of the average absolute wave celerity $V_w = U + c$.
- 3) Calculation of the time when the wave front passes at the different positions along the channel assuming a constant celerity (front tracking). Within the macro-rough channel reach, the absolute wave front celerity was found more or less constant which is explained by a Froude number close to 0.5. For most of the tests, the assumption of constant absolute wave celerity is acceptable along the 38.33 m long channel (Figure 5-17).

The water levels are then identified according to Figure 5-16 from which the height of the wave front as well as the evolution of the water level in the wave body is described. The exact height of the wave front can be identified only in the prismatic reference. In all macro-rough channel configurations, due to surface wave reflections and super-position as well as due to its attenuation, the wave front height is impossible to isolate and must be estimated as $h'^+ = h_{21} - h_1$ (positive surge) respectively as $h'^- = h_3 - h_{41}$.

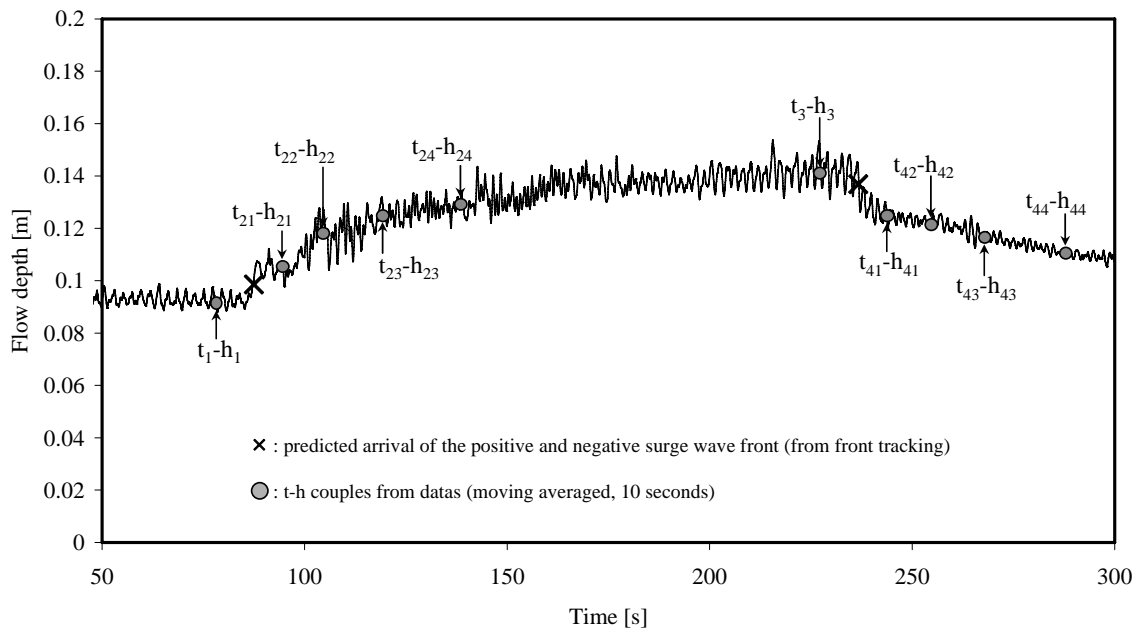


Figure 5-16: Finally extracted couples $h-t$ from the semi-automatic procedure. t_1 , t_3 are 9 seconds before the predicted arrival time of the wave front. t_{21} , t_{22} , t_{23} , t_{24} respectively 7, 17, 32 and 52 seconds after the predicted arrival. Idem for t_{41} , t_{42} , t_{43} , t_{44} . Example of a non-prismatic configuration.

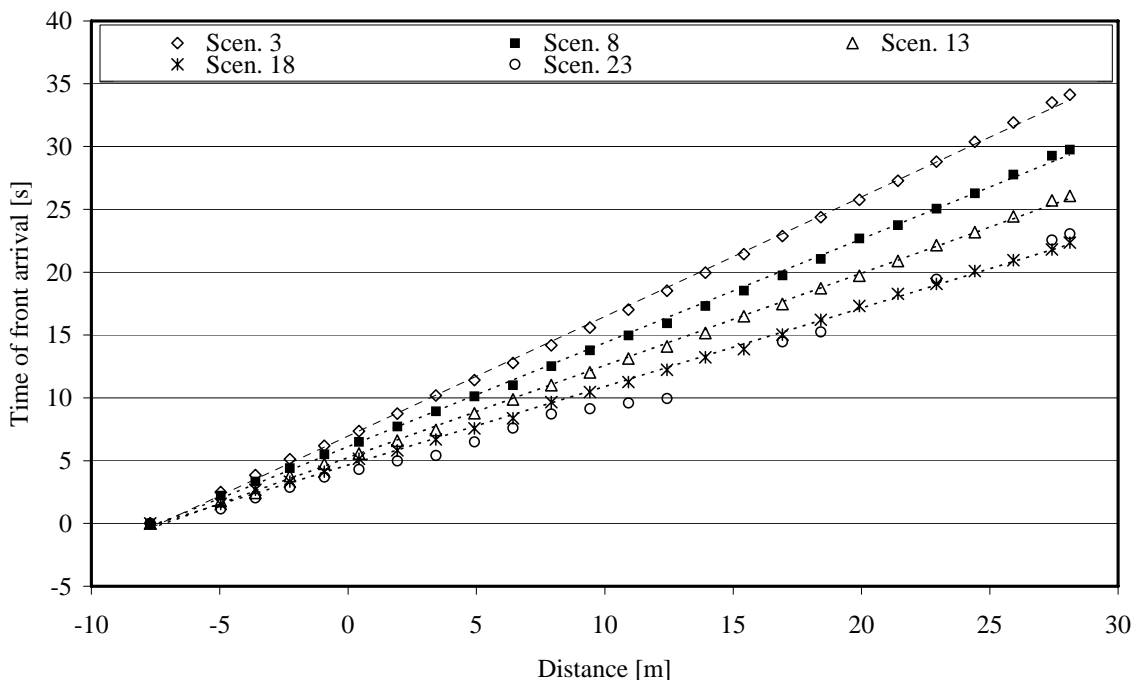


Figure 5-17: Characteristic lines for the positive surge wave front for configuration 222 (Scenarios 3, 8, 13, 18 and 23). The absolute celerity of the surge wave front of scenario 23 is not correctly detected.

The times t_1 and t_3 are shifted 9 seconds before the predicted arrival of the wave front (Figure 5-16, \times): 5 s are necessary since the extracted water levels are calculated from the moving average over 10 s and 4 s are considered as security to exclude the influence of the wave front. The times t_{21} and t_{41} are shifted 7 seconds after the predicted arrival of the wave front: 5 s due to the moving average and 2 s as security. Security is reduced behind the wave front in order to be as close to the wave front as possible and also only little influenced by the further decrease of the water level following the front.

For the prismatic reference, all 30 scenarios have been analysed. The analysis of the macro-rough configuration has been done systematically for scenarios 3, 8, 13, 18 and 23.

5.6 *Characteristic values of positive and negative surge waves from upstream*

5.6.1 Decrease of the observed absolute wave celerity

The absolute celerity $V_w = U + c$ is exemplarily shown as a function of the dimensionless wave parameter $HP_I = (Q_b + Q_w) / Q_b$ in Figure 5-18 (positive surge waves from upstream) and Figure 5-19 (negative surge waves from upstream) for the macro-rough configurations 221 to 224 and the randomly generated macro-rough configuration. All other tests are shown in the Appendix 5-1. The comparison is based on the discharges since they are practically the same for corresponding scenarios whereas flow depths are influenced by backwater-curve effects in the macro-rough configurations. Alternatively, a comparison based on the upstream surge Froude number Fr_s , calculated at the end of the inlet reach, is also shown in Appendix 5-1.

The analysis of the absolute celerity $V_w = U + c$ in the configurations with macro-roughness at the banks reveals the following (Figure 5-18, Figure 5-19 and Appendix 5-1):

- The absolute wave celerity of the positive surge waves $V_w^+ = U + c^+$ is decreased in all macro-rough configurations compared to the prismatic one.
- The decrease generally increases with increasing ΔB and decreasing L_c for a given length of the cavity L_b .
- The asymmetric configurations 112 asy., 121 asy. and 212 asy. have practically an identical decrease of V_w^+ as the corresponding symmetric configurations 112, 121 and 212. The randomly generated macro-rough configuration has a decrease similar to the one of configuration 222, which can be considered as the “average” axisymmetric macro-rough configuration.
- The absolute wave celerity of the negative surge waves $V_w^- = U + c^-$ is decreased compared to the prismatic reference configuration too.
- The absolute wave celerity of the negative surge waves is more difficult to identify and some erroneous values have been skipped from the figures (e.g. 144 scenarios 13, 18 and 23).

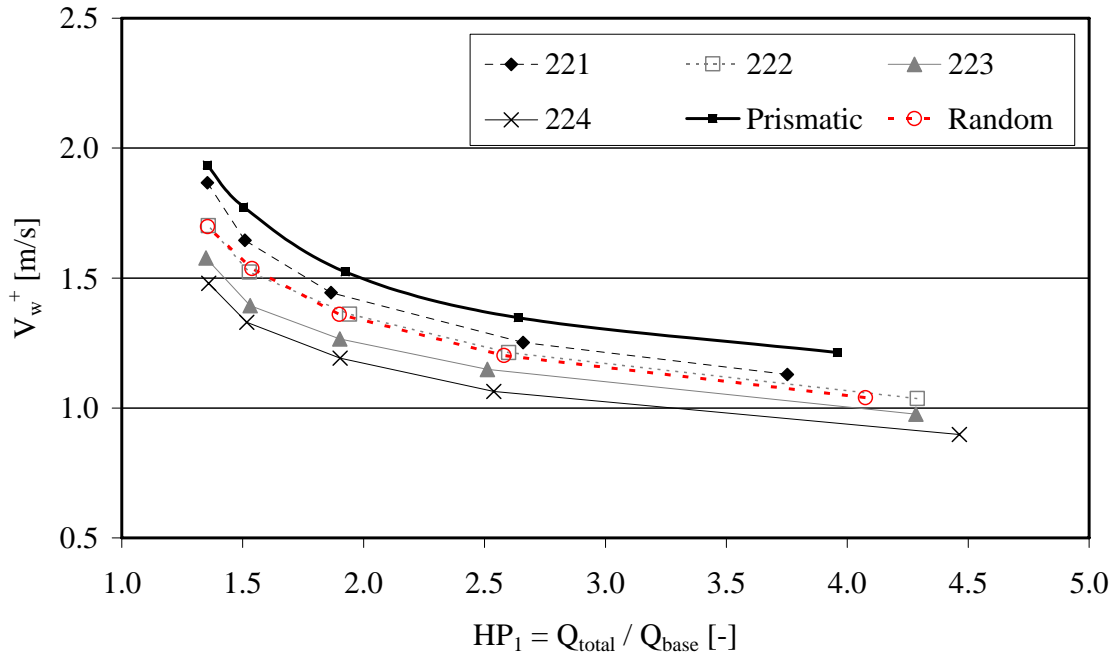


Figure 5-18: Observed absolute wave celerities V_w^+ (positive waves from upstream) as a function of the dimensionless wave parameter $HP_1 = Q_{total} / Q_b$ for the macro-rough configurations 221 to 224 and the randomly generated macro-rough configuration. The macro-rough configurations are compared to the prismatic reference.

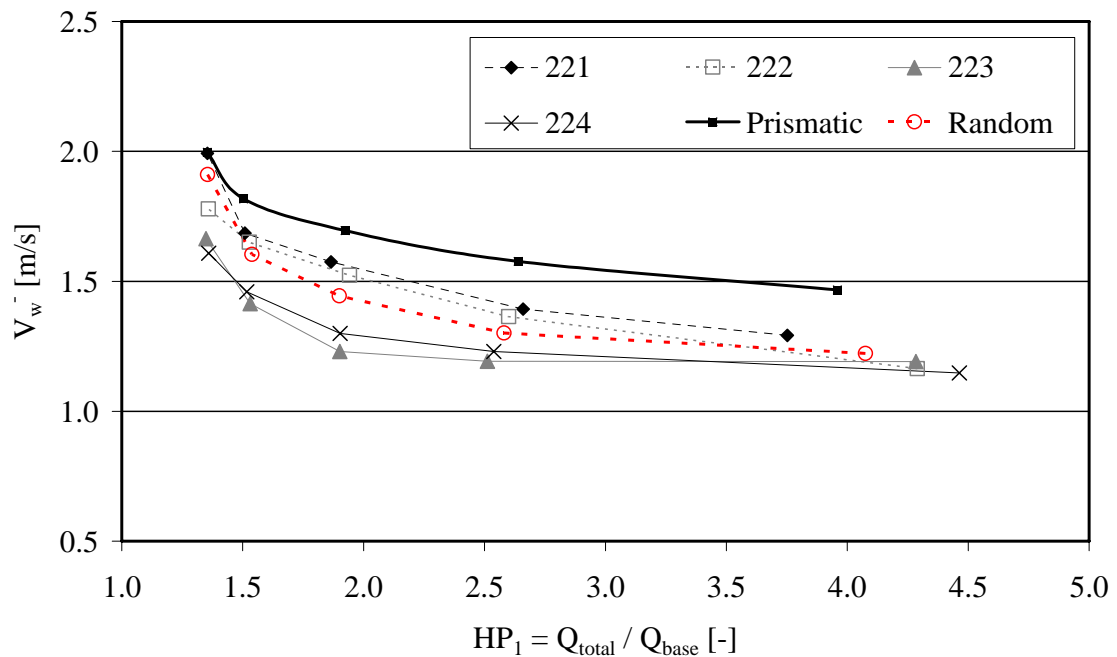


Figure 5-19: Observed absolute wave celerities V_w^- (negative waves from upstream) as a function of the dimensionless wave parameter $HP_1 = Q_{total} / Q_b$ for the macro-rough configurations 221 to 224 and the randomly generated macro-rough configuration. The macro-rough configurations are compared to the prismatic reference.

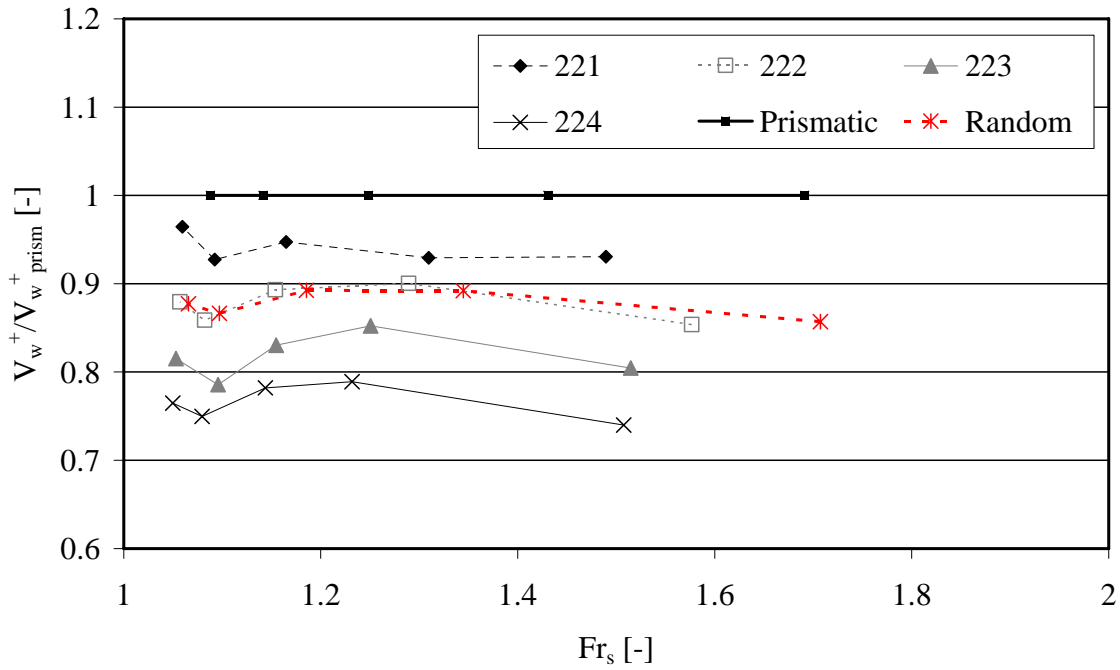


Figure 5-20: Absolute wave celerity of the macro-rough configurations relative to the prismatic reference $V_w^+ / V_w^+_{prism}$ as a function of the upstream surge Froude number for the macro-rough configurations 221 to 224 and the randomly generated macro-rough configuration.

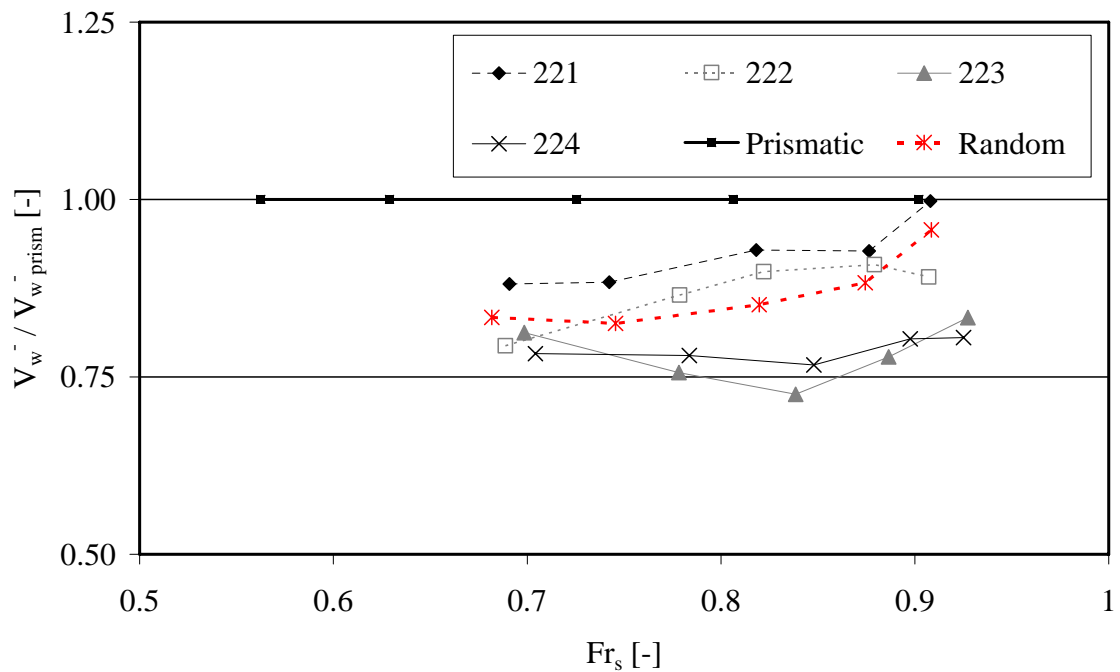


Figure 5-21: Absolute wave celerity of the macro-rough configurations relative to the prismatic reference $V_w^- / V_w^-_{prism}$ as a function of the upstream surge Froude number for the macro-rough configurations 221 to 224 and the randomly generated macro-rough configuration.

Figure 5-20, Figure 5-21 and Appendix 5-1 compare the ratio $V_w^+ / V_w^{+ prism}$ (absolute wave celerity of the macro-rough configurations relative to the prismatic configuration) of the different macro-rough configurations as a function of the surge Froude number Fr_s . Following points could be noticed:

- The ratio $V_w^+ / V_w^{+ prism}$ (absolute wave celerity of the macro-rough configurations relative to the prismatic configuration) is quite constant for a given geometry and thus independent of the upstream surge Froude number Fr_s .
- The absolute surge wave celerity is more significantly reduced (decreasing values of the ratio $V_w^+ / V_w^{+ prism}$) for increasing ΔB and decreasing L_c .
- Higher scattering occurs for surge Froude numbers close to $Fr_s = 1$. This is due to the difficulty to detect precisely the absolute wave celerity of small surge waves in macro-rough configurations.
- The decrease of V_w^+ ranges between approximately 5% (configurations 141, 241 and 441) and 25% (configurations 114, 214 and 414) compared to the prismatic reference.
- The ratio $V_w^- / V_w^{- prism}$ (absolute wave celerity of the macro-rough configurations relative to the prismatic configuration) is also quite constant for a given configuration except for surge Froude numbers close to $Fr_s = 1$ for which the reduction is less. These cases are characterized by a high baseflow discharge and a small reduction of the discharge due to the generation of the negative surge.
- The decrease of V_w^- ranges approximately around 15% (25% for 114 to 5% for 441) compared to the prismatic reference.

5.6.2 Attenuation of the wave front height

In the prismatic reference configurations, the positive and negative waves are characterized by a sudden increase respectively sudden decrease of the flow depth at the wave front. The sudden change is followed by a more progressive increase/decrease of the flow depth in the wave body until steady flow conditions are reached. The point separating the sudden from the progressive increase/decrease can be clearly seen for the prismatic configuration (Figure 5-3) but is hardly detectable for the macro-rough configurations (Figure 5-4). The height of the surge wave front is characterized by $h'^+ = h_{21} - h_1$ (positive wave, Figure 5-14) and $h'^- = h_3 - h_{41}$ (negative wave, Figure 5-14). Strictly spoken, this wave characteristic only describes the wave front height for the prismatic reference configuration. In the macro-rough configurations h' quantifies an increase/decrease of the mean water level during the first 7 s seconds after the calculated arrival of the wave. Figure 5-22 (positive surge wave) and Figure 5-23 (negative surge wave) show the relative decrease h'_{ds} / h'_{us} of the surge wave front height between a section at the beginning (h'_{us}) and the end (h'_{ds}) of the macro-rough reach for the example of the macro-rough configurations 221 to 224. All other tests are presented in the Appendix 5-1.

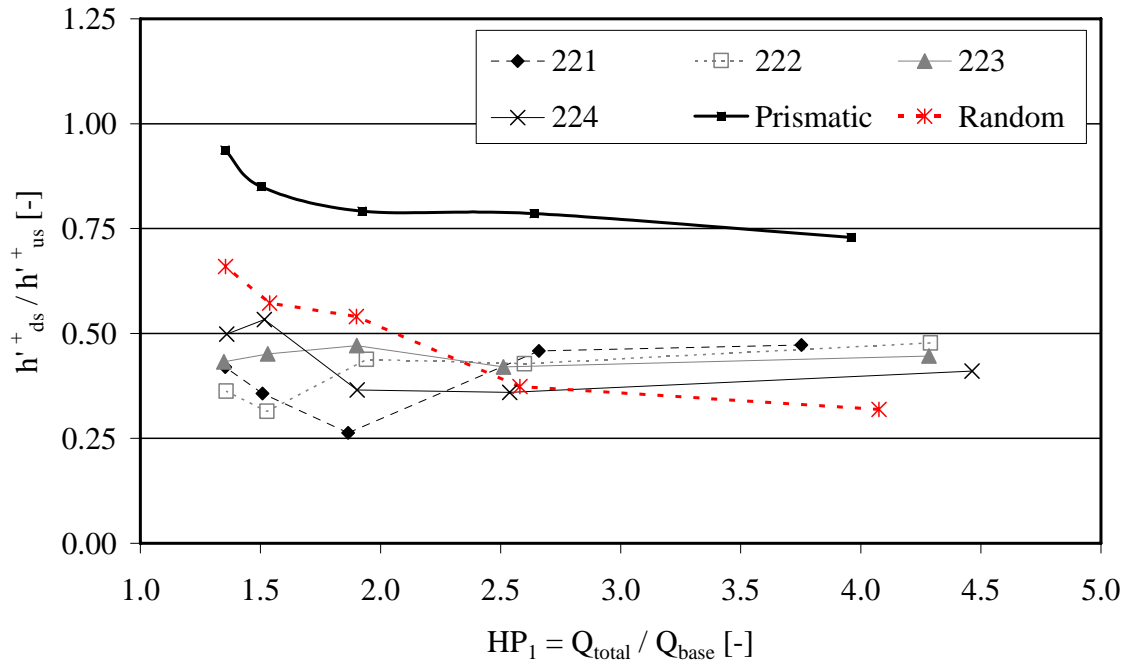


Figure 5-22: Observed surge wave height ratio between the beginning and the end of the macro-rough reach h^+_{ds} / h^+_{us} (positive wave from upstream) as a function of $HP_1 = Q_{total} / Q_b$ for the macro-rough configurations 221 to 224 and the randomly generated macro-rough configuration.

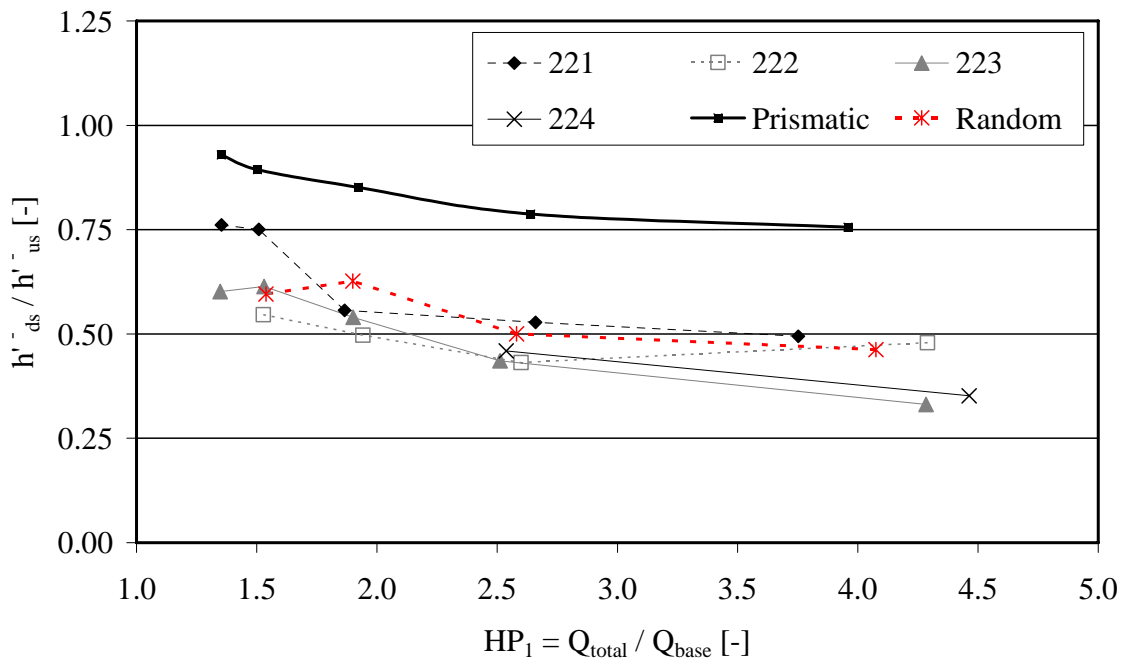


Figure 5-23: Observed surge wave height ratio between the beginning and the end of the macro-rough reach h^-_{ds} / h^-_{us} (negative wave from upstream) as a function of $HP_1 = Q_{total} / Q_b$ for the macro-rough configurations 221 to 224 and the randomly generated macro-rough configuration.

The following can be noticed from Figure 5-22, Figure 5-23 and Appendix 5-1 which describe the attenuation of the surge wave front height along the macro-rough reach for the scenarios 3, 8, 13, 18 and 23:

- For the prismatic configuration, the ratio h'_{ds} / h'_{us} indicates a decrease of 5% to 25% of the surge wave front height along the channel. The decrease results from the combination of bottom slope and friction slope. In the macro-rough configurations, the decrease is significantly higher (up to 70%) except for some scenarios with low ratios Q_{total} / Q_b .
- High scattering is observed for relatively small surges due to the already mentioned difficulty to locate exactly the wave front. Clearly erroneous values identified by the semi-automatic procedure have been skipped.
- A comparable attenuation for the positive surge wave can be observed for the negative surge wave front height along the prismatic channel (h'_{ds} / h'_{us}) ranging between 5% and 25%. The decrease of h'^- ranges between 10% and 75% along the channel for the macro-roughness configurations. The observed decrease is generally less for scenarios with low discharge ratios Q_{total} / Q_b .
- High scattering of h'_{ds} / h'_{us} for scenarios 18 and 23 (having a ratio of $Q_{total} / Q_b < 2$) is observed. Since the upstream surge wave height of these scenarios is quite small (18: ca. 0.022 m; 23: ca. 0.017 m) small errors in the determination of the water levels before and after the front rapidly lead to significant scattering.
- For both, positive and negative surge waves, the asymmetric configurations normally show quite similar behaviour to the corresponding axi-symmetric ones.

The decrease of the positive and negative surge wave heights along the macro-rough channel relative to the prismatic configuration as a function of the upstream surge Froude number Fr_s is shown in Appendix 5-1.

5.6.3 Reasons for the reduction of the absolute wave celerity

The preceding paragraph showed that the average absolute wave celerity V_w^+ (positive wave) and V_w^- (negative wave) are reduced in the macro-rough channel when compared to the prismatic reference configurations. Since the discharges Q_b and Q_{total} are practically the same for corresponding scenarios in macro-rough configurations, basically four reasons should be pointed out for the observed reduction, namely (Figure 5-24):

- The varying **flow depths** along the channel: The macro-roughness elements lead to a backwater-curve in the macro-rough channel. The flow depths increase from downstream to upstream and the mean flow velocities consequently decrease. Since the absolute surge wave celerity V_w is the sum of the mean flow velocity U and the celerity c , a reduction of U theoretically leads to a reduction of V_w , for both, positive and negative waves. However, the decrease of the mean flow velocity might be compensated by the celerity since c increases with increasing flow depths (§ 2.5). Compensation especially occurs at Froude numbers of the baseflow close to 0.5.

- The attenuation of the **height of the surge wave front**: The height of the surge wave front decreases along the channel for both, the prismatic and the macro-rough configurations. The attenuation of the surge wave height leads to a reduction of the celerity c according formula (eq. 2.49).
- The **expansion of the flow** in the widened channel reaches: In the macro-rough channel configurations, the flow can partially or completely expand from B to B' . Furthermore, the local increase of the flow width is coupled with a local increase of the flow depth (subcritical flow through a sudden enlargement). Both effects reduce locally the mean flow velocity.
- The increased **friction**: Macro-roughness elements at the banks increase the flow resistance under steady flow conditions (§ 4.3). According to the theoretical development in § 2.3.3.5, the celerity c should be reduced too. However, reduction becomes only noticeable for high flow resistance f and length L of the control volume.

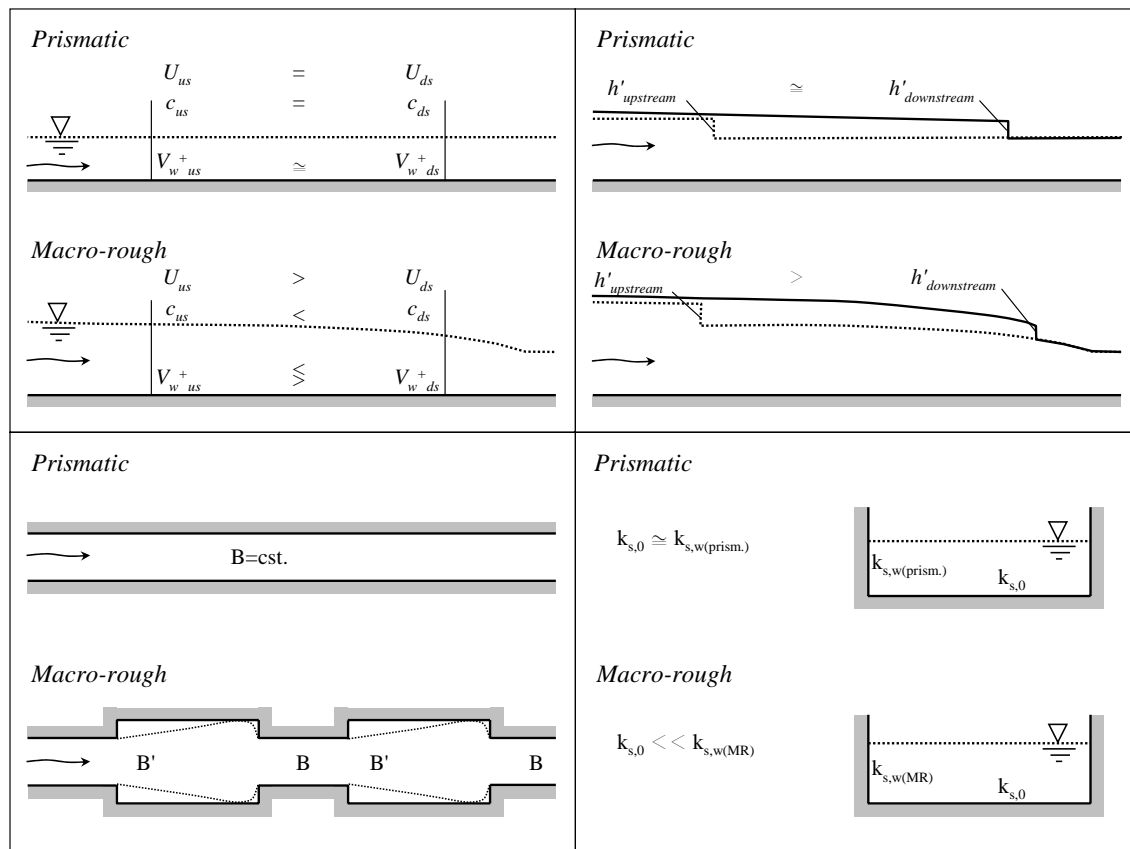


Figure 5-24: Top left: Varying flow depths. Top right: Attenuation of the surge wave height. Bottom left: Expansion of the flow. Bottom right: Increased channel bank roughness.

5.6.4 Distinction of the effects influencing the absolute wave celerity V_w

5.6.4.1 Wave celerity c in the prismatic configuration

In the prismatic case, the flow depth and the channel width are quite constant for a given baseflow discharge. The channel slope is practically balanced by the friction since in this configuration the flow depth is uniform. The above-mentioned effects (increasing flow depth, decreasing surge wave height, flow expansion and friction) are almost negligible along the experimental flume. The celerity c is obtained by subtracting the mean flow velocity U from the observed absolute celerity V_w . Since the width $B = 0.485$ m is constant, the mean flow velocity at baseflow conditions is given by:

$$U_{1,mean}^+ = \frac{\sum_i x_i \cdot (Q_{base}) / B \cdot h_i}{x_{total}} \quad (\text{eq. 5.8})$$

where x_i is the length for which h_i (flow depth measured at sensor i) is representative and x_{total} the sum of all x_i . The celerity of the positive surge is thus estimated as:

$$c_{prism}^+ = V_w^+ - U_{1,mean}^+ \quad (\text{eq. 5.9})$$

The mean flow velocity for the situation before the initiation of the negative surge is calculated assuming steady flow as:

$$U_{1,mean}^- = \frac{\sum_i x_i \cdot (Q_{base} + Q_{wave}) / B \cdot h_i}{x_{total}} \quad (\text{eq. 5.10})$$

where x_i is again the length for which h_i is representative and x_{total} the sum of all x_i . The celerity of the negative surge is thus estimated as:

$$c_{prism}^- = V_w^- - U_{1,mean}^- \quad (\text{eq. 5.11})$$

The observed values of c_{prism}^+ and c_{prism}^- can be compared to the theoretical values either obtained with the simplified (eq. 2.56) or exact (eq. 2.49) formula for the surge wave celerity. Observed values of c_{prism}^+ and c_{prism}^- mean that the celerity c has been obtained from the observed absolute celerity V_w by subtracting the observed mean flow velocity of the baseflow. For calculating the theoretical celerities, the measured flow depths at every ultrasonic sensor are used assuming locally a horizontal and frictionless channel. The values of h_1 and h_{2l} are used for the calculation of the positive surge wave celerity and the values of h_3 and h_{4l} for the calculation of the negative surge wave celerity. The obtained celerities are representative values at the ultrasonic sensors and they take into account the dispersive character of the surge along the prismatic channel. The local celerities are weighted with the distance and thus the theoretical celerity along the whole channel is obtained.

Figure 5-25 compares the theoretical and observed values of c^+_{prism} and c^-_{prism} for all 30 investigated scenarios. The observed values of $c^+_{prism} = V_w^+ - U^+_{1,mean}$ are in good agreement with the theory of the surge wave celerity according (eq. 2.49) found from the combination of the momentum and continuity equation in a rectangular, prismatic, horizontal and frictionless channel. The slight overestimation of the calculated values (c^+_{prism} theoretical) can be explained by the bottom and wall friction of the prismatic reference configuration. The simplified formula $c^+_{prism} = (g \cdot h_1)^{0.5}$ does not allow calculating correctly the observed celerity since the small surge height hypothesis of is not valid for most scenarios.

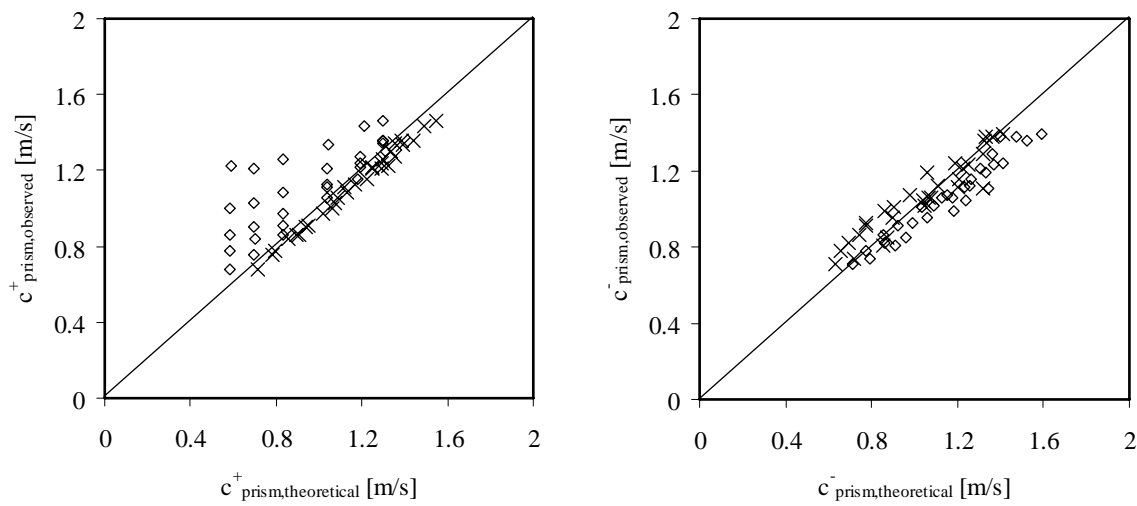


Figure 5-25: Observed and theoretical wave celerities of all investigated positive (left) and negative (right) surge waves from upstream according to the simplified (\diamond , eq. 2.56) and exact (\times , eq. 2.49) formula. All scenarios of the prismatic reference configurations are included in the graphs.

The observed values of $c^-_{prism} = V_w^- - U^-_{1,mean}$ are in quite good agreement with the theory of the surge wave celerity according eq. 2.49 or eq. 2.56. The simplified formula $c^-_{prism} = (g \cdot h_3)^{0.5}$ slightly overestimates the observed surge wave celerity whereas the “exact” formula (eq. 2.49) slightly underestimates it. The relatively high scattering comes from the difficulty to: 1) determine exactly the observed absolute celerity V_w^- and 2) find the exact values of the flow depths h_3 (before) and h_{41} (after the negative surge wave “front”).

The formulas of Zairov and Listrovoy (1983) and Ünsal (1983) have also been applied to the test data. Agreement between them and the measured celerities is significantly less than for formula (eq. 2.49). Furthermore, comparison of the observed celerities with the kinematic wave theory assuming Manning or Chezy relationship (Graf and Altinkar 1996) confirms that the investigated waves do not follow this theory. Finally, the procedure described in Favre (1935) for the calculation of a positive surge from upstream has been applied to some scenarios (3, 8, 13, 18, 23) in the prismatic configuration between the sections $x = 0.42$ m and $x = 24.42$ m. Very good agreement between the experimental data and results from this approach is obtained.

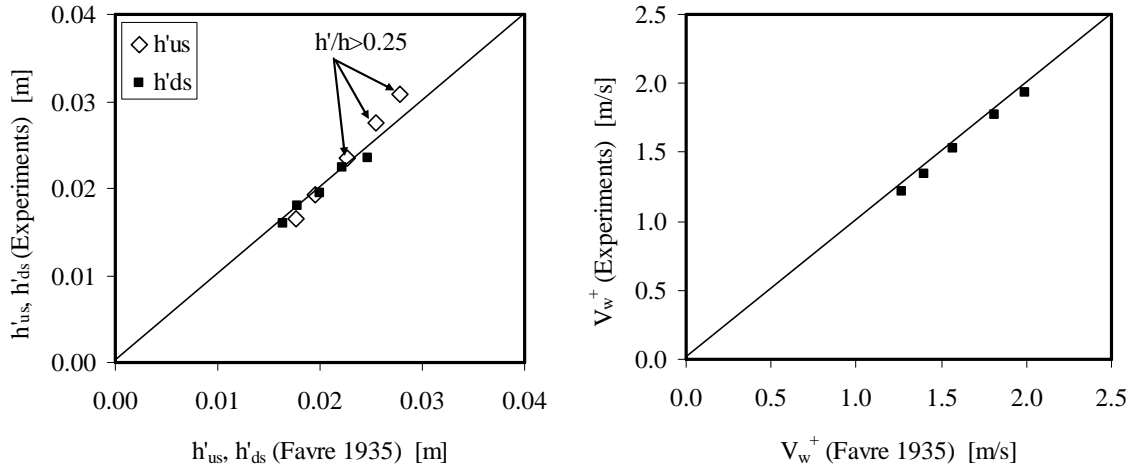


Figure 5-26: Application of the theory of Favre (1935) to the scenarios 3, 8, 13, 18 and 23 of the prismatic configuration (us: section $x = 0.42$ m; ds: section $x = 24.42$ m).

5.6.4.2 Wave celerity in the channel with macro-roughness at the banks

In the macro-rough configurations, the different effects (increasing flow depth, decreasing surge wave height, flow expansion and friction, § 5.6.3) are not any more negligible. They can be separated by subtracting a representative mean flow velocity of the baseflow. The formulas (eq. 5.8) and (eq. 5.9) are applied where B is replaced by B' in the widened reaches. Three techniques can be used to calculate B' assuming different hypotheses, namely:

- 1) The cavities do not to interact with the flow in the main channel. The representative mean flow velocity is calculated using $B' = B = 0.485$ m as for the prismatic configuration (Figure 5-27, above). By this operation, the effect of the backwater-curve is eliminated.
- 2) The flow is assumed to reattach fully to the cavity side walls and the flow width $B' = B + 2\Delta B$ is used along the widened reach (Figure 5-27, middle) to calculate the mean flow velocity. Along the small reaches, $B' = B = 0.485$ m is used. Hence, the effect of the backwater-curve and the expansion of the flow are at least compensated (but probably overcompensated).
- 3) The flow is assumed to expand inside the cavities (Figure 5-27, below). If the cavity is long enough, it reattaches at a distance $L_l = x \cdot \Delta B$ to the cavity side wall.

In the third case, the flow width B' allows calculating the representative mean flow velocity. It is found as described hereafter. First the expansion of the flow, expressed by x , is determined from the results of the steady flow tests:

$$x = \left(\frac{Re_{lim}}{Re_m} + x_0 \right) \left(\frac{L_b}{\Delta B} \right)^{0.18} \quad (\text{eq. 4.47})$$

where $Re_{lim} = 150'000$ and $x_0 = 4.5$. Then, the flow width B_{eff} is calculated for two cases.

If $x \geq L_b / \Delta B$, the flow does not reattach and B_{eff} becomes:

$$B_{eff} = \left(B + \frac{L_b}{x} \right) \tag{eq. 5.12}$$

If $x < L_b / \Delta B$, the flow reattaches to the side wall and B_{eff} becomes:

$$B_{eff} = (B + \Delta B) \left(\frac{x \cdot \Delta B}{L_b} \right) + (B + 2\Delta B) \left(\frac{L_b - \Delta B}{L_b} \right) \tag{eq. 5.13}$$

$B' = B_{eff}$ found by these formulas allows then to calculate the mean flow velocity of the baseflow $U^+_{1,mean}$ respectively $U^-_{1,mean}$ used for the determination of c^+_{MR} respectively c^-_{MR} .

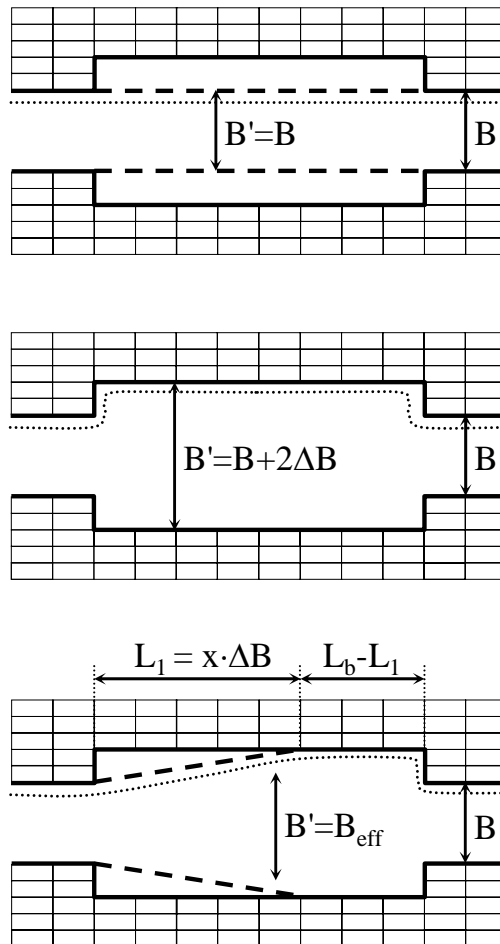


Figure 5-27: Above: Cavity does not contribute to the flow. Middle: Cavity fully contributes to the flow. Below: Cavity contributes partially to the flow.

The observed celerities are compared to the theoretical celerities (eq. 2.49 with h_1 and h_{21} respectively h_3 and h_{41}), calculated by assuming locally horizontal and frictionless channel. Since the celerities are calculated locally at the ultrasonic sensors measuring h_i , they are weighted with the distance x_i such as in the prismatic configuration.

When no expansion of the flow is considered ($B' = B$, Figure 5-28), the observed positive and negative celerities are significantly smaller than the theoretical ones from the flow depths at the wave front (eq. 2.49). This is not surprising since the subtracted mean flow velocity of the baseflow is overestimated for most of the geometrical configurations.

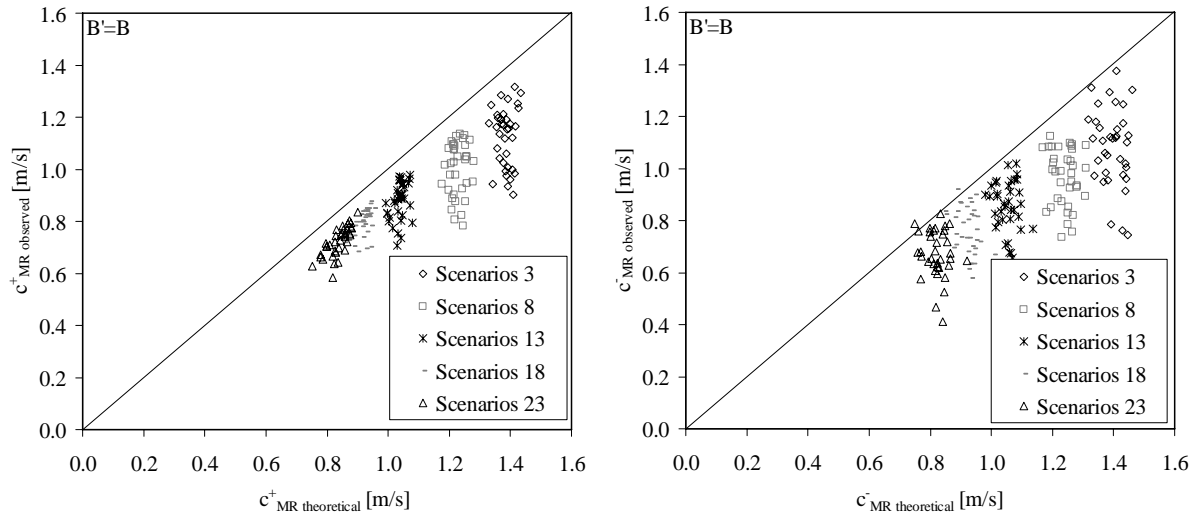


Figure 5-28: Positive (left) and negative (right) surge wave celerities after subtraction of the mean flow velocity with the assumption that the cavities do not contribute to the flow.

When the total expansion is considered ($B' = B + 2\Delta B$, Figure 5-29), the observed positive and negative celerities are closer to the theoretical ones (eq. 2.49 with h_1 and h_{21} respectively h_3 and h_{41}) since the subtracted mean flow velocity U_1 is significantly decreased. However, in general the observed celerities remain below the theoretical ones. Thus, even under the assumption of a total expansion of the flow, the observed celerities are smaller than the theoretical ones calculated with eq. 2.49. Macro-rough flow resistance and other complex phenomena (partial reflections, surface waves) consequently contribute to the decrease of the surge wave celerity c^+ and c^- .

A partial expansion in the widened channel reaches according to the conceptual model (eq. 5.12 and eq. 5.13) seems to be the most reasonable approach. The celerities obtained from this assumption are between the ones obtained from the assumptions $B' = B$ and $B' = B + 2\Delta B$ respectively (Figure 5-30). For some geometrical configurations, the observed macro-rough positive and negative celerities are close to the calculated ones from the flow depths. For other geometrical configurations, the observed celerities are reduced by almost 40%. However, for most scenarios and configurations, the observed celerities are reduced between 5% and 20% for the positive and between 0% and 20% for the negative surge waves from upstream. The difficulty to identify the absolute wave celerities for scenarios with high baseflow discharge leads to a few points close to the line indicating a decrease of 40% (negative wave).

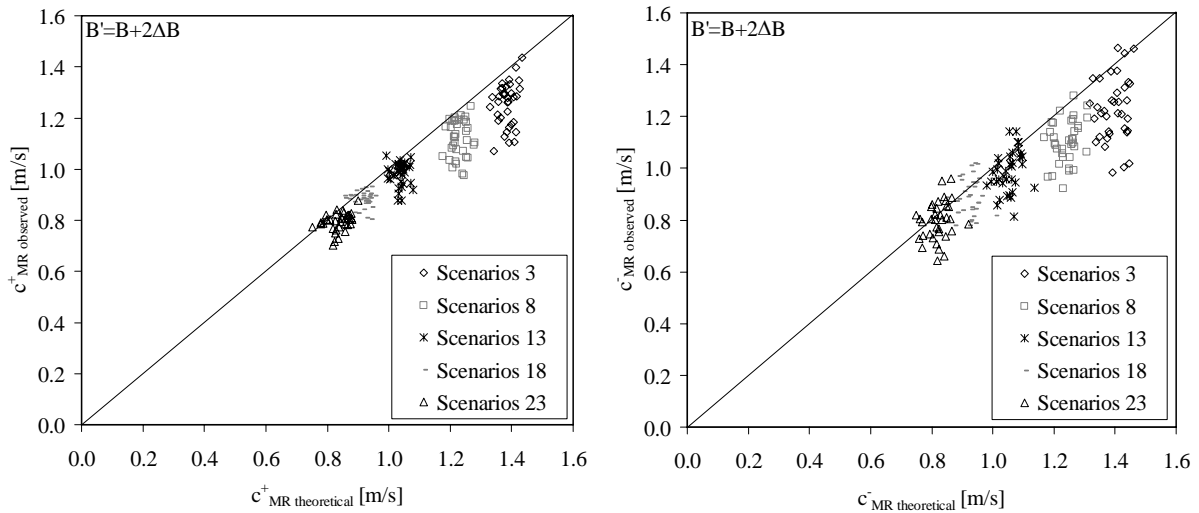


Figure 5-29: Positive (left) and negative (right) surge wave celerities after subtraction of the mean flow velocity with the assumption that the cavities fully contribute to the flow.

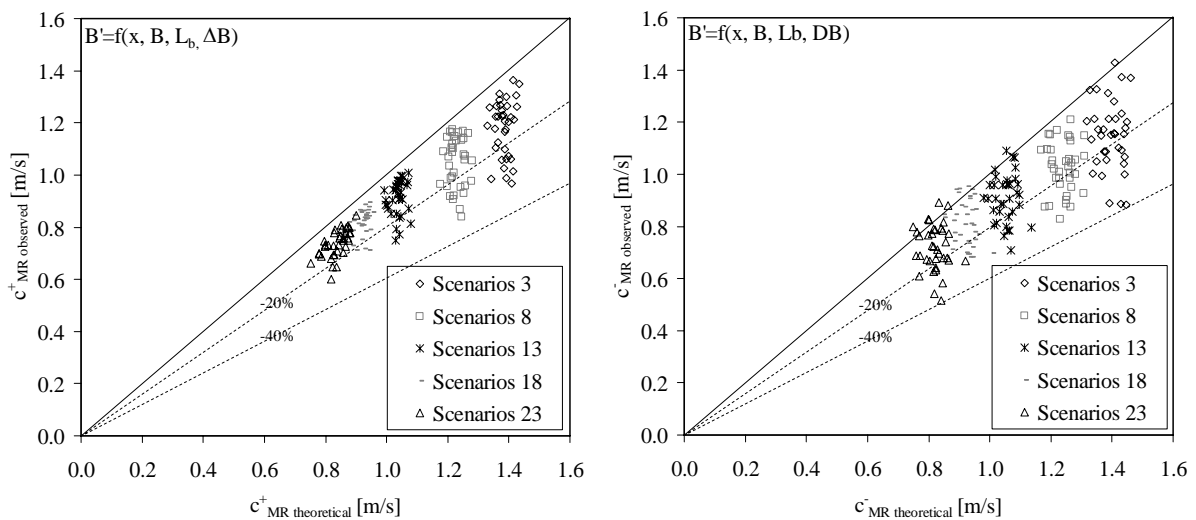


Figure 5-30: Positive (left) and negative (right) surge wave celerities after subtraction of the mean flow velocity with the assumption that the cavities contribute partially to the flow.

The difference between the theoretical, frictionless celerities in the horizontal channel $c_{MR th}$ and the observed celerities $c_{MR obs}$ for the positive and negative surge waves correlates with the identified friction coefficient $f_m = f_{prism} + f_{MR}$ under steady flow conditions. This observation supports the assumption that the decrease of the celerities in the macro-rough configurations depends at least partially on the flow resistance similar to the observed decrease of the front celerity of a dam break wave under the influence of friction (Dressler 1954, Whitham 1955, Lauber and Hager 1998a 1998b, Leal et al. 2006).

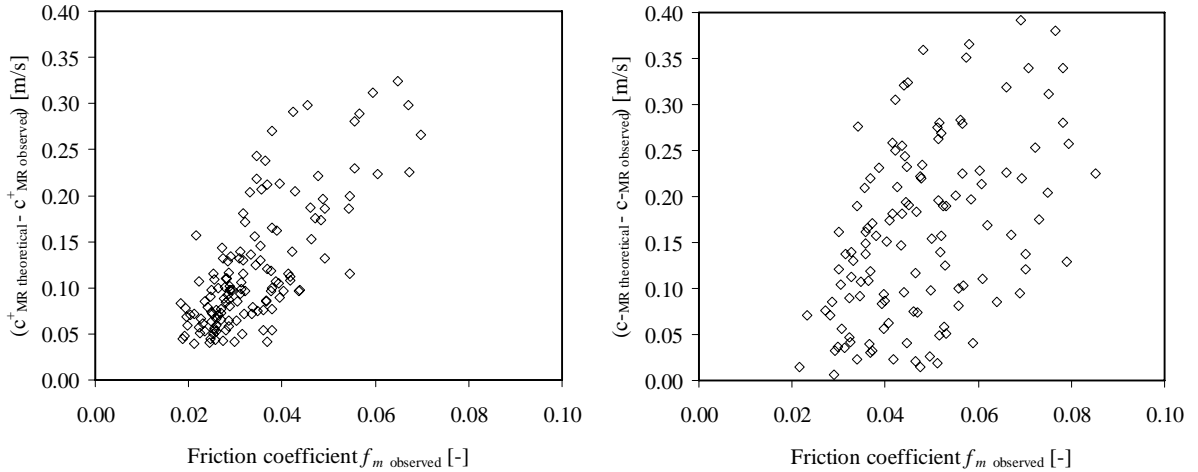


Figure 5-31: The difference $c_{MR th} - c_{MR obs}$ as a function of the friction coefficient $f_m = f_{prism} + f_{MR}$. The friction coefficient for the positive surge is relative to Q_b . The friction coefficient for the negative surge is relative to $Q_b + Q_w$.

5.6.5 Mathematical description of the attenuation of the wave front height

The mathematical description of the attenuation of the surge wave front height is based on a slightly modified approach presented by Lai et al. (2000). They investigated the peak attenuation of short, middle and long duration floods in compound channels. The filling and emptying of floodplains in a compound channel during a flood leads to an exponential attenuation of the flood peak (h_p) along the channel.

In the present study, the decrease of the wave front height of positive ($h'^+ = h_{21} - h_1$) and negative ($h'^- = h_3 - h_{41}$) surge waves was found to be exponential with the distance. Such as the filling and emptying of flood plains, the filling and emptying of depression roughness elements influences on the surge wave front height. Increased flow resistance leads to an additional decrease of the front height since it makes the surge more dispersive.

The following formula describing the attenuation of the flood peak is loan from Lai et al. (2000):

$$\frac{h_p(x)}{h_{p0}} = Ae^{(-BX)} \quad (\text{eq. 5.14})$$

where $h_p(x)$ is the flood peak height at a distance x of the channel and h_{p0} is the maximum height at the upstream channel end (x_0). A (close to 1.0) and B are parameters calibrated by the experimental results of Lai et al. (2000). The parameter B is reported as 0.42, 0.58 and 0.97 for long, middle and short duration floods respectively, indicating a higher attenuation for short duration floods. The dimensionless distance X takes the channel slope into account and is expressed as:

$$X = \frac{x - x_0}{(h_b / S_0)} \quad (\text{eq. 5.15})$$

where x is the location along the channel, x_0 the location of the reference height h_{p0} , h_b the baseflow water depth (a priori uniform) and S_0 the mean channel slope (a priori constant).

For the description of the attenuation of the wave front height the formula (eq. 5.14) is modified as follows:

$$\frac{h'(x)}{h'(x_0)} = e^{-(a+b) \cdot X} \quad (\text{eq. 5.16})$$

where $h'(x)$ is the wave front height at a distance x of the channel. $h'(x_0)$ is the wave front height at the beginning of the macro-rough reach ($x = 0$). $a + b$ is the sum used for the calibration of the observed and the calculated surge wave front heights along the channel. Separation between a (attenuation parameter of the wave front height of in the prismatic channel) and b (attenuation parameter of the wave front height due to macro-roughness elements) is considered in order to identify the additional contribution due to the depression macro-roughness elements on $h'(x)$ separately. The dimensionless distance is calculated according formula (eq. 5.15) where h_b is the baseflow depth at the beginning of the macro-rough reach and S_0 the mean channel slope of the macro-rough reach. Formulas (eq. 5.16) and (eq. 5.15) apply to the positive surge wave height h'^+ as well as to the negative one h'^- .

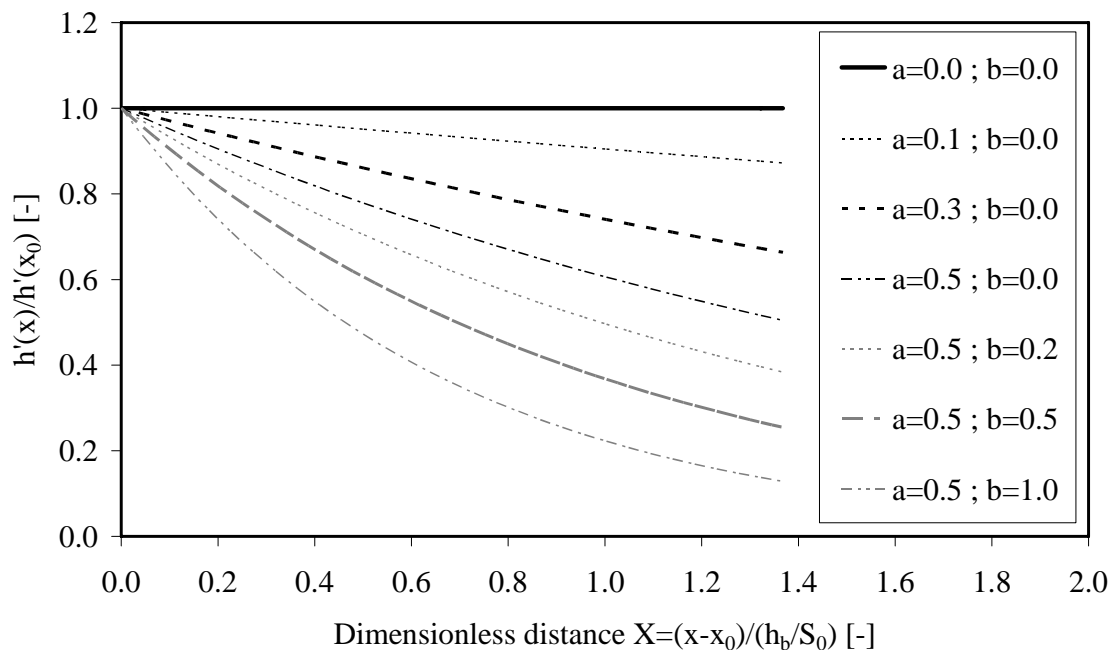


Figure 5-32: Attenuation of the surge wave front height shown schematically for different values of the attenuation parameter of the surge wave front height a and b .

The influence of the attenuation parameter of the surge wave front height a and b is shown in Figure 5-32 as an example. First, the influence of prismatic and macro-rough friction and channel slope are completely neglected. No surge wave height attenuation is observed ($a = 0 ; b = 0$). Then, the effects of the prismatic friction and the channel slope are considered leading to attenuation of the surge wave front height due to the dispersive character of the wave ($a \neq 0 ; b = 0$). Finally the macro-rough friction is considered too ($a \neq 0 ; b \neq 0$).

5.6.5.1 Attenuation parameter of the wave front height in the prismatic configuration

At a first step, the value of the attenuation parameter of the surge wave front height a (attenuation parameter of the wave front height of in the prismatic channel) for the positive and negative surge waves has been investigated and optimized for scenarios 3, 8, 13, 18 and 23 of the prismatic reference configuration. The result of the measured and theoretical attenuation of the surge wave front $h'(x)$ after calibration is shown in Figure 5-33 for the positive and Figure 5-34 for the negative surge waves from upstream.

The corresponding values of the attenuation parameter of the surge wave front height a^+ and a^- are 0.39 and 0.99 respectively. Using these values, the root mean square-errors between observed and calibrated front heights are 0.0011 m for h'^+ and 0.0009 m for h'^- .

$a^- > a^+$ indicates that the negative surge waves in the prismatic channel are more dispersive than the positive ones. The mentioned values of a^+ and a^- , allow reproducing rather well the decrease of the surge wave front height also for the others 30 prismatic scenarios. The values of $a^+ = 0.39$ and $a^- = 0.99$ are taken into consideration for the determination of b . When a (from the prismatic configuration) and the sum $a + b$ (from the calibration of the macro-rough configurations) are known, the value of b (resulting from the macro-rough friction and the filling/emptying of the depression roughness elements) is easily determined.

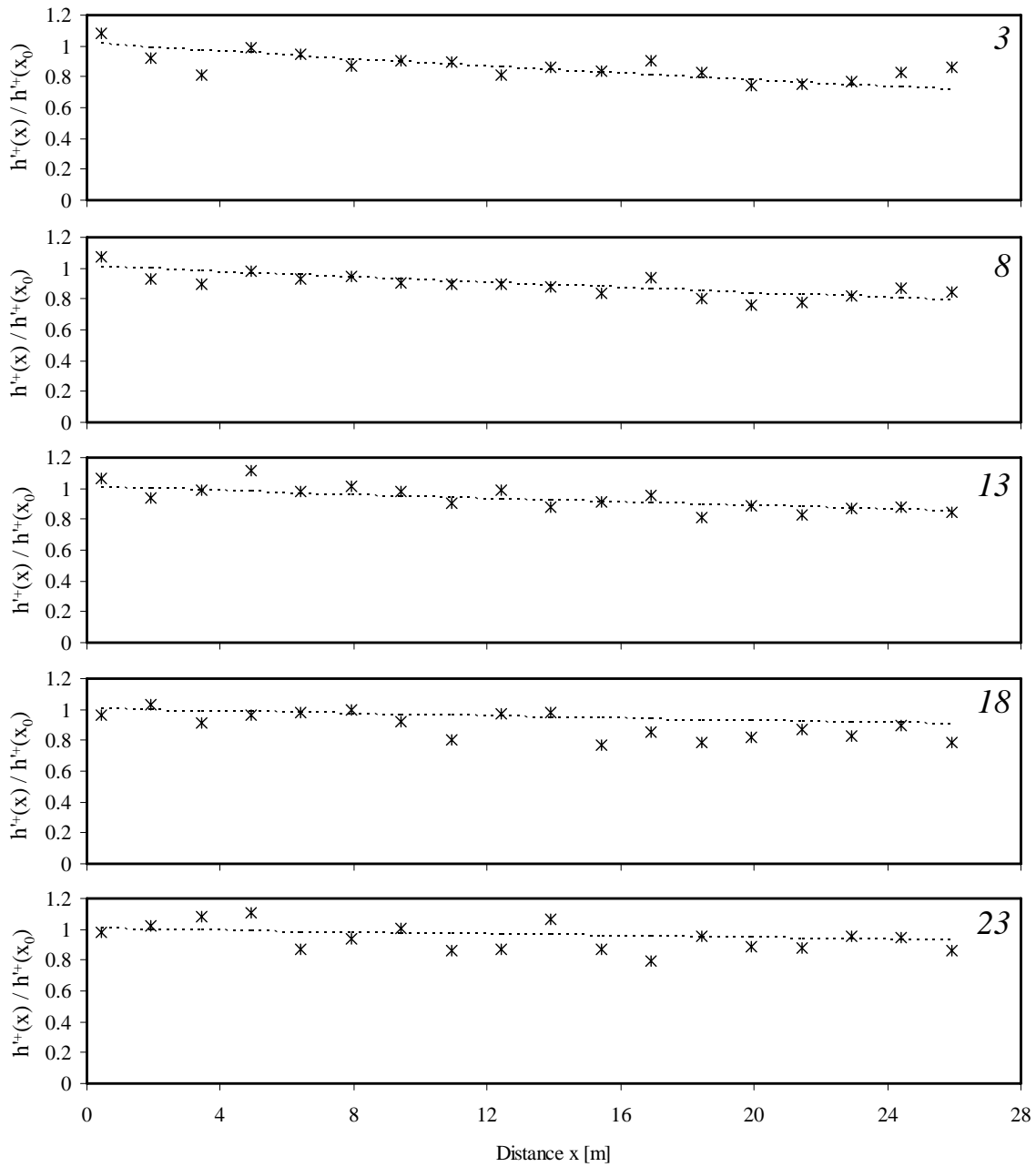


Figure 5-33: Attenuation of the front height for the positive surge wave along the channel. Scenarios 3, 8, 13, 18 and 23 of the prismatic reference configuration. Attenuation parameter of the positive surge wave front height $a^+ = 0.39$.

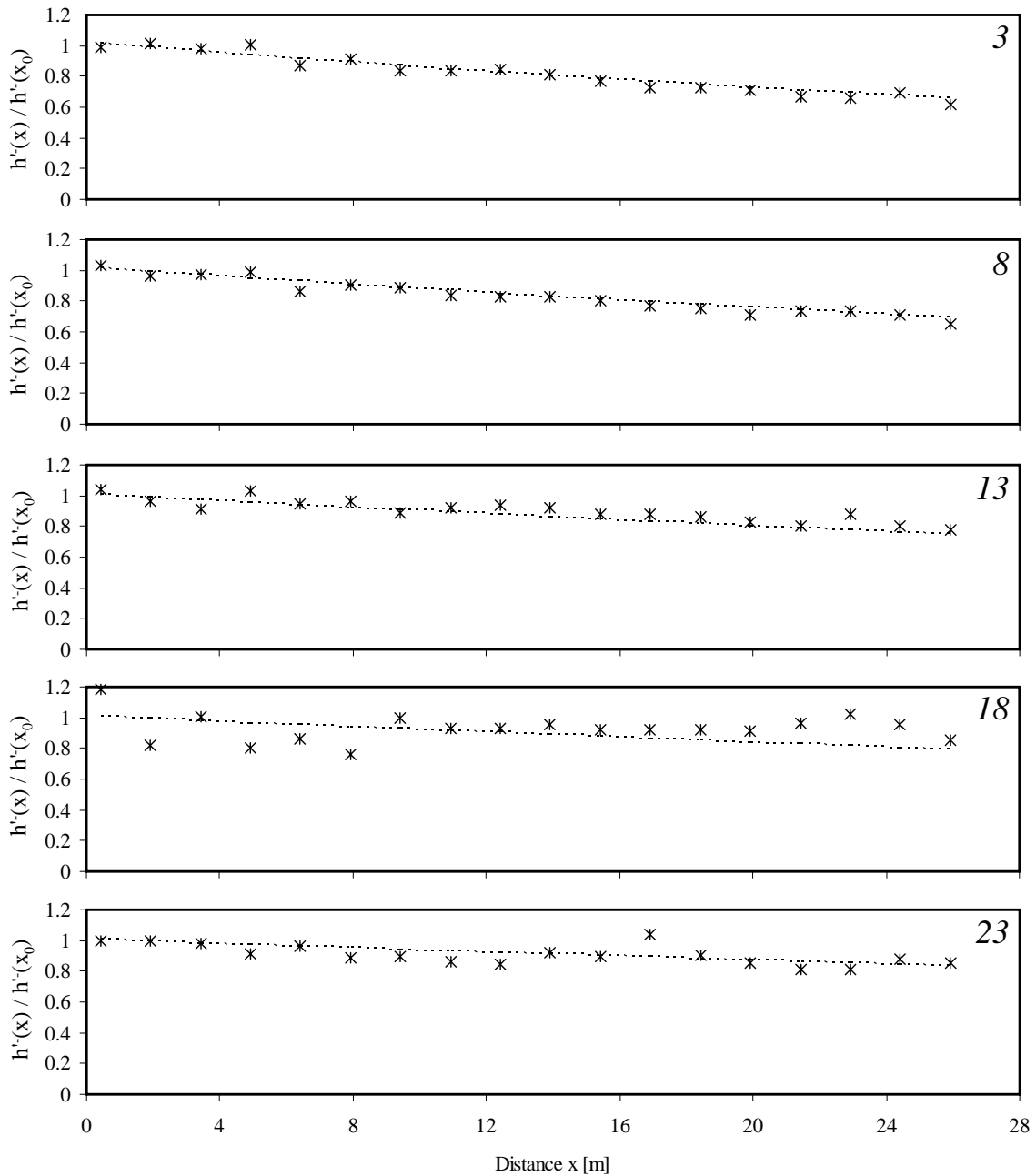


Figure 5-34: Attenuation of the front height for the negative surge wave along the channel. Scenarios 3, 8, 13, 18 and 23 of the prismatic reference configuration. Attenuation parameter of the positive surge wave front height $\alpha^+ = 0.99$.

5.6.5.2 Attenuation parameter of the wave front height due to macro-roughness

The parameter b (attenuation parameter of the wave front height due to macro-roughness) of formula (eq. 5.16) has been determined with the observed values of $h'(x)/h'(x_0)$ for the 36 axi-symmetric, the 4 asymmetric and the randomly generated macro-rough configurations (scenarios 3, 8, 13, 18 and 23). The adjustment has been done by minimizing the sum of the mean absolute errors between the measured and calculated surge wave front heights.

As an example in Figure 5-35 (positive surge) and Figure 5-36 (negative surge), the adjustment between the measured and calibrated ratio $h^+(x)/h^+(x_0)$ along the channel for the positive and negative surge waves from upstream are given.

The calculated line represents the general, exponential decrease of the surge wave front height along the channel whereas the measured points include some scattering due to:

- the location of the ultrasonic sensor along the macro-rough reach (at the beginning, in the middle or at the end of a widened reach respectively in the middle of the contracted reach)
- complex phenomena such as partial reflections of surges in the macro-rough reach.

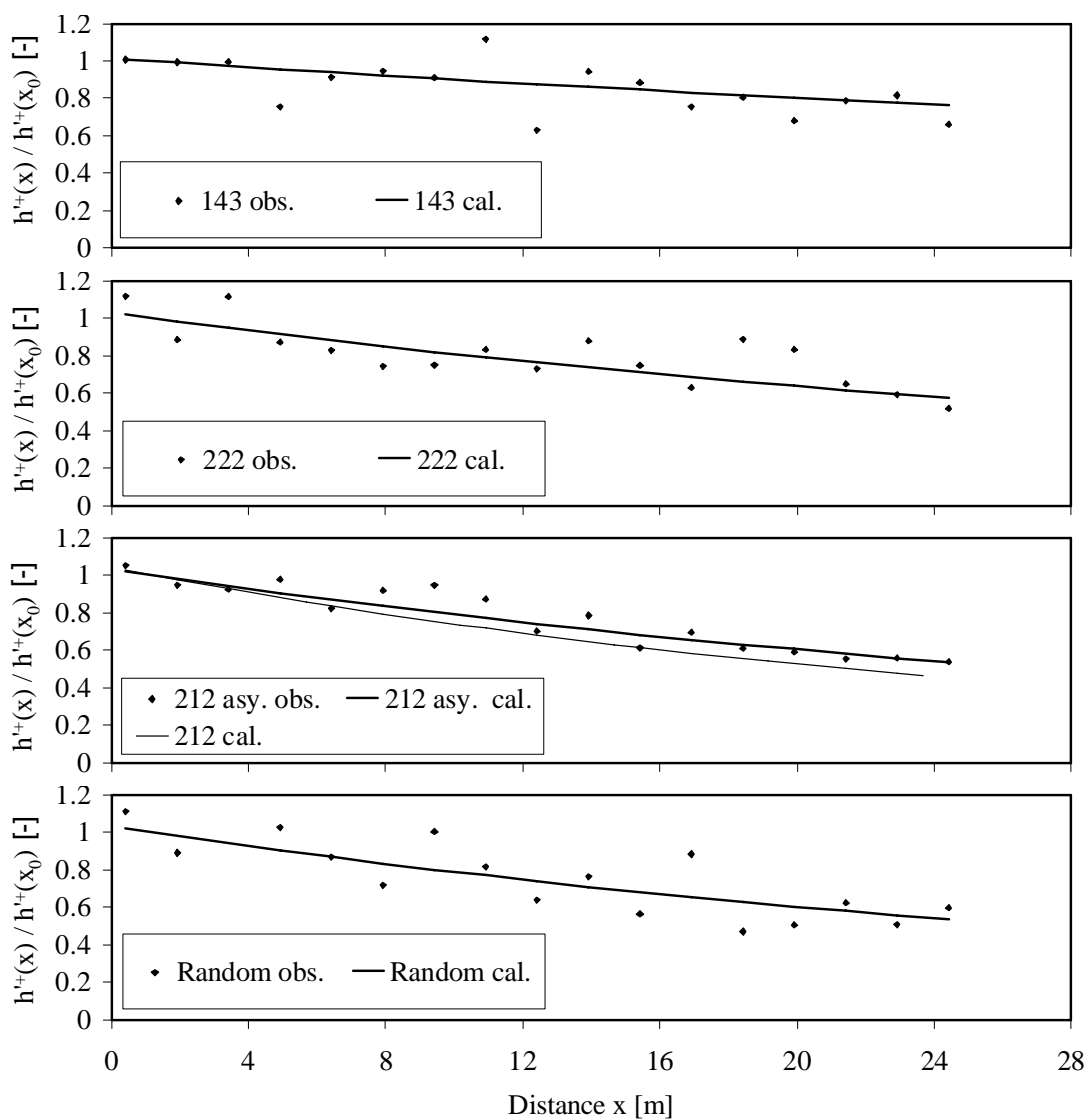


Figure 5-35: Examples of observed and calibrated $h^+(x)/h^+(x_0)$ along the macro-rough channel. All examples for scenario 8. (a + b) dependent on geometry.

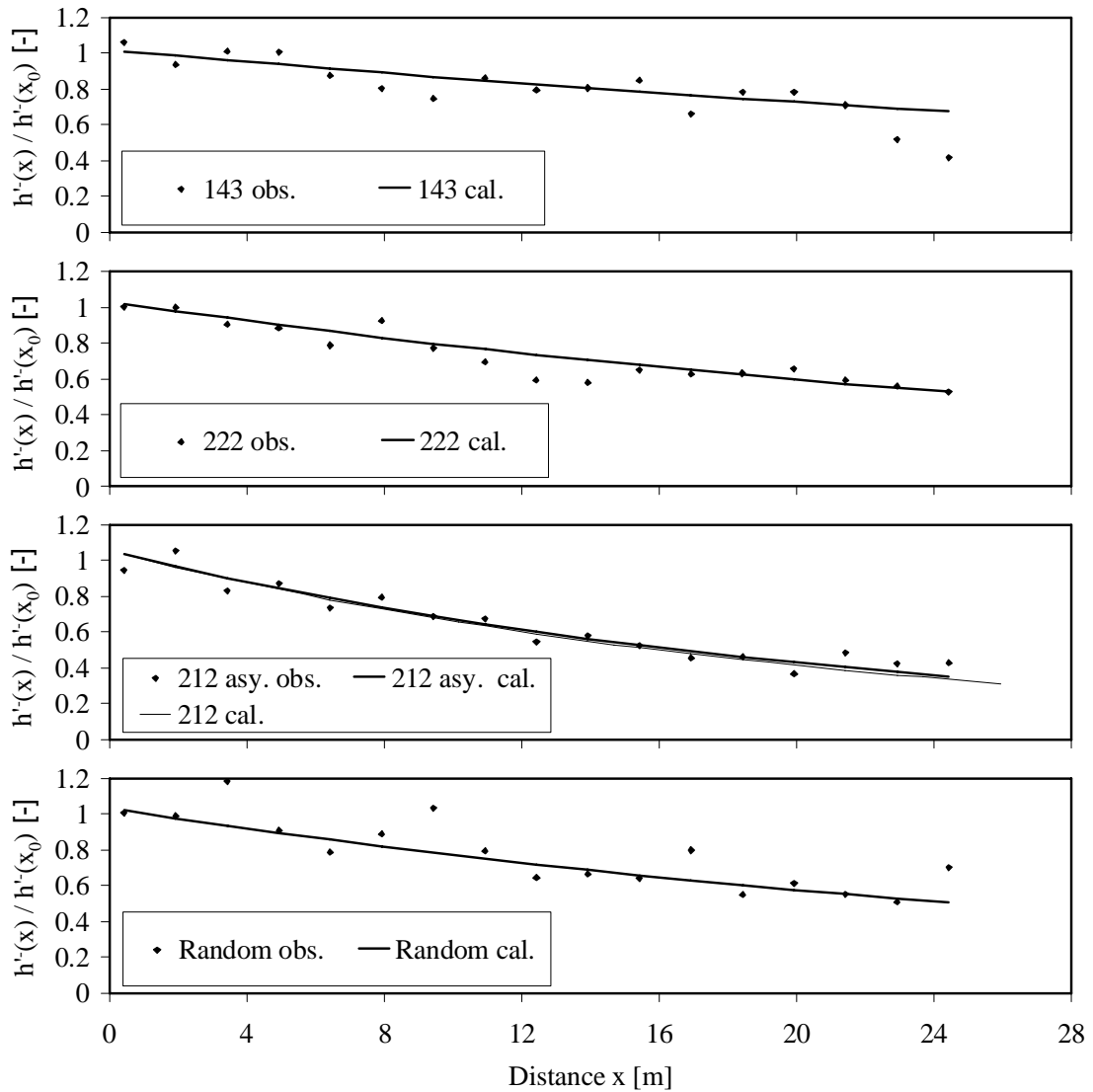


Figure 5-36: Examples of observed and calibrated $h^-(x)/h^-(x_0)$ along the macro-rough channel. All examples for scenario 8. ($a + b$) dependent on geometry.

The positive surges from upstream are found less dispersive than the negative ones and the configuration 143, having a higher longitudinal roughness spacing, attenuates the surge wave front height less than the other configurations. The surge wave front attenuation of the randomly generated configuration is comparable with the one of configuration 222 which can be considered as an “average” axi-symmetric macro-rough configuration. The asymmetric configuration 212 asy. shows quite good agreement with the corresponding symmetric one for both, positive and negative surge waves from upstream.

The values of b , which are calculated knowing that $a^+ = 0.39$ and $a^- = 0.99$ are given in the Appendix 5-1. Figure 5-37 shows the relationships between b and different dimensionless geometrical parameters of the macro-rough configurations, as well as between b and the macro-rough friction coefficient f_{MR} relative to the baseflow conditions.

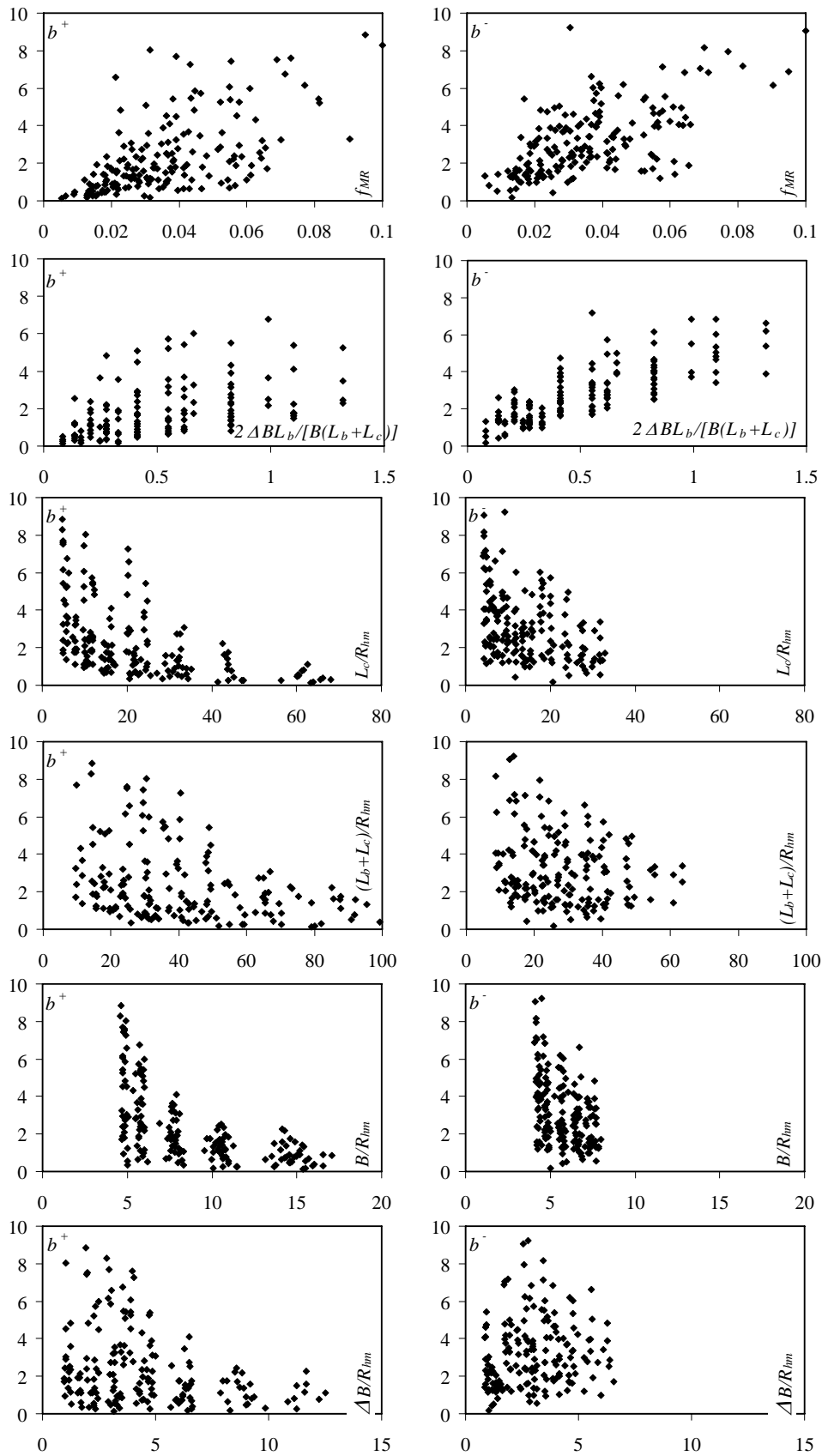


Figure 5-37: Relationship between attenuation parameter of the surge wave front height b and the different macro-rough dimensionless parameters respectively the friction coefficients f_{MR} . The friction coefficients and the dimensionless parameters are relative to the baseflow conditions.

Figure 5-37 and the values of the attenuation parameter of the surge wave front height b due to macro-roughness (Appendix 5-1) reveal the following:

- The value of b increases for positive as well as for negative surges with increasing macro-rough friction coefficients f_{MR} . The same trend can also be shown for the value of $(a + b)$ as a function of the total friction of the composite channel section $f_m = f_{prism} + f_{MR}$. In the present experiments, the friction thus makes positive (Henderson 1966) but also the negative waves more dispersive.
- The increase of the relative distance between two depression roughness elements L_c / R_{hm} respectively the relative roughness spacing $(L_b + L_c) / R_{hm}$ reduces the attenuation parameter of the surge wave front height, for both, positive and negative surges.
- For positive surge waves and less significantly also for negative surge waves, a decreasing base flow depth (parameter B / R_{hm}) leads to a decrease of b^+ (b^-).
- The response relative to an increase of $\Delta B / R_{hm}$ is astonishing. Neither b^+ nor b^- clearly increases with an increase of $\Delta B / R_{hm}$,
- The b^+ and b^- values are found often erroneous for scenario S23. Erroneous values are characterized by an abnormal increase respectively sudden decrease compared to scenarios S3 to S18.
- Other investigated dimensionless geometrical parameters do not correlate at all with the macro-rough attenuation parameters b of the surge wave height expect the surface density of depression roughness elements defined as $2\Delta B L_b / [B(L_b + L_c)]$. This parameter is characterizing the storage volume.

The relationship between the values of b , the flow resistance and dimensionless geometrical parameters of the macro-rough configurations is unknown and it is identified by using the EPR programming (§ 5.6.7).

5.6.6 Discharge estimation directly behind the wave front at the end of the macro-rough channel reach

The discharge directly after the surge wave front can roughly be estimated using the elementary surge wave theory in the frictionless and horizontal channel. The estimation is done at the channel position $x = 24.42$ m. Formula (eq. 2.65) is employed for the negative wave. For the negative wave, the absolute front celerity is not necessary to know and the discharge after the front becomes:

$$Q(h_{41}) = (U_3 - 2\sqrt{gh_3} + 2\sqrt{gh_{41}}) \cdot B \cdot h_{41} \quad (\text{eq. 5.17})$$

where U_3 and h_3 are the mean flow velocity and the flow depth before the passage of the negative surge. h_{41} is the flow depth assumed after the passage of the wave front according to Figure 5-16. $Q(h_{41})$ is the discharge immediately after the negative surge wave front.

For the positive surge, the absolute celerity V_w^+ is necessary to know (from experiments). Formula (eq. 2.44b) is used for the calculation of $U(h_{21})$. The formula for the discharge after the front becomes:

$$Q(h_{21}) = \left(\frac{U_1 h_1 + V_w^+ (h_{21} - h_1)}{h_2} \right) B h_{21} \quad (\text{eq. 5.18})$$

where U_1 and h_1 are the mean flow velocity and the flow depth before the passage of the positive surge wave. h_{21} is the flow depth after the passage of the wave front according to Figure 5-16. V_w^+ is the absolute celerity of the wave front. $Q(h_{21})$ is the discharge immediately after the positive surge wave front.

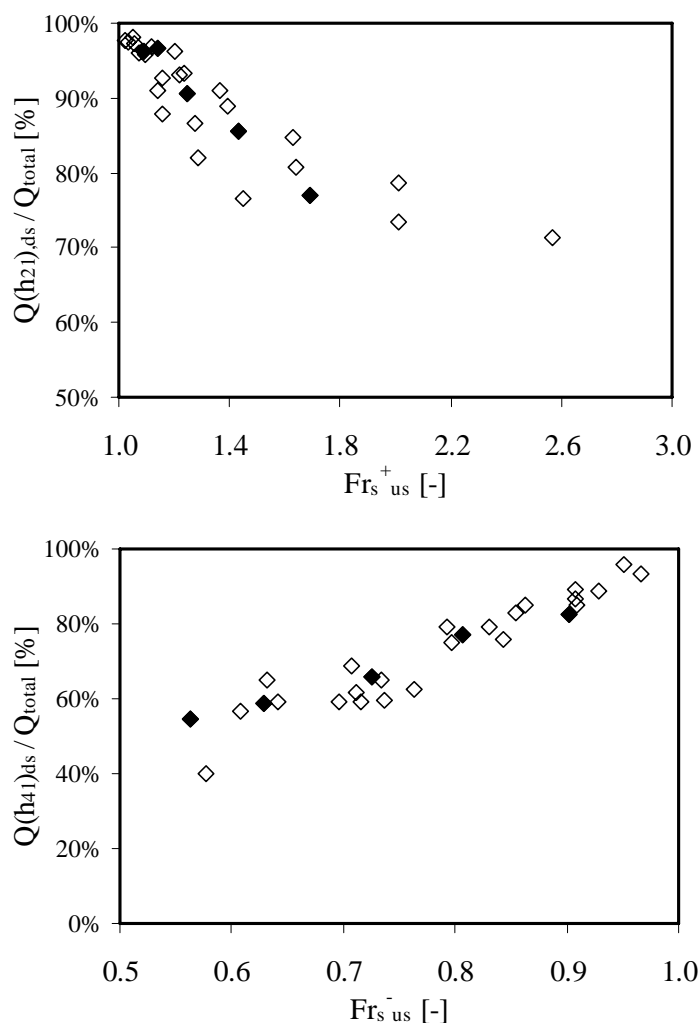


Figure 5-38: Normalized estimated discharge directly after the wave front for the positive ($Q(h_{21})$) and negative ($Q(h_{41})$) surge waves in the prismatic configurations shown as a function of the upstream surge Froude number Fr_s . (\diamond): Scenarios 1-30; (\blacklozenge): Scenarios 3, 8, 13, 18, 23.

For the calculation of the discharge behind the wave front, the flow depths h_{21} and h_{41} have been determined using first (eq. 5.16) for the height of the surge wave front $h^{+}(x)$

and $h'^-(x)$. The flow depths becomes then $h_{2l}(x) = h_l(x) - h'^+(x)$ for the positive and $h_{4l}(x) = h_3(x) - h'^-(x)$ for the negative surge from upstream.

For the positive waves from upstream in the prismatic configuration (Figure 5-38, above) the discharge at the wave front at position $x = 24.42$ m is reduced of 5% (scenario 23) to 25% (scenario 3) compared to the total discharge $Q_{total} = Q_b + Q_w$ introduced at the upstream limit of the channel. This confirms again the dispersive character of the positive surge waves from upstream. Figure 5-38 (below) shows the same result for the negative waves from upstream in the prismatic configuration. At position $x = 24.42$ m the discharge after the wave front still represents between 55% (scenario 3) to 80% (scenario 23) of the total discharge $Q_{total} = Q_b + Q_w$ before the passage of the negative wave.

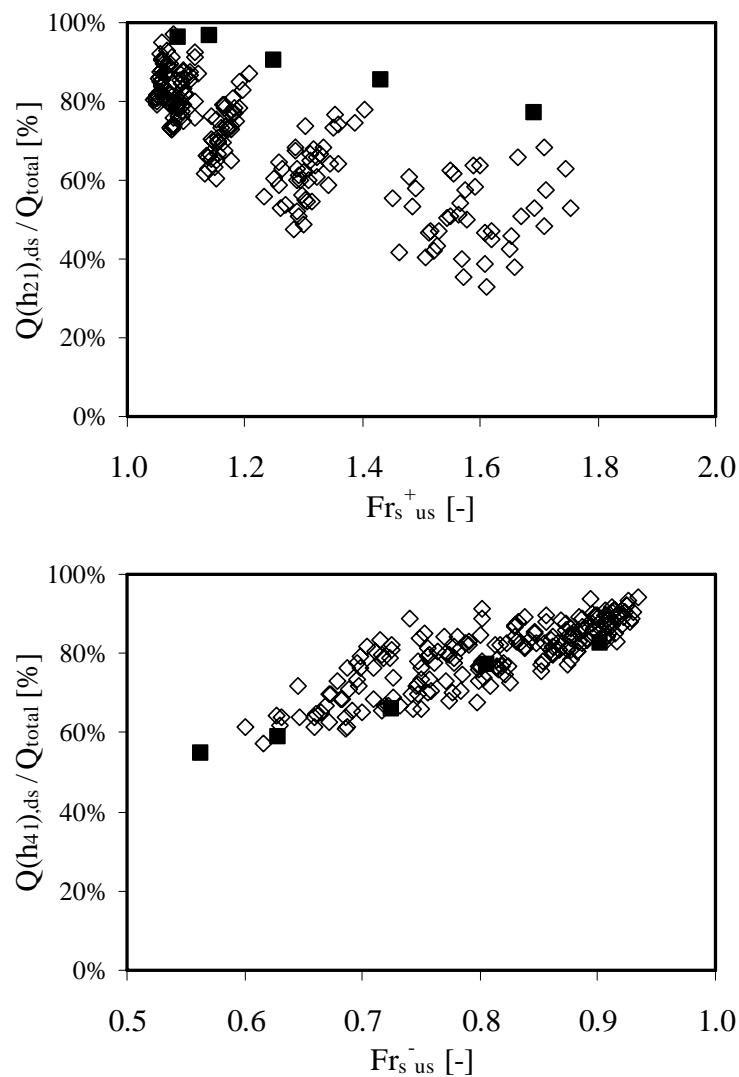


Figure 5-39: Normalized estimated discharge directly after the wave front for the positive ($Q(h_{2l})$) and negative ($Q(h_{4l})$) surge waves in the macro-rough (\diamond) and prismatic (\blacksquare) configurations as a function of the upstream surge Froude number Fr_s (scenarios 3, 8, 13, 18 and 23).

The discharge directly after the wave front has also been estimated for the configurations with macro-roughness at the banks assuming locally frictionless and horizontal channel (Figure 5-39). The part of sudden change of discharge at the end of the macro-rough reach, even if roughly estimated, is significantly diminished under the influence of the depression macro-roughness elements for the positive surge wave from upstream. The decrease results from the storage in the cavities on one hand and the increased friction on the other hand. For the negative waves from upstream, the discharge after the wave front (eq. 5.17) generally also indicates a reduction of the sudden change in discharge compared to the prismatic configuration. However, some macro-rough configurations behave rather similar than the prismatic configurations regarding the discharge after the wavefront.

It may be concluded that the channel bank macro-roughness and the storage of a certain amount of water in the cavities lead to a decrease of the sudden change of discharge at the wave front compared to the prismatic configuration. Discharges have been roughly estimated from the experimental data assuming locally a horizontal and frictionless channel. With regard to the formulas (eq. 5.17) and (eq. 5.18) which both depend on h' , the discharge after the surge wave front and the attenuation of the surge wave front height are correlated.

5.6.7 Empirical relationships for the surge wave celerity and the attenuation of the surge wave front height obtained by the EPR-method

With regard to Figure 5-37 and Figure 5-31 it can be desired that the establishment of empirical relationships is possible for a dimensionless reduction of the celerity and the attenuation parameter of the height of the surge wave front. Since the surge wave characteristics are issued from the specific situation of the experiments, namely a backwater-curve of the type M2, and a mean bottom slope of $S_0 = 0.0011$, the results and formulas shown hereafter are quantitatively applicable to similar situations. Comparative results can also be extended to other situations.

5.6.7.1 Attenuation parameters of the surge wave front height

The additional attenuation of the surge wave front height due to macro-roughness and storage of water inside the cavities can be described with the parameter b . It can be used in formula (eq. 5.16) for the prediction of the exponential decrease of the surge wave front height¹. Based on scenarios 3, 8, 13 and 18, the following empirical formula can be proposed for the attenuation parameter of the height of the positive surge wave front b^+ :

$$b^+ = 26.5 \cdot \left(\frac{L_b + L_c}{\Delta B} \right) \cdot f_{MR} \cdot \ln \left(\frac{2\Delta B L_b}{B(L_b + L_c)} + 1 \right) \quad (R^2 = 0.71) \quad (\text{eq. 5.19})$$

¹ Alternatively to a selection of parameters b^+ and b^- directly issued from the experimental results.

The attenuation parameter depends on geometrical parameters of the macro-rough configurations as well as on the macro-rough friction coefficient f_{MR} corresponding to the situation before the passing of the positive surge from upstream. The parameter in the natural logarithm describes the density of the cavities.

For the attenuation of the height of the negative surge wave front, the parameter is calculated with the following formula:

$$b^- = 1.47 \cdot \left(\frac{2\Delta BL_b}{B(L_b + L_c)} \right) \cdot \ln \left(\frac{L_b + L_c}{\Delta B} + 1 \right) + 37.7 \cdot f_{MR} \quad (R^2 = 0.77) \quad (\text{eq. 5.20})$$

The considered geometrical parameters of the macro-rough configurations are the same than for b^+ . Here, the macro-rough friction coefficient f_{MR} corresponds to the situation before the passing of the negative surge from upstream. The application of the fully empirical formulas is limited to the range summarized in Table 5-7.

Table 5-7: Application range of the formulas for the attenuation parameters of the surge wave front height due to macro-roughness.

	Friction	$(L_b + L_c) / \Delta B$	Cavity density
Positive surge from upstream (b^+)	$\sim 0 < f_{MR} < 0.065$	$2.5 < (L_b + L_c) / \Delta B < 40$	$0.08 < 2\Delta BL_b / [B(L_b + L_c)] < 1.3$
Positive surge from upstream (b^-)	$\sim 0 < f_{MR} < 0.090$	$2.5 < (L_b + L_c) / \Delta B < 40$	$0.08 < 2\Delta BL_b / [B(L_b + L_c)] < 1.3$

* : additional restrictions: The mean bottom slope should range around $S_0 = 0.0011$. Furthermore, the flow conditions during the experiments corresponded to a backwater-curve of the type M2.

5.6.7.2 Reduction of the surge wave celerity

The normalized reduction of the positive and negative surge wave front celerity in the macro-rough configurations can be defined as:

$$\Delta c_{MR,adim} = (c_{MR,obs}^2 - c_{MR,th}^2) / c_{MR,th}^2 \quad (\text{eq. 5.21})$$

where $c_{MR,th}$ is the theoretical celerity calculated as described in § 5.6.4 based on the flow depths and by assuming the elementary surge wave theory at the wave front. $c_{MR,obs}$ is the celerity determined according to Figure 5-30.

The prediction of the parameter $\Delta c_{MR,adim}^+$ of the positive surge wave from upstream is again based on scenarios 3, 8, 13 and 18 and the following empirical formula can be proposed:

$$\Delta c_{MR,adim}^+ = - \left[0.82 \cdot \left(\frac{L_b + L_c}{\Delta B} \right)^{-1} + 3.3 \cdot f_m \right] \quad (R^2 = 0.61) \quad (\text{eq. 5.22})$$

The difference between the observed $c_{MR,obs}$ and the theoretical celerity $c_{MR,th}$ increases

with the friction coefficient $f_m = f_{prism} + f_{MR}$ corresponding to the flow conditions before the passing of the positive surge wave and with increasing depth of the cavities. The increase of the roughness spacing $L_b + L_c$ reduces the difference between observed and theoretical celerities. The application range is limited to mean bottom slopes around $S_0 = 0.0011$ and the flow conditions during the experiments corresponded to a back-water-curve of the type M2. The dimensionless geometrical parameter ranged between $2.5 < (L_b + L_c) / \Delta B < 40$ and the total friction coefficient between $0.018 < f_m < 0.079$.

For the corresponding normalized reduction of the negative surge wave $\Delta c_{MR,adim}^-$, no empirical formula is proposed since even the best identified correlation coefficient was only $R^2 = 0.31$.

5.7 *Conclusions for surge wave experiments in the prismatic and macro-rough configurations*

Elementary surge wave theory experimentally verified in the prismatic configuration

For the prismatic reference configuration the analysis of the surge wave experiments confirms the elementary surge wave theory (§ 2.3.3) and the developments of Favre (1935). Due to the curvature of the wave front, which is leading to extra pressure terms, secondary waves can be observed for surge Froude numbers between $1.06 < Fr_s < 1.5$. For higher surge Froude numbers, secondary waves disappear. Unsteady velocity measurements of the streamwise velocity components $u(z)$ have been done using an Ultrasonic Doppler Velocity Profiler (UVP). For surge waves with breaking conditions of the wave front the measurements revealed that the non hydrostatic pressure distributions (accelerated velocity profile) are limited to a small part of the wave under breaking conditions. This explains physically the disappearance of the secondary waves at the wave front.

Reduction of the absolute celerity V_w and the celerity c of the surge wave

The absolute wave celerities along the macro-rough reach V_w have been found practically constant, but reduced when compared to the prismatic reference. The constant values of V_w^+ and V_w^- along the channel must be explained by Froude numbers relatively close to $Fr = 0.5$. The reduction of V_w^+ lies between 5% (configurations 141, 241 and 441) and 25% (configurations 114, 214 and 414) compared to the prismatic reference. The decrease of V_w^- ranges approximately around 15% (25% for 114 to 5% for 441) compared to the prismatic reference.

The reduction of the absolute surge wave celerities V_w^+ and V_w^- in the macro-rough configurations has four reasons:

- 1) Due to a backwater-curve, the flow depths increase and thus the mean flow velocity decreases from downstream to upstream along the channel. The absolute surge wave celerity $V_w = U + c$ should therefore a priori decreased when compared to the prismatic reference. However, the decrease of U is partially balanced by the increase of the celerity c due to the higher water levels.
- 2) An additional decrease of the mean flow velocity results from the partial expansion of the flow in the widened channel reaches.
- 3) The surge wave front height is attenuated along the macro-rough reach which leads to an attenuation of the celerity according to formula (eq. 2.49).
- 4) Finally, due to macro-roughness at the channel banks, the flow resistance (friction coefficients) is increased.

It is difficult to separate the different effects. However, assuming a conceptual flow expansion model (§ 5.6.4), the difference between the observed celerity and the theoretical

celerity (calculated based on the flow depths before and after the surge wave front) can be explained to some extent by the friction coefficients. The friction coefficients concern the steady flow situation before the positive and before the negative surge wave.

Attenuation of the surge wave front height

The analysis of the surge wave front height confirms the dispersive character of surge waves, which is increased in the macro-rough configurations compared to the prismatic reference. The extra dispersion is the result of the macro-rough flow resistance and other phenomena such as the partial reflections of the surge wave in the cavities of the macro-roughness elements and the passive retention in the cavities.

The ratio between the surge wave height upstream and downstream of the experimental channel h'^+_{ds} / h'^+_{us} indicates a decrease of 5% (low Q_{total} / Q_b) to 25% (height Q_{total} / Q_b) of the surge wave front height along the prismatic channel. The decrease is the result of the combination of bottom and friction slope. In the macro-rough configurations, the decrease is significantly higher (up to 70%). The height of the negative surge wave front (h'^-_{ds} / h'^-_{us}), estimated from the level measurements, decreases along the prismatic channel of 5% to 25%. The decrease of h'^- ranges between 10% and 75% along the channel with macro-roughness at the banks.

The attenuation of the surge wave front height can be described with the empirical formula:

$$\frac{h'(x)}{h'(x_0)} = e^{-(a+b) \cdot X} \quad (\text{eq. 5.16})$$

where $h'(x)$ is the wave front height at a distance x of the channel. $h'(x_0)$ is the initial wave front height. a and b are the attenuation parameters of the wave front height in the prismatic channel (a) and due to the macro-roughness elements at the channel banks (b) respectively. The attenuation parameters of the wave front height in the prismatic channel are $a^+ = 0.39$ for the positive surge wave and $a^- = 0.99$ for the negative surge wave. The values of b can be determined directly from the experiments with different macro-rough configurations or they can be estimated with the empirical formulas (eq. 5.19) and (eq. 5.20).

The dimensionless distance X takes into account the channel slope S_0 (a priori constant) and the depth of the baseflow h_b (a priori uniform and steady) at the reference location x_0 . It is expressed as:

$$X = \frac{x - x_0}{(h_b / S_0)} \quad (\text{eq. 5.15})$$

The uniform baseflow depth conditions are verified in the present experimental study only for the prismatic reference. This limits the range of application for quantitative

results in the macro-rough configurations to bottom slope close to 0.001 and backwater-curve of the type M2.

Discharge estimation behind the wave front

The discharge at the downstream end of the macro-rough reach has been roughly estimated. The continuity equation through the surge front (eq. 5.18) was used in combination with experimental values for the absolute wave celerity V_w^+ and the flow depth downstream and upstream of the wave front. At the end of the macro-rough reach, the part of sudden increase of the discharge immediately behind the positive wave front is significantly reduced comparing to the prismatic configuration.

For the negative surge wave from upstream the sudden change in discharge directly behind the negative front (eq. 5.17) is generally also reduced but the difference compared to the prismatic configuration is less significant.

Asymmetric and randomly generated configurations with macro-roughness at banks

Independent on the considered parameter it can be concluded that the asymmetric macro-rough configurations conduct similar to the corresponding axi-symmetric configurations. The behaviour of the macro-rough configuration with randomly generated channel banks lies in the range of the macro-rough axi-symmetric configurations 222 characterized by “average” geometrical macro-rough parameters.

6 NUMERICAL SIMULATIONS

6.1 2D-simulations of the steady flow experiments

6.1.1 Introduction

Dam break and surge wave flows are usually simulated using 1D or 2D shallow water equations assuming hydrostatic pressure distribution. Turbulent stresses are generally neglected. However, Soares et al. (2003) reveals that under certain conditions such as flows in highly non-prismatic geometries, the integration of the turbulent stress terms might be important. The experimentally investigated macro-rough configurations of the present work have to be attributed to these situations. In their work, Soares et al. (2003) present a numerical 2D-scheme including the momentum exchange through turbulence at the vertical shear layers. The source term of the two-dimensional shallow water equations is completed by depth averaged terms related to turbulent stresses as (see Soares et al. 2003 for the complete formulation):

$$\mathbf{S}(\mathbf{U}) = \begin{bmatrix} 0 \\ gh(S_{0,x} - S_{f,x}) + \frac{\partial}{\partial x}(h\tau_{xx}/\rho) + \frac{\partial}{\partial y}(h\tau_{xy}/\rho) \\ gh(S_{0,y} - S_{f,y}) + \frac{\partial}{\partial x}(h\tau_{yx}/\rho) + \frac{\partial}{\partial y}(h\tau_{yy}/\rho) \end{bmatrix} \quad (\text{eq. 6.1})$$

where the turbulent stresses are expressed as¹:

$$\frac{\tau_{xx}}{\rho} = 2\nu_t \frac{\partial u}{\partial x}, \quad \frac{\tau_{yx}}{\rho} = \frac{\tau_{xy}}{\rho} \nu_t \left(\frac{\partial u}{\partial y} + \frac{\partial v}{\partial x} \right), \quad \frac{\tau_{yy}}{\rho} = 2\nu_t \frac{\partial v}{\partial y} \quad (\text{eq. 6.2})$$

ν_t is the depth averaged turbulent viscosity. According Rodi (1993) or Nezu and Nakagawa (1993) one possibility to express ν_t is to relate the depth averaged turbulent viscosity to the friction velocity u_* and the flow depth h as:

$$\nu_t = \lambda \cdot u_* \cdot h \quad (\text{eq. 6.3})$$

where λ is dimensionless eddy viscosity. Rodi (1993) emphasizes that the approach is valuable when the turbulence is mainly bed generated. Other possibilities to express ν_t consist in assuming the turbulent (or eddy) viscosity constant or to apply a mixing length model. The approach according formula (eq. 6.3) is integrated in the numerical

¹ Turbulent kinetic energy terms are neglected.

2D-model of Soares et al. (2003). The range of possible values of λ reported in Rodi (1993), Nezu and Nakagawa (1993) or French (1985) on the basis of experimental works and field measurements is presented in Figure 6.1.



Figure 6-1: Range of reported values of the dimensionless eddy viscosity λ .

Preliminary computations for some steady test cases, done by the Civil Engineering Department of the Université catholique de Louvain in the framework of a collaboration, clearly showed that the experimental backwater-curves observed in the laboratory flume “Vevey” under steady flow conditions cannot be reproduced without depth averaged terms describing turbulent stresses. The objectives of the 2D-simulations of steady flow tests given in this chapter have consequently been defined as:

- To apply the numerical model including turbulent stresses to test cases and verify the ability of reproduction of the experiments.
- To calibrate the depth-averaged turbulent viscosity and especially to investigate whether the dimensionless eddy viscosity λ can be considered as constant for the macro-rough configurations.
- To validate the numerical model under steady flow conditions since its application to highly unsteady dam-break flow (Soares et al. 2003) did not allow concluding definitely on the necessity to include or not turbulence stress in 2D-shallow water equations.

6.1.2 Simulations and results

Macro-rough channel configurations 221 and 224 have been investigated by the 2D-simulations with different discharges (Table 6-1). The geometry, the initial conditions and the boundary conditions (steady discharge upstream, constant water level downstream) have been integrated into the 2D-model. The calculation time was sufficient to get completely steady flow conditions. Furthermore, the investigation of two different mesh sizes allowed exclude effects related to the spatial resolution of the geometry.

At a first step, different dimensionless eddy viscosities λ allowed the calibration for the geometrical configuration 221 at the steady discharge Q5. At a second and third step, additional discharges for the geometrical configuration 221 and the second configuration 224 have been simulated using the best value of λ (0.630). The comparisons of flow depths are presented in Figure 6-2 to Figure 6-4.

Table 6-1: Characteristics of the macro-rough test cases for the 2D-simulations.

Test case	$L_b ; L_c ; \Delta B$ [m]	Q_b [m ³ /s]	h_{ds} [m]	λ [-]	Mesh size [m]
221 Q5 g 0.000	1.0 ; 1.0 ; 0.1	0.0483	0.1482	0.000	0.05
221 Q5 f 0.420	1.0 ; 1.0 ; 0.1	0.0483	0.1482	0.420	0.025
221 Q5 g 0.420	1.0 ; 1.0 ; 0.1	0.0483	0.1482	0.420	0.05
221 Q5 g 0.630	1.0 ; 1.0 ; 0.1	0.0483	0.1482	0.630	0.05
221 Q5 g 0.840	1.0 ; 1.0 ; 0.1	0.0483	0.1482	0.840	0.05
221 Q3 g 0.630	1.0 ; 1.0 ; 0.1	0.0176	0.0636	0.630	0.05
221 Q8 g 0.630	1.0 ; 1.0 ; 0.1	0.1032	0.2664	0.630	0.05
224 Q5 g 0.000	1.0 ; 1.0 ; 0.4	0.0480	0.1470	0.000	0.05
224 Q5 g 0.630	1.0 ; 1.0 ; 0.4	0.0480	0.1470	0.630	0.05

Figure 6-2 allows pointing out:

- Without turbulent stresses, the backwater-curve is not simulated correctly. To consider the skin friction only, introduced by a Manning coefficient of the channel (without macro-roughness), does not allow to simulate the total head-loss.
- The mesh size does not influence the result.
- From different investigated dimensionless eddy viscosities λ , the value of 0.630 leads to the best fit between measured and simulated water depths (at channel axis).
- For the geometrical configuration 221 and the discharge Q5 (reattachment flow type), the flow depth along the channel axis is influenced by the expansion and contraction of the flow leading to the typical rise and dip of the water surface, conformal to the measurements.

From Figure 6-3 the following can be concluded:

- For the test case “221 Q3 g 0.630”, the flow depths are still quite well reproduced.
- For the test case “221 Q8 g 0.630” considering the highest steady discharge investigated in this configuration, the numerical simulations ($\lambda = 0.630$) overestimate the flow depths. The overestimation is of about 10% at a distance of 28.8 m upstream of the downstream boundary.

From Figure 6-4 following points can be concluded:

- For the test case “224 Q5 g 0.630”, the numerical simulation ($\lambda = 0.630$) underestimates the measured flow depths. The underestimation is of about 6% at a distance of 28.8 m upstream of the downstream boundary.

- Without turbulent stresses, the backwater-curve of the test case “224 Q5 g 0.630” is not simulated correctly as for configuration 221.
- Configuration 224 at a discharge of Q5 has to be considered as a normal recirculating flow type. The flow only expands in the widened reach, but does not reattach to the side walls. Compared to the reattachment flow type (configuration 221), the typical rise and dip of the water surface along the channel are reduced.

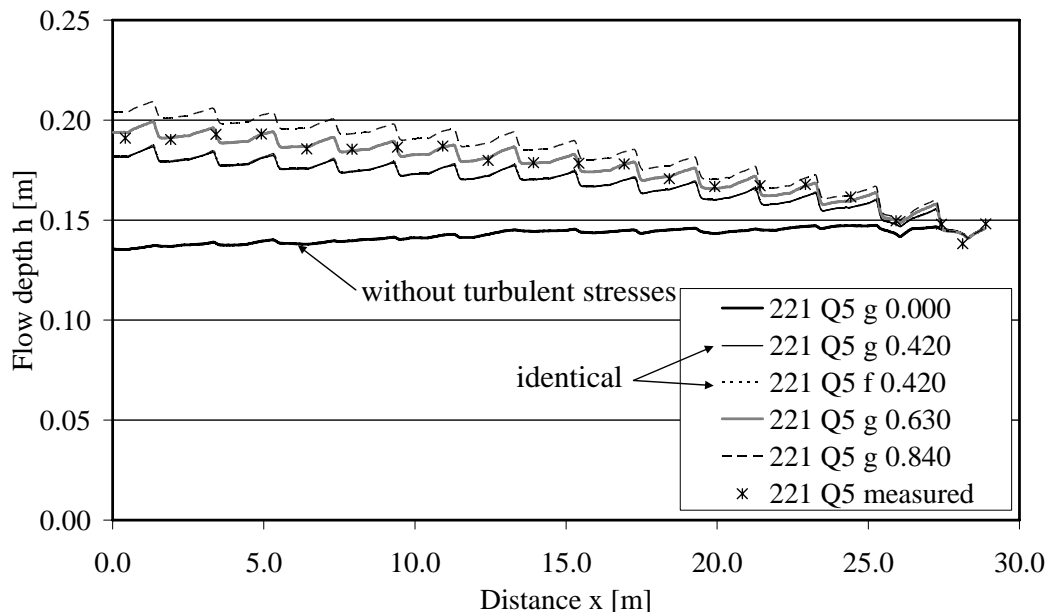


Figure 6-2: Experimental and numerical results with and without turbulence stress terms for different λ and two mesh sizes for the configuration 221 and discharge Q5.

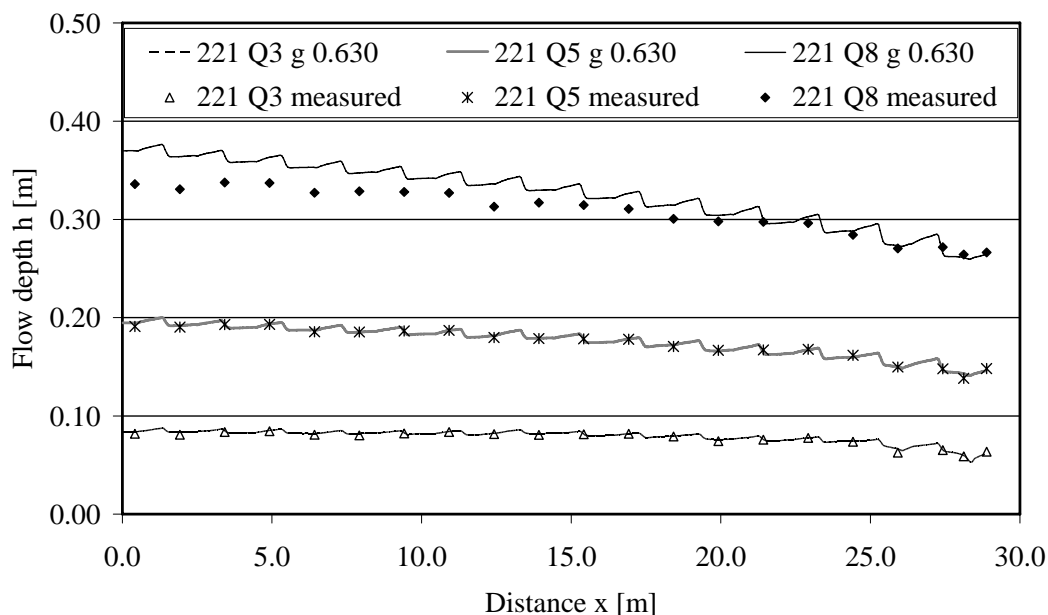


Figure 6-3: Experimental and numerical results for $\lambda = 0.630$ for the configuration 221 (Q3, Q5, Q8).

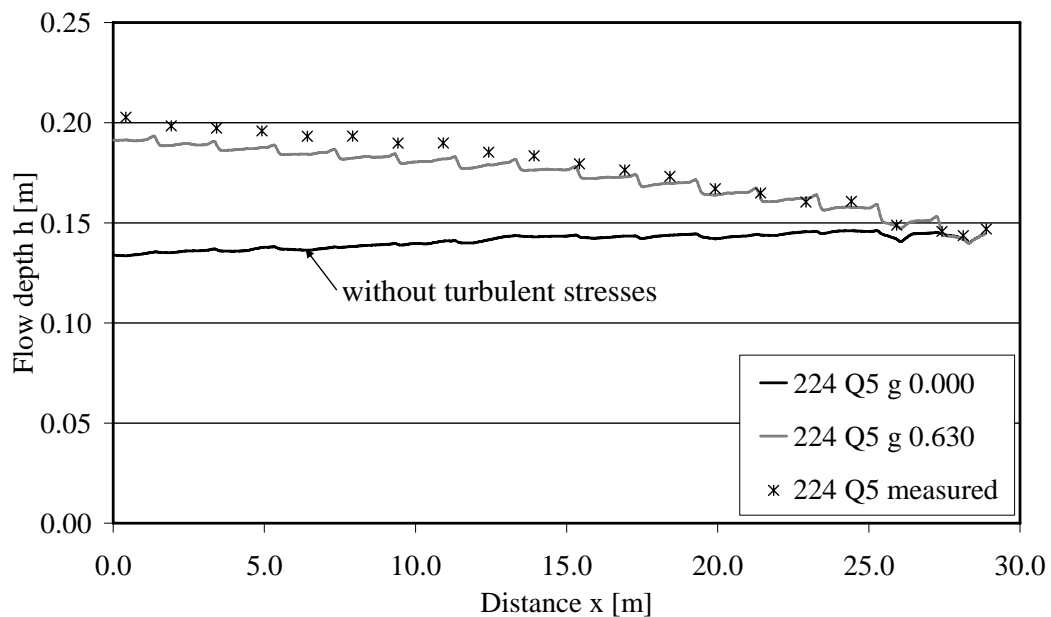


Figure 6-4: Experimental and numerical results with and without turbulence for the configuration 221 and discharge Q5.

6.1.3 Conclusions for the 2D-steady flow simulations

The channel configurations with macro-roughness elements at the banks generate turbulence stresses which have to be included in the numerical models. Skin friction alone does not allow the closure of the two dimensional shallow water equations by the source term (despite when the skin friction is artificially increased, which does however not represent the physic of the problem). It can be easily understood from the source term of the shallow water equations (eq. 6.2) that the friction slope might be used alternatively to the turbulence stresses for the water level calibration.

The dimensionless eddy viscosity λ is situated in a reasonable range compared to the literature (Rodi 1993). However, for the investigated macro-rough configurations, the value of λ is not constant which makes the generalization of the problem impossible. The application of formula (eq. 6.3) has to be questioned and the use of more complex, depth averaged turbulence models might be required (e.g. $k-\varepsilon$ model integrated over the depth).

The steady flow tests in the macro-rough configurations constitute an interesting and important database for the calibration of turbulence models of further developments.

6.2 1D-simulations of the unsteady flow experiments

6.2.1 Objectives

The goals of the 1D-simulations of the unsteady flow experiments can be summarized as follows:

- To test and validate a 1D surge wave simulation tool developed by Dubois (2007, personal communication).
- To integrate the effect of the macro-rough configurations by an adapted continuity equation in order to take into account the storage in the depression macro-roughness elements and by applying the roughness related parameters identified in the steady flow test analysis (§ 4.3).
- To compute the discharge $Q(t)$ from the calibrated 1D model allowing obtaining the discharge at the channel outlet which has not been measured during the tests.

6.2.2 Theoretical background and model description

The 1D tool Dubois (2007, personal communication) is based on a finite volume scheme. The mass and momentum fluxes through the boundaries are calculated using the HLL Riemann solver (Harten 1983). The celerity of the Riemann problem is computed based on the approach of Toro (1999) which determines the maximum celerity taking into account the celerity of a wave front at dry conditions. The 1D code integrates the Saint Venant equations, a finite volume scheme and the hydrostatic pressure reconstruction method through the bottom (Audusse, 2004). The 1D code for unsteady flow simulations has been developed by (Dubois 2007, personal communication) and is implemented into Microsoft Excel. The document contains following worksheets:

- **G**: the channel geometry, the parameters related to the macro-rough configurations, the employed friction law and the channel roughness.
- **CI**: the initial conditions (flow depth and discharge along the geometry at time t_0).
- **CL**: the boundary conditions upstream and/or downstream (flow depth h or discharge Q or Froude number Fr as a function of time).
- **Num**: the parameters for the numerical simulation as Courant number, discretisation, simulation time, time step for the saving of results. This worksheet contains also control parameters which are updated all along the computation.
- **ResQ**: the computed discharges along the channel saved for a chosen time step.
- **Resh**: the computed flow depths along the channel saved for a chosen time step.

At the actual state, the tool is especially adapted for the situation of the experiments in the laboratory flume “Vevey” using rectangular cross sections.

6.2.3 Simulations and results

Simulations are limited to positive surge waves from upstream since boundary conditions are well-known for these situations. The scenarios 3, 8, 10 and 21 of the prismatic configuration have been simulated first. Then, the positive surge of scenario 8 has been simulated for all axi-symmetric macro-rough configurations. The scenario 8 is characterized by a ratio $HP_1 = Q_{total} / Q_b = 2.7$.

The channel geometry has been reproduced between $x = -7.41$ m and $x = 30.92$ m. The boundary conditions as well as the roughness parameters were taken from the experiments. The courant number of all tests was 0.9. The number of finite volumes was 80 (one element per 0.479 m channel distance).

Positive surges from upstream in the prismatic configuration

Experimental flow depths of the prismatic configuration are compared to the simulated ones for four scenarios in Figure 6-5 to Figure 6-8. The baseflow Q_b and the additional flow Q_w due to the surge, introduced at the upstream limit of the channel, are:

- Prismatic S3: $Q_b = 6.0$ l/s, $Q_w = 17.7$ l/s
- Prismatic S8: $Q_b = 10.7$ l/s, $Q_w = 17.6$ l/s
- Prismatic S10: $Q_b = 10.7$ l/s, $Q_w = 53.4$ l/s
- Prismatic S21: $Q_b = 49.1$ l/s, $Q_w = 6.4$ l/s

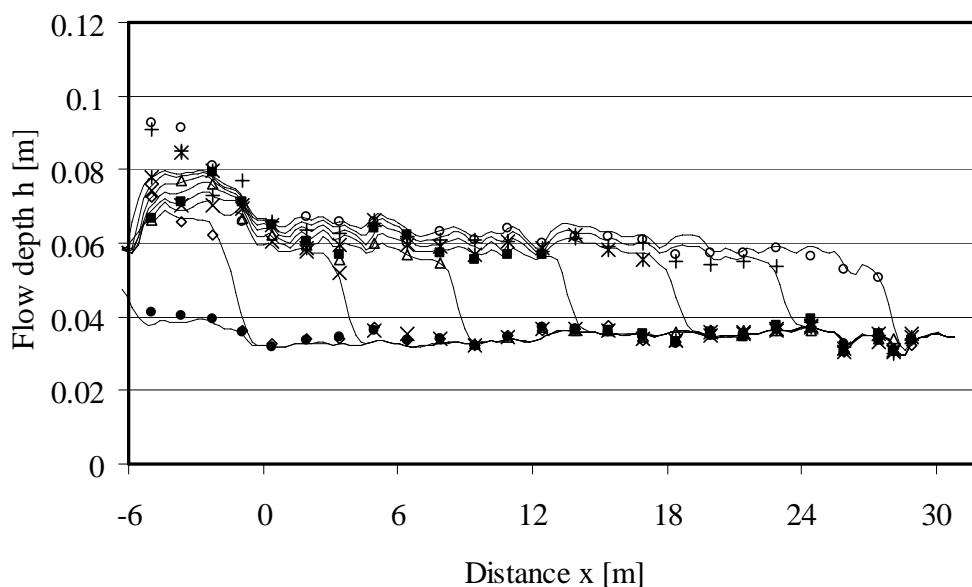


Figure 6-5: Flow depths along the channel for the prismatic configurations (Scenario 3). Lines=simulated values, points=measurements. The time step between the presented curves is $\Delta t=4$ s.

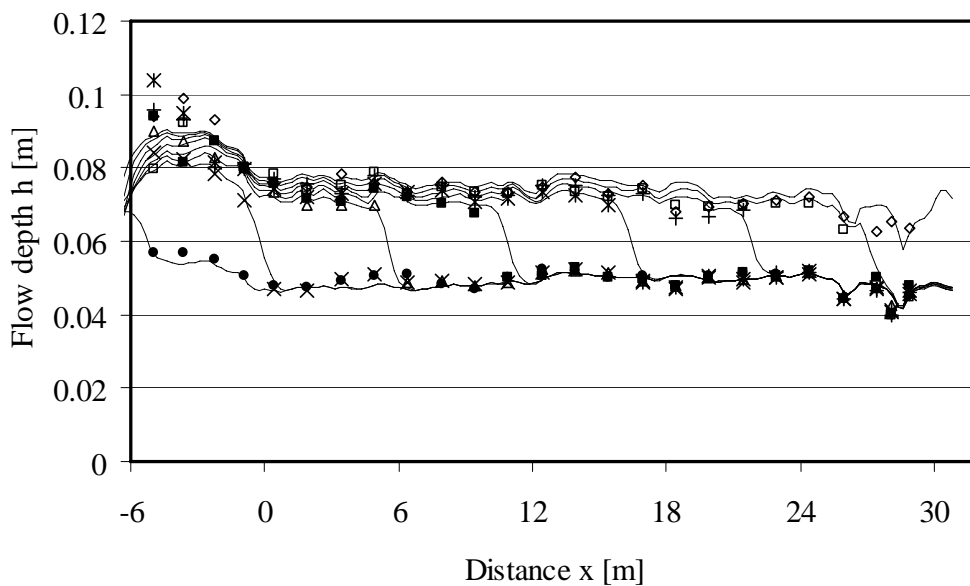


Figure 6-6: Flow depths along the channel for the prismatic configurations (Scenario 8). Lines=simulated values, points=measurements. The time step between the presented curves is $\Delta t=4$ s.

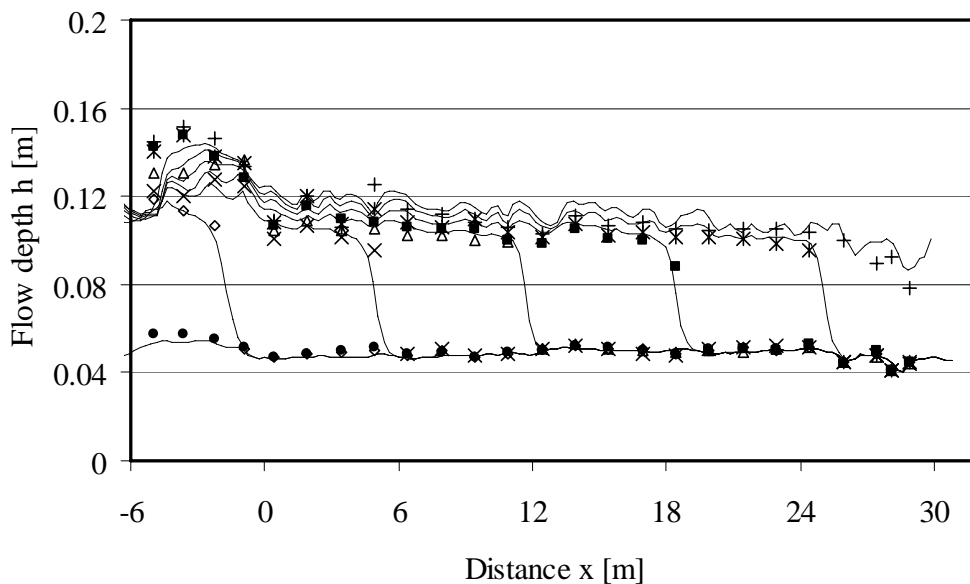


Figure 6-7: Flow depths along the channel for the prismatic configurations (Scenario 10). Lines=simulated values, points=measurements. The time step between the presented curves is $\Delta t=4$ s.

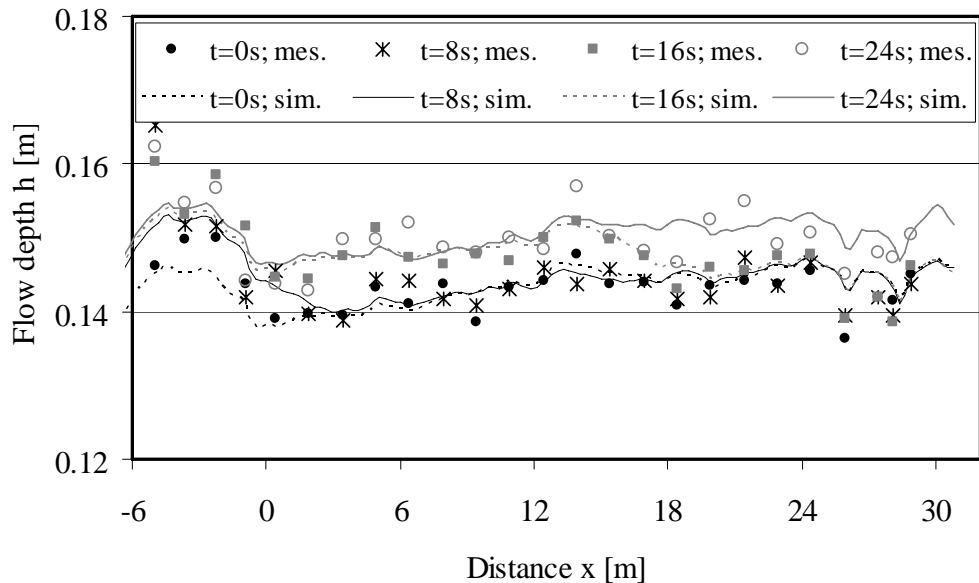


Figure 6-8: Flow depths along the channel for the prismatic configurations (Scenario 21). Lines=simulated values, points=measurements. The time step between the presented curves is $\Delta t=4$ s.

The following can be noticed from the simulations in the prismatic configurations:

- With appropriate boundary conditions as well as the observed skin friction of the prismatic configurations, the 1D simulation tool solved well the positive surge wave problem from upstream. Agreement between calculated and measured water level is good.
- For scenario 21, which is characterized by a high baseflow discharge and low additional discharge generating the positive surge, the propagation speed of the wave front is still quite well reproduced. Since the surge wave height is small in this case, some differences are observed for the water levels.
- The most important differences between measurements and simulation occur at the upstream boundary of the channel. They are due to the channel inlet geometry leading to an undulated hydraulic jump. The propagation of the surge further downstream is not influenced by these differences.
- The waves seem very steep but the vertical distortion on the figures should be taken into consideration. In fact, the channel is 38.33 m long (x -axis) whereas the height of the numerically investigated surges varied between less than 0.01 m and 0.08 m (y -axis).

Positive surges from upstream in axi-symmetric macro-rough configurations

For the simulation of the macro-rough configurations, the continuity equation (influencing the mass fluxes) has been adapted in order to take into account the storage of water in the depressions (e. g. Jirka and Lang 2005). Along the macro-rough reach, the channel width B (rectangular section) is replaced in the continuity equation by B^{**}

taking into account the cavity characteristics It is important to note that B is replaced by B^{**} only in the continuity equation, but not in the dynamic equation. B^{**} is expressed as:

$$B^{**} = B + 2 \frac{\Delta B L_b}{L_b + L_c} \quad (\text{eq. 6.4})$$

The increased friction is taken into account in the dynamic equation by using the roughness parameters identified by the experiments with steady flow presented in § 4.3. Separate bottom and wall roughness coefficients are considered ($K_{st,0}$ and $K_{st,w}$ considered in eq. 2.17).

Calculations have been done for all macro-rough configurations (scenario 8). In Figure 6-9 to Figure 6-11 the results for scenarios 141, 222 and 423 are shown as examples. Test characteristics are given in Table 6-2.

Table 6-2: Characteristics of the macro-rough test cases for the unsteady 1D-simulations.

Geometry ; Scenario	$L_b ; L_c ; \Delta B$ [m]	Q_b [m ³ /s]	Q_w [m ³ /s]	$K_{st,0}$ [m ^{1/3} /s]	$K_{st,w}$ [m ^{1/3} /s]	B^{**} [m]
141, S8	0.5 ; 2.0 ; 0.1	0.0101	0.0175	115	86	0.0525
222, S8	1.0 ; 1.0 ; 0.2	0.0110	0.0175	115	48	0.685
423, S8	2.0 ; 1.0 ; 0.3	0.0113	0.0175	115	56	0.885

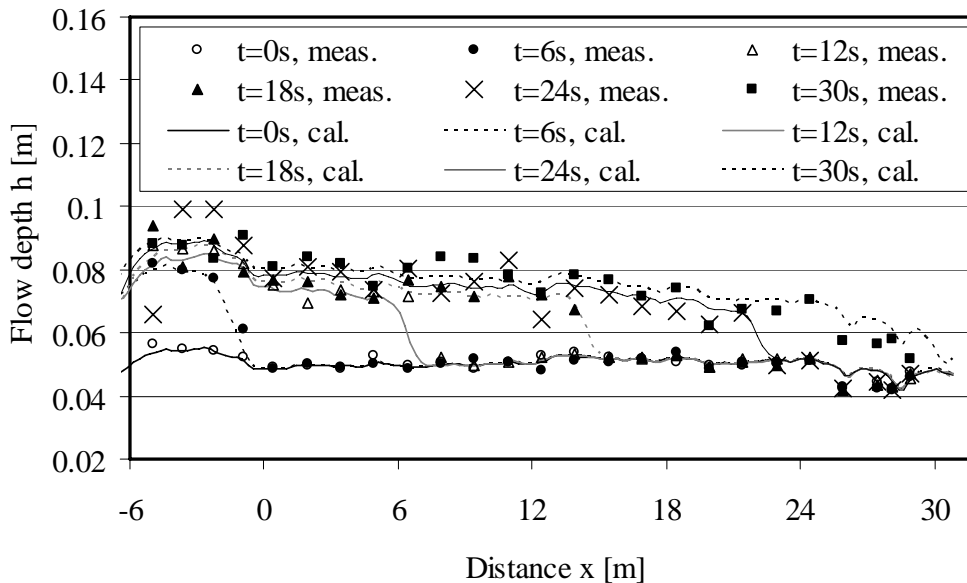


Figure 6-9: Flow depths along the channel for the macro-rough configuration 141 (Scenario 8). Lines=simulated values, points=measurements. The time step between the presented curves is $\Delta t=4$ s.

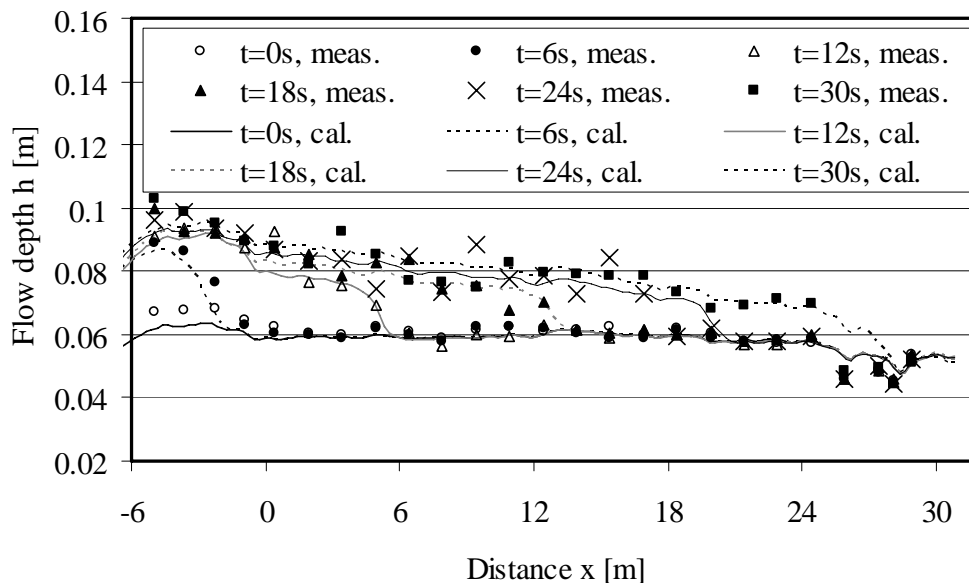


Figure 6-10: Flow depths along the channel for the macro-rough configuration 222 (Scenario 8). Lines=simulated values, points=measurements. The time step between the presented curves is $\Delta t=4$ s.

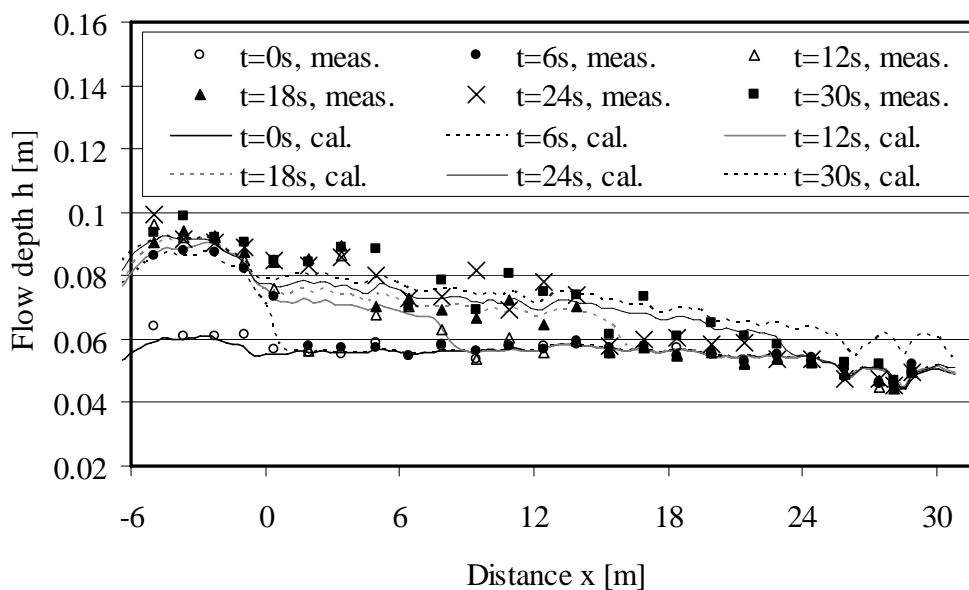


Figure 6-11: Flow depths along the channel for the macro-rough configuration 423 (Scenario 8). Lines=simulated values, points=measurements. The time step between the presented curves is $\Delta t=4$ s.

The results show the following:

- Propagation speed and flow levels are still well reproduced for scenario 8 in the macro-rough configurations, 141 and 222. Configuration 423, characterized by important cavities ($B^{**} = 1.82 \cdot B$), experimentally and numerically reduces the

surge the most significantly along the channel. Up to a time of $t = 18$ sec from the surge wave initiation, flow levels and propagation speed are quite well solved even for this highly, non-prismatic test case. After $t = 18$ sec, some major differences are observed.

- Compared to the prismatic configuration, positive surge waves from upstream deform significantly more when travelling downstream. It is however important to remember that behind the wave front, the water surface reaches a higher level than in the prismatic reference configuration due to increased roughness.
- The differences observed for configuration 423 might be explained by the fact that only the continuity equation has been modified. Since the flow expands significantly for this kind of configurations and since an significant part of the unsteady flow discharge is stored in the widenings, momentum flux might be modified too.

Nonetheless, flow depths fit quite well for the three, basically different, macro-rough configurations. It can thus be assumed that the downstream discharge can be calculated using the 1D-tool. This discharge is compared to the discharge estimated from the elementary surge wave theory. Globally, good agreement is observed despite for the configurations having cavity length of 2.0 m for which the computed discharge is consequently higher than the estimated one (§ 5.5.5).

The retention along the macro-rough reach, resulting from the increased friction and the storage in the depressions, has been quantified by comparison of the prismatic to the macro-rough configuration as:

$$\Delta V(x) = \int_{t=t_0}^{t=t_1} [(Q_{prism}(x,t) - Q_{MR}(x,t)) - (Q_{b,prism} - Q_{b,MR})] dt \quad (\text{eq. 6.5})$$

where t_0 corresponds to the arrival of the positive surge of the prismatic configuration. t_1 is arbitrarily chosen 40 s. All other parameters are shown in Figure 6-12 hereafter. The second term in the brackets is necessary to allow the comparison of tested scenarios even if the baseflow discharge is not identical.

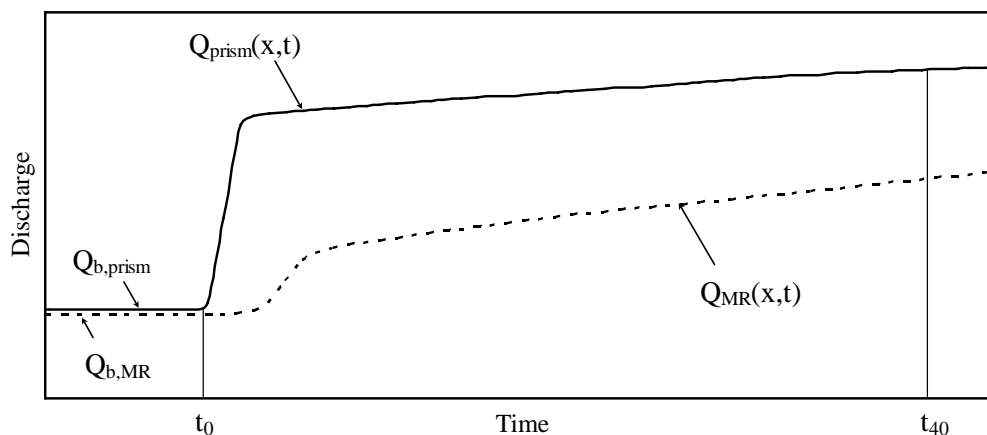


Figure 6-12: Definition of the parameters according formula (eq. 6.5).

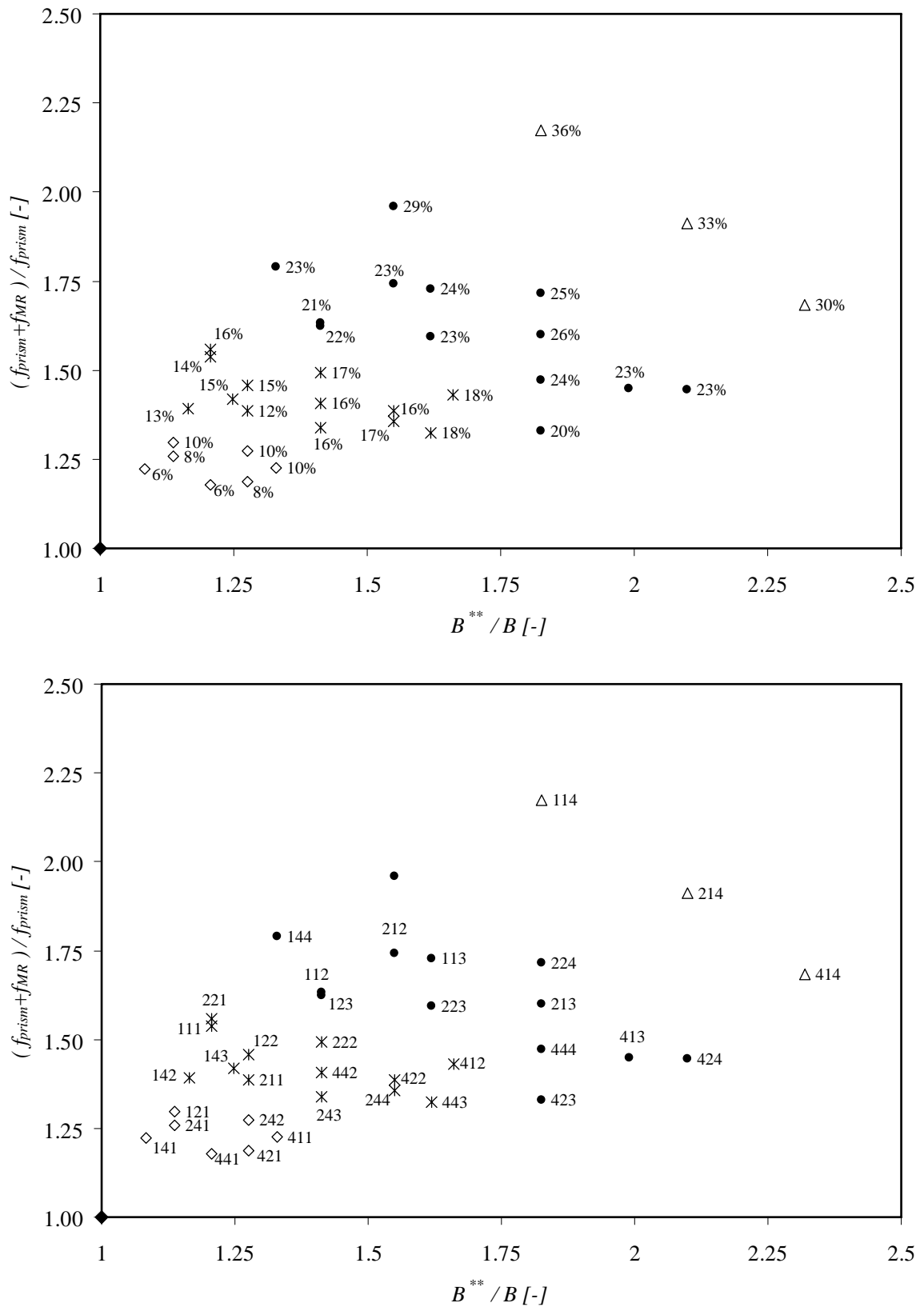


Figure 6-13: The relative reduction of the transited volume (%; above) as a function of the relative friction f_m / f_{prism} and the ratio B^{**} / B for scenario 8 after 40 seconds. The corresponding macro-rough configurations are indicated below.

In Figure 6-13 the result for all axi-symmetric macro-rough configurations of scenario 8 are summarized. The values of the relative reduction of the transited volume $\Delta \nabla(x) / \nabla(x)_{prism}$, (calculated at $x=27.42$ m; $\cong 57 \cdot B$) are compared to the parameter B^{**} / B and the flow resistance including macro-roughness $f_m / f_{prism} = (f_{prism} + f_{MR}) / f_{prism}$. Some intuitively expected results are confirmed and quantified by Figure 6-13 namely:

- In order to reduce the proportion of the sudden change in discharge compared to the total change, one can increase the flow resistance (expressed by f_m / f_{prism}) and/or the passive retention expressed by B^{**} / B .
- As expected, the most significant reductions of the sudden change compared to the total change are observed for rough configurations having large passive retention. The smallest reduction is observed for configurations with small passive retention and roughness.
- B^{**} / B and f_m / f_{prism} are somehow correlated since both depend on the geometrical properties of the depression roughness elements. Thus, points having high B^{**} / B and low f_m / f_{prism} respectively low B^{**} / B and high f_m / f_{prism} do not exist on Figure 6-13.

It must be remembered that Figure 6-13 characterizes the increased retention of the macro-rough configurations during the first 40 seconds after the arrival of the positive surge from upstream (prismatic configuration). According Figure 6-12 this retention is due to a delay and a slower increase of the discharge in the macro-rough configuration. At a given section, the difference of discharge between the prismatic and macro-rough configurations decreases with increasing time until reaching a value close to zero for high duration impulses of positive waves. Furthermore, the calculated retention corresponds to a distance $x=27.42$ m (end of the macro-rough reach). In order to get an idea about the order of magnitude of some characteristic values, Table 6-3 summarizes the values of the model and prototype scale assuming Froude similitude and two different length scales.

Table 6-3: Characteristic values of Figure 6-13 at model and prototype scale.

Parameter	Model (1:1)	Prototype (25:1)	Prototype (50:1)
Froude Fr	0.57	0.57	0.57
Width B	0.485 m	12 m	24 m
Baseflow Q_0	0.010 m ³ /s	31.2 m ³ /s	176 m ³ /s
Wave discharge Q_w	0.017 m ³ /s	53.1 m ³ /s	300 m ³ /s
$x_{us}-x_{ds}$	27.42 m	686 m	1370 m
Time to peak t_p^*	4 to 6 s	20 to 30 s	30 to 45 s
t_I-t_0	40 s	3 min 20 s	4 min 40 s
Baseflow depth h_n (prism.)	0.05 m	1.25 m	2.50 m

* corresponds to a very sudden start of turbines.

When considering a channel of about 12 m width and 0.7 km length including large scale depression roughness elements at the channel banks (increased flow resistance and passive retention) for example, a retention of about 6% to 36% of the discharge of the prismatic configuration during the first 3.5 minutes can be expected. These values are based on the assumption of a baseflow of $Q_b = 31 \text{ m}^3/\text{s}$ and additional flow of $Q_w = 53 \text{ m}^3/\text{s}$.

6.2.4 Conclusions for the 1D-unsteady flow simulations

One dimensional modeling of the surge waves has been done with success for the prismatic reference configuration as well as for different macro-rough configurations. The continuity equation has to be adapted for taking into account the additional volumes in the depression macro-roughness elements. The increased roughness was considered from the steady flow experiments in the dynamic equation. The most significant differences occurred for the important cavities for which the dynamic equation might be adapted too.

If the initial water surface corresponds to the observed one before the initiation of the surge wave, water depths and surge front propagation speed are well reproduced. The discharge at the end of the macro-rough reach has therefore been determined with the purpose to define a retention capacity of the different macro-rough configurations.

The calculated volumes retained during 40 s (model scale) confirm some intuitive ideas. Higher retention is reached either with increased roughness (e.g. macro-roughness) or by providing passive retention volumes.

However, in natural river morphologies influenced by sediment transport, erosion and deposition, waves will have more dispersive character compared to an artificial prismatic channel only when:

1. The increase of the discharge leads to a higher volume of water contained in a reach of a given length than in a prismatic channel.
2. The natural morphology effectively has an increased flow resistance.

The first point has been investigated within a student semester project (Ferrari 2007) under the author's supervision using the 2-D software "Basement" from the VAW-ETHZ (Minor et al. 2006). Different steady flow situations have been simulated in three river morphologies namely a channel, a channel with alternate bars and a braided river. The geometries were upscaled from laboratory experiments (Ackerman 2004, Requena et al. 2006).

On one hand, the results allow to quantify the increasing flow variability with the complexity of the morphology, suitable from an environmental point of view. On the other hand, the results show no significant extra volumes available with increasing complexity of real river morphologies. Hence, retention capacity of a river reach would be only notably increased by increasing actively the roughness or by the arrangement of passive retention volumes by river engineering works.

One dimensional simulation with an adequate roughness and an adapted continuity equation allows calculating the propagation and attenuation of (surge)waves in rivers influenced by hydropeaking. Since each river basin, characterized by its watersheds (geometry, slope) and its energy production units, is unique, the generalization of the problem is difficult. Diagrams for the estimation of the effect of morphological measures, such as proposed by Stranner (1996) are useful but durations of the impulses longer than 90 minutes should also be considered.

7 SUMMARY, CONCLUSIONS AND OUTLOOK

7.1 *Summary and conclusions*

Field of research

Rapidly varied unsteady flow is of relevance in hydraulic engineering applications influenced by sluice gate operations, flushing of reservoirs, debris jam and break up, ice jam and break up, flashfloods, dambreaks or sudden stopping and start up of turbines of runoff river and storage hydropower plants. Appropriate morphological measures increasing the roughness and the passive retention downstream of rejections of hydropower plants can influence the propagation and attenuation of surge waves. This has been shown by a systematic parameter study using a 1D-numerical model (Stranner 1996).

A literature review showed that surge wave experiments have been mainly conducted for prismatic channels (e.g. Favre 1935). The aim of this research was to investigate surge flows under the influence of large scale roughness at the channel banks for which no systematic studies existent to date. Furthermore, the effect of large scale roughness at the channel banks on the flow resistance could be determined under steady flow conditions.

Laboratory tests

Surge waves have been investigated in a 40 m long laboratory flume with a small slope of 1.14 ‰. Subcritical flow conditions are relevant with Froude numbers between $\sim 0.35 < Fr < \sim 0.65$. The aim of the experimental work was to investigate the influence of large scale roughness at the channel banks on the propagation and the deformation of surge waves.

The first part of the experiments was related to steady flow tests in 36 axi-symmetric macro-rough configurations (§ 4). Moreover, four asymmetric and one randomly generated macro-rough configuration have been analyzed. The large scale roughness consisted in rectangular cavities integrated in the channel banks (depression roughness). The aspect ratios of the cavities varied between $0.8 > \Delta B / L_b > 0.05$. The cavity depths varied between $0.4 > \Delta B > 0.1$ m for a channel base width of $B = 0.485$ m and the distance L_c between the cavities varied from 0.5 m to 2 m. The roughness parameters of the macro-rough configurations (Chezy, Strickler and friction coefficients) are of relevance for the unsteady flow tests. They have been identified by modeling the backwater-curves induced by the macro-rough channel banks for various steady discharges (5 l/s to 120 l/s).

Positive and negative surge waves from upstream have then been investigated for the same geometries. The unsteady flow was induced by a surge wave generating setup developed for these experiments. With this setup, 15 different additional discharges ranging between 7 l/s and 78 l/s could be added to the channel baseflow at the upstream boundary within 2 to 3 seconds. The waves generated by this way are classified in the domain of gravity waves. Totally, 235 positive and 235 negative surge waves from upstream have been tested and analyzed mainly based on water-level measurements. The ratio of the total discharge (including the surge) to the baseflow discharge ranged between $10.0 > Q_{total} / Q_b > 1.1$.

Steady flow in a channel with macro-roughness at the banks (large scale depressions)

The cavity geometry and also the flow conditions in the main channel have an influence on the flow pattern inside the cavity. For cavity aspect ratios $\Delta B / L_b \leq 0.1$, the flow reattaches to the sidewalls except for very low discharge conditions with $h / B < 0.12$. With increasing mean flow velocities and flow depths, the flow becomes complex. It is governed by different phenomena which are responsible for the additional head-loss along the macro-rough channel namely recirculation gyres, coherent structures, vertical mixing layers, wake-zones and transverse oscillations of the flow.

Important transverse oscillations of the flow at particular values of the Strouhal number

Important oscillations transverse to the main flow direction occur at Strouhal numbers close to 0.42 and 0.84. This flow feature creates water surface oscillations inside the cavity. It is produced by a hydrodynamic feedback effect provided from the backflow inside the cavity. Since the main frequency of the observed water surface oscillations and the main frequency of the measured transverse velocity components are identical with the one of vortices which shed periodically at the cavity leading edge, the phenomena are assumed to be coupled.

Flow resistance induced by the macro-roughness elements

The experimentally investigated cavities can be considered as macro-roughness elements (depression roughness) since their size is important compared to the hydraulic radius. The backwater curve computation allowed to identify the overall flow resistance in terms of friction coefficients f , Chezy coefficient C and Strickler coefficient K_{st} . It appears that disturbing the flow by macro-roughness elements leads to a significant increase of the flow resistance compared to the prismatic reference configuration. The increase becomes clearly visible with increasing relative flow depths h / B respectively increasing values of the Reynolds number. The difference between the prismatic configuration and the 36 macro-rough configurations is important whereas the differences between the 36 macro-rough configurations itself are more difficult to identify (Figure 4-30). The relative roughness spacing was found to be the most important parameter for the determination of the friction coefficients.

Empirical formulas for the computation of the flow resistance induced by form drag

Three approaches have been considered to develop empirical formulas which allow to calculate friction coefficients for the channel bank macro-roughness: the first one is based on a Powerlaw optimization, the second on a form drag coefficient model, and the third on the Evolutionary Polynomial Regression method. For the experiments, they have all comparable performance. The formulas suggested for use in river engineering applications are summarized Table 4.15 and § 7.3.

In order to obtain the total friction of the channel cross section f_m , the friction coefficient from the empirical formulas for the channel bank macro-roughness f_{MR} is summed up with the friction coefficient of the channel without macro-roughness f_{prism} . The friction coefficient of the prismatic channel f_{prism} (natural or artificial) can be determined by commonly used formulas presented in § 2.1.

The formulas based on the form drag coefficient model could be extended to channel banks having macro-roughness elements different from rectangular cavities by the determination of corresponding drag coefficients.

Unsteady flow – Main differences between the prismatic reference and the configurations with macro-roughness at the banks

For the prismatic reference configuration the analysis of the surge wave experiments confirms the elementary surge wave theory. Secondary waves can be observed for surge Froude numbers between $1.06 < Fr_s < 1.5$. For higher surge Froude numbers, secondary waves disappear. Unsteady velocity measurements of the streamwise velocity components $u(z)$ have been done using an Ultrasonic Doppler Velocity Profiler (UVP). For surge waves with breaking conditions at the wave front the measurements revealed that the non hydrostatic pressure distributions are limited to a small part of the wave. This explains physically the disappearance of the secondary waves at the wave front under breaking conditions.

In the macro-rough configurations, the surge wave front deforms and it becomes 3 dimensional in the widened channel reaches. Partial reflections and surface waves lead to a weak water-surface which makes the identification of the front difficult. The attenuation of the height of the surge wave front along the channel with macro-roughness at banks is significantly increased.

Reduction of the absolute celerity V_w and the celerity c of the surge wave

The absolute wave celerities along the macro-rough reach $V_w = U + c$ have been found practically constant, but reduced when compared to the prismatic reference. The constant values along the channel must be explained by Froude numbers relatively close to $Fr = 0.5$ for which the effects of mean flow velocity U and celerity c compensate. The reduction compared to the prismatic reference lies between 5% and 25% for both, positive and negative surge waves from upstream. The reduction of the absolute surge wave celerities in the macro-rough configurations has four reasons:

- 1) Due to a backwater-curve, the flow depths increase and thus the mean flow velocity decreases from downstream to upstream along the channel. The absolute surge wave celerity $V_w = U+c$ thus decreases. However, the decrease of U is partially balanced by the increase of the celerity c due to the higher water levels.
- 2) An additional decrease of the mean flow velocity results from the partial expansion of the flow in the widened channel reaches.
- 3) The surge wave front height diminishes along the macro-rough reach which leads to an attenuation of the celerity according to the elementary surge wave theory.
- 4) Finally, due to macro-roughness at the channel banks, the flow resistance (friction coefficient) is increased.

Assuming a conceptual flow expansion model (§ 5.6.4), the difference between the observed celerity and the theoretical celerity (calculated based on the flow depths before and after the surge wave front) can be explained to some extent by the friction coefficients.

Attenuation of the height of the surge wave front

The analysis of the surge wave front height confirms the diffusive character of surge waves, which is increased in the macro-rough configurations compared to the prismatic reference. The extra diffusion is the result of the macro-rough flow resistance, the partial reflections in the cavities and the passive retention.

The ratio between the surge wave height upstream and downstream of the experimental channel h'^+_{ds}/h'^+_{us} indicates a decrease of 5% (low Q_{total}/Q_b) to 25% (height Q_{total}/Q_b) of the surge wave front height along the prismatic channel. In the macro-rough configurations, the decrease is significantly higher (up to 70%).

The height of the negative surge wave front (h'^-_{ds}/h'^-_{us}), estimated from the level measurements, decreases along the prismatic channel of 5% to 25%. The decrease of h'^- ranges between 10% and 75% along the channel with macro-roughness at the banks.

The attenuation of the surge wave front height can be described with the empirical formula:

$$\frac{h'(x)}{h'(x_0)} = e^{-(a+b) \cdot x} \quad (\text{eq. 5.16})$$

where $h'(x)$ is the wave front height at a distance x of the channel. $h'(x_0)$ is the initial wave front height. a and b are the attenuation parameters of the wave front height in the prismatic channel (a) and due to the macro-roughness elements at the channel banks (b) respectively. The attenuation parameters of the wave front height in the prismatic channel are $a^+ = 0.39$ for the positive surge wave and $a^- = 0.99$ for the negative surge wave. The values of b can be determined directly from the experiments with different macro-rough configurations or they can be estimated with the empirical formulas (eq. 5.19) and (eq. 5.20).

The dimensionless distance X takes into account the channel slope S_0 (a priori constant) and the depth of the baseflow h_b (a priori uniform and steady) at the reference location x_0 . It is expressed as:

$$X = \frac{x - x_0}{(h_b / S_0)} \quad (\text{eq. 5.15})$$

The uniform baseflow depth conditions are verified in the present experimental study only for the prismatic reference. This limits the range of application for quantitative results in the macro-rough configurations to bottom slope close to 0.001 and backwater-curve of the type M2.

Asymmetric and randomly generated configurations with macro-roughness at banks

For both, steady and unsteady flow tests, the asymmetric macro-rough configurations generally show comparable roughness parameters and characteristics of the surge wave propagation. The configuration with randomly generated macro-rough banks acts usually like configurations having "average" macro-rough characteristics.

7.2 Outlook

This study provides answers to cavity flows, macro-rough flow resistance and surge wave flow in macro-rough, complex morphologies. Furthermore, the research revealed some questions, which would be interesting to analyse in future researches namely:

- To investigate the influence of uneven bed topographies, including sediment transport, on the amplitude and frequency of water surface oscillations and to investigate the influence of the base width B , which influences the frequency of the oscillations but also the ability of axi-symmetric cavities to interact.
- The semi-empirical flow resistance formula based on the form drag coefficient model performs well in the laboratory field. For practical applications, the empirical part concerning the expansion of the flow might be eliminated (or confirmed) by investigations on a shorter model at a scale allowing higher Reynolds numbers. However, the basic architecture of the semi-empirical equation should be generally valid. Furthermore, the drag coefficients of other shapes than rectangular slots could be investigated.
- Only few geometric configurations were characterized by the square grooved flow type. The application range and performance of formulas for this flow type might be increased by tests in geometries with other base widths.
- Steady and unsteady flow data are available for the validation of numerical models. In particular, the question of an adequate turbulence model for steady flow conditions and the question whether turbulent stresses have to be considered or not for

highly unsteady flow can be highlighted.

- Some surge wave experiments have not been analyzed yet. With additional input data, the attenuation parameter for the surge wave front height might be predicted better.

7.3 Recommendations for practical engineers

Cavity oscillations

The results issued from the analysis of the cavity oscillations are of relevance for practical applications dealing with embayments and groinfields. Strouhal numbers close to 0.42 and 0.84 should be avoided in order to eliminate or reduce water-surface oscillations and transverse velocity components of the flow which might cause problems for navigation. When knowing the range of flow depths and mean flow velocities, the geometric parameters L_b and ΔB can be adjusted to avoid Strouhal numbers close to 0.42 and close to 0.84 (eq. 7.1). This equation results from the combination of (eq. 4.6) assuming the first mode of sloshing and (eq. 4.9):

$$St = \frac{1}{2\pi} \frac{\sqrt{\frac{\pi g}{W} \tanh\left(\frac{\pi h}{W}\right)} L_b}{U} \quad (\text{eq. 7.1})$$

where $W = B + 2\Delta B$ is the width at the enlarged reach, h the flow depth, U the mean flow velocity relative to the channel base width B and L_b the length of the cavity.

Computation of the flow resistance of channel banks including macro-roughness

For the estimation of the flow resistance of large scale channel bank roughness, three basic flow types have been identified: the square grooved flow type, the reattachment flow type and the normal recirculating flow type. From the different developed formulas, those of Table 4.15 are recommended for the calculation of normal depth h_n or for friction slopes S_f up to 0.005. Froude numbers varied approximately between $0.35 < Fr < 0.65$ in the experiments. The range of characteristic, dimensionless geometrical parameters during the tests were:

- $10 > B / R_{hm} > 3.2$
- $70 > (L_b + L_c) / R_{hm} > 10$
- $40 > (L_b + L_c) / \Delta B > 3.33$

For the physically based formulas issued from the approach based on form drag, an extension of the application range of the dimensionless geometrical parameters should be possible.

The formulas of Table 4.15 provide the form drag induced contribution of the channel banks f_{MR} to the total flow resistance coefficient which can be calculated as:

$$f_m = f_{prism} + f_{MR}$$

where f_m is the friction coefficient of the cross section as used in the Weisbach-Darcy equation and f_{prism} the friction coefficient without large scale roughness at the banks. In the present study, this friction coefficient f_{prism} was calculated using the Colebrook-White formula for the experimental flume without macro-roughness. For practical applications, the friction coefficient of the prismatic channel (natural or artificial) can be determined by commonly used formulas presented in § 2.1.

Table 4.15: Recommended formulas issued from the empirical and semi-empirical approaches for the calculation of the macro-rough friction coefficient of the channel bank macro-roughness f_{MR} . $C_d = 0.475$ is the drag coefficient of a rectangular cavity and $Re_{lim} = 150 \cdot 000$ and $x_0 = 4.5$, respectively, are empirical parameters describing the flow expansion.

Flow type	Geometrical criteria	Formula
		issued from the Powerlaw optimization:
Square grooved flow type	$L_b \cong \Delta B \cong B$	$C_{adim\ MR,sg} = \sqrt{\frac{8}{f_{MR,sg}}} = 5 \cdot \left(\frac{L_b + L_c}{R_{hm}}\right)^{1/3}$ (eq. 4.38)
		issued from the form drag based approach:
Reattachment flow type	$\Delta B / L_b \leq 0.1$	$f_{MR,re} = C_d \frac{8R_{hm}\Delta B}{B(L_b + L_c)}$ (eq. 4.46)
		issued from the approach based on form drag:
Normal recirculating flow type	$0.1 \leq \Delta B / L_b \leq 0.8$	$f_{MR,nc} = C_d \frac{8R_{hm}\Delta B^*}{B(L_b + L_c)}$ (eq. 4.42)
		$\Delta B^* = \min(\Delta B ; (L_b / x))$ (eq. 4.43)
		$x = \left(\frac{Re_{lim}}{Re_m} + x_0\right) \left(\frac{L_b}{\Delta B}\right)^{0.18}$ (eq. 4.47)

The formula for the normal recirculating flow includes some engineering safety, since the expansion of the flow might be overestimated for Reynolds numbers at prototype scales. Furthermore, it can be noticed that the macro-rough flow resistance at the banks becomes significant with increasing ratios h/B .

Surge wave propagation in channels with large scale roughness at banks

The results of the unsteady flow experiments showed qualitatively the decrease of the propagation velocity of the surge wave front and the attenuation of the height of the surge wave front. For all macro-rough configurations, the attenuation parameter of the

surge wave front height is increased when compared to the prismatic configuration.

By numerical simulations it has been shown that for most engineering applications, the propagation of surge waves might be accurately solved by 1D-models. An adequate roughness estimation can be derived from the results shown above and the continuity equation of 1D-models can be adapted following § 6 for taking into account passive retention.

Concerning morphological measures, engineers should be aware of the following points:

- Channel bank macro-roughness produces additional flow resistance which has to be considered for flood protection.
- Surge waves become more diffusive than in a prismatic channel only when the morphological measures effectively increase the resistance of the flow in a range of discharges typical for hydropeaking. Furthermore, higher passive retention only occurs when the increase of the discharge increases the volume of water contained in a reach more significantly than in a prismatic channel. For the range of discharges typical for hydropeaking, these effects become substantial only by river engineering works increasing artificially the roughness or by the arrangement of passive retention volumes.
- Morphological measures increase the variability of the flow pattern which is desirable from an environmental point of view. Particular attention should be addressed for limiting the areas regularly submerged and emerged.
- For long duration impulses of hydropeaking, which are dominant in most of the alpine rivers, morphological measures as macro-roughness at banks make the (surge)waves more diffusive and reduce the rate of increase of the flow depth or the discharge. However, they will not significantly influence on the maximum daily discharge such as managed detention basins with important volumes.

Notations

Regularly used variables and constants are summarized hereafter. The present list of notations is valid throughout the whole work, unless otherwise mentioned explicitly in the text below formulas or in captions of figures and tables. The regularly used subscript and exponents are described after the variables and constants.

Geometrical parameters of the configurations and the channel:

ΔB	:	[m]	:	Widening depth
B	:	[m]	:	Base width of the channel
L_b	:	[m]	:	Widening length
L_c	:	[m]	:	Longitudinal distance between two widenings
W	:	[m]	:	Width at the enlarged sections = $B+2\Delta B$
x	:	[m]	:	x-axis of channel ($x = 0.0$ m at begin macro-rough reach)
y	:	[m]	:	y-axis of channel ($y = 0.0$ m at the channel axis)
z	:	[m]	:	z-axis of channel ($z = 0.0$ m at downstream section)
i	:	[-]	:	relative to the channel section i

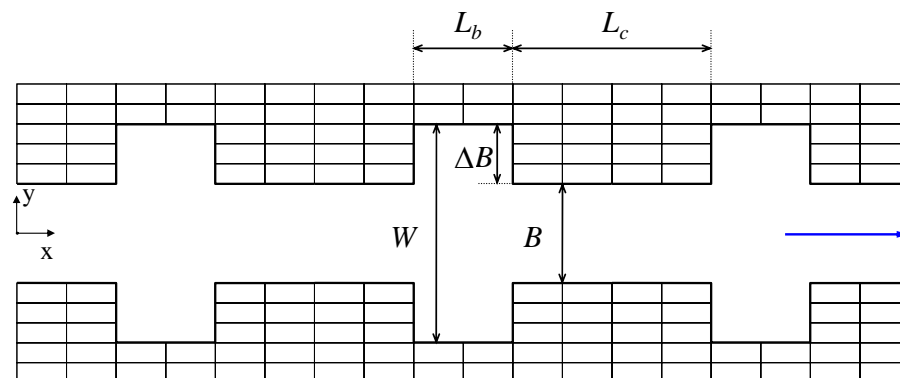


Figure N-1: Definition of the geometrical parameters of the configurations and the channel.

Variables and constants

A	:	[m ²] or [-]	:	Cross sectional flow area or Log-law constant
B	:	[m] or [-]	:	Flow width at the water-surface or Log-law constant
C & C_c	:	[m ^{0.5} s ⁻¹]	:	Chezy coefficient & composite Chezy coefficient
C_d	:	[-]	:	Drag coefficient
CoD	:	[-]	:	Coefficient of determination (also Nash coefficient)
C_r	:	[-]	:	Surge reflection coefficient
D	:	[m]	:	Pipe diameter
E	:	[J]	:	Energy
Fr	:	[-]	:	Froude number = $U/(gh)^{0.5}$

NOTATIONS

Fr_s	:	[-]	:	Surge Froude number
G	:	[-]	:	Dimensionless head-loss correction factor
H	:	[m]	:	Head <u>or</u> height of transverse bars (step-pool configurations)
HP_1	:	[-]	:	Dimensionless discharge parameter
HP_2	:	[-]	:	Dimensionless discharge parameter
K_{st}	:	[m ^{1/3} s ⁻¹]	:	Strickler coefficient
L	:	[m]	:	Length of the control volume of the front
(L/z)	:	[-]	:	Ratio of the distance to the height of macro-scale bottom rib roughness
P	:	[m] <u>or</u> [°]	:	Total wetted perimeter [m] <u>or</u> Phase [°]
Q	:	[m ³ s ⁻¹];	:	Discharge
Q_b	:	[m ³ s ⁻¹];	:	Baseflow discharge
Q_{total}	:	[m ³ s ⁻¹];	:	Total discharge = $Q_b + Q_w$
Q_w	:	[m ³ s ⁻¹];	:	Additional discharge due to surge
R	:	[-] <u>or</u> [m]	:	Linear correlation coefficient in statistical analysis <u>or</u> Pipe radius
Re	:	[-]	:	Reynolds number
R_h	:	[m]	:	Hydraulic radius
S_0	:	[-]	:	Bottom slope
S_e	:	[-]	:	Head-loss (slope) for steady flow conditions
S_f	:	[-]	:	Friction slope
S_a	:	[-]	:	Additional head loss due to channel-floodplain interaction
St	:	[-]	:	Strouhal number
T	:	[s]	:	Period
U	:	[ms ⁻¹]	:	Mean flow velocity at the channel base width B if not explicitly mentioned otherwise
V_v	:	[ms ⁻¹]	:	Tangential velocity of depression vortex
V_w	:	[ms ⁻¹]	:	Absolute surge wave celerity = $U+c$ <u>or</u> Velocity near wall in the approach of Morris (1955)
V_F	:	[ms ⁻¹]	:	Dam break front velocity
We	:	[-]	:	Weber number
Δl	:	[m]	:	Unit length
Δp	:	[Nm ⁻²]	:	Pressure drop per unit length
a	:	[m] <u>or</u> [-]	:	Wave amplitude of an oscillatory wave <u>or</u> log-law constant
\mathbf{a}	:	[-]	:	Prismatic attenuation parameter of the front height
\mathbf{b}	:	[-]	:	Macro-rough attenuation parameter of the front height
c	:	[ms ⁻¹]	:	Celerity of a gravity wave (despite c_k : kinematic wave)
d_c	:	[m]	:	Characteristic diameter of the particle size distribution curve, c : can be 90, 84, 50, m(mean), ...
d_x & d_z	:	[m]	:	Roughness element streamwise & vertical dimensions
e	:	[m]	:	Spacing of secondary wave crests
f	:	[-]	:	Friction coefficient used with different subscripts

f_{cal}	:	[Hz]	:	Frequency calculated from (eq. 4.6) or (eq. 4.7)
f_{FFT}	:	[Hz]	:	Frequency of the observed transverse oscillations
f_{shed}	:	[Hz]	:	Frequency of the vortex shedding
g	:	[ms ⁻²]	:	Gravitational constant
h	:	[m]	:	Flow depth
h'	:	[m]	:	Surge wave front height
h'_{min} & h'_{max}	:	[m]	:	Surge wave front height at crest & trough of Favre waves
h_0	:	[m]	:	Water depth in the reservoir of the dam break problem
k	:	[m]	:	Geometrical roughness height
K_1 to K_3	:	[-]	:	Constants in the logarithmic law of type Colebrook
k_s	:	[m]	:	Equivalent sand roughness height
n & n_c	:	[m ^{-1/3} s ¹]	:	Manning coefficient & composite Manning coefficient
p	:	[m]	:	Part of the wetted perimeter covered with roughness elements
t ; t_p	:	[s]	:	Time; time to peak
u	:	[ms ⁻¹]	:	Streamwise velocity component
u_*	:	[ms ⁻¹]	:	Friction velocity = $(gS_f R_h)^{0.5}$
v	:	[ms ⁻¹]	:	Spanwise velocity component
w	:	[ms ⁻¹]	:	Vertical velocity component
Γ	:	[-]	:	Spatial pebble density
Δ or Δ	:	[-] or [m]	:	Difference <u>or</u> height of ripples and dunes
Λ	:	[-] or [m]	:	Inundation ratio h/k <u>or</u> length of ripples and dunes
Π	:	[-]	:	Wake parameter
Φ	:	[-]	:	Correction factor of the hydraulic radius
			:	
α	:	[°]	:	Flow expansion angle $\tan(\alpha) = I/x$
α	:	[°]	:	Non-uniformity coefficient of the velocity profile
α	:	[°]	:	Roughness param. for flow resistance computation (eq. 2.9)
α_s ; β_s	:	[°]	:	Sediment transport correction parameters
β	:	[°]	:	US-transducer downstream angle
γ_r & γ_d	:	[-]	:	Presence factor for ripples & dunes
γ	:	[N/m ³]	:	Specific weight
δ_r & δ_d	:	[-]	:	Steepness of ripples & dunes
δ	:	[m] <u>or</u> [°]	:	Boundary layer thickness <u>or</u> angle channel bank / watersurf.
ε	:	[-]	:	Relative roughness height = k_s/D
κ	:	[-]	:	Von Karman integration constant
λ	:	[m] <u>or</u> [-]	:	Longitudinal spacing of roughness elements <u>or</u> solidity
μ	:	[-]	:	Contraction coefficient
ν	:	[m ² s ⁻¹]	:	Kinematic viscosity
ξ	:	[-]	:	(Power-law) constant

ρ	:	$[\text{m}^3\text{s}^{-1}]$:	Fluid density
τ^* ; τ^*_{cr}	:	[-]	:	Shields parameter; critical Shields parameter
τ_0	:	$[\text{N}/\text{m}^2]$:	Shear stress
χ_1 ; χ_2	:	[-]	:	Exponents in eq. 2.9 for flow resistance computation

Subscripts and exponents

-	relative to the negative wave
+	relative to the positive wave
α, β, \dots	Power law exponents
<i>adim</i>	relative to a dimensionless parameter
<i>cal</i>	calculated
<i>cr</i>	relative to critical flow conditions
<i>ds</i>	downstream
<i>i</i>	relative to an US-probe along the channel
<i>m</i>	relative to the composite channel section including effect of macro-roughness
<i>max</i>	relative to a maximum value
<i>min</i>	relative to a minimum value
<i>MR</i>	relative to the macro-roughness
<i>nc</i>	relative to normal recirculating flow type
<i>obs</i>	observed
<i>prism</i>	relative to the prismatic configuration (without MR)
<i>re</i>	relative to reattachment flow type
<i>sg</i>	relative to square grooved flow type
<i>th</i>	theoretical
<i>us</i>	upstream
<i>w</i>	relative to the side-walls of the channel
<i>ch</i>	relative to the main channel (in composite channels)
<i>fr and fl</i>	relative to the right side and left side floodplain (in composite channels)
<i>0</i>	relative to the bottom of the channel
<i>1</i>	just before the positive surge wave front (or negative surge wave front § 2)
<i>2</i>	just after the positive surge wave front (or negative surge wave front § 2)
<i>3</i>	just before the negative surge wave (§ 5)
<i>4</i>	just after the negative surge wave (§ 5)

References

- Abrahams, A. D., Li, G., and Atkinson, J. F.** (1995). "Step-pool streams - adjustment to maximum flow resistance." *Water Resources Research*, 31(10), 2593-2602.
- Ackerman, S.** (2004). "Seitenerosion in verzweigten Flüssen II." Diplomarbeit an der Versuchsanstalt für Wasserbau, Hydrologie und Glaziologie - VAW der ETH Zürich (unveröffentlicht), Zürich, Switzerland.
- Alcrudo, F.** (2002). "State of the Art review on Flood Propagation " An introduction to the IMPACT Project, HR Wallingford, Wallingford.
- André, S.** (2004). "High velocity aerated flows on stepped chutes with macro-roughness elements." *Communication du Laboratoires de Constructions Hydrauliques - LCH, N°20*, EPFL, Lausanne, Switzerland.
- Audusse, E.** (2004). "Hyperbolic Models and Numerical Analysis for Shallow Water Flows," Ph.D. Thesis TU-1131, Université Paris VI, Paris, France.
- Back, L. H., and Roshke, E. J.** (1972). "Shear-layer flow regimes and wave instabilities and reattachment lengths downstream of an abrupt circular channel expansion." *Journal of Applied Mechanics*, 94, 677-781.
- Bandyopadhyay, P. R.** (1987). "Rough-wall turbulent boundary layers in the transition regime." *Journal of Fluid Mechanics*, 180, 231–266.
- Bathurst, J. C.** (1978). "Flow resistance of large-scale roughness." *Journal of the Hydraulics Division-ASCE*, 104(12), 1587–1603.
- Bathurst, J. C.** (1985). "Flow resistance estimation in mountain rivers." *Journal of Hydraulic Engineering - ASCE*, 111(4), 625–643.
- Baumann, P., and Klaus, I.** (2003). "Gewässerökologische Auswirkungen des Schwallbetriebes - Ergebnisse einer Literaturstudie." Bundesamt für Umwelt, Wald und Landschaft (BUWAL), Bern, Switzerland.
- Baumann, P., and Meile, T.** (2004). "Makrozoobenthos und Hydraulik in ausgewählten Querprofilen der Rhone." *Wasser, energie, luft – eau, énergie, air*, 96(11/12), 320-325.
- Baumann, P., Meile, T., and Fette, M.** (2005). "Synthesebericht Schwall/Sunk." Publikation des Rhone-Thur Projektes, Eawag, WSL, LCH-EPFL, VAW-ETHZ, Pdf auf www.rivermanagement.ch.
- Bazin, H.** (1865). "Recherches expérimentales relatives aux remous et à la propagation des ondes." Dunod, Paris, 528-553.
- Benet, F., and Cunge, J. A.** (1971). "Analysis of Experiments on Secondary Undulations caused by Surge Waves in Trapezoidal Channels." *Journal of Hydraulic Research - IAHR*, 9(1), 11-33.
- Bezzola, G. R.** (2002). "Fließwiderstand und Sohlenstabilität natürlicher Gerinne," Ph.D. Thesis N°14433, ETHZ, Zürich, Switzerland.
- Birkhofer, B. H., Windhab, E. J., and Jeelani, S. A. K.** (2006). "Monitoring of fat crystallization process using UVP-PD technique." *Fifth International Symposium on Ultrasonic Doppler Methods for Fluid Mechanics and Fluid Engineering*, Eidgenössisch Technische Hochschule Zürich, Switzerland, 149-153.
- Bousmar, D., and Zech, Y.** (1999). "Momentum transfer for practical flow computation in compound channels." *Journal of Hydraulic Engineering - ASCE*, 125(7), 696-706.
- Bray, D. I.** (1987a). "Estimating average velocity in cobble-bed channels." National Conference on Hydraulic Engineering, R. M. Ragan, ed., ASCE, Williamsburg, Virginia, USA.
- Bray, D. I.** (1987b). "A review of flow resistance in gravel-bed rivers." *Leggi morfologiche e loro verifica di campo*, Università della Calabria, Cosenza, Italy.

- Brückner, E. (1895).** "Untersuchungen über die tägliche Periode der Wasserführung und die Bewegung von Hochfluten in der oberen Rhone." *Mitteilungen aus Justus Perthes' Geographischer Anstalt*, Mitteilungen 41, 159-169.
- BWG. (2001).** "Rauheiten in ausgesuchten schweizerischen Fließgewässern." Serie Wasser, No.1, Berichte des Bundesamts für Wasser und Geologie (BWG).
- BWG. (2002).** "Hochwasser 2000 - Les crues 2000. Ereignisanalyse und Fallbeispiele." Serie Wasser, Nr. 2, Berichte des Bundesamts für Wasser und Geologie (BWG).
- Canovaro, F., Paris, E., and Solari, L. (2003).** "Analysis of resistance of flow over macro-scale roughness: first results." *XXX IAHR Congress*, Thessaloniki, Greece, 1-8.
- Canovaro, F., Paris, E., and Solari, L. (2004).** "Influence of macro-roughness arrangement on flow resistance." *International Conference on Fluvial Hydraulics, River Flow 2004*, Naples, Italy, 287-293.
- Canovaro, F., and Solari, L. (2005).** "Macro-roughness flow resistance: a new experimental formula." *XXXI IAHR Congress*, Seoul, Korea, 5434-5443.
- Cao, Z., Meng, J., Pender, G., and Wallis, S. (2006).** "Flow Resistance and Momentum Flux in Compound Open Channels." *Journal of Hydraulic Engineering - ASCE*, 132(12), 1272-1282.
- Carlier, M. (1988).** *Hydraulique générale et appliquée*, Eyrolles, Paris, France.
- Carollo, F. G., Ferro, V., and Termini, D. (2005).** "Flow Resistance Law in Channels with Flexible Submerged Vegetation." *Journal of Hydraulic Engineering - ASCE*, 131(7), 554-564.
- Chanson, H. (1996).** "Free-surface flows with near-critical flow conditions." *Canadian Journal of Civil Engineering*, 23(6), 1272-1284.
- Chaudhry, M. H. (1982).** "Numerical Solution of Transient-Flow." *Applying Research to Hydraulic Practice*, Jackson - Mississippi, USA, 633-660.
- Chaudhry, M. H. (1987).** *Applied Hydraulic Transients*, Van Nostrand Reinhold Company Inc., New York, USA.
- Chen, F., and Ikeda, S. (1996).** "Experimental study on horizontal separation eddies in open-channel flow with groins." *Annual Journal of Hydraulic Engineering - JSCE*, 40, 787-792.
- Chow, V. T. (1959).** *Open-channel hydraulics*, McGraw-Hill New York, USA.
- Chung, W., and Kang, Y. (2006).** "Classifying River Waves by the Saint Venant Equations Decoupled in the Laplacian Frequency Domain." *Journal of Hydraulic Engineering - ASCE*, 132(7), 666-680.
- Deck, D. (1984).** "Controlling River Ice to Alleviate Ice Jam Flooding." *Water for Resource Development*, Coer d'Alene, Idaho, USA, 524-528.
- Dressler, R. F. (1954).** "Comparison of theories and experiments for the hydraulic dambreak wave." *International Association of Scientific Hydrology*, 3(38), 319-328.
- Dubois, J. (1998).** "Comportement hydraulique et modélisation des écoulements de surface." *Communication du Laboratoires de Constructions Hydrauliques - LCH, N°8*, EPFL, Lausanne, Switzerland.
- East, L. F. (1966).** "Aerodynamically Induced Resonance in Rectangular Cavities." *Journal of Sound and Vibrations*, 3(3), 277-287.
- Eichinger, P., and Lein, G. (1992).** "The influence of friction on unsteady pipe flow." *International Conference on Unsteady Flow and Fluid Transients*, H. Wallingford, ed., Durham UK, 41-50.
- Einstein, H. A. (1934).** "Der hydraulische oder Profilradius." *Schweizerische Bauzeitung*, 103(8), 147-150.
- Einstein, H. A., and Banks, R. (1950).** "Fluid resistance of composite roughness." *Transactions American Geophysical Union*, 31(4), 603-610.

- Erickson, D. D., Durgin, W. W., Maguire, C. F., and Moeller, M. J.** (1986). "Shear layer coupling with side-branch resonators." Forum on Unsteady Flow, ASME Publication No. FED39, 43-45.
- Faure, J., and Nahas, N.** (1961). "Etude numérique et expérimental d'intumescences à forte courbure du front." *Intumescences - Société hydrotechnique de France*, 5, 579-587.
- Favre, H.** (1935). *Etude théorique et expérimentale des ondes de translation dans les canaux découverts*, Dunod, Paris.
- Ferrari, E.** (2007). "Influence de la renaturation des cours d'eau sur les conditions d'écoulements pour différents débits." Projet ENAC, EPFL, Lausanne, Switzerland.
- Ferro, V.** (1999). "Evaluating Friction Factor for Gravel-Bed Channel with High Boulder Concentration" *Journal of Hydraulic Engineering - ASCE*, 125(7), 771-778.
- French, R. H.** (1985). *Open-Channel Hydraulics*, McGraw-Hill Book Co, New York.
- Gharib, M., and Roshko, A.** (1987). "The effect of flow oscillations on cavity drag." *Journal of Fluid Mechanics*, 177, 501-530.
- Giezendanner, W.** (1983). "Die Simulation instationärer Abflüsse in offenen Kanälen." *Schweizer Ingenieur und Architekt*, 101(10), 307-311.
- Giustolisi, O., and Savic, D. A.** (2003). "Evolutionary Polynomial Regression (EPR)." Development and Applications. Report 2003/01, School of Engineering, Computer Science and Mathematics, Centre for Water Systems, University of Exeter.
- Giustolisi, O., and Savic, D. A.** (2006). "A Symbolic Data-driven Technique Based on Evolutionary Polynomial Regression." *Journal of Hydroinformatics*, 8(3), 207-222.
- Graf, W. H., and Altinakar, M. S.** (1995). *Hydraulique fluviale, écoulement permanent uniforme et non uniforme*, Presses polytechniques et universitaires romandes PPUR, Lausanne, Switzerland.
- Graf, W. H., and Altinakar, M. S.** (1995). *Hydrodynamique, une introduction*, Presses polytechniques et universitaires romandes PPUR, Lausanne, Switzerland.
- Graf, W. H., and Altinakar, M. S.** (1996). *Hydraulique fluviale, écoulement non permanent et phénomènes de transport*, Presses polytechniques et universitaires romandes PPUR, Lausanne, Switzerland.
- Hager, W. H., Fritz, H. M., and Zweifel, A.** (2004). "Impulse waves from laboratory scale to mega-tsunami." *Hydraulics of Dams and River Structures*, Tehran, Iran, 93-108.
- Halleraker, J. H., Saltveit, S. J., Harby, A., Arnekleiv, J. V., Fjeldstad, H.-P., and Kohler, B.** (2003). "Factors influencing stranding of wild juvenile brown trout (*salmo trutta*) during rapid and frequent flow decreases in an artificial stream." *River Research and Applications*, 19, 589-603.
- Harris, W.** (1950). "An Engineering Concept of Flow in Pipes." *Transactions American Society of Civil Engineers*, 115, 909.
- Harten, A., Lax, P. D., and van Leer, B.** (1983). "On upstream differencing and Godunov-type schemes for hyperbolic conservation laws." *SIAM Review*, 25, 35-61.
- Heller, P., Pellaud, M., Bollaert, E., Schleiss, A. J., and Schlaepfer, R.** (2007). "River rehabilitation through a multi-purpose reservoir." *XXXII IAHR Congress, Abstracts Volume 1*, Venice, Italy, 1.
- Henderson, F. M.** (1966). *Open Channel Flow*, Macmillan, New York, USA.
- Herbich, J. B., and Shulits, S.** (1964). "Large-Scale Roughness in Open-Channel Flow." *Journal of Hydraulics Division - ASCE*, 90(HY6), 203-230.
- Heritage, G. L., Moon, B. P., Broadhurst, L. J., and James, C. S.** (2004). "The frictional resistance characteristics of a bedrock-influenced river channel." *Earth Surface Processes and Landforms*, 29, 611-627.
- Hersberger, D.** (2003). "Wall roughness effects on flow scouring in curved channels with gravel bed." *Communication du Laboratoires de Constructions Hydrauliques - LCH, N°14*, EPFL, Lausanne, Switzerland.

- Hicks, F. E., Steffler, P. M., and Gerard, R.** (1991). "Finite element modeling of surge propagation and an application to the Hay River." *Canadian Journal of Civil Engineering*, 19(3), 454-462.
- Honsowitz, H.** (1988). "Die Abschätzung der Veränderung der hydraulischen Leistungsfähigkeit von revitalisierten Fließgewässerquerschnitten." Institut für Wassergüte und Landschaftswasserbau, Technische Universität Wien, Wien, Austria, 307-348.
- Ikeda, S., Yoshike, T., and Sugimoto, T.** (1999). "Experimental Study on the Structure of Open Channel Flow with Impermeable Spur Dikes." *Annual Journal of Hydraulic Engineering - JSCE*, 43, 281-286.
- Indlekofer, H. M. F.** (1981). "Überlagerung von Rauigkeitseinflüssen beim Abfluß in offenen Gerinnen." *Mitteilung 37*, Institut für Wasserbau und Wasserwirtschaft, Rheinisch-Westfälische Technische Hochschule Aachen.
- Indlekofer, H. M. F.** (2003). "Die Bestimmung des hydraulischen Einflusses von flexiblen Bewuchs auf die Abflusskapazität von Fließgewässern." *Wasserbau - Heft 7*, Wasserbau und Wasserwirtschaft FH Aachen.
- Jaeggi, M.** (1984). "Abflussberechnungen in kiesführenden Flüssen." *Wasserwirtschaft*, 5, 263-267.
- Jain, A. K., Raju, K. G. R., and Garde, R. J.** (1978). "Vortex formation at vertical pipe intake." *Journal of Hydraulics Division - ASCE*, 100(HY10), 1427-1445.
- Jiménez, J.** (2004). "Turbulent Flows over Rough Walls." *Annual Review of Fluid Mechanics*, 36, 173-196.
- Jirka, G. H., and Lang, C.** (2004). "Instationärer Abfluss: Wellenbewegungen in Gerinnen." *Gerinnehydraulik, Vorlesungsskript*, Karlsruhe, Germany, 99-118.
- Kimura, I., and Hosoda, T.** (1997). "Fundamental properties of flows in open channels with dead zone." *Journal of Hydraulic Engineering - ASCE*, 123(2), 98-107.
- Kirschmer, O.** (1949a). "Reibungsverluste in Röhren und Kanälen." *Die Wasserwirtschaft, Stuttgart*, 39(7), 137-142.
- Kirschmer, O.** (1949b). "Reibungsverluste in Röhren und Kanälen." *Die Wasserwirtschaft, Stuttgart*, 39(8), 168-174.
- Lagarrigue, T., Céréghino, R., Lim, P., Reyes-Marchant, P., Chappaz, R., Lavandier, P., and Belaud, A.** (2002). "Diel and seasonal variations in brown trout (*Salmo trutta*) feeding patterns and relationship with invertebrate drift under natural and hydropeaking conditions in mountain stream." *Aquatic Living Resources*, 15, 129-137.
- Lai, C.-J., Liu, C. L., and Lin, Y.-Z.** (2000). "Experiments on flood-wave propagation in compound channel." *Journal of Hydraulic Engineering - ASCE*, 126(7), 492-501.
- Lauber, G.** (1997). "Experimente zur Talsperrenbruchwelle im glatten geneigten Rechteckkanal." *Mitteilungen der Versuchsanstalt für Wasserbau, Hydrologie und Glaziologie - VAW, N°152*, ETHZ, Zürich, Switzerland.
- Lauber, G., and Hager, W. H.** (1998). "Experiments to dambreak wave: Horizontal channel." *Journal of Hydraulic Research - IAHR*, 36(3), 291-307.
- Lauber, G., and Hager, W. H.** (1998). "Experiments to dambreak wave: Sloping channel." *Journal of Hydraulic Research - IAHR*, 36(5), 761-773.
- Laucelli, D., Berardi, L., and Doglioni, A.** (2005). "Evolutionary Polynomial Regression EPR TOOLBOX." Technical University Bari, Bari, Italy.
- Lawrence, D. S. L.** (1997). "Macroscale surface roughness and frictional resistance in overland flow." *Earth Surface Processes and Landforms*, 22, 365-382.
- Lawrence, D. S. L.** (2000). "Hydraulic resistance in overland flow during partial and marginal surface inundation: Experimental observations and modeling." *Water Resources Research*, 36, 2381-2393.
- Lawson, N. J., and Davidson, M. R.** (2001). "Self-sustained oscillation of a submerged jet in a thin rectangular cavity." *Journal of Fluids and Structures*, 15, 59-81.

- Leal, J. G. A. B., Ferreira, R. M. L., and Cardoso, A. H.** (2006). "Dam-break Wave Front Celerity." *Journal of Hydraulic Engineering - ASCE*, 132(1), 69-76.
- Leonardi, S., Orlandi, P., Smalley, R. J., Djenidi, L., and Antonia, R. A.** (2003). "Direct numerical simulation of turbulent channel flow with transverse square bars on one wall." *Journal of Fluid Mechanics*, 491, 229-238.
- Lindner, K.** (1982). "Der Strömungswiderstand von Pflanzenbeständen." *Mitteilung des Leichtweiss-Institut für Wasserbau N°75*, TU Braunschweig, Braunschweig, Germany.
- Loizeau, J.-L., and Dominik, J.** (2000). "Evolution of the Upper Rhone River discharge and suspended sediment load during the last 80 years and some implications for Lake Geneva." *Aquatic Sciences*, 62, 54-67.
- Lyapin, V. Y.** (1994). "Hydraulic analysis of channels with increased bottom roughness." *Hydrotechnical construction*, 25(5), 290-293.
- Manciola, P. G., Mazzoni, A., and Savi, F.** (1994). "Formation and propagation of steep waves: An investigative experimental interpretation." Specialty Conference on Modelling of Flood Propagation Over Initially Dry Areas, Milano, Italy, 283-297.
- Manning, R.** (1891). "On the flow of water in open channels and pipes." *Transactions Institute of Civil Engineering Ireland*, 20, 161-207.
- Martin, H.** (1983). "Dam-break in horizontal channels with parallel and divergent side walls." *XX IAHR Congress*, Moscow, U.S.S.R., 494-505.
- McCoy, A., Constantinescu, G., and Weber, L.** (2006). "Exchange processes in a channel with two vertical emerged obstructions." *Flow, Turbulence and Combustion* 77, 97-126.
- McGahey, C., Samuels, P. G., and Knight, D. W.** (2006). "A practical approach to estimating the flow capacity of rivers - Application and analysis." *International Conference on Fluvial Hydraulics, River Flow 2006*, Lisbon, Portugal.
- Meile, T.** (2005). "Flussbauliche Massnahmen zur Verminderung von Schwall- und Sunkerscheinungen infolge Kraftwerkbetrieb." *JuWi-Treffen 2005*, Graz, Austria, 85-90.
- Meile, T.** (2006d). "Schwall und Sunk in Fliessgewässern." *Eawag News* (61d), 28-29.
- Meile, T., Boillat, J.-L., Dubois, J., and Schleiss, A. J.** (2006c). "Experimental study on steady flow in a channel with macro-roughness at the side walls." *International Conference on Fluvial Hydraulics, River Flow 2006*, Lisbon, Portugal, 1059-1068.
- Meile, T., Boillat, J.-L., Dubois, J., and Schleiss, A. J.** (2007a). "Oscillations in a channel with rectangular widenings at the side walls." *XXXII IAHR Congress, Abstracts Volume 2*, Venice, Italy, 700.
- Meile, T., Boillat, J.-L., and Schleiss, A. J.** (2006b). "Influence of dams and reservoirs on the flow regime of the Upper-Rhone-River." *Vingt Deuxième Congrès des Grands Barrages*, Barcelone, Spain, 449-465.
- Meile, T., De Cesare, G., Blanckaert, K., and Schleiss, A. J.** (2006a). "Improving acoustic Doppler velocimetry in steady and unsteady flow by means of seeding with hydrogen bubbles." *Fifth International Symposium on Ultrasonic Doppler Methods for Fluid Mechanics and Fluid Engineering*, ETH Zurich, Switzerland, 97-100.
- Meile, T., De Cesare, G., Blanckaert, K., and Schleiss, A. J.** (2007 accepted for publication). "Improvement of Acoustic Doppler velocimetry in steady and unsteady turbulent open-channel flows by means of seeding with hydrogen bubbles." *Flow Measurement and Instrumentation*, doi:10.1016/j.flowmeasinst.2007.08.009.
- Meile, T., Schleiss, A., and Boillat, J.-L.** (2005c). "Entwicklung des Abflussregime des Rhone seit dem Beginn des 20. Jahrhunderts." *Wasser, energie, luft – eau, énergie, air*, 97(5/6), 133-142.
- Meile, T., Schleiss, A. J., and Boillat, J.-L.** (2005b). "Flow regime in a river influenced by morphological changes and hydropower plants." *8th International Conference on Fluvial Sedimentology*, Delft, Netherlands, Abstract p.199.

- Meile, T., Schleiss, A. J., Boillat, J.-L., and Dubois, J.** (2005a). "Influence of macro-roughness on steady flow in channels." *8th International Conference on Fluvial Sedimentology*, Delft, Netherlands, Abstract p.200.
- Meile, T., Schleiss, A. J., and Boillat, J.-L.** (submitted). "Analysis of flow regimes influenced by high-head storage power plants – Application to the Upper-Rhone River." *River Research and Applications*.
- Mertens, W.** (1989). "Zur Frage hydraulischer Berechnungen naturnaher Fließgewässer." *Wasserwirtschaft*, 79(4), 170-179.
- Mertens, W.** (1994). "Zum Strömungswiderstand naturnaher Fließgewässer." *Wasserwirtschaft*, 84(3), 138-141.
- Met-Flow SA.** (2002). "UVP Monitor – Model UVP-DUO Users guide." Metflow SA, Lausanne, Switzerland, www.met-flow.com.
- Meyer-Peter, E., and Müller, R.** (1948). "Formulas for bed-load transport." *Report on the 2nd meeting of the IAHSR (today IAHR)*, Stockholm, Sweden, 39-64.
- Mingham, C. G., and Causon, D. M.** (1998). "High-resolution finite-volume method for shallow water flows." *Journal of Hydraulic Engineering - ASCE*, 124(6), 605-614.
- Minor, H.-E., Fäh, R., Farshi, D., Müller, R., Rousselot, P., and Vetsch, D.** (2006). "System manual of Basement, Version 1.1, October 2006." Versuchsanstalt für Wasserbau, Hydrologie und Glaziologie - VAW, Zurich, Switzerland.
- Mishuev, A. V., and Komarov, A. A.** (1996). "Mathematical modeling of the process of surge wave propagation in open channels with a variable cross-sectional area." *Hydrotechnical Construction*, 30(1), 8-14.
- Mohamed, H. I.** (2004). "Effect of lateral variation of roughness on flow conveyance within a trapezoidal channel cross-section." *International Conference on Fluvial Hydraulics, River Flow 2004*, Naples, Italy, 363-368.
- Mohapatra, P. K., and Chaudhry, H.** (2004). "Numerical Solution of Boussinesq Equations to Simulate Dam-Break Flows." *Journal of Hydraulic Engineering - ASCE*, 130(2), 156-159.
- Moog, O., Jungwirth, M., Muhar, S., and Schönbauer, B.** (1993). "Berücksichtigung ökologischer Gesichtspunkte bei der Wasserkraftnutzung durch Ausleitungskraftwerke." *Österreichische Wasserwirtschaft*, 45(7/8), 1-14.
- Morris, H. M.** (1955). "Flow in Rough Conduits." *Transactions of the American Society of Civil Engineers*, 120, 373-410.
- Morris, H. M., and Wiggert, J. M.** (1972). *Applied hydraulics in engineering*, The Ronald Press Company, New York, USA.
- Morse, B., and Hicks, F.** (2005). "Advances in river ice hydrology 1999-2003." *Hydrological Processes*, 19, 247-263.
- Muser, R., and Meder, G.** (1970). *Schwall- und Sunkerscheinungen aus Schleusenbetrieb in Schiffahrtskanälen - Massnahmen zur Sicherung des Schiffahrtsbetriebes*, Versuchsanstalt für Wasserbau und Kulturtechnik, Universität Fridericiana Karlsruhe, Karlsruhe, Germany.
- Musleh, F. A., and Cruise, J. F.** (2006). "Functional Relationships of Resistance in Wide Flood Plains with Rigid Unsubmerged Vegetation." *Journal of Hydraulic Engineering - ASCE*, 132(2), 163-171.
- Muto, Y., Imamoto, H., and Ishigaki, T.** (2000). "Turbulence characteristics of a shear flow in an embayment attached to a straight open channel." *4th International Conference on Hydrosience and Engineering*, Seoul, Korea, 232-241.
- Naudascher, E.** (1963). "On the role of eddies in flow-induced vibrations." *X IAHR Congress*, London, UK, 61-72.
- Nezu, I., and Nakagawa, H.** (1993). *Turbulence in open channel flows*, A.A. Balkema, Rotterdam, Brookfield.

- Nezu, I., and Onitsuka, K.** (2002). "PIV measurements of side-cavity open-channel flows - Wando model in rivers." *Journal of Visualization*, 5(1), 77-84.
- Nikuradse, J.** (1933). "Strömungsgesetze in rauhen Röhren." Forschungsheft 361 (Beilage zur 'Forschung auf dem Gebiet des Ingenieurwesens', Ausgabe B Band 4, Juli/August 1933), VDI-Verlag GmbH, Berlin, Germany.
- Nuding, A.** (1991). "Fließwiderstandsverhalten in Gerinnen mit Ufergebüsch." *Wasserbau-Mitteilung* 35, Technische Hochschule Darmstadt, Darmstadt, Germany.
- Nuding, A.** (1998). "Zur Durchflußermittlung bei gegliederten Gerinnen." *Wasserwirtschaft*, 88(3), 130-132.
- Ohomoto, T., Nirakawa, R., and Watanabe, K.** (2005). "Interaction between water surface oscillations and large eddies in an open channel with spur dikes." *XXXI IAHR Congress*, Seoul, Korea.
- Pagliara, S., and Chiavaccini, P.** (2006). "Energy Dissipation on Reinforced Block Ramps." *Journal of Irrigation and Drainage Engineering*, 132(3), 293-297.
- Pagliara, S., and Chiavaccini, P.** (2006). "Flow Resistance of Rock Chutes with Protruding Boulders." *Journal of Hydraulic Engineering - ASCE*, 132(6), 545-552.
- Pasche, E., and Rouvé, G.** (1985). "Overbank flow with vegetatively roughened flood plains." *Journal of Hydraulic Engineering - ASCE*, 111(9), 1262-1278.
- Pellaud, M.** (2007). "Ecological response of a multi-purpose river development project using macro-invertebrates richness and fish habitat value," Thèse N° 3807, EPFL, Lausanne, Switzerland.
- Perry, A. E., Schofield, W. H., and Joubert, P.** (1969). "Rough wall turbulent boundary layers." *Journal of Fluid Mechanics*, 37, 383-413.
- Peter, A.** (2004). "Ökologie der Rhone - Resultate aktueller Erhebungen des Forschungsprojekts "Rhone-Thur"." *Wasser, energie, luft - eau, énergie, air*, 95(11/12), 299-330.
- Peter, A., Meile, T., Reichert, P., and Truffer, B.** (2005). "Alles im Fluss aber bitte nachhaltig." *Eawag - aquatic research*(Jahresbericht 2005), 7-11.
- Petryk, S., and Basmajian, G.** (1975). "Analysis of flow through vegetation." *Journal of Hydraulics Division - ASCE*, 101(HY7), 871-884.
- Poff, N. L., Allan, D. J., Bain, M. B., Karr, J. R., Prestegard, K. L., Richter, B. D., Sparks, R. E., and Stromberg, J. C.** (1997). "The Natural Flow Regime." *BioScience*, 47(11), 769-784.
- Ponce, V. M., Li, R. M., and Simons, D. B.** (1978). "Applicability of kinematic and diffusive models." *Journal of Hydraulic Division - ASCE*, 104(3), 353-360.
- Verbund-Autrian Hydropower Power (2004).** "Strom aus Enns, Mur und Teigitsch. Die steirischen Wasserkraftwerke."
- Proust, S., Rivière, N., Bousmar, D., Paquier, A., Zech, Y., and Morel, R.** (2006). "Flow in Compound Channel with Abrupt Floodplain Contraction." *Journal of Hydraulic Engineering - ASCE*, 132(9), 958-970.
- Pyle, R., and Novak, P.** (1981). "Coefficient of Friction in Conduits with large Scale Roughness." *Journal of Hydraulic Research - IAHR*, 19(2), 119-140.
- Requena, P., Weichert, R., and Minor, H.-E.** (2006). "Self widening by lateral erosion in gravel bed rivers." *International Conference on Fluvial Hydraulics, River Flow 2006*, Lisbon, Portugal, 1801-1809.
- Rice, C. E., Kadavy, K. C., and Robinson, K. M.** (1998). "Roughness of loose rock riprap on steep slopes." *Journal of Hydraulic Engineering - ASCE*, 124(2), 179-185.
- Rickenmann, D.** (1996). "Fließgeschwindigkeit in Wildbächen und Gebirgsflüssen." *Wasser, energie, luft - eau, énergie, air*, 88(11/12), 298-303.
- Ritter, A.** (1892). "Die Fortpflanzung der Wasserwellen." *Zeitschrift Verein deutscher Ingenieure*, 36(33), 947-954.

- Rockwell, D., and Naudascher, E.** (1978). "Review - self-sustaining oscillations of flow past cavities." *Journal of Fluids Engineering*, 100, 152-165.
- Rockwell, D., and Naudascher, E.** (1979). "Self-Sustained Oscillations of impinging free shear layers." *Annual Review of Fluid Mechanics*, 11, 67-94.
- Rodi, W.** (1993). *Turbulence Models and their Application in Hydraulics*, A.A. Balkema, Rotterdam, Brookfield.
- Rosier, B.** (2007). "Interaction of side weir overflow with bed-load transport and bed morphology in a channel." *Communication du Laboratoires de Constructions Hydrauliques - LCH, in prep.*, EPFL, Lausanne, Switzerland.
- Rouse, H.** (1946). *Elementary mechanics of fluids*, John Wiley and Sons, New York.
- Rouse, H.** (1965). "Critical Analysis of Open-Channel Resistance." *Journal of Hydraulics Division*, 91(HY4), 1-25.
- Rowley, C. W., and Williams, D. R.** (2006). "Dynamics and Control of High-Reynolds-number Flow over Open Cavities." *Annual Review of Fluid Mechanics*, 38, 251-276.
- Rutschmann, P., and Hager, W. H.** (1996). "Diffusion of floodwaves." *Journal of Hydrology*, 178(1), 19-32.
- Schleiss, A.** (2002). "Potentiel hydroélectrique de l'arc alpin." *Bulletin SEV/VSE*, 02(2), 13-21.
- Schleiss, A.** (2007). "L'hydraulique suisse: Un grand potentiel de croissance par l'augmentation de la puissance." *Bulletin SEV/VSE*, 07(2), 24-29.
- Schlichting, H.** (1936). "Experimentelle Untersuchungen zum Rauigkeitsproblem." *Ingenieur-Archive*, 7(1).
- Schoklitsch, A.** (1917). "Ueber Dambruchwellen." *Sitzungsberichte der Kaiserlichen Akademie der Wissenschaften in Wien*, 126(10), 1489-1514.
- Schröder, R. C. M.** (1990). "Bestimmung von Rauheiten." *Hydraulische Methoden zur Erfassung von Rauheiten*, DVWK, ed., Verlag Paul Parey, Berlin, 1-144.
- Schröder, W.** (1999). "Hydraulik." *Grundlagen des Wasserbaus*, Werner-Verlag, Düsseldorf.
- Sieben, J.** (2003). "Estimation of effective hydraulic roughness in non-uniform flow." *XXX IAHR Congress*, Thessaloniki, Greece, 17-24.
- Simons, D. B., and Richardson, E. V.** (1966). "Resistance to flow in alluvial channels." *U. S. Geological Survey Prof. Paper*, 422(J).
- Sinniger, R. O., and Hager, W. H.** (1989). *Constructions hydrauliques - Ecoulement stationnaires*, Presses polytechniques et universitaires romandes PPUR, Lausanne, Switzerland.
- Smart, G.** (2004). "A improved flow resistance formula." *International Conference on Fluvial Hydraulics, River Flow 2004*, Naples, Italy, 259-262.
- Smart, G. M., Duncan, M. J., and Walsh, J. M.** (2002). "Relatively Rough Flow Resistance Equations." *Journal of Hydraulic Engineering - ASCE*, 128(6), 568-578.
- Smart, G. M., and Jäggi, M. N. R.** (1983). "Sediment transport on steep slopes." *Mitteilungen der Versuchsanstalt für Wasserbau, Hydrologie und Glaziologie -VAW, N°64*, ETHZ, Zürich, Switzerland.
- Soares-Fraza, S., Lories, D., Taminiau, S., and Zech, Y.** (2003). "Dam break flow in channel with sudden enlargement." *XXX IAHR Congress*, Thessaloniki, Greece, 221-228.
- Soares-Fraza, S., and Zech, Y.** (2002). "Undular bores and secondary waves - Experiments and hybrid finite - volume modelling." *Journal of Hydraulic Research - IAHR*, 40(1), 33-43.
- Sorensen, R. M.** (1978). *Basic Coastal Engineering*, John Wiley and Sons, Brisbane.
- Stansby, P. K., Chegini, A., and Barnes, T. C. D.** (1998). "The initial stages of dam-break flow." *Journal of Fluid Mechanics*, 374, 407-424.
- Stoker, J. J.** (1975). *Water Waves*, Interscience Publication Inc., New York, USA.

- Stranner, H.** (1996). "Schwallwellen im Unterwasser von Spitzenkraftwerken und deren Reduktion durch flussbauliche Massnahmen." *Schriftenreihe zur Wasserwirtschaft N°20*, Technische Universität Graz, Austria.
- Straub, L. G., and Morris, H. M.** (1950). "Hydraulic Data Comparison of Concrete and Corrugated Metal Culvert Pipes." University of Minnesota, St. Anthony Falls Hydr. Lab., Minneapolis.
- Straub, L. G., and Morris, H. M.** (1950). "Hydraulic Tests on Concrete Culvert Pipes." University of Minnesota, St. Anthony Falls Hydr. Lab., Minneapolis.
- Streeter, V. L., and Wylie, E. B.** (1967). *Hydraulic Transients*, McGraw-Hill, Inc., New York, USA.
- Strickler, A.** (1923). "Beiträge zur Frage der Geschwindigkeitsformel und der Rauheitszahlen für Ströme, Kanäle und geschlossene Leitungen." *Mitteilung Nr. 16*, Amt für Wasserwirtschaft, Eidgenössisches Department des Innern, Bern, Switzerland.
- Tani, I.** (1987). "Turbulent boundary layer development over rough surfaces." *Perspectives in Turbulence Studies*, H. U. Meier and P. Bradshaw, eds., Springer, Berlin, Germany, 223–249.
- Thompson, S. M., and Campbell, P. L.** (1979). "Hydraulics of a large channel paved with boulders." *Journal of Hydraulic Research - IAHR*, 17(4), 341–354.
- Toro, E. F.** (1999). *Riemann solvers and numerical methods for fluid dynamics*, Springer, Berlin.
- Treske, A.** (1994). "Undular Bores (Favre-Waves) in Open Channels - Experimental Studies." *Journal of Hydraulic Research - IAHR*, 32(3), 355-370.
- Trikha, A. K.** (1975). "An efficient method for simulating frequency-dependent friction in transient liquid flow." *Journal of Fluids Engineering - ASME*, 97, 97-105.
- Uensal, I.** (1983). "Propagation of dam-break waves in channels of varying section." *XX IAHR Congress*, Moscow, U.S.S.R., 539-545.
- Uijttewaal, W. S. J.** (2005). "Effects of Groyne Layout on the Flow in Groyne Fields: Laboratory Experiments." *Journal of Hydraulic Engineering - ASCE*, 131(9), 782-791.
- Uijttewaal, W. S. J., Lehmann, D., and van Mazijk, A.** (2001). "Exchange processes between a river and its groyne fields: Model experiments." *Journal of Hydraulic Engineering - ASCE*, 127(11), 928-936.
- USACE.** (2002). "Engineering and design, coastal engineering manual, harbour hydrodynamics." *Report EM 1110-2-1100*, Departement of the army, U.S. Army Corps of Engineers, Washington DC, USA.
- van Prooijen, B. C., Battjes, J. A., and Uijttewaal, W. S. J.** (2005). "Momentum Exchange in Straight Uniform Compound Channel Flow." *Journal of Hydraulic Engineering - ASCE*, 131(3), 175-183.
- van Rijn, L. C.** (1993). *Principles of sediment transport in rivers, estuaries and coastal seas*, Aqua Publications, Amsterdam, Netherlands.
- van Rijn, L. C.** (1994). "Principles of fluid flow and surface waves." *Rivers, Estuaries, Seas, and Oceans*, Aqua Publications, Amsterdam, Netherlands.
- Vanoni, V. A., and Brooks, N. H.** (1957). "Laboratory studies of the roughness and suspended load of alluvial streams." *Report E-68, C*, Sedimentation Laboratory, California Institute of Technology, Pasadena, California.
- Vardy, A.** (1992). "Approximating unsteady friction at high Reynolds numbers." *Unsteady Flow and Fluid Transients*, R. Bettess and J. Watts, eds., Balkema, Rotterdam, Brookfield, 21-29.
- VAW-LCH.** (2006). "Kraftwerksbedingter Schwall und Sunk, Eine Standortbestimmung." *VAW 4232, LCH 05-2006*.
- Vibert, R.** (1939). "Répercussions piscicoles du fonctionnement par éclusées des usines hydroélectriques." *Bulletin français de pisciculture*, 117, 137-155.

- Vibert, R.** (1939). "Répercussions piscicoles du fonctionnement par éclusées des usines hydroélectriques." *Bulletin français de pisciculture*, 116, 109-115.
- Viessman, W., Harbough, T., and Knapp, J.** (1972). *Introduction to Hydrology*, Intext Educational Publishers, New York, USA.
- Webb, R. L., Eckert, E. R. G., and Goldstein, R. J.** (1971). "Heat transfer and friction in tubes with repeated-rib roughness." *Journal of International Heat Mass Transfer*, 14, 601-617.
- Weichert, R.** (2006). "Bed Morphology and Stability in Steep Open Channels," Ph.D. Thesis N°16316, ETHZ, Zürich, Switzerland.
- Weitbrecht, V.** (2004). "Influence of dead-water zones on the dispersive mass transport in rivers," Dissertationsreihe am Institut für Hydromechanik der Universität Karlsruhe (TH) Heft 2004/1, Karlsruhe, Germany.
- Weitbrecht, V., and Jirka, G. H.** (2001). "Flow patterns and exchange processes in dead zones of rivers." *International Symposium on Environmental Hydraulics ISEH and IAHR*, Pheonix, USA, 1-6.
- Whitham, G. B.** (1955). "The effects of hydraulic resistance in the dam-break problem." *Proceedings of the Royal Society A*, 227, 399-407.
- Willi, H.-P.** (2002). "Synergism between flood protection and stream ecology - space as the key parameter." *EAWAG news*, 51e, 26-28.
- Wilson, B. W.** (1972). "Seiches." *Advances in Hydrosience*, Academic Press, New York, USA, 1-94.
- Wirtz, C.** (2004). "Hydromorphologische und morphodynamische Analyse von Bühnenfeldern der unteren Mittelelbe im Hinblick auf eine ökologische Gewässerunterhaltung," Ph.D. Thesis, Freie Universität Berlin, Berlin, Germany.
- Yalin, M. S., and da Silva, A. M. F.** (2001). *Fluvial processes*, IAHR, Delft, The Netherlands.
- Yen, B. C.** (2002). "Open Channel Flow Resistance." *Journal of Hydraulic Engineering - ASCE*, 128(1), 20-39.
- Yoo, D. H., and Singh, V. P.** (2005). "Two Methods for the Computation of Commercial Pipe Friction Factors." *Journal of Hydraulic Engineering - ASCE*, 131(8), 694-704.
- Zairov, K. I., and Listrovoy, P. P.** (1983). "Experimental investigation of the positive traveling surges fore-part observed in canals." *XX IAHR Congress*, Moscow, U.S.S.R., 210-218.
- Zelt, J. A.** (1986). "Tsunamis: The Response of Harbors with Sloping Boundaries to Long Wave Excitation." *Report KH-R-47*, W.M. Keck Laboratory of Hydraulics and Water Resources, California Institute of Technology.
- Ziada, S.** (1993). "A flow visualization study of flow-acoustic coupling at the mouth of a resonant side-branch." *Journal of Fluids and Structures* 8(4), 391-416.
- Zielke, W.** (1968). "A short review of resistance laws for unsteady flow through pipes and orifices." *Proceedings IAHR working group on the behaviour of hydraulic machinery under oscillatory conditions*, Milan, Italy, K1-K15.
- Zoppou, C., and Roberts, S.** (2000). "Numerical solution of the two-dimensional unsteady dam break." *Applied Mathematical Modelling*, 24(7), 457-475.
- Zweifel, A.** (2004). "Impulswellen: Effekte der Rutschdicke und der Wassertiefe " Ph.D. Thesis N°15596, Eidgenössische Technische Hochschule ETH Zürich, Zürich, Switzerland.
- Zweifel, A., Hager, W. H., and Minor, H.-E.** (2006). "Plane Impulse Waves in Reservoirs." *Journal of Waterway, Port, Coastal, and Ocean Engineering*, 132(5), 358-368.

Acknowledgments

Special thanks to Prof. Dr. A. Schleiss, initiator of this research project allowing me to carry out an interesting work dealing with several topics in the field of hydraulics. This thank includes the good research conditions and the confidence in my person.

The financing of the project was ensured by the Swiss Federal Office for Water and Geology FOWG (now Federal Office for the Environment FOEN) in the framework of the project "Rhone-Thur - sustainable use of rivers". To work as PhD Student in an interdisciplinary research such as the "Rhone-Thur" project was a good experience and opportunity to exchange ideas with other researchers. I want to thank all researches and partner-institutes of the "Rhone-Thur" project. Special thanks to Dr. Armin Peter, one of the driving forces of this interdisciplinary project and to Peter Baumann and Markus Fette for the pleasant collaboration for the hydropeaking synthesis report.

At the beginning, experimental research demands technical assistance and support for which I thank Louis Schneiter and his team. Thanks also to Metflow SA for the support and Dr. Beat Birkhofer for its contribution to UVP velocity measurements. Experiments need to be carried out and data demand analysis. I would like to thank Ronny Moser for moving thousands of limestone-bricks, Jean-Luc Lacouture and Simon Colin for her practical work and Frédéric Loup for the Master work contributing to this research. Special thanks to Dr. Jean Louis Boillat, Dr. Jérôme Dubois and Dr. Koen Blankaert for helping me to keep the path and for their scientific support and advices.

Within this project, I had the chance to work and discuss with other researchers to which I address my gratitude: Prof. Yves Zech and Dr. Sandra Soares-Frazao from the Université catholique de Louvain for the collaboration about 1D- and 2D-modeling of experiments and the suggestions of Yves Zech during his stays in Lausanne. Prof. Orazio Giustolisi from the Technical University of Bari to make available Evolutionary Polynominal Regression for the data interpretation of my experiments as well as for his support in the use of the software. Prof. Dr. Michel Pirotton and Dr. Sebastian Erpicum for the interesting inputs I got during their stay in Lausanne. Many other researchers I met during conferences for discussions.

Gratitude is dedicated to the members of the jury, Prof. Yves Zech, Prof. Willi H. Hager and Dr. Martin Jaeggi for acting as co-examiners, their comments and proof reading.

Whoever worked at the Laboratory of Hydraulic Constructions knows that it is the opportunity to have dynamic colleagues from all over the world. Thanks to all my colleagues for solving scientific questions and others.

Finally, I am very grateful to my mother, my sister, Carole and many good friends for their support and distraction, outside of the scientific environment, as well as for the comprehension for my absences during the last months.

List of the Appendices

Appendix 3-1:	Mathematical model for the discharge computation of the surge wave generating setup.....	A.1
Appendix 3-2:	Calibrated emptying of the upper basin for the 15 different pipe opening combinations.....	A.7
Appendix 3-3:	Positions of the US sensor for the unsteady flow tests.....	A.10
Appendix 3-4:	Overview of the tested scenarios for the unsteady flow tests.....	A.11
Appendix 4-1:	Summarized test results for the steady flow tests.....	A.13
Appendix 4-2:	Aspect of the flow for two test series	A.51
Appendix 4-3:	Flow visualization with dye tests	A.53
Appendix 4-4:	Horizontal velocity profiles in configurations 221, 222, 223 and 224	A.64
Appendix 4-5:	Head-loss computation through sudden channel transitions: Enlargement and contraction.....	A.67
Appendix 4-6:	Test results for the cavity oscillations	A.69
Appendix 4-7:	Alternative formulation of the drag force based headloss computation model	A.76
Appendix 4-8:	Overview of the Evolutionary Polynomial Regression parameters.....	A.78
Appendix 4-9:	Calculated and measured water levels for the reattachment flow type using single head- and friction-losses	A.79
Appendix 5-1:	Summarized test results for the unsteady flow tests.....	A.85
Appendix 5-2:	Conditions at the wavefront for all tests.....	A.121

A 3-1: Mathematical model of the surge wave generation setup

Subdivision of the setup

The mathematical model of the setup generating the positive surge waves is based on its subdivision into four elements:

- The upper basin with the crest spillway
- The pipes connecting the upper basin and the inlet basin
- The inlet basin with the rectangular opening
- The outflow into the inlet reach

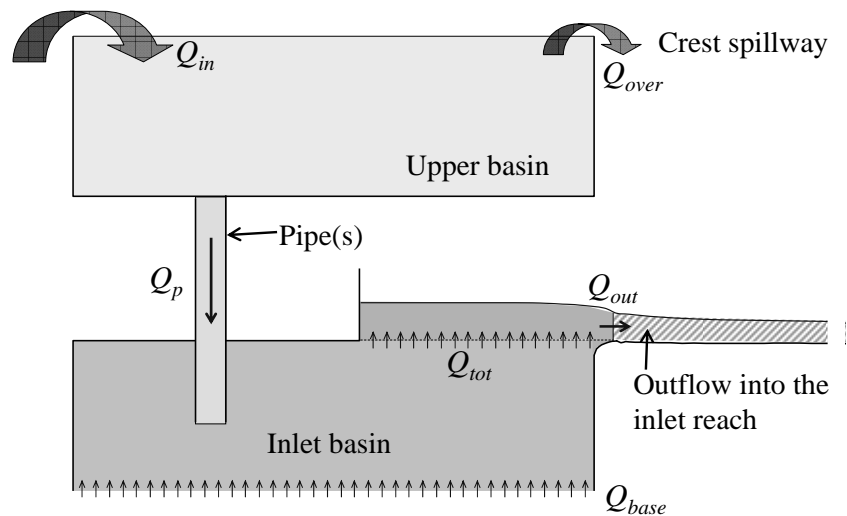


Fig-A3.1: Definition of the elements of the surge wave generation setup considered for the mathematical model and denomination of the discharge at different locations.

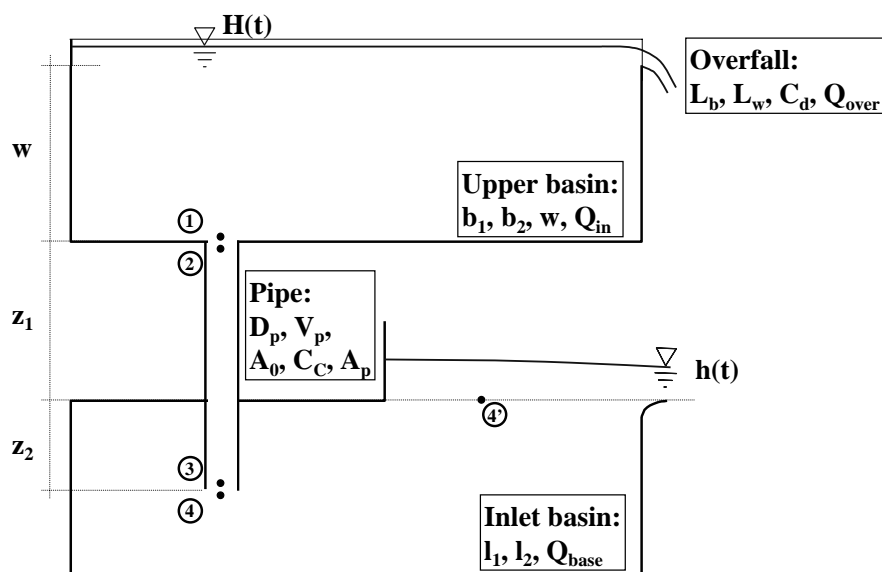


Fig-A3.2: Schematic view and definition of the parameters of the upper basin, the pipe and the inlet basin including the rectangular opening.

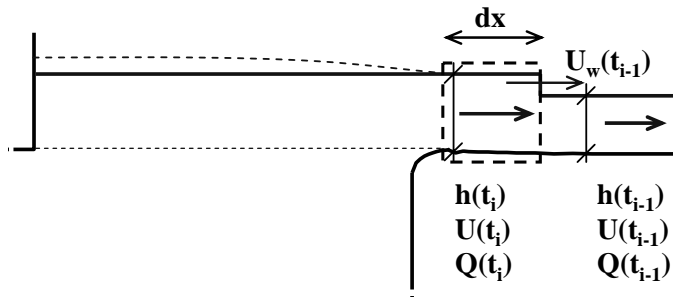


Fig-A3.3: Schematic view of the surge wave generation at the first section of the inlet reach.

Assumptions

- vertical velocity of the water surface in the upper basin is zero
- the water is non compressible
- the pipes are non extensible
- no linear headloss between 3 and 4' (no headloss between 4 and 4') is considered
- the wave height is considered small compared to the flow depth at the section $x = -7.4$ m (which is admissible if small time steps Δt are considered)
- velocity gradients dV/dt in the upper basin and dV/dt in the inlet basin are considered as small (which is admissible for the important flow areas)

Notations (used in this Appendix 3-1)

Upper basin:

- $z_l + w$: weir overfall crest level measured form the bottom level of the section $x = -7.4$ m
- b_1 : upper basin length
- b_2 : upper basin width
- L_w : overfall crest width
- L_b : effective overfall length
- C_d : overfall coefficient
- Q_{in} : upper basin inflow
- Q_{over} : weir overflow
- H : upper basin water level measured form the bottom level of the section $x = -7.4$ m
- A_1 : surface of a horizontal section of the upper basin

Pipe:

- z_1 : pipe length above reference level (bottom level of the section $x = -7.4$ m)
- z_2 : pipe length under reference level (bottom level of the section $x = -7.4$ m)
- D_p : diameter of the pipe p; $p = 1$ to 4
- A_{0p} : surface at the pipe entrance (if there is no diaphragm, $A_0 = A_2$)
- C_{Cp} : contraction coefficient for A_0 (contraction due to diaphragm)
- A_{2p} : section of pipe p; $p = 1$ to 4

- Q_p : flow in pipe p; p = 1 to 4
 Q_{tot} : baseflow and sum of pipeflows
 V_p : mean flow velocity in the pipe; p = 1 to 4
 h_{s1p} : single headloss at the entrance of the pipe p; p = 1 to 4
 h_{s2p} : single headloss at the outlet of the pipe p; p = 1 to 4
 h_{rp} : headloss due to friction in the pipe p; p = 1 to 4
 k_s : equivalent sand roughness coefficient
 Re : Reynolds Number
 ν : cinematic viscosity

Inlet basin with the rectangular opening and outflow section into the inlet reach:

- Q_{base} : inlet basin inflow (= channel baseflow)
 Q_{tot} : baseflow and sum of pipeflows
 Q_{out} : outflow into the inlet reach at section $x=-7.4$ m
 h : outflow level into the inlet reach at section $x=-7.4$ m
 U : outflow velocity into the channel at section $x=-7.4$ m
 U_w : absolute wave propagation velocity $U_w=U+c$
 l_1 : width of the opening of inlet basin = channel width of the inlet reach B
 l_2 : length of the opening of inlet basin
 A_3 : “hypothetic” lower basin section assumed as $l_1 * l_2$

Equations

Pipe:

The momentum equation of the flow in the pipe can be written as:

$$\sum F = ma \quad (I.0)$$

$$P_2 - P_3 + G - F = \rho \frac{\pi D_p^2}{4} L \frac{dV_p}{dt} \quad (I.1)$$

where P are the pressure forces, G the gravity force and F the flow resistance.

By dividing (I.1) with

$$\left(g \rho \pi D_p^2 / 4 \right)$$

one obtains:

$$H_2 - H_3 - h_r = \frac{L}{g} \frac{dV_p}{dt} \quad (I.2)$$

where H is the total head containing the pressure and gravity components. H_2 and H_3 can be calculated as:

$$H_2 = H_1 - \xi_2 \frac{V_p^2}{2g} = H - \xi_2 \frac{V_p^2}{2g} \quad (\text{II.1})$$

$$H_3 = H_4 + \xi_3 \frac{V_p^2}{2g} = h + \frac{(Q_{tot}/l_1 l_2)^2}{2g} + \xi_3 \frac{V_p^2}{2g} \quad (\text{II.2})$$

Replacement of (II.1) and (II.2) in (I.2) leads to:

$$H - \left[h + \frac{(Q_{tot}/l_1 l_2)^2}{2g} \right] + (\xi_2 - \xi_3) \frac{V_p^2}{2g} - h_r = \frac{L}{g} \frac{dV_p}{dt} \quad (\text{I.3})$$

The single headloss-coefficient at the transition between the upper basin and the pipe can be calculated as:

$$\xi_{2p} = \left(\frac{A_{2p}}{A_{0p} C_{cp}} - 1 \right)^2 \quad \text{with}$$

$$C_{cp} = 0.63 + 0.37 \left(\frac{A_{0p}}{A_{1p}} \right)^3 \quad (\text{Graf and Altinakar 1995})$$

The single headloss-coefficient at the transition between the pipe and the lower basin can be calculated as:

$$\xi_{3p} = \left(1 - \frac{A_{2p}}{A_{3p}} \right)^2 \quad (\text{Graf and Altinakar 1995})$$

The linear headloss in the pipe can be calculated as:

$$h_{rp} = f \frac{z_1 + z_2}{D_p} \frac{V_p^2}{2g}$$

where f is the friction coefficient which can be calculated with the Colebrook-White formula:

$$\frac{1}{f} = -2 \log \left[\frac{k_s}{D_p 3.71} + \frac{2.51}{\text{Re} \sqrt{f}} \right] \quad \text{with}$$

$$\text{Re} = \frac{D_p V_p}{\nu} \quad (\text{Colebrook-White 1939})$$

Upper basin:

The continuity equation of the upper basin is written as:

$$Q_{in} - \sum_{p=1}^4 Q_p - Q_{over} = b_1 b_2 \frac{dH}{dt} \quad (\text{III.0})$$

where the overflow Q_{over} can be calculated as:

$$Q_{over} = C_d L_b \sqrt{2g} (H - z_1 - w)^{3/2}$$

C_d is the overfall coefficient which can be calculated as:

$$C_d = 0.326 \left[\frac{1 + (9/7)\zeta_w^4}{1 + \zeta_w^4} \right] \quad \text{with}$$

$$\zeta_w = (H - w - z_1) / L_w \quad (\text{Hager 1995})$$

Finally, the replacement of Q_{over} in equation (III.0) leads to:

$$Q_{in} - \sum_{p=1}^4 V_p \frac{D_p^2 \pi}{4} - C_d L_b \sqrt{2g} (H - z_1 - w)^{3/2} = b_1 b_2 \frac{dH}{dt} \quad (\text{III.1})$$

Inlet basin including the rectangular opening:

The continuity equation of the inlet basin (including the volume of the water over the rectangular opening with $l_1=0.5$ m and $l_2=0.9$ m) is written as:

$$\sum_{p=1}^4 Q_p + Q_{base} - Q_{out} = l_1 l_2 \frac{dh}{dt} \quad (\text{IV.0})$$

$$\sum_{p=1}^4 V_p \frac{D_p^2 \pi}{4} + Q_{base} - Q_{out} = l_1 l_2 \frac{dh}{dt} \quad (\text{IV.1})$$

Outflow of the inlet basin including the rectangular opening

The outflow of the inlet basin including the rectangular opening is equal to the inflow into the inlet reach. As the additional flow through the pipe(s) leads to an increase of the water level h a rapidly varied uniformly progressive flow is produced in the inlet reach. The increase of h leads therefore to a change of the outlet flow Q_{out} .

The continuity equation for a small channel reach dx immediately downstream of the section $x=-7.4$ m is written as:

$$\frac{dA}{dt} + \frac{dQ}{dx} = 0 \quad (\text{V.0})$$

The multiplication with dx leads to:

$$\frac{d\forall}{dt} = dQ \quad (\text{V.1})$$

where $d\forall$ is the variation of the volume. After discretization for a small time step $\Delta t = t_{i-1} - t_i$ the equation (V.1) is written as:

$$\Delta\forall = (Q_e - Q_s) \Delta t = U_i h_i B \Delta t - U_{i-1} h_{i-1} B \Delta t \quad (\text{V.2})$$

with $Q_e = Q_{out\ i} = U_i h_i B$ and $Q_s = Q_{out\ i-1} = U_{i-1} h_{i-1} B$

$\Delta\forall$ can also be expressed considering the absolute wave velocity U_w :

$$\Delta\forall = \Delta A \Delta x = (h_i - h_{i-1}) B U_{w\ i-1} \Delta t \quad (V.3)$$

with $U_{w\ i-1} = U_{i-1} + \sqrt{gh_{i-1}}$

The replacement of (V.3) in (V.2) leads to:

$$(h_i - h_{i-1}) B U_{w\ i-1} \Delta t = U_i h_i B \Delta t - U_{i-1} h_{i-1} B \Delta t \quad (V.4)$$

after replacement of $U_{w\ i-1}$ with $U_{i-1} + (gh_{i-1})^{0.5}$ and $U_i h_i B$ with $Q_{out\ i}$ equation (V.4) becomes:

$$Q_{out\ i} = U_{i-1} h_{i-1} B + (h_i - h_{i-1})(U_{i-1} + \sqrt{gh_{i-1}}) B \quad (V.5)$$

Discretization in time of equations (I.3), (III.1) and (IV.1)

The steady inflow to the upper basin Q_{in} and the steady inflow to the inlet basin $Q_{baseflow}$ as well as all geometrical parameters are considered constant. After the opening of the flap gate(s), the water in the pipe(s) is accelerated. Q_p , H and h as well as all depending parameters are therefore a function of time after the gate(s) opening. Equations (I.3), (III.1) and (IV.1) can be discretized in time as follows, where X_i means $X(t_i)$.

$$V_{p\ i+1} = V_{p\ i} + \frac{g(t_{i+1} - t_i)}{L} \left[H_i - h_i - \frac{(Q_{tot\ i} / l_1 l_2)^2}{2g} - \frac{V_{p\ i}^2}{2g} \left(\xi_{2i} + \xi_{3i} + f_i \frac{L}{D_p} \right) \right] \quad (I.4)$$

$$H_{i+1} = H_i + \frac{(t_{i+1} - t_i)}{b_1 b_2} \left[Q_{in} - \sum_{p=1}^4 V_{p\ i} \frac{D_p^2 \pi}{4} - C_{d\ i} L_b \sqrt{2g} (H_i - Z_1 - w)^{3/2} \right] \quad (III.2)$$

$$h_{i+1} = h_i + \frac{(t_{i+1} - t_i)}{l_1 l_2} \left[\sum_{p=1}^4 V_{p\ i} \frac{D_p^2 \pi}{4} + Q_{base} - Q_{out\ i} \right] \quad (IV.1)$$

and after replacement of $Q_{out\ i}$ (V.5):

$$h_{i+1} = h_i + \frac{(t_{i+1} - t_i)}{l_1 l_2} \left[\sum_{p=1}^4 V_{p\ i} \frac{D_p^2 \pi}{4} + Q_{base} - B \left(h_{i-1} U_{i-1} + (h_i - h_{i-1})(U_{i-1} + \sqrt{gh_{i-1}}) \right) \right] \quad (IV.2)$$

Finally, equations (I.4), (III.2) and (IV.2) allows to calculate the pipe flow, the water level in the upper basin and the outflow level at section $x=-7.4$ m at time t_{i+1} .

A 3-2: Measured and calibrated emptying of the upper basin (part 1)

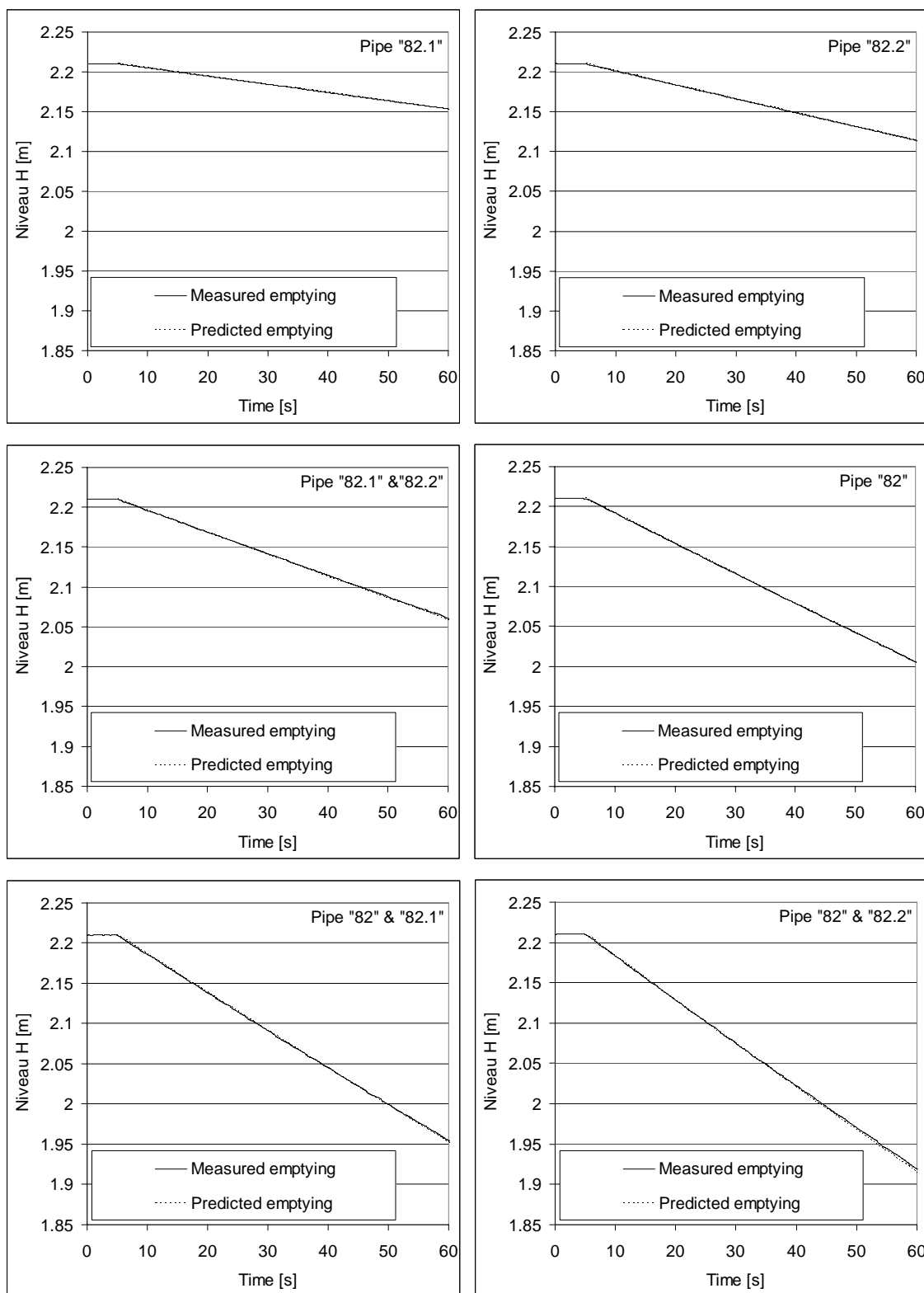


Fig-A3.4: Measured and predicted water levels in the upper basin during its emptying for different openings of one or several pipes with the calibrated mathematic model. Case 1 to 6.

A 3-2: Measured and calibrated emptying of the upper basin (part 2)

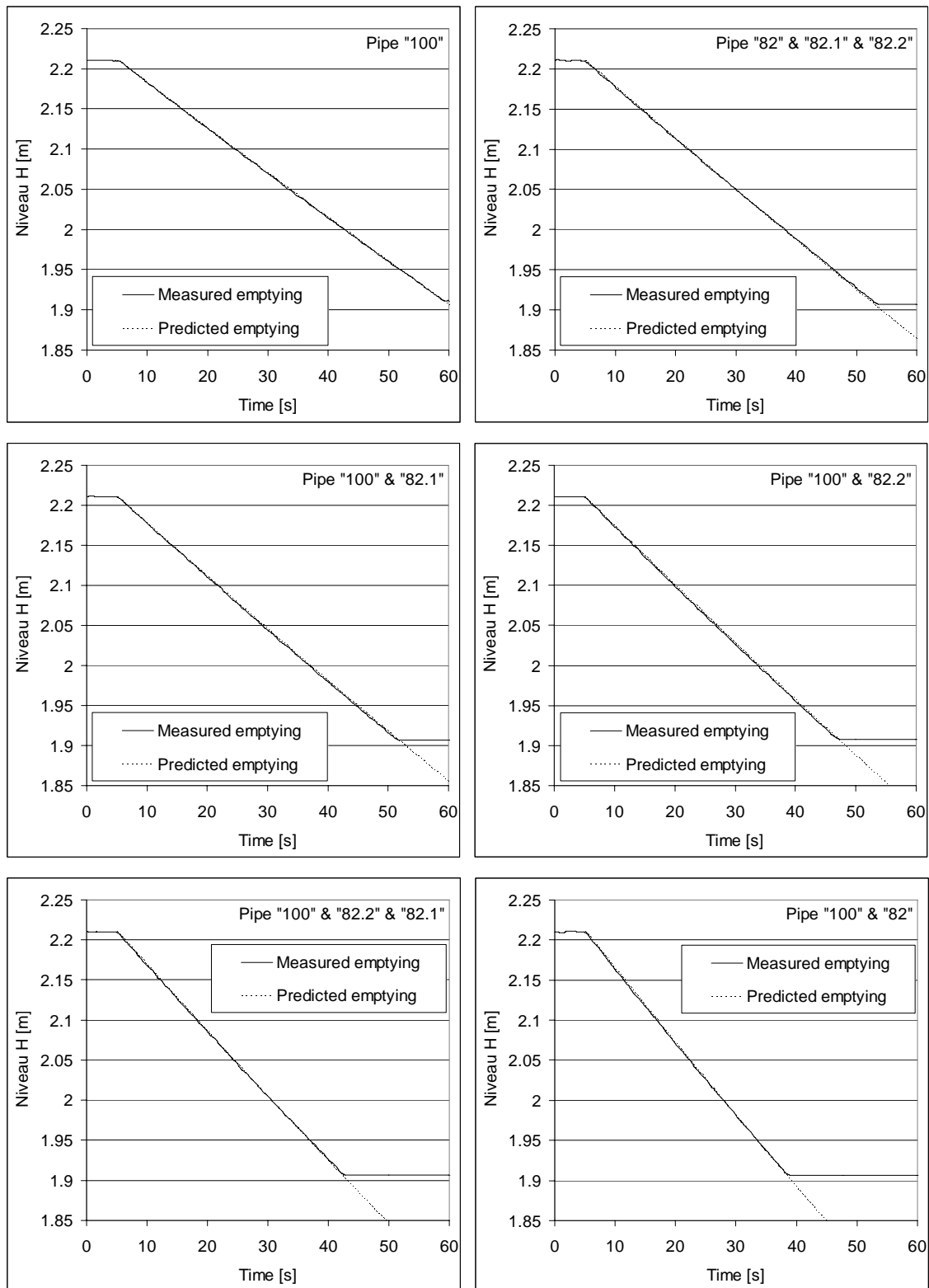


Fig-A3.5: Measured and predicted water levels in the upper basin during its emptying for different openings of one or several pipes with the calibrated mathematic model. Case 7 to 12.

A 3-2: Measured and calibrated emptying of the upper basin (part 3)

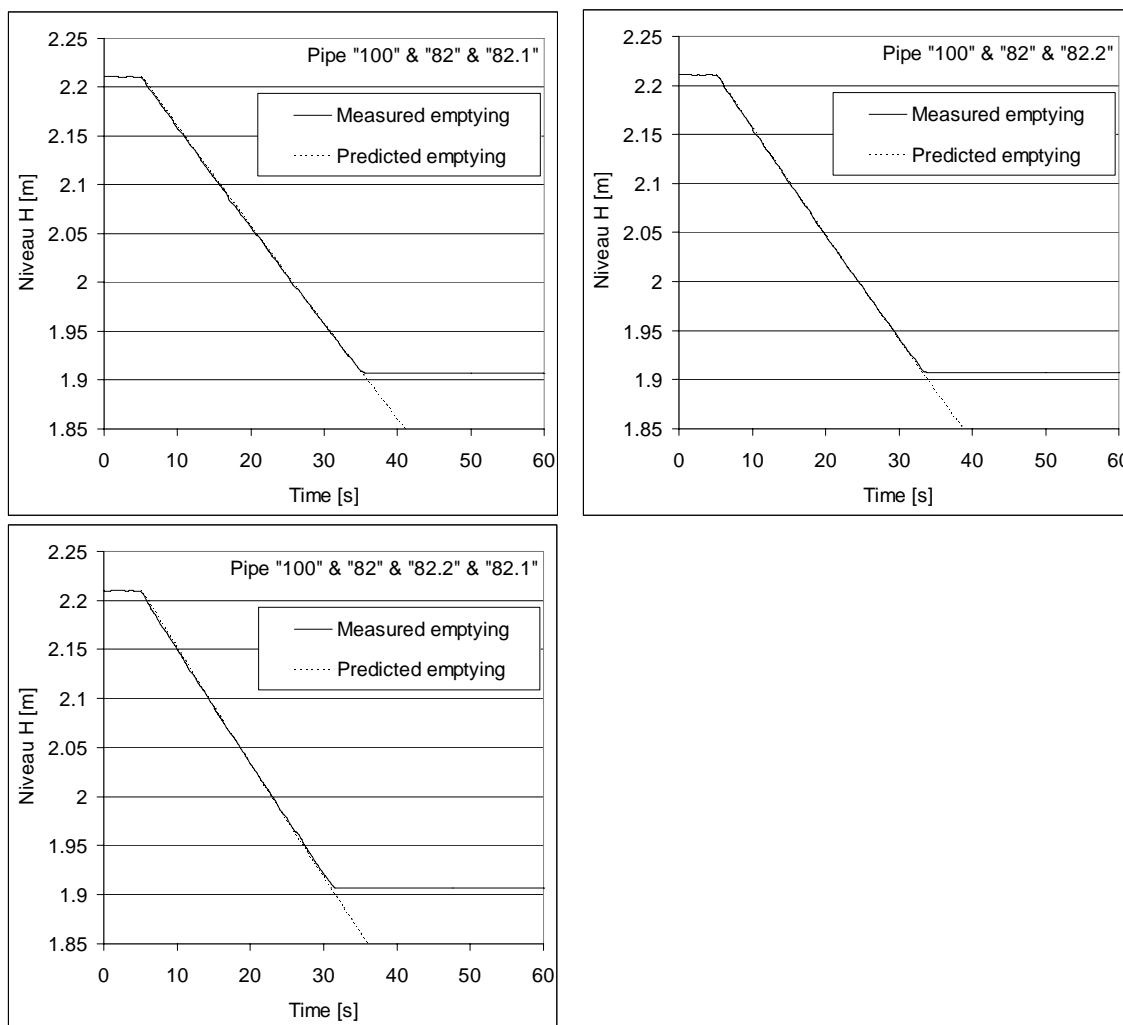


Fig-A3.6: Measured and predicted water levels in the upper basin during its emptying for different openings of one or several pipes with the calibrated mathematic model. Case 13 to 15.

US-probe [-]	Prismatic channel [m]	Configuration 111 to 114 [m]	Configuration 121 to 124 [m]	Configuration 141 to 144 [m]	Configuration 211 to 214 [m]	Configuration 221 to 224 [m]	Configuration 241 to 244 [m]	Configuration 411 to 414 [m]	Configuration 421 to 424 [m]	Configuration 441 to 444 [m]
0	-7.71	-7.71	-7.71	-7.71	-7.71	-7.71	-7.71	-7.71	-7.71	-7.71
1	-4.96	-4.96	-4.96	-4.96	-4.96	-4.96	-4.96	-4.96	-4.96	-4.96
2	-3.615	-3.615	-3.615	-3.615	-3.615	-3.615	-3.615	-3.615	-3.615	-3.615
3	-2.27	-2.27	-2.27	-2.27	-2.27	-2.27	-2.27	-2.27	-2.27	-2.27
4	-0.925	-0.925	-0.925	-0.925	-0.925	-0.925	-0.925	-0.925	-0.925	-0.925
5	0.42	0.42	0.42	0.42	0.42	0.42	0.42	0.42	0.42	0.42
6	1.92	1.92	1.92	1.92	1.92	1.92	1.92	1.92	1.92	1.92
7	3.42	3.42	3.42	3.42	3.42	3.42	3.42	3.17	3.42	3.42
8	4.92	4.92	5.67	4.92	5.67	4.92	4.92	4.92	4.92	4.92
9	6.42	6.42	6.42	6.42	6.42	6.42	6.42	6.42	6.42	6.42
10	7.92	7.92	7.92	7.92	7.92	7.92	7.92	8.17	7.92	7.92
11	9.42	9.42	10.17	9.42	10.17	9.42	9.42	9.42	9.42	9.42
12	10.92	10.92	10.92	10.92	10.92	10.92	10.92	10.67	10.92	10.92
13	12.42	12.42	12.42	12.42	12.42	12.42	12.42	12.42	12.42	12.42
14	13.92	13.92	14.67	13.92	14.67	13.92	13.92	13.92	13.92	13.92
15	15.42	15.42	15.42	15.42	15.42	15.42	15.42	15.67	15.42	15.42
16	16.92	16.92	16.92	16.92	16.92	16.92	16.92	16.92	16.92	16.92
17	18.42	18.42	18.42	18.42	18.42	18.42	18.42	18.17	18.42	18.42
18	19.92	19.92	19.17	19.92	19.17	19.92	19.92	19.92	19.92	19.92
19	21.42	21.42	21.42	21.42	21.42	21.42	21.42	21.42	21.42	21.42
20	22.92	22.92	22.92	22.92	22.92	22.92	22.92	23.17	22.92	22.92
21	24.42	24.42	23.67	24.42	23.67	24.42	24.42	24.42	24.42	24.42
22	25.92	25.92	25.92	25.92	25.92	25.92	25.92	25.92	25.92	25.92
23	27.42	27.42	27.42	27.42	27.42	27.42	27.42	27.42	27.42	27.42
24	28.12	28.12	28.12	28.12	28.12	28.12	28.12	28.12	28.12	28.12
25	28.92	28.92	28.92	28.92	28.92	28.92	28.92	28.92	28.92	28.92

Fig-A3.7: Position of the ultrasonic sensors along the channel for the unsteady flow tests. The positions depend on the configuration (prismatic or axi-symmetric macro-rough) but are fixed for the different scenarios. $x=0.0$ m at the begin of the macro-rough reach.

	Sc 1	Sc 2	Sc 3	Sc 4	Sc 5	Sc 6	Sc 7	Sc 8	Sc 9	Sc 10	Sc 11	Sc 12	Sc 13	Sc 14	Sc 15	Sc 16	Sc 17	Sc 18	Sc 19	Sc 20	Sc 21	Sc 22	Sc 23	Sc 24	Sc 25	Sc 26	Sc 27	Sc 28	Sc 29	Sc 30	
Prismatic																															
111																															
112																															
113																															
114																															
121																															
122																															
123																															
124																															
141																															
142																															
143																															
144																															
211																															
212																															
213																															
214																															
221																															
222																															
223																															
224																															
241																															
242																															
243																															
244																															
411																															
412																															
413																															
414																															
421																															
422																															
423																															
424																															
441																															
442																															
443																															
444																															
112 asy.																															
121 asy.																															
211 asy.																															
Random																															

tested scenario not tested scenario

Fig-A3.8: Tested scenarios for all geometrical configurations.

A 4-1: Summarized test results for the steady flow tests: 111 to 114

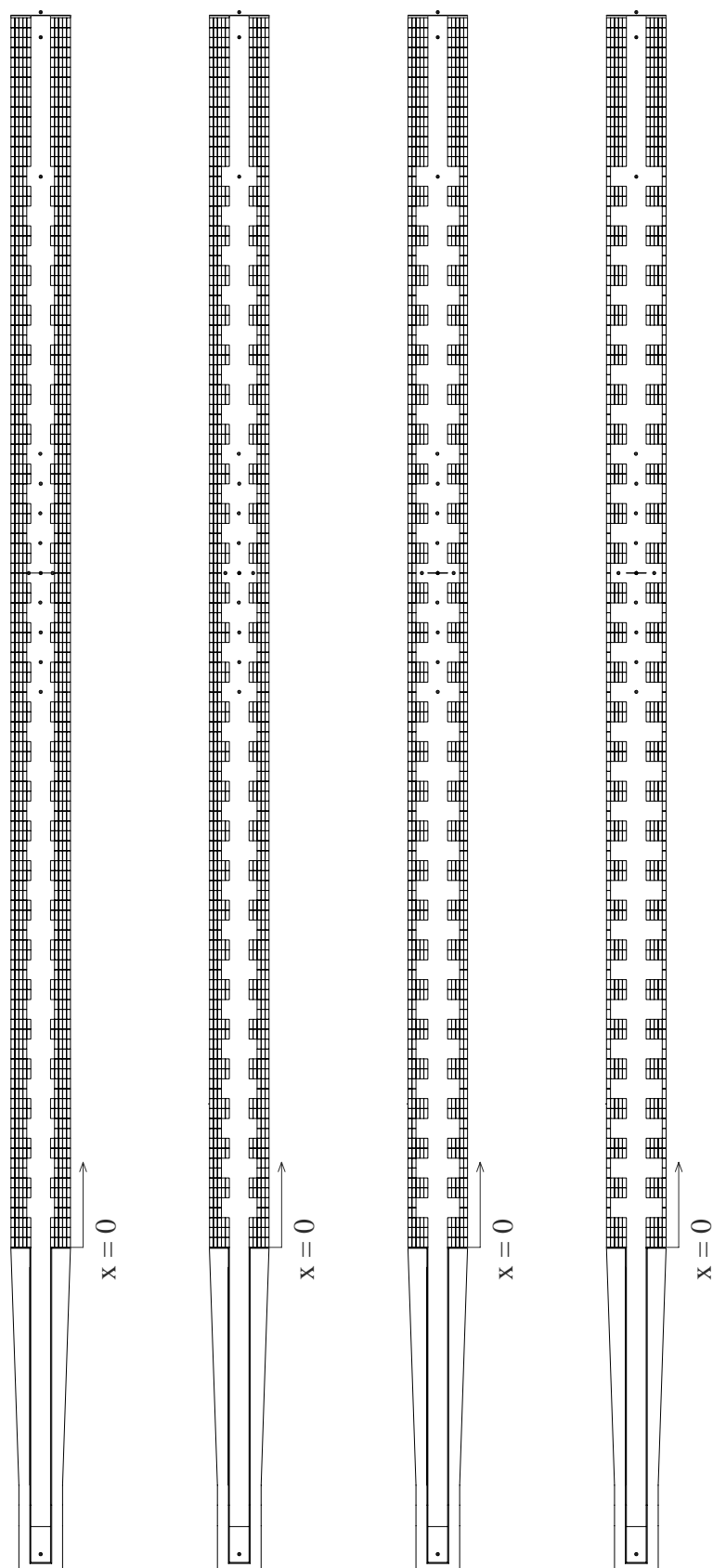


Fig-A4.1: Configurations 111, 112, 113 and 114. Flow direction from bottom to top.

Table with flow resistance parameters of the tests in configurations 111-114. f_{MR} can be calculated as $f_{MR} = f_m - f_{prism}$.

Conf.	Q	$h(x=16.92m)$	$k_{s,w}$	$K_{st,w}$	$K_{st,m}$	C_w	C_m	Re_w	Re_m	Fr	f_w	f_m	f_{prism}
[-]	[m ³ /s]	[m]	[mm]	[m ¹ /3s ⁻¹]	[m ¹ /3s ⁻¹]	[m0.5s ⁻¹]	[m0.5s ⁻¹]	[-]	[-]	[-]	[-]	[-]	[-]
111	0.0063	0.040	16.6	47.7	91.9	32.0	52.4	29787	11121	0.52	0.0765	0.0286	0.0193
111	0.0109	0.058	28.3	42.8	82.3	30.3	49.4	48018	18012	0.51	0.0856	0.0321	0.0174
111	0.0193	0.087	46.0	38.5	70.7	28.4	44.7	72220	29093	0.49	0.0975	0.0393	0.0159
111	0.0324	0.135	121.1	29.5	51.3	22.6	34.1	97926	42761	0.43	0.1541	0.0673	0.0148
111	0.0491	0.181	120.0	29.9	47.6	23.0	32.6	115928	57714	0.42	0.1484	0.0739	0.0140
111	0.0626	0.216	123.1	29.7	45.1	23.0	31.4	126775	67888	0.41	0.1484	0.0795	0.0136
112	0.0062	0.039	14.6	49.0	93.1	32.7	53.0	28671	10952	0.52	0.0732	0.0280	0.0193
112	0.0109	0.058	25.4	43.9	83.4	31.0	50.1	47426	18120	0.52	0.0819	0.0313	0.0174
112	0.0191	0.085	33.4	41.7	74.8	30.4	47.1	69688	29064	0.51	0.0847	0.0353	0.0159
112	0.0350	0.137	77.9	33.9	57.1	25.7	38.0	100561	45979	0.46	0.1188	0.0543	0.0146
112	0.0484	0.177	103.7	31.3	49.8	24.0	34.0	115418	57455	0.43	0.1360	0.0677	0.0140
112	0.0616	0.206	78.4	34.1	51.4	26.2	35.7	126650	68453	0.43	0.1141	0.0616	0.0136
113	0.0053	0.039	59.5	34.4	80.2	24.1	45.5	33583	9409	0.46	0.1353	0.0379	0.0200
113	0.0109	0.060	50.1	37.1	75.5	26.7	45.6	52077	17915	0.49	0.1099	0.0378	0.0174
113	0.0191	0.088	58.5	36.2	67.5	26.8	42.8	73392	28759	0.48	0.1095	0.0429	0.0159
113	0.0342	0.135	85.3	33.0	56.0	25.0	37.3	99704	45014	0.45	0.1251	0.0565	0.0146
113	0.0501	0.176	75.4	34.4	53.9	26.3	36.9	116875	59576	0.45	0.1133	0.0577	0.0139
113	0.0645	0.208	55.4	37.6	55.6	28.8	38.6	128338	71334	0.45	0.0948	0.0527	0.0135
114	0.0057	0.042	104.5	29.1	71.8	20.9	41.2	38559	9938	0.43	0.1790	0.0461	0.0197
114	0.0106	0.064	130.5	27.8	61.8	20.7	37.6	56658	17125	0.43	0.1837	0.0555	0.0176
114	0.0195	0.099	156.8	26.7	52.2	20.3	33.5	77919	28447	0.41	0.1911	0.0698	0.0159
114	0.0344	0.145	154.4	27.2	47.0	20.9	31.5	100134	44204	0.41	0.1793	0.0792	0.0147
114	0.0484	0.179	121.5	29.7	47.5	22.9	32.5	115241	57087	0.42	0.1497	0.0741	0.0140
114	0.0609	0.214	135.5	28.8	44.0	22.3	30.6	125207	66385	0.40	0.1580	0.0838	0.0137

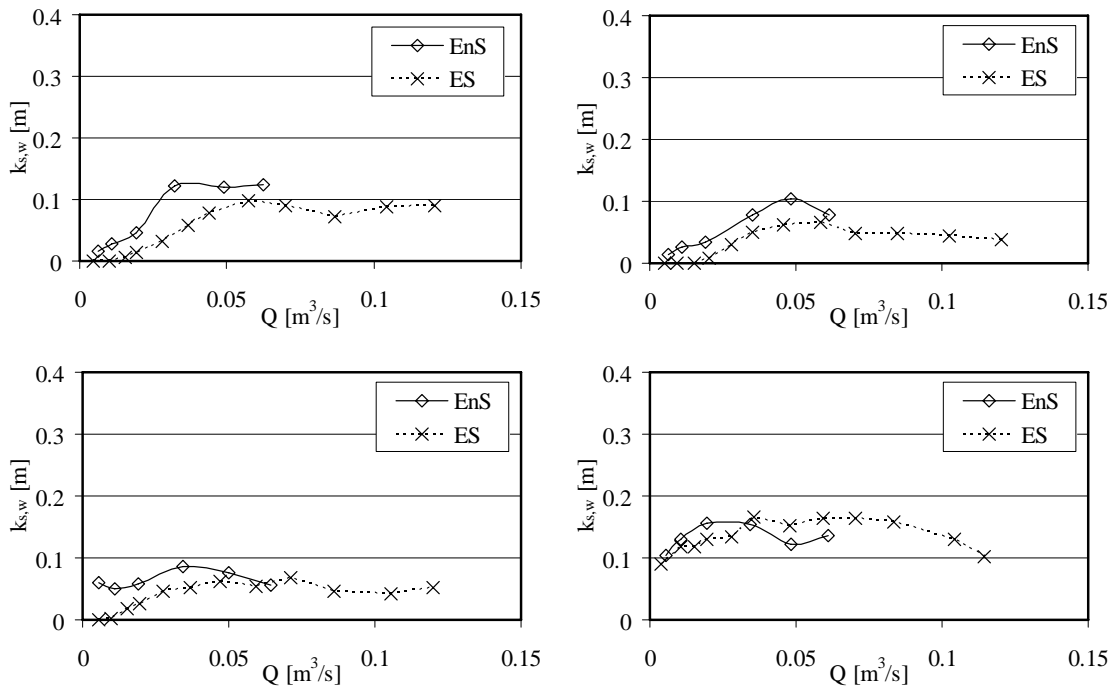


Fig-A4.2: Equivalent sand roughness of the wall $k_{s,w}$ for configurations 111 (top left), 112 (top right), 113 (bottom left) and 114 (bottom right). ES: first test series. EnS: second test series.

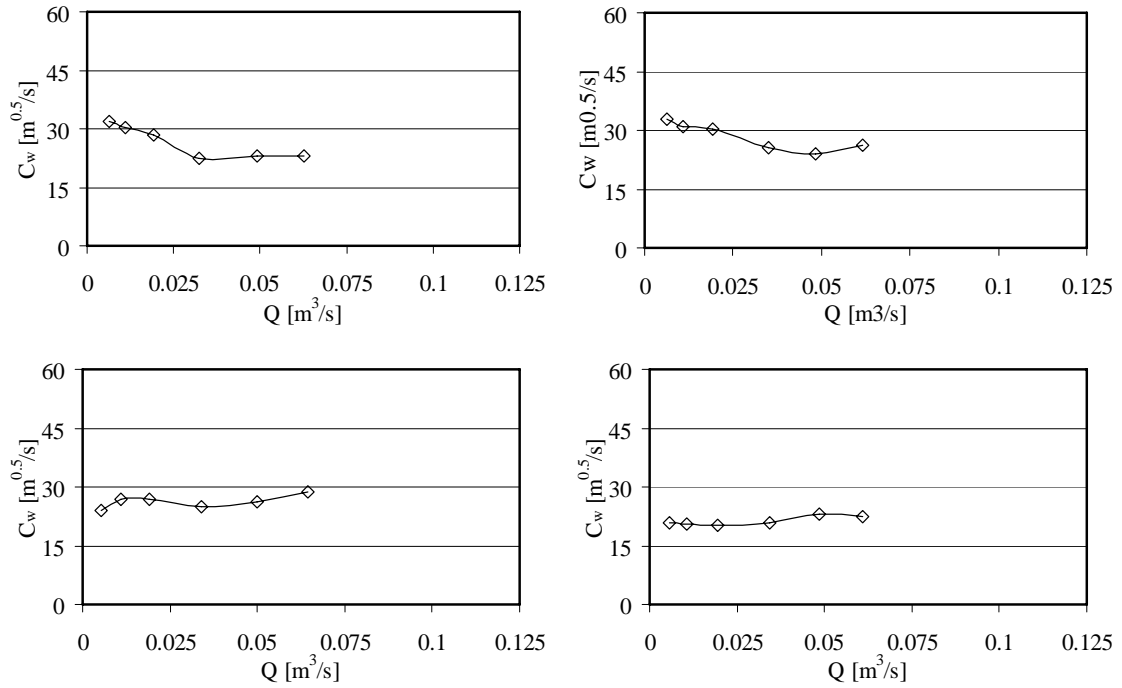


Fig-A4.3: Chezy coefficient related to the wall C_w for configurations 111 (top left), 112 (top right), 113 (bottom left) and 114 (bottom right).

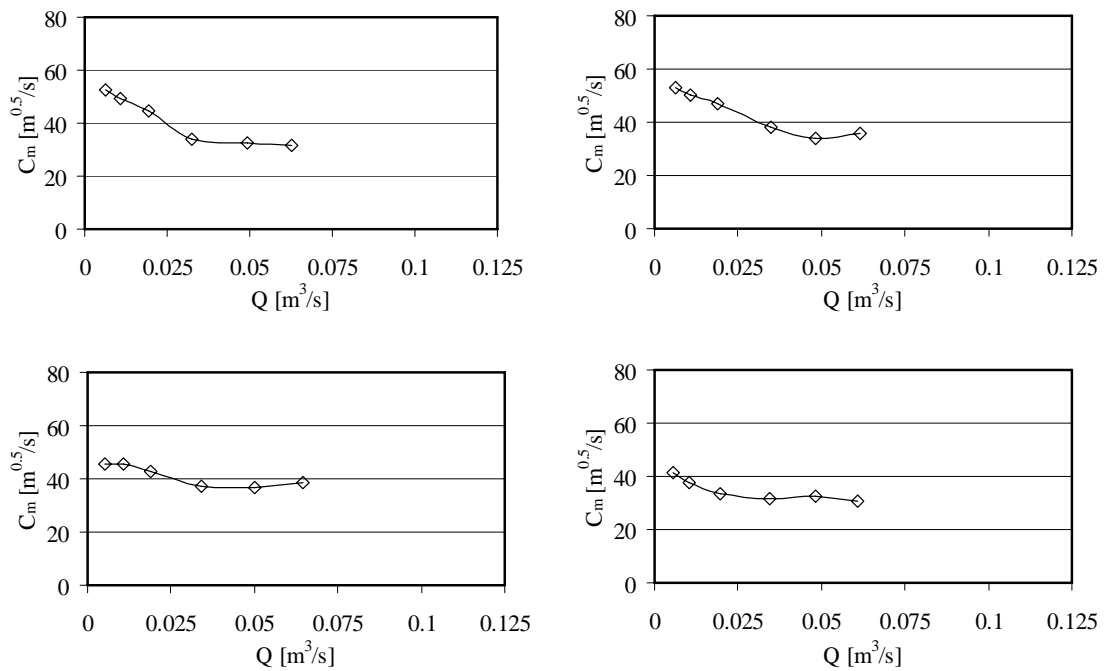


Fig-A4.4: Chezy coefficient related to the cross section C_m for configurations 111 (top left), 112 (top right), 113 (bottom left) and 114 (bottom right).

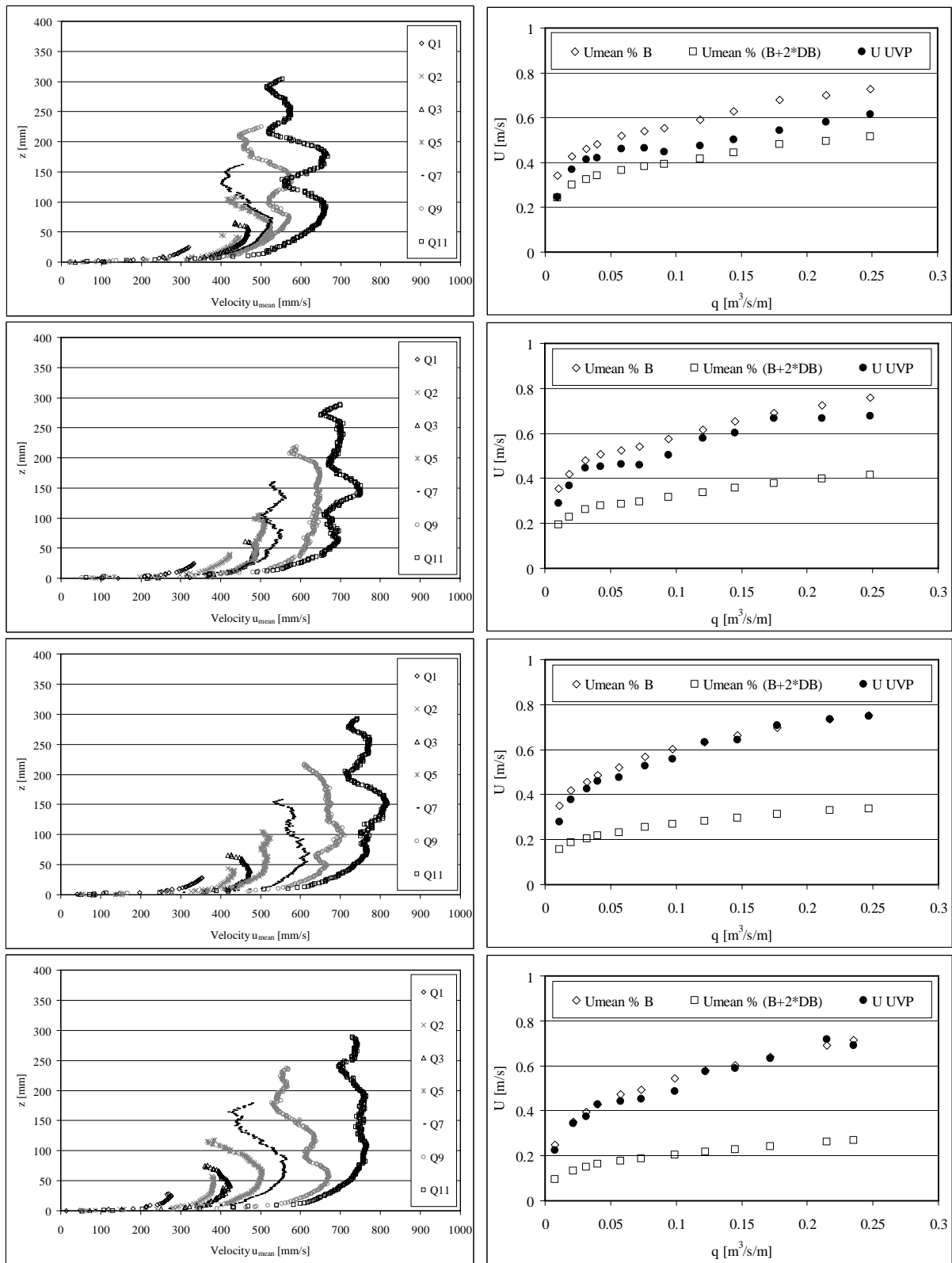


Fig-A4.5: Configurations 111 (above) to 114 (below). Left side: Vertical velocity profiles for different discharges (first test series ES). Right side: Mean velocity of the profiles measured by UVP technique and the theoretical velocities $U_{mean}^+ = Q/(Bh)$ and $U_{mean}^- = Q/((B+2\Delta B)h)$.

A 4-1: Summarized test results for the steady flow tests: 121 to 124

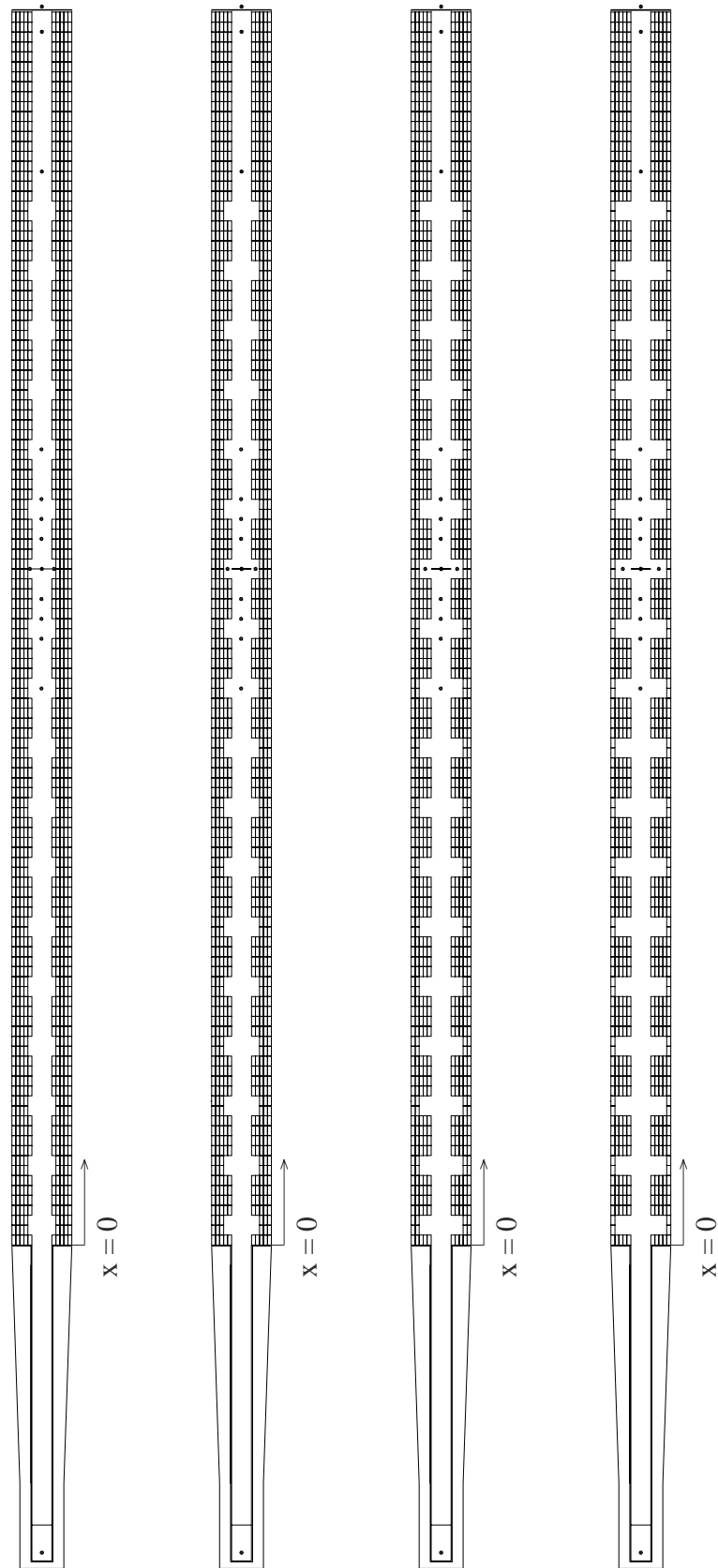


Fig-A4.6: Configurations 121, 122, 123 and 124. Flow direction from bottom to top.

Table with flow resistance parameters of the tests in configurations 121-124. f_{MR} can be calculated as $f_{MR} = f_m - f_{prism}$.

Conf.	Q	$h(x=16.92m)$	$k_{s,w}$	$K_{st,w}$	$K_{st,m}$	C_w	C_m	Re_w	Re_m	Fr	f_w	f_m	f_{prism}
[-]	[m ³ /s]	[m]	[mm]	[m ¹ /3s ⁻¹]	[m ¹ /3s ⁻¹]	[m0.5s ⁻¹]	[m0.5s ⁻¹]	[-]	[-]	[-]	[-]	[-]	[-]
121	0.0055	0.036	11.1	51.8	96.0	33.9	53.9	24575	9747	0.53	0.0681	0.0270	0.0198
121	0.0118	0.054	0.3	94.4	110.2	58.3	65.5	24960	19784	0.62	0.0231	0.0183	0.0171
121	0.0194	0.080	9.5	54.8	87.9	38.6	55.1	60841	29938	0.56	0.0526	0.0259	0.0158
121	0.0349	0.127	31.8	42.7	69.0	31.8	45.6	96515	46963	0.51	0.0774	0.0377	0.0145
121	0.0496	0.170	58.0	37.0	57.7	28.2	39.3	116540	59830	0.46	0.0990	0.0508	0.0139
121	0.0624	0.199	43.4	40.0	59.1	30.5	40.9	126636	70443	0.46	0.0845	0.0470	0.0136
121	0.0846	0.247	38.0	41.4	57.9	31.7	40.8	142301	86068	0.45	0.0779	0.0471	0.0131
121	0.1051	0.292	39.3	41.2	55.7	31.7	39.7	153941	97984	0.44	0.0781	0.0497	0.0128
122	0.0064	0.041	28.9	41.9	86.9	28.8	49.7	33400	11182	0.50	0.0947	0.0317	0.0192
122	0.0107	0.056	17.8	47.6	87.3	33.1	52.2	44404	17887	0.53	0.0716	0.0288	0.0175
122	0.0181	0.077	9.0	55.4	89.0	38.8	55.4	57654	28264	0.56	0.0521	0.0255	0.0160
122	0.0346	0.129	42.8	39.8	65.4	29.8	43.3	98041	46445	0.49	0.0883	0.0418	0.0146
122	0.0483	0.166	51.0	38.2	59.6	29.0	40.5	114744	58903	0.47	0.0931	0.0478	0.0140
122	0.0618	0.197	44.5	39.7	58.9	30.3	40.7	126224	69921	0.46	0.0856	0.0474	0.0136
123	0.0058	0.039	27.0	42.4	88.3	28.9	50.1	30747	10239	0.50	0.0940	0.0313	0.0196
123	0.0111	0.056	11.2	52.6	91.2	36.1	54.5	42210	18479	0.55	0.0604	0.0264	0.0173
123	0.0191	0.083	23.2	45.5	79.1	32.8	49.7	67293	29298	0.53	0.0729	0.0317	0.0158
123	0.0330	0.123	37.6	41.0	67.6	30.6	44.5	94973	44878	0.50	0.0838	0.0396	0.0146
123	0.0471	0.161	42.0	40.1	62.4	30.4	42.3	112611	58120	0.48	0.0851	0.0439	0.0140
123	0.0628	0.198	36.6	41.7	61.1	31.7	42.2	126239	71056	0.47	0.0781	0.0440	0.0135
123	0.0859	0.246	34.1	42.5	59.3	32.5	41.7	144209	87667	0.46	0.0741	0.0450	0.0131
123	0.1040	0.293	41.1	40.7	55.1	31.4	39.3	151909	96678	0.43	0.0797	0.0507	0.0129
124	0.0063	0.043	80.4	31.7	74.8	22.7	43.2	39480	10884	0.45	0.1527	0.0421	0.0194
124	0.0105	0.061	89.0	31.4	68.1	23.0	41.1	54693	17148	0.46	0.1478	0.0463	0.0176
124	0.0191	0.092	101.9	30.8	59.6	23.1	37.9	76615	28411	0.45	0.1470	0.0545	0.0159
124	0.0345	0.139	118.2	29.8	51.2	22.8	34.2	101402	44980	0.44	0.1513	0.0671	0.0146
124	0.0466	0.177	148.7	27.8	45.0	21.4	30.8	114185	55383	0.41	0.1711	0.0830	0.0141
124	0.0629	0.211	100.9	31.7	47.9	24.4	33.3	128520	69022	0.43	0.1315	0.0706	0.0136

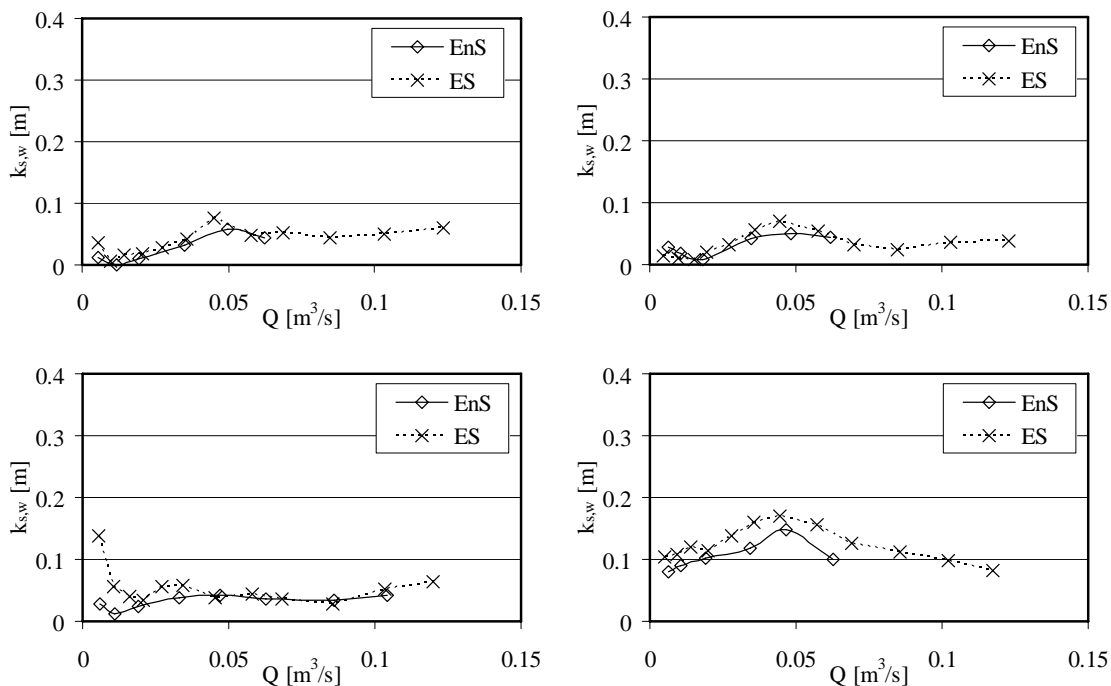


Fig-A4.7: Equivalent sand roughness of the wall $k_{s,w}$ for configurations 121 (top left), 122 (top right), 123 (bottom left) and 124 (bottom right). ES: first test series. EnS: second test series.

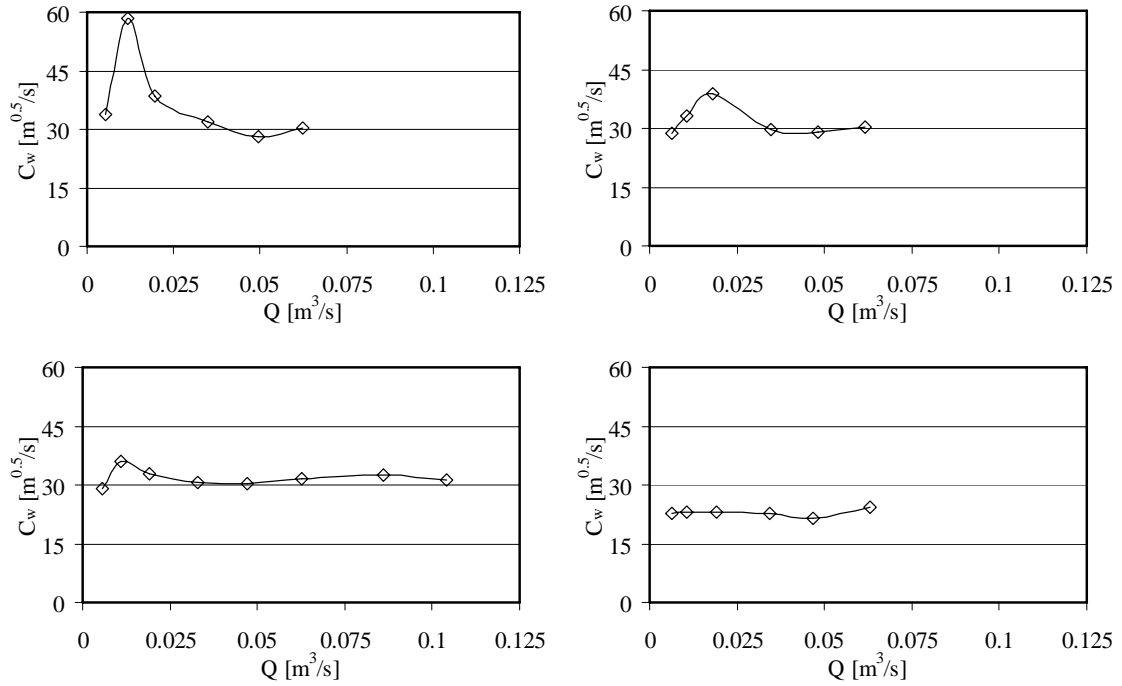


Fig-A4.8: Chezy coefficient related to the wall C_w for configurations 121 (top left), 122 (top right), 123 (bottom left) and 124 (bottom right).

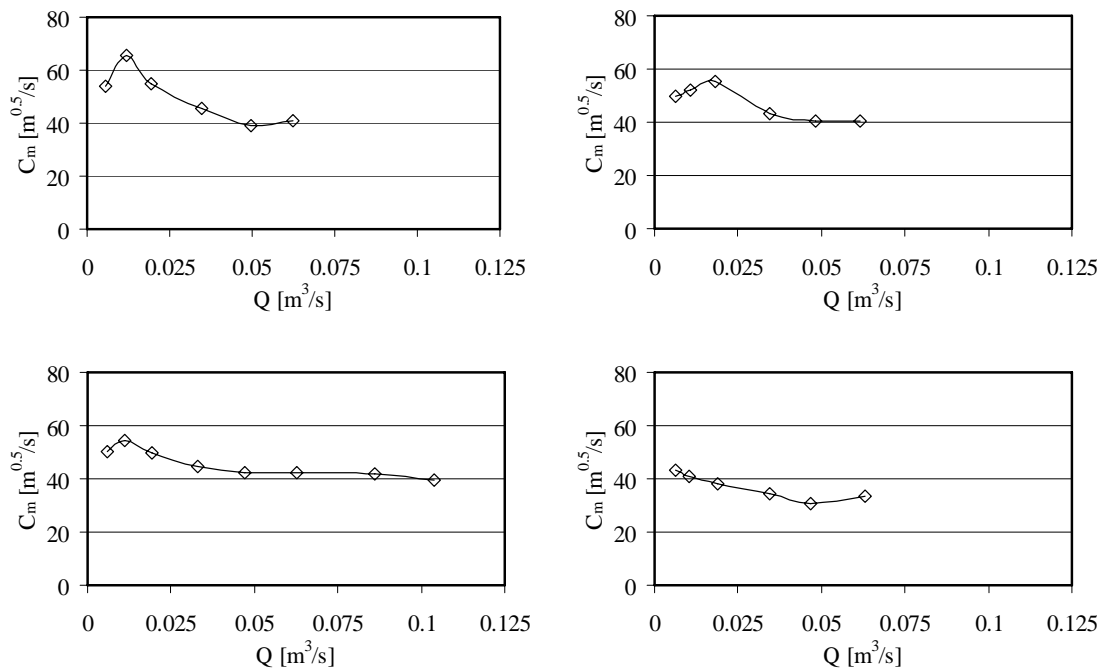


Fig-A4.9: Chezy coefficient related to the cross section C_m for configurations 121 (top left), 122 (top right), 123 (bottom left) and 124 (bottom right).

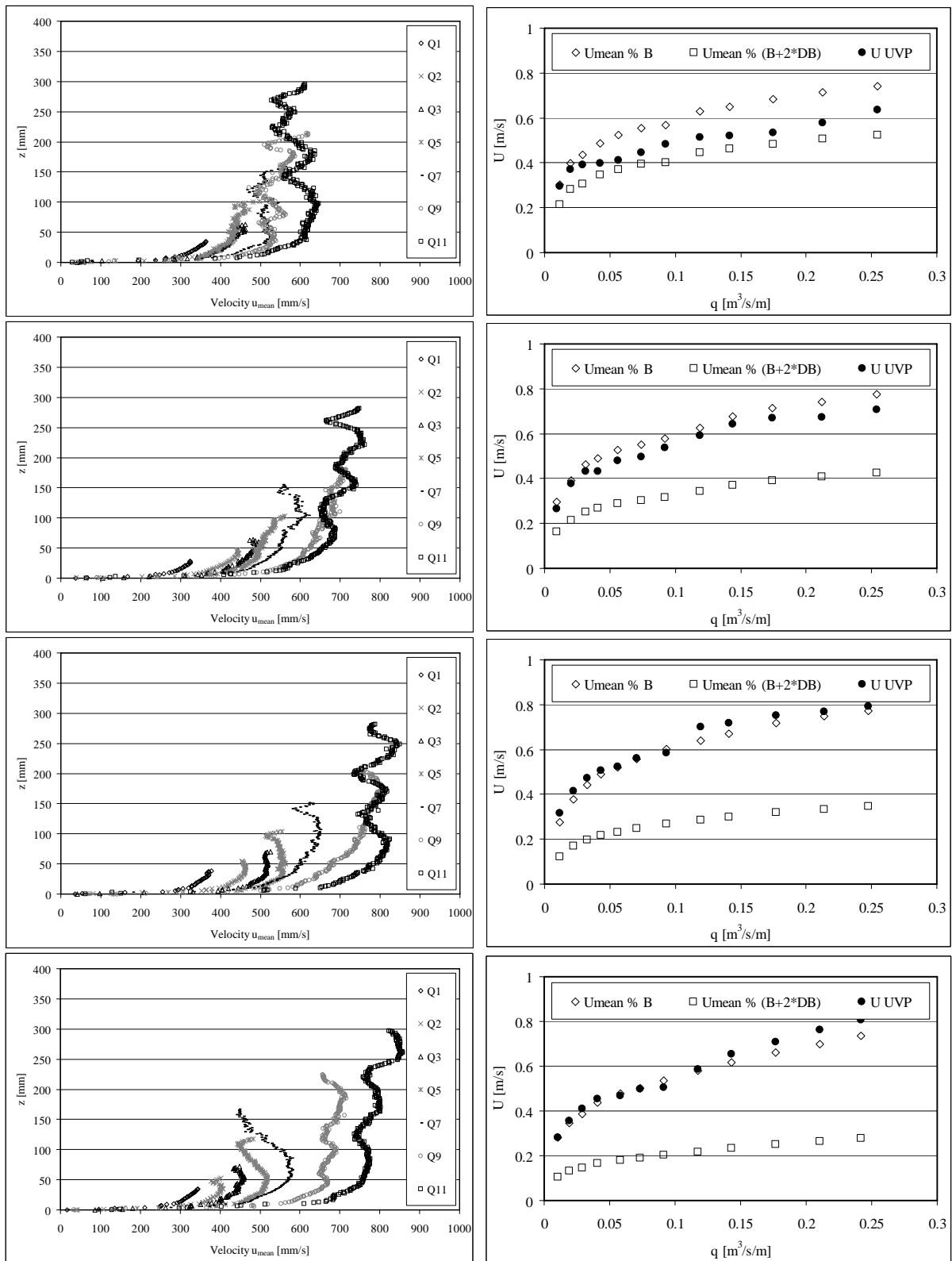


Fig-A4.10: Configurations 121 (above) to 124 (below). Left side: Vertical velocity profiles for different discharges (first test series ES). Right side: Mean velocity of the profiles measured by UVP technique and the theoretical velocities $U_{mean}^+ = Q/(Bh)$ and $U_{mean}^- = Q/((B+2\Delta B)h)$.

A 4-1: Summarized test results for the steady flow tests: 141 to 144

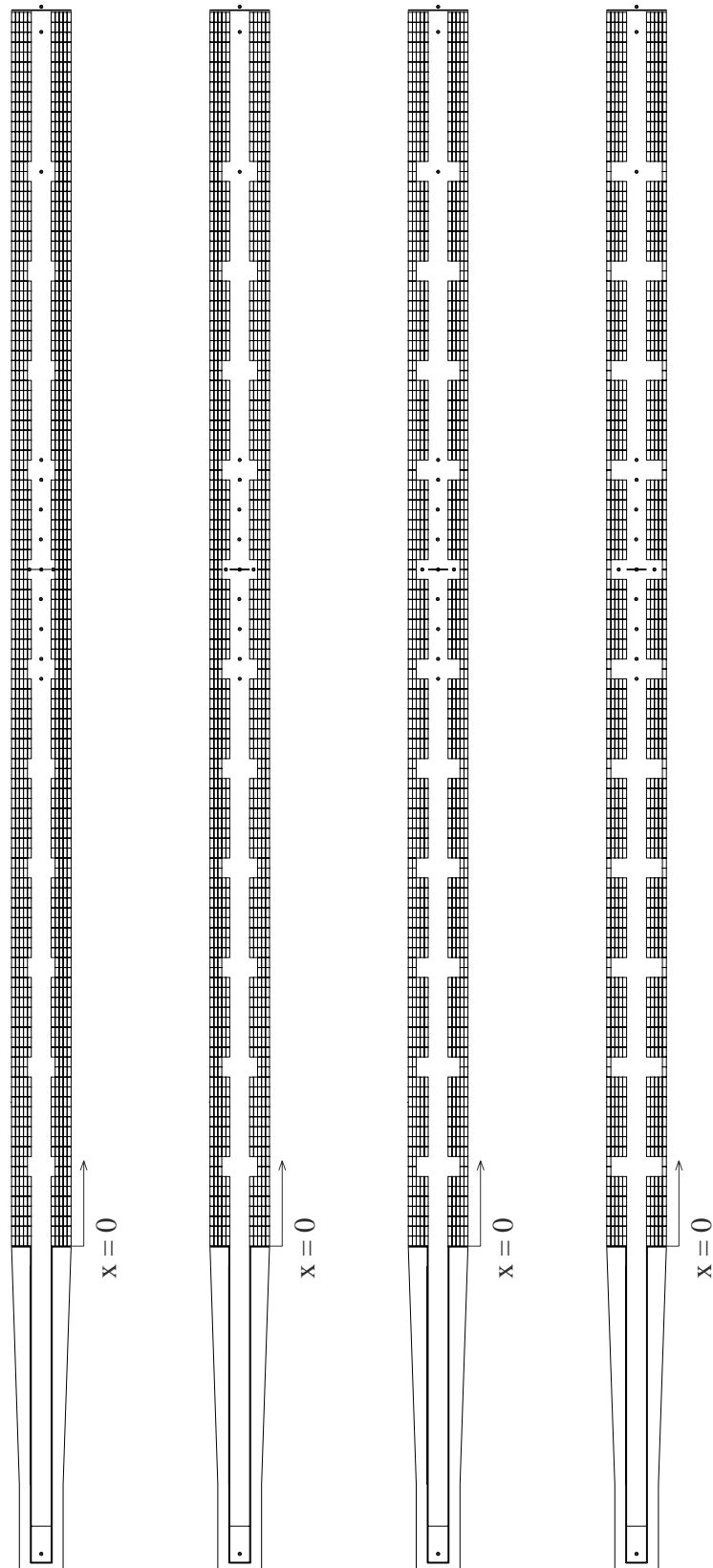


Fig-A4.11: Configurations 141, 142, 143 and 144. Flow direction from bottom to top.

Table with flow resistance parameters of the tests in configurations 141-144. f_{MR} can be calculated as $f_{MR} = f_m - f_{prism}$

Conf.	Q	$h(x=16.92m)$	$k_{s,w}$	$K_{s,w}$	$K_{s,m}$	C_w	C_m	Re_w	Re_m	Fr	f_w	f_m	f_{prism}
[-]	[m ³ /s]	[m]	[mm]	[ml/3s-1]	[ml/3s-1]	[m0.5s-1]	[m0.5s-1]	[-]	[-]	[-]	[-]	[-]	[-]
141	0.0062	0.036	0.1	104.1	112.5	59.6	63.2	12504	11130	0.59	0.0221	0.0196	0.0193
141	0.0107	0.051	0.6	86.3	108.1	53.9	63.8	25472	18193	0.61	0.0270	0.0193	0.0174
141	0.0191	0.076	2.0	71.8	99.5	48.5	62.0	48659	29807	0.59	0.0334	0.0204	0.0158
141	0.0337	0.115	3.8	64.9	90.7	46.2	59.3	77331	46868	0.57	0.0368	0.0223	0.0145
141	0.0486	0.155	7.7	57.4	80.8	42.2	54.5	101488	60892	0.53	0.0440	0.0264	0.0139
141	0.0649	0.196	11.6	53.3	73.7	39.9	50.9	119846	73772	0.49	0.0493	0.0303	0.0134
141	0.0852	0.243	15.0	50.8	68.3	38.5	48.1	136199	87322	0.47	0.0530	0.0340	0.0131
141	0.1120	0.302	19.4	48.3	63.1	36.9	45.1	153212	102530	0.45	0.0575	0.0385	0.0128
142	0.0053	0.036	16.6	47.4	93.1	31.5	52.2	25898	9410	0.51	0.0791	0.0288	0.0200
142	0.0098	0.051	6.0	59.5	96.8	39.6	57.1	34465	16594	0.56	0.0500	0.0241	0.0177
142	0.0192	0.081	11.7	52.6	86.0	37.3	53.9	61674	29515	0.55	0.0565	0.0270	0.0158
142	0.0342	0.123	18.3	48.3	75.5	35.6	49.7	90936	46580	0.52	0.0620	0.0317	0.0146
142	0.0488	0.161	20.6	47.3	70.4	35.4	47.7	109204	60239	0.50	0.0626	0.0345	0.0139
142	0.0631	0.195	19.0	48.2	68.6	36.4	47.3	121771	71849	0.48	0.0594	0.0350	0.0135
143	0.0051	0.035	13.0	50.0	95.2	32.8	53.2	24021	9158	0.52	0.0728	0.0277	0.0201
143	0.0112	0.056	7.9	56.4	93.8	38.3	56.1	40064	18693	0.55	0.0535	0.0250	0.0173
143	0.0196	0.083	16.2	49.2	82.5	35.2	51.9	65126	29967	0.54	0.0633	0.0291	0.0158
143	0.0354	0.127	19.0	48.0	74.7	35.4	49.4	92790	47741	0.52	0.0626	0.0322	0.0145
143	0.0497	0.164	24.2	45.7	68.3	34.3	46.4	111103	60784	0.49	0.0666	0.0365	0.0139
143	0.0628	0.194	18.6	48.5	68.9	36.5	47.5	121379	71660	0.48	0.0588	0.0347	0.0135
143	0.0865	0.246	14.8	50.9	68.3	38.6	48.1	136973	88177	0.47	0.0527	0.0339	0.0131
143	0.1098	0.290	7.6	57.8	73.2	43.8	52.2	146309	102671	0.46	0.0410	0.0288	0.0128
144	0.0062	0.042	40.0	38.5	83.4	26.8	47.8	34730	10902	0.48	0.1092	0.0343	0.0193
144	0.0106	0.060	60.6	35.2	73.2	25.5	44.2	52195	17390	0.47	0.1208	0.0402	0.0176
144	0.0190	0.089	61.0	35.8	66.9	26.5	42.4	73103	28567	0.47	0.1117	0.0436	0.0159
144	0.0347	0.134	61.7	36.1	60.3	27.3	40.1	98833	45863	0.47	0.1052	0.0488	0.0146
144	0.0469	0.168	72.5	34.8	55.0	26.5	37.4	113084	56783	0.45	0.1115	0.0560	0.0141
144	0.0625	0.205	56.9	37.3	55.5	28.5	38.4	126243	69618	0.44	0.0963	0.0531	0.0136

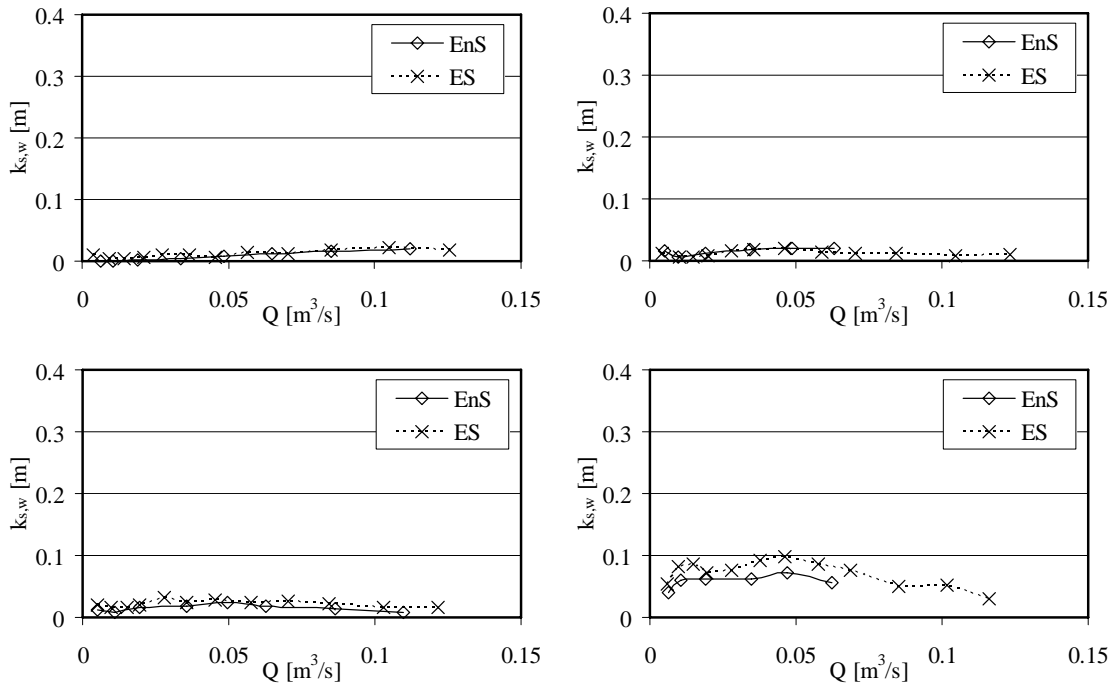


Fig-A4.12: Equivalent sand roughness of the wall $k_{s,w}$ for configurations 141 (top left), 142 (top right), 143 (bottom left) and 144 (bottom right). ES: first test series. EnS: second test series.

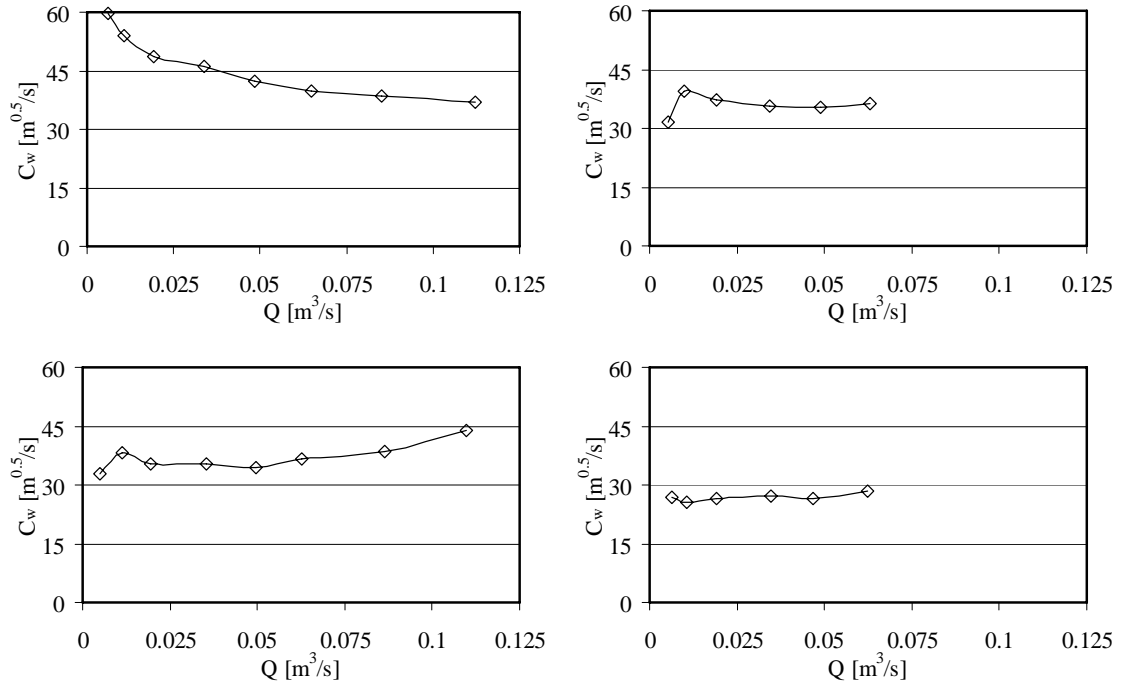


Fig-A4.13: Chezy coefficient related to the wall C_w for configurations 141 (top left), 142 (top right), 143 (bottom left) and 144 (bottom right).

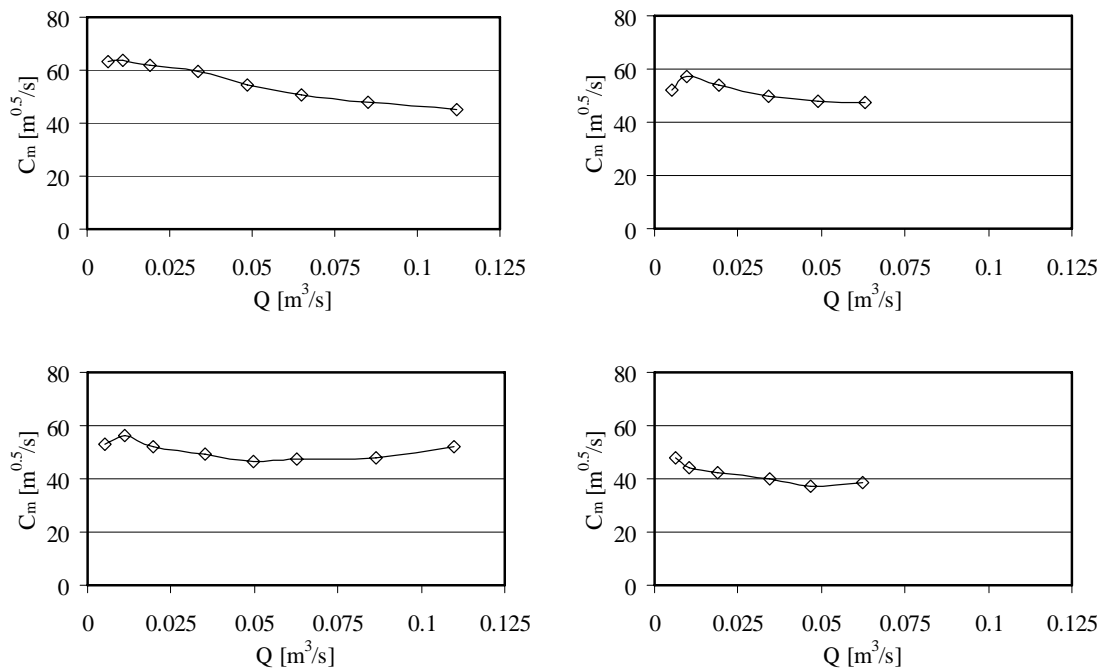


Fig-A4.14: Chezy coefficient related to the cross section C_m for configurations 141 (top left), 142 (top right), 143 (bottom left) and 144 (bottom right).

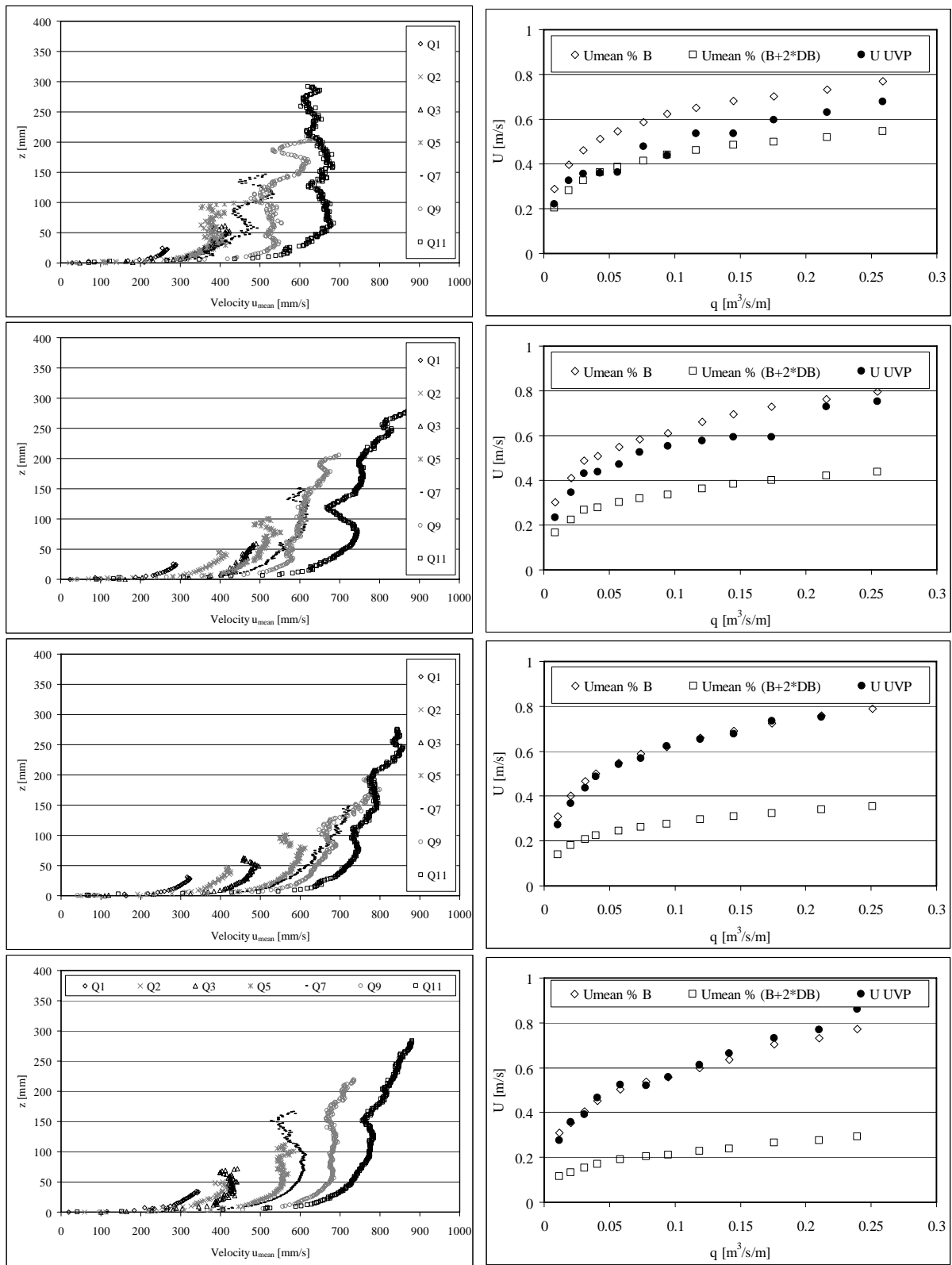


Fig-A4.15: Configurations 141 (above) to 144 (below). Left side: Vertical velocity profiles for different discharges (first test series ES). Right side: Mean velocity of the profiles measured by UVP technique and the theoretical velocities $U_{mean}^+ = Q/(Bh)$ and $U_{mean}^- = Q/((B+2\Delta B)h)$.

A 4-1: Summarized test results for the steady flow tests: 211 to 214

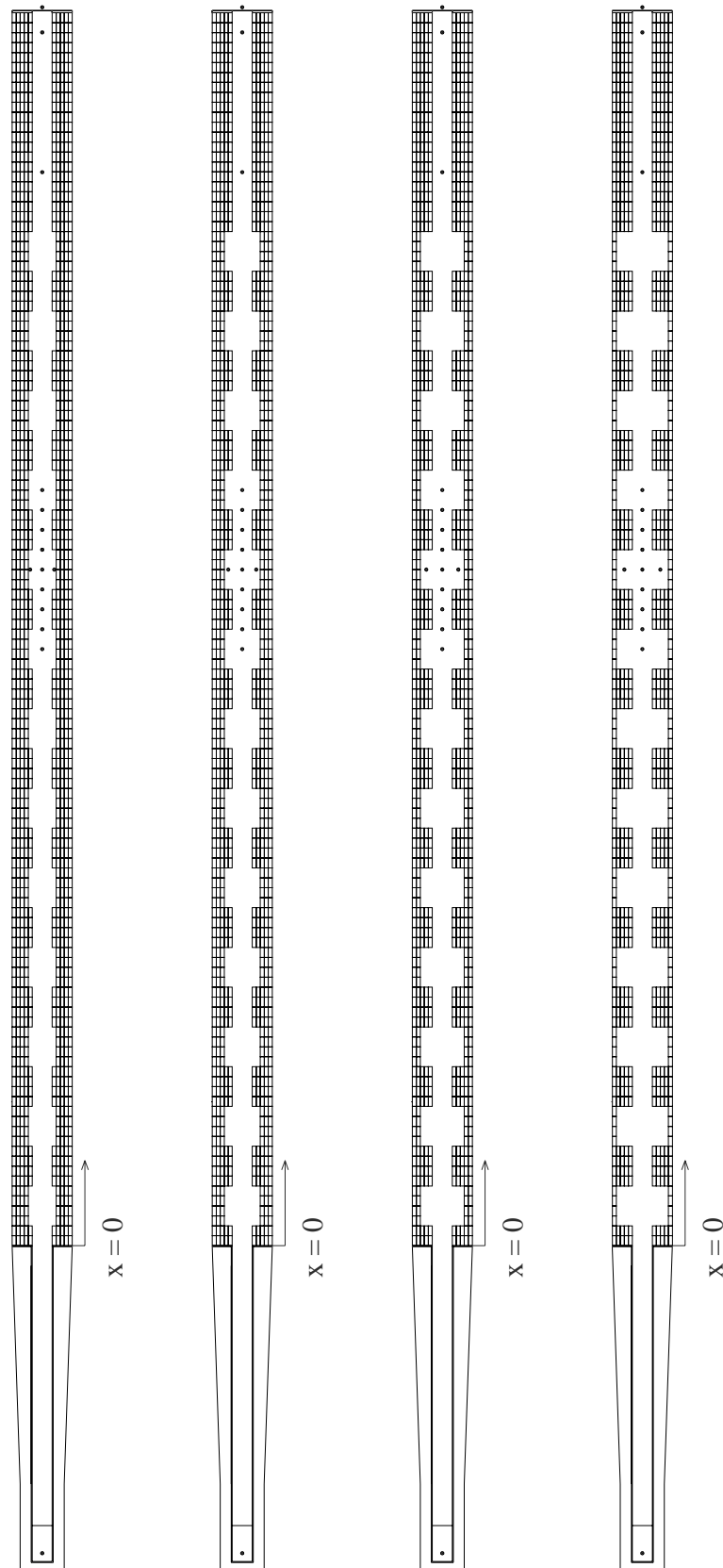


Fig-A4.16: Configurations 211, 212, 213 and 214. Flow direction from bottom to top.

Table with flow resistance parameters of the tests in configurations 211-214. f_{MR} can be calculated as $f_{MR} = f_m - f_{prism}$.

Conf.	Q	$h(x=16.92m)$	$k_{s,w}$	$K_{st,w}$	$K_{st,m}$	C_w	C_m	Re_w	Re_m	Fr	f_w	f_m	f_{prism}
[-]	[m ³ /s]	[m]	[mm]	[m ^{1/3} s ⁻¹]	[m ^{1/3} s ⁻¹]	[m ^{0.5} s ⁻¹]	[m ^{0.5} s ⁻¹]	[-]	[-]	[-]	[-]	[-]	[-]
211	0.0052	0.035	14.0	49.3	94.6	32.5	53.0	24978	9391	0.52	0.0744	0.0280	0.0200
211	0.0110	0.055	9.3	54.6	92.8	37.2	55.4	40648	18340	0.55	0.0568	0.0256	0.0174
211	0.0198	0.087	35.5	41.2	73.8	30.1	46.6	71862	29924	0.51	0.0866	0.0361	0.0158
211	0.0332	0.131	80.8	33.5	57.2	25.4	38.0	99080	44315	0.46	0.1218	0.0545	0.0147
211	0.0494	0.178	107.6	30.9	49.2	23.8	33.7	117295	58433	0.43	0.1389	0.0692	0.0140
211	0.0634	0.215	111.3	30.7	46.5	23.7	32.4	128733	69100	0.42	0.1394	0.0748	0.0136
211	0.0872	0.272	113.4	30.7	43.7	23.8	31.0	143824	84492	0.41	0.1386	0.0814	0.0132
212	0.0053	0.037	36.7	39.1	85.9	26.9	48.5	30539	9388	0.49	0.1087	0.0334	0.0200
212	0.0108	0.060	54.0	36.3	74.7	26.2	45.1	52630	17832	0.49	0.1141	0.0387	0.0175
212	0.0189	0.087	55.5	36.7	68.5	27.1	43.3	73095	28622	0.49	0.1069	0.0419	0.0159
212	0.0335	0.140	147.8	27.6	48.1	21.2	32.1	100051	43598	0.42	0.1748	0.0762	0.0147
212	0.0486	0.186	173.5	26.3	42.3	20.3	29.0	115367	56570	0.40	0.1897	0.0930	0.0141
212	0.0622	0.225	197.1	25.2	38.5	19.6	26.9	125154	66242	0.38	0.2050	0.1085	0.0137
213	0.0059	0.039	26.2	42.8	88.4	29.1	50.2	31069	10451	0.50	0.0924	0.0311	0.0195
213	0.0110	0.059	35.8	40.4	79.6	28.8	47.9	50311	18200	0.51	0.0945	0.0342	0.0174
213	0.0205	0.089	36.2	41.0	73.2	30.0	46.4	73551	30844	0.51	0.0869	0.0365	0.0157
213	0.0325	0.133	113.8	30.1	52.4	23.0	34.8	98842	43101	0.44	0.1486	0.0648	0.0148
213	0.0483	0.188	196.5	25.1	40.4	19.4	27.8	114407	55944	0.39	0.2076	0.1015	0.0141
213	0.0620	0.226	209.9	24.6	37.6	19.1	26.3	124488	65831	0.38	0.2151	0.1137	0.0137
213	0.0905	0.295	199.3	25.2	35.8	19.7	25.6	141923	83787	0.37	0.2031	0.1199	0.0132
214	0.0063	0.042	41.2	38.2	83.2	26.6	47.7	35322	11007	0.49	0.1106	0.0345	0.0193
214	0.0108	0.063	100.8	30.3	65.8	22.3	40.0	56543	17646	0.45	0.1575	0.0492	0.0175
214	0.0186	0.090	106.9	30.3	59.2	22.8	37.6	75756	27751	0.45	0.1516	0.0555	0.0160
214	0.0322	0.124	53.5	37.5	63.3	28.2	41.7	95930	43755	0.48	0.0989	0.0451	0.0147
214	0.0483	0.178	121.5	29.7	47.6	22.9	32.6	116215	57292	0.43	0.1498	0.0739	0.0140
214	0.0626	0.221	162.7	27.0	41.2	21.0	28.8	126748	67292	0.40	0.1786	0.0948	0.0137

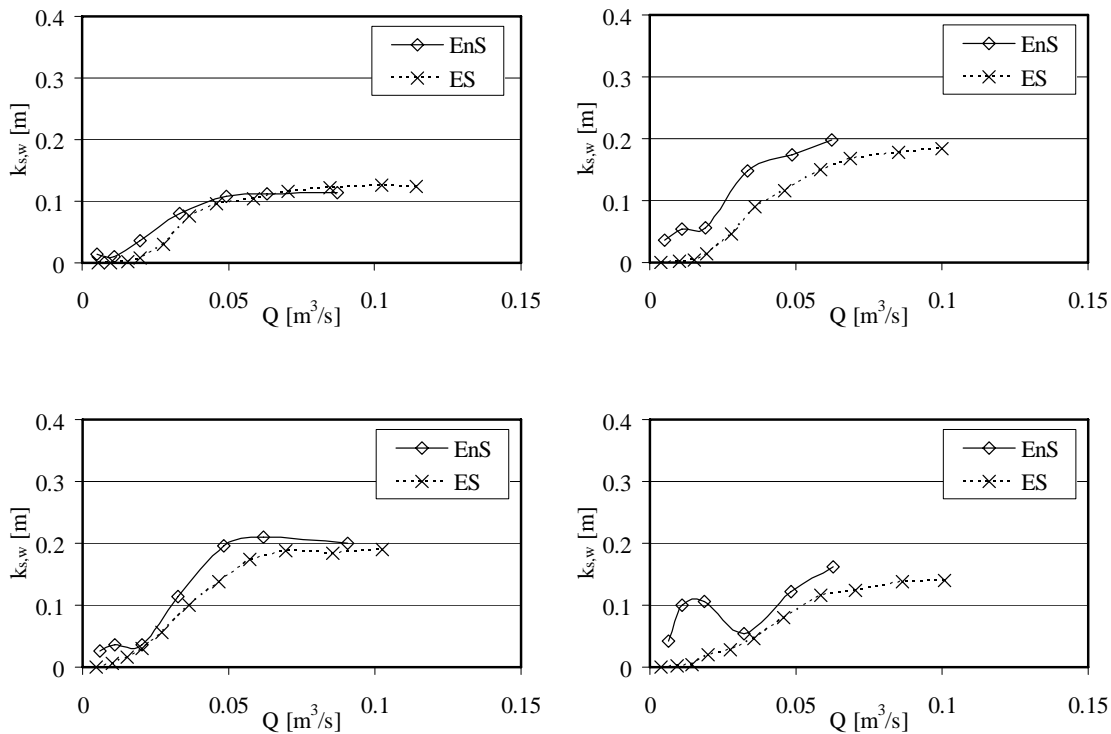


Fig-A4.17: Equivalent sand roughness of the wall $k_{s,w}$ for configurations 211 (top left), 212 (top right), 213 (bottom left) and 214 (bottom right). ES: first test series. EnS: second test series.

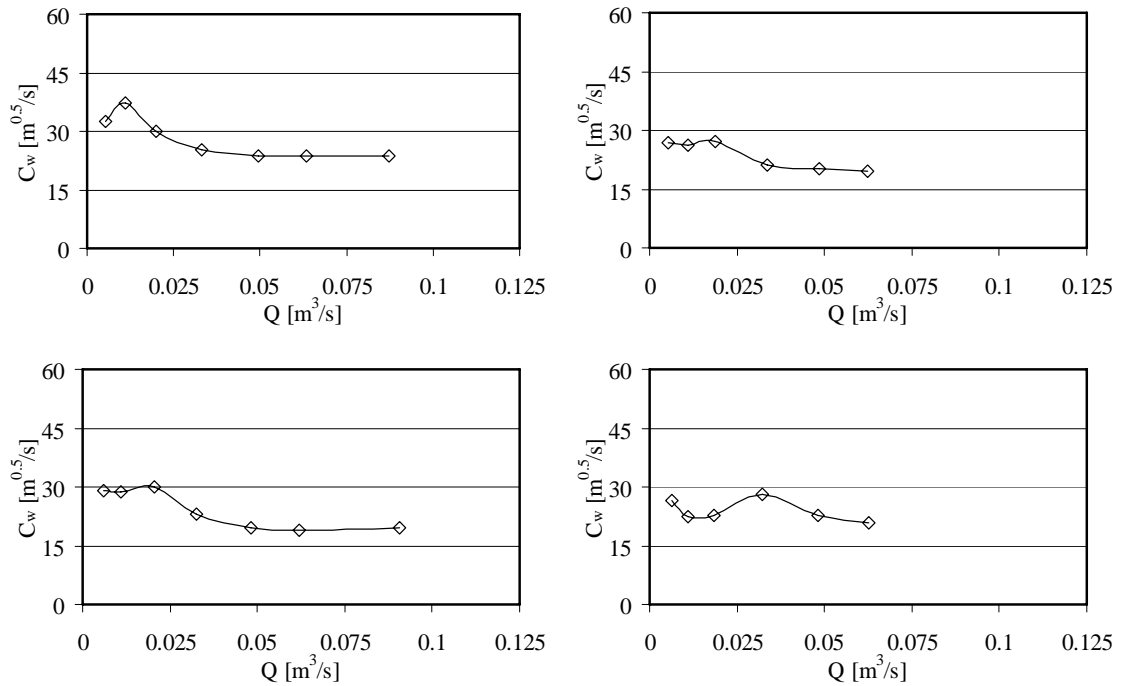


Fig-A4.18: Chezy coefficient related to the wall C_w for configurations 211 (top left), 212 (top right), 213 (bottom left) and 214 (bottom right).

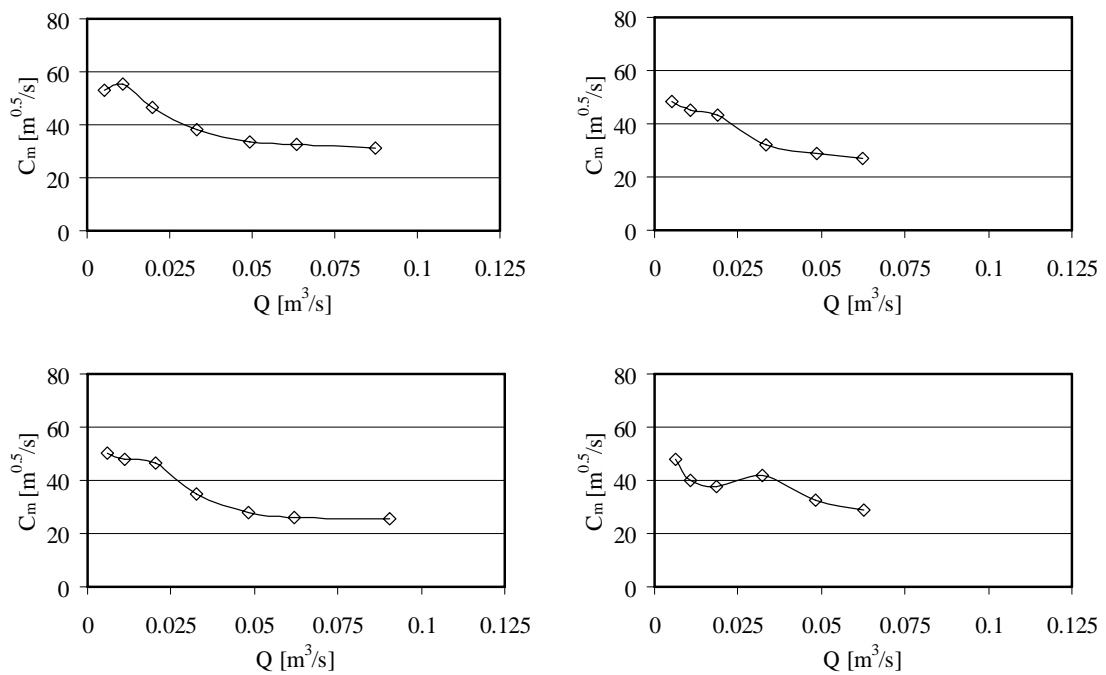


Fig-A4.19: Chezy coefficient related to the cross section C_m for configurations 211 (top left), 212 (top right), 213 (bottom left) and 214 (bottom right).

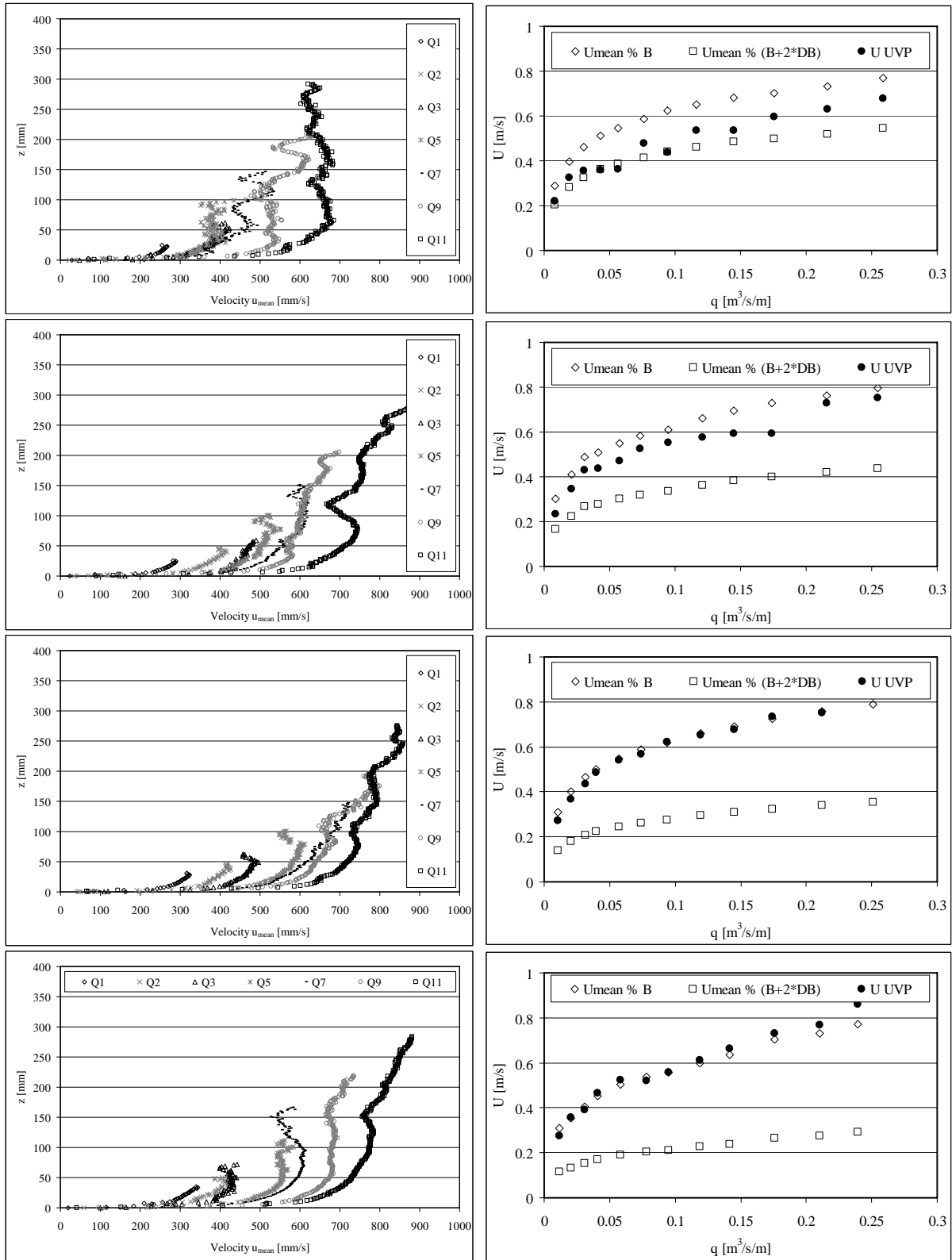


Fig-A4.20: Configurations 211 (above) to 214 (below). Left side: Vertical velocity profiles for different discharges (first test series ES). Right side: Mean velocity of the profiles measured by UVP technique and the theoretical velocities $U_{mean}^+ = Q/(Bh)$ and $U_{mean}^- = Q/((B+2\Delta B)h)$.

A 4-1: Summarized test results for the steady flow tests: 221 to 224

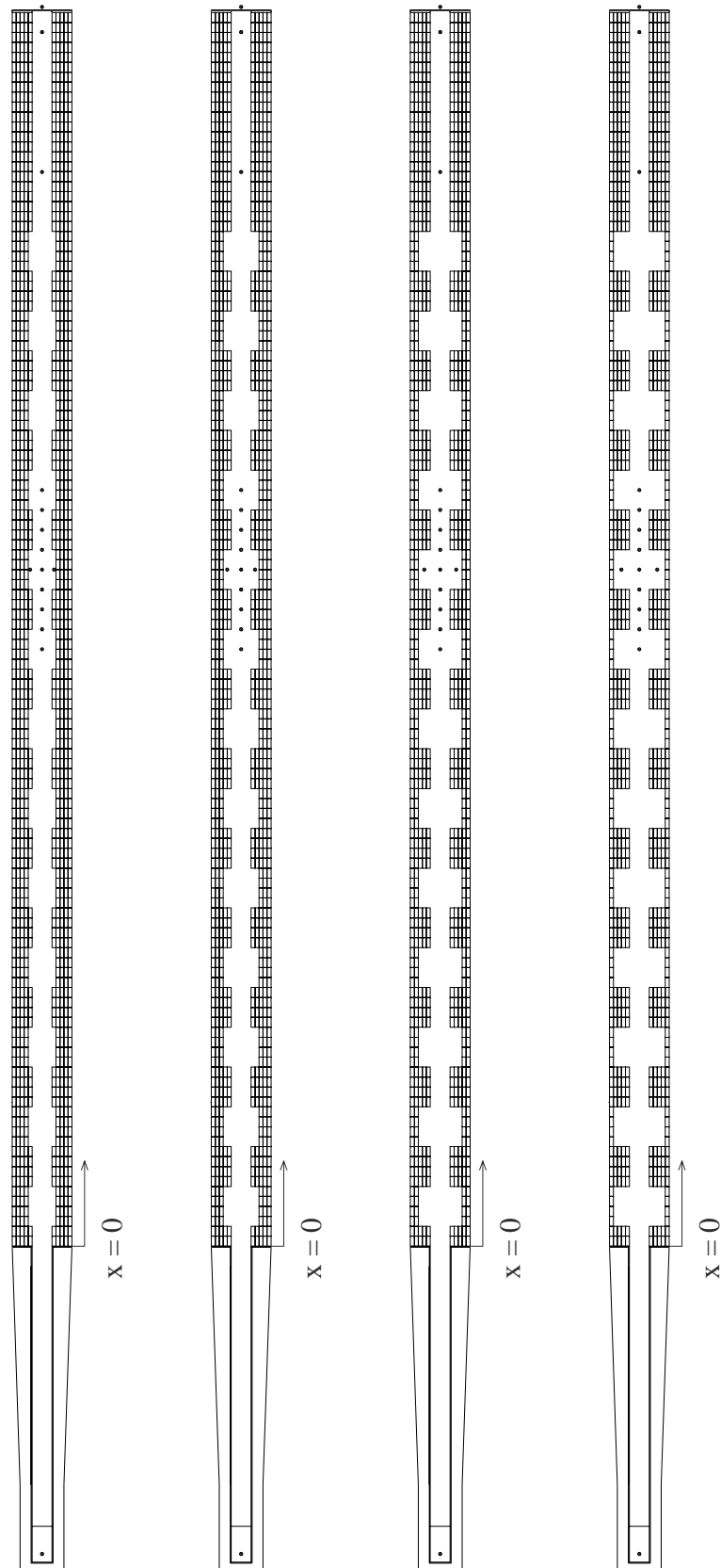


Fig-A4.21: Configurations 221, 222, 223 and 224. Flow direction from bottom to top.

Table with flow resistance parameters of the tests in configurations 221-224. f_{MR} can be calculated as $f_{MR} = f_m - f_{prism}$

Conf.	Q	$h(x=16.92m)$	$k_{s,w}$	$K_{s,w}$	$K_{s,m}$	C_w	C_m	Re_w	Re_m	Fr	f_w	f_m	f_{prism}
[-]	[m ³ /s]	[m]	[mm]	[ml/3s-1]	[ml/3s-1]	[m0.5s-1]	[m0.5s-1]	[-]	[-]	[-]	[-]	[-]	[-]
221	0.0048	0.032	2.5	68.9	104.5	42.2	57.7	16345	8738	0.55	0.0440	0.0235	0.0203
221	0.0110	0.055	7.5	56.9	94.3	38.5	56.3	39140	18347	0.56	0.0529	0.0248	0.0174
221	0.0176	0.078	19.7	47.1	81.6	33.7	50.9	62318	27327	0.53	0.0690	0.0303	0.0161
221	0.0340	0.132	61.1	36.2	60.7	27.3	40.3	97962	45196	0.47	0.1050	0.0484	0.0146
221	0.0483	0.174	81.5	33.6	53.1	25.7	36.3	114732	57780	0.44	0.1185	0.0597	0.0140
221	0.0632	0.213	88.0	33.0	49.6	25.4	34.5	127249	69143	0.42	0.1214	0.0660	0.0136
221	0.0831	0.260	86.7	33.3	47.5	25.7	33.6	140355	82327	0.41	0.1184	0.0695	0.0132
221	0.1032	0.306	89.0	33.1	45.5	25.7	32.6	151235	93751	0.40	0.1189	0.0737	0.0129
222	0.0055	0.039	52.3	35.7	81.4	24.9	46.3	33480	9708	0.47	0.1263	0.0366	0.0198
222	0.0112	0.058	17.0	48.1	87.2	33.5	52.3	45192	18528	0.53	0.0699	0.0286	0.0173
222	0.0190	0.087	52.9	37.2	68.9	27.4	43.6	72230	28610	0.48	0.1042	0.0413	0.0159
222	0.0328	0.129	62.0	36.1	60.8	27.2	40.3	96455	44011	0.47	0.1061	0.0484	0.0147
222	0.0486	0.179	109.5	30.8	48.9	23.6	33.5	114988	57375	0.42	0.1404	0.0700	0.0140
222	0.0634	0.216	101.5	31.6	47.6	24.4	33.2	127204	68875	0.42	0.1318	0.0714	0.0136
222	0.0846	0.272	125.7	29.7	42.4	23.0	30.1	140039	81910	0.39	0.1479	0.0865	0.0132
222	0.1036	0.316	128.6	29.5	40.7	23.0	29.3	149830	92396	0.38	0.1487	0.0917	0.0130
223	0.0055	0.037	15.7	48.1	93.3	32.0	52.6	26554	9841	0.51	0.0767	0.0284	0.0198
223	0.0113	0.057	12.8	51.2	89.8	35.3	53.8	43585	18776	0.54	0.0629	0.0271	0.0173
223	0.0201	0.087	26.6	44.1	76.9	32.0	48.6	69949	30401	0.52	0.0764	0.0332	0.0157
223	0.0332	0.128	53.2	37.6	62.8	28.3	41.6	96301	44575	0.47	0.0982	0.0454	0.0147
223	0.0480	0.171	73.0	34.7	54.7	26.5	37.3	114276	57729	0.45	0.1117	0.0564	0.0140
223	0.0626	0.213	94.8	32.3	48.7	24.9	33.8	126733	68510	0.42	0.1268	0.0685	0.0136
223	0.0860	0.272	108.6	31.1	44.3	24.1	31.4	141424	83276	0.40	0.1349	0.0795	0.0132
223	0.1037	0.315	122.9	30.0	41.3	23.3	29.7	150136	92651	0.39	0.1444	0.0891	0.0130
224	0.0052	0.040	112.5	28.3	71.5	20.3	40.8	36776	9141	0.42	0.1898	0.0472	0.0201
224	0.0114	0.061	40.8	39.2	77.5	28.1	46.9	52095	18725	0.49	0.0992	0.0357	0.0173
224	0.0190	0.086	41.5	39.6	72.0	29.0	45.5	70765	28790	0.50	0.0932	0.0379	0.0159
224	0.0333	0.132	71.5	34.7	58.7	26.2	38.9	97587	44286	0.46	0.1140	0.0517	0.0147
224	0.0480	0.178	112.0	30.5	48.7	23.5	33.3	114396	56820	0.42	0.1424	0.0707	0.0141
224	0.0644	0.218	100.5	31.7	47.6	24.5	33.2	127985	69650	0.42	0.1309	0.0712	0.0136
224	0.0834	0.271	133.2	29.1	41.7	22.6	29.6	139034	80934	0.39	0.1537	0.0894	0.0132
224	0.1049	0.318	125.3	29.8	41.0	23.2	29.5	150631	93214	0.39	0.1462	0.0905	0.0130

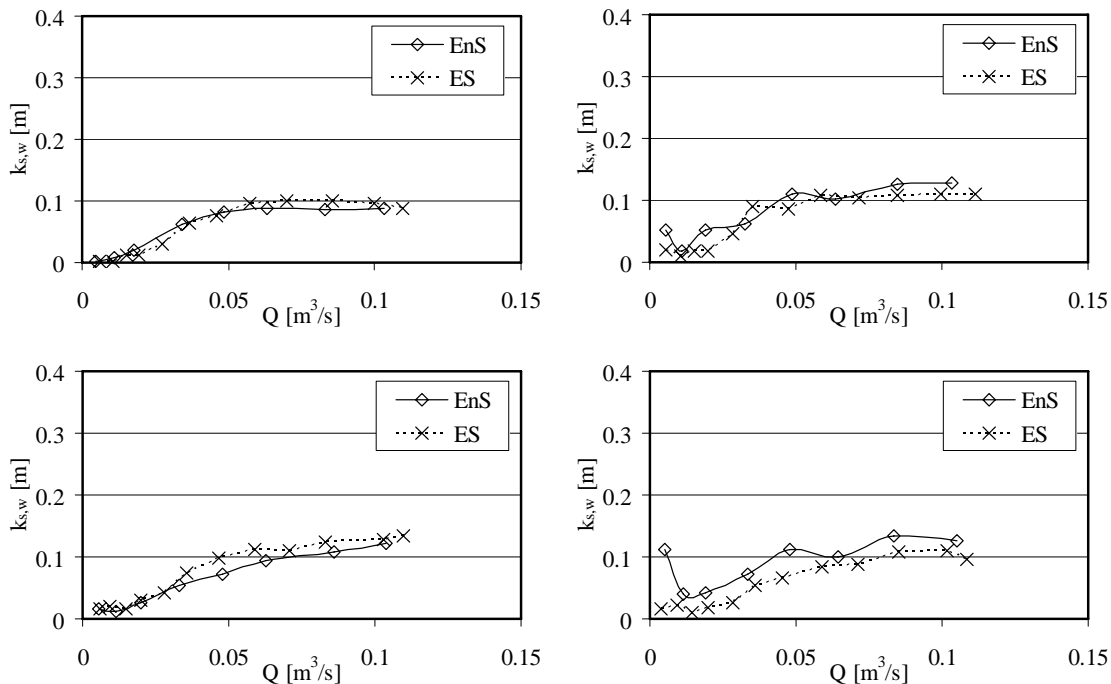


Fig-A4.22: Equivalent sand roughness of the wall $k_{s,w}$ for configurations 221 (top left), 222 (top right), 223 (bottom left) and 224 (bottom right). ES: first test series. EnS: second test series.

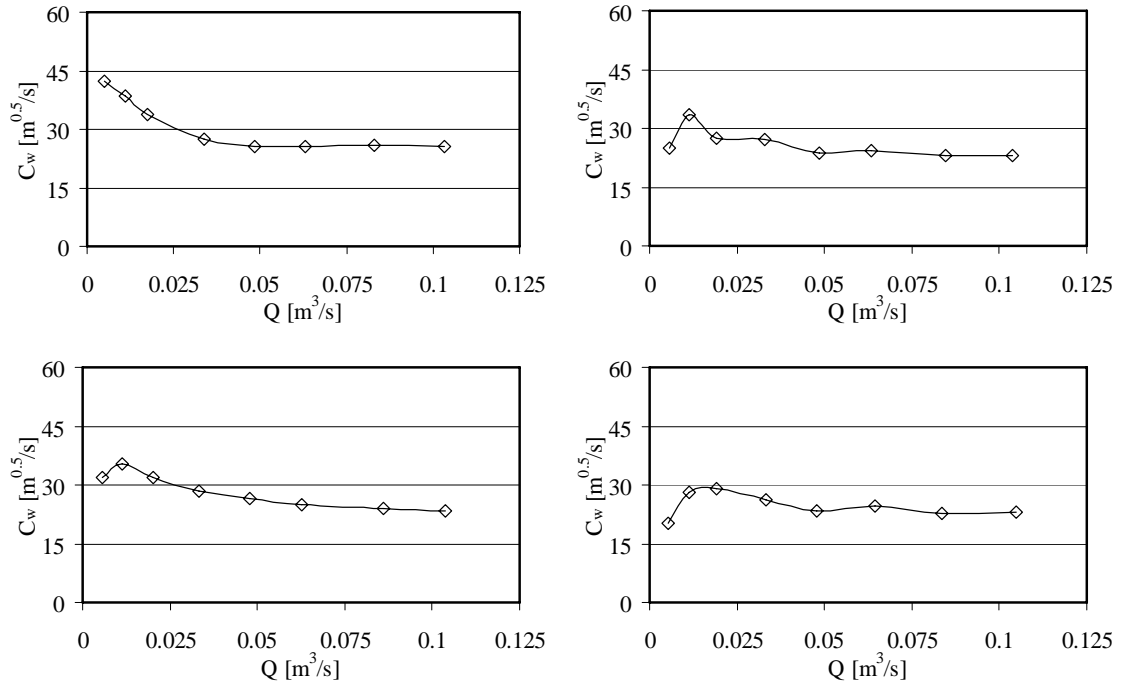


Fig-A4.23: Chezy coefficient related to the wall C_w for configurations 221 (top left), 222 (top right), 223 (bottom left) and 224 (bottom right).

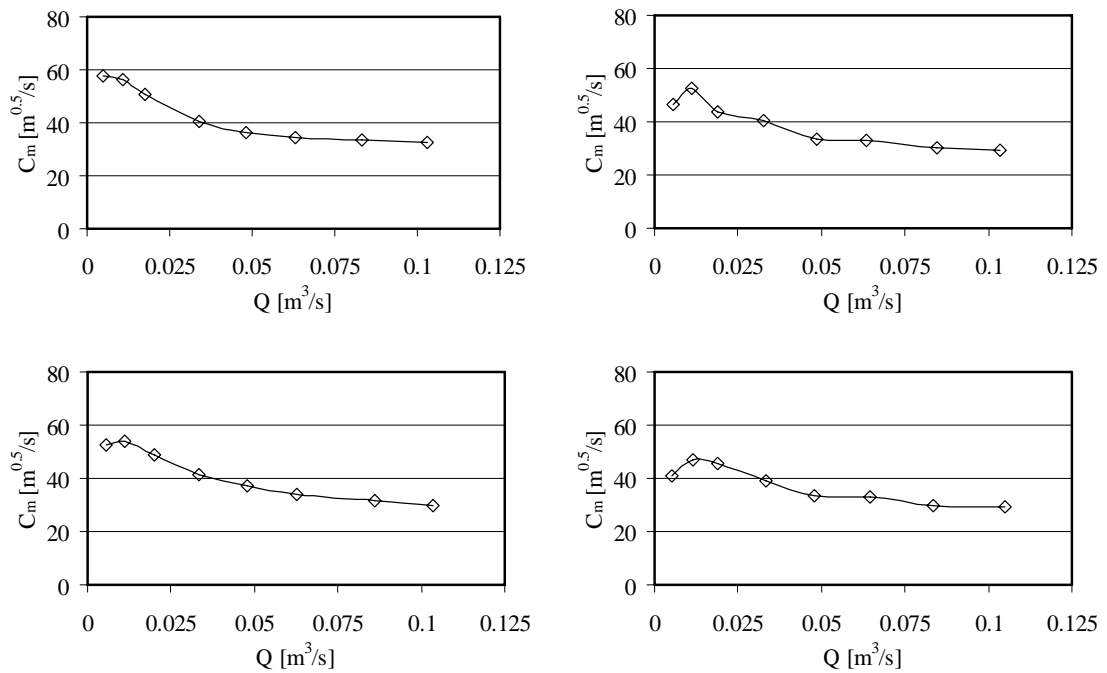


Fig-A4.24: Chezy coefficient related to the cross section C_m for configurations 221 (top left), 222 (top right), 223 (bottom left) and 224 (bottom right).

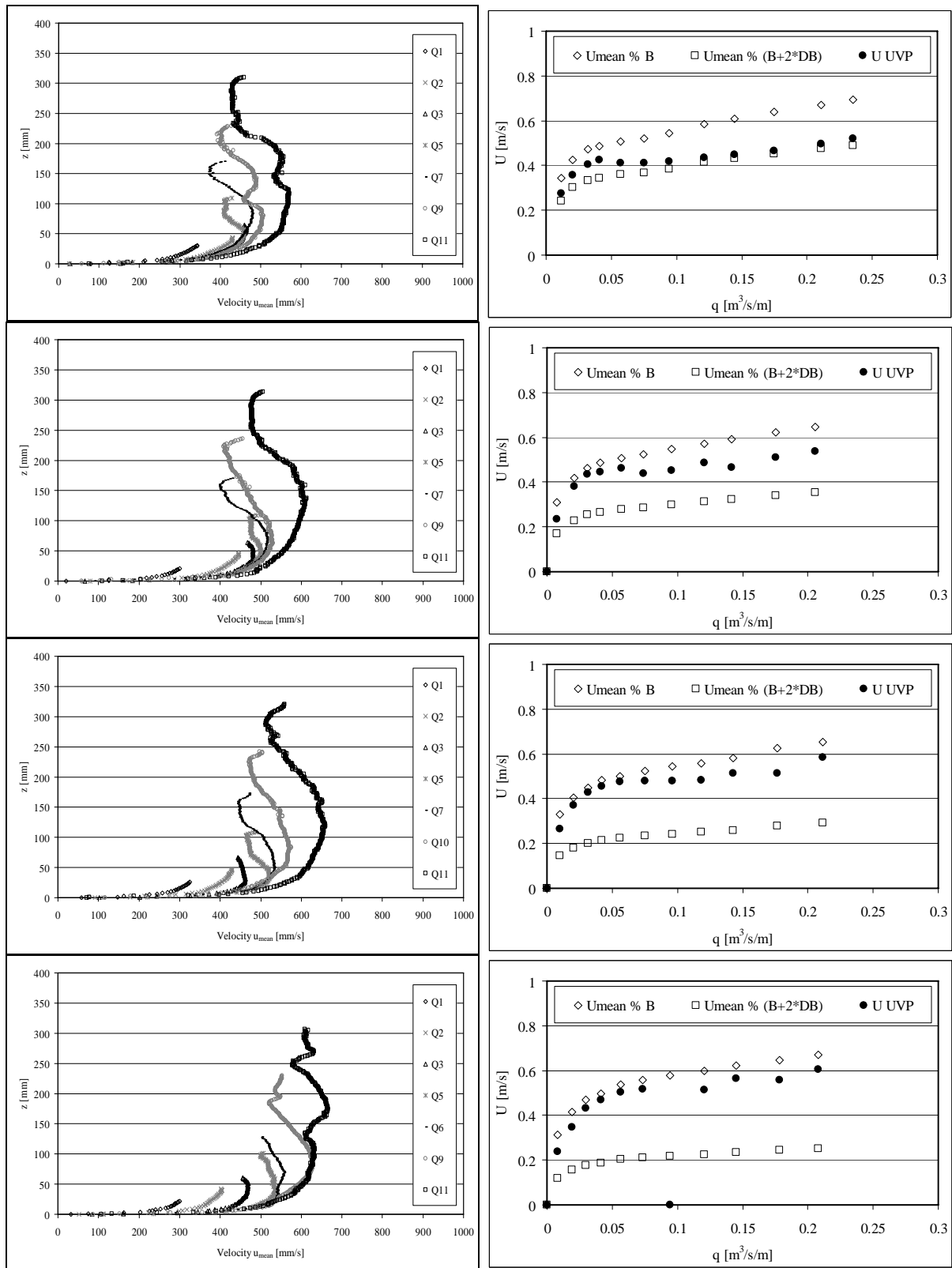


Fig-A4.25: Configurations 221 (above) to 224 (below). Left side: Vertical velocity profiles for different discharges (first test series ES). Right side: Mean velocity of the profiles measured by UVP technique and the theoretical velocities $U_{mean}^+ = Q/(Bh)$ and $U_{mean}^- = Q/((B+2\Delta B)h)$.

A 4-1: Summarized test results for the steady flow tests: 241 to 244

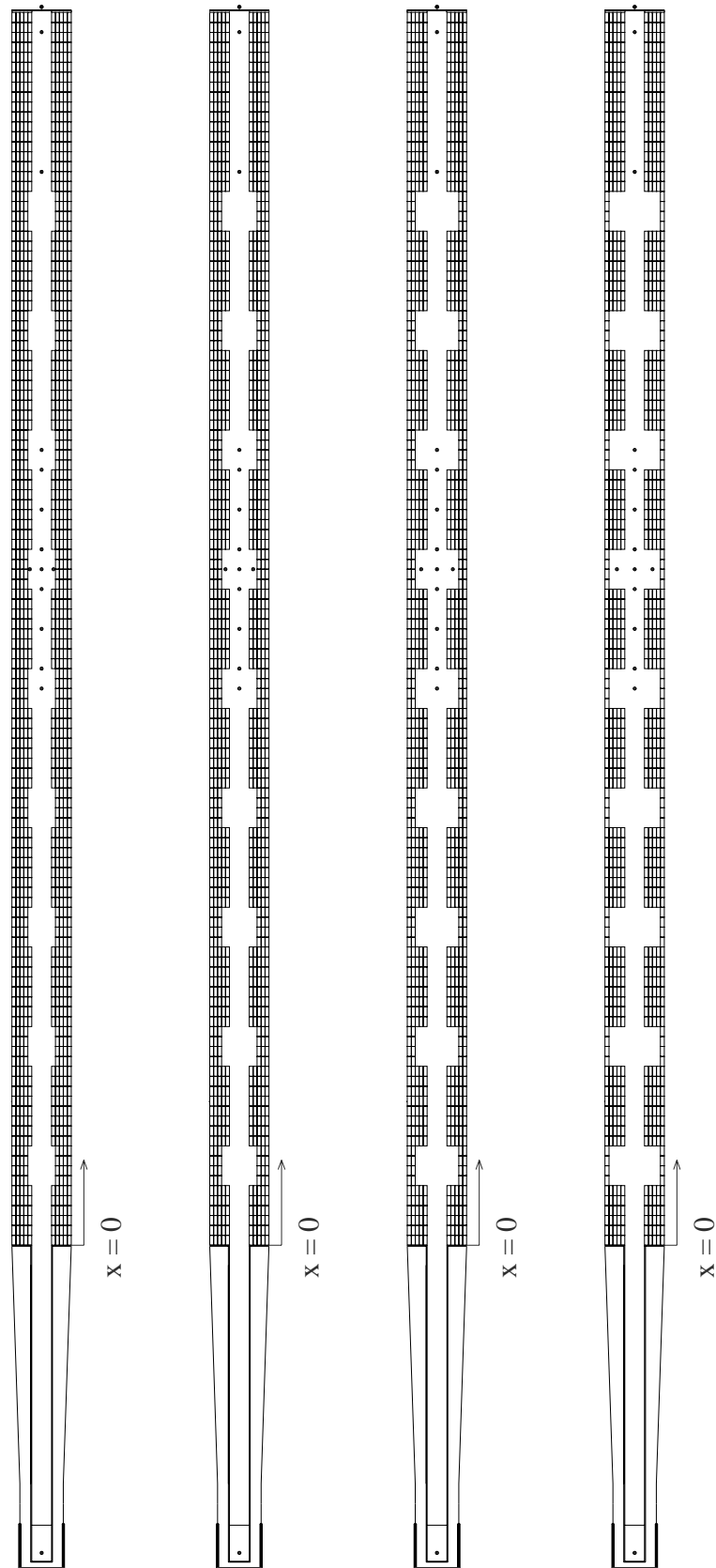


Fig-A4.26: Configurations 241, 242, 243 and 244. Flow direction from bottom to top.

Table with flow resistance parameters of the tests in configurations 241-224. f_{MR} can be calculated as $f_{MR} = f_m - f_{prism}$.

Conf.	Q	$h(x=16.92m)$	$k_{s,w}$	$K_{st,w}$	$K_{st,m}$	C_w	C_m	Re_w	Re_m	Fr	f_w	f_m	f_{prism}
[-]	[m ³ /s]	[m]	[mm]	[m ^{1/3} s ⁻¹]	[m ^{1/3} s ⁻¹]	[m0.5s ⁻¹]	[m0.5s ⁻¹]	[-]	[-]	[-]	[-]	[-]	[-]
241	0.0049	0.033	8.5	54.7	98.3	35.2	54.6	21244	8809	0.53	0.0635	0.0263	0.0203
241	0.0109	0.054	4.5	62.8	98.1	41.7	58.3	35757	18303	0.57	0.0451	0.0231	0.0174
241	0.0183	0.078	9.5	54.7	88.3	38.5	55.1	58471	28523	0.56	0.0530	0.0259	0.0159
241	0.0327	0.121	25.4	45.0	72.3	33.3	47.5	91461	44825	0.51	0.0709	0.0347	0.0147
241	0.0478	0.164	41.6	40.3	62.2	30.5	42.2	112700	58631	0.48	0.0846	0.0440	0.0140
241	0.0623	0.200	46.4	39.3	58.2	30.0	40.3	126101	70055	0.46	0.0872	0.0484	0.0136
241	0.0853	0.254	47.4	39.2	55.0	30.2	38.9	141977	85544	0.44	0.0863	0.0520	0.0131
241	0.1013	0.287	42.3	40.4	55.0	31.1	39.2	150830	95201	0.43	0.0810	0.0511	0.0129
242	0.0052	0.035	6.6	57.6	99.5	36.9	55.5	21309	9383	0.54	0.0578	0.0254	0.0200
242	0.0111	0.055	5.2	61.0	96.9	40.8	57.7	37136	18525	0.57	0.0472	0.0235	0.0173
242	0.0190	0.081	12.8	51.7	85.3	36.7	53.4	62203	29334	0.55	0.0583	0.0275	0.0158
242	0.0336	0.121	18.8	48.0	75.5	35.4	49.6	90454	45933	0.52	0.0627	0.0319	0.0146
242	0.0494	0.172	61.8	36.4	56.8	27.7	38.7	115770	59356	0.46	0.1022	0.0524	0.0139
242	0.0624	0.203	55.6	37.5	55.9	28.7	38.7	126718	69774	0.45	0.0952	0.0524	0.0136
242	0.0840	0.252	50.4	38.6	54.4	29.7	38.4	141290	84563	0.44	0.0890	0.0533	0.0132
242	0.1025	0.296	62.0	36.7	50.2	28.3	35.9	151960	94847	0.42	0.0977	0.0610	0.0129
243	0.0065	0.038	1.4	76.4	106.2	47.0	60.2	18932	11548	0.57	0.0355	0.0217	0.0191
243	0.0113	0.057	8.7	55.4	93.1	37.7	55.7	41061	18866	0.55	0.0551	0.0253	0.0173
243	0.0202	0.084	12.3	52.1	85.0	37.1	53.5	64403	30860	0.55	0.0572	0.0274	0.0157
243	0.0344	0.126	29.7	43.4	69.9	32.3	46.2	94976	46472	0.50	0.0752	0.0368	0.0146
243	0.0497	0.168	38.4	41.1	62.8	31.1	42.7	114226	60384	0.48	0.0813	0.0430	0.0139
243	0.0842	0.259	75.2	34.7	49.3	26.8	34.9	141779	83659	0.42	0.1094	0.0645	0.0132
243	0.0842	0.259	75.2	34.7	49.3	26.8	34.9	141779	83659	0.42	0.1094	0.0645	0.0132
244	0.0053	0.038	45.7	36.9	83.4	25.6	47.2	31844	9383	0.47	0.1198	0.0353	0.0200
244	0.0114	0.056	7.5	57.0	94.1	38.6	56.3	40256	18957	0.56	0.0526	0.0248	0.0172
244	0.0196	0.083	15.2	49.8	83.2	35.6	52.3	64869	30056	0.54	0.0619	0.0287	0.0158
244	0.0333	0.122	25.0	45.1	72.3	33.4	47.6	92197	45464	0.51	0.0702	0.0346	0.0146
244	0.0476	0.160	30.6	43.3	66.0	32.6	44.7	110892	58879	0.49	0.0739	0.0392	0.0140
244	0.0643	0.208	56.4	37.4	55.4	28.6	38.4	128238	71158	0.45	0.0957	0.0531	0.0135
244	0.0844	0.258	72.4	35.1	49.8	27.1	35.2	141891	83873	0.42	0.1071	0.0633	0.0132
244	0.1011	0.296	74.8	34.8	48.0	27.0	34.3	151128	93468	0.41	0.1080	0.0668	0.0129

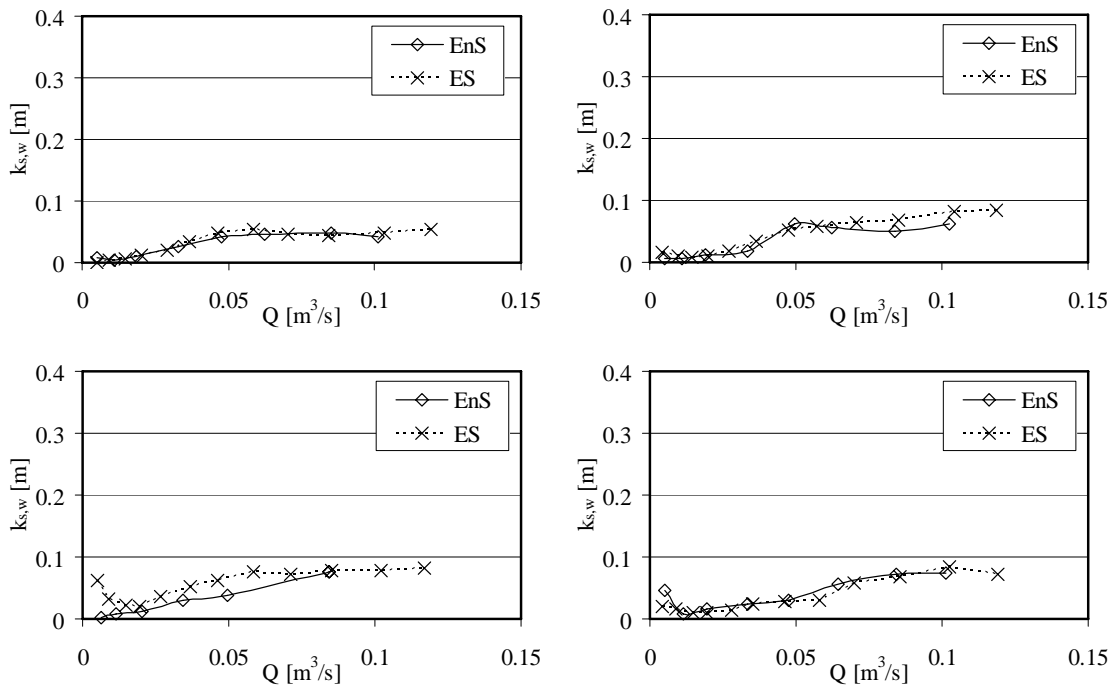


Fig-A4.27: Equivalent sand roughness of the wall $k_{s,w}$ for configurations 241 (top left), 242 (top right), 243 (bottom left) and 244 (bottom right). ES: first test series. EnS: second test series.

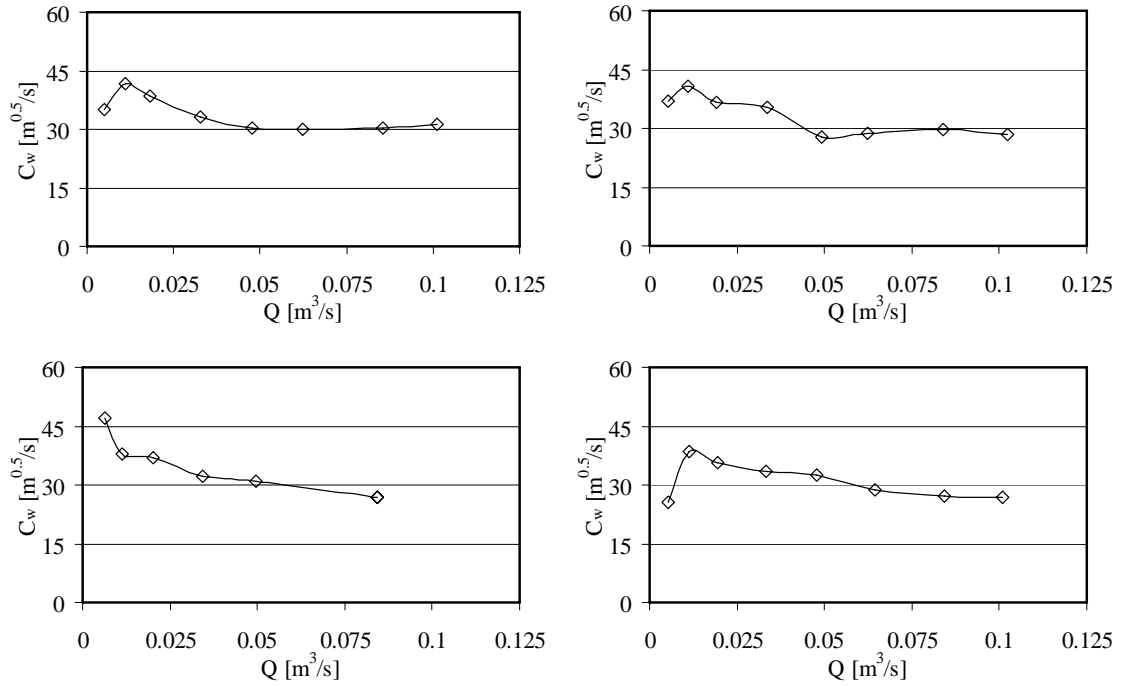


Fig-A4.28: Chezy coefficient related to the wall C_w for configurations 241 (top left), 242 (top right), 243 (bottom left) and 244 (bottom right).

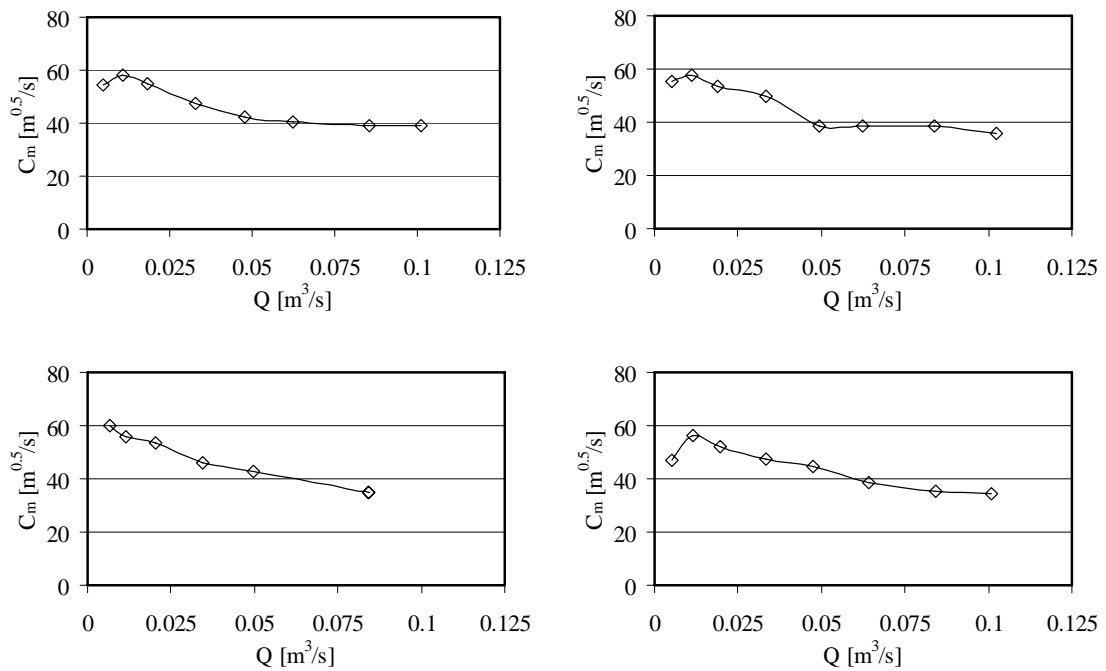


Fig-A4.29: Chezy coefficient related to the cross section C_m for configurations 241 (top left), 242 (top right), 243 (bottom left) and 244 (bottom right).

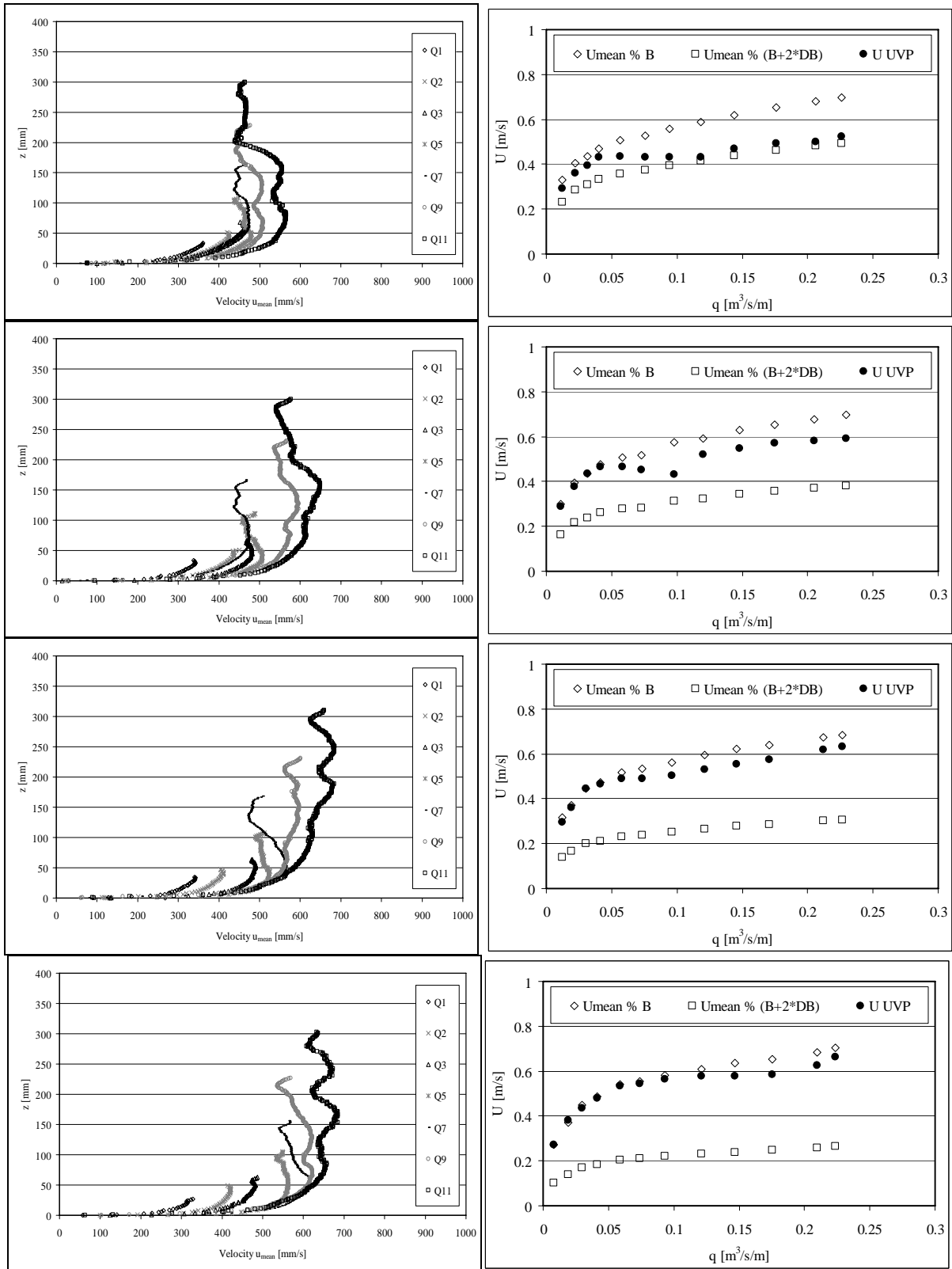


Fig-A4.30: Configurations 241 (above) to 244 (below). Left side: Vertical velocity profiles for different discharges (first test series ES). Right side: Mean velocity of the profiles measured by UVP technique and the theoretical velocities $U_{mean}^+ = Q/(Bh)$ and $U_{mean}^- = Q/((B+2\Delta B)h)$.

A 4-1: Summarized test results for the steady flow tests: 411 to 414

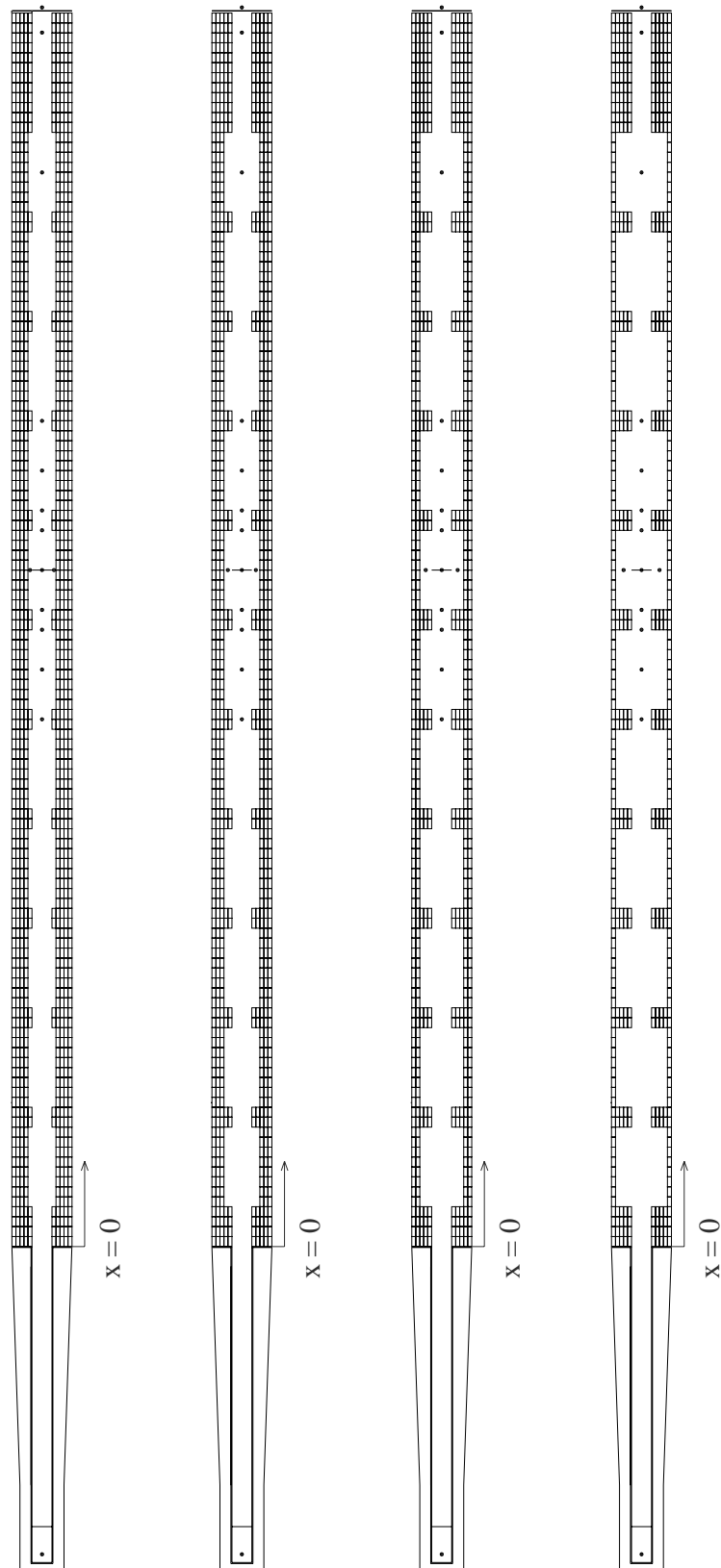


Fig-A4.31: Configurations 411, 412, 413 and 414. Flow direction from bottom to top.

Table with flow resistance parameters of the tests in configurations 411-414. f_{MR} can be calculated as $f_{MR} = f_m - f_{prism}$

Conf.	Q	h(x=16.92m)	$k_{s,w}$	$K_{s,w}$	$K_{s,m}$	C_w	C_m	Re_w	Re_m	Fr	f_w	f_m	f_{prism}
[-]	[m ³ /s]	[m]	[mm]	[ml/3s-1]	[ml/3s-1]	[m0.5s-1]	[m0.5s-1]	[-]	[-]	[-]	[-]	[-]	[-]
411	0.0063	0.036	0.0	114.0	113.9	64.1	64.0	11268	11287	0.60	0.0191	0.0191	0.0192
411	0.0111	0.054	3.4	65.9	99.8	43.5	59.3	34780	18659	0.58	0.0415	0.0223	0.0173
411	0.0200	0.082	11.8	52.5	85.8	37.3	53.9	64052	30684	0.56	0.0564	0.0270	0.0157
411	0.0337	0.123	33.2	42.3	69.1	31.5	45.5	95909	45895	0.51	0.0792	0.0379	0.0146
411	0.0493	0.165	41.5	40.3	62.2	30.5	42.2	115768	60311	0.49	0.0844	0.0440	0.0139
411	0.0627	0.199	50.1	38.6	57.4	29.4	39.7	128481	70713	0.47	0.0905	0.0498	0.0135
411	0.0851	0.249	44.2	39.9	56.1	30.6	39.5	143519	86212	0.45	0.0836	0.0502	0.0131
411	0.1047	0.291	42.8	40.3	54.7	31.1	39.1	154561	97807	0.44	0.0813	0.0515	0.0129
412	0.0063	0.039	7.3	56.7	98.1	36.9	55.6	25284	11094	0.55	0.0578	0.0253	0.0193
412	0.0109	0.056	15.6	49.0	88.6	34.0	52.9	44180	18208	0.54	0.0680	0.0280	0.0174
412	0.0192	0.085	41.9	39.4	72.2	28.9	45.6	72396	29210	0.51	0.0937	0.0378	0.0159
412	0.0315	0.120	50.9	37.9	64.4	28.5	42.3	95452	43187	0.50	0.0969	0.0439	0.0147
412	0.0476	0.173	123.4	29.6	47.8	22.8	32.6	116979	56963	0.43	0.1516	0.0738	0.0140
412	0.0621	0.212	133.3	29.0	44.3	22.4	30.8	128922	68041	0.42	0.1565	0.0826	0.0136
412	0.0858	0.269	134.1	29.0	41.7	22.6	29.6	144065	83551	0.41	0.1543	0.0895	0.0132
412	0.1025	0.307	139.6	28.7	40.0	22.3	28.7	152680	92851	0.40	0.1572	0.0956	0.0130
413	0.0061	0.040	23.4	44.0	89.3	29.9	50.8	31331	10823	0.51	0.0879	0.0304	0.0194
413	0.0111	0.057	17.4	47.9	87.4	33.3	52.3	45400	18397	0.54	0.0708	0.0287	0.0174
413	0.0197	0.086	38.2	40.4	73.2	29.6	46.2	72702	29830	0.52	0.0897	0.0368	0.0158
413	0.0328	0.131	101.3	31.3	54.3	23.8	36.0	100260	43786	0.46	0.1387	0.0606	0.0147
413	0.0483	0.179	151.9	27.6	44.6	21.3	30.5	117302	57093	0.42	0.1733	0.0843	0.0140
413	0.0626	0.216	153.4	27.6	42.2	21.4	29.4	128824	67990	0.41	0.1717	0.0906	0.0136
413	0.0861	0.275	163.4	27.1	39.0	21.1	27.7	143219	82952	0.39	0.1763	0.1021	0.0132
413	0.0983	0.304	171.4	26.7	37.5	20.8	26.8	149267	89615	0.39	0.1813	0.1089	0.0130
414	0.0057	0.040	68.1	33.1	78.3	23.4	44.6	36197	9963	0.47	0.1434	0.0395	0.0197
414	0.0106	0.058	46.2	37.8	77.2	27.1	46.3	51067	17512	0.50	0.1067	0.0366	0.0175
414	0.0195	0.086	45.5	38.7	71.0	28.4	44.9	73680	29586	0.51	0.0970	0.0390	0.0158
414	0.0330	0.131	97.7	31.6	54.8	24.0	36.3	100390	43997	0.46	0.1358	0.0595	0.0147
414	0.0488	0.173	96.6	32.0	51.0	24.5	34.8	118169	58542	0.45	0.1306	0.0647	0.0140
414	0.0644	0.219	141.2	28.4	43.2	22.0	30.1	130411	69510	0.41	0.1621	0.0864	0.0136
414	0.0861	0.275	166.7	26.9	38.7	20.9	27.5	143077	82851	0.39	0.1788	0.1036	0.0132
414	0.0990	0.306	172.9	26.6	37.3	20.7	26.7	149537	89935	0.39	0.1824	0.1097	0.0130

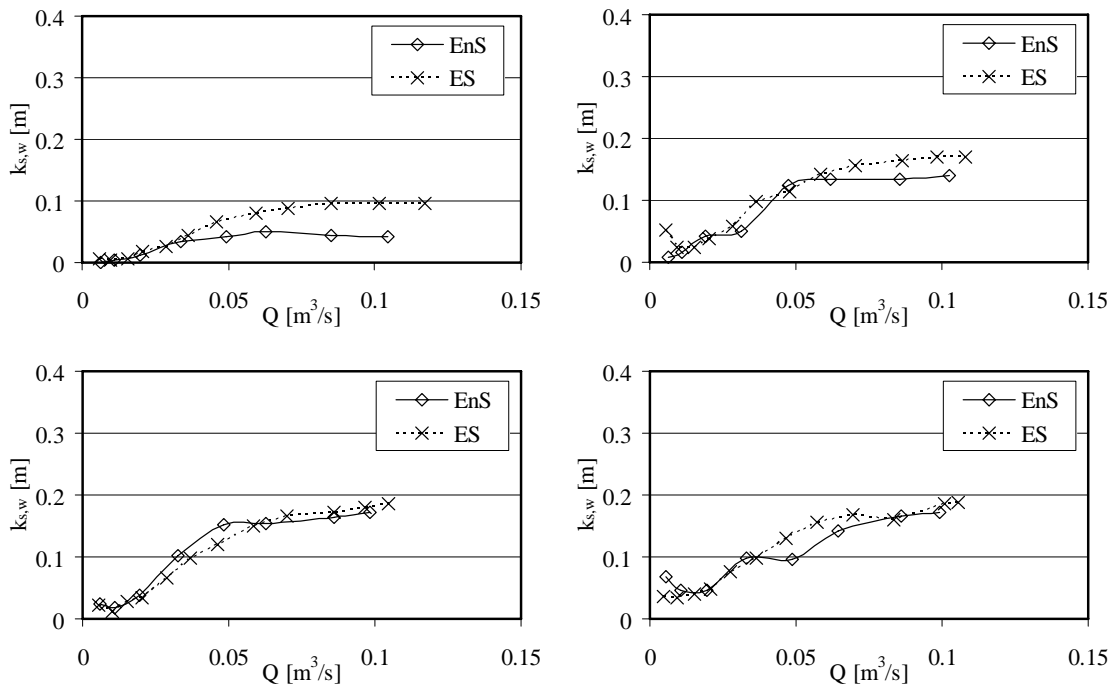


Fig-A4.32: Equivalent sand roughness of the wall $k_{s,w}$ for configurations 411 (top left), 412 (top right), 413 (bottom left) and 414 (bottom right). ES: first test series. EnS: second test series.

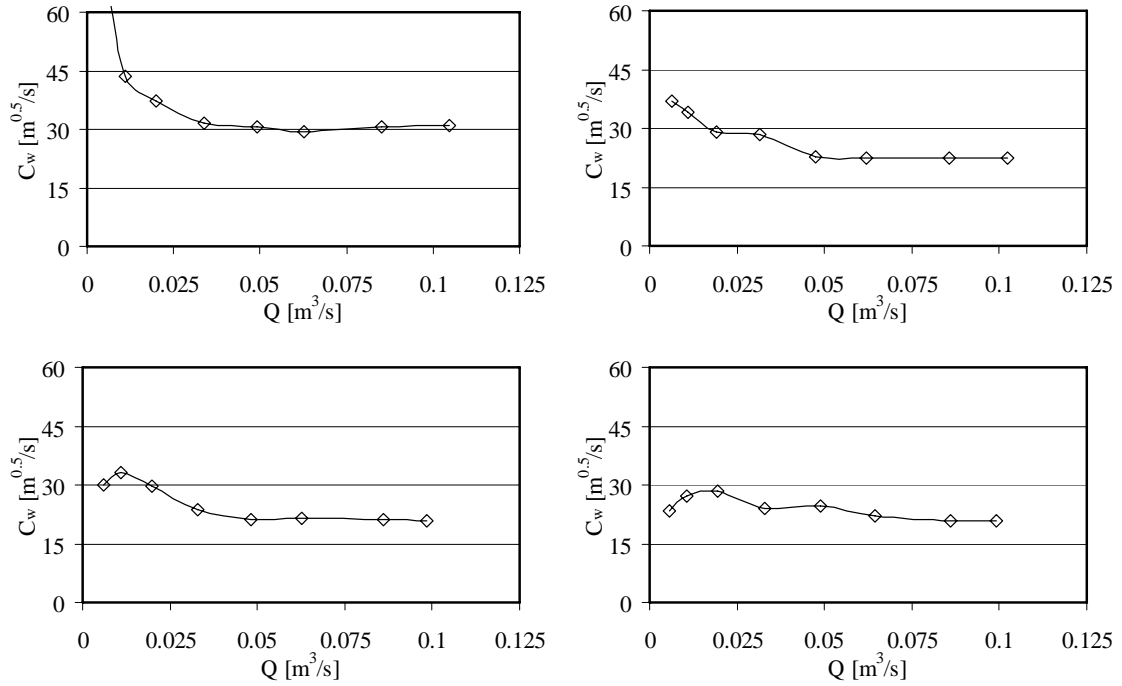


Fig-A4.33: Chezy coefficient related to the wall C_w for configurations 411 (top left), 412 (top right), 413 (bottom left) and 414 (bottom right).

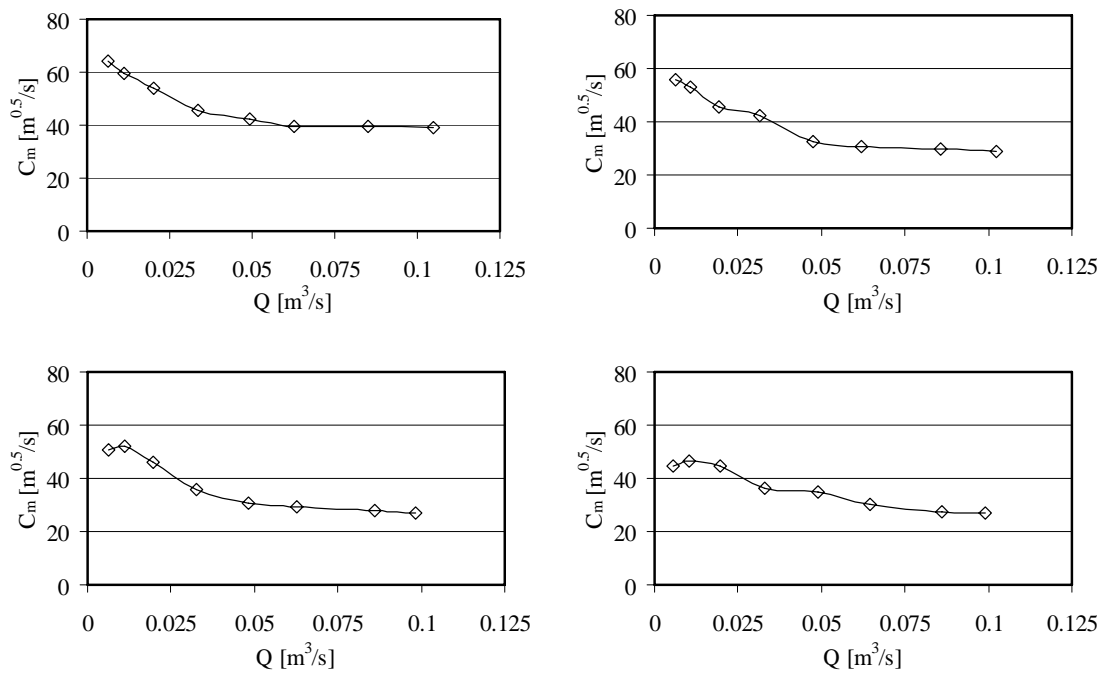


Fig-A4.34: Chezy coefficient related to the cross section C_m for configurations 411 (top left), 412 (top right), 413 (bottom left) and 414 (bottom right).

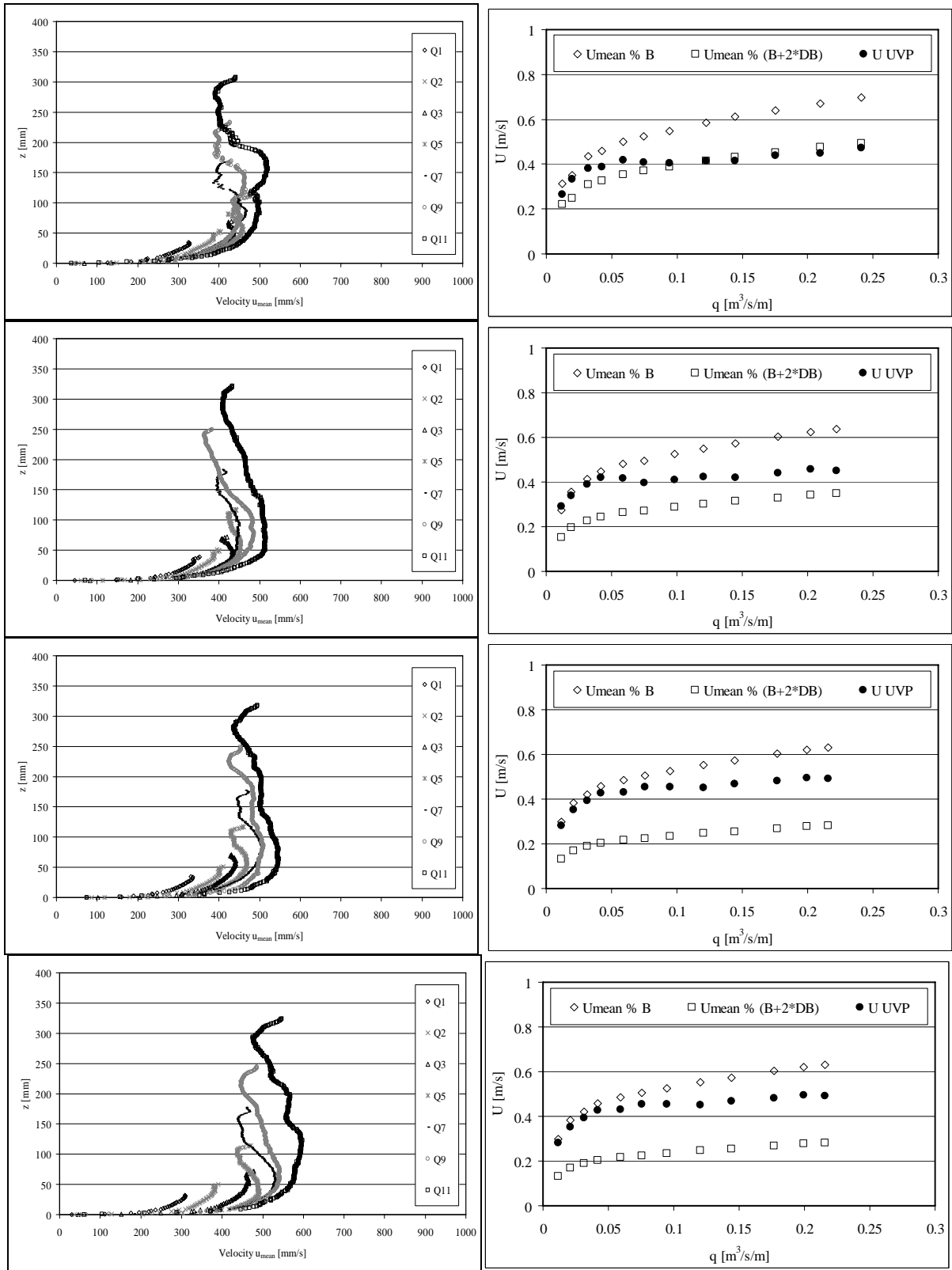


Fig-A4.35: Configurations 411 (above) to 414 (below). Left side: Vertical velocity profiles for different discharges (first test series ES). Right side: Mean velocity of the profiles measured by UVP technique and the theoretical velocities $U_{mean}^+ = Q/(Bh)$ and $U_{mean}^- = Q/((B+2\Delta B)h)$.

A 4-1: Summarized test results for the steady flow tests: 421 to 424

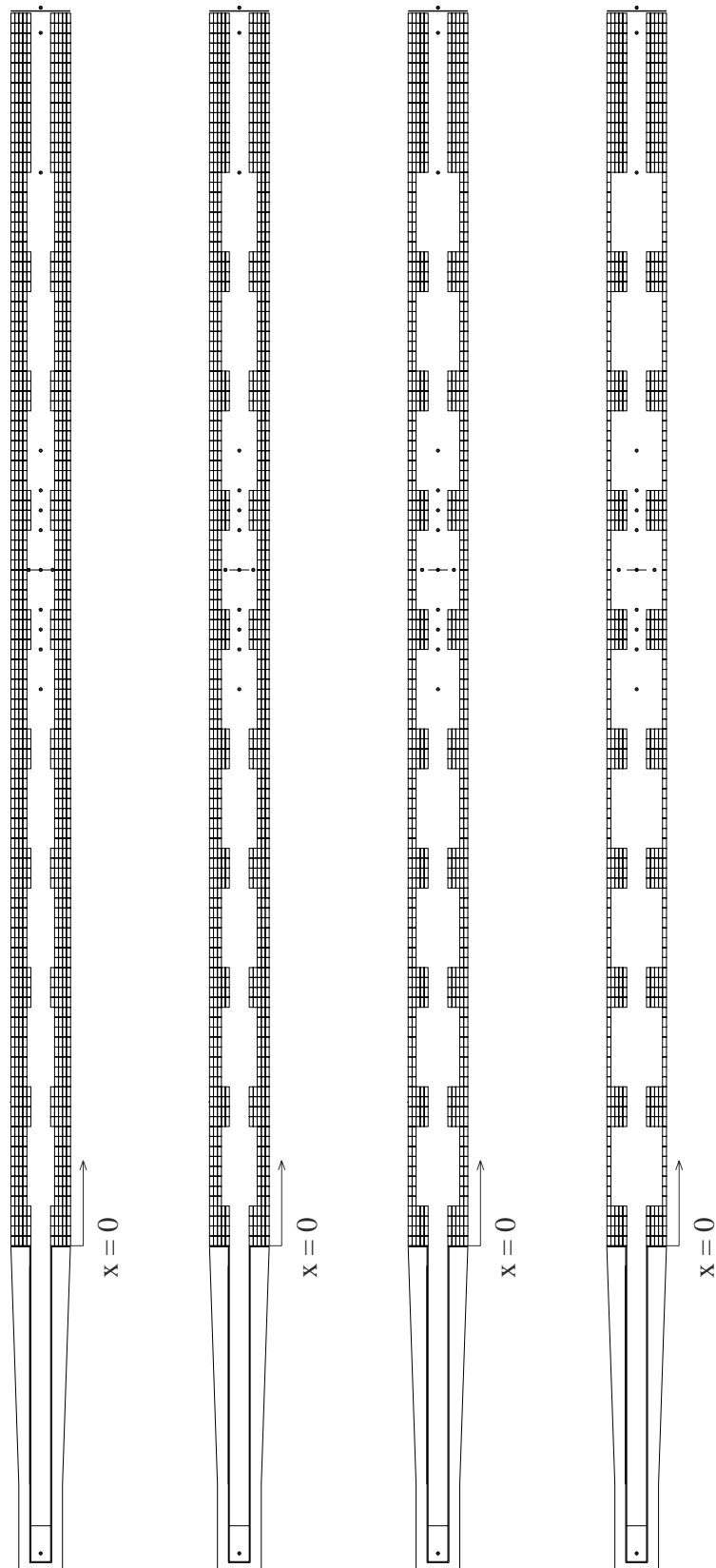


Fig-A4.36: Configurations 421, 422, 423 and 424. Flow direction from bottom to top.

Table with flow resistance parameters of the tests in configurations 421-424. f_{MR} can be calculated as $f_{MR} = f_m - f_{prism}$.

Conf.	Q	$h(x=16.92m)$	$k_{s,w}$	$K_{st,w}$	$K_{st,m}$	C_w	C_m	Re_w	Re_m	Fr	f_w	f_m	f_{prism}
[-]	[m ³ /s]	[m]	[mm]	[m ¹ /3s ⁻¹]	[m ¹ /3s ⁻¹]	[m0.5s ⁻¹]	[m0.5s ⁻¹]	[-]	[-]	[-]	[-]	[-]	[-]
421	0.0055	0.033	0.0	113.8	113.7	63.2	63.1	9859	9875	0.59	0.0197	0.0197	0.0198
421	0.0107	0.052	2.1	71.4	102.6	46.3	60.7	31045	18019	0.59	0.0367	0.0213	0.0174
421	0.0194	0.081	9.6	54.7	87.8	38.6	55.0	60792	29931	0.56	0.0527	0.0259	0.0158
421	0.0328	0.122	30.7	43.1	70.0	32.0	46.1	92879	44757	0.50	0.0766	0.0369	0.0147
421	0.0506	0.166	24.7	45.5	67.9	34.2	46.2	112578	61675	0.49	0.0672	0.0368	0.0139
421	0.0624	0.199	38.7	41.1	60.4	31.3	41.8	125476	70436	0.46	0.0801	0.0450	0.0136
421	0.0853	0.251	36.8	41.8	58.1	32.0	41.0	141244	86103	0.45	0.0766	0.0467	0.0131
421	0.1055	0.294	34.5	42.5	57.0	32.7	40.7	152548	98030	0.44	0.0736	0.0473	0.0128
422	0.0059	0.036	2.0	71.6	104.9	44.2	58.9	18587	10475	0.56	0.0401	0.0226	0.0195
422	0.0109	0.055	9.7	54.2	92.5	36.9	55.2	40601	18206	0.55	0.0575	0.0258	0.0174
422	0.0193	0.085	28.4	43.4	76.6	31.5	48.3	68913	29375	0.52	0.0790	0.0337	0.0158
422	0.0330	0.131	80.3	33.5	57.2	25.4	38.0	98031	43955	0.46	0.1214	0.0544	0.0147
422	0.0491	0.175	83.0	33.5	52.8	25.6	36.1	116073	58566	0.44	0.1196	0.0603	0.0140
422	0.0633	0.213	95.9	32.2	48.5	24.8	33.7	127854	69156	0.42	0.1275	0.0690	0.0136
422	0.0946	0.288	101.3	31.8	44.5	24.7	31.8	147097	88792	0.40	0.1288	0.0778	0.0131
423	0.0057	0.038	17.3	47.1	92.3	31.5	52.2	27801	10132	0.51	0.0791	0.0288	0.0197
423	0.0113	0.056	8.1	56.1	93.5	38.1	56.0	40677	18888	0.56	0.0540	0.0251	0.0173
423	0.0191	0.083	21.3	46.3	80.0	33.4	50.3	66268	29212	0.53	0.0705	0.0311	0.0159
423	0.0323	0.127	64.9	35.6	60.4	26.9	40.0	96379	43545	0.47	0.1088	0.0491	0.0147
423	0.0500	0.176	75.8	34.4	53.9	26.3	36.8	116801	59491	0.45	0.1137	0.0579	0.0139
423	0.0629	0.216	116.4	30.3	45.8	23.4	31.9	127217	68332	0.41	0.1433	0.0770	0.0136
423	0.0858	0.272	119.4	30.2	43.1	23.4	30.6	141672	83064	0.40	0.1432	0.0839	0.0132
423	0.1044	0.316	127.3	29.6	40.9	23.0	29.3	151045	93147	0.39	0.1478	0.0911	0.0130
424	0.0062	0.040	18.2	46.7	91.3	31.5	52.0	30053	11002	0.51	0.0792	0.0290	0.0193
424	0.0111	0.057	16.6	48.4	87.6	33.6	52.5	44888	18439	0.53	0.0693	0.0285	0.0173
424	0.0189	0.082	22.4	45.8	79.5	33.0	50.0	66320	29003	0.53	0.0719	0.0314	0.0159
424	0.0334	0.129	59.7	36.4	61.3	27.5	40.6	97428	44680	0.47	0.1039	0.0477	0.0147
424	0.0481	0.177	108.3	30.9	49.2	23.7	33.7	115145	57141	0.43	0.1396	0.0693	0.0140
424	0.0619	0.210	95.4	32.2	48.7	24.8	33.9	126786	68131	0.42	0.1274	0.0684	0.0136
424	0.0933	0.290	122.3	30.0	42.1	23.3	30.1	145653	87306	0.39	0.1447	0.0868	0.0131

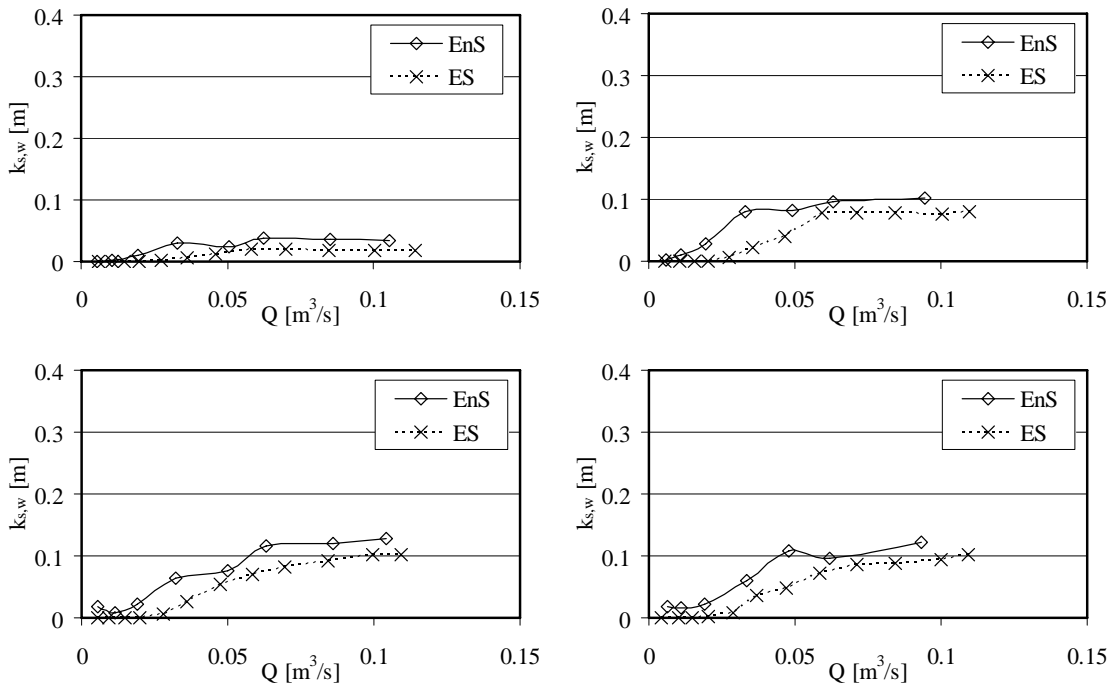


Fig-A4.37: Equivalent sand roughness of the wall $k_{s,w}$ for configurations 421 (top left), 422 (top right), 423 (bottom left) and 424 (bottom right). ES: first test series. EnS: second test series.

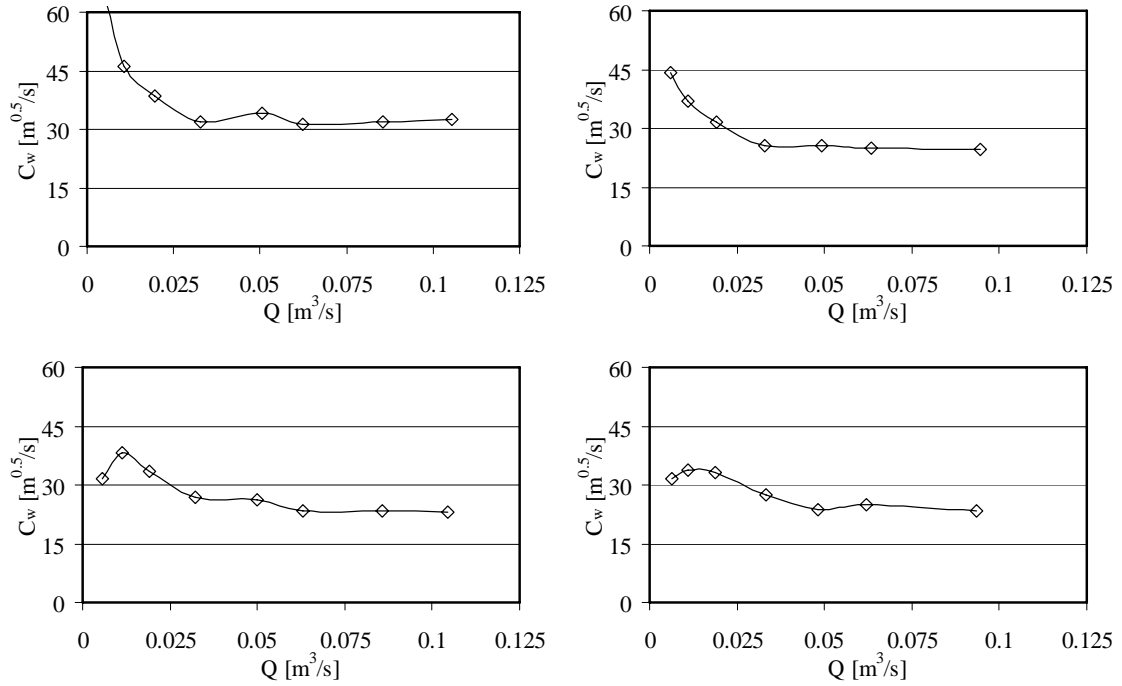


Fig-A4.38: Chezy coefficient related to the wall C_w for configurations 421 (top left), 422 (top right), 424 (bottom left) and 424 (bottom right).

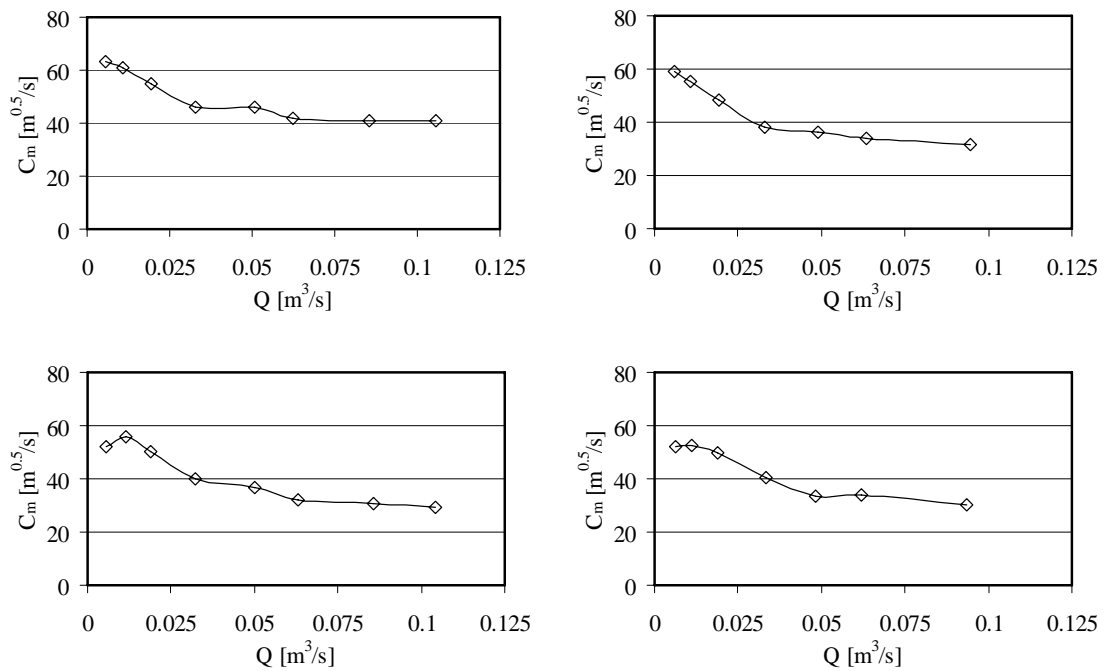


Fig-A4.39: Chezy coefficient related to the cross section C_m for configurations 421 (top left), 422 (top right), 423 (bottom left) and 424 (bottom right).

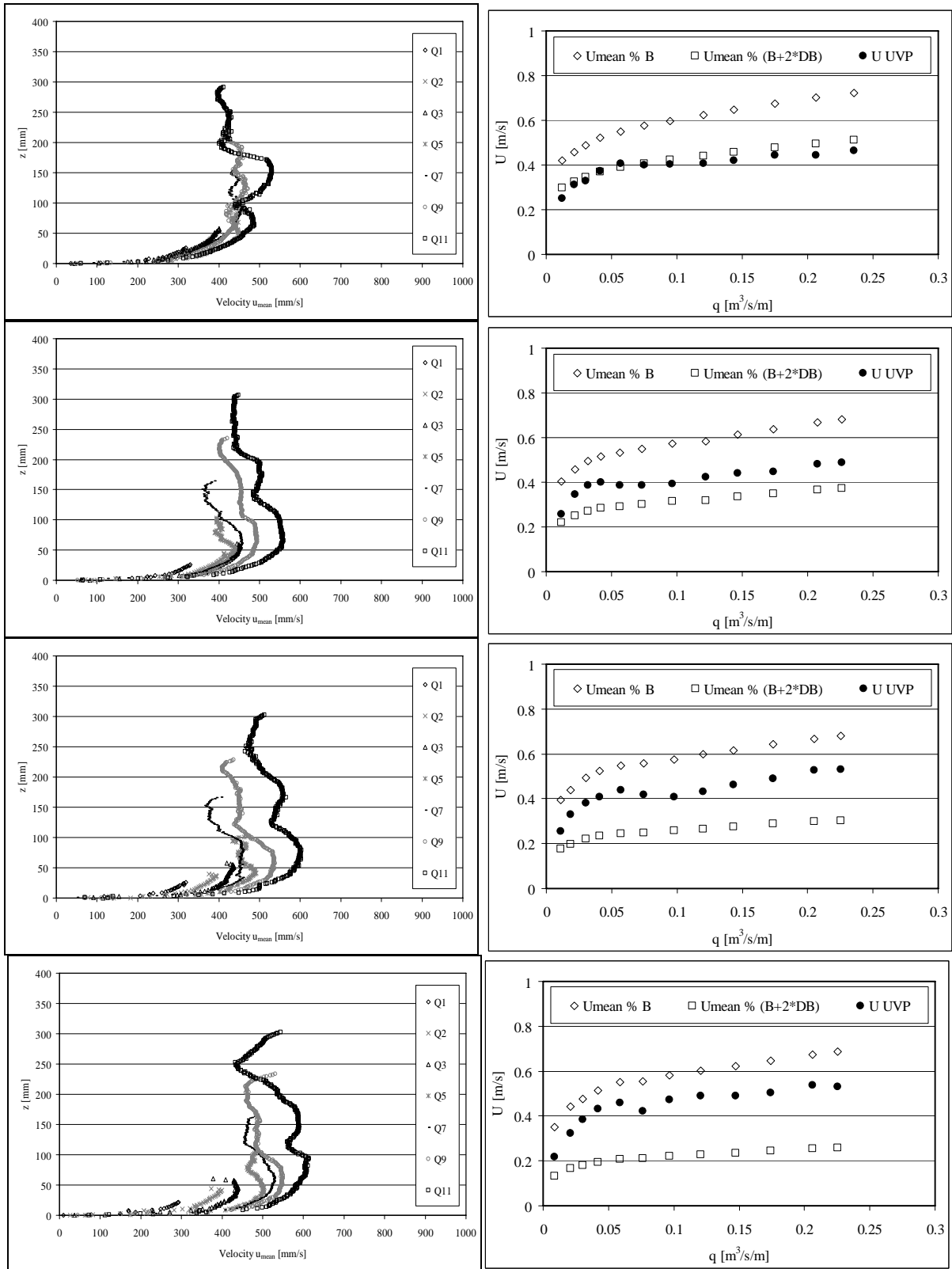


Fig-A4.40: Configurations 421 (above) to 424 (below). Left side: Vertical velocity profiles for different discharges (first test series ES). Right side: Mean velocity of the profiles measured by UVP technique and the theoretical velocities $U_{mean}^+ = Q/(Bh)$ and $U_{mean}^- = Q/((B+2\Delta B)h)$.

A 4-1: Summarized test results for the steady flow tests: 441 to 444

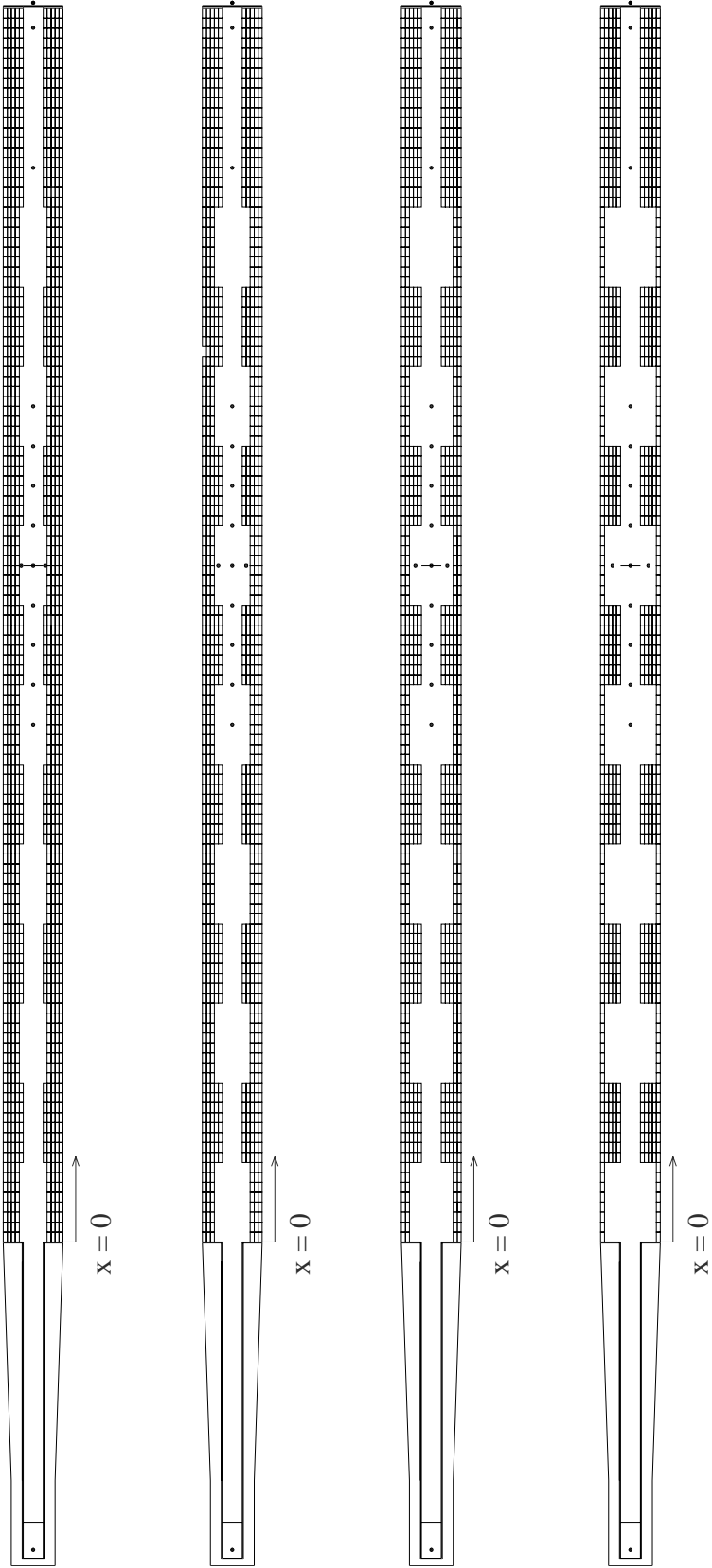


Fig-A4.41: Configurations 441, 442, 443 and 444. Flow direction from bottom to top.

Table with flow resistance parameters of the tests in configurations 441-444. f_{MR} can be calculated as $f_{MR} = f_m - f_{prism}$.

Conf.	Q	$h(x=16.92m)$	$k_{s,w}$	$K_{st,w}$	$K_{st,m}$	C_w	C_m	Re_w	Re_m	Fr	f_w	f_m	f_{prism}
[-]	[m ³ /s]	[m]	[mm]	[m ¹ /3s ⁻¹]	[m ¹ /3s ⁻¹]	[m0.5s ⁻¹]	[m0.5s ⁻¹]	[-]	[-]	[-]	[-]	[-]	[-]
441	0.0070	0.039	0.0	114.2	114.0	64.7	64.7	12313	12334	0.61	0.0187	0.0188	0.0188
441	0.0119	0.056	2.2	71.0	101.9	46.5	60.9	34069	19831	0.59	0.0364	0.0212	0.0171
441	0.0207	0.082	4.1	64.0	94.3	44.3	59.2	56745	31732	0.58	0.0401	0.0224	0.0156
441	0.0342	0.121	14.6	50.7	78.1	37.1	51.4	89514	46769	0.53	0.0569	0.0297	0.0145
441	0.0492	0.159	14.8	50.7	74.1	37.7	50.1	107781	61036	0.51	0.0552	0.0312	0.0139
441	0.0621	0.193	23.4	46.2	66.5	34.9	45.9	122952	71067	0.48	0.0645	0.0373	0.0135
441	0.0848	0.243	19.4	48.2	65.6	36.6	46.1	138247	87014	0.47	0.0586	0.0369	0.0131
441	0.1011	0.283	33.1	42.9	57.9	32.9	41.2	150492	95846	0.44	0.0724	0.0461	0.0129
442	0.0063	0.038	5.4	60.2	99.9	38.7	56.6	23817	11132	0.55	0.0524	0.0245	0.0193
442	0.0114	0.058	13.7	50.5	89.2	34.9	53.5	44557	18973	0.54	0.0644	0.0274	0.0172
442	0.0196	0.085	28.0	43.5	76.7	31.6	48.4	69544	29738	0.52	0.0784	0.0335	0.0158
442	0.0327	0.121	28.6	43.7	71.0	32.5	46.7	92587	44793	0.51	0.0745	0.0360	0.0147
442	0.0483	0.168	62.8	36.2	56.9	27.6	38.7	115251	58519	0.46	0.1032	0.0524	0.0140
442	0.0630	0.206	68.9	35.4	53.0	27.2	36.8	128147	69908	0.44	0.1063	0.0580	0.0136
442	0.0844	0.256	66.9	35.8	50.9	27.6	35.9	142499	84315	0.43	0.1027	0.0608	0.0132
442	0.1022	0.294	61.4	36.8	50.4	28.4	36.0	152403	94940	0.42	0.0972	0.0606	0.0129
443	0.0059	0.037	8.4	55.1	97.5	35.9	55.1	24653	10479	0.54	0.0609	0.0259	0.0195
443	0.0113	0.056	7.8	56.6	94.0	38.4	56.2	40274	18813	0.56	0.0533	0.0249	0.0173
443	0.0186	0.079	14.2	50.5	84.5	35.9	52.9	62234	28770	0.55	0.0608	0.0281	0.0159
443	0.0331	0.123	32.5	42.5	69.3	31.6	45.6	94069	45125	0.50	0.0785	0.0377	0.0146
443	0.0483	0.168	59.1	36.8	57.6	28.0	39.2	115083	58635	0.46	0.1002	0.0510	0.0140
443	0.0639	0.208	68.8	35.4	52.9	27.2	36.7	128874	70609	0.44	0.1061	0.0581	0.0135
443	0.0833	0.256	76.5	34.5	49.2	26.7	34.8	141879	83275	0.42	0.1105	0.0648	0.0132
443	0.1036	0.301	79.1	34.3	47.1	26.6	33.7	153014	94898	0.41	0.1112	0.0690	0.0129
444	0.0058	0.037	6.1	58.7	99.5	37.7	56.1	22929	10377	0.54	0.0552	0.0250	0.0195
444	0.0113	0.058	19.2	46.9	86.1	32.8	51.7	46684	18774	0.53	0.0730	0.0294	0.0173
444	0.0191	0.082	21.1	46.4	80.1	33.4	50.4	66465	29319	0.53	0.0702	0.0309	0.0158
444	0.0335	0.126	44.7	39.3	65.2	29.5	43.1	96551	45215	0.49	0.0904	0.0423	0.0146
444	0.0482	0.166	51.6	38.1	59.5	28.9	40.4	114475	58756	0.47	0.0936	0.0481	0.0140
444	0.0622	0.204	66.6	35.7	53.6	27.4	37.2	127483	69403	0.45	0.1044	0.0569	0.0136
444	0.0966	0.286	78.4	34.3	47.8	26.6	34.0	149351	91031	0.42	0.1111	0.0677	0.0130

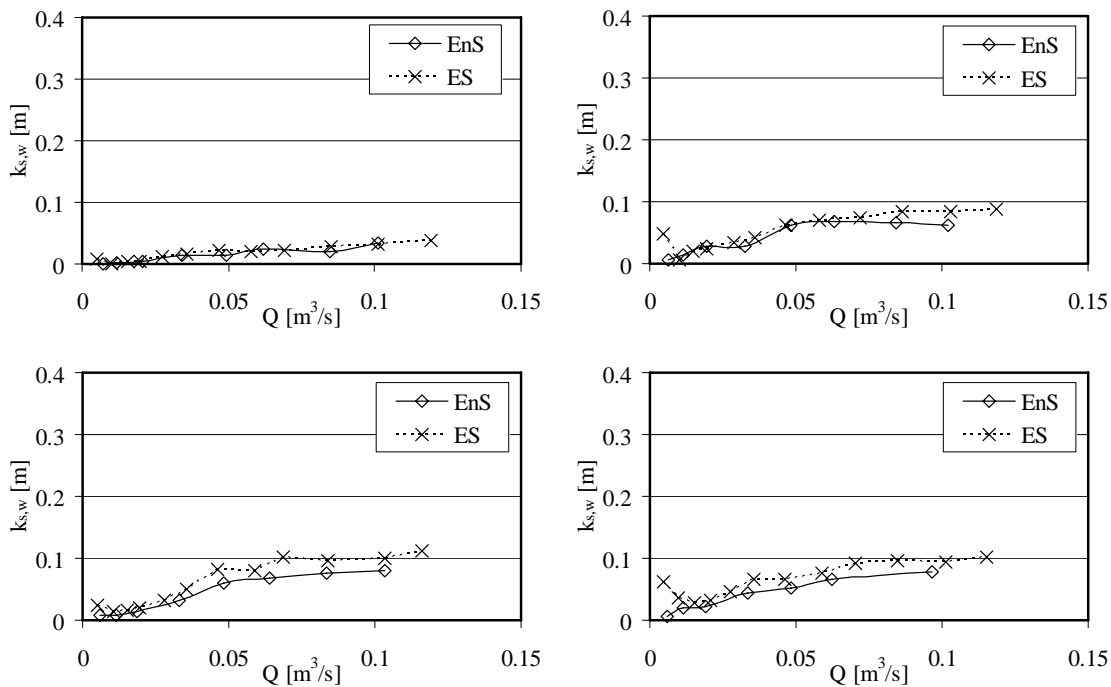


Fig-A4.42: Equivalent sand roughness of the wall $k_{s,w}$ for configurations 441 (top left), 442 (top right), 443 (bottom left) and 444 (bottom right). ES: first test series. EnS: second test series.

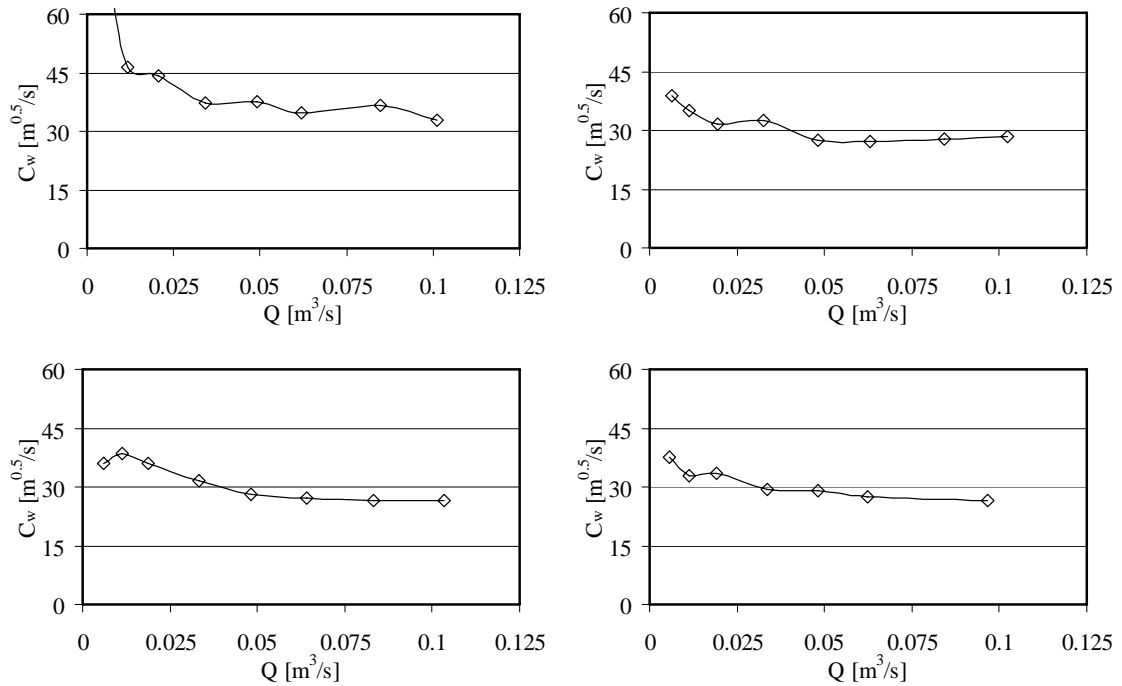


Fig-A4.43: Chezy coefficient related to the wall C_w for configurations 441 (top left), 442 (top right), 443 (bottom left) and 444 (bottom right).

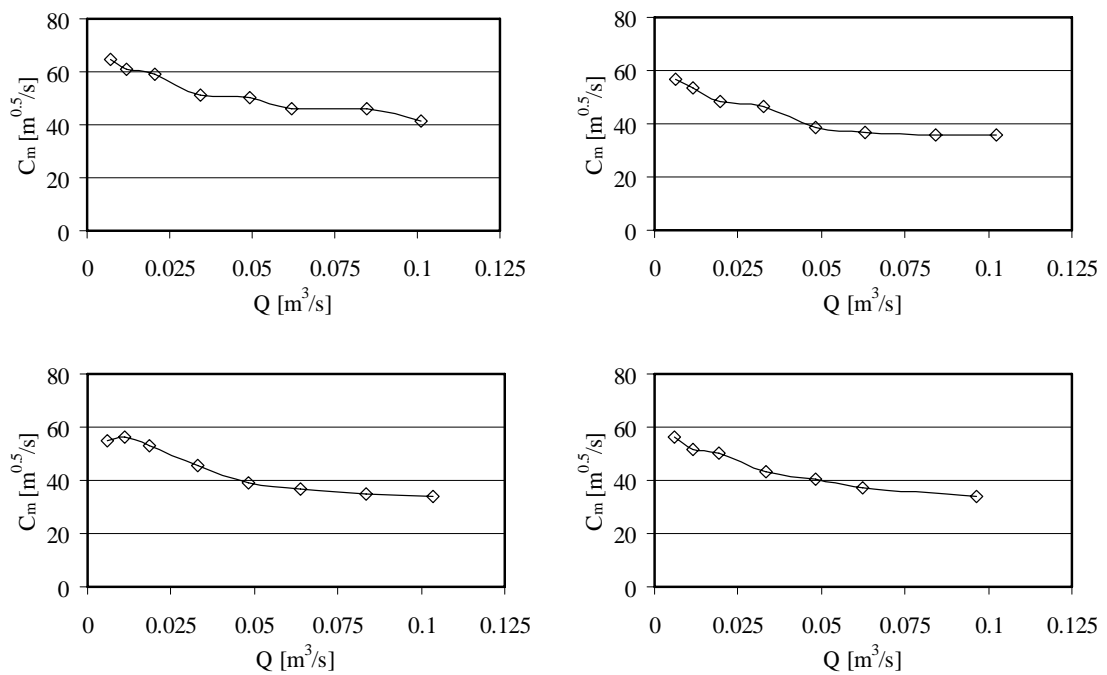


Fig-A4.44: Chezy coefficient related to the cross section C_m for configurations 441 (top left), 442 (top right), 443 (bottom left) and 444 (bottom right).

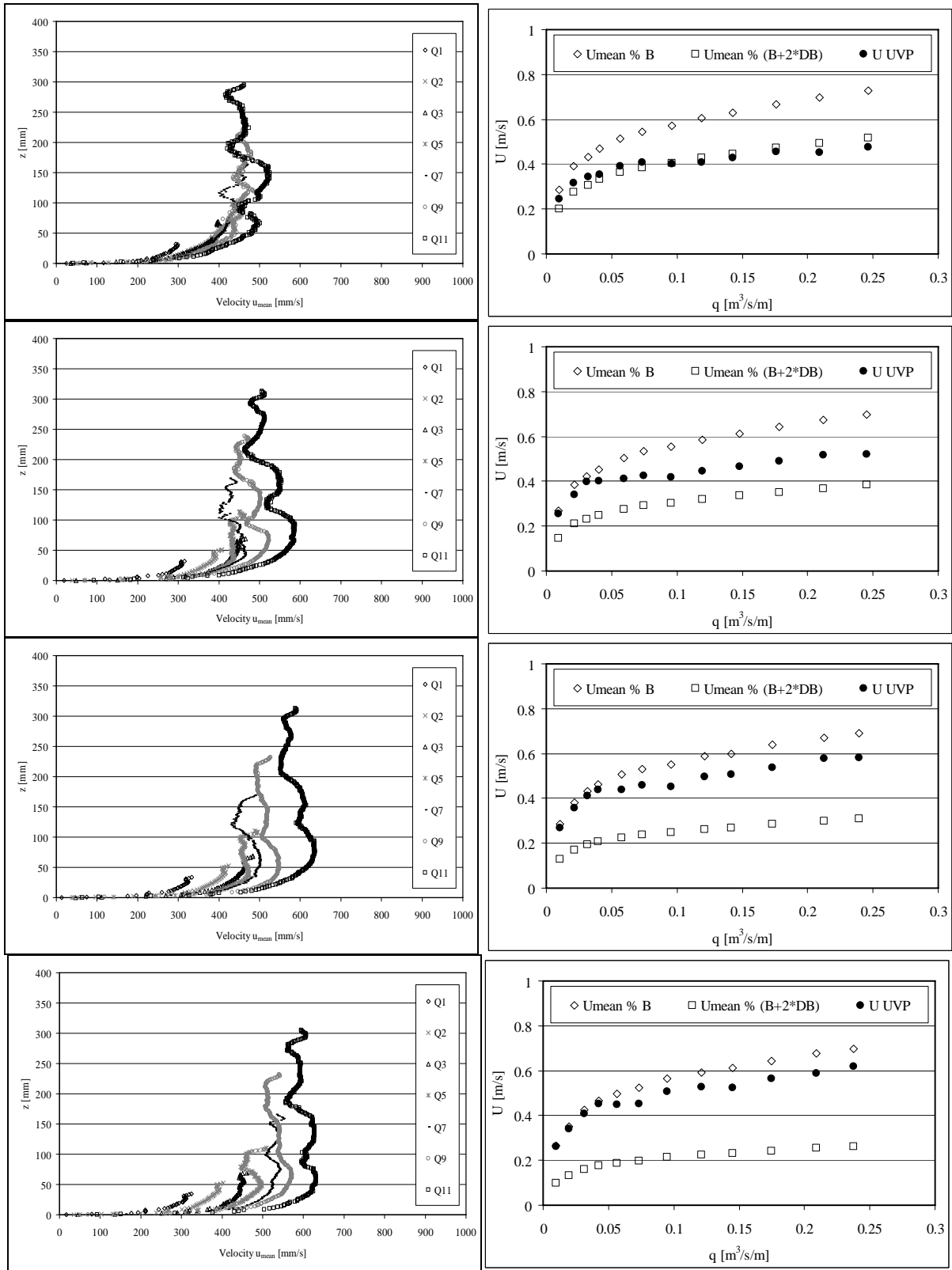


Fig-A4.45: Configurations 441 (above) to 444 (below). Left side: Vertical velocity profiles for different discharges (first test series ES). Right side: Mean velocity of the profiles measured by UVP technique and the theoretical velocities $U_{mean}^+ = Q/(Bh)$ and $U_{mean}^- = Q/((B+2\Delta B)h)$.

A 4-1: Summarized test results for the steady flow tests: 112 asy., 122 asy., 212 asy., Random

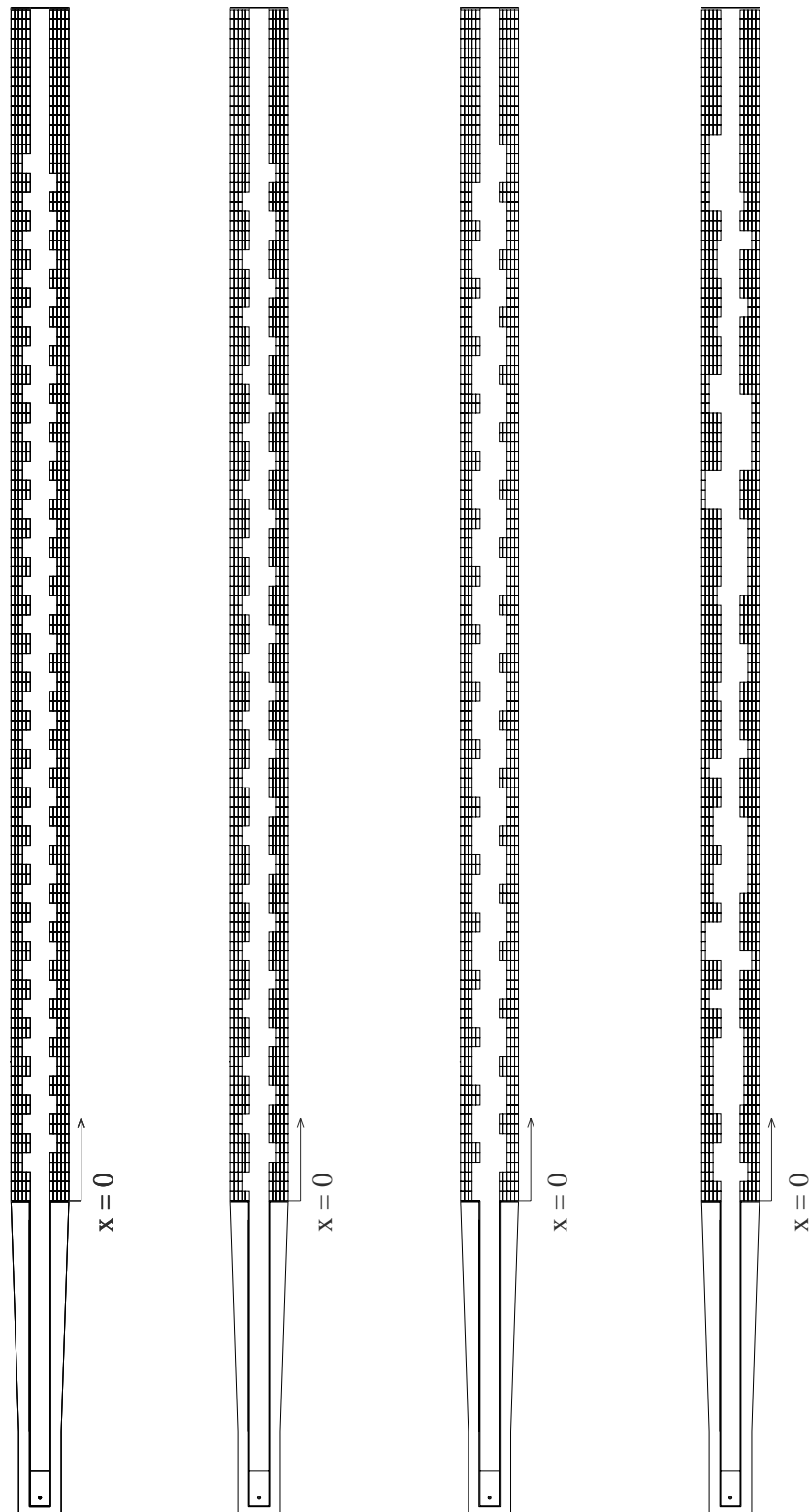


Fig-A4.46: Configurations from left to right: 112 asy., 122 asy., 212 asy. and Random. Flow direction from bottom to top.

Table with flow resistance parameters of the tests in configurations 441-444. f_{MR} can be calculated as $f_{MR} = f_m - f_{prism}$.

Conf. [-]	Q [m ³ /s]	$h(x=16.92m)$ [m]	$k_{s,w}$ [mm]	$K_{st,w}$ [m ¹ /3s-1]	$K_{st,m}$ [m ¹ /3s-1]	C_w [m0.5s-1]	C_m [m0.5s-1]	Re_w [-]	Re_m [-]	Fr [-]	f_w [-]	f_m [-]	f_{prism} [-]
112 asy.	0.0061	0.040	25.3	43.2	88.4	29.5	50.4	31639	10808	0.502	0.090	0.031	0.019
112 asy.	0.0100	0.055	30.3	42.0	82.3	29.7	49.1	46025	16789	0.507	0.089	0.033	0.018
112 asy.	0.0186	0.086	53.9	37.0	68.9	27.3	43.5	71893	28222	0.485	0.105	0.041	0.016
112 asy.	0.0321	0.131	95.4	31.8	55.0	24.2	36.5	97286	42846	0.446	0.134	0.059	0.015
112 asy.	0.0477	0.177	115.5	30.2	48.4	23.2	33.1	114719	56674	0.423	0.145	0.072	0.014
112 asy.	0.0626	0.211	94.1	32.4	48.8	24.9	34.0	127324	68676	0.424	0.126	0.068	0.014
112 asy.	0.0821	0.258	92.1	32.7	46.9	25.3	33.1	140334	81771	0.413	0.123	0.071	0.013
112 asy.	0.1024	0.296	62.6	36.6	50.1	28.3	35.8	151932	94789	0.419	0.098	0.061	0.013
122 asy.	0.0052	0.034	2.7	68.4	104.2	42.3	58.0	17710	9418	0.554	0.044	0.023	0.020
122 asy.	0.0111	0.055	6.1	59.3	95.9	39.8	57.2	38262	18591	0.566	0.049	0.024	0.017
122 asy.	0.0194	0.080	7.2	57.8	90.3	40.4	56.5	58686	30008	0.569	0.048	0.025	0.016
122 asy.	0.0311	0.118	34.9	41.7	69.2	31.0	45.3	91759	42992	0.505	0.081	0.038	0.015
122 asy.	0.0481	0.169	68.5	35.3	55.8	27.0	38.0	115597	58291	0.458	0.108	0.054	0.014
122 asy.	0.0643	0.199	26.7	44.8	64.7	34.0	44.7	125759	72633	0.478	0.068	0.039	0.013
122 asy.	0.0850	0.245	23.6	46.2	63.4	35.2	44.6	139659	86901	0.463	0.063	0.039	0.013
122 asy.	0.1032	0.284	26.7	45.0	60.2	34.5	42.9	150981	97524	0.448	0.066	0.043	0.013
212 asy.	0.0058	0.040	41.4	38.1	83.9	26.4	47.7	33383	10212	0.484	0.113	0.034	0.020
212 asy.	0.0111	0.062	70.5	33.7	70.8	24.6	42.9	55254	18170	0.472	0.130	0.043	0.017
212 asy.	0.0191	0.091	92.9	31.7	61.0	23.7	38.8	76289	28518	0.459	0.140	0.052	0.016
212 asy.	0.0328	0.135	126.2	29.1	50.7	22.3	33.8	99231	43183	0.433	0.158	0.069	0.015
212 asy.	0.0489	0.180	128.5	29.2	46.7	22.5	32.0	116636	57617	0.421	0.155	0.077	0.014
212 asy.	0.0623	0.220	160.4	27.2	41.5	21.1	28.9	126578	67098	0.398	0.177	0.094	0.014
212 asy.	0.0843	0.275	170.7	26.7	38.4	20.8	27.3	139951	81016	0.384	0.182	0.105	0.013
212 asy.	0.1025	0.318	175.5	26.5	36.8	20.7	26.4	149088	90973	0.375	0.184	0.112	0.013
Random	0.0057	0.036	6.0	58.3	100.2	37.4	56.3	22530	10213	0.542	0.056	0.025	0.020
Random	0.0111	0.055	6.0	59.3	96.3	39.9	57.4	38023	18559	0.565	0.049	0.024	0.017
Random	0.0194	0.084	23.0	45.6	78.6	33.0	49.5	67622	29602	0.527	0.072	0.032	0.016
Random	0.0322	0.125	54.1	37.5	62.2	28.2	41.0	95544	43635	0.480	0.099	0.047	0.015
Random	0.0484	0.169	62.9	36.3	55.8	27.7	38.0	115116	58555	0.458	0.103	0.054	0.014
Random	0.0616	0.204	70.5	35.3	52.0	27.1	36.1	126793	68732	0.441	0.107	0.060	0.014
Random	0.0827	0.252	65.0	36.2	50.6	27.9	35.7	141141	83222	0.430	0.101	0.062	0.013
Random	0.1027	0.298	70.3	35.5	47.9	27.5	34.3	152331	94668	0.416	0.104	0.067	0.013

A 4-2: Aspect of the flow in the macro-rough configuration 142

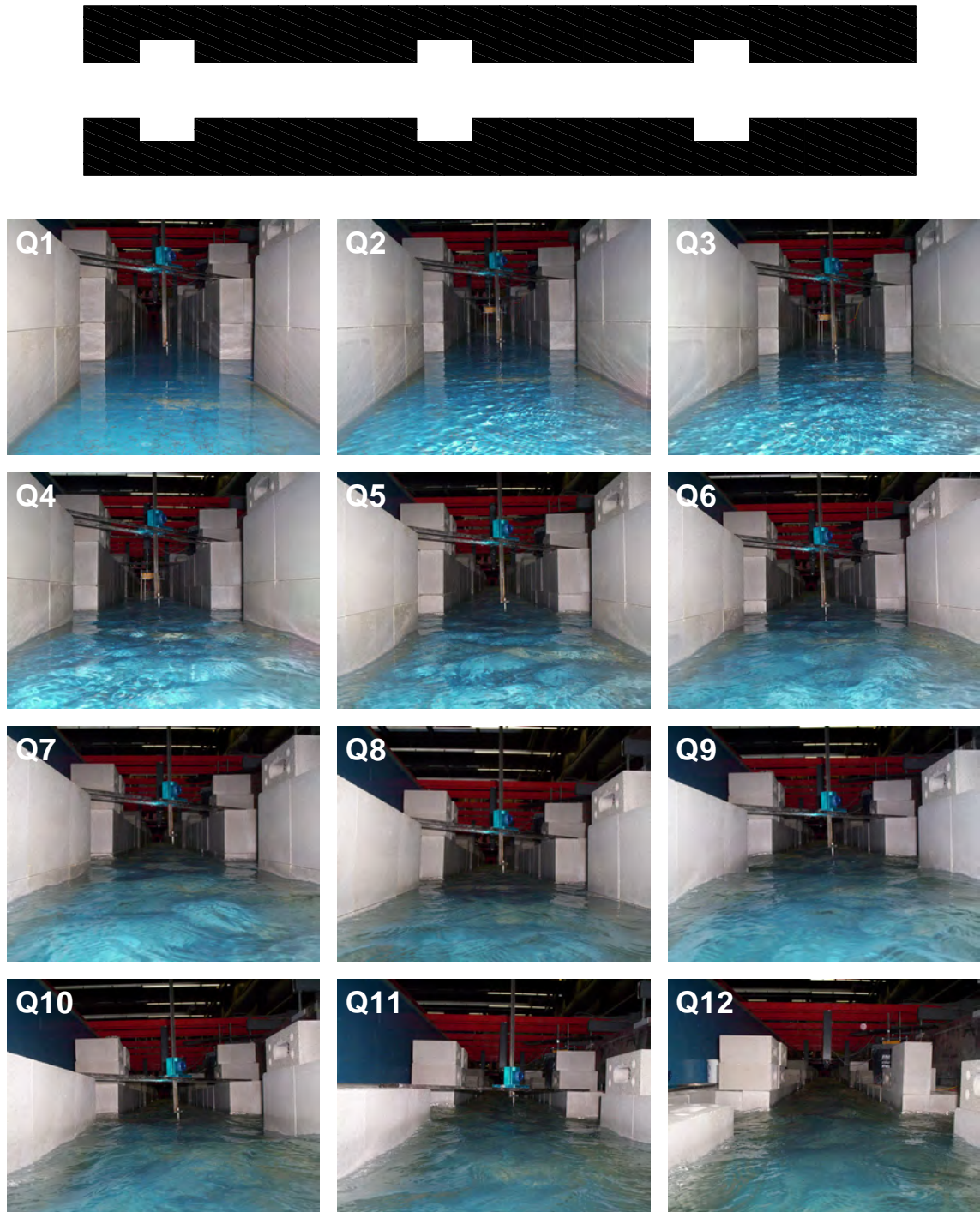


Fig-A4.47: Aspect of the flow for different discharges in configuration 142 ($L_b = 0.5$ m, $L_c = 2.0$ m, $\Delta B = 0.2$ m) at the channel location $x = 16$ m. $Q1 = 4.4$ l/s, $Q2 = 10.1$ l/s, $Q3 = 15.0$ l/s, $Q4 = 19.9$ l/s, $Q5 = 28.0$ l/s, $Q6 = 35.6$ l/s, $Q7 = 46.0$ l/s, $Q8 = 58.8$ l/s, $Q9 = 70.3$ l/s, $Q10 = 84.3$ l/s, $Q11 = 104.7$ l/s, $Q12 = 123.4$ l/s.

A 4-2: Aspect of the flow in the macro-rough configuration 222

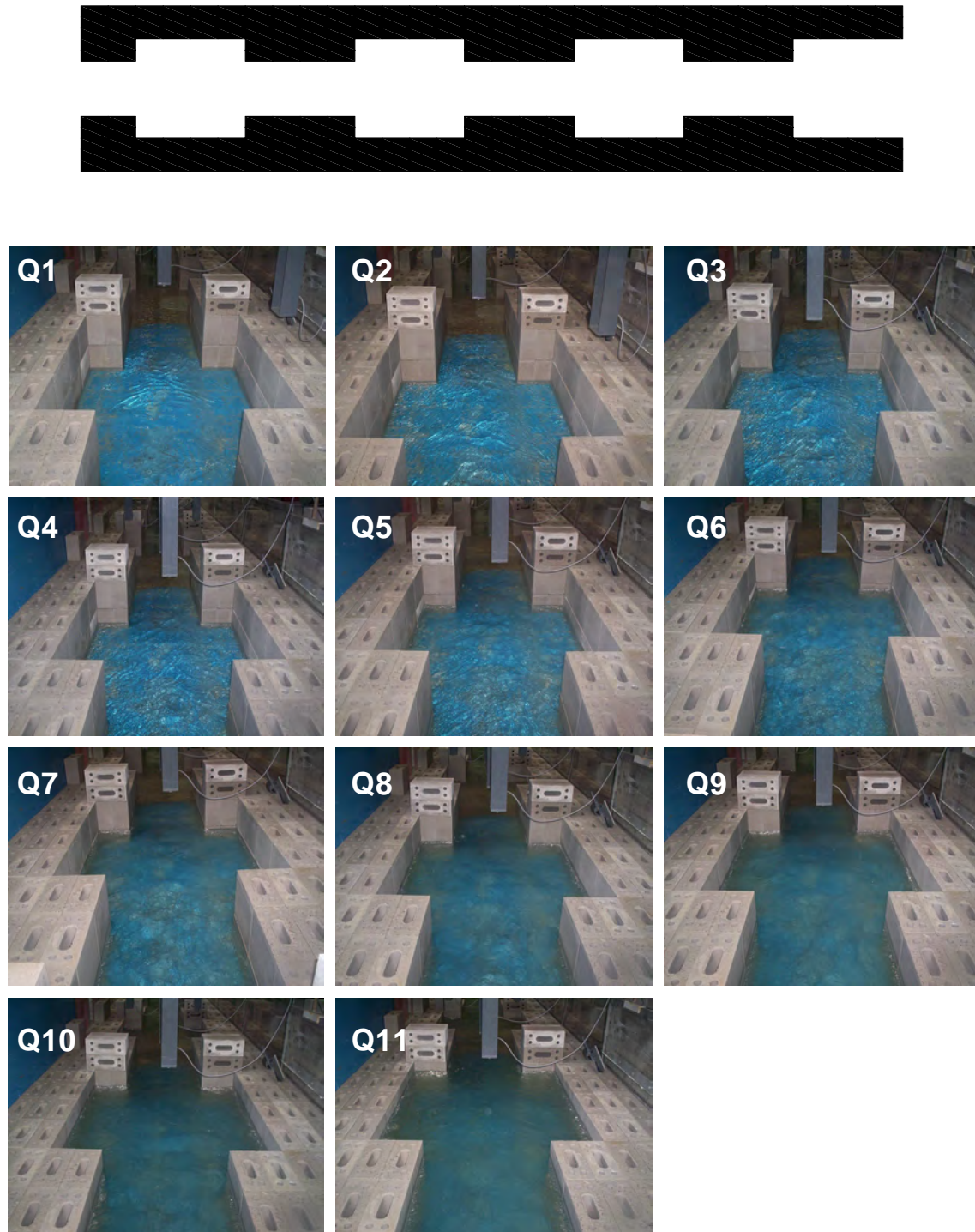


Fig-A4.48: Aspect of the flow for different discharges in configuration 222 ($L_b = 1.0$ m, $L_c = 1.0$ m, $\Delta B = 0.2$ m) at the channel location $x = 16$ m. $Q1 = 5.5$ l/s, $Q2 = 10.5$ l/s, $Q3 = 15.2$ l/s, $Q4 = 20.0$ l/s, $Q5 = 28.3$ l/s, $Q6 = 35.3$ l/s, $Q7 = 47.4$ l/s, $Q8 = 58.3$ l/s, $Q9 = 71.6$ l/s, $Q10 = 84.8$ l/s, $Q11 = 99.5$ l/s, $Q12 = 111.4$ l/s.

A 4-3: Flow visualization with dye tests

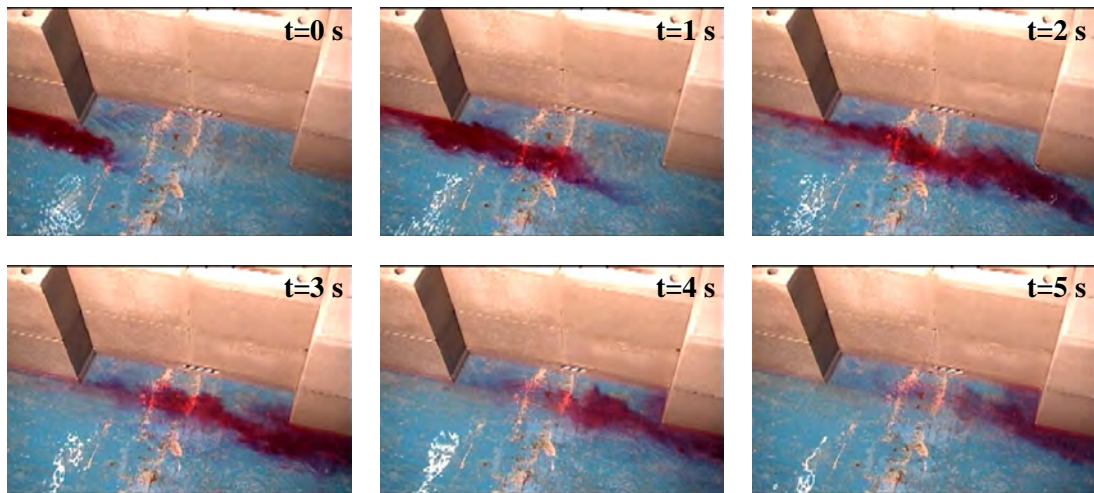


Fig-A4.49: Dye test in a cavity of configuration 111 ($L_b = 0.5$ m, $L_c = 0.5$ m; $\Delta B = 0.1$ m, Aspect ratio = $\Delta B/L_b = 0.2$, Expansion ratio = $(B+2\Delta B)/B = 1.41$, $(B+2\Delta B)/L_b = 1.37$) for a low discharge ($Q = 5$ l/s, $Re_m = 12'000$; $Fr = 0.58$). Flow direction is **from the left to the right side**. The dye is introduced upstream of the cavity in the main flow.

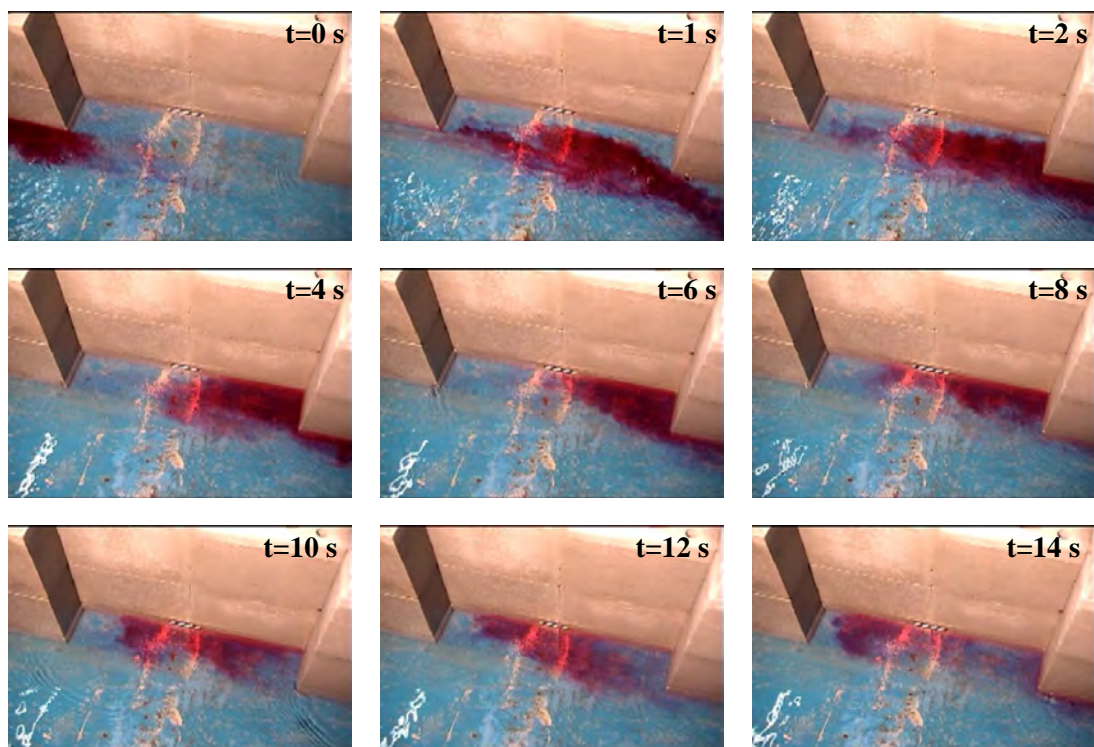


Fig-A4.50: Dye test in a cavity of configuration 111 ($L_b = 0.5$ m, $L_c = 0.5$ m; $\Delta B = 0.1$ m, Aspect ratio = $\Delta B/L_b = 0.2$, Expansion ratio = $(B+2\Delta B)/B = 1.41$, $(B+2\Delta B)/L_b = 1.37$) for a low discharge ($Q = 5$ l/s, $Re_m = 12'000$; $Fr = 0.58$). Flow direction is **from the left to the right side**. The dye is introduced upstream of the cavity in the main flow.

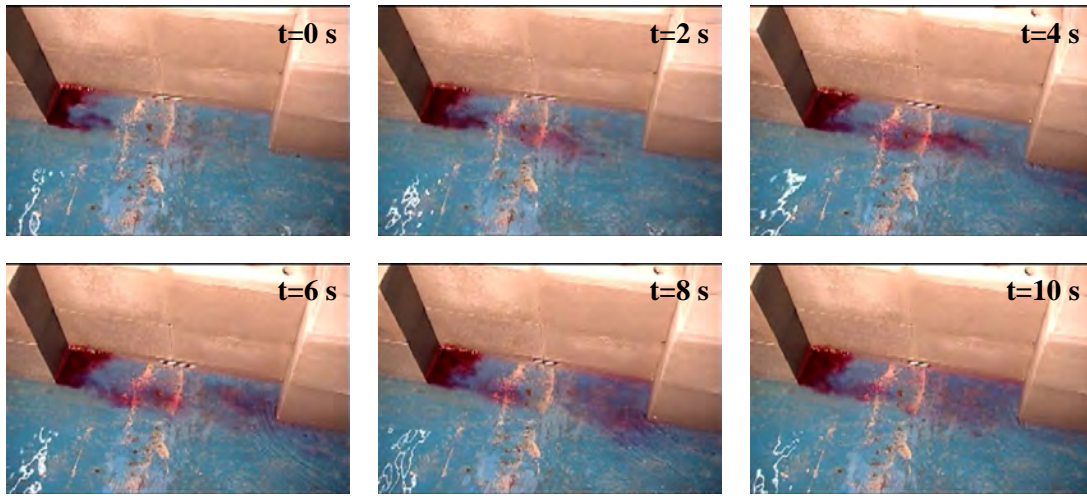


Fig-A4.51: Dye test in a cavity of configuration 111 ($L_b = 0.5$ m, $L_c = 0.5$ m; $\Delta B = 0.1$ m, Aspect ratio = $\Delta B/L_b = 0.2$, Expansion ratio = $(B+2\Delta B)/B = 1.41$, $(B+2\Delta B)/L_b = 1.37$) for a low discharge ($Q = 5$ l/s, $Re_m = 12'000$; $Fr = 0.58$). Flow direction is **from the left to the right side**. The dye is introduced into the small secondary gyre in the upstream part of the cavity.

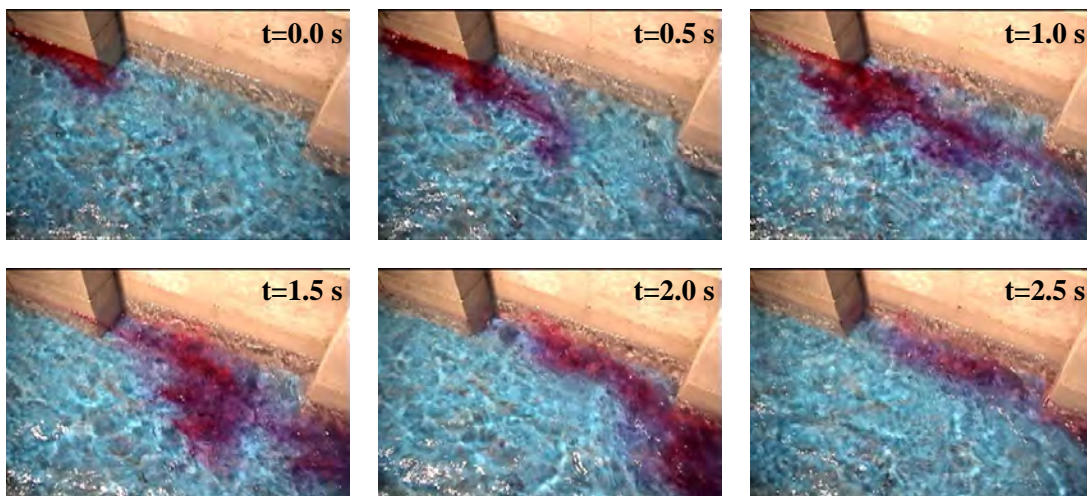


Fig-A4.52: Dye test in a cavity of configuration 111 ($L_b = 0.5$ m, $L_c = 0.5$ m; $\Delta B = 0.1$ m, Aspect ratio = $\Delta B/L_b = 0.2$, Expansion ratio = $(B+2\Delta B)/B = 1.41$, $(B+2\Delta B)/L_b = 1.37$) for a medium discharge ($Q = 37$ l/s, $Re_m = 48'000$; $Fr = 0.47$). Flow direction is **from the left to the right side**. The dye is introduced upstream of the cavity in the main flow.

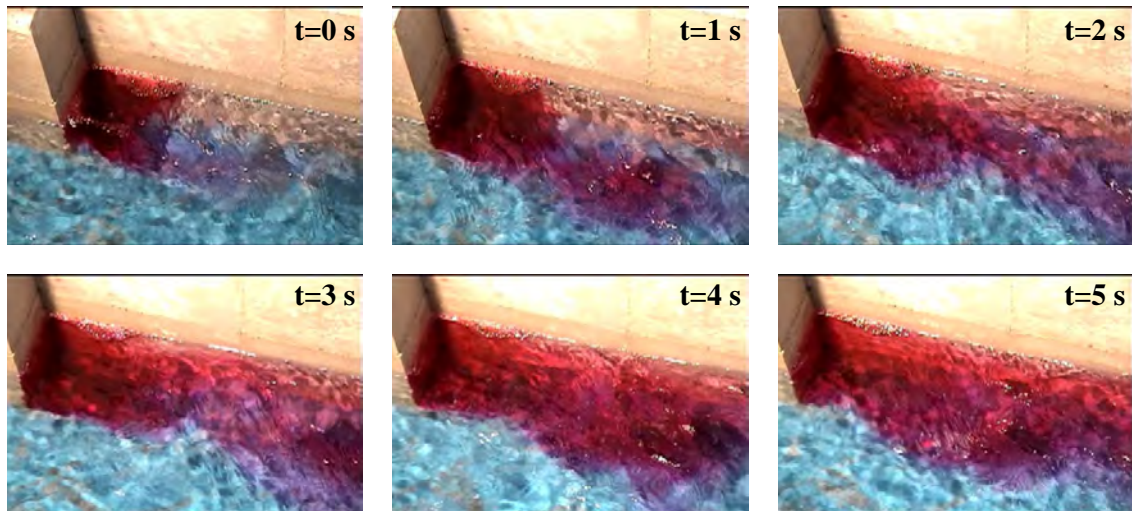


Fig-A4.53: Dye test in a cavity of configuration 111 ($L_b = 0.5$ m, $L_c = 0.5$ m; $\Delta B = 0.1$ m, Aspect ratio = $\Delta B/L_b = 0.2$, Expansion ratio = $(B+2\Delta B)/B = 1.41$, $(B+2\Delta B)/L_b = 1.37$) for a medium discharge ($Q = 37$ l/s, $Re_m = 48'000$; $Fr = 0.47$). Flow direction is **from the left to the right side**. The dye is introduced into the small secondary gyres in the upstream part of the cavity.

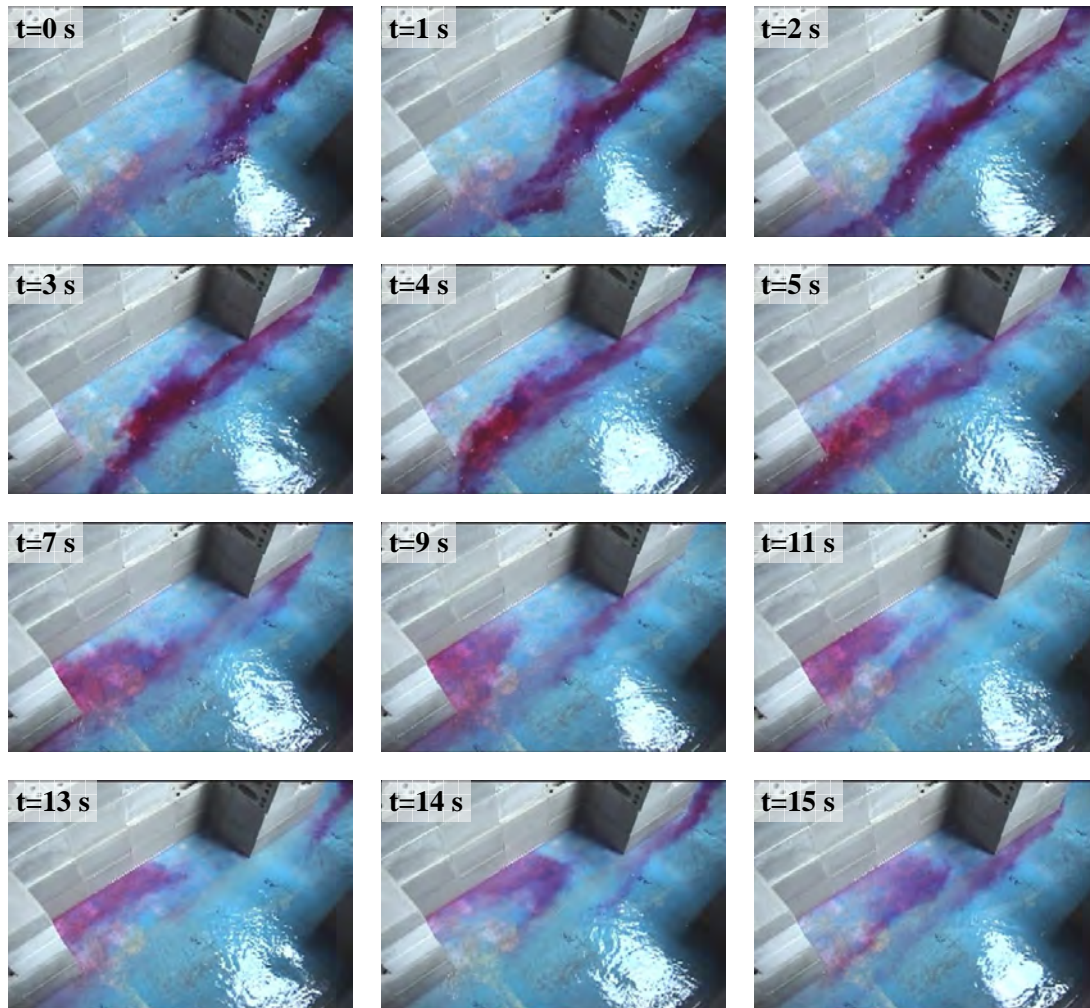


Fig-A4.54: Dye test in a cavity of configuration 213 ($L_b = 1.0$ m, $L_c = 0.5$ m; $\Delta B = 0.3$ m, Aspect ratio = $\Delta B/L_b = 0.3$, Expansion ratio = $(B+2\Delta B)/B = 2.24$, $(B+2\Delta B)/L_b = 1.09$) for a low discharge ($Q = 5$ l/s, $Re_m = 10'000$; $Fr = 0.58$). Flow direction is **from the right to the left side**. The dye is introduced into the downstream part of the next upstream cavity.

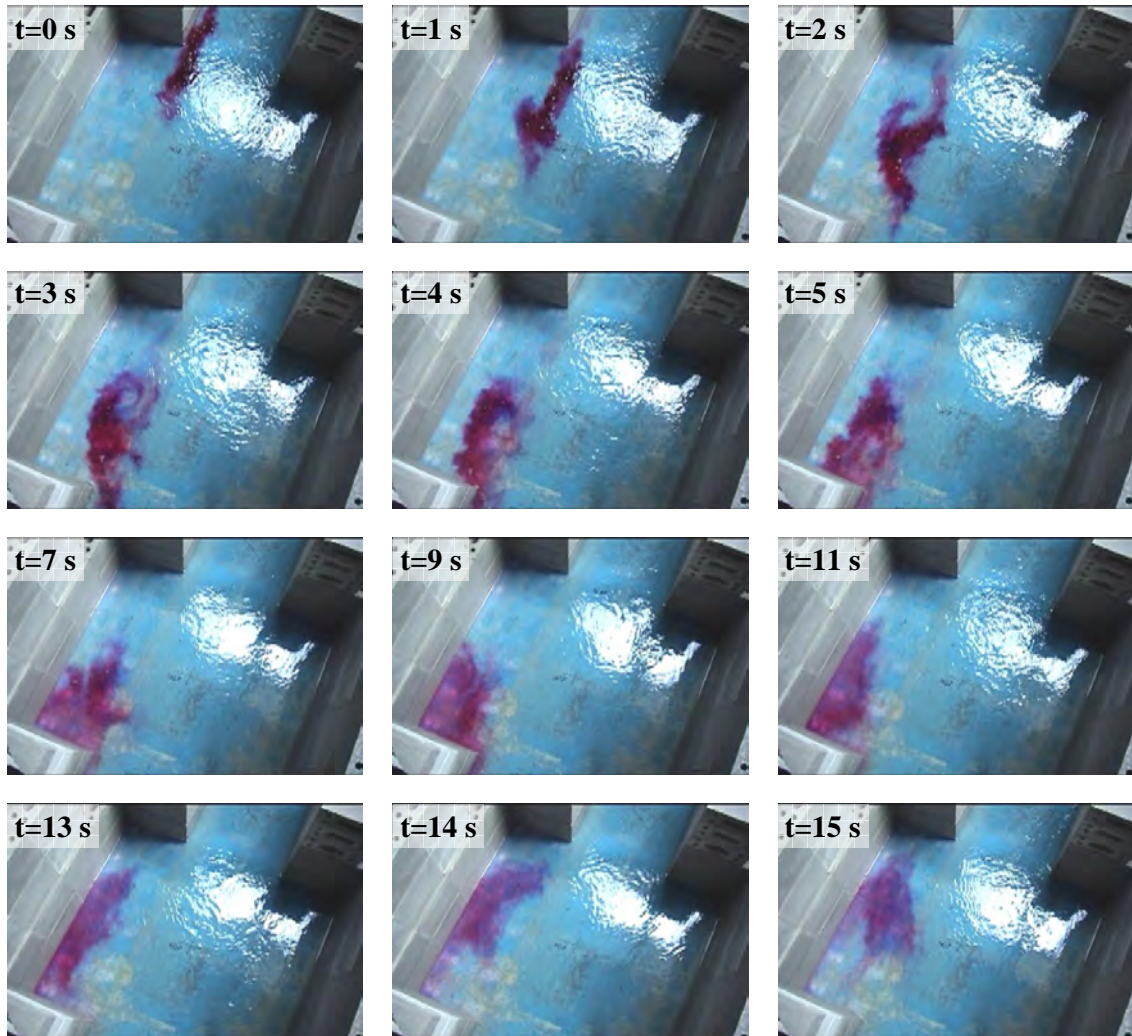


Fig-A4.55: Dye test in a cavity of configuration 213 ($L_b = 1.0$ m, $L_c = 0.5$ m; $\Delta B = 0.3$ m, Aspect ratio = $\Delta B/L_b = 0.3$, Expansion ratio = $(B+2\Delta B)/B = 2.24$, $(B+2\Delta B)/L_b = 1.09$) for a low discharge ($Q = 5$ l/s, $Re_m = 10'000$; $Fr = 0.58$). Flow direction is **from top to bottom**. The dye is introduced into the main stream upstream of the cavity.

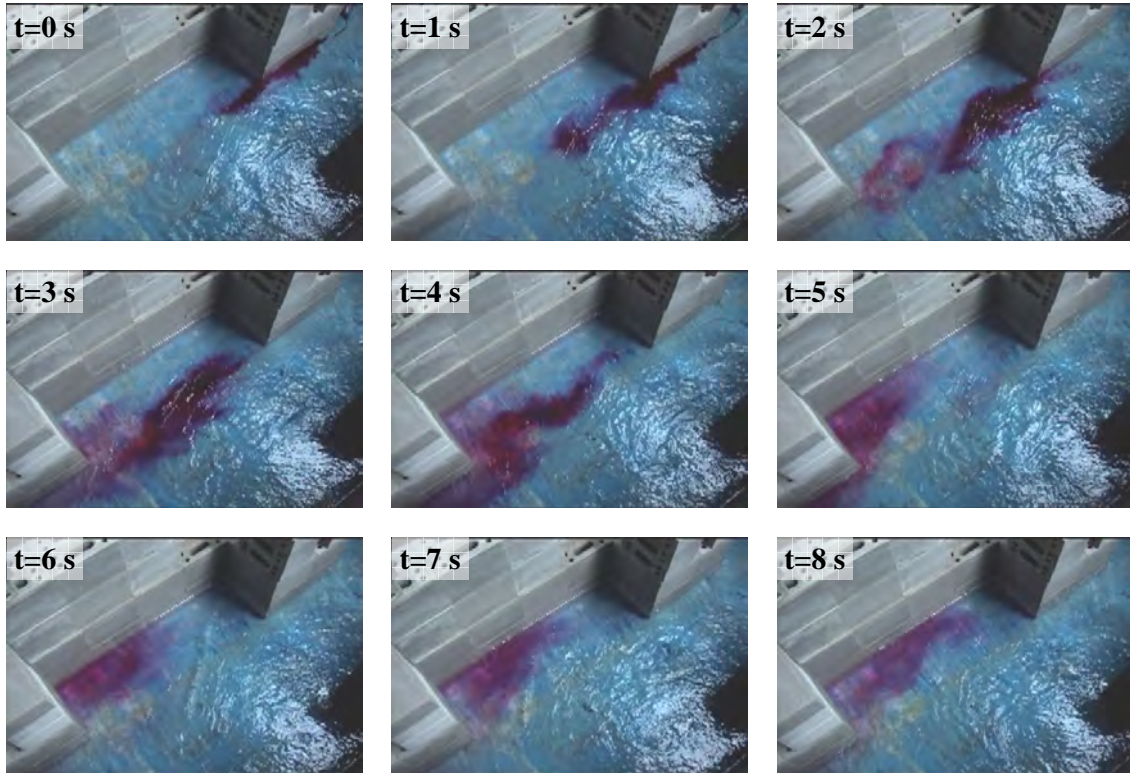


Fig-A4.56: Dye test in a cavity of configuration 213 ($L_b = 1.0$ m, $L_c = 0.5$ m; $\Delta B = 0.3$ m, Aspect ratio = $\Delta B/L_b = 0.3$, Expansion ratio = $(B+2\Delta B)/B = 2.24$, $(B+2\Delta B)/L_b = 1.09$) for a medium discharge ($Q = 27$ l/s, $Re_m = 38'000$; $Fr = 0.49$). Flow direction is **from the right to the left side**. Dye is introduced into the main stream upstream of the cavity.

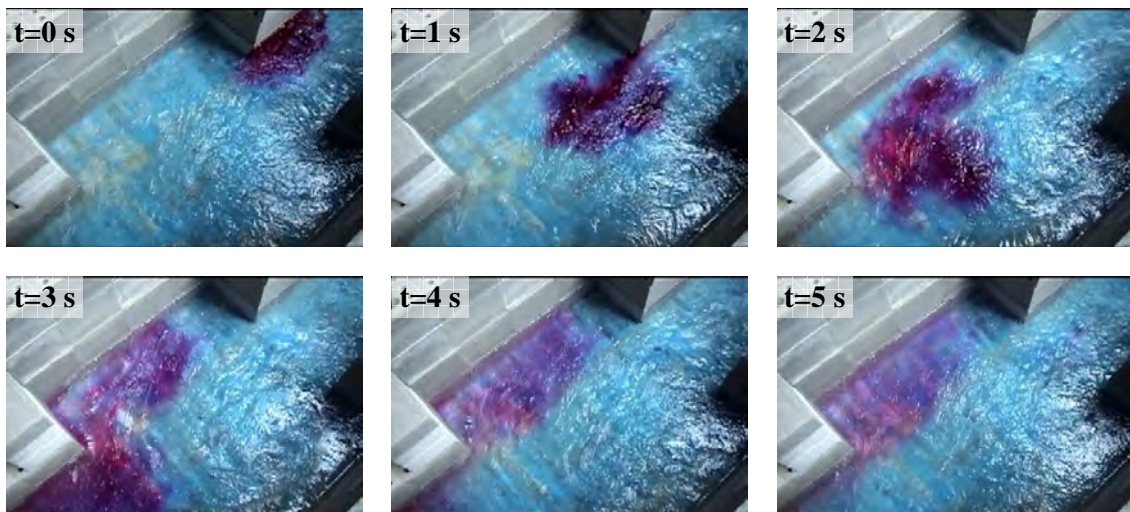


Fig-A4.57: Dye test in a cavity of configuration 213 ($L_b = 1.0$ m, $L_c = 0.5$ m; $\Delta B = 0.3$ m, Aspect ratio = $\Delta B/L_b = 0.3$, Expansion ratio = $(B+2\Delta B)/B = 2.24$, $(B+2\Delta B)/L_b = 1.09$) for a high discharge ($Q = 47$ l/s, $Re_m = 56'000$; $Fr = 0.42$). Flow direction is **from the right to the left side**. The dye is introduced into the main stream upstream of the cavity.

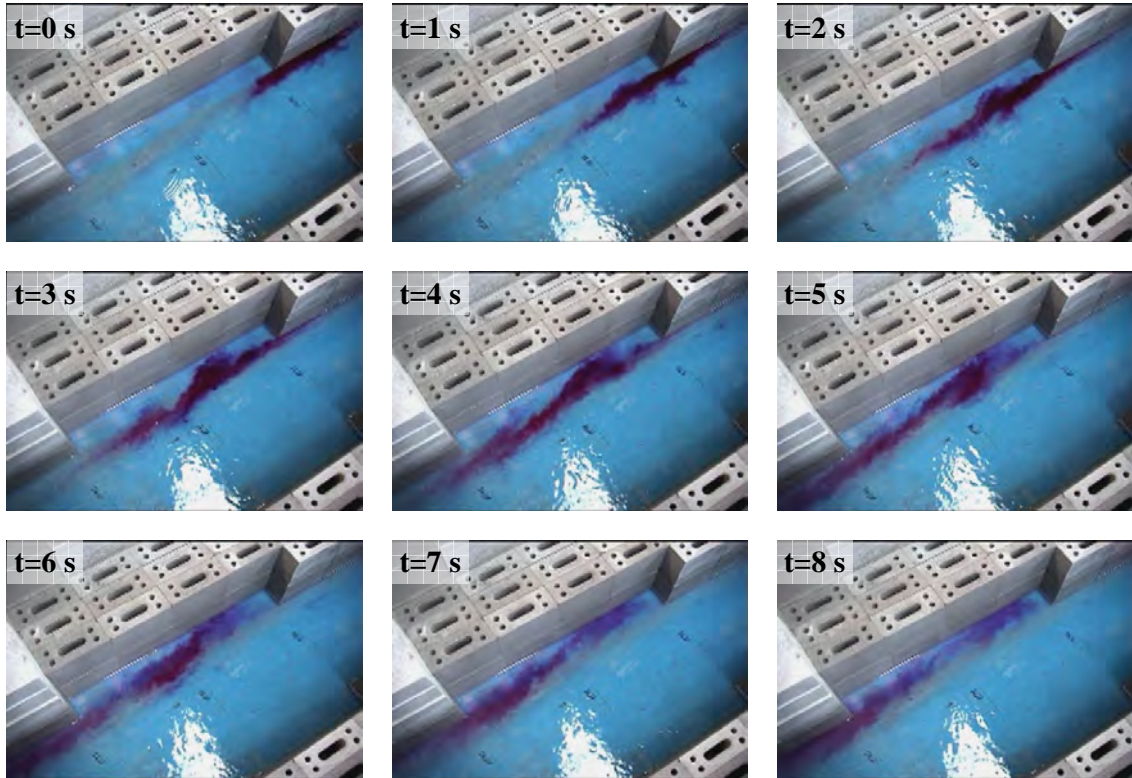


Fig-A4.58: Dye test in a cavity of configuration 221 ($L_b = 1.0$ m, $L_c = 1.0$ m; $\Delta B = 0.1$ m, Aspect ratio = $\Delta B/L_b = 0.1$, Expansion ratio = $(B+2\Delta B)/B = 1.41$, $(B+2\Delta B)/L_b = 0.69$) for a low discharge ($Q = 5$ l/s, $Re_m = 10'000$; $Fr = 0.57$). Flow direction is **from the right to the left side**. The dye is introduced into the main stream upstream of the cavity.

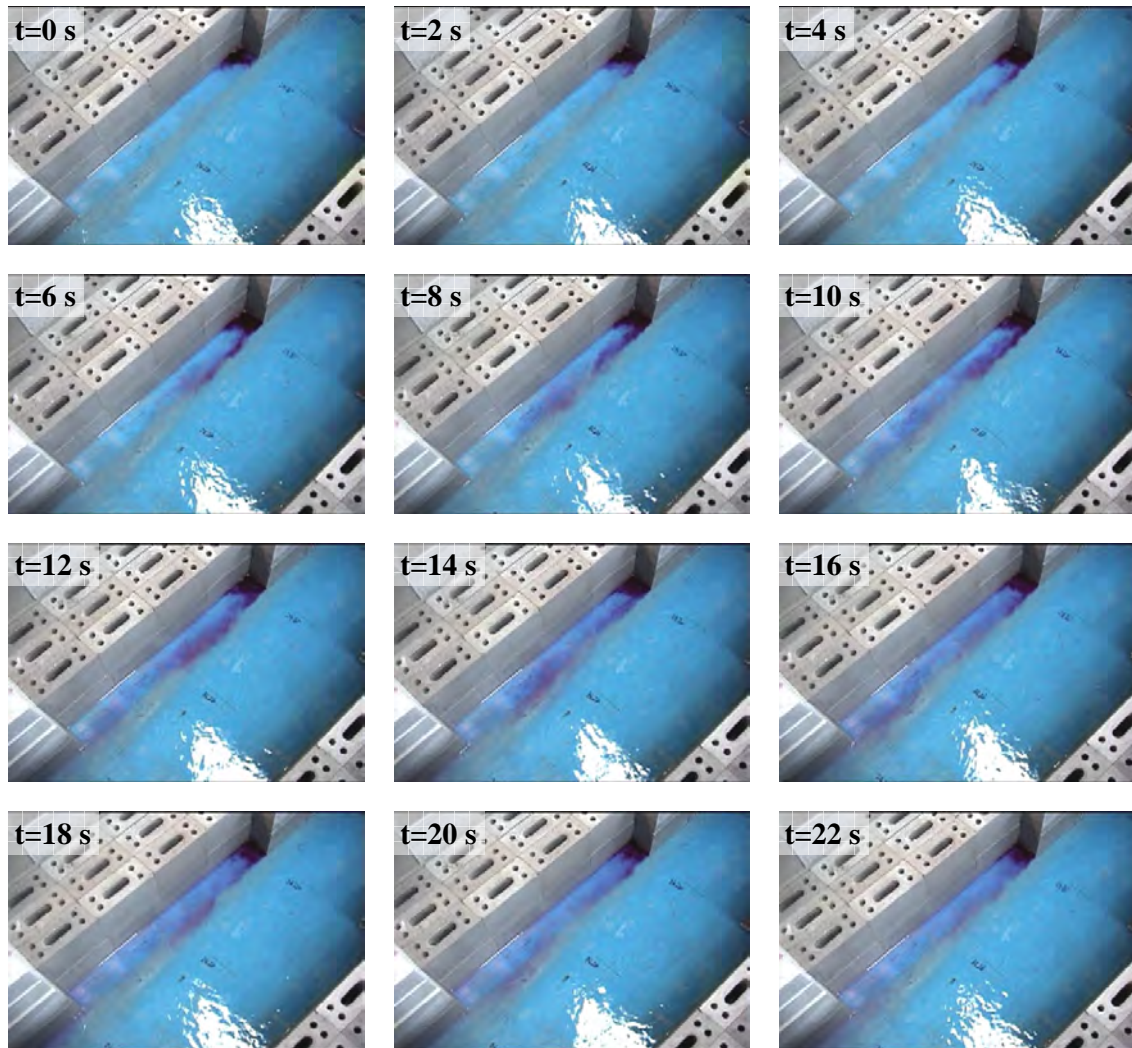


Fig-A4.59: Dye test in a cavity of configuration 221 ($L_b = 1.0$ m, $L_c = 1.0$ m; $\Delta B = 0.1$ m, Aspect ratio = $\Delta B/L_b = 0.1$, Expansion ratio = $(B+2\Delta B)/B = 1.41$, $(B+2\Delta B)/L_b = 0.69$) for a low discharge ($Q = 5$ l/s, $Re_m = 10'000$; $Fr = 0.57$). Flow direction is **from the right to the left side**. The dye is introduced into the small secondary gyre (quasi dead zone) in the upstream part of the cavity.

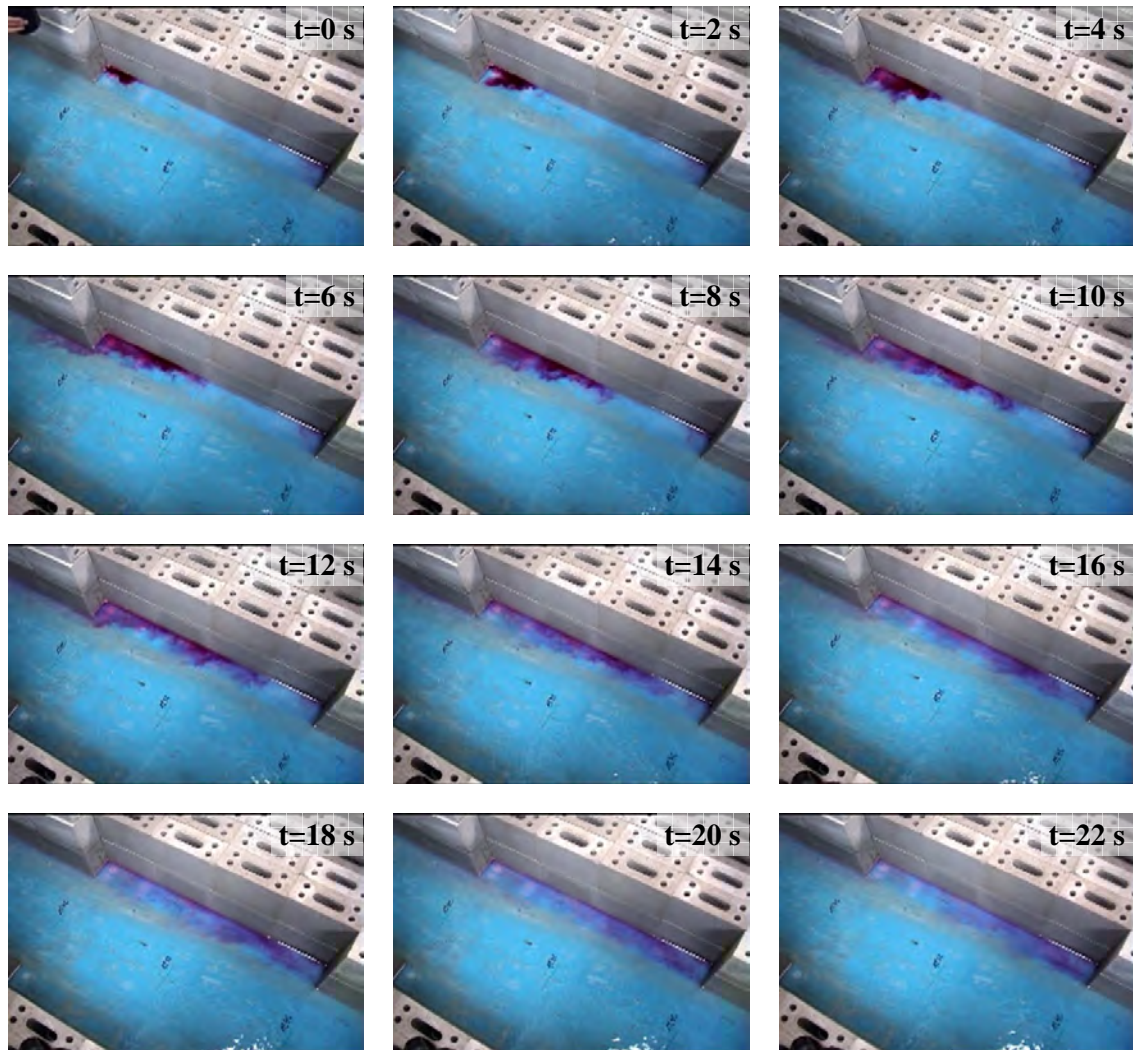


Fig-A4.60: Dye test in a cavity of configuration 221 ($L_b = 1.0$ m, $L_c = 1.0$ m; $\Delta B = 0.1$ m, Aspect ratio = $\Delta B/L_b = 0.1$, Expansion ratio = $(B+2\Delta B)/B = 1.41$, $(B+2\Delta B)/L_b = 0.69$) for a low discharge ($Q = 5$ l/s, $Re_m = 10'000$; $Fr = 0.57$). Flow direction is **from the right to the left side**. The dye is introduced in the downstream part of the cavity. The flow does not reattach completely, the dye moves very slowly upstream.

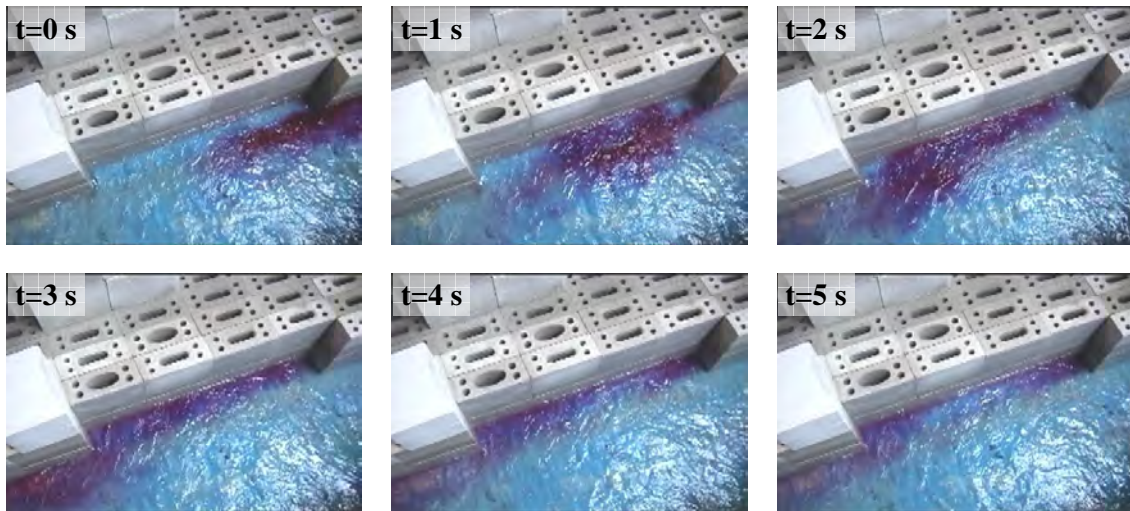


Fig-A4.61: Dye test in a cavity of configuration 221 ($L_b = 1.0$ m, $L_c = 1.0$ m; $\Delta B = 0.1$ m, Aspect ratio = $\Delta B/L_b = 0.1$, Expansion ratio = $(B+2\Delta B)/B = 1.41$, $(B+2\Delta B)/L_b = 0.69$) for a medium discharge ($Q = 40$ l/s, $Re_m = 52'000$; $Fr = 0.47$). Flow direction is **from the right to the left side**. The dye is introduced in the main stream upstream of the cavity.

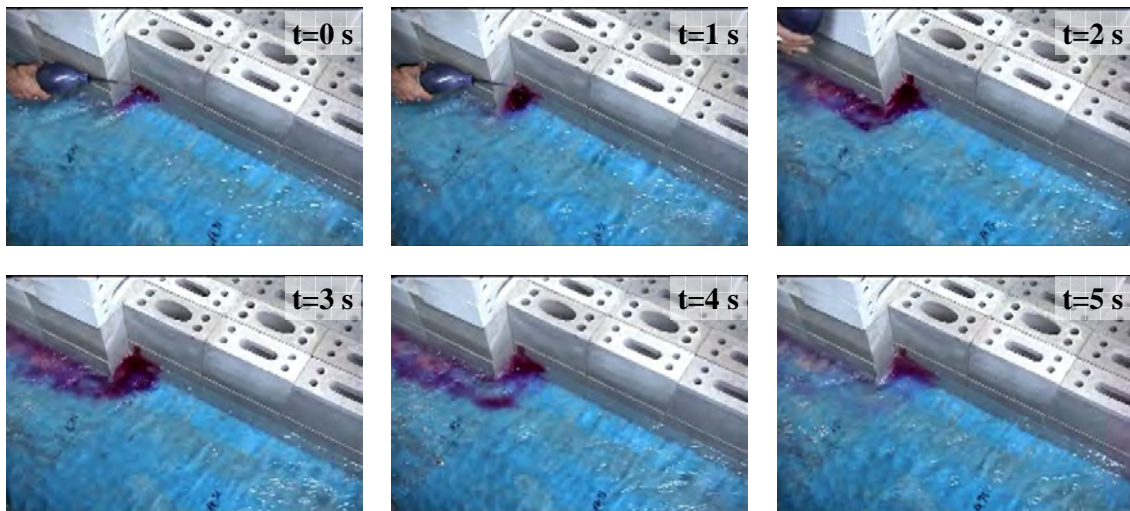


Fig-A4.62: Dye test in a cavity of configuration 221 ($L_b = 1.0$ m, $L_c = 1.0$ m; $\Delta B = 0.1$ m, Aspect ratio = $\Delta B/L_b = 0.1$, Expansion ratio = $(B+2\Delta B)/B = 1.41$, $(B+2\Delta B)/L_b = 0.69$) for a medium discharge ($Q = 40$ l/s, $Re_m = 52'000$; $Fr = 0.47$). Flow direction is **from the right to the left side**. The dye is introduced in the downstream part of the cavity. The flow does reattach, the dye can't move upstream.

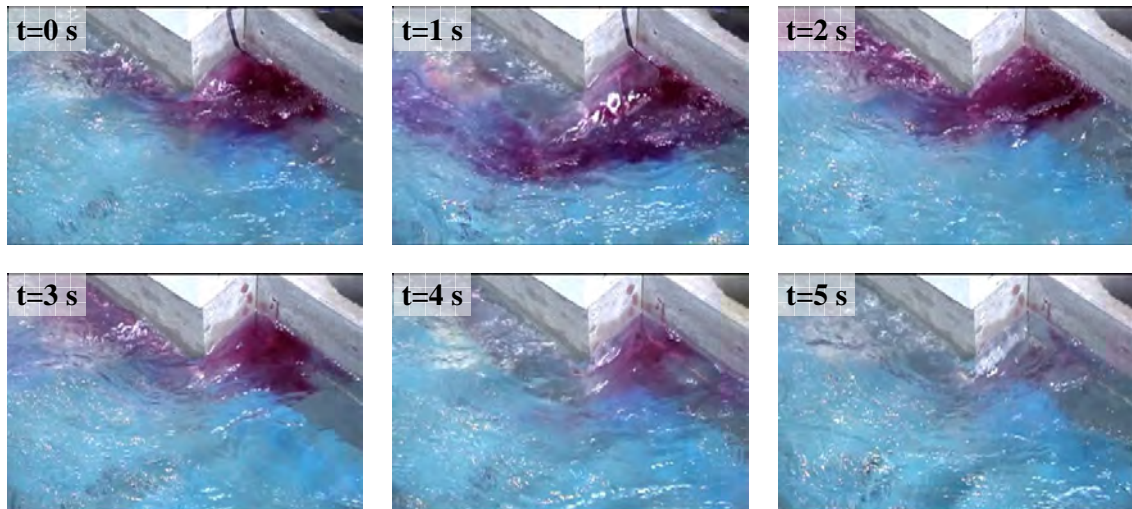
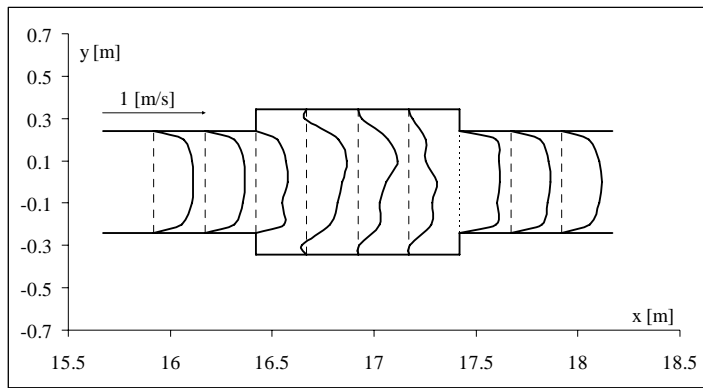
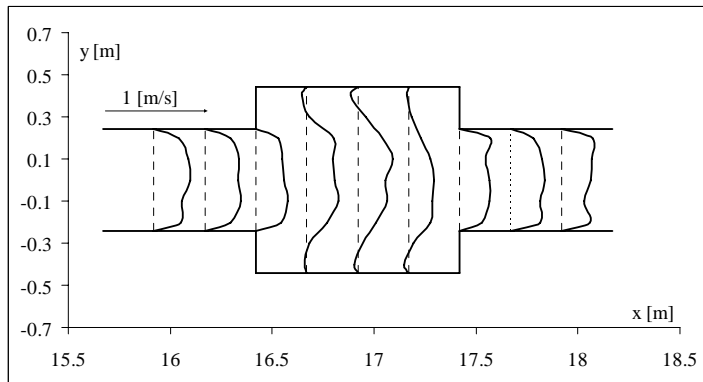


Fig-A4.63: Dye test in a cavity of configuration 221 ($L_b = 1.0$ m, $L_c = 1.0$ m; $\Delta B = 0.1$ m, Aspect ratio = $\Delta B/L_b = 0.1$, Expansion ratio = $(B+2\Delta B)/B = 1.41$, $(B+2\Delta B)/L_b = 0.69$) for a high discharge ($Q = 57$ l/s, $Re_m = 66'000$; $Fr = 0.44$). Flow direction is **from the right to the left side**. The dye is introduced in the downstream part of the cavity. The flow does reattach, the dye can't move upstream.

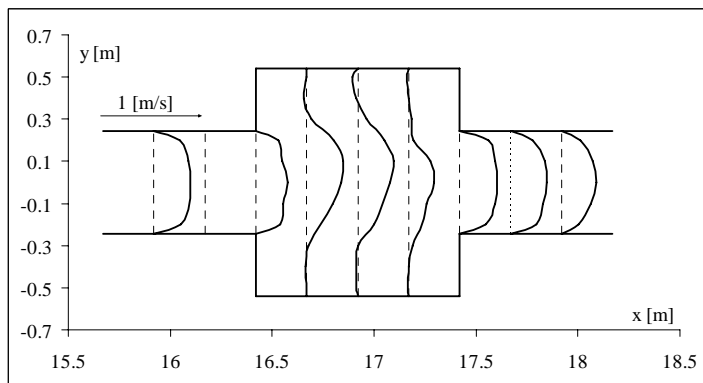
A 4-4: Horizontal velocity profiles in configurations 221, 222, 223 and 224



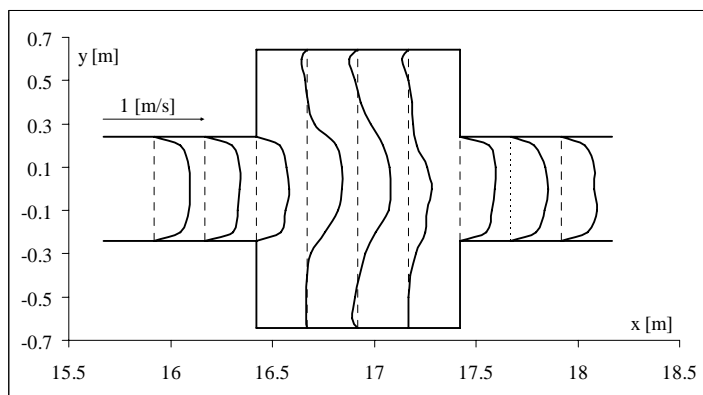
221



222

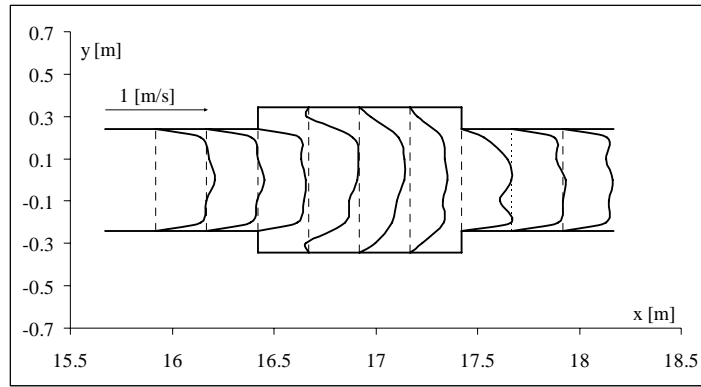


223

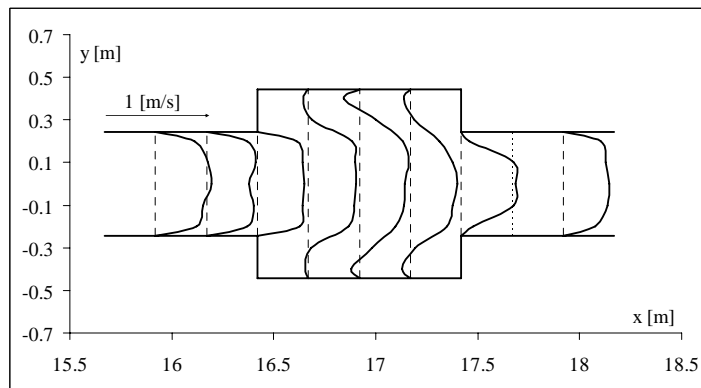


224

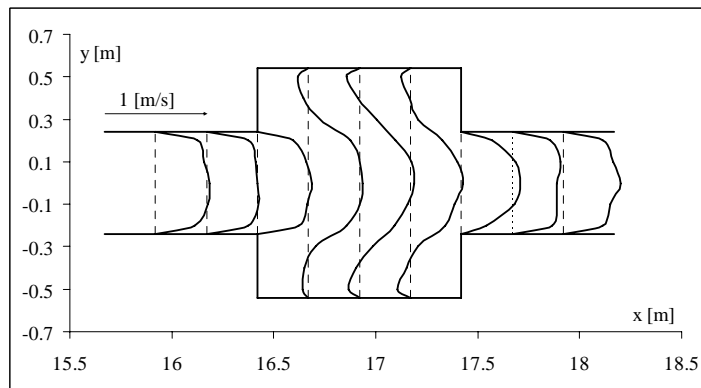
Fig-A4.64: Velocity profiles (horizontal) at z -levels $z = 0.5 \div 0.6 h_{max}$ for configurations 221, 222, 223 and 224. The dashed line indicates a velocity of $u = 0$ [m/s] for a given section. Discharge is $5 \div 6$ l/s.



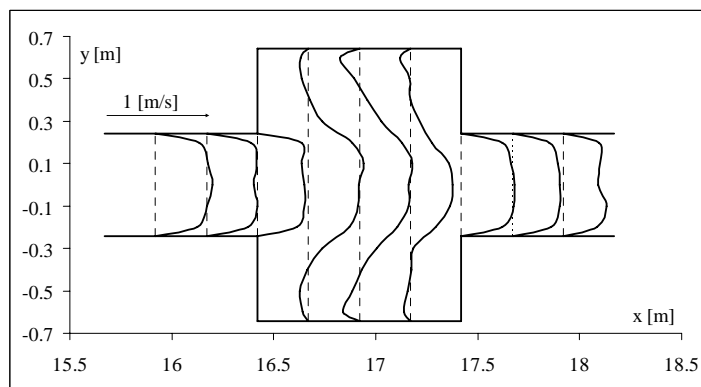
221



222

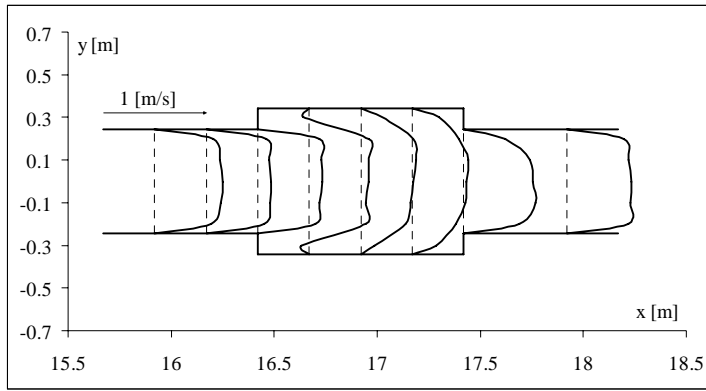


223

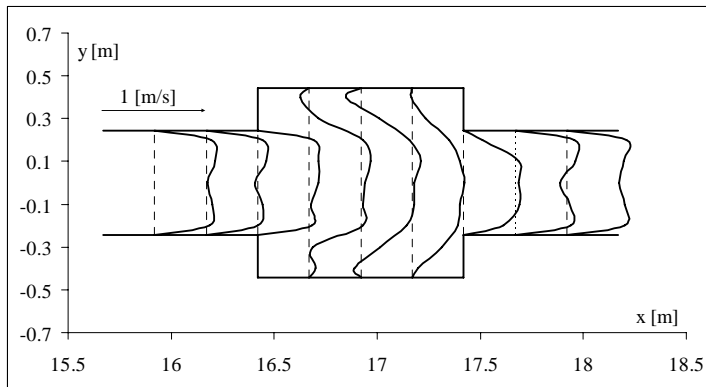


224

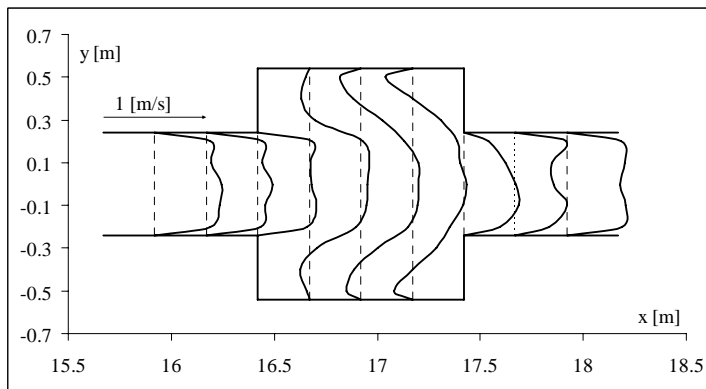
Fig-A4.65: Velocity profiles (horizontal) at z -levels $z = 0.5 \div 0.6 h_{max}$ for configurations 221, 222, 223 and 224. The dashed line indicates a velocity of $u = 0$ [m/s] for a given section. Discharge is $19 \div 20$ l/s.



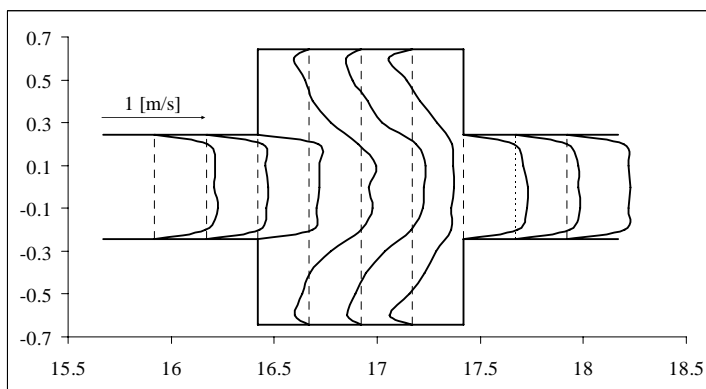
221



222



223



224

Fig-A4.66: Velocity profiles (horizontal) at z -levels $z = 0.5 \div 0.6 h_{max}$ for configurations 221, 222, 223 and 224. The dashed line indicates a velocity of $u = 0$ [m/s] for a given section. Discharge is $48 \div 49$ l/s.

A 4-5: Head-loss computation through sudden channel transitions: Enlargement and contraction

When considering a sudden enlargement (Figure A4.21, left side) one can find the headloss ΔH_{exp} by using the theorems of Belanger and Borda (Carlier 1986). It is expressed as:

$$\Delta H_{exp} = \frac{U_2^2}{2g} \left(\frac{1}{m-1} \right)^2 \quad (\text{eq. A4.1})$$

where U_2 is the mean flow velocity in the large section and $m = A_1/A_2$ the ratio between the flow area at the small (A_1) and the large (A_2) channel section.

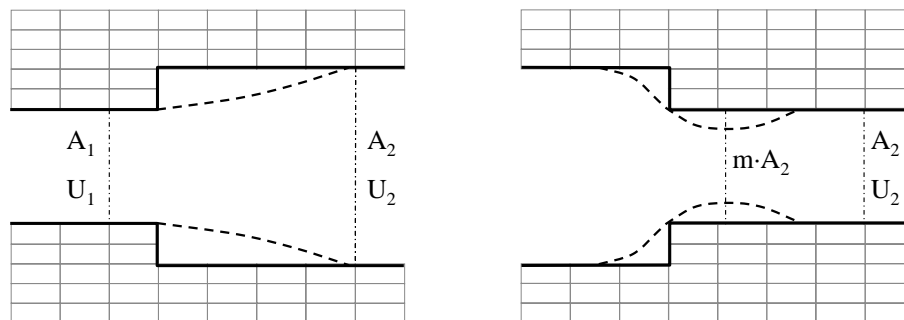


Fig-A4.67: Flow through channel transitions. Enlargement (left) and contraction (right side).

This formulation is however based on several assumptions namely:

- the flow must reattach to the side wall
- zero velocity of the water in the recirculation zone
- no wall friction
- $\beta_2 = \beta_1 = 1$ where β_2 and β_1 are the momentum correction coefficients respectively
- $\alpha_2 = \alpha_1 = 1$ where α_2 and α_1 are the energy correction coefficients respectively

When considering the sudden contraction of a significant length, the same formulation is used. A minimum length is necessary in order to ensure that the flow can reattach to the side wall after the contraction. If not, the contraction has to be considered as a diaphragm.

$$\Delta H_{cont} = \frac{U_2^2}{2g} \left(\frac{1}{m-1} \right)^2 \quad (\text{eq. A4.2})$$

where m is the ratio between the flow area at the contracted section and the flow area after the reattachment of the streamlines to the side walls (Figure A4.21, right side).

Furthermore, comparison with experiments showed more accurate results when using following formula:

$$\Delta H = \frac{U_2^2}{2g} \left[\left(\frac{1}{m} - 1 \right)^2 + \frac{1}{9} \right] \quad (\text{eq. A4.3})$$

Alternatively, the headloss of channel transitions can be computed by combining the energy (eq. A4.4) and the momentum (eq. A4.5) equation:

$$h_r + h_s = z_1 - z_2 + \frac{p_1 - p_2}{\gamma} + (1 + a_1) \frac{U_1^2}{2g} - (1 + a_2) \frac{U_2^2}{2g} \quad (\text{eq. A4.4})$$

$$\frac{\Sigma F}{\gamma \cdot A_2} = z_1 - z_2 + \frac{p_1 - p_2}{\gamma} = \frac{U_2}{g} [U_2(1 + b_2) - U_1(1 + b_1)] \quad (\text{eq. A4.5})$$

where h_r and h_s are the linear and single headlosses and z_1 and z_2 the bottom elevation. p_1 and p_2 are the pressure head.

The combination of these two equations neglecting the linear headloss leads to:

$$h_s = \frac{U_2}{g} [U_2(1 + b_2) - U_1(1 + b_1)] + (1 + a_1) \frac{U_1^2}{2g} - (1 + a_2) \frac{U_2^2}{2g} \quad (\text{eq. A4.6})$$

And after simplifications:

$$J_{12} \cdot \Delta x = \frac{U_2^2}{g} \left[\left(\frac{A_2}{A_1} - 1 \right)^2 + \left(\frac{A_2}{A_1} \right)^2 a_1 - \frac{A_2}{A_1} 2b_1 + (2b_2 - a_2) \right] \quad (\text{eq. A4.7})$$

where J_{12} expresses the energy slope between the two sections 1 (upstream) and 2 (downstream) at a distance Δx . a_i and b_i corresponds to $(\alpha_i - 1)$ and $(\beta_i - 1)$ respectively where α and β are the energy and momentum correction coefficients respectively. They are expressed as:

$$\alpha_i = \frac{1}{A_i} \int_{A_i} \left(\frac{u}{U_i} \right)^3 dA_i \quad (\text{eq. A4.8})$$

$$\beta_i = \frac{1}{A_i} \int_{A_i} \left(\frac{u}{U_i} \right)^2 dA_i \quad (\text{eq. A4.9})$$

where the index i corresponds to the section 1 respectively 2. u is the local velocity perpendicular to the flow area A_i .

Thus, by measuring the flow depths h_1 and h_2 , the local velocities in the two sections, the steady discharge Q and knowing the width B_1 and B_2 , the total headloss J_{12} between two sections can be calculated. Furthermore, from (eq. A4.6) it can be easily understood that the formulation from the theorems of Belanger and Borda is found assuming a_1 , b_1 , a_2 and b_2 equal to zero. Finally, the term $1/9$ in (eq. A4.3) found from the experiments expresses the influence of the non-uniformity of the velocity in the sections 1 and 2.

A 4-6: Test results for the cavity oscillations

- Q : Discharge
- h : Flow depth
- Re_m : Reynolds number relative to the base width B
- a_+ : Mean wave height at $y = \pm B/2 + \Delta B$
- a_+/h : Relative mean wave height at $y = \pm B/2 + \Delta B$
- $a_{B/2}$: Mean wave height at $y = \pm B/2$
- $f_{cal(n=1)} \text{ (simpl.)}$: Calculated frequency of the transverse oscillations assuming mode $n=1$ with the simplified formula (seiching)
- $f_{cal(n=1)} \text{ (exact)}$: Calculated frequency of the transverse oscillations assuming mode $n=1$ with the complete formula (sloshing)
- f_{FFT} : Observed frequency of the most powerful watersurface oscillations detected with FFT-analysis
- St_{Lb} : Calculated Strouhal number with L_b (cavity length)
- \bar{V}_{max} : transverse velocity averaged in space for situation 2 (= horizontal water-surface)
- V_{max} : maximum horizontal velocity at the node in situation 2
- $\Delta E_{pot1-2}/(L_b+L_c)$: difference in potential energy for the two situations with inclined and horizontal surface per distance
- $\Delta E_{pot1-2}/\Delta E_f$: upper limit for the part of energy loss due to transverse oscillations

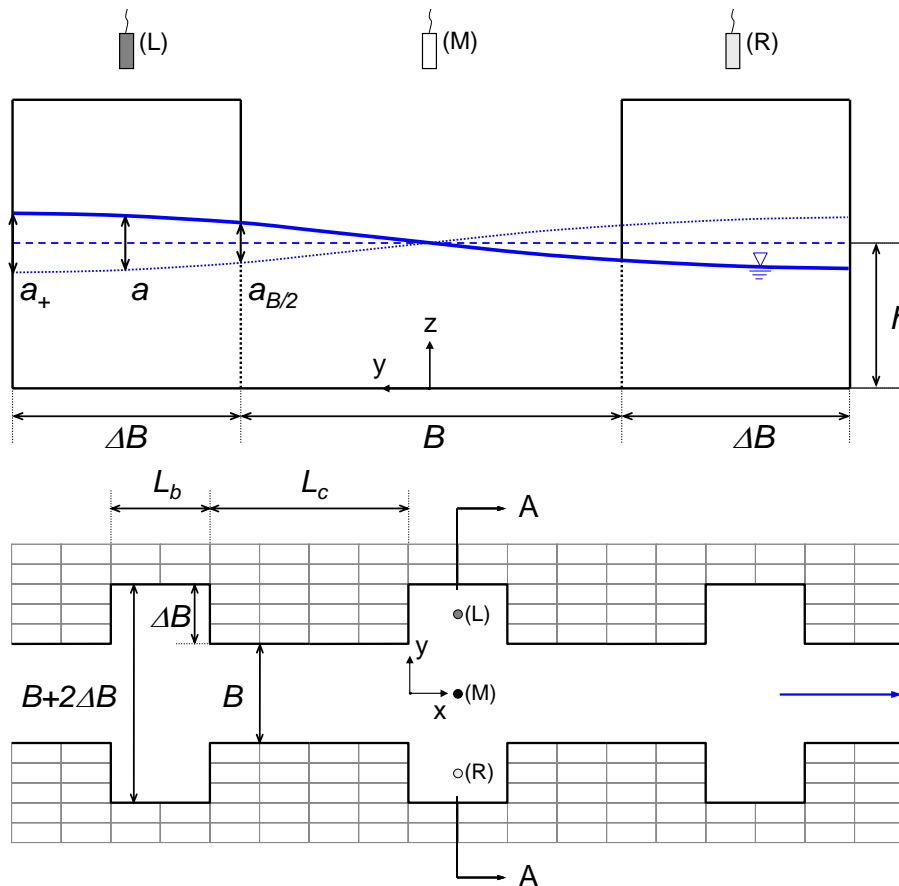


Fig-A4.68: Definition of the parameters relative to the transverse oscillations of the flow.

APPENDIX 4-6

Conf.	Q	h	Re	a_s	a_s/h	a_{B2}	$f_{cal(n=1)}$ (simpl)	$f_{cal(n=1)}$ (exact)	f_{FFT}	Score n=1	Score n=2	St_{Lb}	\bar{V}_{max}	V_{max}	$(\Delta E_{post-2}) / (L_p + L_c)$	$(\Delta E_{post-2}) / \Delta E_f$
[]	[m3/s]	[m]	[]	[m]	[%]	[m]	[Hz]	[Hz]	[Hz]	[]	[]	[]	[m/s]	[m/s]	[J/m]	[%]
111	0.0045	0.0274	8267	0.0014	5.2%	0.00127	0.378	0.377	0.450	0	1	0.610	0.009	0.013	0.0004	0.3%
111	0.0100	0.0485	17169	0.0026	5.5%	0.00238	0.504	0.500	0.533	3	0	0.590	0.013	0.019	0.0015	0.6%
111	0.0154	0.0689	24630	0.0043	6.3%	0.00387	0.600	0.590	0.617	3	0	0.637	0.018	0.026	0.0039	1.0%
111	0.0193	0.0825	29592	0.0056	6.8%	0.00505	0.657	0.642	0.667	3	0	0.660	0.022	0.031	0.0067	1.2%
111	0.0283	0.1126	39887	0.0085	7.6%	0.00765	0.767	0.736	0.767	3	0	0.698	0.028	0.040	0.0153	1.7%
111	0.0369	0.1409	48237	0.0081	5.8%	0.00727	0.858	0.805	0.817	3	0	0.733	0.024	0.034	0.0138	1.0%
111	0.0441	0.1646	54460	0.0066	4.0%	0.00594	0.928	0.853	0.867	2	0	0.755	0.018	0.026	0.0092	0.5%
111	0.0574	0.2008	64817	0.0110	5.5%	0.00989	1.024	0.910	0.917	3	0	0.763	0.027	0.039	0.0256	1.0%
111	0.0699	0.2298	73947	0.0111	4.8%	0.00997	1.096	0.945	0.933	3	0	0.747	0.026	0.036	0.0260	0.8%
111	0.0868	0.2640	85484	0.0074	2.8%	0.00660	1.175	0.977	0.967	0	1	0.718	0.016	0.022	0.0114	0.3%
111	0.1043	0.3078	94732	0.0100	3.2%	0.00895	1.268	1.006	0.983	0	2	0.715	0.020	0.028	0.0209	0.4%
111	0.1206	0.3426	103052	0.0112	3.3%	0.01003	1.338	1.022	0.933	0	2	0.700	0.021	0.030	0.0263	0.4%
112	0.0052	0.0299	9328	0.0013	4.3%	0.00097	0.306	0.306	0.267	1	2	0.468	0.008	0.012	0.0004	0.3%
112	0.0092	0.0451	15818	0.0022	4.8%	0.00165	0.376	0.374	0.317	0	1	0.455	0.011	0.016	0.0013	0.6%
112	0.0151	0.0648	24479	0.0040	6.2%	0.00305	0.450	0.447	0.383	1	1	0.463	0.018	0.025	0.0044	1.3%
112	0.0205	0.0834	31407	0.0064	7.6%	0.00482	0.511	0.504	0.433	1	1	0.496	0.024	0.034	0.0109	2.1%
112	0.0281	0.1106	39753	0.0072	6.5%	0.00548	0.588	0.574	0.500	1	1	0.544	0.024	0.034	0.0142	1.6%
112	0.0350	0.1337	46562	0.0057	4.3%	0.00432	0.647	0.624	0.383	0	2	0.571	0.017	0.024	0.0088	0.7%
112	0.0459	0.1642	56402	0.0086	5.2%	0.00653	0.717	0.680	0.017	0	2	0.585	0.024	0.033	0.0201	1.1%
112	0.0585	0.1963	66552	0.0081	4.1%	0.00613	0.784	0.729	1.117	0	2	0.590	0.020	0.029	0.0177	0.8%
112	0.0703	0.2215	75766	0.0095	4.3%	0.00717	0.833	0.761	1.167	0	1	0.576	0.022	0.031	0.0242	0.9%
112	0.0848	0.2531	85309	0.0094	3.7%	0.00714	0.890	0.794	0.600	0	2	0.573	0.021	0.029	0.0240	0.8%
112	0.1027	0.2920	96053	0.0086	2.9%	0.00652	0.956	0.828	1.267	0	2	0.566	0.018	0.025	0.0201	0.5%
112	0.1203	0.3275	105813	0.0091	2.8%	0.00689	1.013	0.851	0.933	0	2	0.555	0.018	0.025	0.0224	0.5%
113	0.0054	0.0318	9748	0.0034	10.6%	0.00217	0.257	0.257	0.283	3	0	0.386	0.021	0.030	0.0038	2.5%
113	0.0096	0.0474	16385	0.0059	12.5%	0.00382	0.314	0.313	0.333	3	0	0.390	0.030	0.043	0.0116	4.7%
113	0.0154	0.0699	24491	0.0073	10.4%	0.00471	0.382	0.379	0.417	3	0	0.426	0.031	0.043	0.0177	3.9%
113	0.0195	0.0829	29718	0.0105	12.7%	0.00679	0.416	0.412	0.433	2	1	0.434	0.040	0.057	0.0367	6.1%
113	0.0274	0.1086	38613	0.0070	6.4%	0.00452	0.476	0.468	0.483	2	0	0.458	0.024	0.033	0.0163	1.7%
113	0.0369	0.1341	48380	0.0091	6.8%	0.00585	0.529	0.516	0.500	2	0	0.466	0.027	0.039	0.0273	2.0%
113	0.0472	0.1613	57503	0.0166	10.3%	0.01073	0.580	0.560	0.583	3	0	0.478	0.046	0.065	0.0918	5.1%
113	0.0592	0.1927	67481	0.0085	4.4%	0.00547	0.634	0.604	0.600	1	1	0.480	0.021	0.030	0.0238	1.1%
113	0.0711	0.2209	75518	0.0195	8.8%	0.01256	0.678	0.637	0.650	3	0	0.492	0.046	0.065	0.1259	4.3%
113	0.0860	0.2538	86092	0.0217	8.6%	0.01404	0.727	0.671	0.683	3	0	0.482	0.048	0.068	0.1572	5.0%
113	0.1054	0.2955	97642	0.0260	8.8%	0.01679	0.785	0.707	0.717	3	0	0.480	0.053	0.075	0.2248	6.0%
113	0.1198	0.3288	104660	0.0311	9.5%	0.02010	0.828	0.730	0.733	3	0	0.484	0.060	0.085	0.3222	6.9%
114	0.0038	0.0314	6841	0.0044	14.1%	0.00247	0.216	0.216	0.217	3	0	0.449	0.028	0.039	0.0077	4.6%
114	0.0105	0.0617	17020	0.0113	18.3%	0.00631	0.303	0.302	0.333	3	0	0.443	0.050	0.071	0.0503	10.8%
114	0.0152	0.0795	23350	0.0122	15.3%	0.00681	0.344	0.342	0.367	3	0	0.442	0.048	0.068	0.0585	8.5%
114	0.0196	0.0942	28772	0.0167	17.7%	0.00932	0.374	0.371	0.400	3	0	0.444	0.060	0.085	0.1096	11.9%
114	0.0280	0.1218	38052	0.0180	14.7%	0.01003	0.425	0.419	0.450	3	0	0.449	0.057	0.081	0.1270	9.2%
114	0.0357	0.1492	45286	0.0120	8.1%	0.00673	0.471	0.461	0.483	3	0	0.469	0.035	0.049	0.0571	2.9%
114	0.0480	0.1820	56220	0.0108	6.0%	0.00605	0.520	0.504	0.517	3	0	0.464	0.028	0.040	0.0462	1.7%
114	0.0594	0.2118	64653	0.0204	9.6%	0.01139	0.561	0.538	0.567	3	0	0.472	0.049	0.069	0.1638	4.6%
114	0.0704	0.2412	72246	0.0126	5.2%	0.00703	0.598	0.567	0.583	3	0	0.474	0.028	0.040	0.0624	1.5%
114	0.0835	0.2697	80570	0.0221	15.6%	0.02351	0.633	0.593	0.633	3	0	0.471	0.090	0.127	0.6976	13.6%
114	0.1044	0.3119	93142	0.0409	13.1%	0.02283	0.681	0.625	0.667	3	0	0.458	0.081	0.115	0.6574	10.9%
114	0.1142	0.3294	99313	0.0438	13.3%	0.02446	0.699	0.637	0.667	3	0	0.446	0.084	0.119	0.7551	12.7%

Conf.	Q	h	Re	a_s	a_s/h	a_{B2}	$f_{cal(n=1)}$ (simpl)	$f_{cal(n=1)}$ (exact)	f_{FFT}	Score n=1	Score n=2	St_{Lb}	\bar{V}_{max}	V_{max}	$(\Delta E_{post-2}) / (L_p + L_c)$	$(\Delta E_{post-2}) / \Delta E_f$
[]	[m3/s]	[m]	[]	[m]	[%]	[m]	[Hz]	[Hz]	[Hz]	[]	[]	[]	[m/s]	[m/s]	[J/m]	[%]
121	0.0056	0.0381	9979	0.0023	6.1%	0.00208	0.446	0.444	0.450	2	0	0.732	0.013	0.019	0.0008	0.2%
121	0.0097	0.0507	16567	0.0020	4.0%	0.00184	0.515	0.510	0.467	1	1	0.640	0.010	0.014	0.0006	0.1%
121	0.0142	0.0674	22887	0.0025	3.7%	0.00225	0.594	0.584	0.267	0	1	0.664	0.011	0.015	0.0009	0.1%
121	0.0206	0.0869	31249	0.0038	4.4%	0.00342	0.674	0.657	0.667	1	1	0.661	0.014	0.020	0.0020	0.2%
121	0.0274	0.1079	39095	0.0040	3.7%	0.00360	0.751	0.722	0.750	1	0	0.680	0.014	0.019	0.0023	0.2%
121	0.0360	0.1337	47891	0.0075	5.6%	0.00670	0.836	0.789	0.800	3	0	0.701	0.023	0.032	0.0078	0.4%
121	0.0449	0.1630	55449	0.0089	5.4%	0.00794	0.923	0.850	0.867	1	0	0.739	0.024	0.034	0.0110	0.4%
121	0.0576	0.1888	66737	0.0083	4.4%	0.00749	0.993	0.893	0.900	1	0	0.703	0.021	0.030	0.0098	0.3%
121	0.0686	0.2174	74798	0.0074	3.4%	0.00666	1.066	0.931	0.917	1	1	0.705	0.018	0.025	0.0077	0.2%
121	0.0846	0.2555	85750	0.0082	3.2%	0.00734	1.156	0.970	1.083	0	2	0.692	0.018	0.025	0.0094	0.2%
121	0.1032	0.2981	96403	0.0080	2.7%	0.00720	1.248	1.000	1.133	0	2	0.683	0.016	0.023	0.0090	0.2%
121	0.1236	0.3438	106573	0.0093	2.7%	0.00834	1.341	1.023	0.533	0	2	0.672	0.018	0.025	0.0121	0.2%
122	0.0046	0.0318	8325	0.0011	3.4%	0.00081	0.316	0.315	0.250	0	1	0.537	0.007	0.009	0.0002	0.1%
122	0.0098	0.0514	16600	0.0018	3.5%	0.00136	0.401	0.399	0.367	1	1	0.505	0.009	0.012	0.0006	0.1%
122	0.0152	0.0679	24408	0.0034	5.0%	0.00260	0.461	0.457	0.417	1	1	0.493	0.015	0.021	0.0021	0.3%
122	0.0197	0.0831	30092	0.0045	5.4%	0.00341	0.510	0.503	0.867	0	2	0.516	0.017	0.024	0.0037	0.4%
122	0.0271	0.1060	38750	0.0051	4.8%	0.00386	0.576	0.563	0.983	0	3	0.534	0.017	0.024	0.0047	0.4%
122	0.0358	0.1337	47389	0.0067	5.0%	0.00508	0.647	0.624	1.017	0	2	0.566	0.020	0.029	0.0081	0.4%
122	0.0447	0.1591	55383	0.0088	5.6%	0.00671	0.706	0.672	1.100	0	3	0.580	0.025	0.035	0.0142	0.5%
122	0.0578	0.1904	66668	0.0118	6.2%	0.00898	0.772	0.721	1.150	0	3	0.572	0.030	0.043	0.0254	0.8%
122	0.0699	0.2130	76568	0.0070	3.3%	0.00528	0.817	0.751	1.150	0	1	0.553				

Conf.	Q	h	Re	a_s	a_s/h	$a_{B/2}$	$f_{cal(n=1)}$ (simpl)	$f_{cal(n=1)}$ (exact)	f_{FFT}	Score n=1	Score n=2	St _{Lb}	\bar{V}_{max}	V _{max}	$(\Delta E_{post-2})/$ (L _b +L _c)	$(\Delta E_{post-2})/$ ΔE_f
[]	[m ³ /s]	[m]	[]	[m]	[%]	[m]	[Hz]	[Hz]	[Hz]	[]	[]	[]	[m/s]	[m/s]	[J/m]	[%]
141	0.0039	0.0279	7130	0.0026	9.4%	0.00235	0.382	0.381	0.400	3	0	0.683	0.017	0.025	0.0006	0.2%
141	0.0093	0.0480	15892	0.0024	5.1%	0.00219	0.501	0.497	0.517	2	0	0.623	0.012	0.017	0.0005	0.1%
141	0.0145	0.0652	23616	0.0027	4.1%	0.00238	0.584	0.575	0.600	2	0	0.615	0.012	0.016	0.0006	0.1%
141	0.0210	0.0843	32098	0.0034	4.0%	0.00302	0.664	0.648	0.733	1	1	0.621	0.013	0.018	0.0010	0.1%
141	0.0274	0.1038	39626	0.0040	3.9%	0.00359	0.736	0.710	0.783	1	1	0.640	0.014	0.019	0.0013	0.1%
141	0.0368	0.1298	49778	0.0080	6.2%	0.00720	0.824	0.780	0.817	3	0	0.647	0.025	0.035	0.0054	0.2%
141	0.0456	0.1503	58416	0.0055	3.7%	0.00496	0.886	0.825	0.850	2	1	0.641	0.016	0.022	0.0026	0.1%
141	0.0564	0.1790	67223	0.0058	3.3%	0.00525	0.967	0.877	0.883	1	1	0.662	0.015	0.022	0.0029	0.1%
141	0.0702	0.2119	77855	0.0074	3.5%	0.00664	1.052	0.924	1.100	0	2	0.659	0.018	0.025	0.0046	0.1%
141	0.0852	0.2497	87409	0.0082	3.3%	0.00733	1.142	0.964	1.117	0	1	0.667	0.018	0.026	0.0056	0.1%
141	0.1048	0.2954	98664	0.0099	3.4%	0.00888	1.243	0.999	1.067	0	1	0.662	0.020	0.029	0.0082	0.1%
141	0.1255	0.3358	109988	0.0121	3.6%	0.01085	1.325	1.020	0.517	0	1	0.642	0.023	0.033	0.0123	0.1%
142	0.0044	0.0298	7937	0.0009	2.9%	0.00067	0.305	0.305	0.283	2	1	0.525	0.006	0.008	0.0001	0.0%
142	0.0101	0.0508	17139	0.0030	6.0%	0.00231	0.399	0.397	0.717	0	2	0.490	0.015	0.021	0.0010	0.1%
142	0.0150	0.0651	24128	0.0061	9.4%	0.00462	0.451	0.447	0.833	0	3	0.482	0.026	0.037	0.0040	0.4%
142	0.0199	0.0807	30598	0.0054	6.7%	0.00412	0.503	0.496	0.900	0	3	0.492	0.021	0.030	0.0032	0.2%
142	0.0280	0.1054	40089	0.0074	7.0%	0.00559	0.574	0.562	0.983	0	3	0.513	0.025	0.036	0.0059	0.3%
142	0.0356	0.1261	48127	0.0067	5.3%	0.00510	0.628	0.609	1.067	0	3	0.522	0.021	0.030	0.0049	0.2%
142	0.0460	0.1554	57975	0.0101	6.5%	0.00768	0.698	0.665	1.117	0	3	0.536	0.028	0.040	0.0111	0.3%
142	0.0588	0.1837	69045	0.0067	3.7%	0.00512	0.758	0.711	0.650	0	1	0.532	0.017	0.025	0.0049	0.1%
142	0.0703	0.2081	77994	0.0087	4.2%	0.00657	0.807	0.745	1.217	0	3	0.530	0.021	0.030	0.0082	0.2%
142	0.0843	0.2380	87410	0.0098	4.1%	0.00741	0.863	0.779	0.700	0	0	0.533	0.022	0.031	0.0104	0.2%
142	0.1047	0.2826	100056	0.0096	3.4%	0.00727	0.941	0.820	1.350	0	3	0.529	0.020	0.028	0.0100	0.2%
142	0.1234	0.3197	110008	0.0112	3.5%	0.00853	1.001	0.847	0.750	0	1	0.526	0.022	0.031	0.0137	0.2%
143	0.0051	0.0343	9234	0.0052	15.3%	0.00339	0.267	0.267	0.267	3	0	0.441	0.031	0.044	0.0037	0.8%
143	0.0098	0.0505	16585	0.0140	27.6%	0.00901	0.324	0.323	0.333	3	0	0.419	0.069	0.097	0.0259	3.3%
143	0.0152	0.0672	24243	0.0175	26.0%	0.01130	0.374	0.372	0.383	3	0	0.412	0.075	0.106	0.0407	3.6%
143	0.0193	0.0795	29577	0.0187	23.5%	0.01206	0.407	0.403	0.417	3	0	0.418	0.073	0.104	0.0464	3.2%
143	0.0278	0.1045	39372	0.0260	24.9%	0.01679	0.467	0.460	0.483	3	0	0.438	0.089	0.126	0.0900	4.0%
143	0.0358	0.1252	48120	0.0244	19.5%	0.01578	0.511	0.500	0.517	3	0	0.434	0.076	0.108	0.0794	3.0%
143	0.0454	0.1515	57000	0.0203	13.4%	0.01309	0.562	0.545	0.567	3	0	0.448	0.058	0.082	0.0547	1.6%
143	0.0578	0.1803	67673	0.0268	14.9%	0.01732	0.613	0.587	0.600	3	0	0.450	0.070	0.099	0.0956	2.3%
143	0.0704	0.2104	76990	0.0227	10.8%	0.01465	0.662	0.625	0.633	3	0	0.459	0.055	0.077	0.0685	1.3%
143	0.0845	0.2399	86520	0.0268	11.2%	0.01730	0.707	0.658	0.650	3	0	0.460	0.061	0.086	0.0955	1.6%
143	0.1029	0.2797	98249	0.0320	11.5%	0.02069	0.763	0.694	0.700	3	0	0.457	0.067	0.095	0.1366	2.1%
143	0.1217	0.3179	108286	0.0332	10.5%	0.02147	0.814	0.723	0.717	3	0	0.457	0.065	0.092	0.1470	1.8%
144	0.0058	0.0387	10195	0.0088	22.8%	0.00493	0.240	0.239	0.250	3	0	0.402	0.050	0.070	0.0123	2.1%
144	0.0098	0.0572	16243	0.0179	31.3%	0.01002	0.292	0.291	0.317	3	0	0.419	0.083	0.117	0.0507	5.0%
144	0.0149	0.0760	23170	0.0210	27.6%	0.01174	0.336	0.334	0.350	3	0	0.419	0.084	0.119	0.0695	4.5%
144	0.0197	0.0896	29366	0.0235	26.3%	0.01315	0.365	0.362	0.383	3	0	0.407	0.087	0.123	0.0873	4.5%
144	0.0281	0.1155	38954	0.0288	25.0%	0.01611	0.414	0.409	0.433	3	0	0.413	0.094	0.133	0.1310	4.6%
144	0.0377	0.1450	48307	0.0391	27.0%	0.02184	0.464	0.455	0.483	3	0	0.428	0.114	0.161	0.2407	5.8%
144	0.0460	0.1698	55565	0.0276	16.2%	0.01539	0.502	0.489	0.500	3	0	0.437	0.074	0.105	0.1196	2.3%
144	0.0578	0.1984	65293	0.0318	16.0%	0.01779	0.543	0.523	0.533	3	0	0.435	0.079	0.112	0.1596	2.5%
144	0.0688	0.2234	73568	0.0339	15.2%	0.01896	0.576	0.550	0.567	3	0	0.432	0.079	0.112	0.1815	2.5%
144	0.0854	0.2503	85445	0.0494	19.7%	0.02759	0.610	0.576	0.600	3	0	0.417	0.109	0.155	0.3841	4.8%
144	0.1019	0.2867	95048	0.0504	17.6%	0.02815	0.653	0.606	0.633	3	0	0.420	0.104	0.147	0.4001	4.1%
144	0.1162	0.3106	104194	0.0495	15.9%	0.02765	0.679	0.624	0.650	3	0	0.407	0.098	0.139	0.3860	4.2%

Conf.	Q	h	Re	a_s	a_s/h	$a_{B/2}$	$f_{cal(n=1)}$ (simpl)	$f_{cal(n=1)}$ (exact)	f_{FFT}	Score n=1	Score n=2	St _{Lb}	\bar{V}_{max}	V _{max}	$(\Delta E_{post-2})/$ (L _b +L _c)	$(\Delta E_{post-2})/$ ΔE_f
[]	[m ³ /s]	[m]	[]	[m]	[%]	[m]	[Hz]	[Hz]	[Hz]	[]	[]	[]	[m/s]	[m/s]	[J/m]	[%]
211	0.0056	0.0340	10170	0.0018	5.4%	0.00164	0.421	0.420	0.217	0	2	1.221	0.011	0.016	0.0009	0.4%
211	0.0099	0.0478	16957	0.0025	5.3%	0.00227	0.500	0.496	0.217	1	0	1.158	0.013	0.018	0.0018	0.5%
211	0.0156	0.0680	25160	0.0027	3.9%	0.00238	0.596	0.587	0.150	1	0	1.199	0.011	0.016	0.0020	0.4%
211	0.0199	0.0843	30607	0.0031	3.7%	0.00279	0.664	0.648	0.300	1	0	1.278	0.012	0.017	0.0027	0.4%
211	0.0278	0.1129	39535	0.0036	3.2%	0.00321	0.768	0.737	0.333	1	1	1.385	0.012	0.017	0.0036	0.3%
211	0.0366	0.1447	47743	0.0042	2.9%	0.00372	0.870	0.814	0.400	0	0	1.498	0.012	0.017	0.0048	0.2%
211	0.0459	0.1736	55855	0.0043	2.5%	0.00385	0.953	0.869	0.350	0	2	1.529	0.011	0.016	0.0052	0.2%
211	0.0587	0.2067	65905	0.0048	2.3%	0.00427	1.039	0.918	0.433	0	0	1.521	0.012	0.016	0.0063	0.1%
211	0.0702	0.2371	73821	0.0054	2.3%	0.00489	1.113	0.952	0.900	0	0	1.520	0.012	0.018	0.0083	0.2%
211	0.0849	0.2730	82967	0.0056	2.1%	0.00502	1.195	0.984	0.250	0	1	1.499	0.012	0.017	0.0088	0.1%
211	0.1022	0.3141	92665	0.0071	2.2%	0.00633	1.281	1.009	0.550	0	2	1.468	0.014	0.020	0.0140	0.2%
211	0.1143	0.3400	99010	0.0061	1.8%	0.00548	1.333	1.021	0.517	0	2	1.440	0.012	0.016	0.0104	0.1%
212	0.0037	0.0244	6798	0.0011	4.6%	0.00085	0.276	0.276	0.200	0	1	0.959	0.008	0.011	0.0005	0.3%
212	0.0101	0.0498	17165	0.0030	6.1%	0.00229	0.395	0.393	0.133	0	2	0.945	0.015	0.021	0.0033	0.8%
212	0.0151	0.0672	24365	0.0035	5.2%	0.00262	0.459	0.454	0.317	1	0	0.968	0.015	0.021	0.0043	0.7%
212	0.0197	0.0834	30196	0.0040	4.8%	0.00304	0.511	0.504	0.317	1	0	1.019	0.015	0.022	0.0058	0.7%
212	0.0278	0.1128	39219	0.0052	4.6%	0.00392	0.594	0.579	0.017	0	2	1.117	0.017	0.024	0.0097	0.7%
212	0.0360	0.1418	46920	0.0063	4.5%	0.00481	0.666	0.640	0.017	0	2	1.201	0.019	0.026	0.0145	0.6%
212	0.0462	0.1738	55723	0.0076	4.3%	0.00573	0.738	0.696	0.183	0	1	1.245	0.020	0.028	0.0207	0.6%
212	0.0586	0.2114	64813	0.0101	4.8%	0.00764	0.814	0.749	0.200	0	2	1.286	0.024	0.034	0.0367	0.7%
212	0.0686	0.2389	71373	0.0101	4.2%	0.00765										

APPENDIX 4-6

Conf.	Q	h	Re	a_s	a_s/h	a_{B2}	$f_{cal(n=1)}$ (simpl)	$f_{cal(n=1)}$ (exact)	f_{FFT}	Score n=1	Score n=2	St_{LB}	\bar{V}_{max}	V_{max}	$(\Delta E_{post-2}) / (L_s + L_c)$	$(\Delta E_{post-2}) / \Delta E_f$
[]	[m ³ /s]	[m]	[]	[m]	[]	[m]	[Hz]	[Hz]	[Hz]	[]	[]	[]	[m/s]	[m/s]	[]	[]
221	0.0059	0.0368	10499	0.0016	4.4%	0.00147	0.439	0.437	0.250	0	0	1.295	0.009	0.013	0.0006	0.2%
221	0.0106	0.0543	18006	0.0021	3.9%	0.00189	0.533	0.527	0.217	1	0	1.247	0.010	0.014	0.0009	0.2%
221	0.0152	0.0721	24381	0.0024	3.4%	0.00219	0.614	0.603	0.283	1	0	1.314	0.010	0.014	0.0013	0.2%
221	0.0194	0.0849	29888	0.0029	3.4%	0.00259	0.666	0.650	0.300	1	0	1.308	0.011	0.016	0.0018	0.2%
221	0.0274	0.1117	39145	0.0034	3.1%	0.00306	0.764	0.733	0.333	1	0	1.377	0.011	0.016	0.0024	0.2%
221	0.0367	0.1434	48294	0.0045	3.2%	0.00405	0.866	0.811	0.367	1	1	1.460	0.013	0.019	0.0033	0.2%
221	0.0459	0.1695	56487	0.0050	2.9%	0.00448	0.941	0.862	0.400	0	1	1.475	0.013	0.019	0.0052	0.2%
221	0.0574	0.2016	65474	0.0048	2.4%	0.00429	1.027	0.911	0.417	1	1	1.495	0.012	0.017	0.0048	0.1%
221	0.0698	0.2324	74271	0.0056	2.4%	0.00505	1.102	0.948	0.450	0	1	1.484	0.013	0.018	0.0067	0.1%
221	0.0855	0.2703	84425	0.0081	3.0%	0.00724	1.189	0.982	0.483	0	2	1.457	0.017	0.024	0.0137	0.2%
221	0.1000	0.3033	93020	0.0086	2.8%	0.00773	1.259	1.003	0.500	0	2	1.425	0.017	0.025	0.0156	0.2%
221	0.1097	0.3249	98529	0.0105	3.2%	0.00940	1.303	1.015	0.517	0	2	1.400	0.020	0.029	0.0231	0.2%
222	0.0055	0.0376	9739	0.0023	6.2%	0.00178	0.343	0.342	0.133	1	1	1.110	0.013	0.019	0.0015	0.4%
222	0.0105	0.0546	17627	0.0031	5.7%	0.00238	0.414	0.411	0.167	1	1	1.016	0.015	0.021	0.0027	0.4%
222	0.0152	0.0717	24252	0.0040	5.5%	0.00302	0.474	0.469	0.183	1	1	1.043	0.016	0.023	0.0043	0.5%
222	0.0200	0.0863	30543	0.0053	6.2%	0.00404	0.520	0.512	0.200	1	0	1.037	0.020	0.028	0.0077	0.7%
222	0.0283	0.1149	39873	0.0057	4.9%	0.00429	0.600	0.584	0.233	1	1	1.112	0.019	0.026	0.0087	0.5%
222	0.0353	0.1406	46442	0.0076	5.4%	0.00576	0.664	0.638	0.417	1	1	1.193	0.022	0.032	0.0157	0.6%
222	0.0474	0.1704	57514	0.0077	4.5%	0.00582	0.730	0.690	0.450	1	0	1.185	0.021	0.029	0.0160	0.4%
222	0.0583	0.2031	65845	0.0099	4.9%	0.00753	0.797	0.738	0.483	0	1	1.218	0.024	0.034	0.0267	0.5%
222	0.0716	0.2350	75446	0.0090	3.8%	0.00685	0.858	0.776	0.517	0	1	1.210	0.021	0.029	0.0221	0.4%
222	0.0848	0.2674	83779	0.0102	3.8%	0.00770	0.915	0.808	0.517	0	1	1.209	0.022	0.031	0.0280	0.4%
222	0.0995	0.3031	92188	0.0110	3.6%	0.00835	0.974	0.836	0.550	1	0	1.202	0.022	0.031	0.0329	0.4%
222	0.1114	0.3294	98559	0.0118	3.6%	0.00895	1.016	0.853	0.583	1	1	1.189	0.023	0.032	0.0378	0.4%
223	0.0059	0.0385	10454	0.0065	16.9%	0.00420	0.283	0.283	0.283	3	0	0.884	0.037	0.052	0.0141	3.6%
223	0.0092	0.0513	15659	0.0083	16.3%	0.00539	0.327	0.326	0.333	3	0	0.868	0.041	0.058	0.0232	4.0%
223	0.0147	0.0682	23645	0.0146	21.4%	0.00943	0.377	0.374	0.383	3	0	0.834	0.062	0.088	0.0710	8.6%
223	0.0200	0.0871	30399	0.0149	17.1%	0.00965	0.426	0.422	0.417	3	0	0.874	0.056	0.079	0.0742	6.2%
223	0.0279	0.1115	39486	0.0152	13.7%	0.00983	0.482	0.474	0.483	3	0	0.901	0.050	0.071	0.0771	4.4%
223	0.0355	0.1376	46916	0.0091	6.6%	0.00590	0.535	0.522	0.517	3	0	0.960	0.027	0.039	0.0278	1.1%
223	0.0465	0.1710	56575	0.0105	6.2%	0.00679	0.597	0.574	0.567	3	0	1.001	0.028	0.040	0.0368	1.0%
223	0.0589	0.2040	66138	0.0111	5.5%	0.00719	0.652	0.618	0.600	1	1	1.021	0.027	0.039	0.0412	0.8%
223	0.0707	0.2340	74630	0.0136	5.8%	0.00878	0.698	0.651	0.233	1	1	1.024	0.031	0.044	0.0614	1.0%
223	0.0829	0.2669	82049	0.0129	4.8%	0.00830	0.746	0.683	0.667	2	0	1.041	0.028	0.039	0.0550	0.7%
223	0.1028	0.3141	93380	0.0167	5.3%	0.01082	0.809	0.720	0.700	2	0	1.039	0.033	0.047	0.0933	0.9%
223	0.1099	0.3312	96951	0.0182	5.5%	0.01175	0.831	0.732	0.717	3	0	1.040	0.035	0.050	0.1101	1.0%
224	0.0040	0.0303	7323	0.0012	4.0%	0.00067	0.212	0.212	0.133	0	1	0.769	0.008	0.011	0.0006	0.2%
224	0.0094	0.0525	15941	0.0045	8.6%	0.00252	0.279	0.279	0.300	2	0	0.740	0.022	0.031	0.0080	1.4%
224	0.0144	0.0664	23334	0.0030	4.6%	0.00170	0.314	0.313	0.333	1	1	0.691	0.013	0.018	0.0036	0.5%
224	0.0200	0.0845	30546	0.0052	6.2%	0.00293	0.354	0.352	0.400	3	0	0.712	0.020	0.028	0.0108	1.0%
224	0.0285	0.1085	40428	0.0061	5.6%	0.00340	0.401	0.397	0.433	2	1	0.730	0.020	0.029	0.0146	0.9%
224	0.0360	0.1340	47789	0.0141	10.5%	0.00788	0.446	0.438	0.467	3	0	0.784	0.043	0.060	0.0783	3.3%
224	0.0453	0.1603	56136	0.0204	12.7%	0.01137	0.488	0.476	0.500	3	0	0.811	0.056	0.080	0.1632	5.1%
224	0.0588	0.1992	66791	0.0266	13.3%	0.01485	0.544	0.524	0.533	2	1	0.847	0.066	0.093	0.2784	6.0%
224	0.0711	0.2310	75563	0.0275	11.9%	0.01539	0.586	0.557	0.567	2	1	0.860	0.063	0.090	0.2990	5.2%
224	0.0851	0.2681	83973	0.0287	10.7%	0.01604	0.631	0.591	0.600	3	0	0.884	0.061	0.087	0.3247	4.3%
224	0.1018	0.3065	93480	0.0332	10.8%	0.01854	0.675	0.621	0.633	3	0	0.887	0.066	0.094	0.4338	4.6%
224	0.1086	0.3177	97625	0.0326	10.3%	0.01820	0.687	0.629	0.650	3	0	0.875	0.064	0.090	0.4178	4.4%

Conf.	Q	h	Re	a_s	a_s/h	a_{B2}	$f_{cal(n=1)}$ (simpl)	$f_{cal(n=1)}$ (exact)	f_{FFT}	Score n=1	Score n=2	St_{LB}	\bar{V}_{max}	V_{max}	$(\Delta E_{post-2}) / (L_s + L_c)$	$(\Delta E_{post-2}) / \Delta E_f$
[]	[m ³ /s]	[m]	[]	[m]	[]	[m]	[Hz]	[Hz]	[Hz]	[]	[]	[]	[m/s]	[m/s]	[]	[]
241	0.0049	0.0321	8950	0.0013	4.1%	0.00119	0.410	0.408	0.183	1	0	1.298	0.008	0.012	0.0002	0.1%
241	0.0094	0.0501	16029	0.0025	5.1%	0.00228	0.512	0.507	0.250	1	0	1.287	0.013	0.018	0.0009	0.1%
241	0.0150	0.0696	24051	0.0032	4.7%	0.00291	0.603	0.593	0.300	1	0	1.292	0.014	0.019	0.0015	0.1%
241	0.0203	0.0881	30981	0.0028	3.2%	0.00254	0.679	0.661	0.317	1	0	1.331	0.011	0.015	0.0011	0.1%
241	0.0289	0.1152	40848	0.0039	3.4%	0.00347	0.776	0.743	0.367	1	0	1.367	0.013	0.018	0.0021	0.1%
241	0.0365	0.1396	48431	0.0045	3.2%	0.00401	0.854	0.803	0.383	2	0	1.416	0.013	0.019	0.0028	0.1%
241	0.0464	0.1681	57200	0.0054	3.2%	0.00481	0.937	0.859	0.783	2	0	1.448	0.014	0.020	0.0040	0.1%
241	0.0584	0.1999	66874	0.0055	2.7%	0.00492	1.022	0.909	0.650	0	1	1.451	0.014	0.019	0.0042	0.1%
241	0.0703	0.2289	75870	0.0063	2.8%	0.00569	1.094	0.944	0.483	0	1	1.426	0.015	0.021	0.0056	0.1%
241	0.0842	0.2635	85138	0.0074	2.8%	0.00666	1.173	0.976	0.867	0	1	1.405	0.016	0.023	0.0077	0.1%
241	0.1034	0.3055	96217	0.0086	2.8%	0.00775	1.264	1.005	0.517	1	0	1.379	0.017	0.024	0.0105	0.1%
241	0.1193	0.3406	104304	0.0107	3.1%	0.00961	1.334	1.022	0.533	1	1	1.358	0.020	0.029	0.0161	0.1%
242	0.0043	0.0313	7765	0.0021	6.7%	0.00158	0.313	0.312	0.233	1	1	1.126	0.013	0.018	0.0008	0.2%
242	0.0096	0.0510	16219	0.0028	5.5%	0.00212	0.400	0.397	0.333	1	1	1.033	0.014	0.019	0.0014	0.2%
242	0.0142	0.0658	23010	0.0036	5.5%	0.00274	0.454	0.450	0.350	1	1	1.004	0.016	0.022	0.0024	0.2%
242	0.0201	0.0844	30728	0.0049	5.8%	0.00371	0.514	0.506	0.383	1	1	1.017	0.019	0.026	0.0043	0.3%
242	0.0272	0.1068	39059	0.0061	5.7%	0.00466	0.578	0.565	0.417	1	1	1.054	0.021	0.029	0.0068	0.3%
242	0.0365	0.1349	48392	0.0063	4.7%	0.00478	0.650	0.627	0.200	0	1	1.106	0.019	0.027	0.0072	0.2%
242	0.0473	0.1672	57910	0.0093	5.6%	0.00708	0.724	0.685	0.217	1	1	1.155	0.025	0.036	0.0158	0.3%
242	0.0572	0.1942	65845	0.0102	5.3%	0.00777	0.780	0.726	0.233	1	1	1.171	0.026	0.036	0.0190	0.3%
242	0.0706	0.2292	75427	0.0114	5.0%	0.00864	0.847	0.770	0.250	1	1	1.183	0.0			

Conf.	Q	h	Re	a_s	a_s/h	$a_{B/2}$	$f_{cal(n=1)}$ (simpl)	$f_{cal(n=1)}$ (exact)	f_{FFT}	Score n=1	Score n=2	St _{Lb}	\bar{V}_{max}	V _{max}	$(\Delta E_{post-2}) / (L_b + L_c)$	$(\Delta E_{post-2}) / \Delta E_f$
[-]	[m3/s]	[m]	[-]	[m]	[%]	[m]	[Hz]	[Hz]	[Hz]	[-]	[-]	[-]	[m/s]	[m/s]	[J/m]	[%]
411	0.0058	0.0384	10412	0.0012	3.2%	0.00112	0.448	0.446	0.183	0	1	2.661	0.007	0.010	0.0005	0.1%
411	0.0097	0.0530	16531	0.0017	3.2%	0.00151	0.527	0.521	0.100	1	0	2.572	0.008	0.011	0.0010	0.1%
411	0.0156	0.0738	24916	0.0017	2.3%	0.00153	0.621	0.610	0.217	0	0	2.590	0.007	0.010	0.0010	0.1%
411	0.0207	0.0925	31321	0.0020	2.1%	0.00177	0.695	0.676	0.800	0	1	2.714	0.007	0.010	0.0013	0.1%
411	0.0286	0.1177	40436	0.0022	1.9%	0.00201	0.784	0.750	0.400	0	1	2.784	0.007	0.010	0.0017	0.1%
411	0.0361	0.1419	47767	0.0027	1.9%	0.00238	0.861	0.807	0.800	1	1	2.891	0.008	0.011	0.0024	0.1%
411	0.0458	0.1721	56094	0.0030	1.8%	0.00273	0.948	0.866	0.400	0	1	2.994	0.008	0.011	0.0031	0.1%
411	0.0594	0.2090	66709	0.0032	1.5%	0.00290	1.045	0.921	0.250	0	1	3.010	0.008	0.011	0.0035	0.1%
411	0.0702	0.2367	74186	0.0036	1.5%	0.00319	1.112	0.952	0.350	0	2	3.001	0.008	0.011	0.0043	0.1%
411	0.0852	0.2744	83406	0.0043	1.6%	0.00385	1.198	0.985	0.883	0	1	2.978	0.009	0.013	0.0062	0.1%
411	0.1017	0.3119	92850	0.0044	1.4%	0.00391	1.277	1.008	1.083	1	1	2.909	0.009	0.012	0.0064	0.1%
411	0.1171	0.3464	100820	0.0050	1.4%	0.00448	1.345	1.024	1.033	1	1	2.845	0.009	0.013	0.0084	0.1%
412	0.0056	0.0421	9946	0.0025	5.8%	0.00186	0.363	0.362	0.083	1	0	2.426	0.013	0.019	0.0026	0.5%
412	0.0095	0.0545	15969	0.0026	4.7%	0.00194	0.413	0.411	0.133	1	0	2.183	0.012	0.017	0.0028	0.4%
412	0.0152	0.0755	24110	0.0031	4.1%	0.00237	0.486	0.480	0.150	1	0	2.174	0.013	0.018	0.0042	0.3%
412	0.0204	0.0936	30608	0.0036	3.8%	0.00272	0.542	0.532	0.133	1	0	2.241	0.013	0.018	0.0056	0.3%
412	0.0284	0.1214	39502	0.0052	4.3%	0.00394	0.617	0.599	0.133	1	0	2.347	0.017	0.023	0.0117	0.4%
412	0.0366	0.1518	47072	0.0054	3.6%	0.00410	0.690	0.659	0.167	1	0	2.507	0.015	0.022	0.0127	0.3%
412	0.0478	0.1868	56691	0.0055	2.9%	0.00415	0.765	0.715	0.233	1	0	2.563	0.014	0.020	0.0130	0.2%
412	0.0585	0.2196	64437	0.0055	2.5%	0.00413	0.829	0.759	0.183	1	0	2.627	0.013	0.018	0.0129	0.2%
412	0.0705	0.2534	72358	0.0054	2.1%	0.00406	0.891	0.795	0.167	1	1	2.644	0.012	0.017	0.0124	0.1%
412	0.0863	0.2946	81844	0.0060	2.0%	0.00457	0.960	0.830	0.283	0	1	2.627	0.012	0.017	0.0158	0.1%
412	0.0984	0.3249	88354	0.0074	2.3%	0.00559	1.009	0.850	0.217	0	1	2.608	0.014	0.020	0.0236	0.1%
412	0.1079	0.3475	93292	0.0074	2.1%	0.00562	1.043	0.863	0.783	0	0	2.581	0.014	0.020	0.0238	0.1%
413	0.0056	0.0383	9898	0.0020	5.1%	0.00126	0.283	0.282	0.067	0	1	1.803	0.011	0.016	0.0020	0.4%
413	0.0101	0.0545	17059	0.0027	4.9%	0.00173	0.337	0.336	0.183	1	0	1.689	0.013	0.018	0.0038	0.5%
413	0.0152	0.0744	24079	0.0033	4.4%	0.00212	0.394	0.391	0.183	1	0	1.783	0.013	0.019	0.0058	0.5%
413	0.0202	0.0910	30480	0.0038	4.2%	0.00245	0.436	0.431	0.033	1	0	1.809	0.014	0.020	0.0076	0.5%
413	0.0287	0.1216	39689	0.0054	4.4%	0.00348	0.503	0.493	0.167	1	0	1.948	0.017	0.024	0.0155	0.6%
413	0.0368	0.1500	47265	0.0078	5.2%	0.00507	0.559	0.542	0.167	1	0	2.060	0.022	0.032	0.0328	0.8%
413	0.0460	0.1804	55121	0.0070	3.9%	0.00452	0.613	0.587	0.183	1	1	2.136	0.018	0.026	0.0261	0.5%
413	0.0585	0.2178	64213	0.0078	3.6%	0.00505	0.674	0.634	0.183	1	0	2.211	0.019	0.026	0.0325	0.4%
413	0.0700	0.2519	71787	0.0080	3.2%	0.00514	0.724	0.669	0.150	1	0	2.248	0.018	0.025	0.0337	0.3%
413	0.0860	0.2939	81468	0.0086	2.9%	0.00558	0.782	0.705	0.250	1	0	2.248	0.018	0.025	0.0397	0.3%
413	0.0968	0.3218	87170	0.0079	2.5%	0.00511	0.819	0.725	0.217	0	0	2.252	0.015	0.022	0.0333	0.2%
413	0.1047	0.3427	91144	0.0099	2.9%	0.00641	0.845	0.739	0.183	1	1	2.251	0.019	0.027	0.0524	0.3%
414	0.0048	0.0353	8588	0.0018	5.2%	0.00102	0.229	0.229	0.200	3	0	1.587	0.011	0.015	0.0021	0.4%
414	0.0092	0.0533	15543	0.0035	6.6%	0.00196	0.281	0.281	0.250	2	0	1.534	0.017	0.024	0.0077	0.9%
414	0.0154	0.0757	24228	0.0040	5.3%	0.00222	0.335	0.334	0.300	3	0	1.548	0.016	0.023	0.0100	0.7%
414	0.0207	0.0935	30871	0.0043	4.6%	0.00241	0.373	0.370	0.200	1	0	1.577	0.016	0.022	0.0117	0.6%
414	0.0275	0.1179	38276	0.0052	4.4%	0.00290	0.419	0.413	0.383	2	0	1.672	0.017	0.024	0.0170	0.6%
414	0.0364	0.1461	46928	0.0067	4.6%	0.00376	0.466	0.456	0.167	1	0	1.740	0.019	0.028	0.0285	0.7%
414	0.0468	0.1807	55548	0.0078	4.3%	0.00437	0.518	0.502	0.183	1	0	1.834	0.020	0.029	0.0385	0.6%
414	0.0571	0.2132	63108	0.0087	4.1%	0.00485	0.563	0.539	0.200	1	1	1.899	0.021	0.029	0.0475	0.6%
414	0.0695	0.2476	71383	0.0120	4.8%	0.00668	0.606	0.573	0.200	1	1	1.931	0.027	0.038	0.0902	0.9%
414	0.0836	0.2812	80424	0.0090	3.2%	0.00501	0.646	0.602	0.233	1	0	1.917	0.019	0.026	0.0506	0.4%
414	0.1009	0.3283	89189	0.0126	3.8%	0.00704	0.698	0.636	0.233	1	0	1.956	0.024	0.034	0.1000	0.6%
414	0.1056	0.3404	91537	0.0113	3.3%	0.00631	0.711	0.644	0.233	0	1	1.959	0.021	0.030	0.0804	0.4%

Conf.	Q	h	Re	a_s	a_s/h	$a_{B/2}$	$f_{cal(n=1)}$ (simpl)	$f_{cal(n=1)}$ (exact)	f_{FFT}	Score n=1	Score n=2	St _{Lb}	\bar{V}_{max}	V _{max}	$(\Delta E_{post-2}) / (L_b + L_c)$	$(\Delta E_{post-2}) / \Delta E_f$
[-]	[m3/s]	[m]	[-]	[m]	[%]	[m]	[Hz]	[Hz]	[Hz]	[-]	[-]	[-]	[m/s]	[m/s]	[J/m]	[%]
421	0.0060	0.0295	10748	0.0013	4.5%	0.00118	0.392	0.391	0.150	0	1	2.252	0.008	0.012	0.0005	0.1%
421	0.0105	0.0473	17910	0.0016	3.4%	0.00145	0.497	0.493	0.233	0	0	2.272	0.008	0.012	0.0007	0.1%
421	0.0147	0.0618	24033	0.0021	3.3%	0.00184	0.569	0.561	0.083	1	0	2.280	0.009	0.013	0.0012	0.1%
421	0.0199	0.0784	31242	0.0020	2.5%	0.00179	0.640	0.627	0.217	0	1	2.288	0.008	0.011	0.0011	0.1%
421	0.0276	0.1035	40434	0.0022	2.1%	0.00193	0.736	0.710	0.717	1	1	2.430	0.007	0.011	0.0013	0.1%
421	0.0364	0.1304	49548	0.0028	2.2%	0.00254	0.826	0.781	0.033	0	1	2.573	0.009	0.012	0.0022	0.1%
421	0.0461	0.1590	58405	0.0030	1.9%	0.00265	0.912	0.842	0.550	0	1	2.666	0.008	0.012	0.0024	0.1%
421	0.0584	0.1932	68322	0.0037	1.9%	0.00334	1.005	0.899	0.783	1	1	2.733	0.009	0.013	0.0039	0.1%
421	0.0697	0.2225	76876	0.0037	1.7%	0.00336	1.078	0.937	0.450	0	1	2.727	0.009	0.012	0.0039	0.1%
421	0.0848	0.2591	87041	0.0045	1.7%	0.00403	1.164	0.973	1.117	0	1	2.699	0.010	0.014	0.0056	0.1%
421	0.1001	0.2949	96412	0.0048	1.6%	0.00429	1.241	0.998	0.850	1	1	2.657	0.010	0.014	0.0064	0.1%
421	0.1142	0.3253	104183	0.0053	1.6%	0.00473	1.304	1.015	0.850	0	1	2.614	0.010	0.014	0.0078	0.1%
422	0.0057	0.0292	10281	0.0019	6.5%	0.00143	0.302	0.302	0.167	0	1	1.772	0.012	0.017	0.0013	0.3%
422	0.0106	0.0479	18091	0.0029	6.1%	0.00221	0.387	0.385	0.133	1	1	1.767	0.015	0.021	0.0031	0.4%
422	0.0155	0.0643	25187	0.0032	4.9%	0.00239	0.449	0.445	0.150	1	0	1.772	0.014	0.019	0.0036	0.4%
422	0.0203	0.0810	31738	0.0036	4.4%	0.00270	0.504	0.497	0.067	1	1	1.811	0.014	0.020	0.0046	0.4%
422	0.0275	0.1062	39807	0.0055	5.2%	0.00419	0.577	0.564	0.167	1	0	2.013	0.019	0.027	0.0110	0.6%
422	0.0355	0.1335	47858	0.0043	3.3%	0.00330	0.647	0.624	0.067	1	0	2.167	0.013	0.019	0.0068	0.2%
422	0.0468	0.1680	57863	0.0056	3.3%	0.00426	0.725	0.687	0.150	1	0	2.283	0.015	0.021	0.0114	0.2%
422	0.0592	0.2090	66720	0.0059	2.8%	0.00445	0.809	0.746	0.417	1	0	2.435	0.014	0.020	0.0125	0.2%
422	0.0710	0.2389	75173	0.0062	2.6%	0.00467	0.865	0.780	0.183	1	0	2.429	0.014	0.020	0	

APPENDIX 4-6

Conf.	Q	h	Re	a _s	a _s /h	a _{B2}	f _{cal(n=1)} (simpl)	f _{cal(n=1)} (exact)	f _{FFT}	Score n=1	Score n=2	St _{Lb}	V̄ _{max}	V _{max}	(ΔE _{post1-2}) (L _s +L _c)	(ΔE _{post1-2}) ΔE _f
[]	[m3/s]	[m]	[]	[m]	[%]	[m]	[Hz]	[Hz]	[Hz]	[]	[]	[]	[m/s]	[m/s]	[J/m]	[%]
441	0.0049	0.0353	8815	0.0011	3.2%	0.00103	0.430	0.428	0.217	0	1	2.838	0.007	0.010	0.0003	0.0%
441	0.0102	0.0536	17339	0.0016	3.0%	0.00145	0.530	0.524	0.033	0	1	2.484	0.008	0.011	0.0006	0.1%
441	0.0154	0.0733	24737	0.0021	2.9%	0.00190	0.619	0.608	0.050	0	0	2.588	0.009	0.012	0.0009	0.1%
441	0.0199	0.0873	30776	0.0020	2.3%	0.00183	0.675	0.658	0.150	0	2	2.554	0.008	0.011	0.0009	0.0%
441	0.0273	0.1094	39429	0.0022	2.0%	0.00196	0.756	0.727	0.333	0	1	2.640	0.007	0.010	0.0010	0.0%
441	0.0356	0.1349	48288	0.0028	2.1%	0.00251	0.840	0.792	0.500	0	1	2.695	0.008	0.012	0.0016	0.0%
441	0.0466	0.1684	58428	0.0029	1.7%	0.00257	0.938	0.860	0.817	2	1	2.765	0.008	0.011	0.0017	0.0%
441	0.0575	0.1958	67809	0.0033	1.7%	0.00294	1.012	0.903	0.850	0	1	2.740	0.008	0.012	0.0023	0.0%
441	0.0691	0.2263	76477	0.0040	1.8%	0.00361	1.087	0.941	1.033	0	1	2.743	0.009	0.013	0.0034	0.0%
441	0.0853	0.2642	86906	0.0045	1.7%	0.00403	1.175	0.977	0.817	0	1	2.735	0.010	0.014	0.0042	0.0%
441	0.1013	0.2991	96211	0.0052	1.7%	0.00465	1.250	1.001	0.883	1	1	2.701	0.010	0.015	0.0056	0.0%
441	0.1195	0.3382	105651	0.0056	1.7%	0.00501	1.330	1.021	0.817	0	1	2.656	0.011	0.015	0.0065	0.0%
442	0.0046	0.0358	8340	0.0015	4.2%	0.00115	0.335	0.334	0.200	1	0	2.436	0.009	0.013	0.0006	0.1%
442	0.0104	0.0556	17516	0.0035	6.2%	0.00263	0.417	0.415	0.067	1	1	2.038	0.016	0.023	0.0033	0.3%
442	0.0150	0.0729	23858	0.0027	3.7%	0.00207	0.478	0.473	0.150	1	0	2.139	0.011	0.016	0.0020	0.1%
442	0.0194	0.0887	29648	0.0041	4.6%	0.00307	0.527	0.519	0.150	1	0	2.174	0.015	0.021	0.0045	0.2%
442	0.0288	0.1182	40483	0.0038	3.2%	0.00285	0.608	0.591	0.100	1	0	2.222	0.012	0.017	0.0038	0.1%
442	0.0361	0.1392	47954	0.0048	3.5%	0.00367	0.660	0.635	0.183	1	1	2.260	0.014	0.020	0.0063	0.1%
442	0.0465	0.1725	57052	0.0071	4.1%	0.00538	0.735	0.694	0.200	1	1	2.362	0.019	0.027	0.0137	0.2%
442	0.0579	0.2043	66208	0.0069	3.4%	0.00520	0.800	0.740	0.217	1	1	2.393	0.017	0.024	0.0127	0.1%
442	0.0719	0.2415	76086	0.0068	2.8%	0.00517	0.870	0.783	0.217	1	1	2.407	0.015	0.022	0.0126	0.1%
442	0.0865	0.2782	85107	0.0076	2.7%	0.00576	0.933	0.817	0.233	1	0	2.415	0.016	0.023	0.0156	0.1%
442	0.1030	0.3161	94507	0.0085	2.7%	0.00646	0.995	0.844	0.250	1	0	2.386	0.017	0.024	0.0197	0.1%
442	0.1188	0.3505	102609	0.0113	3.2%	0.00857	1.048	0.864	0.267	1	1	2.357	0.021	0.030	0.0347	0.1%
443	0.0052	0.0373	9290	0.0015	4.0%	0.00097	0.279	0.278	0.133	1	0	1.873	0.009	0.012	0.0007	0.1%
443	0.0105	0.0566	17620	0.0035	6.1%	0.00224	0.343	0.342	0.150	1	1	1.726	0.016	0.023	0.0040	0.3%
443	0.0153	0.0728	24391	0.0034	4.7%	0.00221	0.389	0.387	0.183	1	1	1.720	0.014	0.020	0.0039	0.2%
443	0.0193	0.0859	29625	0.0044	5.1%	0.00285	0.423	0.419	0.200	1	0	1.738	0.017	0.024	0.0065	0.3%
443	0.0278	0.1136	39487	0.0064	5.6%	0.00414	0.487	0.478	0.183	1	0	1.809	0.021	0.030	0.0137	0.4%
443	0.0356	0.1379	47266	0.0065	4.7%	0.00417	0.536	0.522	0.467	1	0	1.888	0.019	0.027	0.0139	0.3%
443	0.0462	0.1728	56354	0.0082	4.8%	0.00531	0.600	0.577	0.517	1	0	2.009	0.022	0.031	0.0225	0.3%
443	0.0588	0.2067	66564	0.0086	4.2%	0.00557	0.656	0.621	0.217	1	1	2.023	0.021	0.030	0.0247	0.2%
443	0.0687	0.2360	73033	0.0098	4.2%	0.00636	0.701	0.654	0.233	1	1	2.083	0.022	0.032	0.0323	0.2%
443	0.0841	0.2714	83196	0.0100	3.7%	0.00648	0.752	0.687	0.617	1	0	2.065	0.021	0.030	0.0335	0.2%
443	0.1033	0.3170	94031	0.0102	3.2%	0.00657	0.813	0.722	0.650	1	1	2.064	0.020	0.028	0.0345	0.2%
443	0.1163	0.3471	100353	0.0123	3.6%	0.00798	0.850	0.741	0.283	1	1	2.067	0.023	0.033	0.0507	0.2%
444	0.0048	0.0377	8630	0.0020	5.4%	0.00113	0.237	0.236	0.117	1	0	1.727	0.012	0.016	0.0016	0.2%
444	0.0096	0.0562	16111	0.0033	5.8%	0.00182	0.289	0.288	0.250	3	0	1.576	0.015	0.022	0.0042	0.3%
444	0.0154	0.0746	24299	0.0053	7.2%	0.00298	0.333	0.331	0.300	3	0	1.511	0.022	0.031	0.0112	0.6%
444	0.0206	0.0913	31012	0.0077	8.4%	0.00431	0.368	0.365	0.333	3	0	1.520	0.028	0.040	0.0234	0.9%
444	0.0275	0.1140	38780	0.0070	6.2%	0.00393	0.411	0.406	0.350	1	0	1.581	0.023	0.033	0.0195	0.5%
444	0.0357	0.1408	46995	0.0076	5.4%	0.00427	0.457	0.449	0.383	1	0	1.654	0.023	0.032	0.0230	0.4%
444	0.0461	0.1685	56622	0.0082	4.9%	0.00461	0.500	0.487	0.250	1	0	1.670	0.022	0.031	0.0268	0.4%
444	0.0588	0.2045	66671	0.0119	5.8%	0.00667	0.551	0.530	0.233	1	1	1.718	0.029	0.041	0.0562	0.6%
444	0.0703	0.2362	74411	0.0102	4.3%	0.00570	0.592	0.562	0.250	0	1	1.767	0.023	0.033	0.0409	0.3%
444	0.0847	0.2713	83586	0.0106	3.9%	0.00593	0.635	0.594	0.250	1	0	1.782	0.023	0.032	0.0444	0.3%
444	0.1013	0.3085	93203	0.0117	3.8%	0.00651	0.677	0.622	0.283	0	0	1.781	0.023	0.033	0.0536	0.3%
444	0.1152	0.3404	100214	0.0111	3.3%	0.00618	0.711	0.643	0.267	1	0	1.787	0.021	0.030	0.0482	0.2%

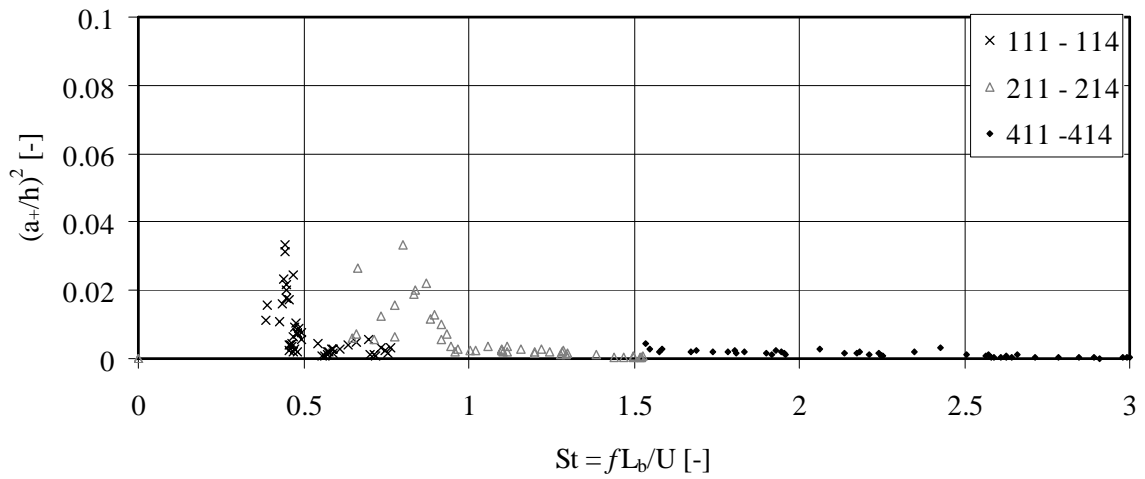


Fig-A4.69: Square value of the relative wave height at $y = B/2 + \Delta B$ as a function of the Strouhal number. $L_c = 0.5$ m.

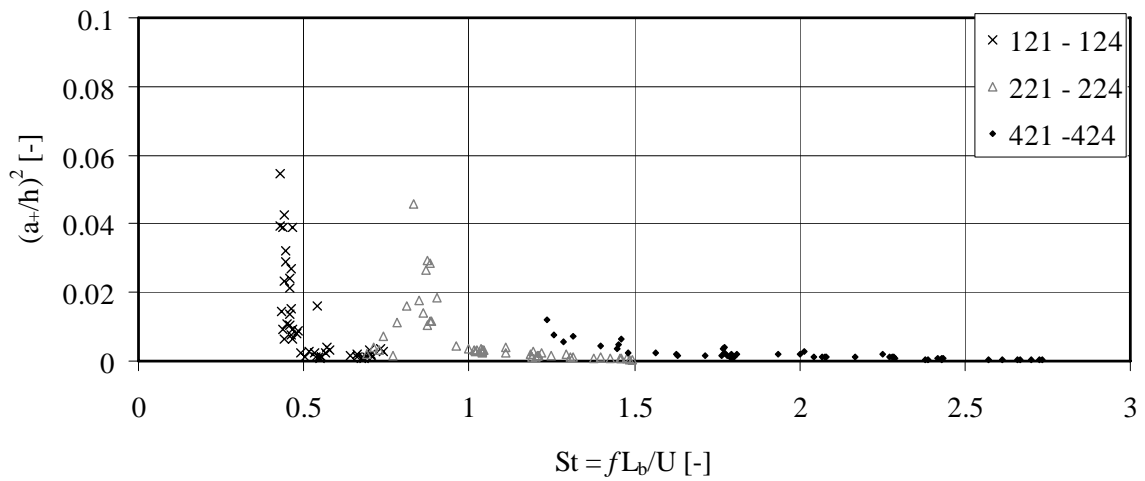


Fig-A4.70: Square value of the relative wave height at $y = B/2 + \Delta B$ as a function of the Strouhal number. $L_c = 1.0$ m.

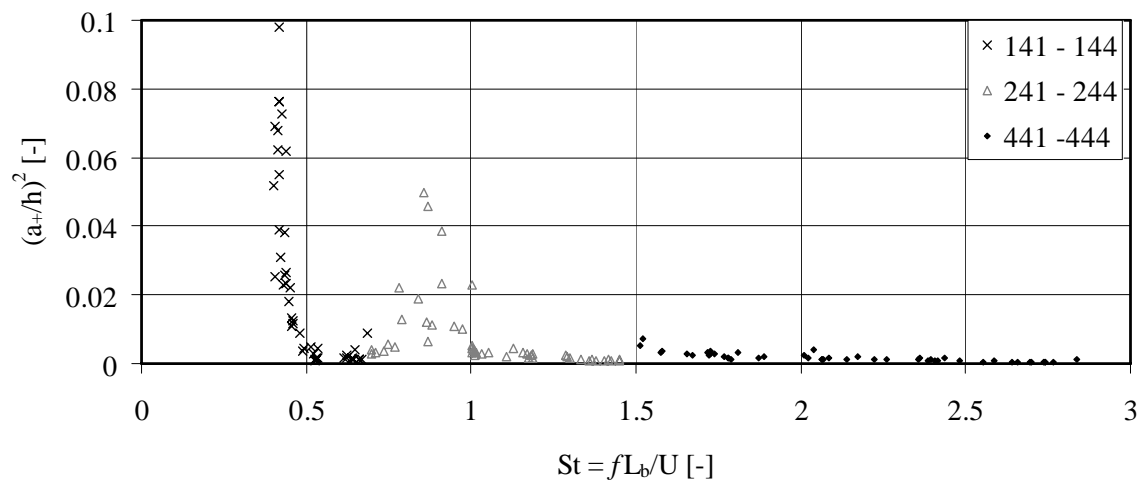


Fig-A4.71: Square value of the relative wave height at $y = B/2 + \Delta B$ as a function of the Strouhal number. $L_c = 2.0$ m.

A 4-7: Alternative formulation of the drag force based computation model

Formulation starts from the drag force formula but the velocity near to the macro-rough element V_w replaces the mean flow velocity U :

$$F_r = C_d A_r \rho \frac{V_w^2}{2} = \Delta p A \tag{1}$$

where F_r is the drag force, C_d the drag coefficient, A_r the surface of application of the drag, Δp the pressure drop and A the flow surface in the main channel. When replacing the pressure drop $\Delta p = \gamma h_r$ and $h_r = S_{f-MR} \Delta x = S_{f-MR}(L_b + L_c)$ one obtains:

$$C_d A_r \frac{V_w^2}{2g} = S_{f-MR} (L_b + L_c) A$$

In this formula, the macro-rough friction slope is replaced by:

$$S_{f-MR} = f_{MR} \frac{U^2}{8gR_{hm}} \quad \text{where} \quad : \quad f_{MR} = f_m - f_{prism}$$

and formula (1) becomes:

$$C_d A_r \left(\frac{V_w}{U} \right)^2 = f_{MR} \frac{1}{4R_h} (L_b + L_c) A$$

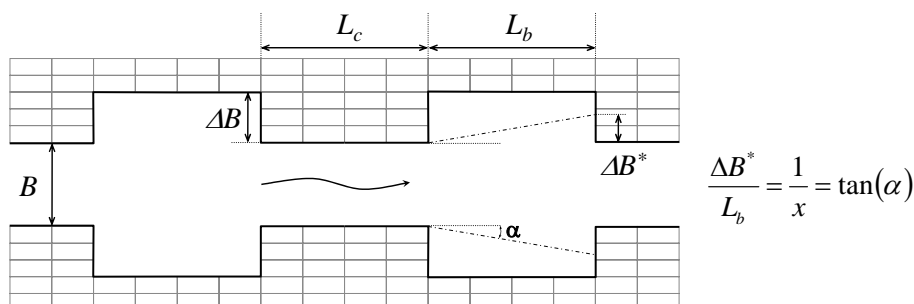


Fig-A4.72: Denomination of the parameters of the drag force based head-loss model.

Furthermore, A respectively A_r can be replaced with $A = B \cdot h$ respectively $A_r = 2\Delta B^* \cdot h$ where $\Delta B^* = \min(\Delta B; L_b / x)$ is the minimum of the geometrical cavity depth and an effective cavity depth taking into account a certain expansion of the flow inside of the cavity. When including all these terms in formula (1), the macro-rough friction coefficient f_{MR} respectively the friction coefficient of the channel section f_m becomes:

$$f_{MR} = C_d \left(\frac{V_w}{U} \right)^2 \frac{8R_h \Delta B^*}{B(L_b + L_c)} \tag{2} \quad \text{with} \quad \Delta B^* = \min(\Delta B; L_b / x) \tag{3}$$

$$f_{m,cal} = f_{m,prismatic} + C_d \left(\frac{V_w}{U} \right)^2 \frac{8R_h \Delta B^*}{B(L_b + L_c)} \tag{4}$$

In this work, the wall velocity ratio (V_w/U) has been assumed to be equal to the unity as

detailed information is not available and since this assumption allows to simplify the approach for practical applications. According to Morris (1972), the ratio (V_w/U) should range between 1/2 to 2/3. As consequence, the drag coefficients identified from the experiments are underestimated and should be multiplied by a factor 2.25 (if $V_w/U = 2/3$) to 4 (if $V_w/U = 1/2$). The few experiments with detailed velocity measurements, namely the configurations 221 to 224 (Q1, Q3 and Q5) indicates quite good agreement with this range (Table A 4.7-1).

Table A 4.7-1: Estimated wall velocity ratios V_w/U from UVP-measurements. U relative to base width B .

221		222		223		224	
Q [L/s]	V_w/U [-]	Q [L/s]	V_w/U [-]	Q [L/s]	V_w/U [-]	Q [L/s]	V_w/U [-]
6.4	0.46	5.3	0.50	5.4	0.47	5.1	0.50
20.1	0.61	18.5	0.52	19.3	0.60	19.3	0.51
48.5	0.66	48	0.60	49.3	0.63	47.8	0.60

A 4-7: Drag coefficients estimated by fixing $x = 6$

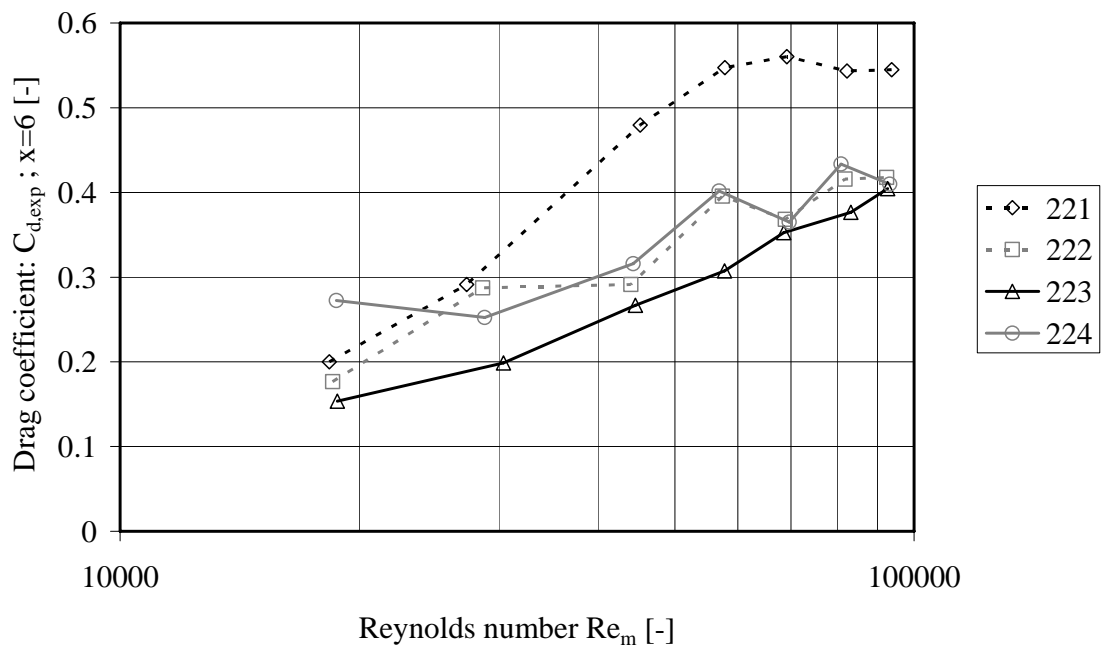


Fig-A4.73: Drag coefficients for configurations 221 to 224 identified by assuming $V_w/U = 1$ and $x = 6$.

A 4-8: Overview of the Evolutionary Polynomial Regression parameters

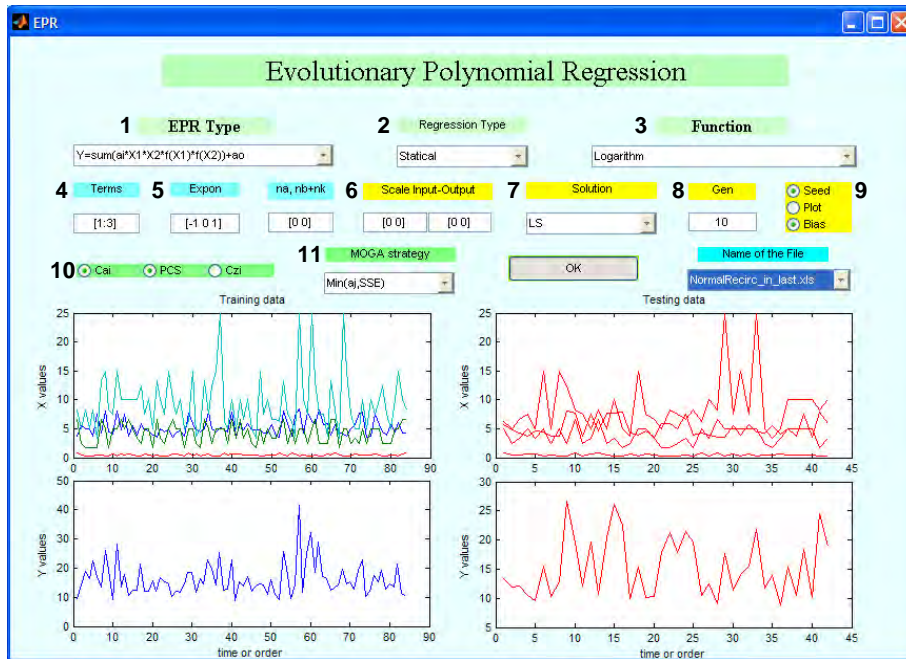


Fig-A4.74: Overview of the EPR toolbox users interface. See also the “Tutorial for the User”: Evolutionary Polynomial Regression EPR, TOOLBOX, Version 1.SA. (Laucelli et al. 2005).

Table A 4-8 1: Summary of the toolbox options and parameters according to Figure-A4.72.

Flow type	1	2	3	4	5	6	7	8	9	10	11
Normal circulating	2	Stat.	no	[1:3]	[-2 -1 0 1 2]	no	LS	10	Seed, Bias	Cai, PCS	MOG A
Reattachment	2	Stat.	no	[1:3]	[-2 -1 0 1 2]	no	LS	10	Seed, Bias	Cai, PCS	MOG A
Square grooved	2	Stat.	no	[1:3]	[-2 -1 0 1 2]	no	LS	10	Seed, Bias	Cai, PCS	MOG A

- ¹ : Corresponds to the general structure of the expression.
- ² : Static modeling corresponds to the type looking for functional relationship. Data are not arranged as time series.
- ³ : Choose of the inner function of the general structure.
- ⁴ : Number of terms of the general expression.
- ⁵ : Possible exponents for the input variables. 0 is necessary to skip unnecessary inputs.
- ⁶ : If input and output variables are not scaled to 0 to 1 values, both fields corresponds to [0 0].
- ⁷ : LS corresponds to the training function by the least square method. LSaj>0 corresponds to the least square method and forcing the constants to be higher than 0.
- ⁸ : Proportionality parameter between the number of generations of EPR and the number of input- and output sets.
- ⁹ : Seed activated allows to formulas mutating randomly. Plot is an output option. Bias activated allows considering a constant value in the model.
- ¹⁰ : Cai activated penalizes small constants (indicates noise modeling). PCS activated allows penalizing complex model structures.
- ¹¹ : MOGA expresses Multi-Objective Genetic Algorithm. At the end of the modeling phase a set of model solutions is returned. The choice is then based on a Pareto front and the SSE (sum of square errors) and the number of a_j coefficients is minimized.

A 4-9: Calculated and measured water levels for the reattachment flow type using single head- and friction-losses

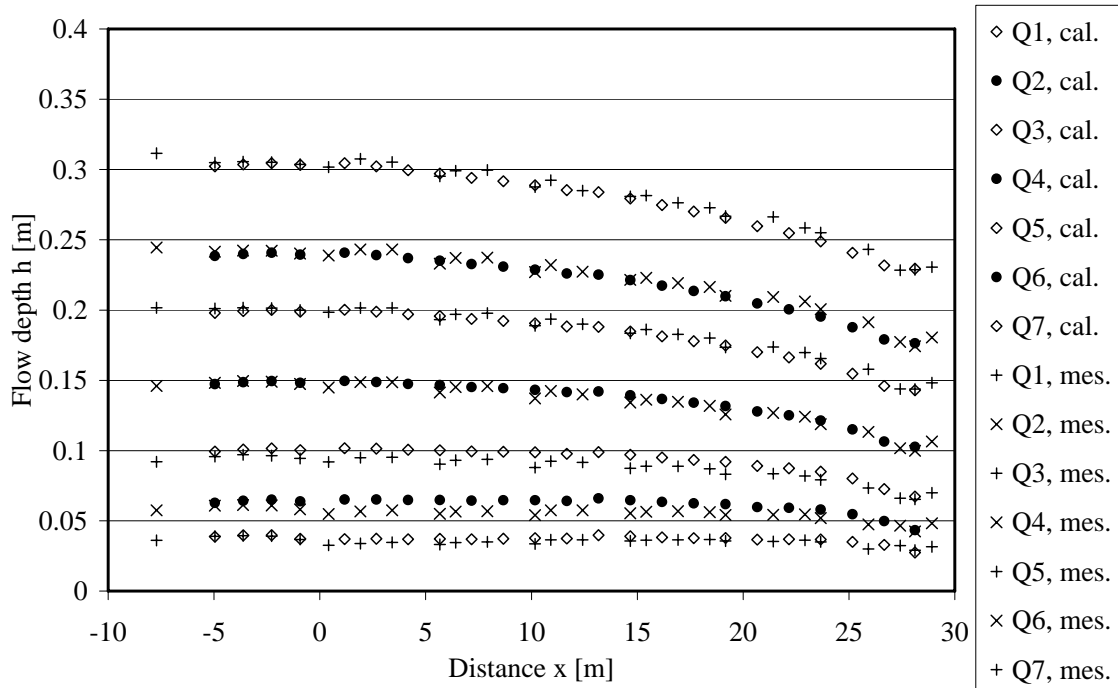


Fig-A4.75: Flow through channel transitions. Configuration 211 with $L_b/\Delta B = 10$ leading to a reattachment of the flow.

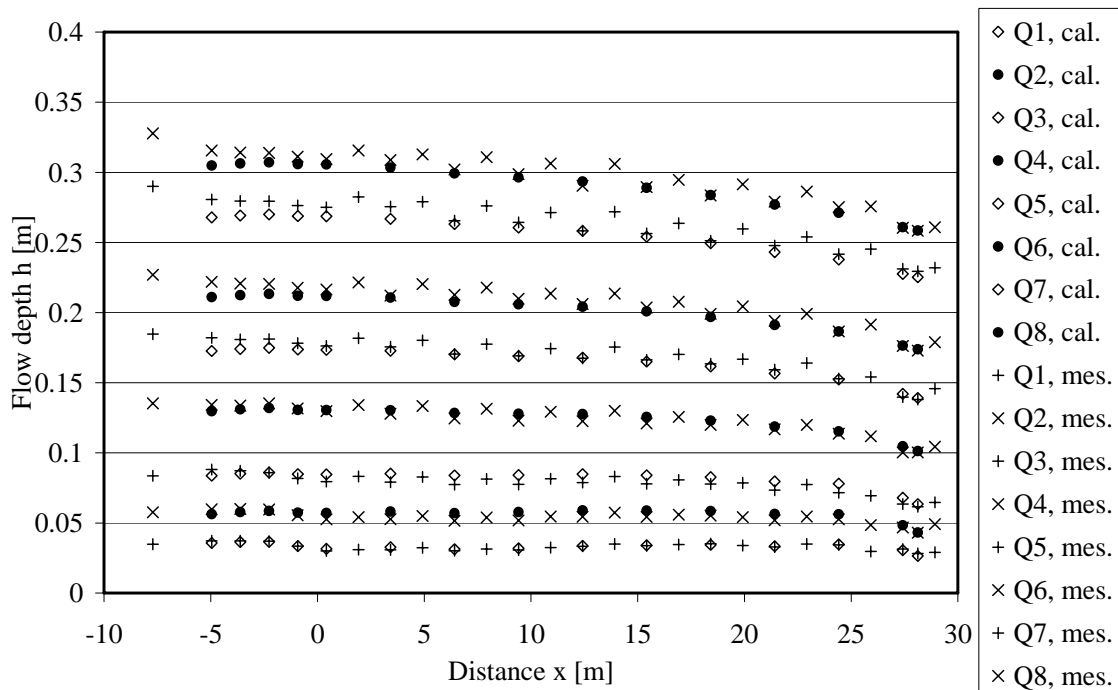


Fig-A4.76: Flow through channel transitions. Configuration 221 with $L_b/\Delta B = 10$ leading to a reattachment of the flow.

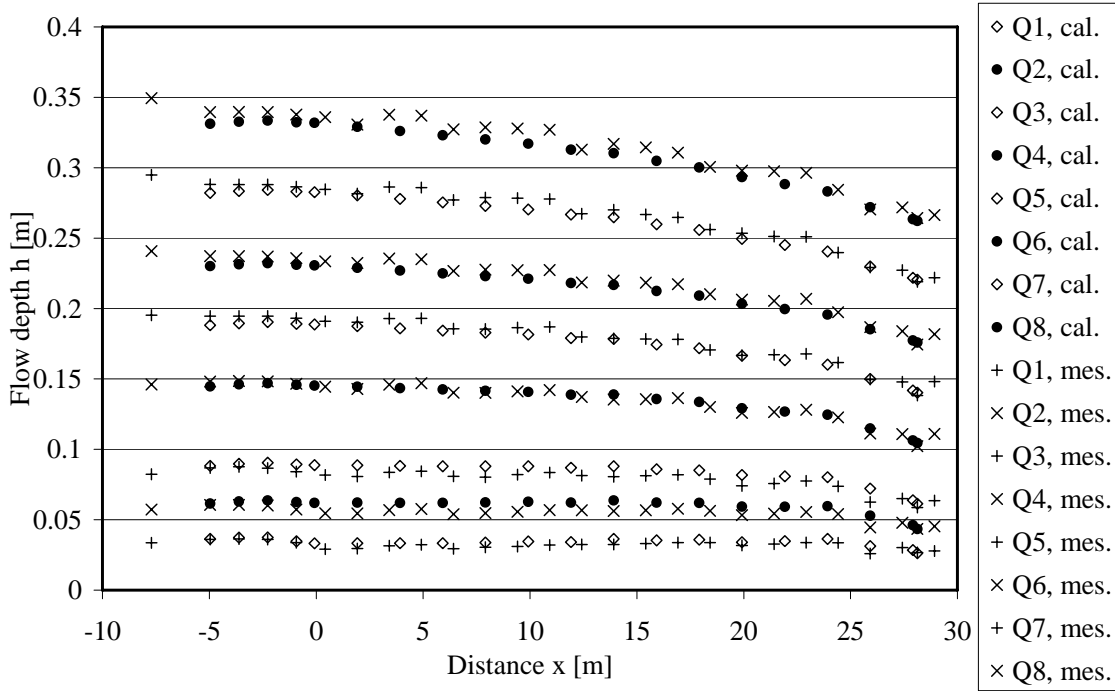


Fig-A4.77: Flow through channel transitions. Configuration 241 with $L_b/\Delta B = 10$ leading to a reattachment of the flow.

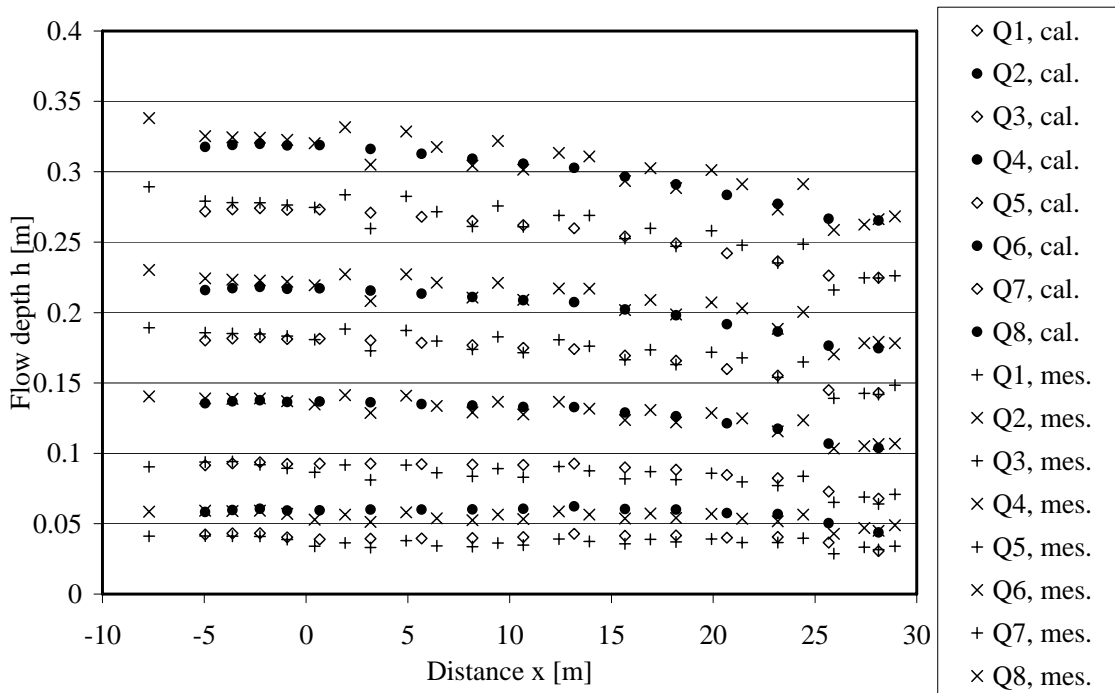


Fig-A4.78: Flow through channel transitions. Configuration 411 with $L_b/\Delta B = 20$ leading to a reattachment of the flow.

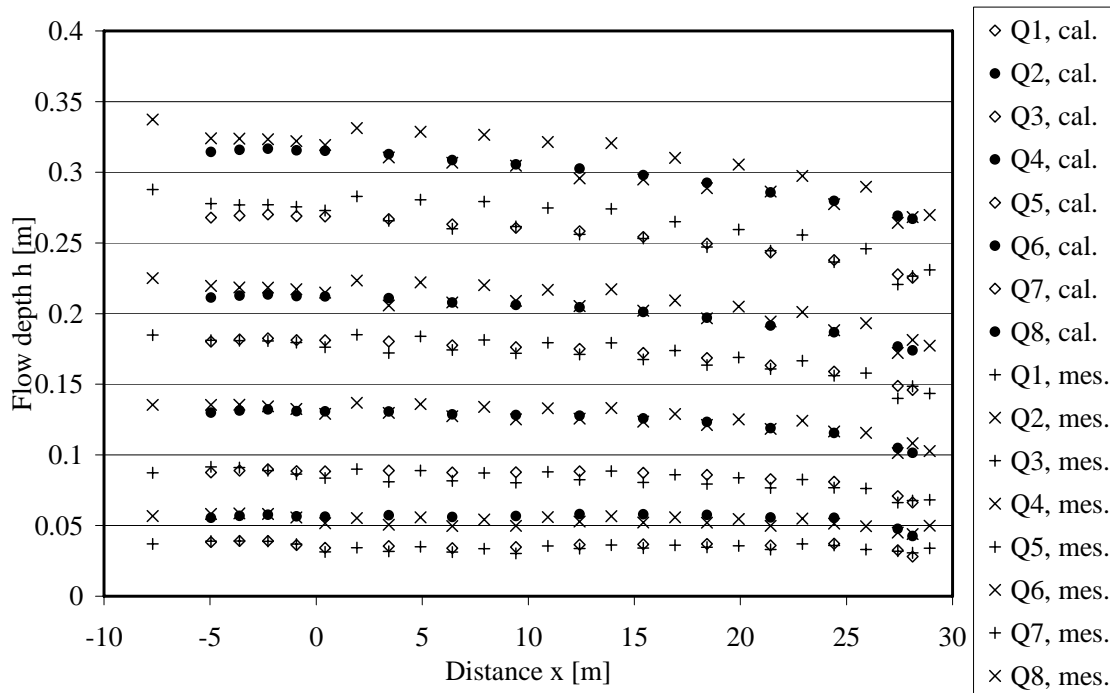


Fig-A4.79: Flow through channel transitions. Configuration 421 with $L_b/\Delta B = 20$ leading to a reattachment of the flow.

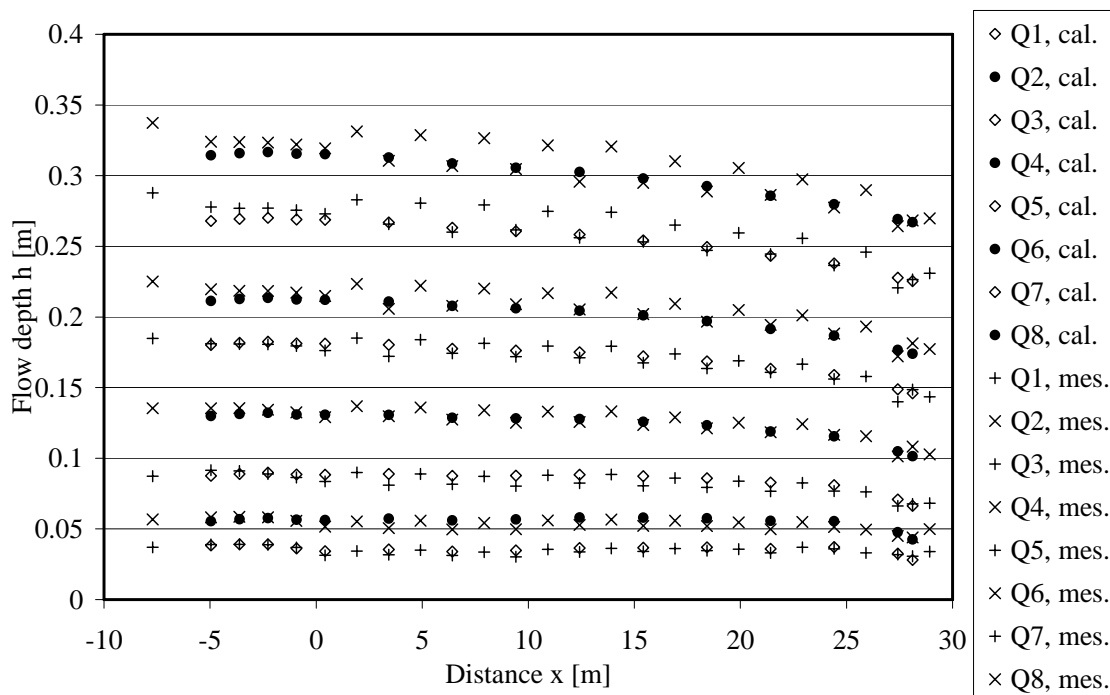


Fig-A4.80: Flow through channel transitions. Configuration 441 with $L_b/\Delta B = 20$ leading to a reattachment of the flow.

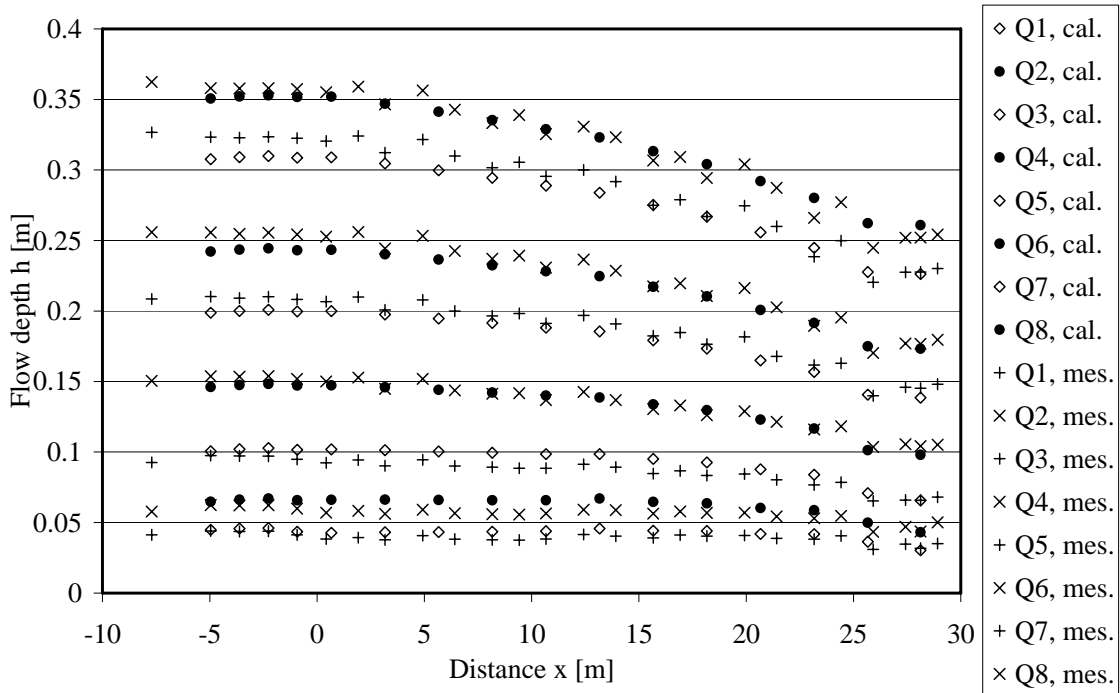


Fig-A4.81: Flow through channel transitions. Configuration 412 with $L_b/\Delta B = 10$ leading to a reattachment of the flow.

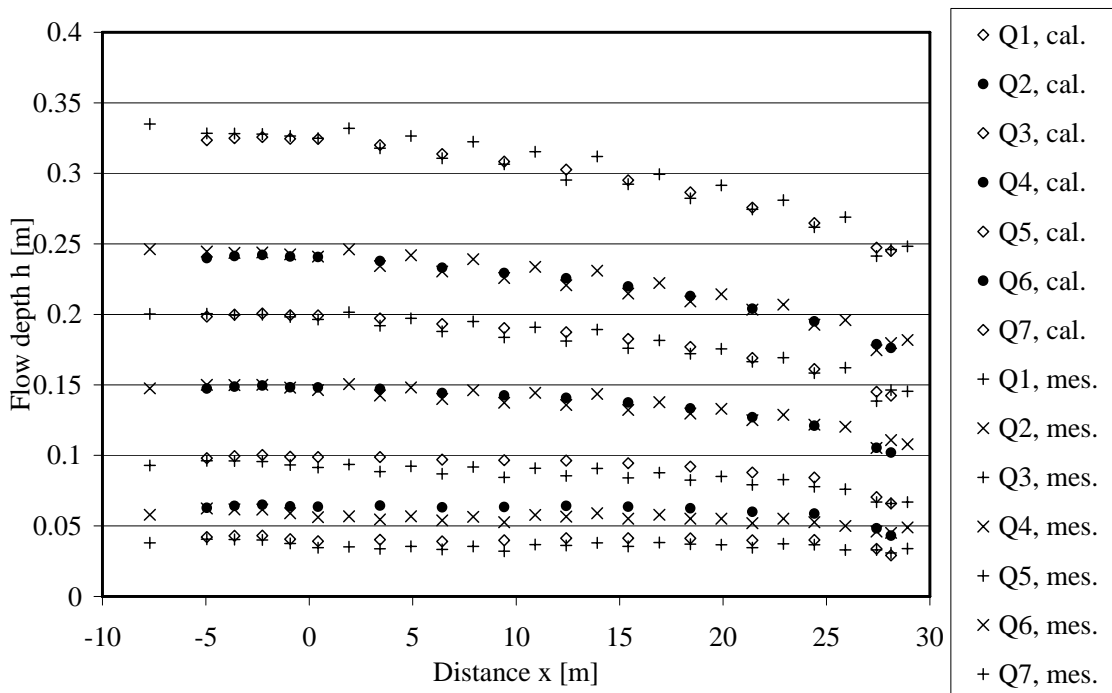


Fig-A4.82: Flow through channel transitions. Configuration 422 with $L_b/\Delta B = 10$ leading to a reattachment of the flow.

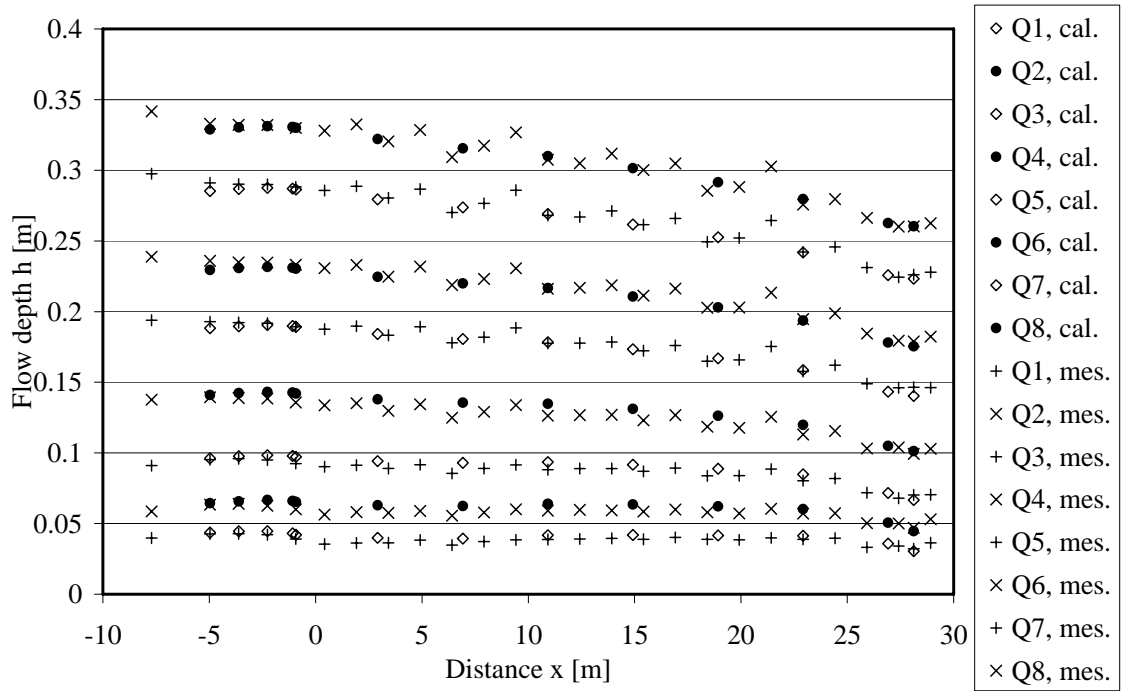


Fig-A4.83: Flow through channel transitions. Configuration 442 with $L_b/\Delta B = 10$ leading to a reattachment of the flow.

A 5-1: Summarized test results for the unsteady flow tests: 111 to 114

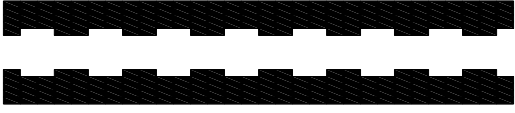

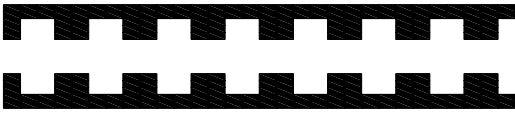
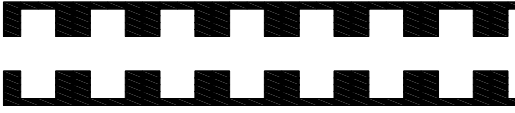
 <p>Configuration 111 $L_b = 0.5 \text{ m}, L_c = 0.5 \text{ m}, \Delta B = 0.1 \text{ m}$</p>	 <p>Configuration 112 $L_b = 0.5 \text{ m}, L_c = 0.5 \text{ m}, \Delta B = 0.2 \text{ m}$</p>
 <p>Configuration 113 $L_b = 0.5 \text{ m}, L_c = 0.5 \text{ m}, \Delta B = 0.3 \text{ m}$</p>	 <p>Configuration 114 $L_b = 0.5 \text{ m}, L_c = 0.5 \text{ m}, \Delta B = 0.4 \text{ m}$</p>

Table: Characteristics of the surge wave experiments and numerical values of the attenuation parameter of the positive (b^+) and the negative (b^-) surge wave front.

Conf.	Scen.	Q_b	Q_{wave}	Q_{total}	HP_1	$Fr_{s,us}^+$	$Fr_{s,us}^-$	b^+	b^-
[-]	[-]	[l/s]	[l/s]	[l/s]	[-]	[-]	[-]	[-]	[-]
111	3	6.45	17.63	24.08	3.73	1.58	0.67	0.66	1.76
111	8	10.85	17.57	28.42	2.62	1.32	0.76	1.11	1.66
111	13	19.13	17.49	36.62	1.91	1.16	0.82	1.10	2.48
111	18	34.42	17.33	51.75	1.50	1.09	0.89	1.38	2.12
111	23	49.40	17.20	66.60	1.35	1.06	0.90	1.72	4.08
112	3	5.92	17.71	23.63	3.99	1.56	0.70	0.74	2.43
112	8	10.85	17.58	28.43	2.62	1.30	0.76	1.20	2.44
112	13	19.02	17.49	36.51	1.92	1.17	0.82	1.74	2.56
112	18	34.66	17.37	52.03	1.50	1.09	0.88	2.87	3.52
112	23	48.51	17.24	65.75	1.36	1.06	0.91	2.38	3.30
112 asy.	3	5.23	17.60	22.83	4.37	1.55	0.71	0.55	1.28
112 asy.	8	11.11	17.53	28.64	2.58	1.32	0.75	1.00	0.62
112 asy.	13	19.41	17.44	36.85	1.90	1.15	0.82	1.63	1.72
112 asy.	18	31.12	17.32	48.44	1.56	1.09	0.87	1.03	3.51
112 asy.	23	48.11	17.17	65.28	1.36	1.06	0.92	-1.12	3.09
113	3	5.35	17.65	23.00	4.30	1.62	0.68	0.88	2.57
113	8	11.02	17.51	28.53	2.59	1.31	0.75	1.03	2.78
113	13	18.88	17.45	36.33	1.92	1.15	0.82	1.89	2.06
113	18	35.94	17.32	53.26	1.48	1.08	0.88	3.67	3.44
113	23	49.12	17.20	66.32	1.35	1.07	0.91	7.69	6.23
114	3	5.72	17.58	23.30	4.07	1.55	0.72	0.80	3.92
114	8	10.53	17.53	28.06	2.66	1.27	0.78	1.10	4.23
114	13	19.43	17.54	36.97	1.90	1.13	0.83	2.57	4.02
114	18	34.13	17.39	51.52	1.51	1.07	0.89	4.31	4.05
114	23	48.36	17.17	65.53	1.36	1.06	0.92	3.25	8.17

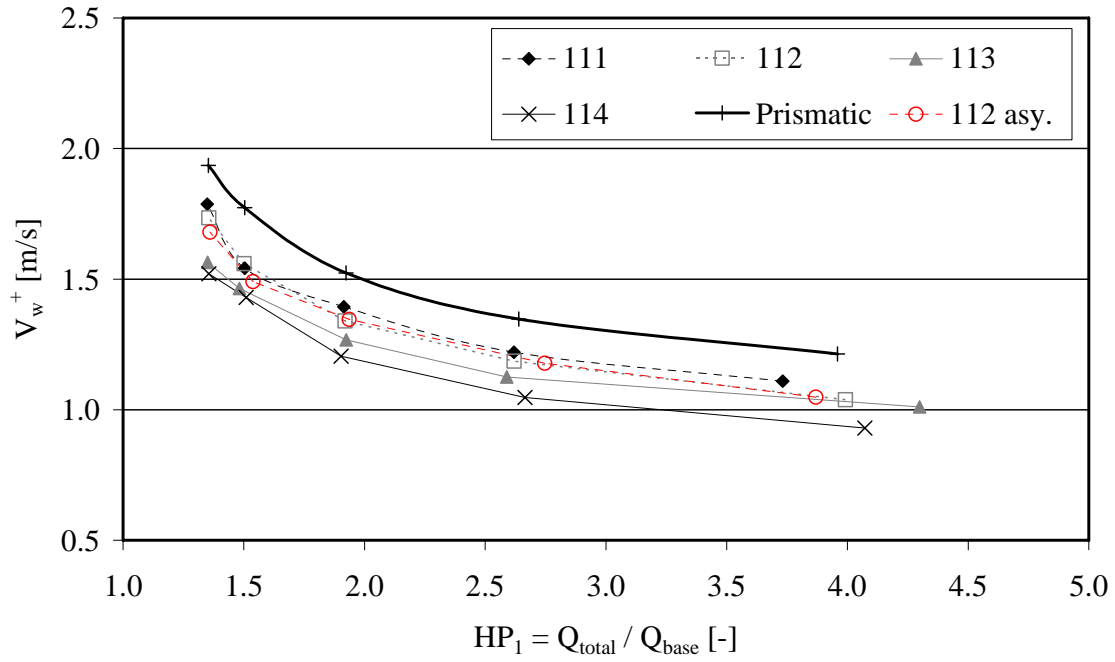


Fig-A5.1: Absolute wave celerity of the positive wave V_w^+ as a function of the discharge ratio $HP_1 = Q_{total} / Q_{base}$. Configurations 111-114.

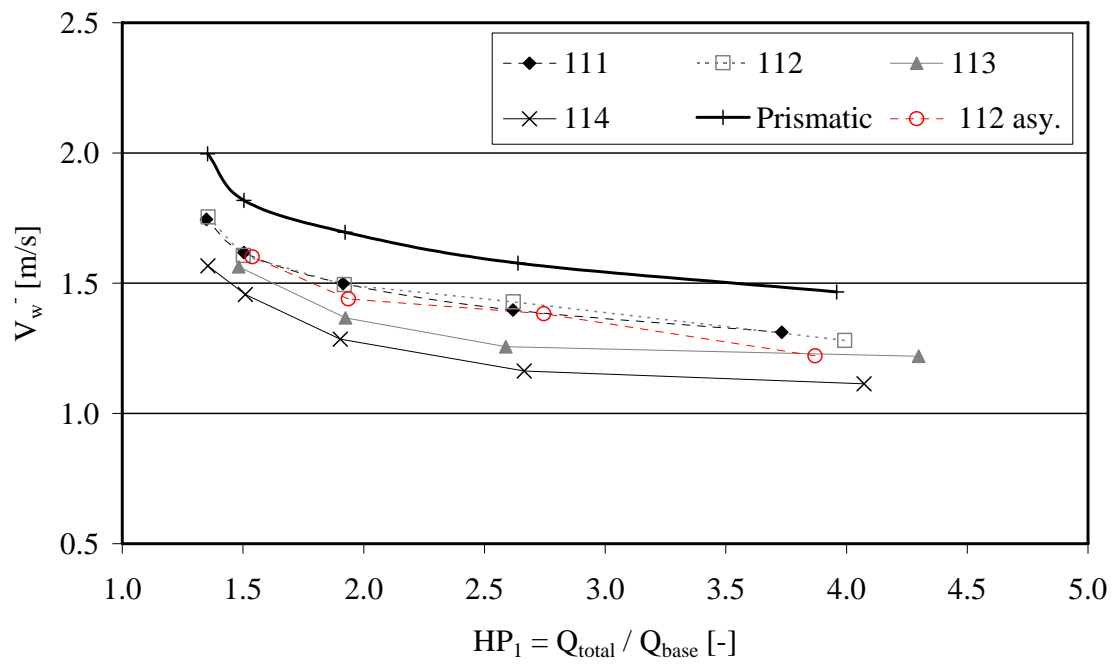


Fig-A5.2: Absolute wave celerity of the negative wave V_w^- as a function of the discharge ratio $HP_1 = Q_{total} / Q_{base}$. Configurations 111-114.

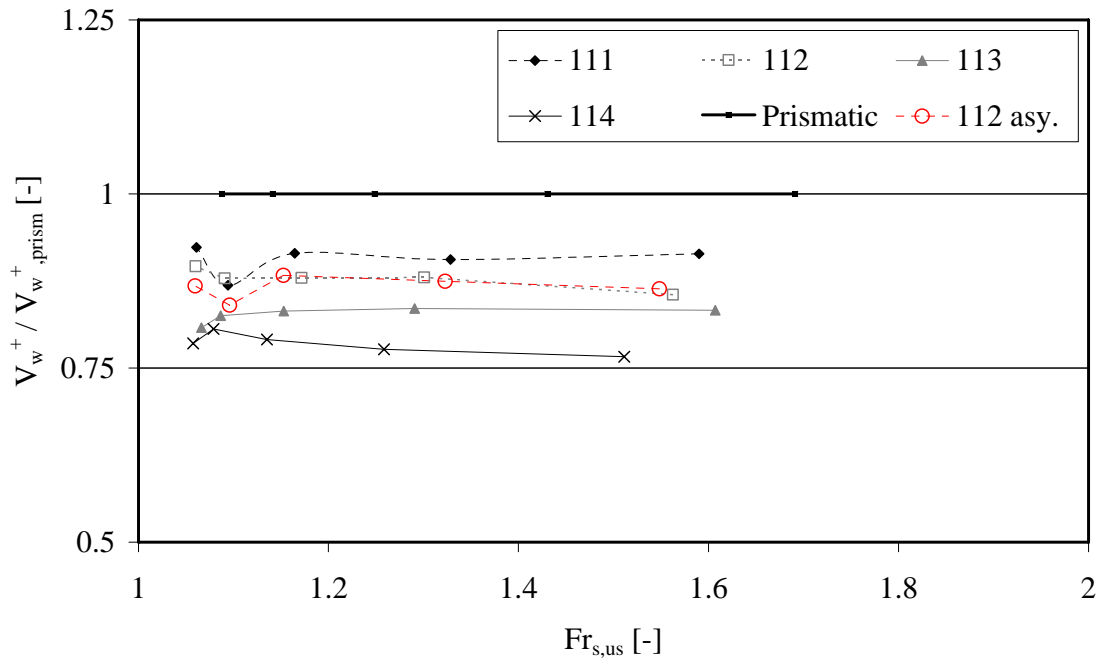


Fig-A5.3: Absolute wave celerity of the macro-rough configurations relative to the prismatic reference $V_w^+ / V_{w,prism}^+$ as a function of the upstream surge Froude number ($x=0.42$ m). Configurations 111-114.

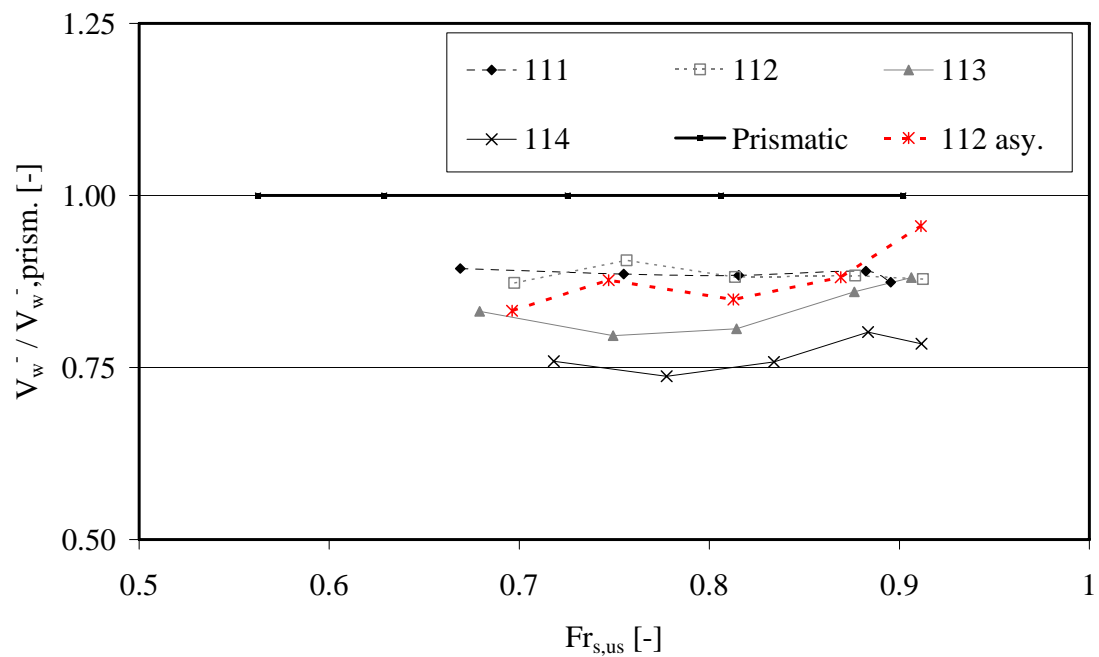


Fig-A5.4: Absolute wave celerity of the macro-rough configurations relative to the prismatic reference $V_w^- / V_{w,prism}^-$ as a function of the upstream surge Froude number ($x=0.42$ m). Configurations 111-114.

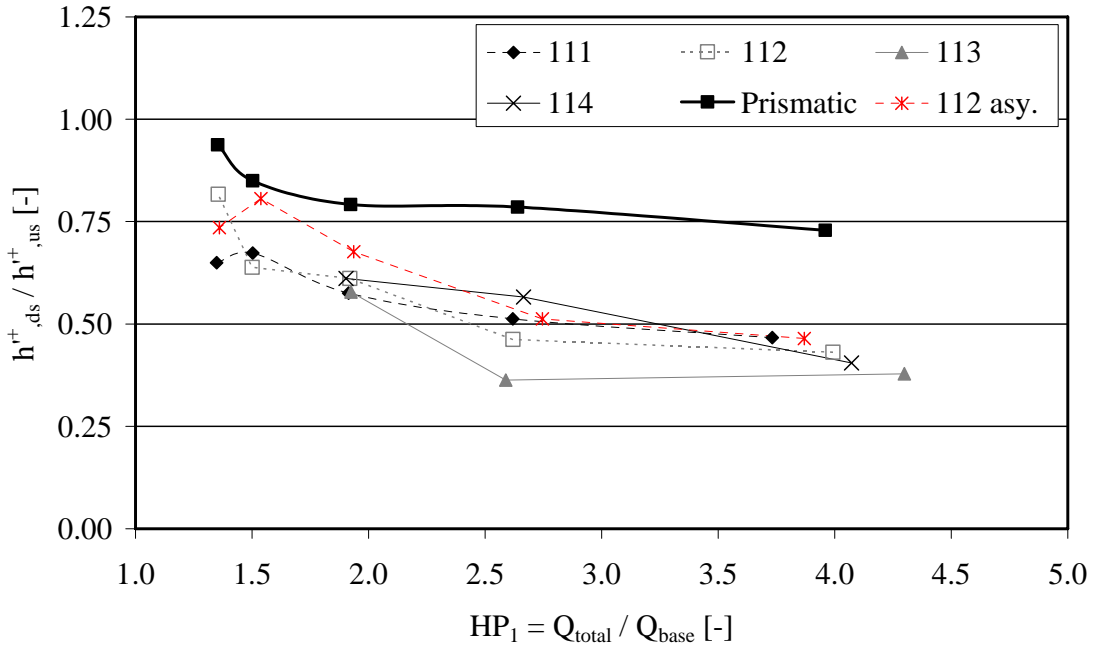


Fig-A5.5: Observed surge wave height ratio between the end and the beginning of the macro-rough reach h^+_{ds}/h^+_{us} (positive wave from upstream) as a function of the discharge ratio $HP_1 = Q_{total}/Q_b$. Configurations 111-114.

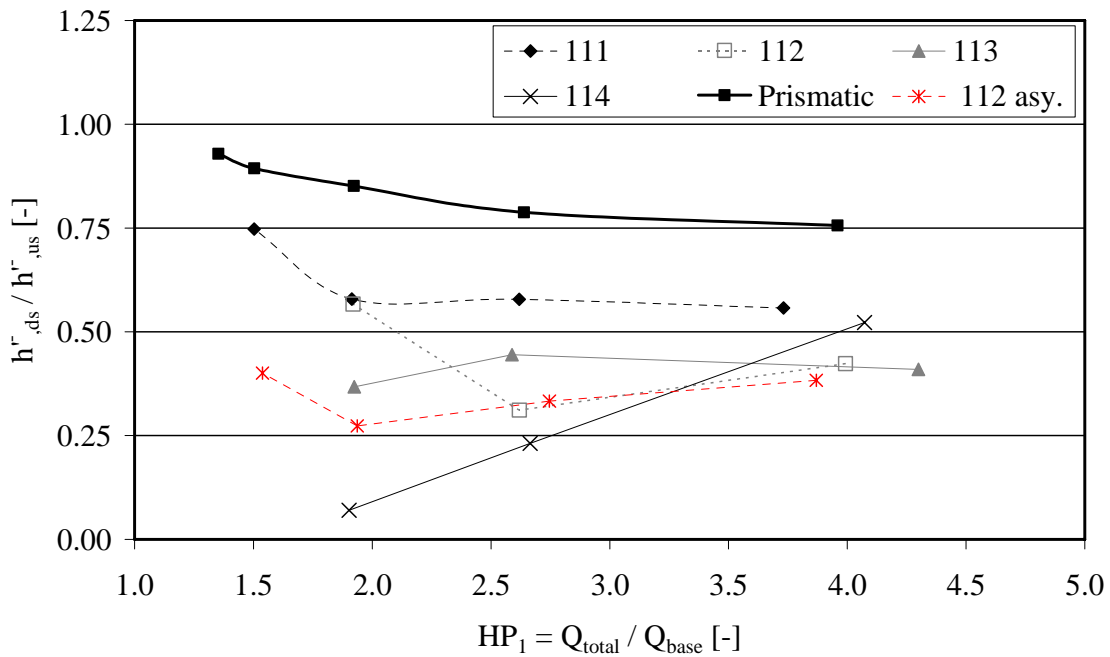


Fig-A5.6: Observed surge wave height ratio between the end and the beginning of the macro-rough reach h^-_{ds}/h^-_{us} (negative wave from upstream) as a function of $HP_1 = Q_{total}/Q_b$. Configurations 111-114.

A 5-1: Summarized test results for the unsteady flow tests: 121 to 124





 <p>Configuration 121 $L_b = 0.5 \text{ m}, L_c = 1.0 \text{ m}, \Delta B = 0.1 \text{ m}$</p>	 <p>Configuration 122 $L_b = 0.5 \text{ m}, L_c = 1.0 \text{ m}, \Delta B = 0.2 \text{ m}$</p>
 <p>Configuration 123 $L_b = 0.5 \text{ m}, L_c = 1.0 \text{ m}, \Delta B = 0.3 \text{ m}$</p>	 <p>Configuration 124 $L_b = 0.5 \text{ m}, L_c = 1.0 \text{ m}, \Delta B = 0.4 \text{ m}$</p>

Table: Characteristics of the surge wave experiments and numerical values of the attenuation parameter of the positive (b^+) and the negative (b^-) surge wave front.

Conf.	Scen.	Q_b	Q_{wave}	Q_{total}	HP_1	$Fr_{s.us}^+$	$Fr_{s.us}^-$	b^+	b^-
[-]	[-]	[L/s]	[L/s]	[L/s]	[-]	[-]	[-]	[-]	[-]
121	3	6.26	17.59	23.85	3.81	1.58	0.66	0.55	1.40
121	8	10.56	17.54	28.10	2.66	1.37	0.72	0.54	1.45
121	13	19.71	17.43	37.14	1.88	1.17	0.80	1.25	0.43
121	18	34.96	17.29	52.25	1.49	1.12	0.87	2.53	2.61
121	23	49.08	17.16	66.24	1.35	1.08	0.90	2.45	4.09
122	3	6.41	17.63	24.04	3.75	1.55	0.66	0.36	0.97
122	8	10.89	17.53	28.42	2.61	1.31	0.72	0.74	0.99
122	13	18.82	17.44	36.26	1.93	1.19	0.78	1.08	2.20
122	18	33.85	17.30	51.15	1.51	1.09	0.86	1.09	2.38
122	23	47.48	17.18	64.66	1.36	1.06	0.90	-0.50	2.69
122 asy.	3	5.78	17.57	23.35	4.04	1.73	0.63	0.71	3.48
122 asy.	8	11.12	17.51	28.63	2.57	1.32	0.75	1.07	4.02
122 asy.	13	19.09	17.43	36.52	1.91	1.17	0.80	2.19	4.81
122 asy.	18	32.77	17.29	50.06	1.53	1.11	0.87	4.49	6.09
122 asy.	23	48.88	17.14	66.02	1.35	1.06	0.91	4.29	8.89
123	3	5.29	17.60	22.89	4.33	1.60	0.66	0.47	1.67
123	8	10.56	17.54	28.10	2.66	1.29	0.74	0.70	1.94
123	13	19.71	17.43	37.14	1.88	1.18	0.80	1.65	1.85
123	18	34.96	17.29	52.25	1.49	1.11	0.86	5.09	2.30
123	23	49.08	17.16	66.24	1.35	1.07	0.90	1.25	9.25
124	3	6.33	17.56	23.89	3.77	1.48	0.70	0.66	2.75
124	8	10.51	17.53	28.04	2.67	1.27	0.76	0.64	3.01
124	13	18.78	17.44	36.22	1.93	1.14	0.82	0.69	1.71
124	18	34.02	17.30	51.32	1.51	1.08	0.88	2.83	1.88
124	23	48.11	17.17	65.28	1.36	1.06	0.91	4.54	1.19

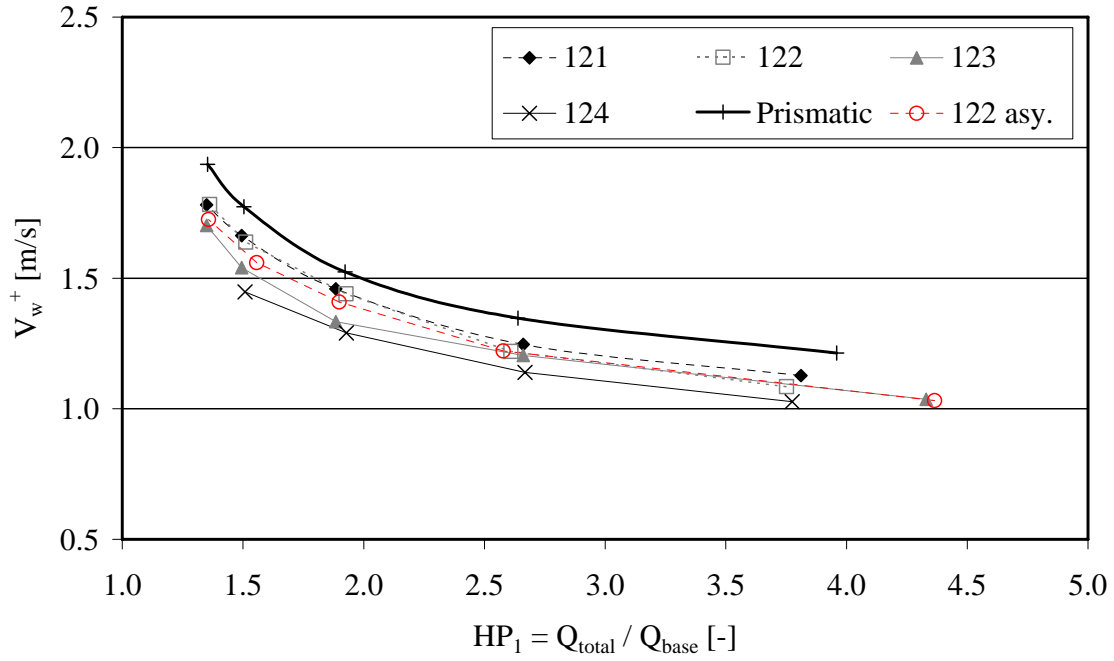


Fig-A5.7: Absolute wave celerity of the positive wave V_w^+ as a function of the discharge ratio $HP_1 = Q_{total} / Q_{base}$. Configurations 121-124.

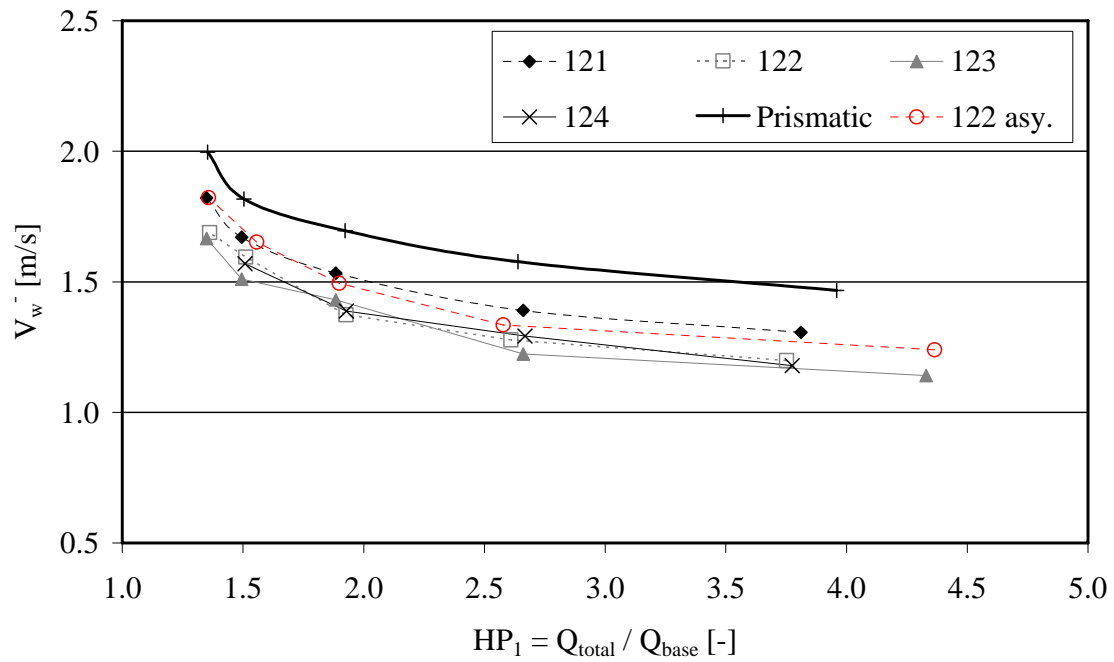


Fig-A5.8: Absolute wave celerity of the negative wave V_w^- as a function of the discharge ratio $HP_1 = Q_{total} / Q_{base}$. Configurations 121-124.

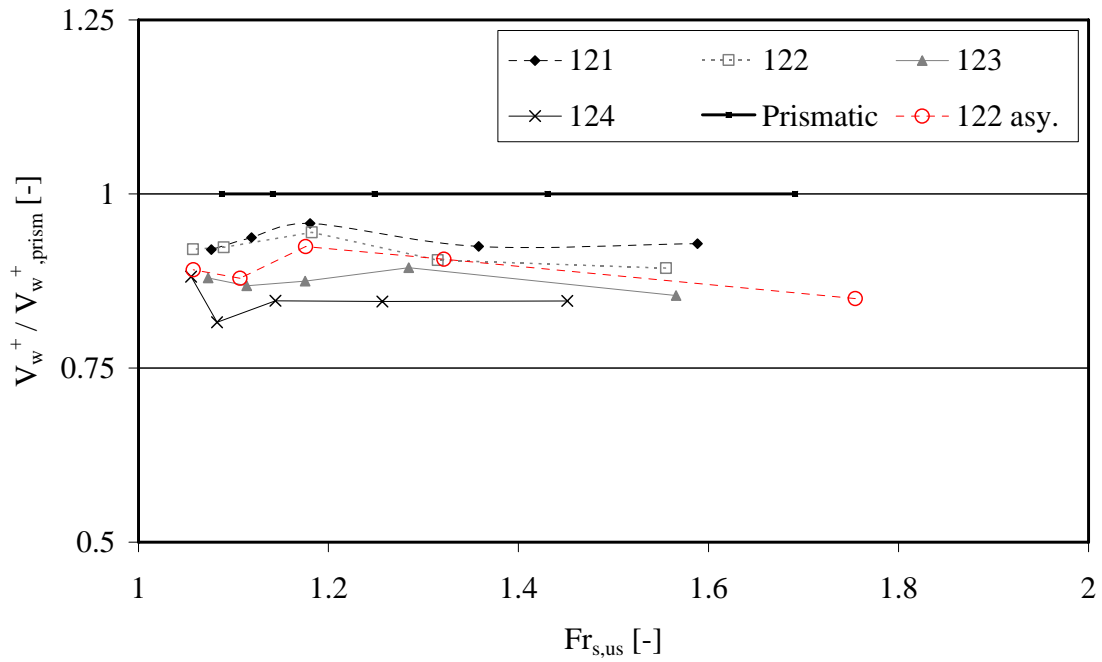


Fig-A5.9: Absolute wave celerity of the macro-rough configurations relative to the prismatic reference $V_w^+ / V_{w,prism}^+$ as a function of the upstream surge Froude number ($x=0.42$ m). Configurations 121-124.

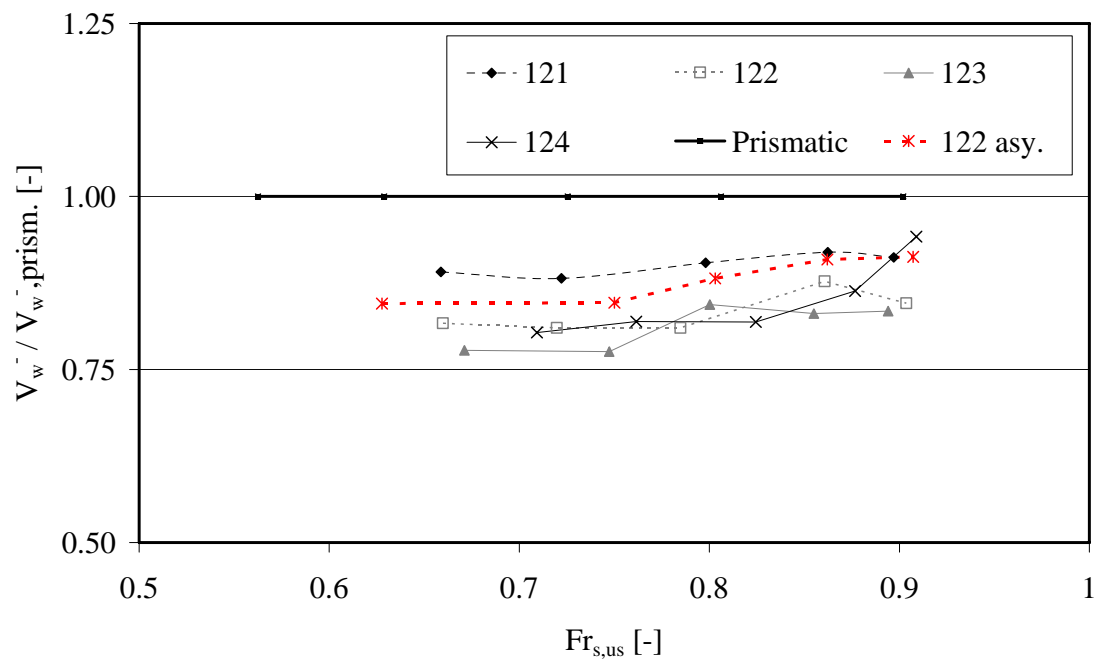


Fig-A5.10: Absolute wave celerity of the macro-rough configurations relative to the prismatic reference $V_w^- / V_{w,prism}^-$ as a function of the upstream surge Froude number ($x=0.42$ m). Configurations 121-124.

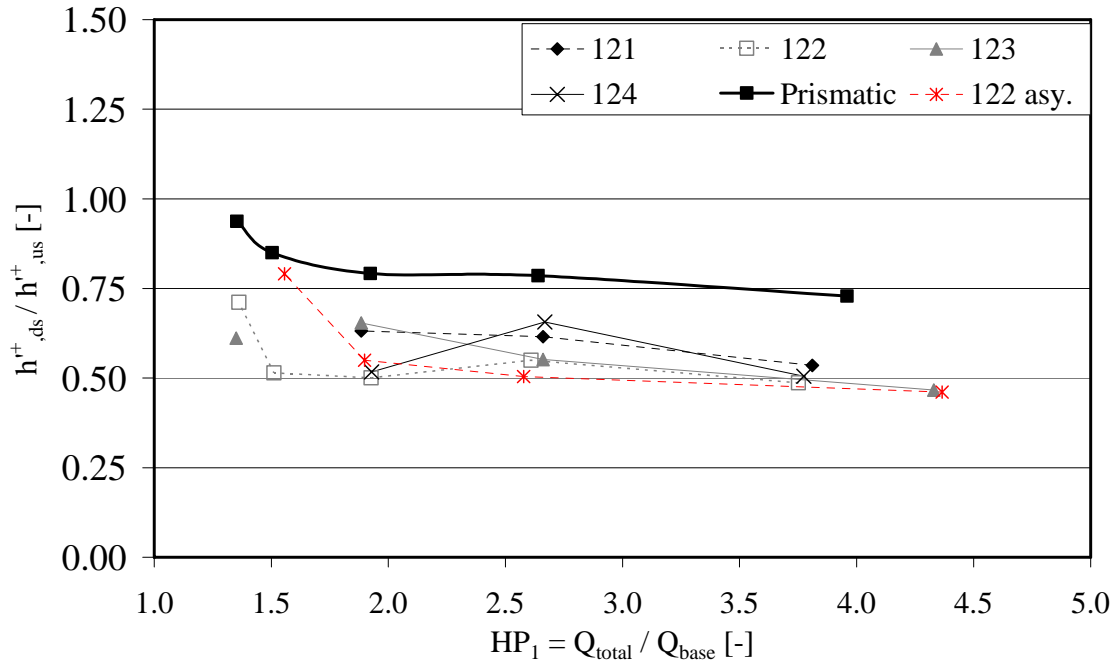


Fig-A5.11: Observed surge wave height ratio between the end and the beginning of the macro-rough reach h^+_{ds}/h^+_{us} (positive wave from upstream) as a function of the discharge ratio $HP_1 = Q_{total} / Q_b$. Configurations 121-124.

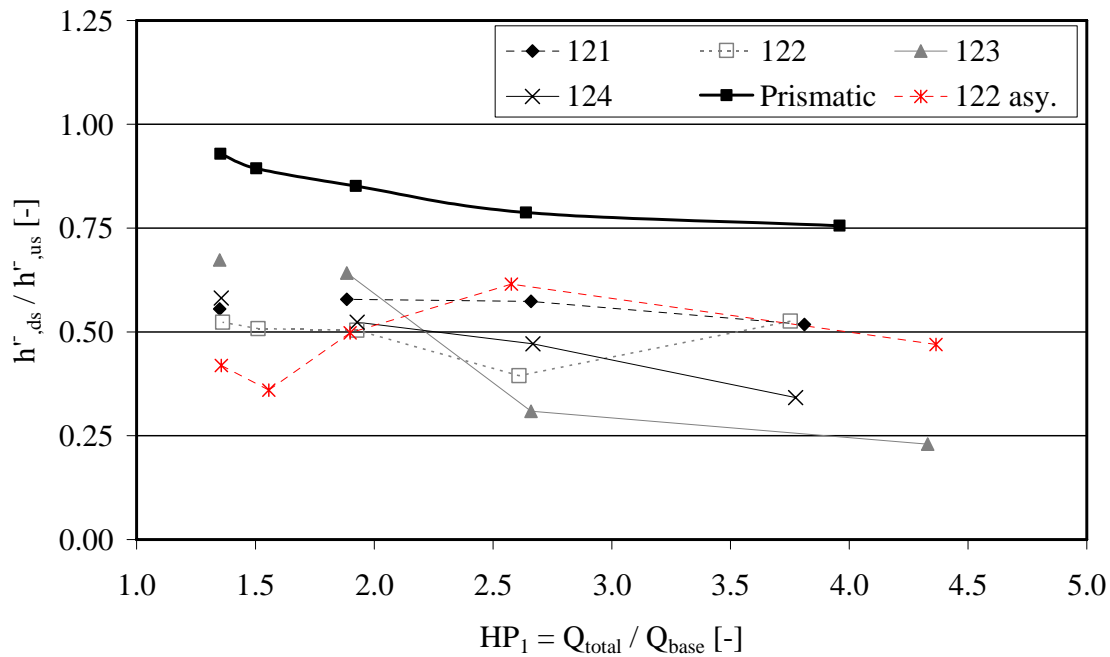


Fig-A5.12: Observed surge wave height ratio between the end and the beginning of the macro-rough reach h^-_{ds}/h^-_{us} (negative wave from upstream) as a function of $HP_1 = Q_{total} / Q_b$. Configurations 121-124.

A 5-1: Summarized test results for the unsteady flow tests: 141 to 144


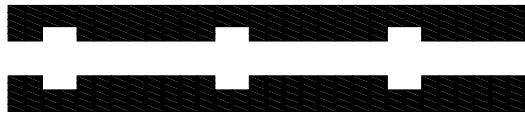
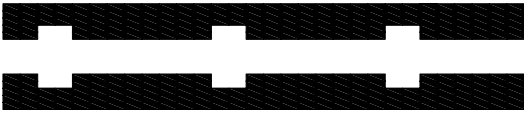
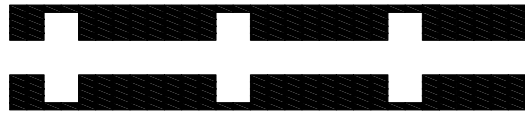
 <p>Configuration 141 $L_b = 0.5 \text{ m}, L_c = 2.0 \text{ m}, \Delta B = 0.1 \text{ m}$</p>	 <p>Configuration 142 $L_b = 0.5 \text{ m}, L_c = 2.0 \text{ m}, \Delta B = 0.2 \text{ m}$</p>
 <p>Configuration 143 $L_b = 0.5 \text{ m}, L_c = 2.0 \text{ m}, \Delta B = 0.3 \text{ m}$</p>	 <p>Configuration 144 $L_b = 0.5 \text{ m}, L_c = 2.0 \text{ m}, \Delta B = 0.4 \text{ m}$</p>

Table: Characteristics of the surge wave experiments and numerical values of the attenuation parameter of the positive (b^+) and the negative (b^-) surge wave front.

<i>Conf.</i> [-]	<i>Scen.</i> [-]	Q_b [U/s]	Q_{wave} [U/s]	Q_{total} [U/s]	HP_1 [-]	$Fr_{s,us}^+$ [-]	$Fr_{s,us}^-$ [-]	b^+ [-]	b^- [-]
141	3	5.13	17.60	22.73	4.43	1.75	0.60	0.12	1.33
141	8	10.10	17.54	27.64	2.74	1.40	0.69	0.26	0.82
141	13	19.50	17.44	36.94	1.89	1.21	0.77	0.34	0.50
141	18	34.46	17.30	51.76	1.50	1.12	0.86	0.51	0.17
141	23	47.48	17.15	64.63	1.36	1.08	0.87	-0.43	5.45
142	3	5.53	17.59	23.12	4.18	1.67	0.61	0.19	0.55
142	8	9.77	17.54	27.31	2.80	1.40	0.69	0.28	0.62
142	13	19.28	17.44	36.72	1.90	1.19	0.77	0.47	1.31
142	18	33.25	17.31	50.56	1.52	1.11	0.86	0.81	1.20
142	23	48.42	17.17	65.59	1.35	1.07	0.88	0.34	1.41
143	3	5.89	17.59	23.48	3.99	1.60	0.64	0.29	1.22
143	8	9.98	17.54	27.52	2.76	1.37	0.70	0.24	1.03
143	13	19.52	17.44	36.96	1.89	1.19	0.78	1.03	0.93
143	18	34.64	17.29	51.93	1.50	1.11	0.87	3.63	1.37
143	23	48.42	17.16	65.58	1.35	1.07	0.89	6.60	3.86
144	3	5.96	17.59	23.55	3.95	1.57	0.67	0.25	0.99
144	8	10.49	17.51	28.00	2.67	1.32	0.73	0.19	1.20
144	13	18.80	17.45	36.25	1.93	1.16	0.80	0.72	2.07
144	18	34.33	17.28	51.61	1.50	1.09	0.87	0.65	1.76
144	23	48.31	17.27	65.58	1.36	1.06	0.89	2.80	6.00

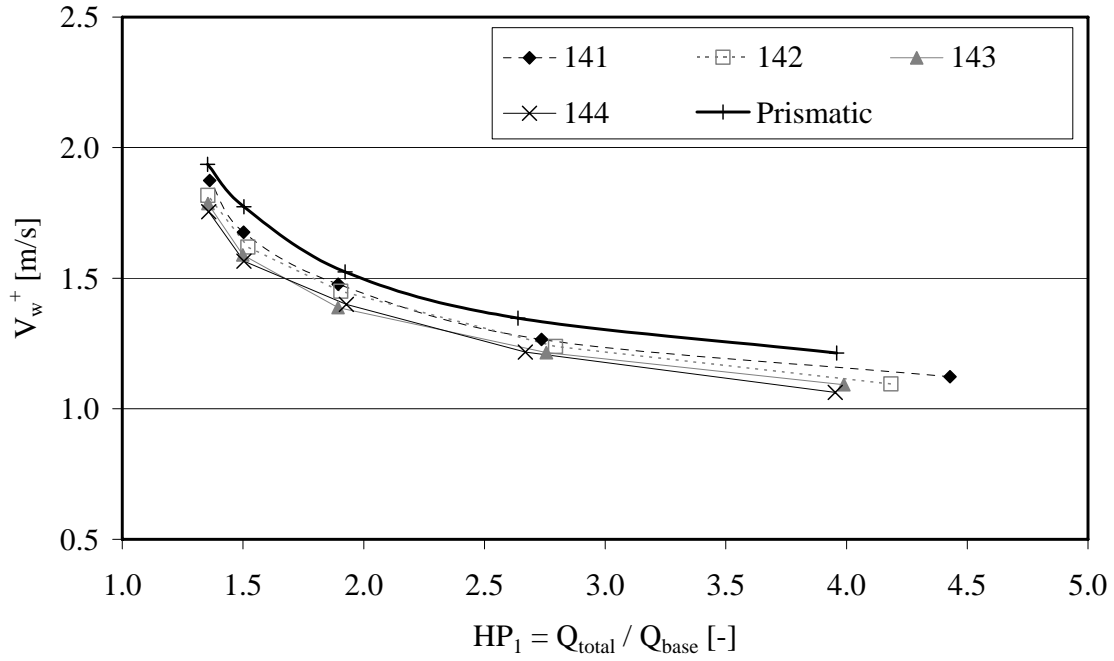


Fig-A5.13: Absolute wave celerity of the positive wave V_w^+ as a function of the discharge ratio $HP_1 = Q_{total} / Q_{base}$. Configurations 141-144.

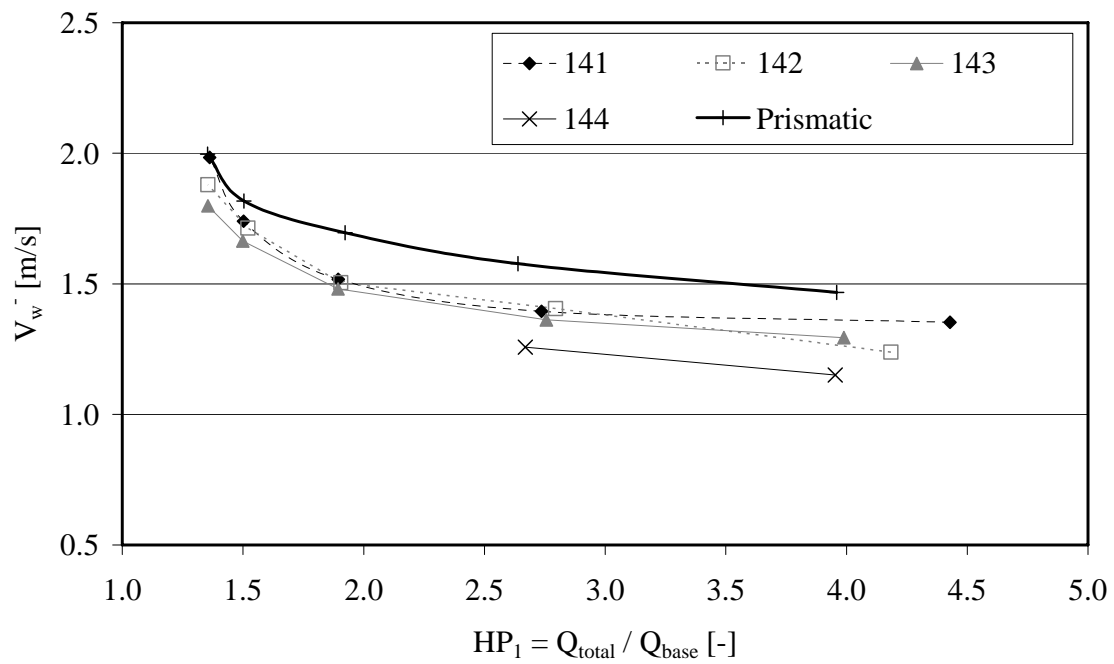


Fig-A5.14: Absolute wave celerity of the negative wave V_w^- as a function of the discharge ratio $HP_1 = Q_{total} / Q_{base}$. Configurations 141-144.

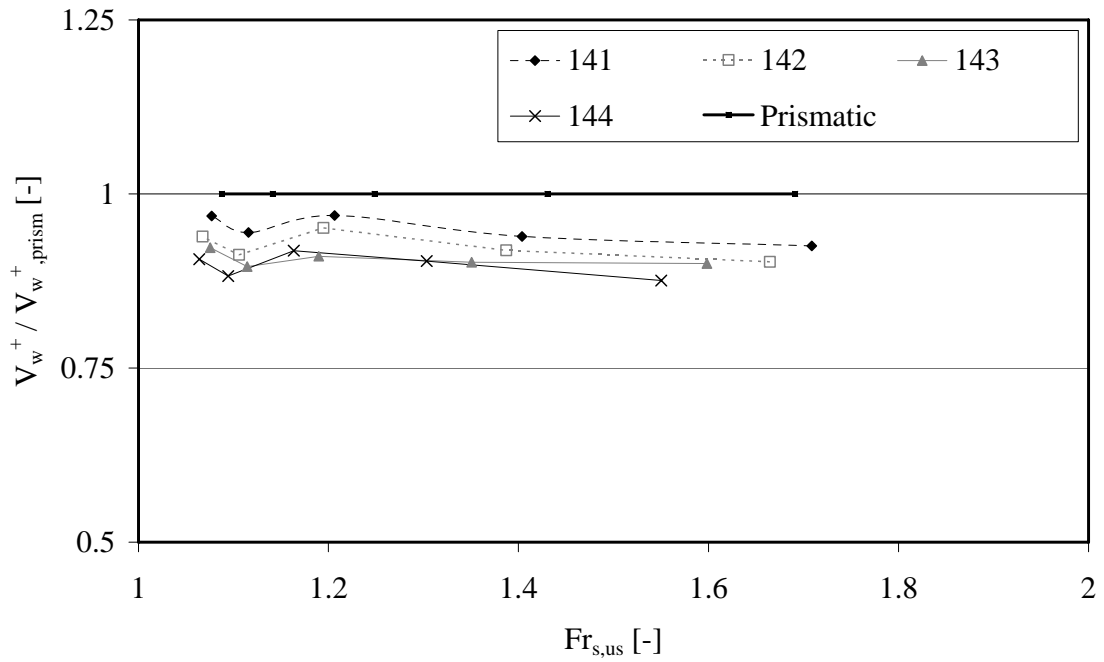


Fig-A5.15: Absolute wave celerity of the macro-rough configurations relative to the prismatic reference $V_w^+ / V_{w,prism}^+$ as a function of the upstream surge Froude number ($x=0.42$ m). Configurations 141-144.

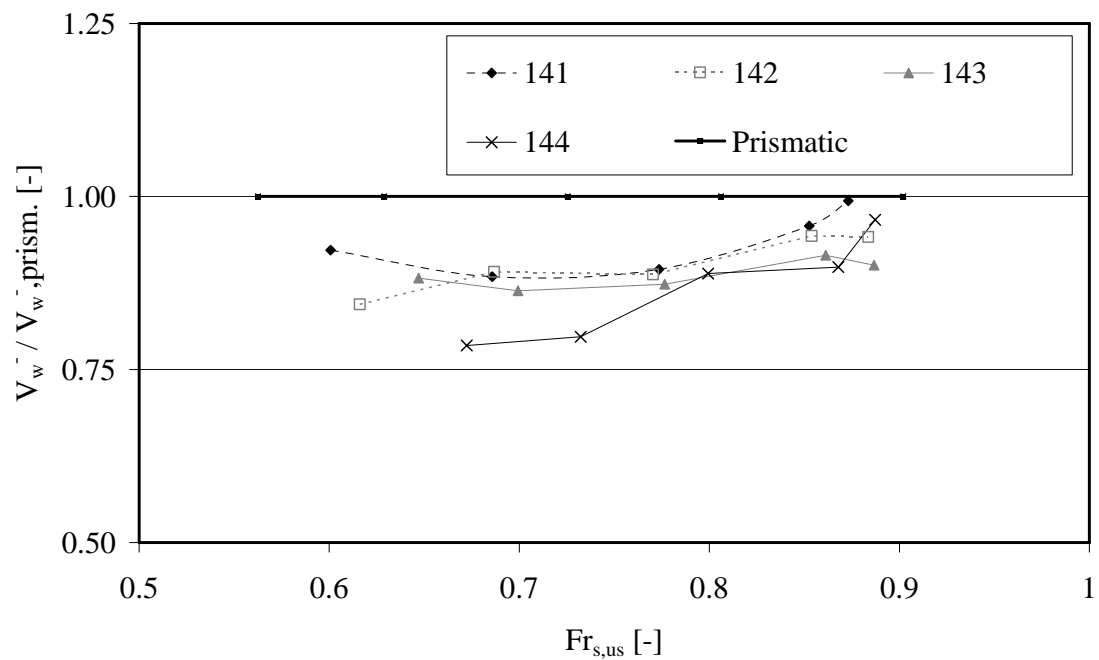


Fig-A5.16: Absolute wave celerity of the macro-rough configurations relative to the prismatic reference $V_w^- / V_{w,prism}^-$ as a function of the upstream surge Froude number ($x=0.42$ m). Configurations 141-144.

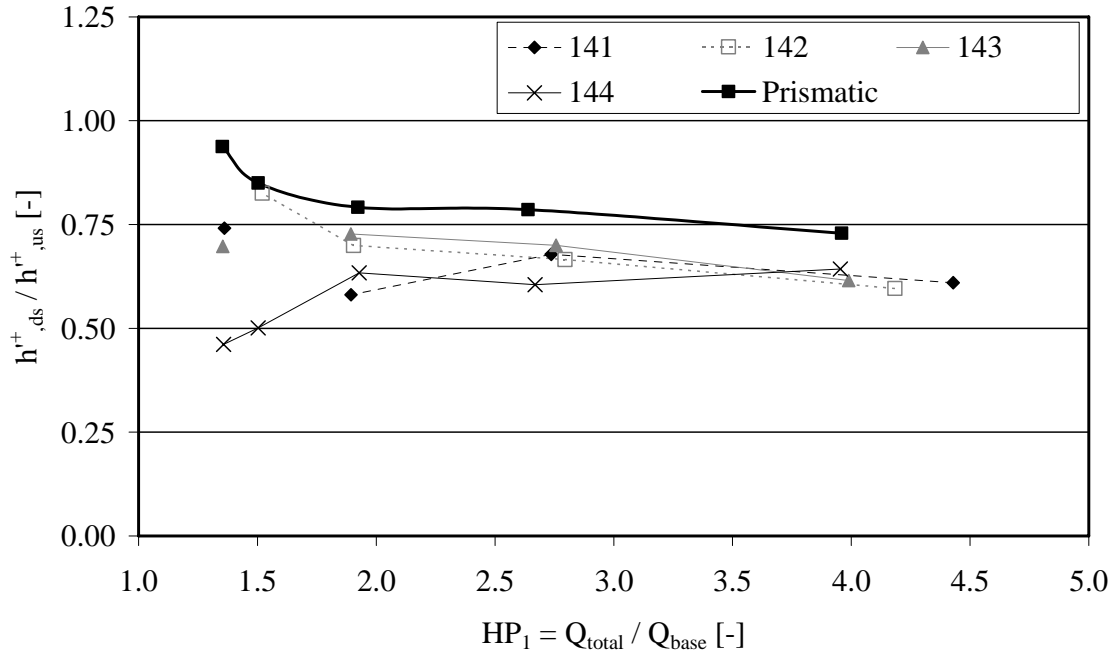


Fig-A5.17: Observed surge wave height ratio between the end and the beginning of the macro-rough reach h^r_{ds}/h^r_{us} (positive wave from upstream) as a function of the discharge ratio $HP_1 = Q_{total}/Q_b$. Configurations 141-144.

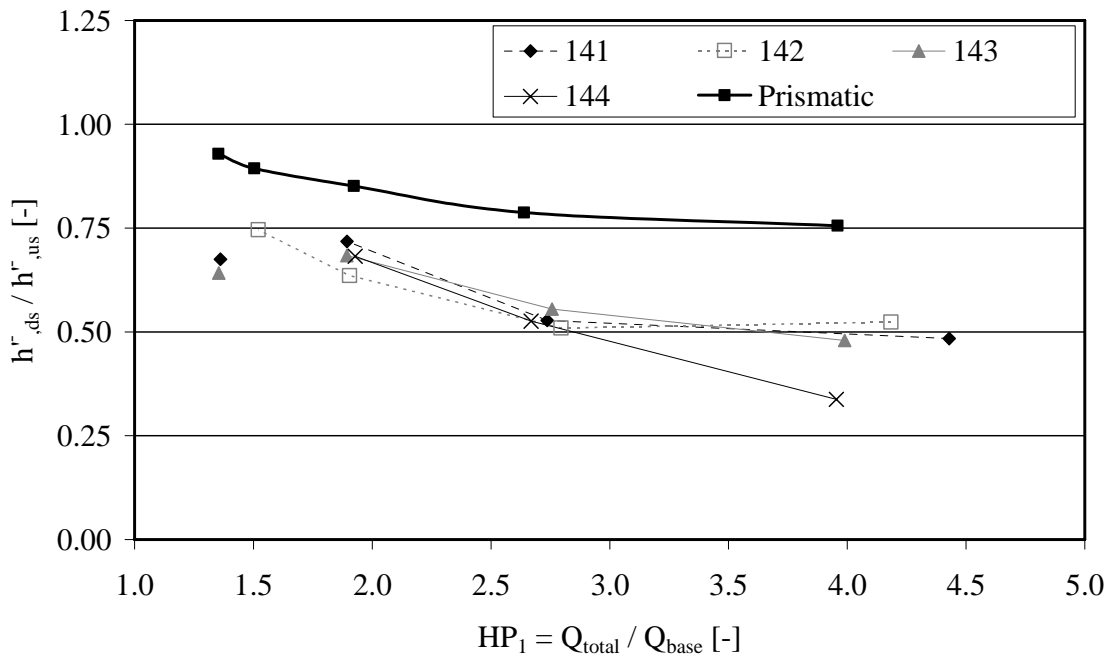


Fig-A5.18: Observed surge wave height ratio between the end and the beginning of the macro-rough reach h^r_{ds}/h^r_{us} (negative wave from upstream) as a function of $HP_1 = Q_{total}/Q_b$. Configurations 141-144.

A 5-1: Summarized test results for the unsteady flow tests: 211 to 214


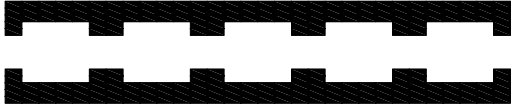


 <p>Configuration 211 $L_b = 1.0 \text{ m}, L_c = 0.5 \text{ m}, \Delta B = 0.1 \text{ m}$</p>	 <p>Configuration 212 $L_b = 1.0 \text{ m}, L_c = 0.5 \text{ m}, \Delta B = 0.2 \text{ m}$</p>
 <p>Configuration 213 $L_b = 1.0 \text{ m}, L_c = 0.5 \text{ m}, \Delta B = 0.3 \text{ m}$</p>	 <p>Configuration 214 $L_b = 1.0 \text{ m}, L_c = 0.5 \text{ m}, \Delta B = 0.4 \text{ m}$</p>

Table: Characteristics of the surge wave experiments and numerical values of the attenuation parameter of the positive (b^+) and the negative (b^-) surge wave front.

Conf. [-]	Scen. [-]	Q_b [L/s]	Q_{wave} [L/s]	Q_{total} [L/s]	HP_1 [-]	$Fr_{s,us}^+$ [-]	$Fr_{s,us}^-$ [-]	b^+ [-]	b^- [-]
211	3	4.91	17.58	22.49	4.58	1.68	0.68	0.68	1.53
211	8	10.22	17.49	27.71	2.71	1.32	0.76	1.14	2.05
211	13	18.25	17.46	35.71	1.96	1.16	0.82	1.94	2.18
211	18	34.25	17.30	51.55	1.51	1.09	0.89	2.21	2.24
211	23	48.30	17.17	65.47	1.36	1.06	0.92	1.89	1.42
212	3	5.50	17.60	23.10	4.20	1.62	0.67	0.93	3.40
212	8	10.78	17.53	28.31	2.63	1.31	0.76	1.34	4.13
212	13	18.67	17.45	36.12	1.93	1.14	0.85	3.19	4.46
212	18	33.42	17.30	50.72	1.52	1.08	0.90	5.21	7.19
212	23	48.43	17.17	65.60	1.35	1.07	0.92	8.85	6.86
212 asy.	3	5.72	17.59	23.31	4.08	1.56	0.76	0.90	1.23
212 asy.	8	11.09	17.53	28.62	2.58	1.26	0.76	0.86	1.41
212 asy.	13	19.39	17.44	36.83	1.90	1.14	0.83	1.23	1.70
212 asy.	18	32.19	17.32	49.51	1.54	1.09	0.90	1.96	1.45
212 asy.	23	48.40	17.17	65.57	1.35	1.06	0.92	2.64	2.87
213	3	6.00	17.59	23.59	3.93	1.55	0.71	1.35	3.69
213	8	10.06	17.54	27.60	2.74	1.33	0.78	1.56	4.65
213	13	18.62	17.44	36.06	1.94	1.17	0.83	2.34	5.53
213	18	34.10	17.29	51.39	1.51	1.08	0.91	3.30	6.17
213	23	48.26	17.16	65.42	1.36	1.07	0.92	8.30	9.05
214	3	6.41	17.60	24.01	3.75	1.49	0.71	1.48	3.44
214	8	10.87	17.53	28.40	2.61	1.29	0.76	1.74	3.99
214	13	18.68	17.44	36.12	1.93	1.14	0.83	1.76	5.36
214	18	33.97	17.29	51.26	1.51	1.08	0.90	2.26	6.86
214	23	48.07	17.16	65.23	1.36	1.05	0.93	5.44	10.56

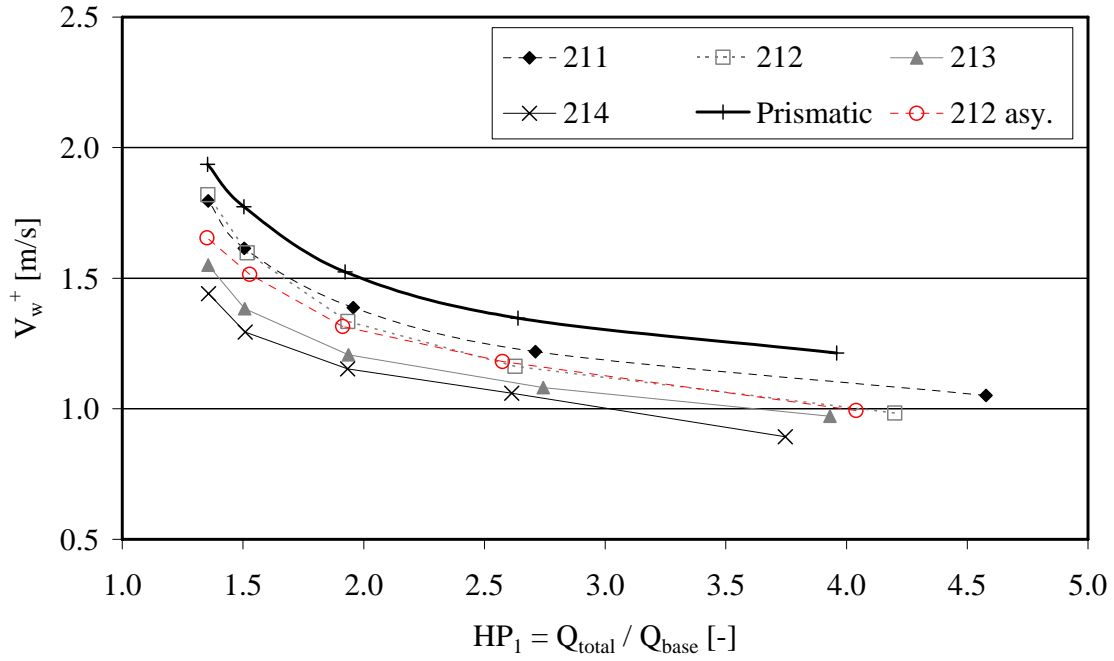


Fig-A5.19: Absolute wave celerity of the positive wave V_w^+ as a function of the discharge ratio $HP_1 = Q_{total} / Q_{base}$. Configurations 211-214.

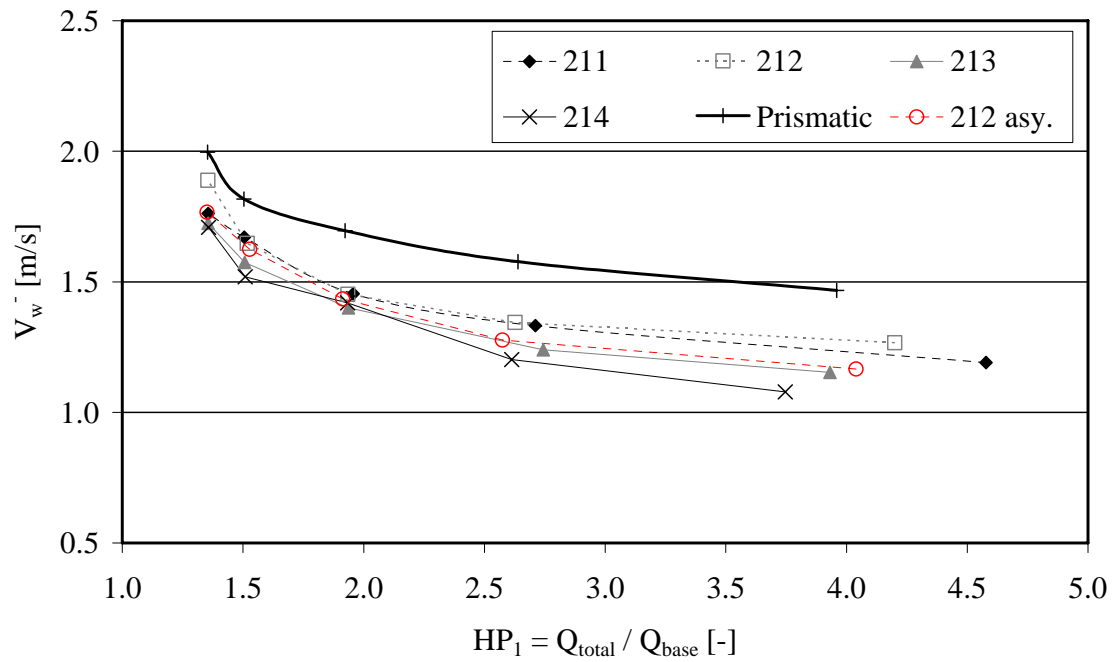


Fig-A5.20: Absolute wave celerity of the negative wave V_w^- as a function of the discharge ratio $HP_1 = Q_{total} / Q_{base}$. Configurations 211-214.

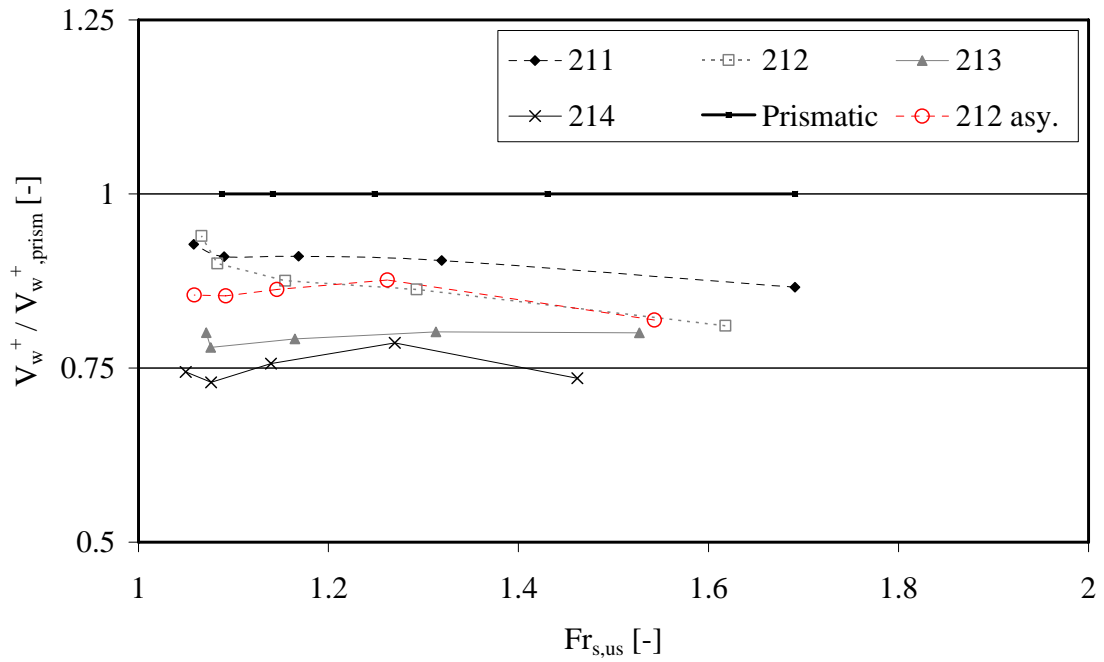


Fig-A5.21: Absolute wave celerity of the macro-rough configurations relative to the prismatic reference $V_w^+ / V_{w,prism}^+$ as a function of the upstream surge Froude number ($x=0.42$ m). Configurations 211-214.

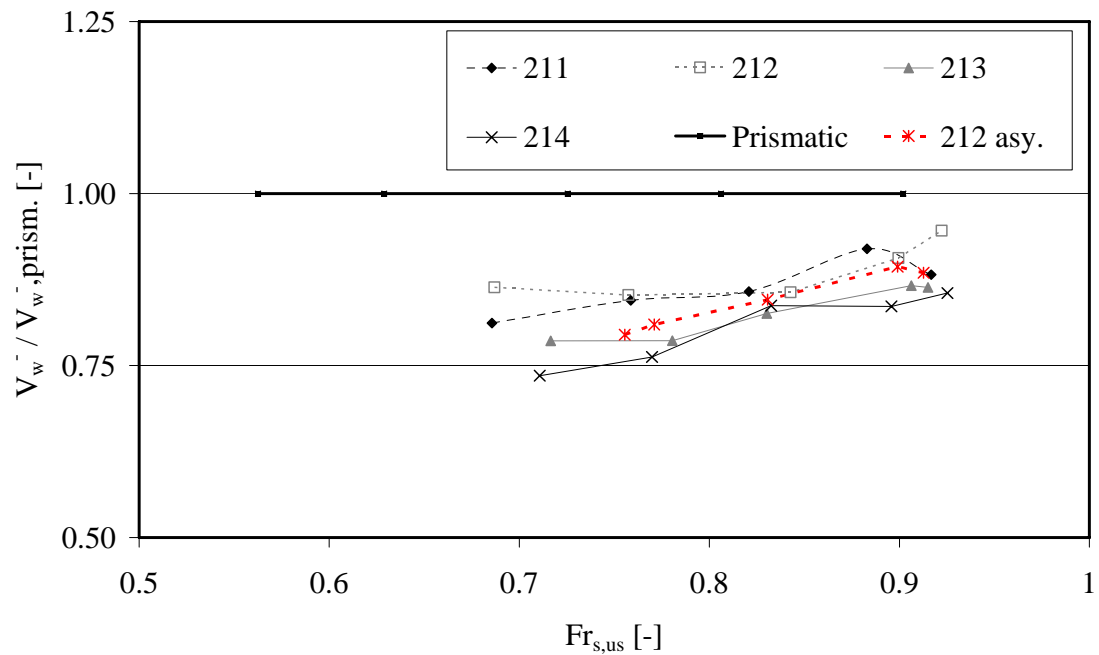


Fig-A5.22: Absolute wave celerity of the macro-rough configurations relative to the prismatic reference $V_w^- / V_{w,prism}^-$ as a function of the upstream surge Froude number ($x=0.42$ m). Configurations 211-214.

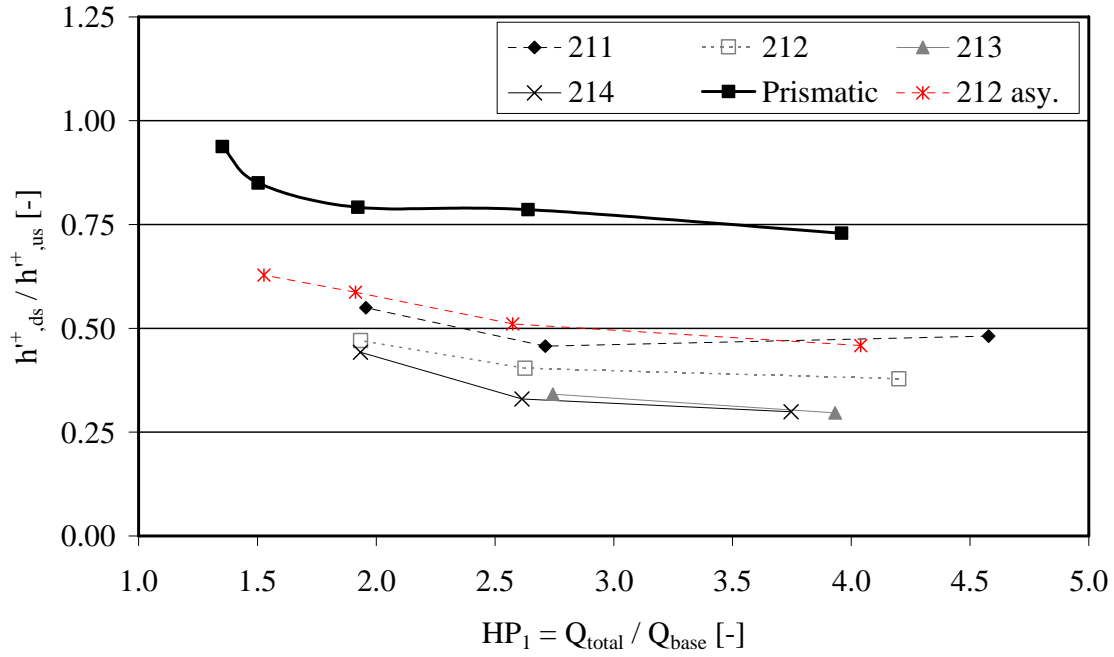


Fig-A5.23: Observed surge wave height ratio between the end and the beginning of the macro-rough reach h^{r+}_{ds}/h^{r+}_{us} (positive wave from upstream) as a function of the discharge ratio $HP_1 = Q_{total}/Q_b$. Configurations 211-214.

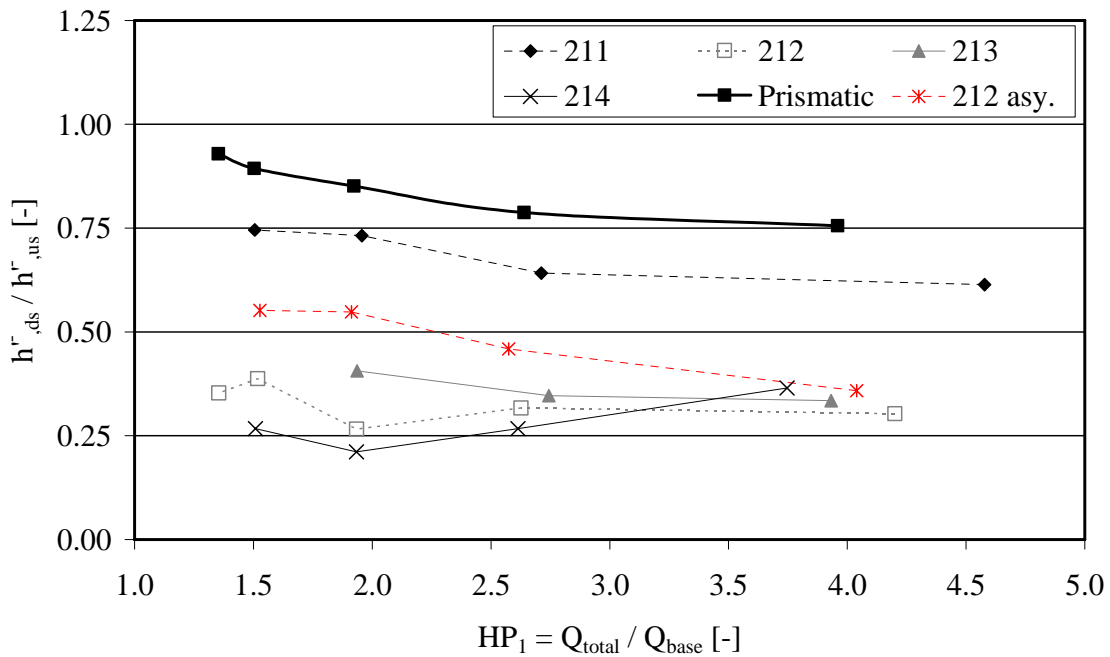


Fig-A5.24: Observed surge wave height ratio between the end and the beginning of the macro-rough reach h^{r-}_{ds}/h^{r-}_{us} (negative wave from upstream) as a function of $HP_1 = Q_{total}/Q_b$. Configurations 211-214.

A 5-1: Summarized test results for the unsteady flow tests: 221 to 224





 <p>Configuration 221 $L_b = 1.0 \text{ m}, L_c = 1.0 \text{ m}, \Delta B = 0.1 \text{ m}$</p>	 <p>Configuration 222 $L_b = 1.0 \text{ m}, L_c = 1.0 \text{ m}, \Delta B = 0.2 \text{ m}$</p>
 <p>Configuration 223 $L_b = 1.0 \text{ m}, L_c = 1.0 \text{ m}, \Delta B = 0.3 \text{ m}$</p>	 <p>Configuration 224 $L_b = 1.0 \text{ m}, L_c = 1.0 \text{ m}, \Delta B = 0.4 \text{ m}$</p>

Table: Characteristics of the surge wave experiments and numerical values of the attenuation parameter of the positive (b^+) and the negative (b^-) surge wave front.

Conf.	Scen.	Q_b	Q_{wave}	Q_{total}	HP_1	$Fr_{s,us}^+$	$Fr_{s,us}^-$	b^+	b^-
[-]	[-]	[L/s]	[L/s]	[L/s]	[-]	[-]	[-]	[-]	[-]
221	3	6.38	17.55	23.93	3.75	1.48	0.69	0.85	1.33
221	8	10.55	17.51	28.06	2.66	1.30	0.74	1.21	1.60
221	13	20.13	17.41	37.54	1.87	1.15	0.83	1.12	2.35
221	18	33.93	17.27	51.20	1.51	1.09	0.88	1.79	2.90
221	23	48.46	17.14	65.60	1.35	1.06	0.91	0.96	1.57
222	3	5.34	17.58	22.92	4.29	1.58	0.69	0.75	1.83
222	8	10.95	17.52	28.47	2.60	1.29	0.78	1.07	2.36
222	13	18.52	17.44	35.96	1.94	1.15	0.83	2.08	3.93
222	18	32.77	17.29	50.06	1.53	1.08	0.88	2.39	4.17
222	23	48.02	17.16	65.18	1.36	1.05	0.91	2.95	4.78
random	3	6.13	17.59	23.72	3.87	1.67	0.68	0.83	2.70
random	8	10.04	17.53	27.57	2.75	1.34	0.75	1.09	3.44
random	13	18.62	17.44	36.06	1.94	1.18	0.83	1.12	4.68
random	18	32.15	17.31	49.46	1.54	1.09	0.88	1.88	7.17
random	23	47.71	17.17	64.88	1.36	1.07	0.91	1.96	6.16
223	3	5.35	17.58	22.93	4.28	1.52	0.70	0.88	3.01
223	8	11.58	17.51	29.09	2.51	1.26	0.78	1.39	2.59
223	13	19.33	17.42	36.75	1.90	1.15	0.84	1.72	2.74
223	18	32.58	17.28	49.86	1.53	1.09	0.89	2.61	2.22
223	23	49.26	17.13	66.39	1.35	1.05	0.93	2.11	2.40
224	3	5.08	17.59	22.67	4.46	1.53	0.70	1.14	2.84
224	8	11.39	17.52	28.91	2.54	1.23	0.79	1.74	2.77
224	13	19.29	17.41	36.70	1.90	1.14	0.85	1.38	2.54
224	18	33.47	17.29	50.76	1.52	1.07	0.90	1.89	4.67
224	23	47.78	17.17	64.95	1.36	1.05	0.93	5.26	7.16

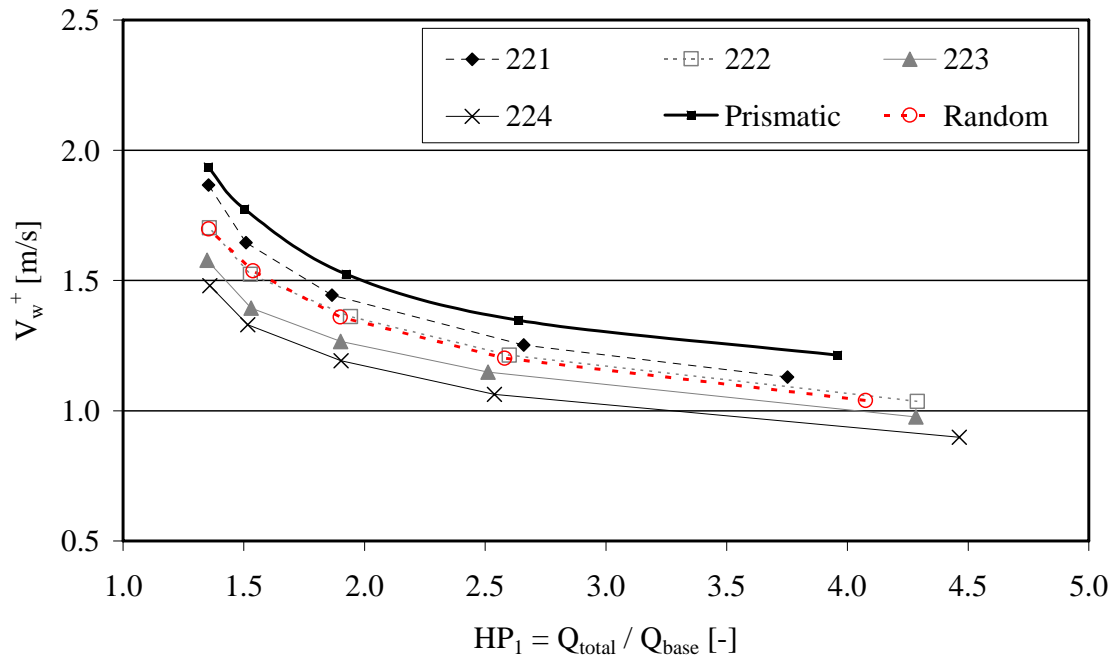


Fig-A5.25: Absolute wave celerity of the positive wave V_w^+ as a function of the discharge ratio $HP_1 = Q_{total} / Q_{base}$. Configurations 221-224.

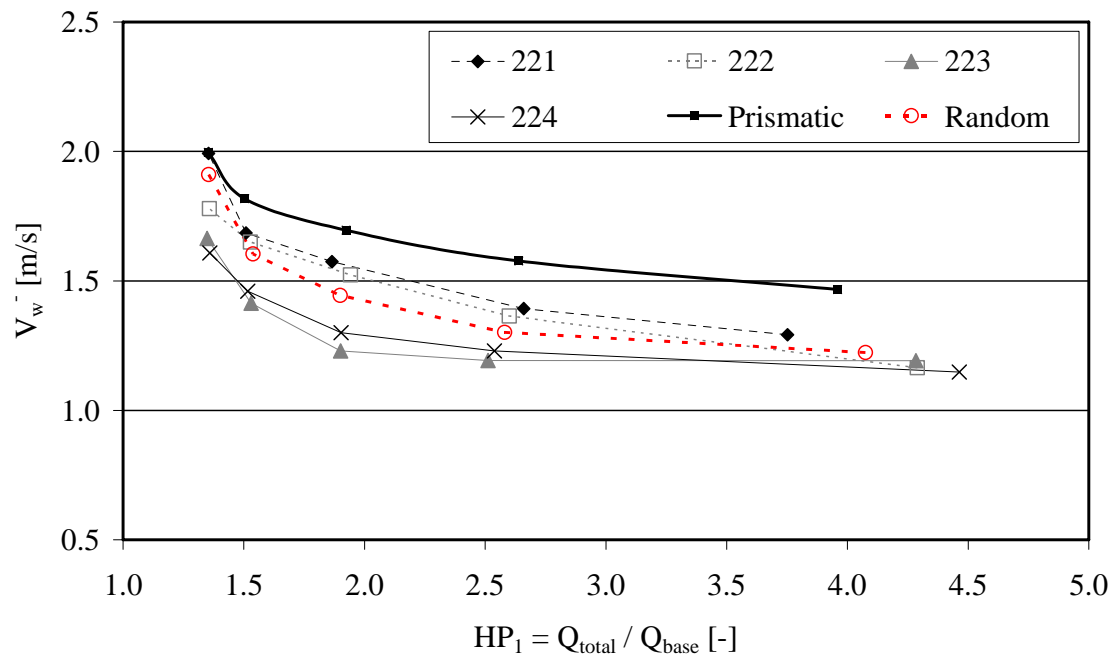


Fig-A5.26: Absolute wave celerity of the negative wave V_w^- as a function of the discharge ratio $HP_1 = Q_{total} / Q_{base}$. Configurations 221-224.

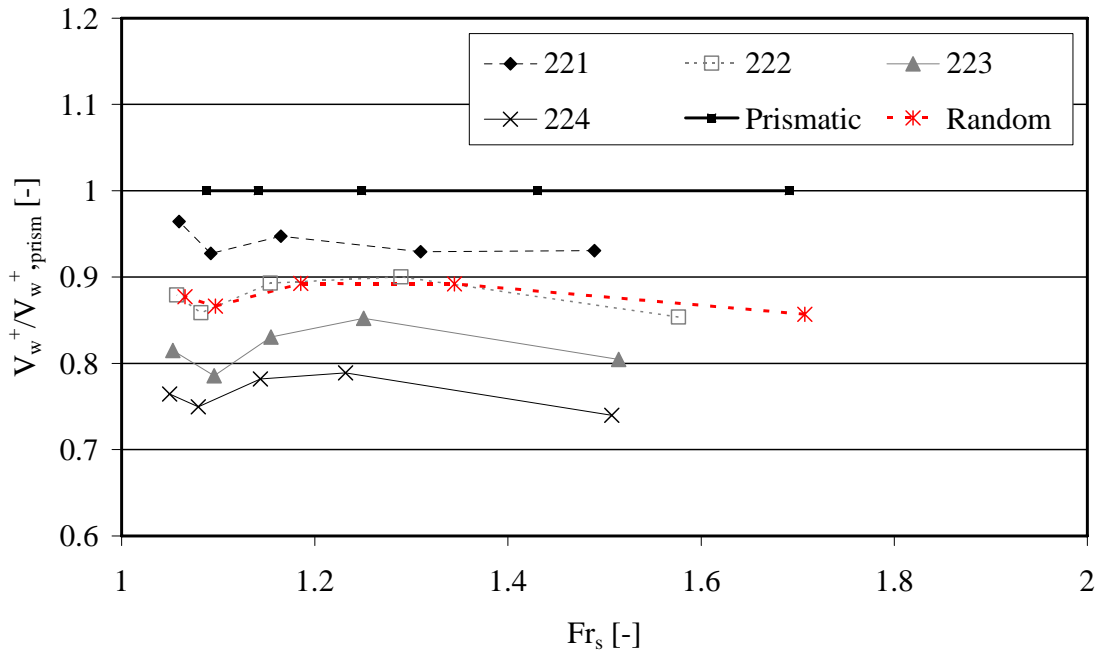


Fig-A5.27: Absolute wave celerity of the macro-rough configurations relative to the prismatic reference $V_w^+ / V_{w,prism}^+$ as a function of the upstream surge Froude number ($x=0.42$ m). Configurations 221-224.

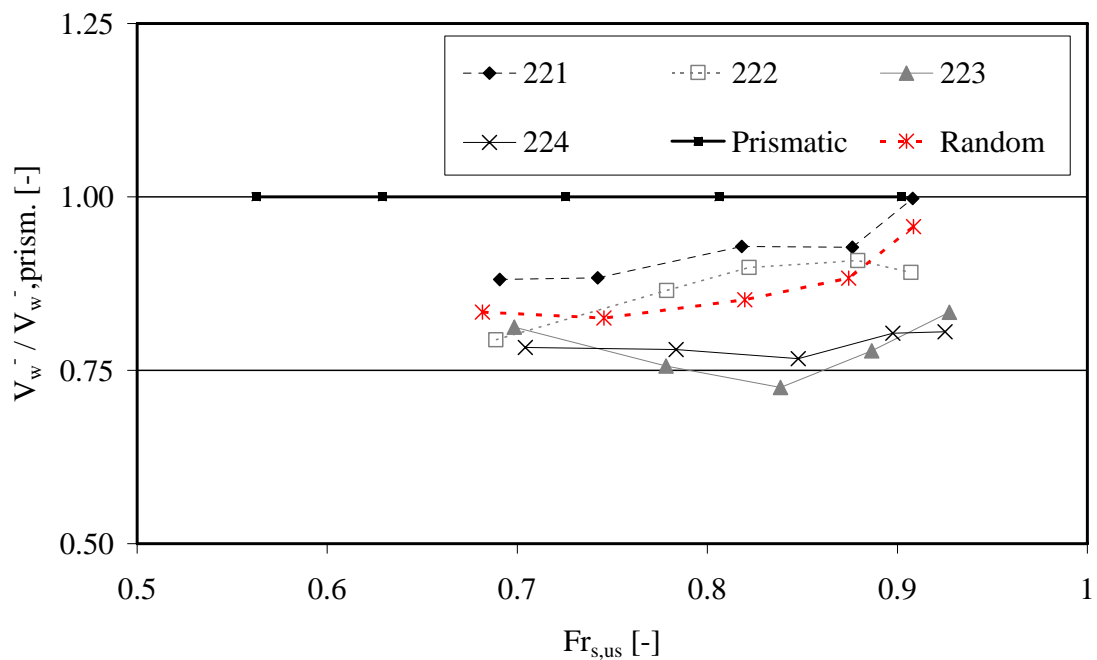


Fig-A5.28: Absolute wave celerity of the macro-rough configurations relative to the prismatic reference $V_w^- / V_{w,prism}^-$ as a function of the upstream surge Froude number ($x=0.42$ m). Configurations 221-224.

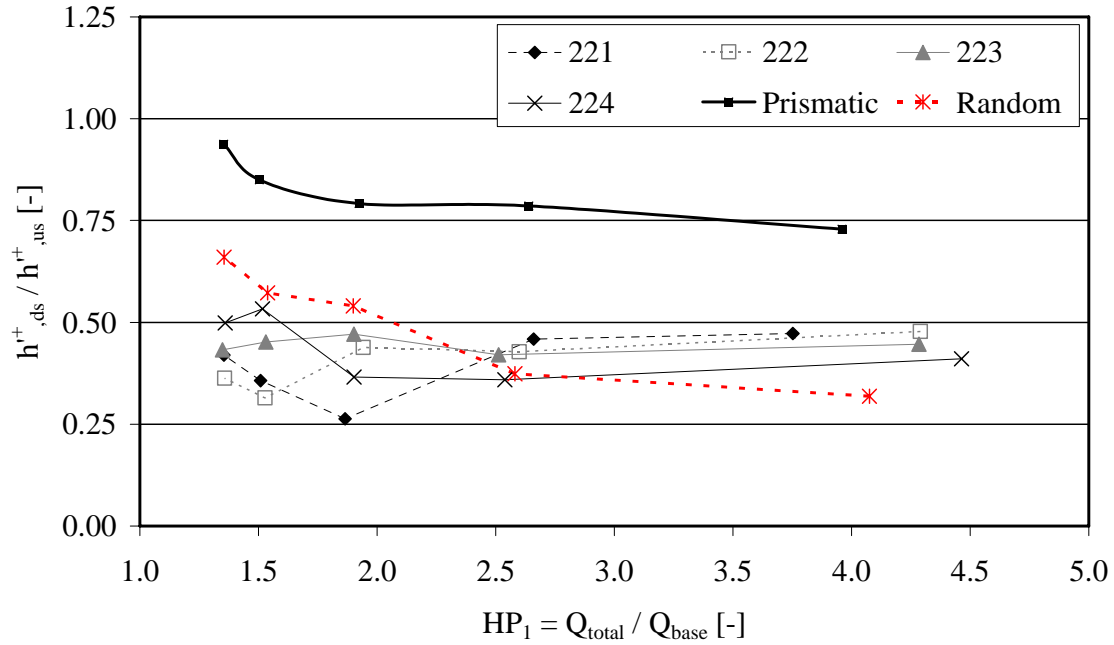


Fig-A5.29: Observed surge wave height ratio between the end and the beginning of the macro-rough reach h^+_{ds}/h^+_{us} (positive wave from upstream) as a function of the discharge ratio $HP_1 = Q_{total}/Q_b$. Configurations 221-224.

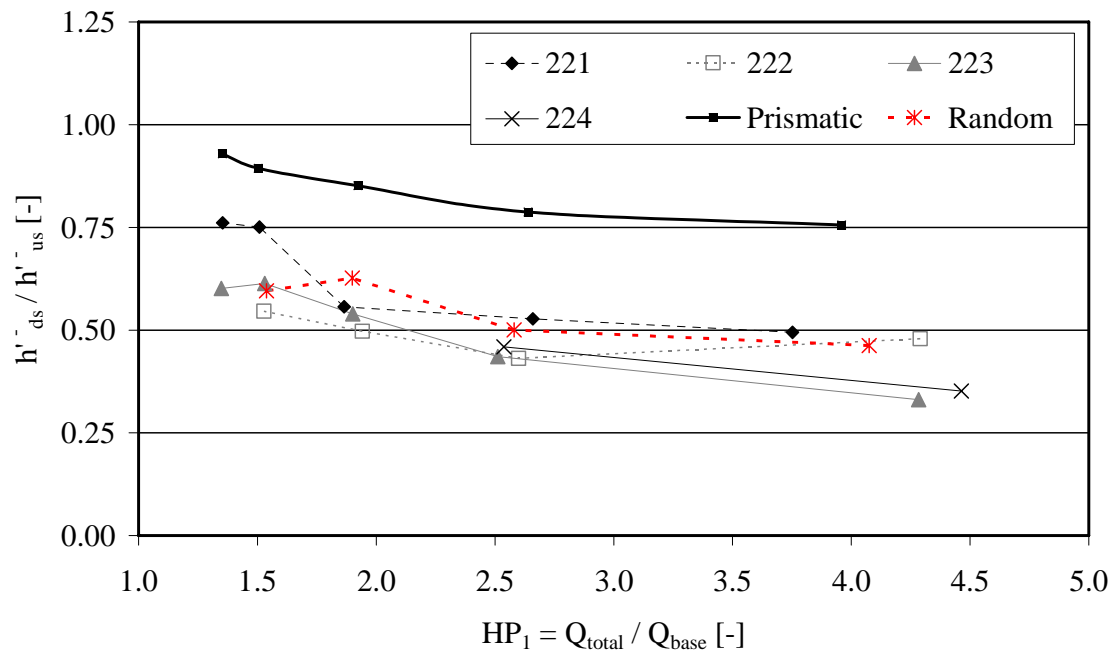


Fig-A5.30: Observed surge wave height ratio between the end and the beginning of the macro-rough reach h^-_{ds}/h^-_{us} (negative wave from upstream) as a function of $HP_1 = Q_{total}/Q_b$. Configurations 221-224.

A 5-1: Summarized test results for the unsteady flow tests: 241 to 244





 <p>Configuration 241 $L_b = 1.0\text{ m}, L_c = 2.0\text{ m}, \Delta B = 0.1\text{ m}$</p>	 <p>Configuration 242 $L_b = 1.0\text{ m}, L_c = 2.0\text{ m}, \Delta B = 0.2\text{ m}$</p>
 <p>Configuration 243 $L_b = 1.0\text{ m}, L_c = 2.0\text{ m}, \Delta B = 0.3\text{ m}$</p>	 <p>Configuration 244 $L_b = 1.0\text{ m}, L_c = 2.0\text{ m}, \Delta B = 0.4\text{ m}$</p>

Table: Characteristics of the surge wave experiments and numerical values of the attenuation parameter of the positive (b^+) and the negative (b^-) surge wave front.

Conf.	Scen.	Q_b	Q_{wave}	Q_{total}	HP_1	$Fr_{s.us}^+$	$Fr_{s.us}^-$	b^+	b^-
[-]	[-]	[L/s]	[L/s]	[L/s]	[-]	[-]	[-]	[-]	[-]
241	3	4.88	17.59	22.47	4.60	1.78	0.62	0.29	1.30
241	8	10.90	17.52	28.42	2.61	1.37	0.72	0.44	1.37
241	13	18.34	17.44	35.78	1.95	1.19	0.79	0.61	1.64
241	18	32.71	17.29	50.00	1.53	1.12	0.85	1.16	1.86
241	23	47.81	17.16	64.97	1.36	1.07	0.89	3.02	2.91
242	3	5.22	17.59	22.81	4.37	1.71	0.63	0.39	1.33
242	8	11.06	17.52	28.58	2.58	1.34	0.71	0.75	1.64
242	13	19.01	17.44	36.45	1.92	1.18	0.80	0.94	1.39
242	18	33.47	17.30	50.77	1.52	1.09	0.86	2.19	2.33
242	23	48.45	17.16	65.61	1.35	1.06	0.90	1.78	4.21
243	3	6.51	17.58	24.09	3.70	1.58	0.67	0.51	1.63
243	8	11.33	17.51	28.84	2.55	1.32	0.75	0.87	1.99
243	13	20.22	17.42	37.64	1.86	1.17	0.82	1.31	2.74
243	18	34.43	17.28	51.71	1.50	1.09	0.86	2.94	3.70
243	23	49.73	17.14	66.87	1.34	1.07	0.91	2.72	1.59
244	3	5.32	17.59	22.91	4.31	1.65	0.64	0.79	1.69
244	8	11.33	17.52	28.85	2.55	1.31	0.73	1.39	1.92
244	13	19.76	17.42	37.18	1.88	1.17	0.80	1.48	2.12
244	18	33.82	17.29	51.11	1.51	1.10	0.87	1.00	2.13
244	23	49.78	17.14	66.92	1.34	1.06	0.91	0.55	5.18

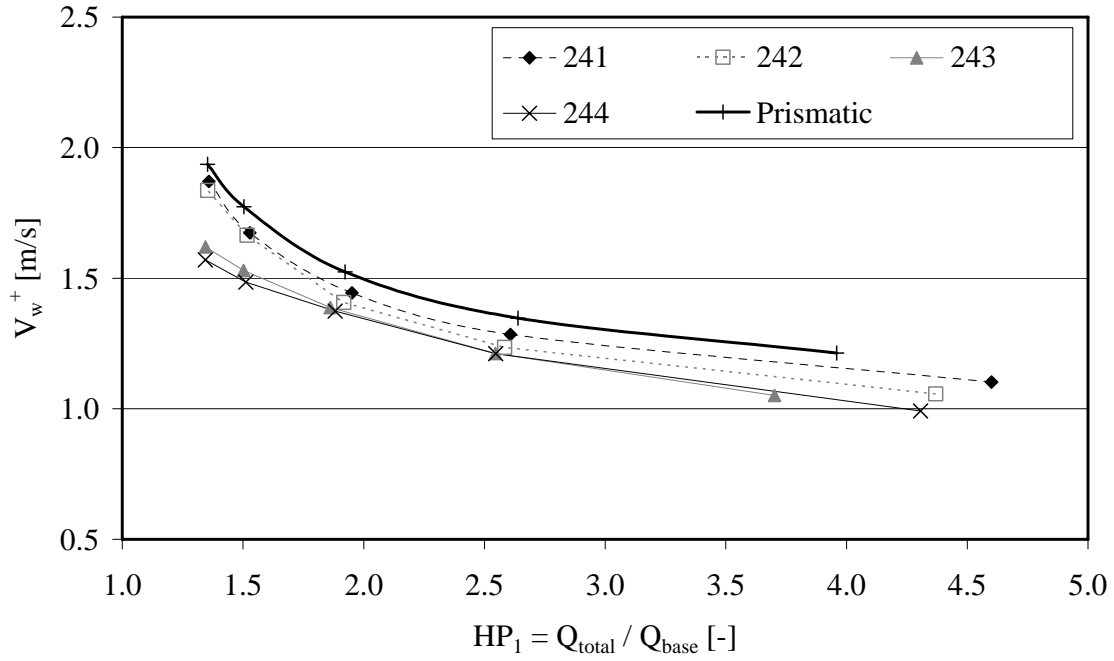


Fig-A5.31: Absolute wave celerity of the positive wave V_w^+ as a function of the discharge ratio $HP_1 = Q_{total} / Q_{base}$. Configurations 241-244.

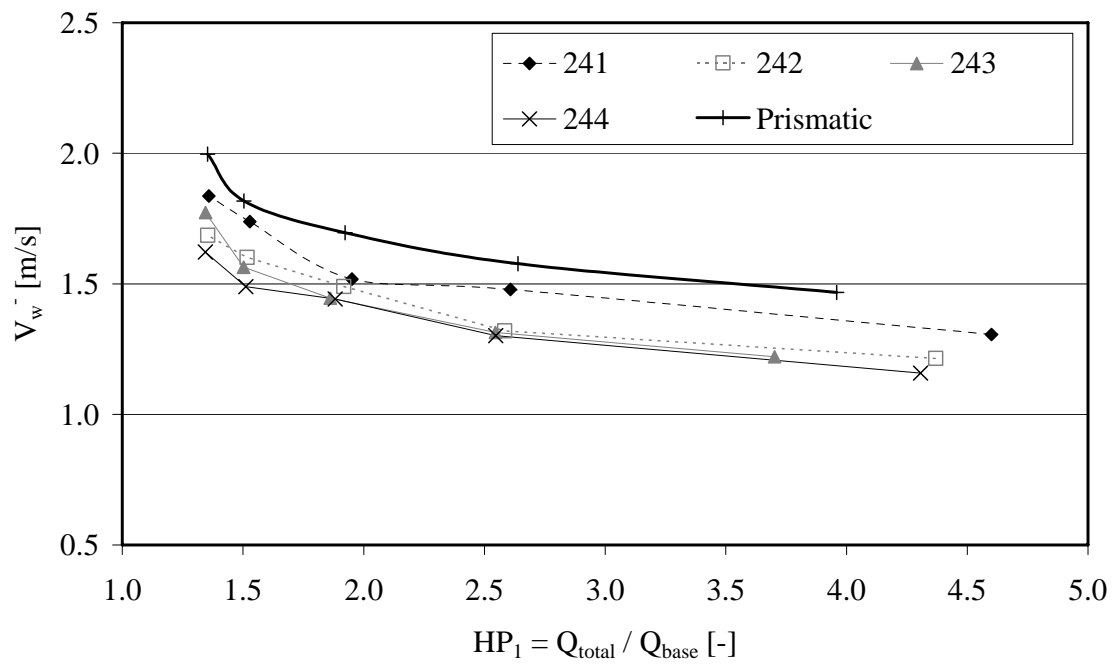


Fig-A5.32: Absolute wave celerity of the negative wave V_w^- as a function of the discharge ratio $HP_1 = Q_{total} / Q_{base}$. Configurations 241-244.

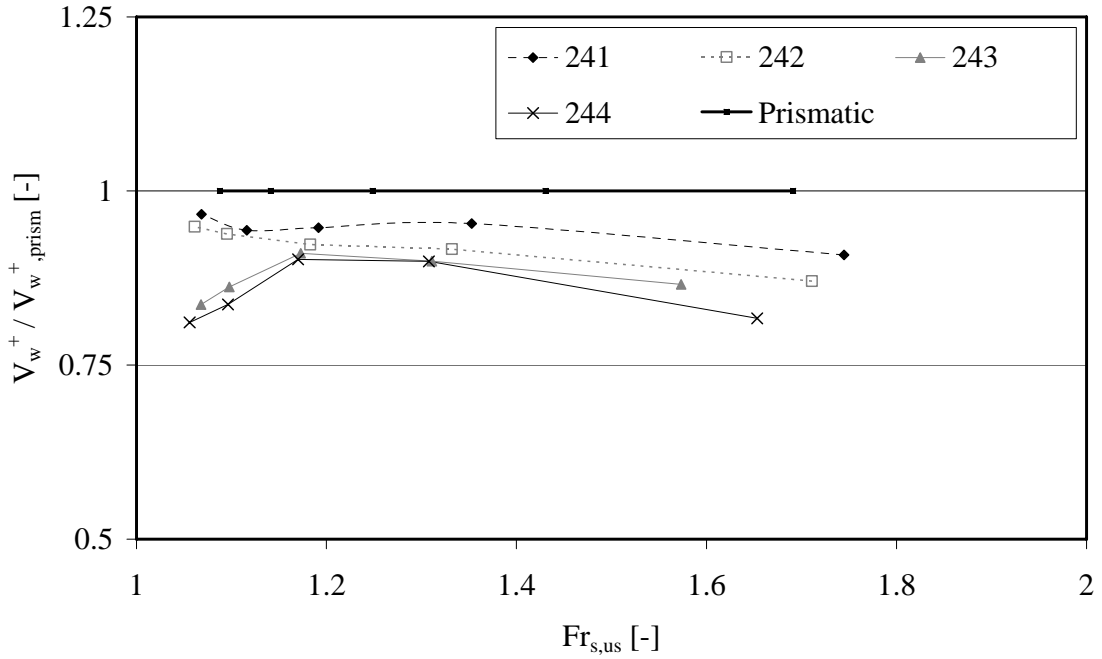


Fig-A5.33: Absolute wave celerity of the macro-rough configurations relative to the prismatic reference $V_w^+ / V_{w,prism}^+$ as a function of the upstream surge Froude number ($x=0.42$ m). Configurations 241-244.

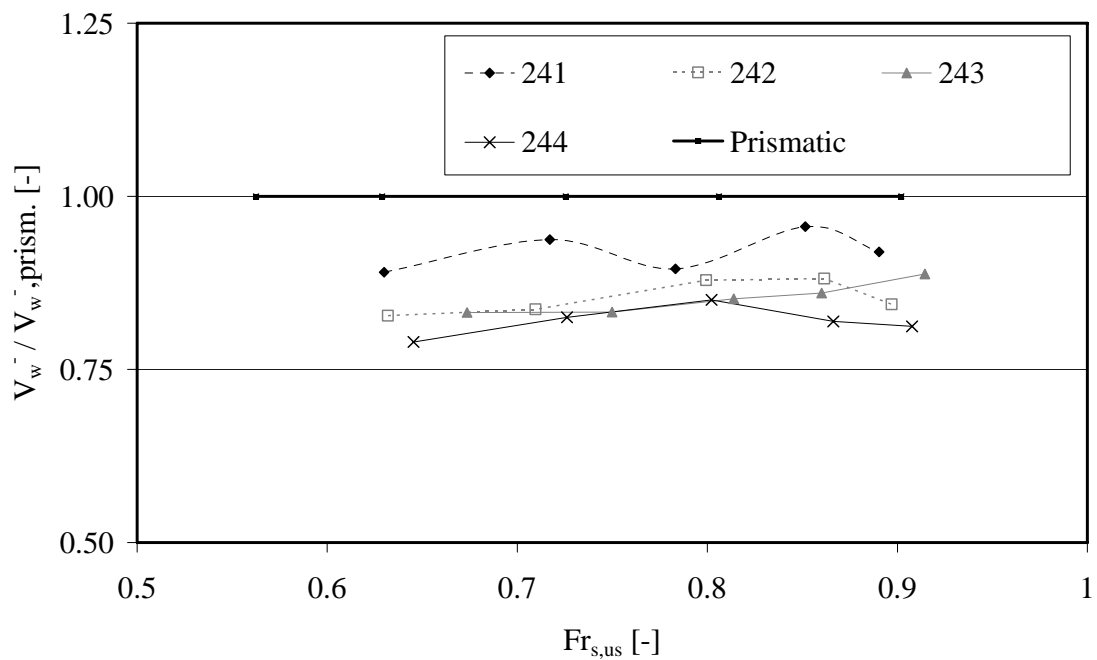


Fig-A5.34: Absolute wave celerity of the macro-rough configurations relative to the prismatic reference $V_w^- / V_{w,prism}^-$ as a function of the upstream surge Froude number ($x=0.42$ m). Configurations 241-244.

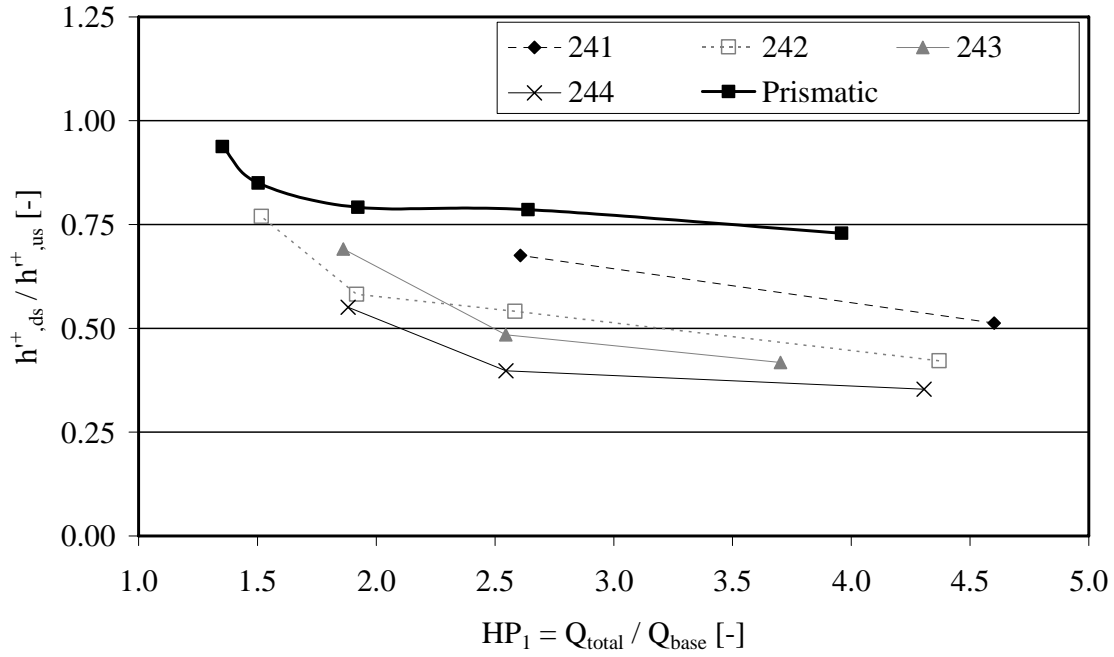


Fig-A5.35: Observed surge wave height ratio between the end and the beginning of the macro-rough reach h^+_{ds}/h^+_{us} (positive wave from upstream) as a function of the discharge ratio $HP_1 = Q_{total}/Q_b$. Configurations 241-244.

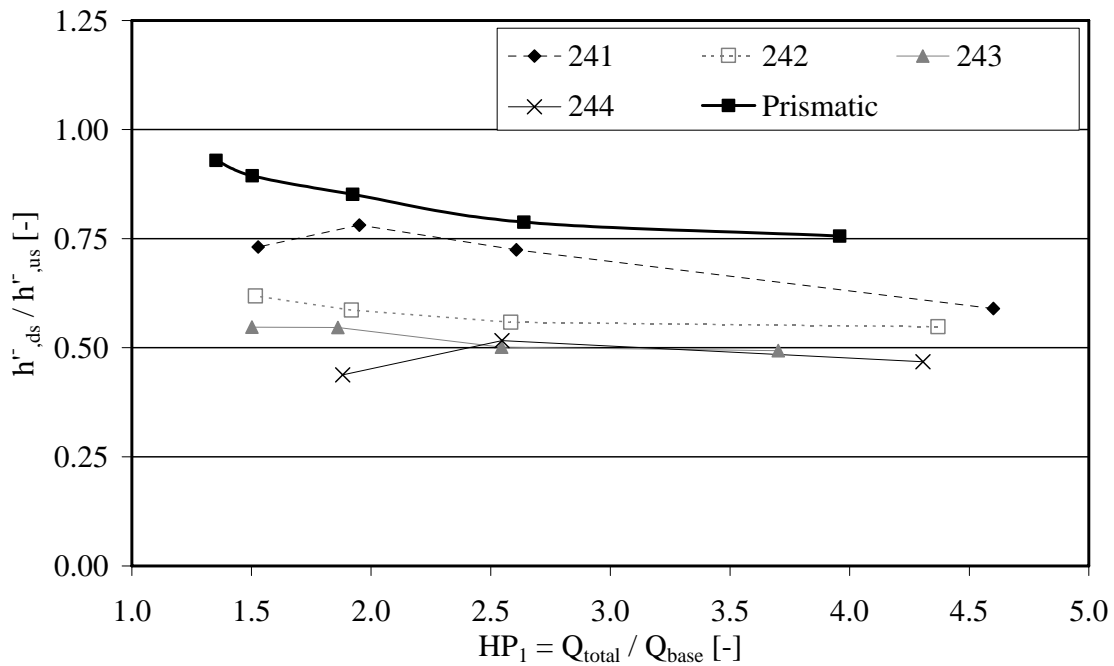


Fig-A5.36: Observed surge wave height ratio between the end and the beginning of the macro-rough reach h^-_{ds}/h^-_{us} (negative wave from upstream) as a function of $HP_1 = Q_{total}/Q_b$. Configurations 241-244.

A 5-1: Summarized test results for the unsteady flow tests: 411 to 414





 <p>Configuration 411 $L_b = 2.0 \text{ m}, L_c = 0.5 \text{ m}, \Delta B = 0.1 \text{ m}$</p>	 <p>Configuration 412 $L_b = 2.0 \text{ m}, L_c = 0.5 \text{ m}, \Delta B = 0.2 \text{ m}$</p>
 <p>Configuration 413 $L_b = 2.0 \text{ m}, L_c = 0.5 \text{ m}, \Delta B = 0.3 \text{ m}$</p>	 <p>Configuration 414 $L_b = 2.0 \text{ m}, L_c = 0.5 \text{ m}, \Delta B = 0.4 \text{ m}$</p>

Table: Characteristics of the surge wave experiments and numerical values of the attenuation parameter of the positive (b^+) and the negative (b^-) surge wave front.

Conf.	Scen.	Q_b	Q_{wave}	Q_{total}	HP_1	$Fr_{s.us}^+$	$Fr_{s.us}^-$	b^+	b^-
[-]	[-]	[L/s]	[L/s]	[L/s]	[-]	[-]	[-]	[-]	[-]
411	3	6.32	17.56	23.88	3.78	1.65	0.68	1.43	1.59
411	8	11.11	17.53	28.64	2.58	1.36	0.75	1.84	1.58
411	13	20.00	17.43	37.43	1.87	1.17	0.83	1.91	1.29
411	18	33.71	17.30	51.01	1.51	1.09	0.87	3.58	1.15
411	23	49.29	17.16	66.45	1.35	1.06	0.91	4.52	2.31
412	3	6.06	17.68	23.74	3.92	1.61	0.72	1.73	3.89
412	8	10.93	17.54	28.47	2.61	1.31	0.79	2.34	3.96
412	13	19.29	17.43	36.72	1.90	1.14	0.85	3.25	4.49
412	18	31.93	17.31	49.24	1.54	1.07	0.89	6.00	4.99
412	23	47.48	17.16	64.64	1.36	1.05	0.92	7.52	7.04
413	3	6.13	17.58	23.71	3.87	1.57	0.74	2.18	3.71
413	8	11.05	17.53	28.58	2.59	1.32	0.80	2.51	3.96
413	13	19.66	17.44	37.10	1.89	1.14	0.86	3.64	5.50
413	18	32.81	17.31	50.12	1.53	1.07	0.90	6.76	6.84
413	23	48.32	17.17	65.49	1.36	1.05	0.93	6.15	7.94
414	3	5.84	17.52	23.36	4.00	1.61	0.75	2.28	3.91
414	8	10.49	17.52	28.01	2.67	1.31	0.80	2.44	6.63
414	13	19.20	17.45	36.65	1.91	1.14	0.86	3.47	6.18
414	18	32.48	17.30	49.78	1.53	1.07	0.91	5.27	5.39
414	23	48.81	17.26	66.07	1.35	1.05	0.94	7.61	10.55

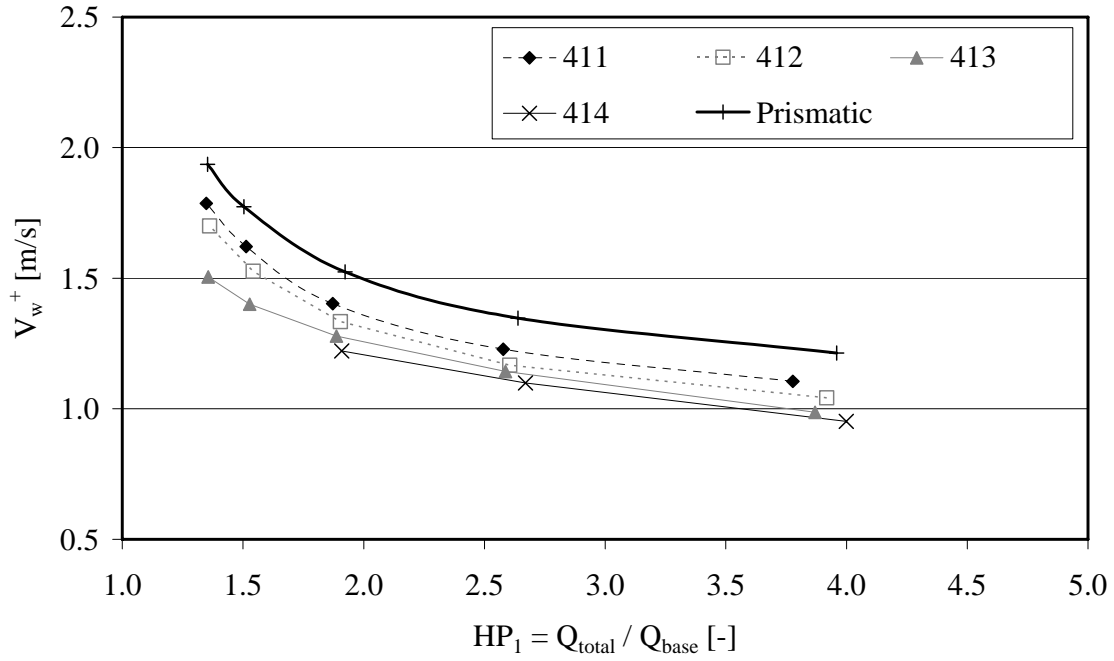


Fig-A5.37: Absolute wave celerity of the positive wave V_w^+ as a function of the discharge ratio $HP_1 = Q_{total} / Q_{base}$. Configurations 411-414.

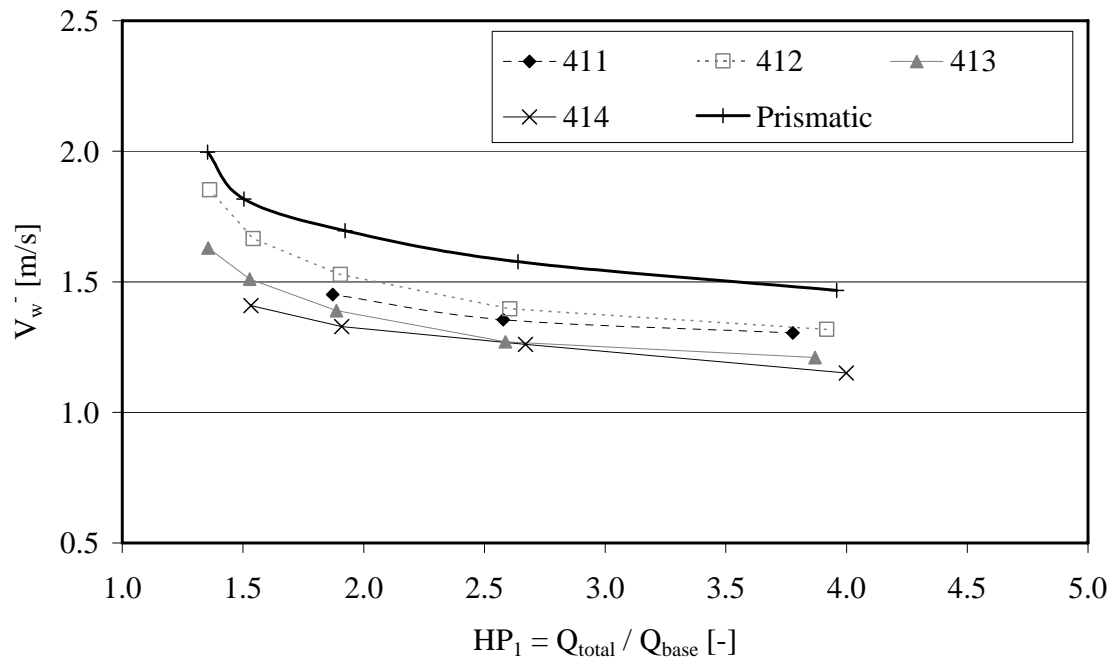


Fig-A5.38: Absolute wave celerity of the negative wave V_w^- as a function of the discharge ratio $HP_1 = Q_{total} / Q_{base}$. Configurations 411-414.

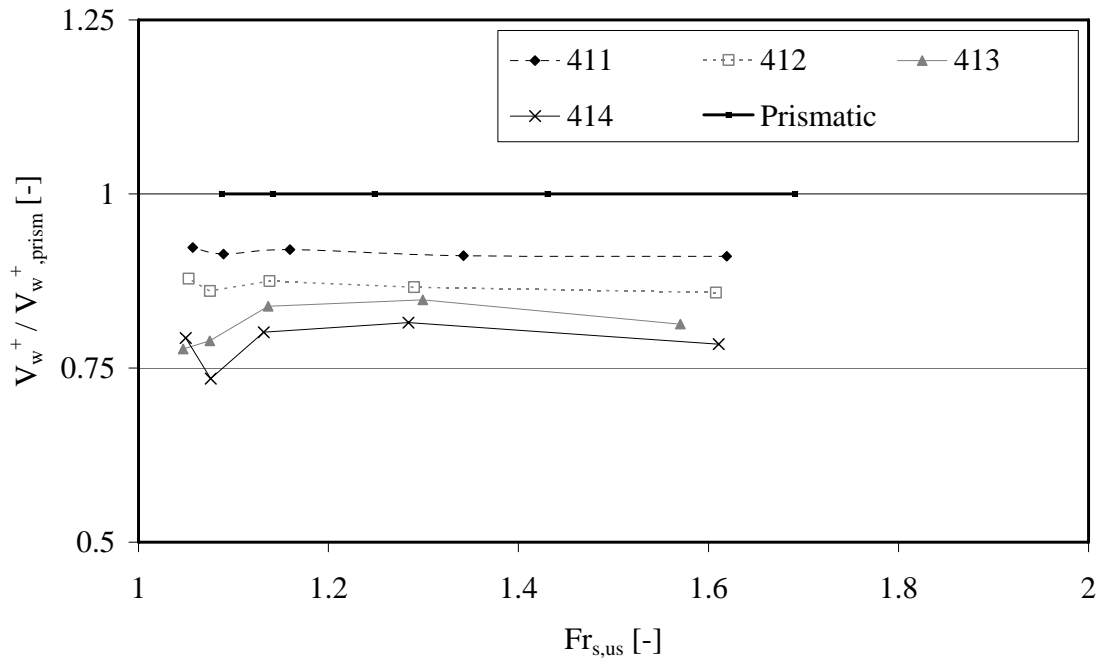


Fig-A5.39: Absolute wave celerity of the macro-rough configurations relative to the prismatic reference $V_w^+ / V_{w,prism}^+$ as a function of the upstream surge Froude number ($x=0.42$ m). Configurations 411-414.

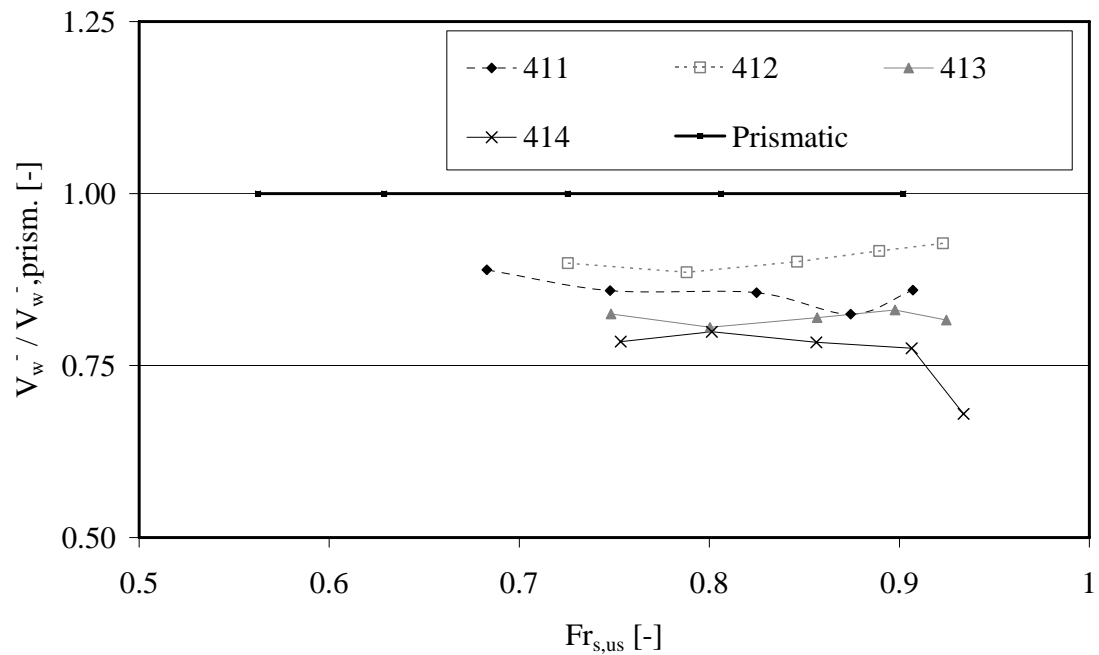


Fig-A5.40: Absolute wave celerity of the macro-rough configurations relative to the prismatic reference $V_w^- / V_{w,prism}^-$ as a function of the upstream surge Froude number ($x=0.42$ m). Configurations 411-414.

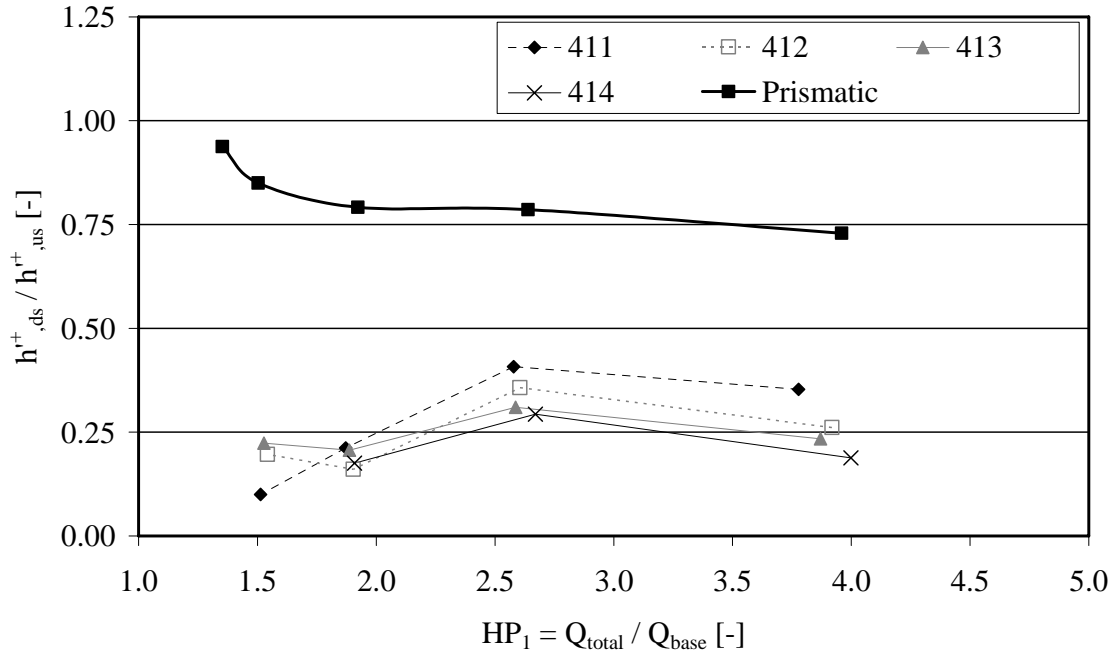


Fig-A5.41: Observed surge wave height ratio between the end and the beginning of the macro-rough reach h^+_{ds}/h^+_{us} (positive wave from upstream) as a function of the discharge ratio $HP_1 = Q_{total}/Q_b$. Configurations 411-414.

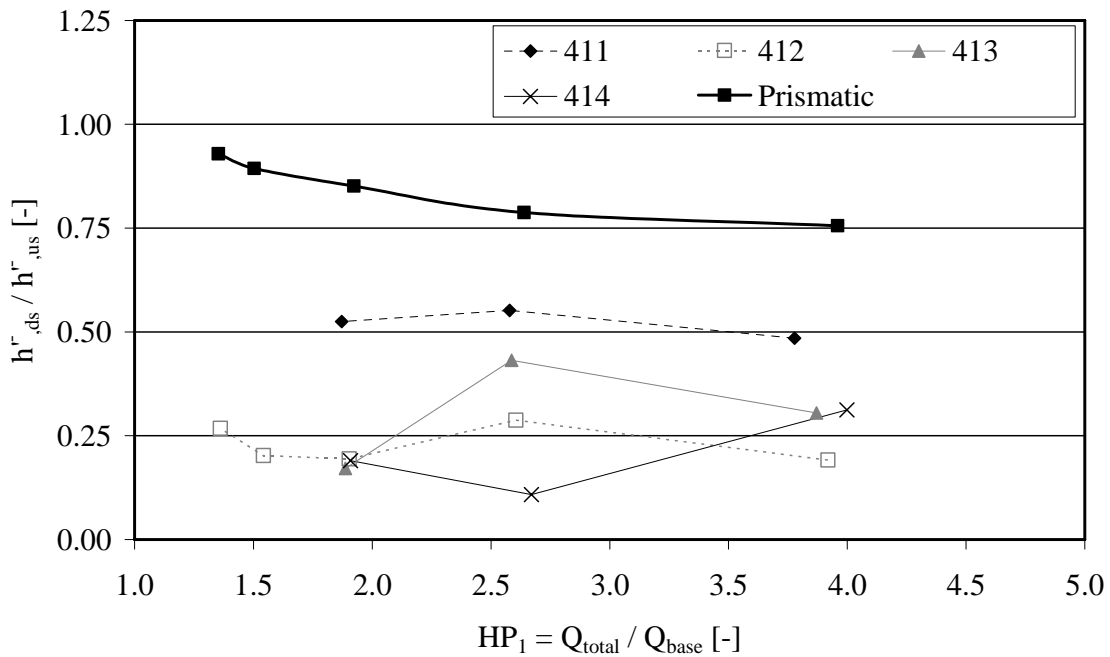


Fig-A5.42: Observed surge wave height ratio between the end and the beginning of the macro-rough reach h^-_{ds}/h^-_{us} (negative wave from upstream) as a function of $HP_1 = Q_{total}/Q_b$. Configurations 411-414.

A 5-1: Summarized test results for the unsteady flow tests: 421 to 424




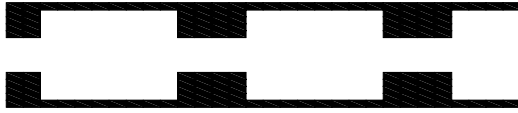
 <p>Configuration 421 $L_b = 1.0 \text{ m}, L_c = 1.0 \text{ m}, \Delta B = 0.1 \text{ m}$</p>	 <p>Configuration 422 $L_b = 1.0 \text{ m}, L_c = 1.0 \text{ m}, \Delta B = 0.2 \text{ m}$</p>
 <p>Configuration 423 $L_b = 1.0 \text{ m}, L_c = 1.0 \text{ m}, \Delta B = 0.3 \text{ m}$</p>	 <p>Configuration 424 $L_b = 1.0 \text{ m}, L_c = 1.0 \text{ m}, \Delta B = 0.4 \text{ m}$</p>

Table: Characteristics of the surge wave experiments and numerical values of the attenuation parameter of the positive (b^+) and the negative (b^-) surge wave front.

Conf.	Scen.	Q_b	Q_{wave}	Q_{total}	HP_1	$Fr_{s.us}^+$	$Fr_{s.us}^-$	b^+	b^-
[-]	[-]	[Us]	[Us]	[Us]	[-]	[-]	[-]	[-]	[-]
421	3	5.47	17.60	23.07	4.22	1.68	0.65	0.90	1.26
421	8	10.67	17.55	28.22	2.64	1.37	0.74	1.36	1.16
421	13	19.43	17.45	36.88	1.90	1.18	0.81	2.15	1.22
421	18	32.79	17.32	50.11	1.53	1.10	0.88	4.82	1.27
421	23	50.60	17.16	67.76	1.34	1.06	0.92	8.04	4.60
422	3	5.88	17.58	23.46	3.99	1.65	0.69	1.34	2.58
422	8	10.96	17.52	28.48	2.60	1.32	0.77	1.97	3.34
422	13	19.27	17.44	36.71	1.90	1.15	0.84	3.55	3.17
422	18	31.82	17.30	49.12	1.54	1.08	0.89	5.73	3.28
422	23	48.79	17.15	65.94	1.35	1.05	0.92	7.43	3.97
423	3	5.70	17.58	23.28	4.08	1.65	0.71	1.58	3.35
423	8	11.34	17.51	28.85	2.54	1.32	0.79	1.58	3.07
423	13	19.07	17.43	36.50	1.91	1.15	0.85	3.14	4.05
423	18	32.34	17.30	49.64	1.54	1.08	0.90	5.49	3.59
423	23	50.01	17.03	67.04	1.34	1.05	0.93	10.80	4.95
424	3	6.45	17.57	24.02	3.72	1.56	0.74	1.59	4.83
424	8	11.04	17.52	28.56	2.59	1.31	0.80	1.73	5.06
424	13	18.70	17.44	36.14	1.93	1.15	0.84	4.10	6.02
424	18	32.86	17.30	50.16	1.53	1.07	0.90	5.40	4.66
424	23	47.85	17.16	65.01	1.36	1.04	0.92	6.06	4.94

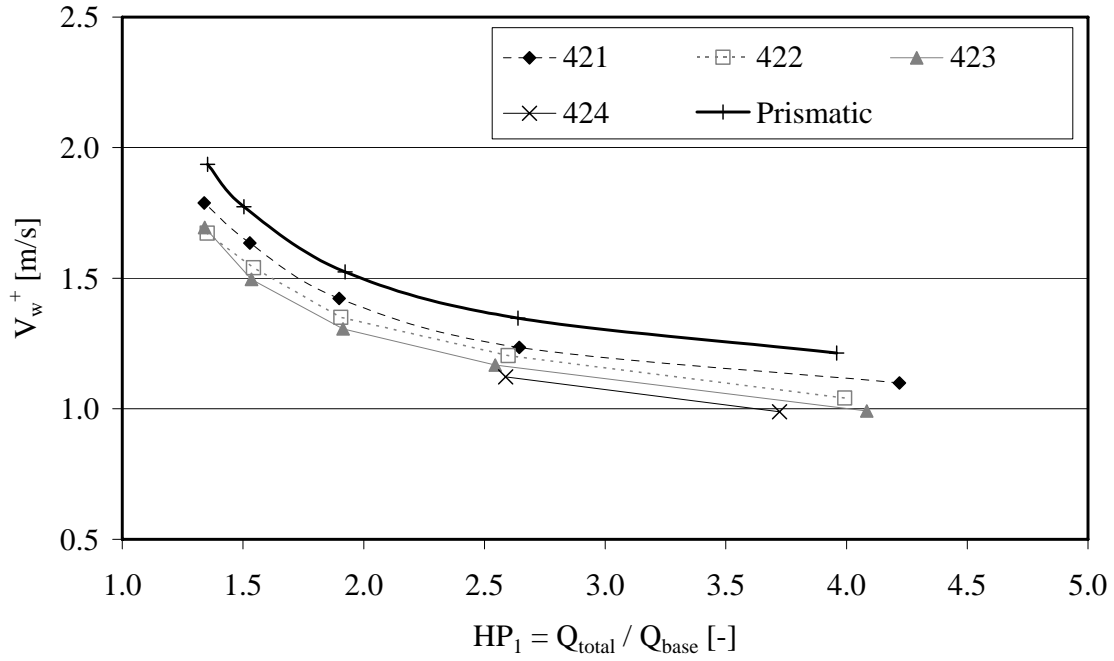


Fig-A5.43: Absolute wave celerity of the positive wave V_w^+ as a function of the discharge ratio $HP_1 = Q_{total} / Q_{base}$. Configurations 421-424.

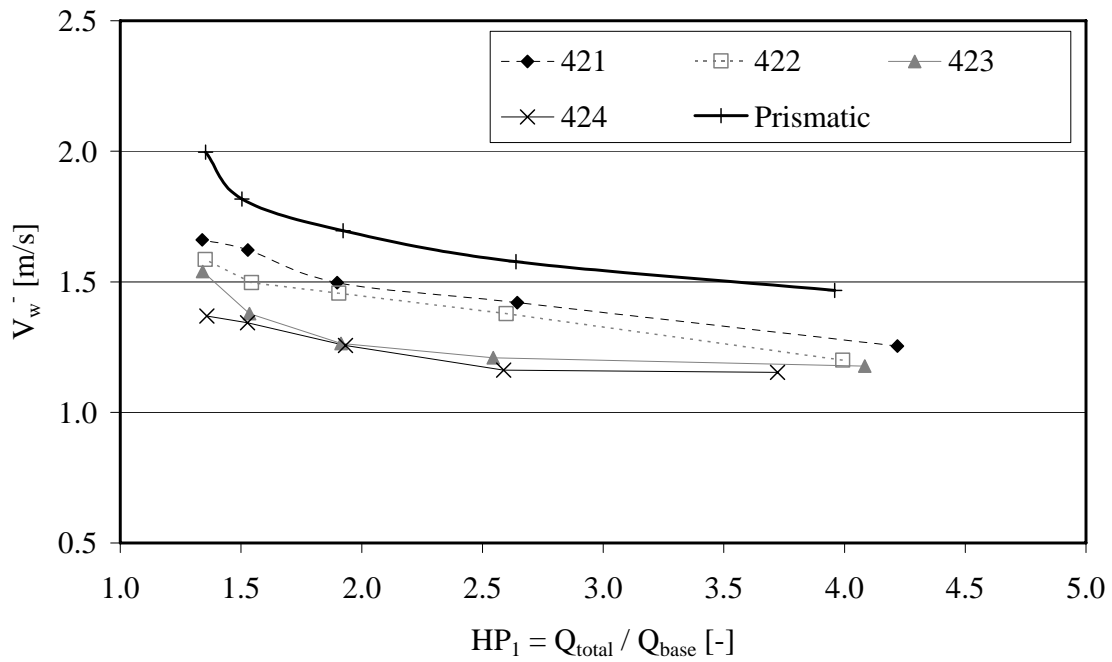


Fig-A5.44: Absolute wave celerity of the negative wave V_w^- as a function of the discharge ratio $HP_1 = Q_{total} / Q_{base}$. Configurations 421-424.

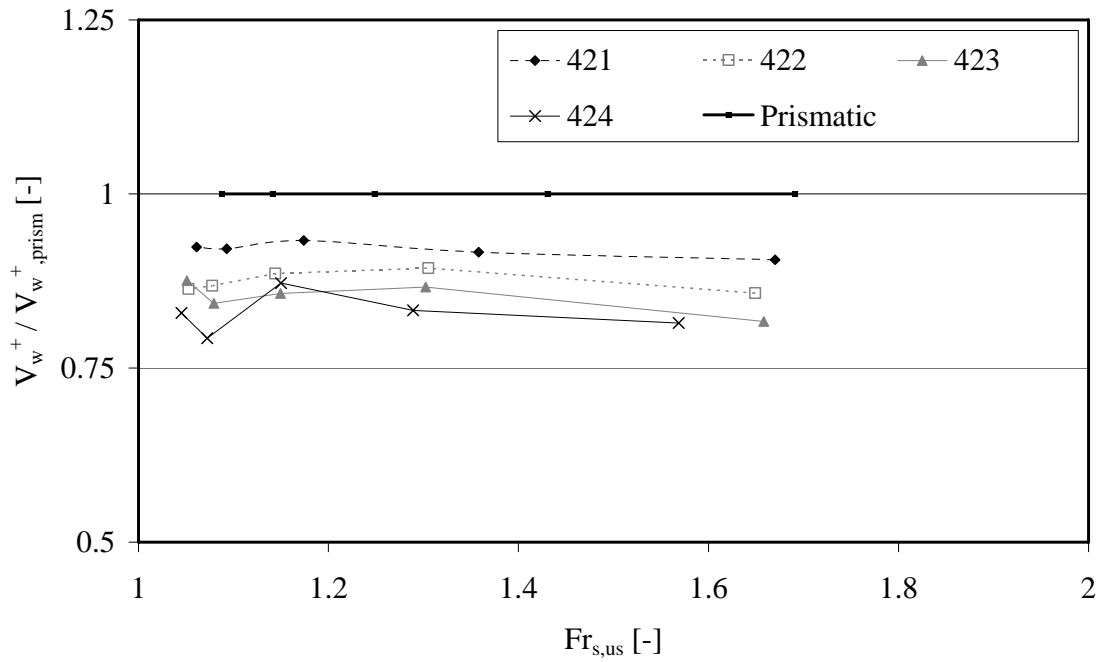


Fig-A5.45: Absolute wave celerity of the macro-rough configurations relative to the prismatic reference $V_w^+ / V_{w,prism}^+$ as a function of the upstream surge Froude number ($x=0.42$ m). Configurations 421-424.

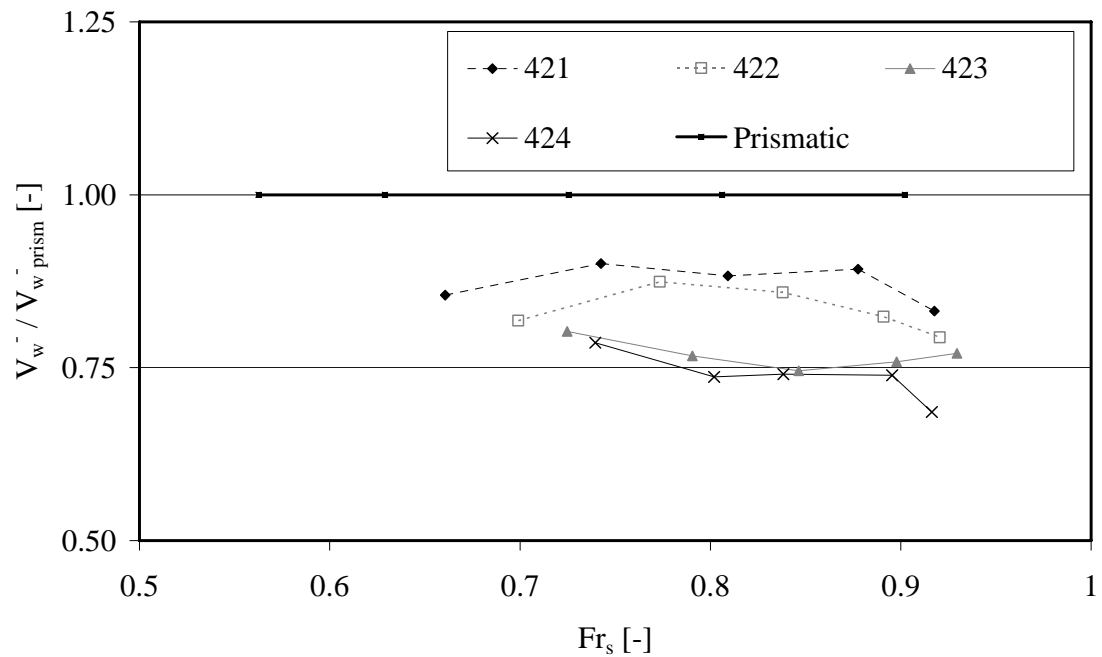


Fig-A5.46: Absolute wave celerity of the macro-rough configurations relative to the prismatic reference $V_w^- / V_{w,prism}^-$ as a function of the upstream surge Froude number ($x=0.42$ m). Configurations 421-424.

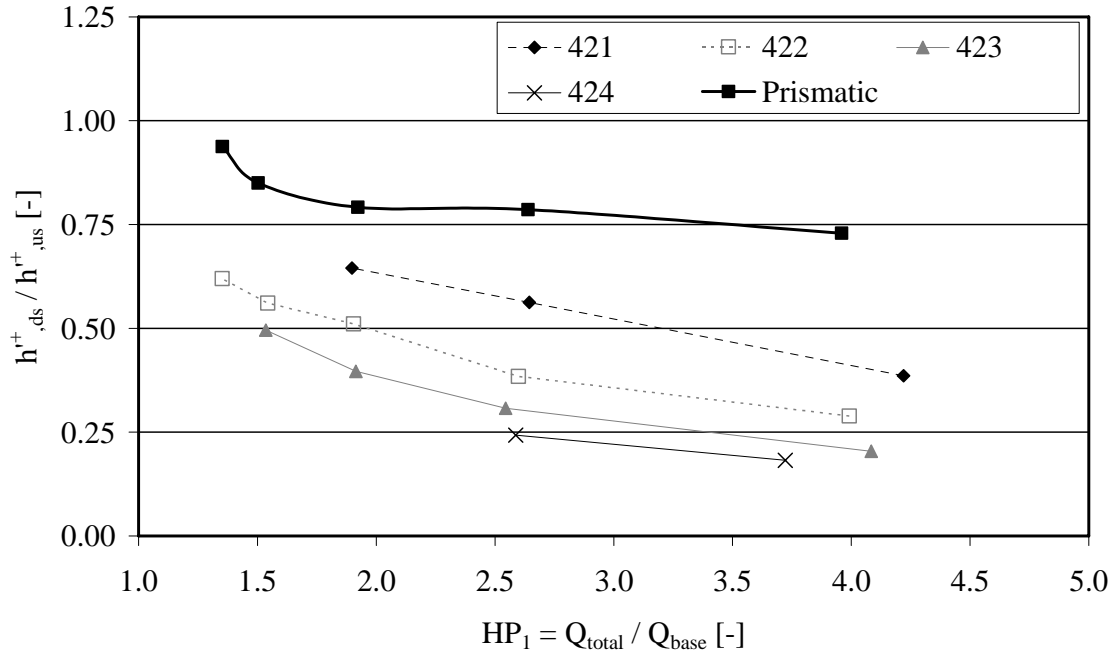


Fig-A5.47: Observed surge wave height ratio between the end and the beginning of the macro-rough reach h^+_{ds}/h^+_{us} (positive wave from upstream) as a function of the discharge ratio $HP_1 = Q_{total}/Q_b$. Configurations 421-424.

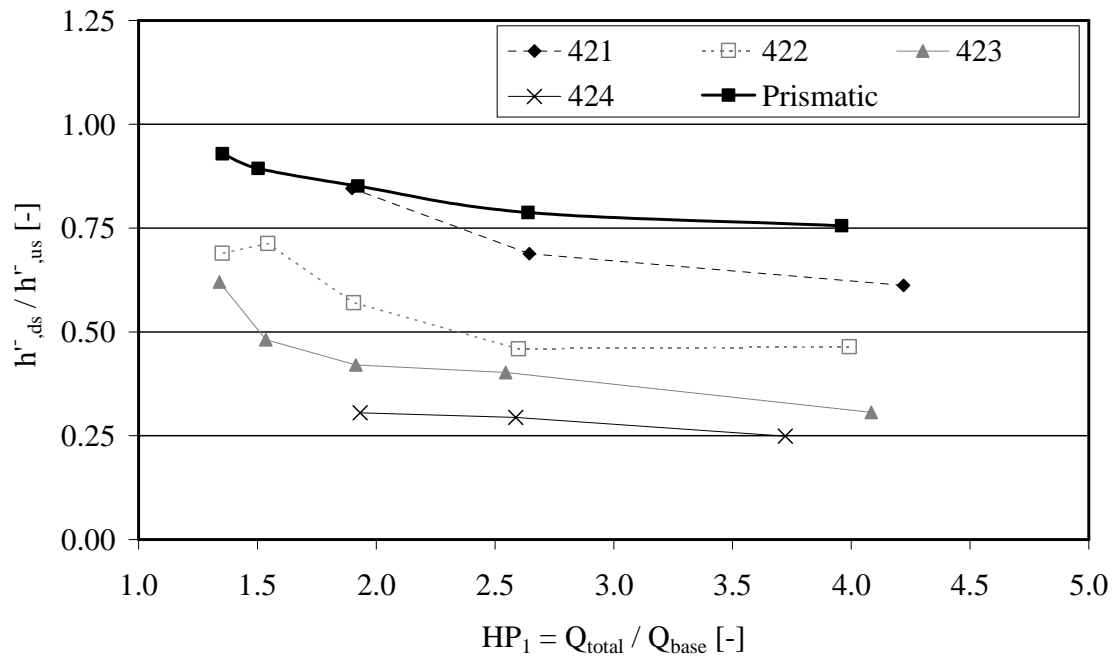


Fig-A5.48: Observed surge wave height ratio between the end and the beginning of the macro-rough reach h^-_{ds}/h^-_{us} (negative wave from upstream) as a function of $HP_1 = Q_{total}/Q_b$. Configurations 421-424.

A 5-1: Summarized test results for the unsteady flow tests: 441 to 444





 <p>Configuration 441 $L_b = 2.0 \text{ m}, L_c = 2.0 \text{ m}, \Delta B = 0.1 \text{ m}$</p>	 <p>Configuration 442 $L_b = 2.0 \text{ m}, L_c = 2.0 \text{ m}, \Delta B = 0.2 \text{ m}$</p>
 <p>Configuration 443 $L_b = 2.0 \text{ m}, L_c = 2.0 \text{ m}, \Delta B = 0.3 \text{ m}$</p>	 <p>Configuration 444 $L_b = 2.0 \text{ m}, L_c = 2.0 \text{ m}, \Delta B = 0.4 \text{ m}$</p>

Table: Characteristics of the surge wave experiments and numerical values of the attenuation parameter of the positive (b^+) and the negative (b^-) surge wave front.

Conf.	Scen.	Q_b	Q_{wave}	Q_{total}	HP_1	$Fr_{s,us}^+$	$Fr_{s,us}^-$	b^+	b^-
[-]	[-]	[U/s]	[U/s]	[U/s]	[-]	[-]	[-]	[-]	[-]
441	3	6.96	17.56	24.52	3.52	1.60	0.67	0.48	1.40
441	8	11.89	17.39	29.28	2.46	1.32	0.73	1.09	1.60
441	13	20.66	17.41	38.07	1.84	1.17	0.80	1.94	2.28
441	18	34.15	17.27	51.42	1.51	1.10	0.87	2.37	3.02
441	23	49.16	17.15	66.31	1.35	1.06	0.91	2.92	4.72
442	3	6.29	17.58	23.87	3.79	1.59	0.69	0.57	2.92
442	8	11.46	17.51	28.97	2.53	1.31	0.76	1.63	3.16
442	13	19.61	17.40	37.01	1.89	1.15	0.82	2.71	3.76
442	18	32.48	17.29	49.77	1.53	1.09	0.88	4.49	4.73
442	23	47.68	17.15	64.83	1.36	1.06	0.91	4.84	3.76
443	3	5.89	17.59	23.48	3.98	1.62	0.72	0.79	3.38
443	8	11.28	17.52	28.80	2.55	1.32	0.77	1.75	2.91
443	13	18.60	17.44	36.04	1.94	1.17	0.84	3.07	4.96
443	18	33.13	17.30	50.43	1.52	1.09	0.89	5.44	5.73
443	23	48.30	17.16	65.46	1.36	1.06	0.92	5.85	5.59
444	3	5.61	17.59	23.20	4.14	1.62	0.72	1.09	2.54
444	8	11.36	17.50	28.86	2.54	1.28	0.80	2.24	3.32
444	13	19.14	17.41	36.55	1.91	1.15	0.83	2.75	4.57
444	18	32.78	17.18	49.96	1.52	1.08	0.88	3.90	4.35
444	23	48.01	17.16	65.17	1.36	1.06	0.93	7.26	3.39

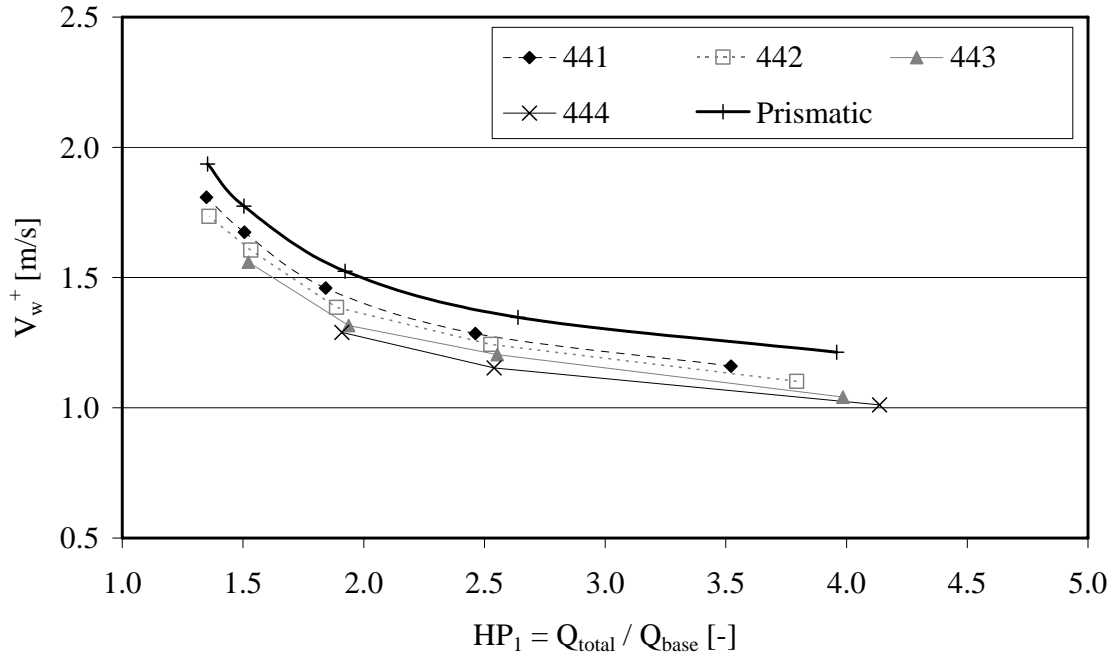


Fig-A5.49: Absolute wave celerity of the positive wave V_w^+ as a function of the discharge ratio $HP_1 = Q_{total} / Q_{base}$. Configurations 441-444.

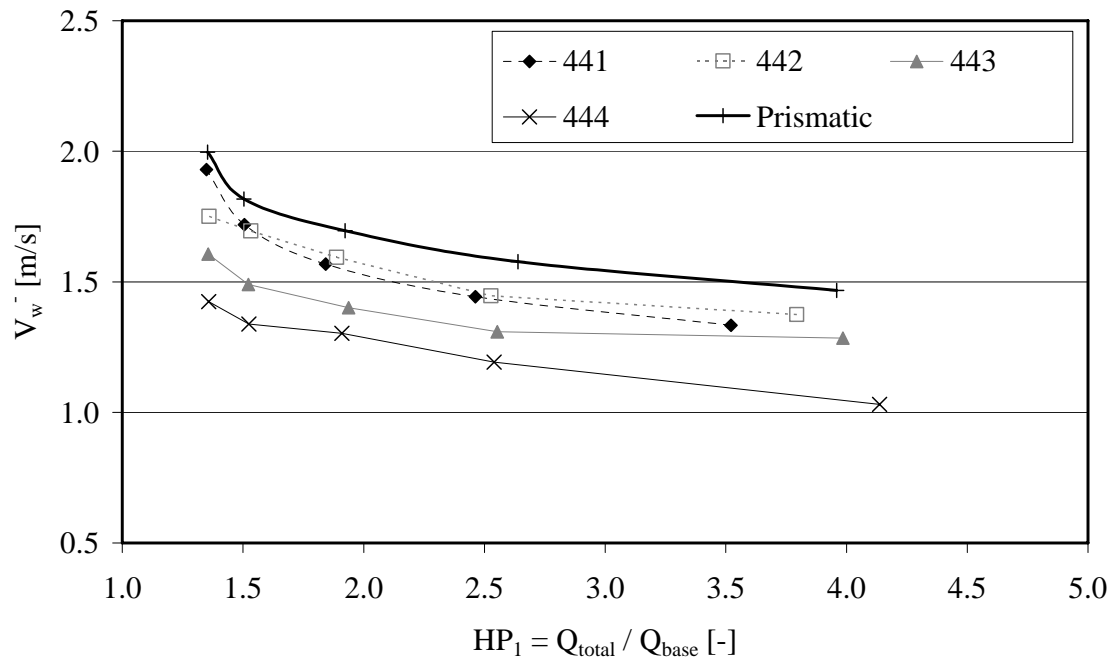


Fig-A5.50: Absolute wave celerity of the negative wave V_w^- as a function of the discharge ratio $HP_1 = Q_{total} / Q_{base}$. Configurations 441-444.

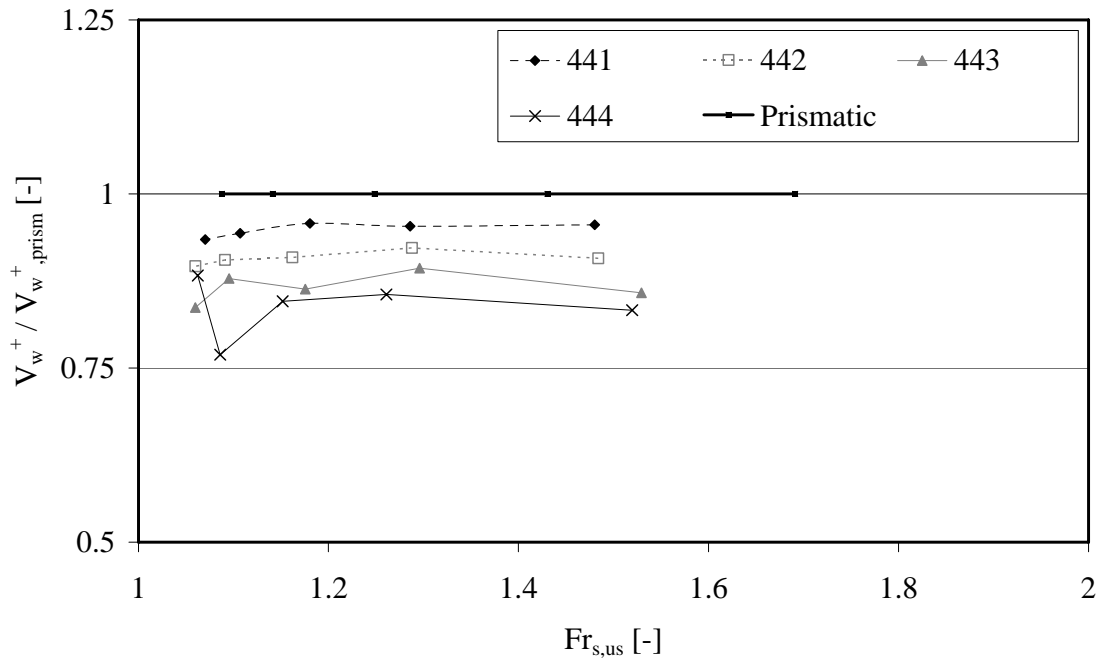


Fig-A5.51: Absolute wave celerity of the macro-rough configurations relative to the prismatic reference $V_w^+ / V_{w,prism}^+$ as a function of the upstream surge Froude number ($x=0.42$ m). Configurations 441-444.

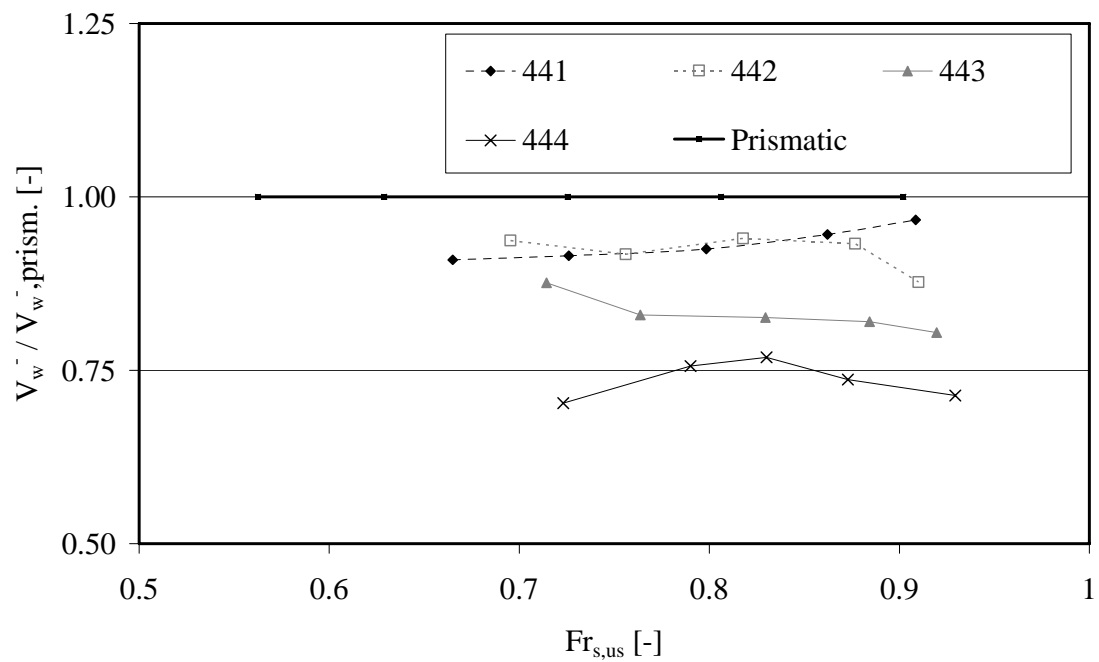


Fig-A5.52: Absolute wave celerity of the macro-rough configurations relative to the prismatic reference $V_w^- / V_{w,prism}^-$ as a function of the upstream surge Froude number ($x=0.42$ m). Configurations 441-444.

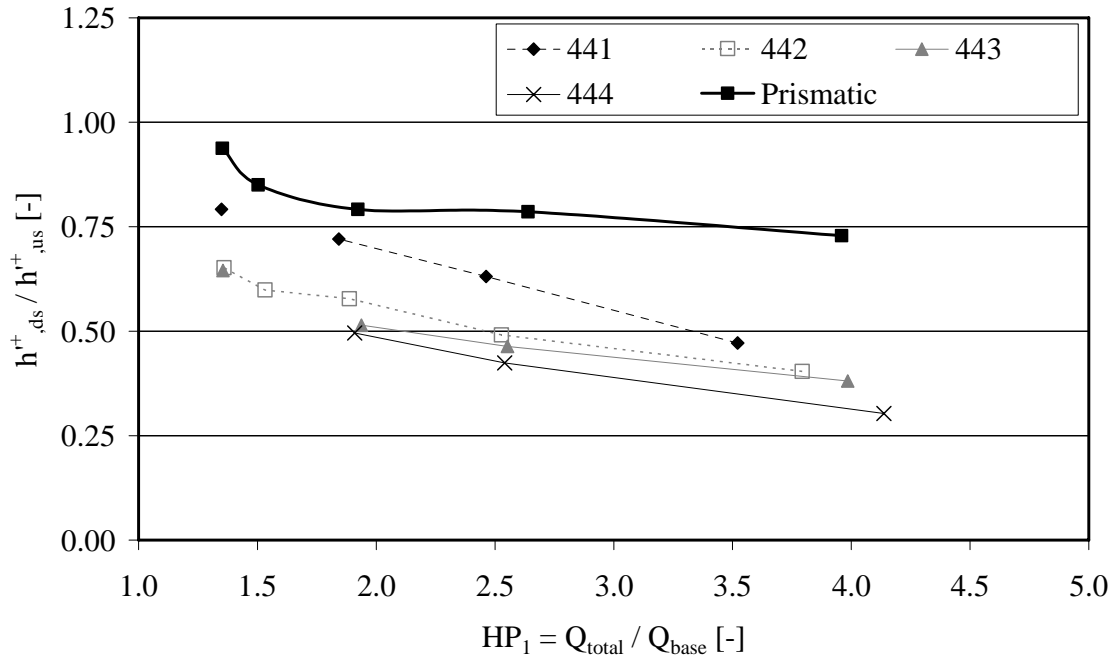


Fig-A5.53: Observed surge wave height ratio between the end and the beginning of the macro-rough reach h^{r}_{ds}/h^{r}_{us} (positive wave from upstream) as a function of the discharge ratio $HP_1 = Q_{total}/Q_b$. Configurations 441-444.

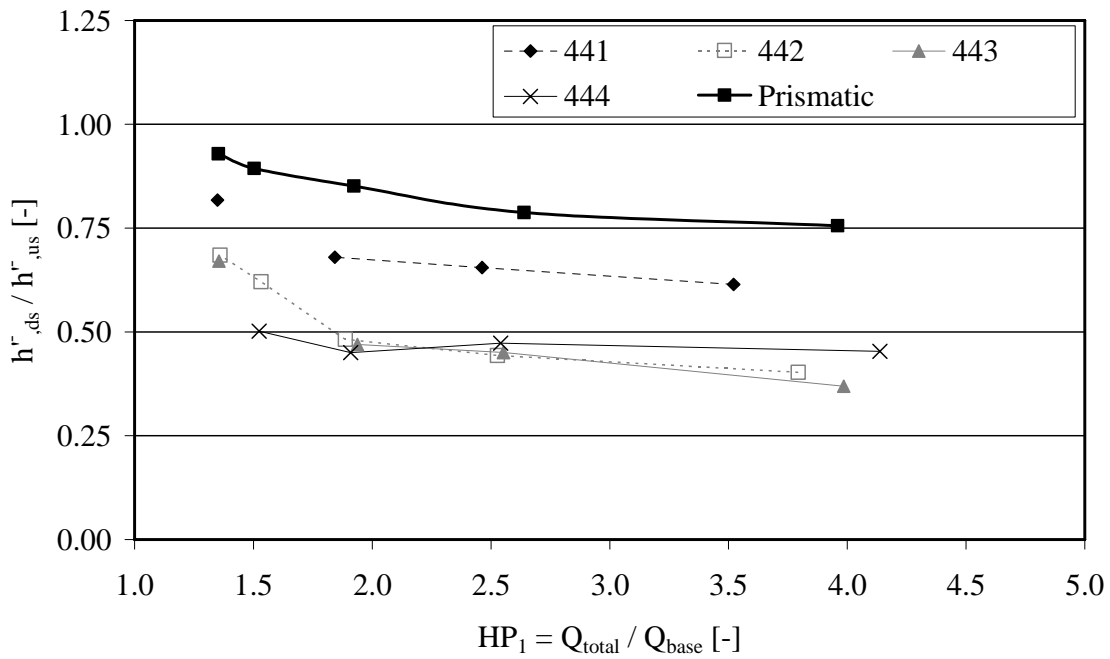


Fig-A5.54: Observed surge wave height ratio between the end and the beginning of the macro-rough reach h^{r}_{ds}/h^{r}_{us} (negative wave from upstream) as a function of $HP_1 = Q_{total}/Q_b$. Configurations 441-444.

A 5-2: Conditions at the wave front for all tests (part 1)

	Sc 1	Sc 2	Sc 3	Sc 4	Sc 5	Sc 6	Sc 7	Sc 8	Sc 9	Sc 10	Sc 11	Sc 12	Sc 13	Sc 14
Prismatic			d	d	d				d	d				d
141			d											
121														
241														
142				d	d					d				
111					d					d				
221														
441			(d)											
143														
122					d					d				
211														
242				(d)	d									
421			(d)											
144					d					d				
411														
123														
243														
112					(d)									
222														
442				(d)	d					d				
124					d					d				
212														
244					(d)									
422					(d)									
113														
223														
443														
412					(d)									
213														
423														
114														
224														
444														
413														
214														
424														
414														

	tested scenario, but no undulations or secondary waves
	secondary waves clearly visible
	secondary waves probable
d	Breaking
(d)	Breaking probable

Fig-A5.55: Observed conditions at the wavefront for all geometrical configurations and scenarios. The configurations are ordered following increasing additional surface.

A 5-2: Conditions at the wave front for all tests (part 2)

	Sc 15	Sc 16	Sc 17	Sc 18	Sc 19	Sc 20	Sc 21	Sc 22	Sc 23	Sc 24	Sc 25	Sc 26	Sc 27	Sc 28	Sc 29	Sc 30
Prismatic	d					d										
141																
121																
241																
142																
111																
221																
441																
143																
122																
211																
242																
421																
144																
411																
123																
243																
112																
222																
442																
124																
212																
244																
422																
113																
223																
443																
412																
213																
423																
114																
224																
444																
413																
214																
424																
414																

	tested scenario, but no undulations or secondary waves
	secondary waves clearly visible
	secondary waves probable
d	Breaking
(d)	Breaking probable

Fig-A5.56: Observed conditions at the wavefront for all geometrical configurations and scenarios. The configurations are ordered following increasing additional surface.

CURRICULUM VITAE

Tobias MEILE

Chemin du Bochet 15, CH-1025 St-Sulpice (VD)

Tel : +41 79 642 26 14

tobias.meile@epfl.ch

PERSONAL DATA

Born on October 19, 1976

unmarried, Swiss nationality

EDUCATION

- since 2002 Ph.D. research at the Laboratory of Hydraulic Constructions LCH-EPFL.
1996 – 2002 Civil Engineering studies at the Ecole Polytechnique Fédérale de Lausanne (EPFL). Diploma project entitled: *Prévision à court terme des débits de fonte des glaciers alpines à l'aide d'un réseau de neurones artificiels*

PROFESSIONAL WORK EXPERIENCE

- since 2002 Laboratory of Hydraulic Constructions – EPFL: Research assistant.
1998/1999 Practical work at H. Bachmann AG, Aadorf (building contractor) and at the administration of the Canton AR (Civil engineering department).

SELECTED ENGINEERING PROJECTS

- since 2002 *Kraftwerk Spullersee – Anpassung der Hochwasserentlastung Hydraulische Modellversuche*, project engineer
La Sionne dans la traversée de Sion – Etude sur modèles physique et numérique de l'aménagement de la Sionne à la place des Tannières, project engineer
L'aménagement hydroélectrique sur l'Avançon à Bex – Note de calcul, project engineer
Hochwasserschutzprojekt der Gamsa in Gamsen (Brig-Glis) - Hydraulische Modellversuche, project engineer
Station Lausanne-Flon – Correction du Flon : Comportement hydraulique de la proposition GIT-LEB, project engineer
Kraftwerksbedingter Schwall und Sunk – eine Standortbestimmung, study in collaboration with VAW-EPFZ

PUBLICATIONS

- Meile T., Bodenmann M., Schleiss A., Boillat J.-L. (2004), **Umsetzung des Hochwasserschutzkonzeptes der Gemeinde Brig - Glis im Kanton Wallis**, *Internationales Symposium INTERPRAEVENT 2004 – Riva/Trient*, Themenkreis VII, pp. 219-230.
- Baumann P., Meile T. (2004), **Makrozoobenthos und Hydraulik in ausgewählten Querprofilen der Rhone**, *Wasser Energie Luft*, 11/12 (2004), pp. 320-325.
- Meile T., Schleiss A., Boillat J.-L. (2005), **Entwicklung des Abflussregimes der Rhone seit dem Beginn des 20. Jahrhundert**, *Wasser Energie Luft*, 5/6 (2005) pp. 133-142.
- Meile T., Schleiss A., Bodenmann M., Boillat J.-L., Jaeggi M. (2005), **Hochwasserschutzmassnahmen an der Gamsa mit eingegrabenen Betonprismen**, *Wasser Energie Luft*, 3/4 (2005) pp. 59-66.
- Meile T., Dubois J., Boillat J.-L., Amberg F. (2005), **Optimization by physical and numerical modelling of the spillway for the Spullersee dam rehabilitation project**, *Proceedings of Hydro 2005: Policy into Practice*, 17-20 October, Villach, Austria, 8.08, pp. 1-8, 2005.
- Meile T., Fette M., Baumann P. (2005), **Synthesebericht Schwall/Sunk**, *Publikation des Rhone-Thur Projektes*, September 2005.
- Meile T., Boillat J.-L., Schleiss A.J. (2006), **Influence of dams and reservoirs on the flow regime of the Upper-Rhone-River**, *Proceeding of the Vingt Deuxième Congrès des Grands Barrages*, Barcelone, pp 449-465.
- Meile T. (2006), **Schwall und Sunk in Fliessgewässern**, *Eawag News*, 61d.
- Meile T., Boillat J.-L., Dubois J., Schleiss A.J. (2006), **Experimental study on steady flow in a channel with macro-roughness at the side walls**, *Proceedings International Conference on Fluvial Hydraulics, River Flow 2006*, Lisbon, Portugal, pp 1059-1068.
- Meile T., Boillat J.-L., Dubois J., Schleiss A.J. (2007), **Oscillations in a channel with rectangular widenings at the side wall**, *Proceedings XXXII IAHR Congress*, Abstracts Volume 1, Venice, Italy, 1-7 July: p 700. 2007 (full record on CD).
- Meile T., De Cesare G., Blanckaert K., Schleiss A. (2007) **Improvement of Acoustic Doppler velocimetry in steady and unsteady turbulent open-channel flows by means of seeding with hydrogen bubbles**, *Flow Measurement and Instrumentation* (accepted for publication).

HONORS AND FLOWSHIPS

- 2004 Best Poster Award of Ph.D. Poster Exhibition at EPFL.
- 2006 Student Paper Award of the 5th ISUD conference.

LANGUAGE SKILLS

- English: fluent, study and research language,
- French: fluent in speaking, good in writing
- German: mother tongue